

THEORY, FIELD MEASUREMENTS, AND LABORATORY EXPERIMENTS
CONCERNING THE CLOUD CONDENSATION NUCLEUS PROPERTIES OF
ORGANIC AND/OR INSOLUBLE AEROSOL COMPONENTS

Thesis by

Tracey Alayne Rissman

In Partial Fulfillment of the Requirements
for the Degree of

Doctor of Philosophy

California Institute of Technology

Pasadena, California

2006

(Defended May 18, 2006)

© 2006

Tracey Alayne Rissman

All Rights Reserved

ACKNOWLEDGEMENTS

This work is dedicated to my Papa, Elmer D. Hale, who passed away while I was at Caltech. He was one of my biggest supporters and role models, and I love and miss him dearly.

I'd especially like to thank my advisors, John H. Seinfeld and Rick C. Flagan. With all the horror stories that I hear about other advisors, I am thankful that I had the unfailing support of John and Rick. I'd like to thank them for trusting in me and helping me to become a more independent scientist and thinker. I only hope that I have made them proud.

None of this would have been possible without my family, who has stood by me through everything. I always knew that they would be there for me, even if I failed. Thank you to my Mom and Dad and my Dad and Mush for always being there and supporting me throughout everything and always encouraging me to do my best. I also thank my Nanny and Grandma Rissman for being strong role models who have been central to my education and upbringing. Then, of course, there are my best friends, my siblings. Thank you Scott, Laura, Kristen, and Christina for making me laugh ... constantly. I'm so proud of all of you.

I was very privileged to work with some great people. Thank you to Tim VanReken, Bill Conant, and Thanos Nenes, who taught me everything I know and were friends, as well as mentors. Also, thanks to past and present group members who have helped me in ways too numerous to list here: Jay Wang, Fred Brechtel, Jose Jimenez, Harmony Gates, Andrea Clements, Shane Murphy, Daven Henze, Anne Chen, Julia Lu, Song Gao, Amir Hakami, Serena Chung, Brian Mader, and Melita Keyword. Thank you to my friends for helping me to laugh my way through Caltech: Roya Bahreini, Jesse Kroll, Jason Surratt, Armin Sorooshian, Kim, Ryan, and Erin Conant, Dean Holunga, Anita Lee, and Paul Skerritt.

I must thank the CIRPAS team because they are some of my favorite people, and the field missions wouldn't be successful (or fun) without them: Haf Jonsson, Nava and Vino Roy, Roy Woods, Mike Hubbell, Gintas Buzorius, Paul Megison, Regie Burch, Sara Moore, Bob Bluth, Bob Rogell, Richard Boyd, Dennis Hamaker, and Rob Taylor-Shaw. Also, thanks to Ann Hilgenfeldt, Yvette Grant, Kathy Bubash, Fran Matzen, Linda Scott, Marty Gould, and Mike Vondrus for their invaluable help and support.

A very special thank you goes to Tomtor Varutbangkul, who has been with me for this entire journey and has made it very interesting. It didn't matter if we were freaking out, stressing out, or just plain hanging out – it was nice to always have someone there who cared and understood.

The past few months have been very stressful, but have been extremely fun because of a few special people who have been incredibly supportive, as well as downright hilarious: Adam Olsen, Sally Ng, Philip Stier, and Marco Seidel. Thanks guys.

ABSTRACT

Predicting how the future climate of Earth will change as a result of increasing human emissions is one of the greatest problems facing science today. The earth's climate is the result of a delicate balance between incoming and outgoing radiation. Anthropogenic emissions of aerosol particles into the atmosphere have the potential to affect the earth's climate in significant ways through both direct and indirect effects on the earth's radiative balance. One of the largest uncertainties in aerosol radiative forcing is associated with the relationship between atmospheric aerosols and cloud formation, properties, and lifetime. Clouds form by water condensing on small particles (aerosols) in the air (referred to as cloud condensation nuclei, or CCN), and how the increasing levels of atmospheric particles will affect Earth's clouds and its hydrologic cycle represents one of the key problems in the science of climate. Through theoretical, field, and laboratory investigations, the results presented here reinforce the importance of atmospheric aerosol chemical composition in determining the ability of an aerosol particle to act as a CCN. A study that incorporates surface tension and limited solubility effects, especially of organic compounds, in parameterizations of cloud droplet activation indicate that these chemical effects can rival those of the meteorological environment. An inverse CCN/aerosol closure study of field measurements indicates that assumptions of simple chemistry and mixing state in the interpretation and analysis of field cloud condensation nuclei (CCN) measurements may not necessarily be sufficient and/or realistic, depending heavily on the location of the field study. Properties of organic compounds, such as functional groups, extent of dissociation, and solubility were found to influence the CCN activity of the compounds in laboratory experiments with pure

organic aerosols. However, the importance of careful planning of laboratory experiments, in consideration of the properties of the organic compounds, was reinforced and results were carefully interpreted to avoid experimental bias in the conclusions.

TABLE OF CONTENTS

Acknowledgements	iii
Abstract	v
Table of Contents	vii
List of Tables	x
List of Figures	xi
Chapter 1: Introduction.....	1-1
1.1 Background and Motivation.....	1-2
1.2 Cloud Activation Theory (Chapter 2).....	1-3
1.3 CCN Field Measurements (Chapter 3)	1-5
1.4 Laboratory CCN Studies of Pure Organic Compounds (Chapter 4)	1-7
1.5 References.....	1-9
Chapter 2: Chemical Amplification (or Dampening) of the Twomey Effect: Conditions Derived from Droplet Activation Theory	2-1
2.1 Abstract.....	2-2
2.2 Introduction.....	2-3
2.3 Analytical Parameterizations of Aerosol Activation.....	2-4
2.3.1 Köhler Theory	2-5
2.3.2 Simplifications of the Full Köhler Expression	2-9
2.3.3 Single-Mode Parameterization Modification	2-10
2.3.4 Analysis of A5d, A5m, and A5c Parameter Simplifications	2-14
2.3.5 The Modified Parameterization (Single-Mode)	2-16
2.3.6 Comparison to a Numerical Parcel Model	2-17
2.3.7 Extension of EAGR Parameterization to Multimodal Aerosol Population	2-19
2.4 Sensitivity Analysis	2-21
2.5 Conclusions.....	2-37
2.6 References.....	2-41
Chapter 3: Characterization of Ambient Aerosol from Measurements of Cloud Condensation Nuclei During the 2003 Atmospheric Radiation Measurement Aerosol Intensive Observational Period at the Southern Great Plains Site in Oklahoma	3-1
3.1 Abstract.....	3-2
3.2 Introduction.....	3-3
3.3 ARM Aerosol IOP.....	3-5
3.4 Instrument Description.....	3-8
3.4.1 Twin Otter Inlet System	3-8
3.4.2 CCN Instrument (CCNC3).....	3-9
3.4.3 Dual Automatic Classified Aerosol Detectors (DACAD)	3-14

3.4.4	Tandem Differential Mobility Analyzer (DMA/TDMA).....	3-16
3.4.5	PILS-IC, TEOM, and Integrating Nephelometer	3-17
3.5	Data Trends During the ARM Aerosol IOP	3-18
3.5.1	Particle Composition (PILS-IC, TEOM, and DMA/TDMA) and Aerosol Mixing State (DMA/TDMA)	3-19
3.5.2	Aerosol Size Distribution (DACAD—Airborne).....	3-20
3.5.3	CCN Concentration (CCNC3—Airborne)	3-22
3.6	Inverse Aerosol/CCN Closure Study: Results and Discussion	3-24
3.6.1	Inverse Aerosol/CCN Closure: Initial Comparison, Assuming 100% (NH ₄) ₂ SO ₄	3-25
3.6.2	Inverse Aerosol/CCN Closure: Inferring Deviations from 100% (NH ₄) ₂ SO ₄	3-35
3.6.2.1	Estimating Aerosol Particle Composition from CCNC3 and DACAD Measurements	3-36
3.6.2.2	CCN and DACAD Derived Insoluble Fraction (Flight 1)	3-37
3.6.3	Inverse Aerosol/CCN Closure: Inferring Aerosol Mixing State.....	3-41
3.6.3.1	Aerosol Mixing State Inferred from Initial Comparison of N_p to N_o	3-41
3.6.3.2	Aerosol Mixing State Inferred with DACAD Derived Insoluble Fraction (Flight 10)	3-42
3.6.3.3	Aerosol Mixing State Discussion	3-43
3.6.4	CCN and DMA/TDMA-Derived Mixing State and Particle Composition.....	3-44
3.7	Case Studies: “Clean” Conditions, Local Pollution, and Siberian Smoke Events	3-53
3.8	Conclusions.....	3-58
3.9	References.....	3-61

Chapter 4: Cloud Condensation Nucleus Properties of Organic Compounds:

	Experimental Results and Theoretical Predictions	4-1
4.1	Abstract.....	4-2
4.2	Introduction.....	4-3
4.3	The Aerosol Diameter Dependent Equilibrium Model (ADDEM)	4-10
4.3.1	Köhler Theory	4-10
4.3.2	Input Parameters.....	4-13
4.3.3	Calculations for Supersaturated Conditions	4-14
4.3.4	Critical Points	4-20
4.4	Experimental Setup	4-22
4.4.1	General Setup	4-22
4.4.2	Three-Column CCN Counter (CCNC3).....	4-26
4.4.3	Dual Automatic Classified Aerosol Detectors (DACAD).....	4-27
4.4.4	Organic Compounds and Experimental Issues.....	4-30
4.4.5	Solvent Comparison	4-37

4.5 Results and Discussion	4-39
4.5.1 Experimental Results.....	4-39
4.5.2 Trends with Chemical Properties.....	4-44
4.5.3 Compound Comparisons.....	4-48
4.5.4 ADDEM Modeling.....	4-50
4.5.4.1 Adipic Acid	4-59
4.5.4.2 Glutaric Acid	4-59
4.5.4.3 DL-Malic Acid	4-60
4.5.4.4 Malonic Acid.....	4-60
4.5.4.5 Oxalic Acid.....	4-61
4.5.4.6 Succinic Acid	4-61
4.6 Conclusions.....	4-62
4.6.1 Experimental Conclusions	4-62
4.6.2 Experiment and Model Comparisons	4-62
4.6.3 Experimental Design Considerations.....	4-63
4.7 References.....	4-67
 Chapter 5: Conclusions and Future Work.....	5-1
5.1 CCN Activation Theory (Chapter 2).....	5-2
5.2 CCN Field Measurements (Chapter 3)	5-3
5.3 Laboratory CCN Studies of Pure Organic Compounds (Chapter 4)	5-4
 APPENDICES	
Appendix A: Black and White Figures for Chapter 3	A-1
Appendix B: Black and White Figures for Chapter 4	B-1
Appendix C: <i>VanReken et al.</i> [2003]: Toward Aerosol/Cloud Condensation Nuclei (CCN) Closure During CRYSTAL-FACE.....	C-1
Appendix D: <i>Ghan et al.</i> [2006]: Use of In Situ Cloud Condensation Nuclei, Extinction, and Aerosol Size Distribution Measurements to Test a Method for Retrieving Cloud Condensation Nuclei Profiles from Surface Measurements	D-1
Appendix E: <i>Lance et al.</i> [2004]: Chemical and Dynamical Effects on Cloud Droplet Number: Implications for Estimates of the Aerosol Indirect Effect	E-1
Appendix F: <i>Conant et al.</i> [2004]: Aerosol-Cloud Drop Concentration Closure in Warm Cumulus.....	F-1
Appendix G: <i>Chen et al.</i> [2005]: Effect of Angle of Attack on the Performance of an Airborne Counterflow Virtual Impactor	G-1
Appendix H: <i>Phillips et al.</i> [2005]: Anvil Glaciation in a Deep Cumulus Updraught over Florida Simulated with the Explicit Microphysics Model. I: Impact of Various Nucleation Processes	H-1
Appendix I: <i>Fridlind et al.</i> [2004]: Evidence for the Predominance of Mid- Tropospheric Aerosols as Subtropical Anvil Cloud Nuclei	I-1

LIST OF TABLES

<i>Number</i>	<i>Page</i>
Chapter 2	
2.1 Aerosol Characteristics Used to Analyze the Accuracy of the Modified Köhler Expression	2-12
2.2 Equations for Physical Parameters G , α , and γ	2-18
2.3 Multimodal Surface Tension Parameterization	2-22
2.4 Derivatives of the Droplet Number Concentration with Respect to Various χ_j for a Multimodal Aerosol Population	2-24
2.5 Cases Examined in Sensitivity Analysis	2-28
Chapter 3	
3.1 Flight Summary with Operating Conditions and Uncertainty Limits for CCNC3 Column 1	3-15
3.2 Average and Standard Deviation of the Ratios of Predicted CCN Concentration to Observed CCN Concentration for All Flights for Which There Were CCN Data	3-28
3.3 Insoluble Volumetric Fractions and Fraction of Particles Unavailable for Activation for Which $\mu(N_P/N_O) \approx 1$	3-38
3.4 Flight 10 Analysis Using $\varepsilon_{ins} = \varepsilon_{ins,DACAD}$, as Determined from DACAD Wet and Dry Cumulative Size Distributions	3-40
3.5 $\mu(N_P/N_O)$ and $\sigma(N_P/N_O)$ Values for Flights 8, 9, and 16 Using ε_{ins} and External Mixing Properties Derived from DMA/TDMA Data	3-46
3.6 Summary of the Values of $\mu(N_P/N_O)$ for Each Flight Divided into Categories Determined from DACAD Size Distributions	3-57
Chapter 4	
4.1 Chemical Properties of Compounds Studied	4-6
4.2 Physical Parameters for the ADDEM Calculations	4-15
4.3 CCNC3 Calibration Summary	4-29
4.4 Comparison Between Methanol and Aqueous Solution Experiments	4-38
4.5 Experimental and ADDEM Results, as the Ratio of the Activation Diameters to Those of Ammonium Sulfate	4-40
4.6 Experimental and ADDEM Results, Given as Activation Diameters	4-42
4.7 Slopes and Intercepts for Linear Fits of Critical Supersaturation and Activation Diameter in Log-Log Space for Experimental Data and ADDEM Predictions for Adipic Acid	4-54
4.8 Slopes and Intercepts for Linear Fits of Critical Supersaturation and Activation Diameter in Log-Log Space for Experimental Data and ADDEM Predictions for Glutaric Acid and DL-Malic Acid	4-55
4.9 Slopes and Intercepts for Linear Fits of Critical Supersaturation and Activation Diameter in Log-Log Space for Experimental Data and ADDEM Predictions for Malonic Acid	4-56
4.10 Slopes and Intercepts for Linear Fits of Critical Supersaturation and	

Activation Diameter in Log-Log Space for Experimental Data and ADDEM Predictions for Oxalic Acid.....	4-57
4.11 Slopes and Intercepts for Linear Fits of Critical Supersaturation and Activation Diameter in Log-Log Space for Experimental Data and ADDEM Predictions for Succinic Acid.....	4-58

LIST OF FIGURES

<i>Number</i>	<i>Page</i>
Chapter 2	
2.1 Köhler curves for the simplified Köhler theory and full Köhler theory for three different dry radii for the aerosol characteristics in Table 2.1	2-11
2.2 Activation ratio as a function of updraft velocity for the full numerical parcel model and the EAGR parameterization, in the presence and absence of dissolved organic material.....	2-20
2.3 Sensitivity ratio based on organic mass fraction for a marine aerosol size distribution with and without surface tension effects	2-29
2.4 Sensitivity ratio based on organic mass fraction for a continental aerosol size distribution with and without surface tension effects	2-32
2.5 Sensitivity ratio based on unimodal mean radius for single-mode aerosol with $N_{ap} = 1000 \text{ cm}^{-3}$ and $\sigma = 2$	2-35
2.6 Sensitivity ratio based on accumulation mode mean radius: marine and continental aerosol size distributions	2-36
Chapter 3	
3.1 ARM Aerosol IOP flight paths for flights with CCN data.....	3-6
3.2 A schematic of a CCNC3 Column.....	3-10
3.3 $(\text{NH}_4)_2\text{SO}_4$ calibration curves for column 1 of the CCNC3 at the temperature gradients used during the ARM Aerosol IOP	3-13
3.4 Aerosol size-distributions from different level legs during flight 16.....	3-21
3.5 Flight traces of CPC, CCNC3, and DACAD data for flight 14	3-23
3.6 Predicted CCN concentration (assuming pure $(\text{NH}_4)_2\text{SO}_4$) versus observed CCN concentration for ARM Aerosol IOP	3-26
3.7 Predicted CCN concentration (assuming pure $(\text{NH}_4)_2\text{SO}_4$) versus observed CCN concentration and linear fits in log-log space for flights 8, 12, 14, and 17.....	3-29
3.8 Altitude versus longitude trace for flights 12 and 14	3-31
3.9 Three-day HYSPLIT back trajectories for 15 May 2003 (flight 8) at the SGP site at altitudes of 450, 650, and 1000 m	3-33
3.10 Three-day HYSPLIT back trajectories for 29 May 2003 (flight 17) at the SGP site at altitudes of 400, 800, and 3000 m and at site EF-19 at altitudes of 650, 800, and 1000 m	3-34
3.11 Flight trace for flight 8, showing a well-mixed boundary layer.....	3-47
3.12 Flight trace for flight 9, showing a well-mixed boundary layer.....	3-48

3.13	Flight trace for flight 16, showing the lack of a well-mixed boundary layer	3-49
3.14	Comparison of DMA/TDMA and DACAD size distributions for flights 8 and 9	3-51
3.15	Comparison of DMA/TDMA and DACAD size distributions for flight 16.....	3-52

Chapter 4

4.1	Hypothetical Köhler curve highlighting the contributions from the Raoult term and the Kelvin factor	4-16
4.2	(a) Difference in RH divided by the Kelvin factor and water activity as a function of water activity (b) Magnification of panel (a) for 3 ambient RH values	4-19
4.3	Predicted Köhler curves for $(\text{NH}_4)_2\text{SO}_4$ and mixed $(\text{NH}_4)_2\text{SO}_4:\text{NH}_4\text{NO}_3$ aerosols.....	4-21
4.4	Negative equilibrium saturation ratio as a function of water activity for $(\text{NH}_4)_2\text{SO}_4$, NaCl , and H_2SO_4 aerosols at 10, 20, 40, and 80 nm	4-23
4.5	Negative saturation ratio for a 10 nm $(\text{NH}_4)_2\text{SO}_4$ aerosol as a function of water activity.....	4-24
4.6	Experimental Setup	4-25
4.7	Calibration curves for CCNC3 using $(\text{NH}_4)_2\text{SO}_4$, NH_4HSO_4 , and NaCl as calibration salts	4-28
4.8	DACAD size distributions for the given DMA selected sized particles.....	4-34
4.9	Experimental CCN activation curves for malonic acid in methanol and water	4-36
4-10	ψ as a function of M_s , aqueous solubility, pK_a , and $M_s/(\rho_s v)$	4-45
4.11	ADDEM and experimental results for adipic acid and glutaric acid	4-51
4.12	ADDEM and experimental results for DL-malic acid and malonic acid	4-52
4.13	ADDEM and experimental results for oxalic acid and succinic acid	4-53

Chapter 1

INTRODUCTION

1.1 Background and Motivation

Predicting how the future climate of the earth will change as a result of increasing human emissions is one of the greatest problems facing science today [Houghton *et al.*, 2001]. The earth's climate is the result of a delicate balance between incoming and outgoing radiation. Anthropogenic emissions of aerosol particles into the atmosphere have the potential to affect the earth's climate in significant ways through both direct and indirect effects on the earth's radiative balance [Seinfeld and Pandis, 1998]. Atmospheric aerosols absorb outgoing longwave radiation from the earth and absorb and scatter incoming shortwave radiation from the Sun, and small changes in atmospheric aerosol loading can have significant effects on the global radiation budget and, thus, on climate [Charlson *et al.*, 1992; Seinfeld and Pandis, 1998; Haywood and Boucher, 2000; McFiggans *et al.*, 2005]. The scattering of incoming shortwave radiation has a cooling effect, while absorption has a heating effect [Charlson and Pilat, 1969]. This is termed the aerosol direct effect on climate.

One of the largest uncertainties in aerosol radiative forcing is associated with the relationship between atmospheric aerosols and cloud formation, properties, and lifetime [Houghton *et al.*, 2001]. Clouds form by water condensing on small particles (aerosols) in the air (referred to as cloud condensation nuclei, or CCN), and how the increasing levels of atmospheric particles will affect Earth's clouds and its hydrologic cycle represents one of the key problems in the science of climate. On average, clouds cover about half of the globe, and clouds are perhaps the most important regulator of the climate system that exists. Small changes in the macro- and microphysical properties of

Earth's clouds can lead to large changes in the overall energy balance on the globe [Lohmann and Feichter, 2005]. Twomey [1974] postulated that an increase in the number concentration of atmospheric aerosol particles would increase the number of cloud droplets formed for a given air mass. For fixed liquid water content, the cloud droplets would also be smaller than those formed under conditions with lower particle concentrations. This increase in number and decrease in mean diameter of cloud droplets would have two indirect effects on climate. Cloud albedo is greater for clouds with more numerous, smaller droplets; this has been termed the first indirect climatic effect of aerosols. Also, the lifetime of a cloud with smaller cloud droplets is greater than that of a cloud with larger droplets because the rain forming mechanisms are less efficient [Warner, 1968; Albrecht, 1989]. This is referred to as the second indirect climatic effect of aerosols. Both effects create clouds that are more reflective and more persistent, leading to cooling of the earth's surface [Albrecht, 1989; Haywood and Boucher, 2000].

Chapters 2 through 4 of this thesis present theoretical, field, and laboratory studies concerned with the CCN activation of insoluble and/or organic aerosols, in an attempt to lead to increased understanding of the relationship between atmospheric aerosols and clouds.

1.2 Cloud Activation Theory (Chapter 2)

The ways in which global climate models (GCMs) treat cloud-related processes is central to the ability to predict future climate changes associated with the effect of increased aerosol loadings on clouds. Due to computational limitations, cloud processes

occur on subgrid levels in GCMs, so parameterizations of cloud activation theory are necessary [McFiggans *et al.*, 2005].

For given particle composition and size, the supersaturation above which the particle undergoes spontaneous condensational growth (activation) into a cloud droplet, the so-called critical supersaturation, is described by Köhler theory [Köhler, 1936]. The activation diameter, the dry diameter at which a particle of known or assumed composition will activate, can also be calculated for a given supersaturation. Prediction of aerosol activation from Köhler theory is very successful for aerosols composed of soluble, inorganic salts, such as ammonium sulfate ((NH₄)₂SO₄), sodium chloride (NaCl), and ammonium bisulfate (NH₄HSO₄) [Seinfeld and Pandis, 1998]. However, the basic assumptions underlying Köhler theory, and thus its predictive ability, break down when considering chemical components, such as organic compounds, that are partially soluble, insoluble, or affect the surface tension of the aqueous solution. The chemical composition of atmospheric aerosol can be very complicated, and individual aerosol components can affect aerosol activation in different and competing ways. It is desirable to expand Köhler theory to include a greater number of aerosol properties, such as surface tension and solute effects of chemical aerosol species, and improve its predictive ability [Laaksonen *et al.*, 1998; Nenes *et al.*, 2002; Raymond and Pandis, 2002; Kumar *et al.*, 2003; Kreidenweis *et al.*, 2005; Koehler *et al.*, 2005].

In assessing the importance of chemical variations in the composition of the CCN population, one has to compare the changes relative to dominant sources of variability, which are total aerosol number and updraft velocity. In doing so, a simple comparison of CCN spectra is not sufficient; droplet formation in clouds is a strongly nonlinear process,

and the full process of activation needs to be considered for a correct treatment. *Nenes et al.* [2002] examined the effects of water-soluble gases, partially soluble species, surface-active species, and condensation kinetics on cloud droplet number concentration and, using a detailed numerical cloud parcel model, compared them with the Twomey effect. Their calculations show that, for a wide range of updraft velocities, chemical effects can rival those of the Twomey effect. The interaction for most cases is positive, indicating that chemical influences mostly act to enhance the Twomey effect. Given that organic compounds are ubiquitous in atmospheric aerosols, it is of interest to examine their influence on activation over the entire parameter space of organic mass fraction.

Chapter 2 of this thesis presents a modification of an activation parameterization [*Abdul-Razzak et al.*, 1998; *Abdul-Razzak and Ghan*, 2000], that is consistent with Köhler theory, to include surface tension and limited solubility effects, especially those associated with organic compounds. The modified parameterization, referred to as the extended Abdul-Razzak, Ghan, and Rivera-Carpio (EAGR) parameterization, is compared with a full, numerical adiabatic cloud parcel model to evaluate its performance in predicting the activation fraction. Sensitivities of cloud droplet number concentration to aerosol size distribution characteristics, organic content, and updraft velocity are then presented.

1.3 CCN Field Measurements (Chapter 3)

Field measurements allow the integration of data from many different instruments at the same time. Large CCN data sets are obtained during field missions by deploying Caltech CCN counting instruments on airplanes for sampling at various locations and

altitudes. The ability of Köhler (or any activation) theory to predict ambient CCN concentrations can be evaluated by comparing atmospheric CCN measurements at a given supersaturation with predicted CCN concentrations, calculated using aerosol size distribution and composition measurements. This type of study, called aerosol/CCN closure, compares the observed CCN concentration at the operating supersaturation of the CCN instrument to that predicted from the aerosol size distribution, which is determined from the aerosol size distribution by summing the concentration of particles with diameters greater than the activation diameter calculated from Köhler theory [VanReken *et al.*, 2003].

When direct measurements of aerosol composition are unavailable, the predicted CCN concentration can be calculated using an assumed aerosol composition or one that is inferred from other available measurements. An “inverse” aerosol/CCN closure study can be undertaken to determine aerosol composition and mixing states that are most consistent with CCN observations when direct measurements of these aerosol characteristics are unavailable. In Chapter 3, data measured by a new Caltech CCN instrument (CCNC3) during the Atmospheric Radiation Measurement (ARM) Program’s aerosol intensive observational period (IOP) in May 2003 are used in an inverse aerosol/CCN closure study of the mid-continental aerosol sampled near the southern great plains (SGP) central facility (CF) to determine aerosol composition and mixing states consistent with the CCN measurements at the operating supersaturations of the instrument. The Texas A&M differential mobility analyzer/tandem differential mobility analyzer (DMA/TDMA) data from the surface are used to infer the mixing state and insoluble fraction of the aerosol population as a function of dry diameter. This

information is used with the airborne CCN and aerosol size distribution measurements to determine conditions under which aerosol composition and mixing states inferred from surface measurements are able to reproduce CCNC3 measurements at altitude. Aerosol properties, categorized by closure ratio and aerosol size distribution shape, during pollution and smoke events are also discussed.

1.4 Laboratory CCN Studies of Pure Organic Compounds (Chapter 4)

Laboratory studies of the CCN properties of organic aerosols are necessary in order to interpret field measurements and provide inputs into aerosol activation models. After sulfate, organic material has been found to be the second most abundant aerosol component in fine aerosols [*Heintzenberg, 1989; Novakov and Penner, 1993; Saxena and Hildemann, 1996; Rudich, 2003; Sun and Ariya, 2006*]. Properties such as solubility, extent of dissociation, and surface activity of the organic compounds found in atmospheric aerosol vary widely and can have complex, and sometimes conflicting, effects on the ability of these particles to act as CCN. Whether the presence of an organic enhances or limits CCN activation depends on the chemical characteristics of the aerosol, as well as the size distribution.

Laboratory studies of the CCN activation of organic aerosol particles are an important element in understanding the aerosol-cloud relationship, and many such studies exist in the literature. Dicarboxylic acids have been studied extensively, and their CCN abilities have been found to vary widely, with some compounds exhibiting CCN activity similar to that of $(\text{NH}_4)_2\text{SO}_4$. The CCN behaviors of some compounds were successfully predicted from Köhler theory modified to include solubility and/or surface tension effects

[Cruz and Pandis, 1997; Corrigan and Novakov, 1999, Prenni *et al.*, 2001; Giebl *et al.*, 2002; Kumar *et al.*, 2003; Broekhuizen *et al.*, 2004].

Some studies have discussed the complications inherent to laboratory experiments concerning the CCN activity of organic compounds. *Raymond and Pandis* [2002] found that some compounds were much more CCN active than their solubilities would suggest and attributed this to the ability of water to wet these compounds. *Huff Hartz et al.* [2006] atomized some compounds from both water and alcohol solutions, and concluded that the CCN activities of some of the compounds were reduced if the aerosol particles were atomized from a non-aqueous solution. They also concluded that the ability of a compound to act as a CCN beyond what would be predicted based on solubility was a result of the existence of particles in a metastable state at low relative humidity (*RH*). *Hori et al.* [2003] found that the drying, morphology and hydrophobicity of particles, as well as solute vaporization, were key factors in theoretical prediction and experimental interpretation.

In the CCN laboratory study presented in Chapter 4, many of these experimental considerations were taken into account and corrections were made when possible. A suite of organic compounds was chosen based on atmospheric relevance and/or use as surrogates in the chemical analysis and component identification of secondary organic aerosol samples. Some of these compounds have been studied previously, and those studies are compared to the present results. The Aerosol Diameter Dependent Equilibrium Model [ADDEM; *Topping et al.*, 2005a; 2005b] was used to predict the CCN behavior of a subset of these compounds, for which experimental surface tension data is available, and a comparison to experimental results is discussed.

1.5 References

- Abdul-Razzak, H., and S. J. Ghan (2000), A parameterization of aerosol activation: 2. Multiple aerosol types, *J. Geophys. Res.*, *105*(D5), 6837 – 6844.
- Abdul-Razzak, H., S. J. Ghan, and C. Rivera-Carpio (1998), A parameterization of aerosol activation: 1. Single aerosol type, *J. Geophys. Res.*, *103*(D6), 6123 – 6131.
- Albrecht, B. A. (1989), Aerosols, cloud microphysics, and fractional cloudiness, *Science*, *245*(4923), 1227 – 1230.
- Broekhuizen, K., P. P. Kumar, and J. P. D. Abbatt (2004), Partially soluble organics as cloud condensation nuclei: Role of trace soluble and surface active species, *Geophys. Res. Lett.*, *31*(1), L01107, doi:10.1029/2003GL018203.
- Charlson, R. J. and M. J. Pilat (1969), Climate: The influence of aerosols, *J. Appl. Meteor.*, *8*(6), 1001 – 1002.
- Charlson, R. J., S. E. Schwartz, J. M. Hales, R. D. Cess, J. A. Coakley, Jr., J. E. Hansen, and D. J. Hofmann (1992), Climate forcing by anthropogenic aerosols, *Science*, *255*(5043), 423 – 430.
- Corrigan, C. E. and T. Novakov (1999), Cloud condensation nucleus activity of organic compounds: A laboratory study, *Atmos. Env.*, *33*(17), 2661 – 2668.
- Cruz, C. N. and S. N. Pandis (1997), A study of the ability of pure secondary organic aerosol to act as cloud condensation nuclei, *Atmos. Env.*, *31*(15), 2205 – 2214.
- Giebl, H., A. Berner, G. Reischl, H. Puxbaum, A. Kasber-Giebl, and R. Hitzemberger (2002), CCN activation of oxalic and malonic test aerosols with the University of Vienna cloud condensation nuclei counter, *J. Aerosol Sci.*, *33*(12), 1623 – 1634.
- Haywood, J. and O. Boucher (2000), Estimates of the direct and indirect radiative forcing due to tropospheric aerosols: A review, *Rev. Geophys.*, *38*(4), 513 – 543.
- Heintzenberg, J. (1989), Fine particles in the global troposphere: A review, *Tellus*, *41B*, 149 – 160.
- Hori, M., S. Ohta, N. Murao, and S. Yamagata (2003), Activation capability of water soluble organic substances as CCN, *J. Aerosol Sci.*, *34*(4), 419 – 448.
- Houghton, J. T., Y. Ding, D. J. Griggs, M. Noguer, P. J. van der Linden, and D. Xiaosu, Eds., (2001), *Climate Change 2001: The Scientific Basis*, 944 pp., Cambridge University Press, Cambridge, U.K.

- Huff Hartz, K. E., J. E. Tischuk, M. N. Chan, C. K. Chan, N. M. Donahue, and S. N. Pandis (2006), Cloud condensation nuclei activation of limited solubility organic aerosol, *Atmos. Env.*, 40(4), 605 – 617.
- Koehler, K. A., S. M. Kreidenweis, P. J. DeMott, A. J. Prenni, C. M. Carrico, B. Ervens, and G. Feingold (2005), Water activity and activation diameters from hygroscopicity data—Part II: Application to organic species, *Atmos. Chem. Phys. Discuss.*, 5, 10,881 – 10,924.
- Köhler, H. (1936), The nucleus in and the growth of hygroscopic droplets, *Trans. Far. Soc.*, 32(2), 1152 – 1161.
- Kreidenweis, S. M., K. A. Koehler, P. J. DeMott, A. J. Prenni, C. M. Carrico, and B. Ervens (2005), Water activity and activation diameters from hygroscopicity data—Part I: Theory and application to inorganic salts, *Atmos. Chem. Phys.*, 5, 1357 – 1370.
- Kumar, P. P., K. Broekhuizen, and J. P. D. Abbatt (2003), Organic acids as cloud condensation nuclei: Laboratory studies of highly soluble and insoluble species, *Atmos. Chem. Phys.*, 3, 509 – 520.
- Laaksonen, A., P. Korhonen, M. Kulmala, and R. J. Charlson (1998), Modification of the Köhler equation to include soluble trace gases and slightly soluble substances, *J. Atmos. Sci.*, 55(5), 853 – 862.
- Lohmann, U. and J. Feichter (2005), Global indirect aerosol effects: A review, *Atmos. Chem. Phys.*, 5, 715 – 737.
- McFiggans, G., P. Artaxo, U. Baltensperger, H. Coe, M. C. Facchini, G. Feingold, S. Fuzzi, M. Gysel, A. Laaksonen, U. Lohmann, T. F. Mentel, D. M. Murphy, C. D. O'Dowd, J. R. Snider, and E. Weingartner (2005), The effect of physical and chemical aerosol properties on warm cloud droplet activation, *Atmos. Chem. Phys. Discuss.*, 5, 8507 – 8646.
- Nenes, A., R. J. Charlson, M. C. Facchini, M. Kulmala, A. Laaksonen, and J. H. Seinfeld (2002), Can chemical effects on cloud droplet number rival the first indirect effect?, *Geophys. Res. Lett.*, 29(17), 1848, doi: 10.1029/2002GL015295.
- Novakov, T. and J. E. Penner (1993), Large contributions of organic aerosols to cloud-condensation-nuclei concentrations, *Nature*, 365(6449), 823 – 825.
- Prenni, A. J., P. J. DeMott, S. M. Kreidenweis, D. E. Sherman, L. M. Russell, and Y. Ming (2001), The effects of low molecular weight dicarboxylic acids on cloud formation, *J. Phys. Chem.*, 105(50), 11,240 – 11,248.

- Raymond, T. M. and S. N. Pandis (2002), Cloud activation of single-component organic aerosol particles, *J. Geophys. Res.*, *107*(D24), 4787, doi:10.1029/2002JD002159.
- Rudich, Y. (2003), Laboratory perspectives on the chemical transformations of organic matter in atmospheric particles, *Chem. Rev.*, *103*(12), 5097 – 5124.
- Saxena, P. and L. M. Hildeman (1996), Water-soluble organics in atmospheric particles: A critical review of the literature and application of thermodynamics to identify candidate compounds, *J. Atmos. Chem.*, *24*(1), 57 – 109.
- Seinfeld, J. H. and S. N. Pandis (1998), *Atmospheric Chemistry: From Air Pollution to Climate Change*, 1326 pp., John Wiley & Sons, Inc., New York.
- Sun, J. and P. A. Ariya (2006), Atmospheric organic and bio-aerosols as cloud condensation nuclei (CCN): A review, *Atmos. Env.*, *40*(5), 795 – 820.
- Topping, D. O., G. B. McFiggans, and H. Coe (2005a), A curved multi-component aerosol hygroscopicity model framework: Part 1—Inorganic compounds, *Atmos. Chem. Phys.*, *5*(5), 1205 – 1222.
- Topping, D. O., G. B. McFiggans, and H. Coe (2005b), A curved multi-component aerosol hygroscopicity model framework: Part 2—Including organic compounds, *Atmos. Chem. Phys.*, *5*(5), 1223 – 1242.
- Twomey, S. (1974), Pollution and the planetary albedo, *Atmos. Env.*, *8*(12), 1251 – 1256.
- VanReken, T. M., T. A. Rissman, G. C. Roberts, V. Varutbangkul, H. H. Jonsson, R. C. Flagan, and J. H. Seinfeld (2003), Toward aerosol/cloud condensation nuclei (CCN) closure during CRYSTAL-FACE, *J. Geophys. Res.*, *108*(D20), 4633, doi:10.1029/2003JD003582.
- Warner, J. (1968), A reduction in rainfall associated with smoke from sugar-cane fires—An inadvertent weather modification?, *J. Appl. Meteor.*, *7*(2), 247 – 251.

Chapter 2

CHEMICAL AMPLIFICATION (OR DAMPENING) OF THE TWOMEY EFFECT: CONDITIONS DERIVED FROM DROPLET ACTIVATION THEORY*

* Full Citation: Rissman, T. A., A. Nenes, and J. H. Seinfeld (2004), Chemical Amplification (or Dampening) of the Twomey Effect: Conditions Derived from Droplet Activation Theory, *Journal of the Atmospheric Sciences*, 61(18), 919 – 930.

© Copyright 2004 American Meteorological Society (AMS). Permission to use figures, tables, and brief excerpts from this work in scientific and educational works is hereby granted provided that the source is acknowledged. Any use of material in this work that is determined to be “fair use” under Section 107 of the U.S. Copyright Act or that satisfies the conditions specified in Section 108 of the U.S. Copyright Act (17 USC §108, as revised by P.L. 94-553) does not require the AMS’s permission. Republication, systematic reproduction, posting in electronic form on servers, or other uses of this material, except as exempted by the above statement, requires written permission or a license from the AMS. Additional details are provided in the AMS Copyright Policy, available on the AMS Web site located at (<http://www.ametsoc.org/AMS>) or from the AMS at 617-227-2425 or copyright@ametsoc.org.

2.1 Abstract

Cloud droplet number concentrations are controlled by both meteorological and microphysical factors, which include aerosol number concentration and composition. This chapter examines the importance of microphysical phenomena, compared to the sensitivity with respect to parcel updraft velocity, in the activation of aerosols to become cloud droplets. Of the compositional (chemical) factors that can influence droplet number concentration, the effect of organics is examined through their ability to alter droplet surface tension and to contribute solute. A recent parameterization of aerosol activation [*Abdul-Razzak et al.*, 1998; *Abdul-Razzak and Ghan*, 2000] is extended to obtain analytical expressions for the sensitivity of activation to microphysical factors relative to updraft velocity. It is demonstrated that, under some conditions, the droplet number concentration can be as much as 1.5 times more sensitive to changes in aerosol composition than to updraft velocity. Chemical effects seem to be most influential for size distributions typical of marine conditions and decrease in importance for strongly anthropogenically perturbed conditions. The analysis indicates that the presence of surface-active species can lead to as much uncertainty in cloud droplet number concentration activation as results from variations in updraft velocity. The presence of surfactant species also drastically changes the response of the cloud condensation nuclei to changes in the updraft velocity spectrum. Conditions are found under which an increase in dissolved organic compounds can actually lead to a decrease in cloud droplet number, a “contra-Twomey effect.” Results presented have more general implications

than just for organic compounds and can apply, in principle, for any chemically induced activation effect.

2.2 Introduction

Cloud optical properties depend on the in-cloud droplet size distribution, which, in turn, is controlled by the availability of atmospheric particles that serve as cloud condensation nuclei (CCN). *Twomey* [1977] suggested that an increase in aerosol number concentration from anthropogenic emissions, and thus an increase in CCN, would lead to a reduction in the size of cloud droplets and higher cloud albedo. This increase in cloud albedo, and the concomitant radiative cooling, is referred to as the first indirect climatic effect of aerosols [*Houghton et al.*, 2001].

In assessing the importance of chemical variations in the composition of the CCN population, one has to compare the changes relative to dominant sources of variability, which are total aerosol number and updraft velocity. In doing so, a simple comparison of CCN spectra is not sufficient; droplet formation in clouds is a strongly nonlinear process, and the full process of activation needs to be considered for a correct treatment. *Nenes et al.* [2002a] examined the effects of water-soluble gases, partially soluble species, surface-active species, and condensation kinetics on cloud droplet number concentration and, using a detailed numerical cloud parcel model, compared them with the Twomey effect. Their calculations show that, for a wide range of updraft velocities, chemical effects can rival those of the Twomey effect. The interaction for most cases is positive, indicating that chemical influences mostly act to enhance the Twomey effect. Given that organic

compounds are ubiquitous in atmospheric aerosols, it is of interest to examine their influence on activation over the entire parameter space of organic mass fraction.

Here, an extension of a parameterization to include surface tension effects consistent with Köhler theory [*Abdul-Razzak et al.*, 1998; *Abdul-Razzak and Ghan*, 2000] is proposed. The modified parameterization is used to examine the sensitivity of the droplet number concentration to total aerosol number concentration, soluble organic mass fraction, and the geometric mean radius and geometric standard deviation of the aerosol size distribution using a normalized sensitivity ratio that compares the sensitivity to that of updraft velocity.

In the following sections, the derivation of the modified Köhler theory is presented, which leads to an aerosol activation parameterization that includes surface tension effects; this will be referred to as the extended Abdul-Razzak, Ghan, and Rivera-Carpio (EAGR) parameterization. The EAGR parameterization is compared with a full, numerical adiabatic cloud parcel model to evaluate its performance in predicting the activation fraction. Sensitivities of cloud droplet number concentration to aerosol size distribution characteristics, organic content, and updraft velocity are then presented.

2.3 Analytical Parameterizations of Aerosol Activation

Before proceeding, it is useful to present a brief overview of current aerosol activation parameterizations. *Cohard et al.* [1998] developed an activation parameterization based on a general description of the CCN spectrum, which depends on four parameters related to the aerosol size distribution characteristics, the solubility of the aerosol species, and the air temperature. They then used the activation parameterization

to analyze the sensitivity of droplet number concentration to the geometric mean radius and the geometric standard deviation of single lognormal aerosol size distributions of marine and continental aerosols. *Khvorostyanov and Curry* [1999] assume the power-law aerosol size distribution of *Junge* [1952] to develop a simple expression relating CCN number concentration to supersaturation with parameters that are related to aerosol characteristics and growth dependence on relative humidity under subsaturation. *Abdul-Razzak et al.* [1998] and *Abdul-Razzak and Ghan* [2000] developed an aerosol activation parameterization involving both unimodal [*Abdul-Razzak et al.*, 1998] and multimodal [*Abdul-Razzak and Ghan*, 2000] lognormal aerosol size distributions.

The parameterizations of *Abdul-Razzak et al.* [1998] and *Abdul-Razzak and Ghan* [2000] are useful to investigate the sensitivity of droplet activation to both microphysical and dynamical factors because of the explicit link of updraft velocity and aerosol size distribution characteristics to droplet number concentration. The lognormal representation of the aerosol size distribution is also a desirable feature. However, these parameterizations lack explicit treatment of surface-active species. For these reasons, the effect of dissolved aerosol organics on droplet surface tension is included in the extended theory presented here.

2.3.1 Köhler Theory

Traditional Köhler theory predicts that the equilibrium saturation ratio for a droplet containing dissolved electrolytes and an insoluble core is [*Seinfeld and Pandis*, 1998]

$$S - 1 = s = \frac{A}{r} - \frac{Ba_d^3}{r^3 - b_1 a_d^3} \quad (2.1)$$

where S is the saturation, s is the supersaturation, A is the curvature coefficient, r is the droplet radius, $B = (M_w \rho_{ap} / \rho_w)[(\varepsilon_s v_s / M_s) + (\varepsilon_o v_o / M_o)]$, $b_1 = \varepsilon_{ins} \rho_{ap} / \rho_{ins}$, $A = 2M_w \sigma_s / (RT \rho_w)$, a_d is the aerosol dry radius, M_w is the molar mass of water, ρ_{ap} is the density of the aerosol particle, ρ_w is the density of water, ε_s is the salt mass fraction, v_s is the number of ions resulting from the dissociation of one salt molecule, M_s is the molar mass of the salt species, ε_o is the dissolved organic mass fraction, v_o is the number of ions resulting from the dissociation of one organic molecule, M_o is the molar mass of the organic species, ε_{ins} is the insoluble mass fraction, ρ_{ins} is the density of the insoluble species, R is the gas constant, and T is the temperature. The density of the aerosol particle is given by

$$\rho_{ap} = \frac{1}{\frac{\varepsilon_o}{\rho_o} + \frac{\varepsilon_s}{\rho_s} + \frac{\varepsilon_{ins}}{\rho_{ins}}} \quad (2.2)$$

where ρ_o is the density of the dissolved organic species and ρ_s is the density of the salt species.

The presence of dissolved organics can change the bulk phase surface tension of the droplet. *Facchini et al.* [1999] have proposed that the droplet surface tension, σ_s , can be expressed as a function of the dissolved organic concentration, C , by

$$\sigma_s = \sigma_s^* - A_1 T \ln(1 + A_2 C) \quad (2.3)$$

where σ_s^* is the surface tension of pure water, and A_1 and A_2 are constants. This relationship is used to represent the change in surface tension from the presence of dissolved organics in the droplet. The presence of inorganic salts may potentially modify the effect of dissolved organic compounds, as the surface tension of electrolytic solutions increases with the molality of inorganic salts. However, the electrolyte concentrations in recently activated CCN are typically not large enough to induce a significant change in surface tension [Pruppacher and Klett, 1997]. This argument is supported by measurements of CCN activity for laboratory-generated particles; no corrections in surface tension are needed for describing the properties of pure-salt CCN. Nevertheless, if inorganic salts appreciably increase surface tension, it would be reflected in the Facchini *et al.* [1999] measurements applied in our study, as their measurements did contain inorganics in their cloud water samples.

Substitution of equation (2.3) into the expression for the curvature coefficient, A , leads to

$$A = \frac{2M_w}{RT\rho_w} [\sigma_s^* - A_1 T \ln(1 + A_2 C)] \quad (2.4)$$

where $C = v_c n_o / V_{drop}$, v_c is the number of moles of carbon in one mole of the soluble organic compound, n_o is the number of moles of the dissolved organic species and $n_o = 4\pi\epsilon_o\rho_{ap}a_d^3/(3M_o)$, V_{drop} is the volume of the droplet, and $V_{drop} = 4\pi r^3/3$. Substituting the expression for C into equation (2.4) gives

$$A = A^* - A_4 T \ln \left(1 + \frac{A_3 a_d^3}{r^3} \right) \quad (2.5)$$

where $A^* = 2M_w \sigma_s^* / (RT\rho_w)$, $A_3 = \varepsilon_o v_o \rho_{ap} A_2 / M_o$, and $A_4 = 2M_w A_1 / (R\rho_w)$. Note that as the droplet grows, the dissolved organic concentration decreases and the droplet surface tension approaches that of pure water. Substituting equation (2.5) into equation (2.1) gives the extended Köhler expression, which includes surface tension changes due to dissolved organic components, as well as insoluble components:

$$s = \frac{A^*}{r} - \frac{A_4}{r} \ln \left(1 + \frac{A_3 a_d^3}{r^3} \right) - \frac{B a_d^3}{r^3 - b_1 a_d^3} \quad (2.6)$$

Compared to an aerosol particle containing a certain amount of inorganic and insoluble species, an increase in the organic mass fraction can (i) decrease the supersaturation by decreasing the surface tension [which is reflected in the second term in equation (2.6)]; (ii) change the supersaturation by changing the moles of dissolved species in the aerosol [reflected by changes in the B coefficient of the third term in equation (2.6)]; depending on the relative proportions of organic and inorganic species, increasing the organic mass fraction can either increase or decrease the supersaturation; and (iii) increase the supersaturation by decreasing the b_1 term in the denominator of the third term in equation (2.6), assuming that the organic mass fraction increases at the expense of the insoluble mass fraction. This influence is important for diameters exceeding the critical diameter.

2.3.2 Simplifications of the Full Köhler Expression

The critical properties for the droplet are determined at the maximum of equation (2.6):

$$\frac{ds}{dr} = 0 = -\frac{A^*}{r_c^2} + \frac{A_4}{r_c^2} \ln\left(1 + \frac{A_3 a_d^3}{r_c^3}\right) + \frac{3A_3 A_4 a_d^3}{\left(1 + \frac{A_3 a_d^3}{r_c^3}\right) r_c^5} + \frac{3Ba_d^3 r_c^2}{(r_c^3 - b_1 a_d^3)^2} \quad (2.7)$$

Certain approximations can be made to obtain an explicit expression for the critical droplet radius. The Köhler curve is approximated with one of constant surface tension and the same critical diameter and critical supersaturation. The constant surface tension, σ_s^* , instead of being that of pure water, is now assigned a value computed from the organic concentration at the critical radius. Classical Köhler theory is used to calculate the critical radius, assuming $\sigma_s = \sigma_s^*$, $r_c^* = (3Ba_d^3/A^*)^{1/2}$ [Seinfeld and Pandis, 1998]. Substitution into equation (2.6) leads to a simplified Köhler equation:

$$s = \frac{A_{5d}}{r} - \frac{Ba_d^3}{r^3} \quad (2.8)$$

where $A_{5d} = A^* - A_4 \ln[1 + (A_3 a_d^3 / r_c^{*3})]$. The critical radius is now explicitly given by

$$r_c = \left(\frac{3Ba_d^3}{A_{5d}}\right)^{1/2} \quad (2.9)$$

Equation (2.8), though a simplification, is self consistent. When $\varepsilon_o \rightarrow 0$, the surface tension goes to that of water ($\sigma_s \rightarrow \sigma_s^*$) and $A_{5d} \rightarrow A$, so the expression reduces to classical Köhler theory. Furthermore, the simplification does not introduce significant error, as is shown by Figure 2.1.

The dry radii examined are 0.025, 0.05, and 0.1 μm , typical of relevant CCN sizes. Table 2.1 summarizes the aerosol properties used, which correspond to a mixture of inorganic and organic compounds and mineral dust. The error in the critical supersaturation (between the simplified and full treatments) is below 10% for critical supersaturations less than 1% and never exceeds 15%, even for supersaturations as high as 3.5%. Since atmospheric supersaturations are typically below 1%, the error incurred in the critical supersaturation by using equations (2.8) and (2.9) for atmospheric conditions is expected to be less than 10%.

2.3.3 Single-Mode Parameterization Modification

The fraction of particles that activates to droplets is given by *Abdul-Razzak et al.* [1998] and *Abdul-Razzak and Ghan* [2000] as

$$\frac{N}{N_{ap}} = \frac{1}{2} [1 - \text{erf}(u)] \quad (2.10)$$

where $u = \ln(a_c/a_m)/[\sqrt{2} \ln(\sigma)]$, N is the droplet number concentration, N_{ap} is the total aerosol number concentration, a_c is the dry radius of the smallest activated particle, a_m is

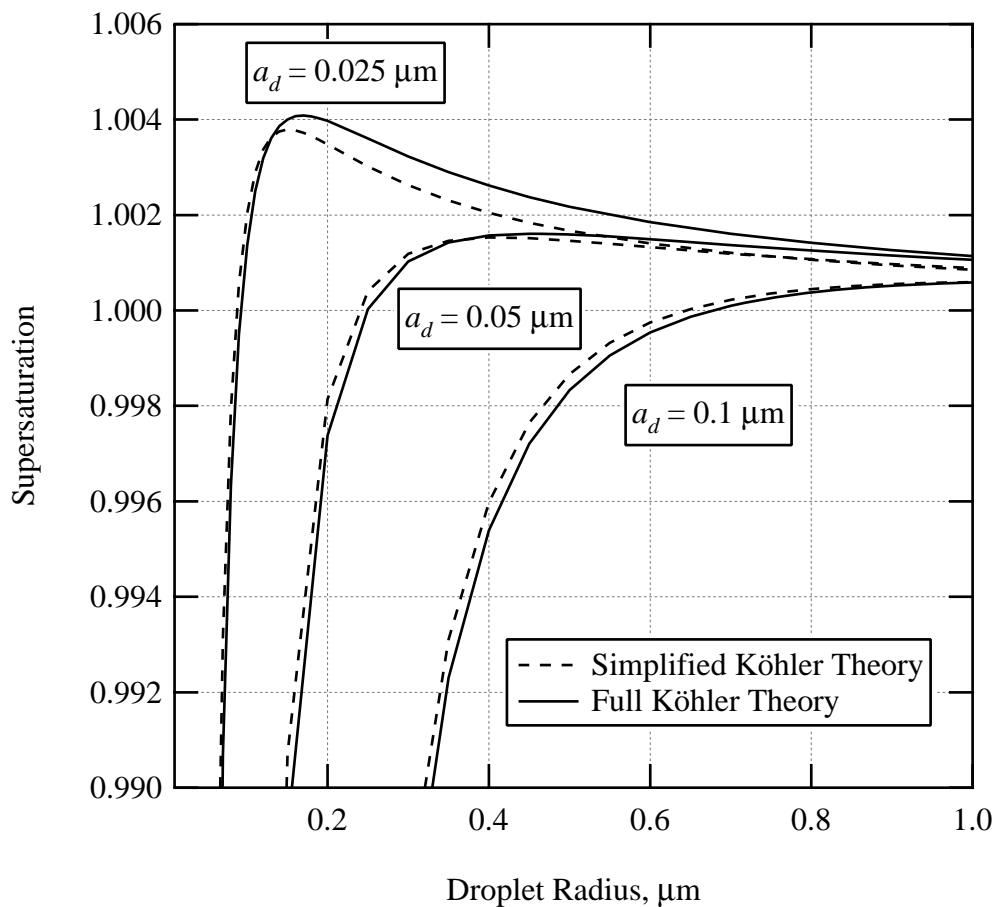


Figure 2.1. Köhler curves for the simplified Köhler theory and full Köhler theory for three different dry radii (a_d) for the aerosol characteristics in Table 2.1. The inorganic compound is assumed to be ammonium sulfate. The soluble organic component is assumed to have the properties of a mixture of 18% levoglucosan, 41% succinic acid, and 41% fulvic acid, by mass [Nenes *et al.*, 2002a]. The insoluble component is assumed to have the properties of typical mineral dust.

Table 2.1. Aerosol Characteristics Used to Analyze the Accuracy of the Modified Köhler Expression

Aerosol Characteristics	Symbol	Value
Organic Mixture Properties	ε_o	0.1
	ρ_o	1.55 g cm ⁻³
	M_o	194.33 g mol ⁻¹
	v_o	2.79
	v_c	8.94
(NH ₄) ₂ SO ₄ Properties	ε_s	0.5
	ρ_s	1.76 g cm ⁻³
	M_S	132 g mol ⁻¹
	v_s	3
Insoluble Compound Properties	ε_{ins}	0.4
	ρ_{ins}	2 g cm ⁻³
Aerosol Size Distribution Properties	N_{ap}	200 cm ⁻³
	σ	2.5
	a_m	0.01 μm
Other Constants	T	273 K
	A_1	1.87x10 ⁻⁷ N cm ⁻¹ K ⁻¹
	A_2	6.28x10 ⁵ cm ³ mol ⁻¹
	σ_s^*	7.28x10 ⁻⁴ N cm ⁻¹

the mean dry radius of the aerosol size distribution, and σ is the geometric standard deviation of the aerosol size distribution.

To account for surface tension changes due to the dissolved organics, the radii a_c and a_m are computed from the simplified Köhler theory through their corresponding critical supersaturations. The maximum supersaturation, s_{\max} , corresponds to the critical supersaturation of the smallest activated particle:

$$s_{\max} = \frac{2}{\sqrt{B}} \left(\frac{A_{5c}}{3a_c} \right)^{3/2} \quad (2.11)$$

where $A_{5c} = A^* - A_4 \ln[1 + (A_3 a_c^3 / r_c^{*3})]$. The critical supersaturation, s_m , of a particle with dry radius equal to the geometric mean radius of the aerosol size distribution is given by

$$s_m = \frac{2}{\sqrt{B}} \left(\frac{A_{5m}}{3a_m} \right)^{3/2} \quad (2.12)$$

where $A_{5m} = A^* - A_4 \ln[1 + (A_3 a_m^3 / r_c^{*3})]$. Equations (2.11) and (2.12) must be solved for a_c and a_m and substituted into the expression for u . The dependencies of A_{5m} and A_{5c} on a_m and a_c , respectively, preclude explicit expressions; however, if $r_c^* \ll A_3 a_d$, then $A_3 a_d^3 / r_c^{*3} \gg 1$, $\ln[1 + (A_3 a_d^3 / r_c^{*3})] \approx \ln(A_3 a_d^3 / r_c^{*3})$, and

$$A_{5i} = A^* - A_4 \ln \left(\frac{A_3 a_i^3}{r_c^{*3}} \right) \quad i = d, m, c \quad (2.13)$$

2.3.4 Analysis of A_{5d} , A_{5m} , and A_{5c} Parameter Simplifications

The errors arising from the assumptions used in the development of equation (2.13) increase with increases in a_d and decreases in a_c and a_m . It can be shown that the absolute error in the A_{5d} parameter is less than 5% for a_d less than 0.1 μm . For the A_{5m} and A_{5c} parameters, the absolute errors are less than 40% for a_d , a_m , and a_c less than 0.1 μm . The accuracy with which the EAGR parameterization is able to assess the sensitivity of the droplet number concentration to chemical and microphysical parameters should be sufficient for this study, although for very low updrafts and very large particle sizes, the error can be large [Nenes and Seinfeld, 2003]. The former situations are infrequent, while the latter case would activate easily, so neither is expected to give a gross error. For most cases, the droplet number concentration is most sensitive to particles that activate at supersaturations close to the maximum supersaturation of the parcel. The radii of such particles are usually in the range of 0.05–0.15 μm [Nenes et al., 2001]. The performance of the EAGR parameterization will be evaluated subsequently by comparing its predictions to those of a full, numerical parcel model.

Equation (2.13) is expanded to

$$\begin{aligned}
 A_{5i} &= A^* - A_4 \ln\left(\frac{A_3 a_i^3}{r_c^{*3}}\right) = A^* - A_4 \ln\left(\frac{A_3 a_i^3 \lambda}{r_c^{*3} \lambda}\right) \\
 &= A^* - A_4 \ln\left(\frac{A_3}{\lambda r_c^{*3}}\right) - A_4 \ln(\lambda a_i^3) \\
 &= A' - 3A_4 \ln\left(\lambda^{1/3} a_i\right) = A' - A_6 \ln(a_i)
 \end{aligned} \tag{2.14}$$

where $A' = A^* - A_4 \ln(A_3/r_c^{*3})$, $A_6 = 3A_4$, and $\lambda = 1$ (length)⁻³. By substituting equation (2.14) into equations (2.12) and (2.11), the following is obtained

$$s_{\max} = \frac{2}{\sqrt{B}} \left(\frac{A' - A_6 \ln(a_c)}{3a_c} \right)^{3/2} \quad (2.15a)$$

$$s_m = \frac{2}{\sqrt{B}} \left(\frac{A' - A_6 \ln(a_m)}{3a_m} \right)^{3/2} \quad (2.15b)$$

To obtain explicit expressions for a_c and a_m , one more approximation to equations (2.15a) and (2.15b) is needed, which is to substitute the logarithmic terms with average values of a_c and a_m that are relevant for the atmosphere. The range of values for a_m is taken from *Whitby* [1978], and the limits for a_m are set at twice the limits of a_c :

$$\ln(a_c) \approx \overline{\ln(a_c)} = \int_{1 \times 10^{-7} \text{ cm}}^{1 \times 10^{-6} \text{ cm}} \ln(a_c) da_c = -14.6 \quad (2.16a)$$

$$\ln(a_m) \approx \overline{\ln(a_m)} = \int_{2 \times 10^{-7} \text{ cm}}^{2 \times 10^{-6} \text{ cm}} \ln(a_m) da_m = -13.9 \quad (2.16b)$$

The total error incurred by the assumptions and approximations that have been made throughout this derivation will be analyzed in section 2.3.6 by comparing the predictions of the approximate model to those of a detailed parcel model. The numerical values used in equations (2.16a) and (2.16b) are not optimized and can be further adjusted based on datasets other than those of *Whitby* [1978].

2.3.5 The Modified Parameterization (Single Mode)

Solving equations (2.15a) and (2.15b) for a_c and a_m , with the aforementioned approximations, results in the following expressions:

$$a_c = \frac{A' - A_6 \overline{\ln(a_c)}}{3} \left(\frac{2}{\sqrt{B} s_{\max}} \right)^{2/3} \quad (2.17a)$$

$$a_m = \frac{A' - A_6 \overline{\ln(a_m)}}{3} \left(\frac{2}{\sqrt{B} s_m} \right)^{2/3} \quad (2.17b)$$

Substituting equations (2.17a) and (2.17b) into the expression for u leads to the following expression:

$$u = \frac{\ln \left[k_c \left(\frac{s_m}{s_{\max}} \right)^{2/3} \right]}{\sqrt{2} \ln(\sigma)} \quad (2.18)$$

where

$$k_c = \frac{A' - A_6 \overline{\ln(a_c)}}{A' - A_6 \overline{\ln(a_m)}} \quad (2.19)$$

The error function of the u parameter [$\text{erf}(u)$] represents the fraction of the total aerosol number concentration that remains as interstitial aerosol after activation has taken place.

The maximum parcel supersaturation is obtained by *Abdul-Razzak et al.* [1998] by using the functions $f_1(\ln\sigma)$ and $f_2(\ln\sigma)$, which are used to fit the ratio of s_m and s_{\max} to a numerical solution of the governing equations:

$$\left(\frac{s_m}{s_{\max}}\right)^2 = f_1(\ln\sigma)\left(\frac{\zeta}{\eta}\right)^{3/2} + f_2(\ln\sigma)\left(\frac{s_m^2}{\eta + 3\zeta}\right)^{3/4} \quad (2.20)$$

where $f_1(\ln\sigma) = 0.5 \exp[2.5 \ln^2(\sigma)]$, $f_2(\ln\sigma) = 1 + 0.25 \ln(\sigma)$, $\zeta = 2/3(\alpha W/G)^{1/2} A_{5c}$, $\eta = [1/(2\pi\rho_w\gamma N_{\text{ap}})](\alpha W/G)^{3/2}$, and W is the updraft velocity. All other parameters are defined in Table 2.2. These expressions for $f_1(\ln\sigma)$ and $f_2(\ln\sigma)$ are the corrected expressions given in *Abdul-Razzak and Ghan* [2000] for a multimodal aerosol. Note also that the expression for ζ differs from the original expression given by *Abdul-Razzak et al.* [1998], in that the A parameter is replaced with the A_{5c} parameter.

Surface tension changes of the growing droplet introduce two new quantities: the k_c parameter in the u function [equation (2.18)] and the A_{5c} parameter in the ζ parameter. The k_c parameter accounts for the differences in the radii, a_m and a_c . The A_{5c} parameter takes into account the surface tension changes. When surface tension effects become negligible, $k_c \rightarrow 1$, and the original parameterization of *Abdul-Razzak et al.* [1998] is obtained.

2.3.6. Comparison to a Numerical Parcel Model

The EAGR parameterization is compared to an adiabatic parcel model with explicit microphysics to evaluate its ability to represent particle activation [Nenes et al.,

Table 2.2. Equations for Physical Parameters G , α , and γ^α

Equation	Symbol Definitions
$\alpha = \frac{gM_w L}{C_{pa} RT^2} - \frac{gM_{air}}{RT}$	α = radius independent coefficient g = acceleration due to gravity L = latent heat of vaporization of water C_{pa} = specific heat of dry air at constant pressure M_{air} = molar mass of air
$\gamma = \frac{RT}{p_s M_w} + \frac{M_w L^2}{C_{pa} p M_{air} T}$	γ = radius independent coefficient p_s = saturation vapor pressure p = pressure
$G = \frac{1}{\frac{\rho_w RT}{p_s D_V M_w} + \frac{L \rho_w}{K_a T} \left(\frac{L M_w}{RT} - 1 \right)}$	G = growth coefficient D_V = diffusivity of water in air K_a = thermal conductivity of air

^aFrom [Pruppacher and Klett, 1997].

2002a]. Figure 2.2 shows the activation ratio as a function of updraft velocity as computed with the parcel model and with the surface tension parameterization. The activation ratio calculated using the EAGR parameterization differs from that calculated using the parcel model. Part of this discrepancy is inherent in the original *Abdul-Razzak et al.* [1998] parameterization (as can be seen by comparing the predictions of droplet number concentration in the absence of surface tension effects). Nevertheless, the EAGR parameterization reasonably captures the relative change in maximum supersaturation and droplet number concentration when a soluble organic compound is introduced into the aerosol. The presence of surface tension effects decreases the maximum supersaturation by 10% in both the EAGR parameterization and the parcel model. Thus, derivatives of the EAGR expression for the number of particles activated should give physically realistic sensitivities to variations of key parameters, and especially relative sensitivities.

2.3.7 Extension of EAGR Parameterization to Multimodal Aerosol Populations

The multimode lognormal aerosol size distribution is given by

$$n(\ln a_d) = \sum_{i=1}^I \frac{N_{api}}{\sqrt{2\pi \ln(\sigma_i)}} \exp \left[-\frac{\ln^2 \left(\frac{a_d}{a_{mi}} \right)}{2 \ln^2(\sigma_i)} \right] \quad (2.21)$$

where the subscript i indicates a quantity that is specific to aerosol population mode i .

The generalized parameterization for a multimodal aerosol population consists of

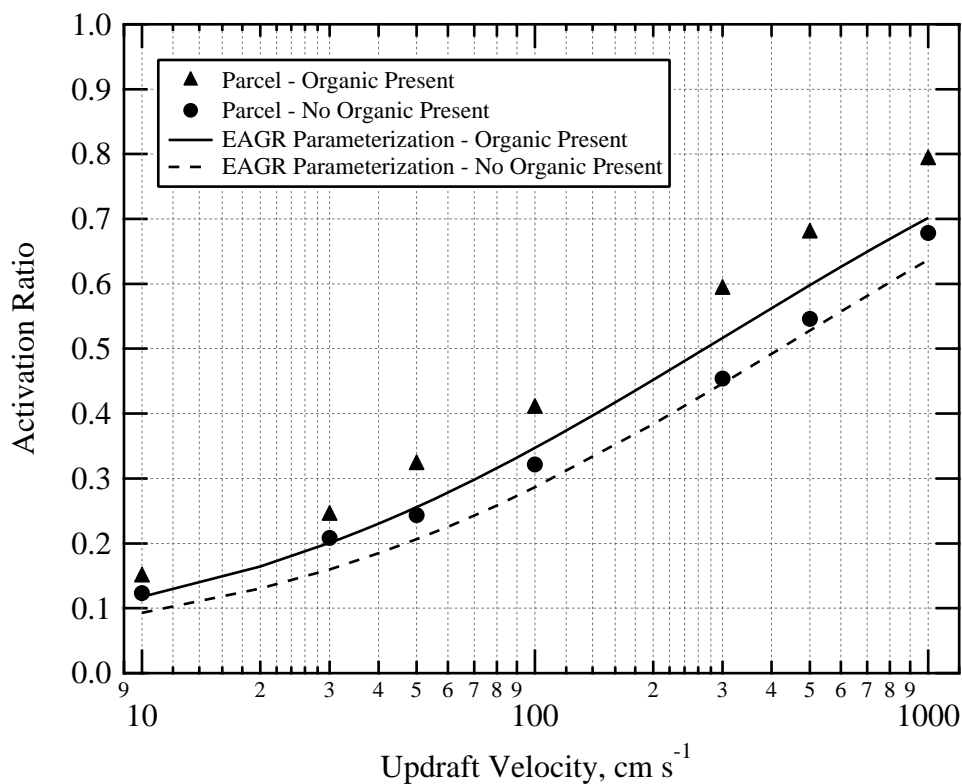


Figure 2.2. Activation ratio as a function of updraft velocity for the full numerical parcel model and the EAGR parameterization, in the presence and absence of dissolved organic material. The aerosol is 10% organic and 90% $(\text{NH}_4)_2\text{SO}_4$ when organics are present. Properties of the organic material and ammonium sulfate and the aerosol size distribution are given in Table 2.1.

the equations in Table 2.3. Some of the parameter definitions differ from those in *Abdul-Razzak and Ghan* [2000] because the Köhler curvature coefficient, A , has been replaced with the modified coefficients, A_{5mi} and A_{5ci} , in the ζ parameter and s_m :

$$s_{mi} = \frac{2}{\sqrt{B_i}} \left(\frac{A_{5mi}}{3a_{mi}} \right)^{3/2} \quad (2.22a)$$

$$\zeta_i = \frac{2}{3} \left(\frac{\alpha W}{G} \right)^{1/2} A_{5ci} \quad (2.22b)$$

where $A_{5ji} = A_i' - A_6 \ln(\bar{a}_j)$. In the expression for A_{5ji} , a_j represents the geometric mean radius ($j = m$) or the radius of the smallest activated aerosol particle ($j = c$). A new parameter, $k_{ci} = A_{5ci}/A_{5mi}$, is introduced in the u_i parameter to account for the differences in the a_c and a_m :

$$u_i = \frac{\ln \left[k_{ci} \left(\frac{s_{mi}}{s_{\max}} \right)^{2/3} \right]}{\sqrt{2} \ln(\sigma_i)} \quad (2.23)$$

2.4 Sensitivity Analysis

Using the EAGR parameterization, the sensitivity of the activated droplet number concentration, N , with respect to any parameter χ , where χ denotes ε_o , σ , N_{ap} , or a_m , is given by

Table 2.3. Multimodal Surface Tension Parameterization

Equation
$N = \sum_{i=1}^I \frac{N_{api}}{2} [1 - \text{erf}(u_i)]^a$
$B_i = \left(\frac{M_w \rho_{api}}{\rho_w} \right) \left(\frac{\varepsilon_{si} v_{si}}{M_{si}} + \frac{\varepsilon_{oi} v_{oi}}{M_{oi}} \right)$
$S_{\max} = \frac{1}{\left\{ \sum_{i=1}^I \frac{1}{S_{mi}^2} \left[f_{1i}(\sigma_i) \left(\frac{\zeta_i}{\eta_i} \right)^{3/2} + f_{2i}(\sigma_i) \left(\frac{S_{mi}^2}{\eta_i + 3\zeta_i} \right)^{3/4} \right] \right\}^{1/2}}^a$
$f_1(\sigma_i) = 0.5 \exp[2.5 \ln^2(\sigma_i)]^a$
$f_2(\sigma_i) = 1 + 0.25 \ln(\sigma_i)^a$
$\eta_i = \frac{1}{2\pi\rho_w\gamma N_{api}} \left(\frac{\alpha W}{G} \right)^{3/2} a$
$A'_i = A^* - A_4 \ln \left(\frac{A_{3i}}{r_{ci}^{*3}} \right)$
$r_{ci}^* = \left(\frac{3B_i a_{mi}^3}{A^*} \right)^{1/2}$
$A_{3i} = \frac{\varepsilon_{oi} v_{ci} \rho_{api} A_2}{M_{oi}}$

^aFrom *Abdul-Razzak et al.* [2000]

$$dN/d\chi_j = (\partial N/\partial\chi_j) + (\partial N/\partial u_j)(\partial u_j/\partial\chi_j) \quad (2.24)$$

where the subscript j indicates that the parameter can be specific to a single mode of a multimodal aerosol size distribution (e.g., the geometric mean radius of the coarse mode) and

$$\frac{\partial N}{\partial u_j} = -\sum_{i=1}^I \left(\frac{N_{api}}{\sqrt{\pi}} \right) \exp(-u_i^2) \quad (2.25)$$

Equation (2.25) can be evaluated for a unimodal aerosol population for $i, j = 1$. Here, $\partial N/\partial\chi_j = 0$ for all χ_j , other than the total aerosol number concentration, N_{apj} :

$$\partial N/\partial N_{apj} = (1/2)[1 - \text{erf}(u_j)] \quad (2.26)$$

Equation (2.24) for $\chi_j = N_{ap}$ is exactly the Twomey effect because it describes the sensitivity of N to N_{ap} . The sensitivities of N to all other aerosol properties, except for size distribution characteristics, are considered to represent the chemical effects, and the sensitivity of N to W describes the dynamical effects.

Expressions for the sensitivity of N with respect to the updraft velocity (W), N_{apj} , organic mass fraction (ε_o), and geometric standard deviation (σ) and geometric mean radius (a_m) of the aerosol size distribution are given in Table 2.4 for unimodal and multimodal aerosols. Although the latter sensitivities (e.g., with respect to σ , a_m) are not from chemical effects on aerosols, they have been included in this study for

Table 2.4. Derivatives of the Droplet Number Concentration with Respect to Various χ_j for a Multimodal Aerosol Population^a

χ_j	$\frac{\partial u_i}{\partial \chi_j}$	$\frac{\partial s_{mj}}{\partial \chi_j}$	$\frac{\partial s_{\max}}{\partial \chi_j}$
W	$-\frac{\sqrt{2}}{3 \ln(\sigma_i) s_{\max}} \frac{\partial s_{\max}}{\partial W}$	0	$\frac{\sum_{i=1}^I \frac{3}{2W s_{mi}^2} \left[-f_{1i}(\sigma_i) \left(\frac{\zeta_i}{\eta_i} \right)^{3/2} + \frac{3f_{2i}(\sigma_i) s_{mi}^{3/2}}{4(\eta_i + 3\zeta_i)^{3/4}} (\eta_i + \zeta_i) \right]}{2 \left\{ \sum_{i=1}^I \frac{1}{s_{mi}^2} \left[f_{1i}(\sigma_i) \left(\frac{\zeta_i}{\eta_i} \right)^{3/2} + f_{2i}(\sigma_i) \left(\frac{s_{mi}^2}{\eta_i + 3\zeta_i} \right)^{3/4} \right] \right\}^{3/2}}$
N_{apj}	$-\frac{\sqrt{2}}{3 \ln(\sigma_i) s_{\max}} \frac{\partial s_{\max}}{\partial N_{apj}}$	0	$\frac{-3}{2s_{mj}^2 N_{apj}} \left[f_{1j}(\sigma_j) \left(\frac{\zeta_j}{\eta_j} \right)^{3/2} - \frac{f_{2j}(\sigma_j) s_{mj}^{3/2} \eta_j}{2(\eta_j + 3\zeta_j)^{3/4}} \right]$ $2 \left\{ \sum_{i=1}^I \frac{1}{s_{mi}^2} \left[f_{1i}(\sigma_i) \left(\frac{\zeta_i}{\eta_i} \right)^{3/2} + f_{2i}(\sigma_i) \left(\frac{s_{mi}^2}{\eta_i + 3\zeta_i} \right)^{3/4} \right] \right\}^{3/2}$
\mathcal{E}_{oj}^b	$\frac{A_4}{\sqrt{2} \ln(\sigma_j)} \left(\frac{1}{A_{5cj}} - \frac{1}{A_{5mj}} \right) \left[\frac{3M_w v_{oj} \rho_{apj}}{2M_{oj} \rho_w B_j} + \frac{\rho_{apj}}{2} \left(\frac{1}{\rho_{insj}} - \frac{1}{\rho_{oj}} \right) - \frac{1}{\varepsilon_{oj}} \right]$ $+ \frac{\sqrt{2}}{3 \ln(\sigma_j)} \left(\frac{1}{s_{mj}} \frac{\partial s_{mj}}{\partial \varepsilon_{oj}} - \frac{1}{s_{\max}} \frac{\partial s_{\max}}{\partial \varepsilon_o} \right) \quad (i = j)$ $-\frac{\sqrt{2}}{3 \ln(\sigma_j) s_{\max}} \frac{\partial s_{\max}}{\partial \varepsilon_{oj}} \quad (i \neq j)$	$\frac{s_{mj} M_w v_{oj} \rho_{apj}}{2B_j M_{oj} \rho_w} \left(\frac{9A_4}{2A_{5mj}} - 1 \right) +$ $\frac{s_{mj} \rho_{apj}}{2} \left(\frac{1}{\rho_{insj}} - \frac{1}{\rho_{oj}} \right) \left(\frac{3A_4}{2A_{5mj}} - 1 \right)$	$\frac{\left[\frac{2f_{1j}(\sigma_j) \left(\frac{\zeta_j}{\eta_j} \right)^{3/2}}{s_{mj}^{3/2}} + \frac{f_{2j}(\sigma_j)}{2(\eta_j + 3\zeta_j)^{3/4}} \right] \frac{1}{s_{mj}^{3/2}} \frac{\partial s_{mj}}{\partial \varepsilon_{oj}}}{2A_{5cj} s_{mj}^{3/2} \left[\frac{3M_w v_{oj} \rho_{apj}}{2M_{oj} \rho_w B_j} + \frac{\rho_{apj}}{2} \left(\frac{1}{\rho_{insj}} - \frac{1}{\rho_{oj}} \right) - \frac{1}{\varepsilon_{oj}} \right] \left[\frac{f_{1j}(\sigma_j) \left(\frac{\zeta_j}{\eta_j} \right)^{3/2}}{\eta_j^{3/2} s_{mj}^{3/2}} - \frac{3f_{2j}(\sigma_j)}{2(\eta_j + 3\zeta_j)^{3/4}} \right]}$ $2 \left\{ \sum_{i=1}^I \frac{1}{s_{mi}^2} \left[f_{1i}(\sigma_i) \left(\frac{\zeta_i}{\eta_i} \right)^{3/2} + f_{2i}(\sigma_i) \left(\frac{s_{mi}^2}{\eta_i + 3\zeta_i} \right)^{3/4} \right] \right\}^{3/2}$
σ_j (Multimodal)	$-\frac{1}{\sqrt{2} \sigma_j \ln^2(\sigma_j)} \ln \left[k_{cj} \left(\frac{s_{mj}}{s_{\max}} \right)^{2/3} \right] - \frac{\sqrt{2}}{3 \ln(\sigma_j) s_{\max}} \frac{\partial s_{\max}}{\partial \sigma_j} \quad (i = j)$ $-\frac{\sqrt{2}}{3 \ln(\sigma_j) s_{\max}} \frac{\partial s_{\max}}{\partial \sigma_j} \quad (i \neq j)$	0	$-\frac{1}{\sigma_j s_{mj}^{1/2}} \left\{ \frac{5 \ln(\sigma_j) f_{1j}(\sigma_j) \left(\frac{\zeta_j}{\eta_j} \right)^{3/2}}{s_{mj}^{3/2}} - \frac{0.25}{(\eta_j + 3\zeta_j)^{3/4}} \right\}$ $2 \left\{ \sum_{i=1}^I \frac{1}{s_{mi}^2} \left[f_{1i}(\sigma_i) \left(\frac{\zeta_i}{\eta_i} \right)^{3/2} + f_{2i}(\sigma_i) \left(\frac{s_{mi}^2}{\eta_i + 3\zeta_i} \right)^{3/4} \right] \right\}^{3/2}$

Table 2.4. Continued...

χ_j	$\frac{\partial u_i}{\partial \chi_j}$	$\frac{\partial s_{mj}}{\partial \chi_j}$	$\frac{\partial s_{\max}}{\partial \chi_j}$
σ (Unimodal)	$-\frac{1}{\sqrt{2}\sigma \ln^2(\sigma)} \ln \left[k_c \left(\frac{s_m}{s_{\max}} \right)^{\frac{2}{5}} \right] - \frac{\sqrt{2}}{3 \ln(\sigma) s_{\max}} \frac{\partial s_{\max}}{\partial \sigma}$	0	$\frac{-\frac{s_m}{\sigma} \left[4.5 \ln(\sigma) f_1 \left(\ln \sigma \right) \left(\frac{\zeta}{\eta} \right)^{\frac{3}{2}} + 0.25 \left(\frac{s_m^2}{\eta + 3\zeta} \right)^{\frac{3}{4}} \right]}{2 \left[f_1 \left(\ln \sigma \right) \left(\frac{\zeta}{\eta} \right)^{\frac{3}{2}} + f_2 \left(\ln \sigma \right) \left(\frac{s_m^2}{\eta + 3\zeta} \right)^{\frac{3}{4}} \right]^{\frac{3}{2}}}$
a_{mj}	$-\frac{9A_{\sigma 4}}{2\sqrt{2}a_{mj} \ln(\sigma_j)} \left(\frac{1}{A_{5cj}} - \frac{1}{A_{5mj}} \right)$ $+ \frac{\sqrt{2}}{3 \ln(\sigma_j)} \left(\frac{1}{s_{mj}} \frac{\partial s_{mj}}{\partial a_{mj}} - \frac{1}{s_{\max}} \frac{\partial s_{\max}}{\partial a_{mj}} \right) \quad (i = j)$ $-\frac{\sqrt{2}}{3 \ln(\sigma_j) s_{\max}} \frac{\partial s_{\max}}{\partial a_{mj}} \quad (i \neq j)$	$\frac{3s_{mj}}{2a_{mj}} \left(\frac{9A_4}{2A_{5mj}} - 1 \right)$	$\frac{\left[\frac{2f_1(\sigma_j) \left(\frac{\zeta_j}{\eta_j} \right)^{\frac{3}{2}}}{s_{mj}^3} + \frac{f_2(\sigma_j)}{2s_{mj}^{\frac{3}{2}} (\eta_j + 3\zeta_j)^{\frac{3}{4}}} \right] \frac{\partial s_{mj}}{\partial a_{mj}}}{-\frac{27A_4 \zeta_j}{4A_{5cj} a_{mj}} \left[\frac{f_1(\sigma_j) \left(\frac{\zeta_j}{\eta_j} \right)^{\frac{3}{2}}}{\eta_j s_{mj}^{\frac{3}{2}}} - \frac{3f_2(\sigma_j)}{2(\eta_j + 3\zeta_j)^{\frac{3}{4}}} \right]}$ $2 \left\{ \sum_{i=1}^I \frac{1}{s_{mi}^2} \left[f_1(\sigma_i) \left(\frac{\zeta_i}{\eta_i} \right)^{\frac{3}{2}} + f_2(\sigma_i) \left(\frac{s_{mi}^2}{\eta_i + 3\zeta_i} \right)^{\frac{3}{4}} \right] \right\}^{\frac{3}{2}}$

^a See Table 2.3 and text for equations for ζ_i , η_i , $f_1(\sigma_i)$, $f_2(\sigma_i)$, A_{5ci} , A_{5mi} , s_{mi} , s_{\max} , B_i , ρ_{api} , and A_4 .

^b Here, ε_{sj} is held constant.

completeness. The unimodal derivatives can be obtained from the multimodal derivatives by letting $i, j = 1$ and replacing the multimodal $f_{1i}(\sigma_i)$ and $f_{2i}(\sigma_i)$ with the unimodal $f_1(\ln \sigma)$ and $f_2(\ln \sigma)$, respectively, except in the σ case.

From these expressions, note that $\partial N / \partial W > 0$ because $\partial u_j / \partial W \geq 0$. For the other variables $\partial N / \partial \chi$ can be either positive or negative, and the sign will determine the relative importance of the chemical effects. This is an important difference between chemical and dynamical effects, as an increase in χ , which corresponds to a region of increased biomass burning or biogenic emissions, can enhance or decrease the sensitivity of N with respect to W . Note that this assumes that $\chi_j = N_{ap}$, σ , and ε_o (or ε_i) usually increase for increasingly polluted aerosols.

To examine the sensitivity of droplet number concentration to chemical effects relative to the sensitivity to dynamical effects (updraft velocity), the sensitivities are scaled to the same order by adopting the nondimensional form:

$$\phi(\chi) = \frac{\chi}{W} \frac{\partial N / \partial \chi}{\partial N / \partial W} \quad (2.27)$$

where the derivatives are evaluated at a nominal set of parameter values, evaluated from equation (2.24). When $|\phi(\chi)| \sim 1$, N is equally sensitive to changes in W and χ . When $|\phi(\chi)| \gg 1$, χ can dominate over changes in W ; while when $|\phi(\chi)| \ll 1$, N is relatively insensitive to χ . Positive values of $\phi(\chi)$ indicate that increasing χ and W both change N in the same direction (either both increase N or both decrease N). Negative values of $\phi(\chi)$ indicate that χ and W change N in opposite directions.

The sensitivity ratio, $\phi(\chi)$, is evaluated for the seven aerosol types given in Table 2.5. The aerosol size distribution characteristics are obtained from *Whitby* [1978]. The parameters chosen for investigation are the soluble organic mass fraction (constant for all modes) and the geometric mean radius (a_m). The presence of insoluble material in the dry aerosol is also considered. The soluble inorganic portion of the aerosol is assumed to be ammonium sulfate. For the trimodal aerosol, the accumulation mode geometric mean radius is chosen as the parameter of interest because it generally has the greatest influence on the droplet number concentration. Surface tension effects are not included in the mean radius sensitivity cases. The sensitivity ratio in the absence of surface tension effects leads to effects of smaller magnitude than with surface tension effects included in the mean radius cases.

Figure 2.3 shows $\phi(\varepsilon_o)$ for marine aerosol with (left panels) and without (right panels) surface tension effects; results are presented in the absence (top panels) and presence (bottom panels) of insoluble species. The rectangles represent the range of updraft velocities and organic mass fractions found in the atmosphere for stratocumulus clouds under marine conditions [*Seinfeld and Pandis*, 1998]. The general trend is that $\phi(\varepsilon_o)$, and thus the relative influence of the chemical effect, increases with increasing ε_o and W . This means that an increase in surface active organic component would tend to further enhance droplet formation compared to an aerosol composed of pure salt. This is clear when comparing to $\phi(\varepsilon_o)$ without surface tension effects; in this case, $\phi(\varepsilon_o)$ is negative because the dissolved moles of salt decrease with increasing organic fraction. Surface tension effects seem to compensate for the decreased hygroscopicity of the organic fraction, and increase the sensitivity of droplet number to variations in the updraft

Table 2.5. Cases Examined in Sensitivity Analysis

χ in $\phi(\chi)$	Case 1 ε_o	Case 2 ε_o	Case 3 ε_o	Case 4 ε_o	Case 5 a_m	Case 6 a_m	Case 7 a_m
Surface Tension Effects	Present	Present	Present	Present	Absent	Absent	Absent
Aerosol Size Distribution	Marine	Marine	Continental	Continental	Continental	Marine	Continental
Unimodal or Trimodal	Trimodal	Trimodal	Trimodal	Trimodal	Unimodal	Trimodal	Trimodal
Insoluble Mass Fraction	0	0.5	0	0.5	0	0	0

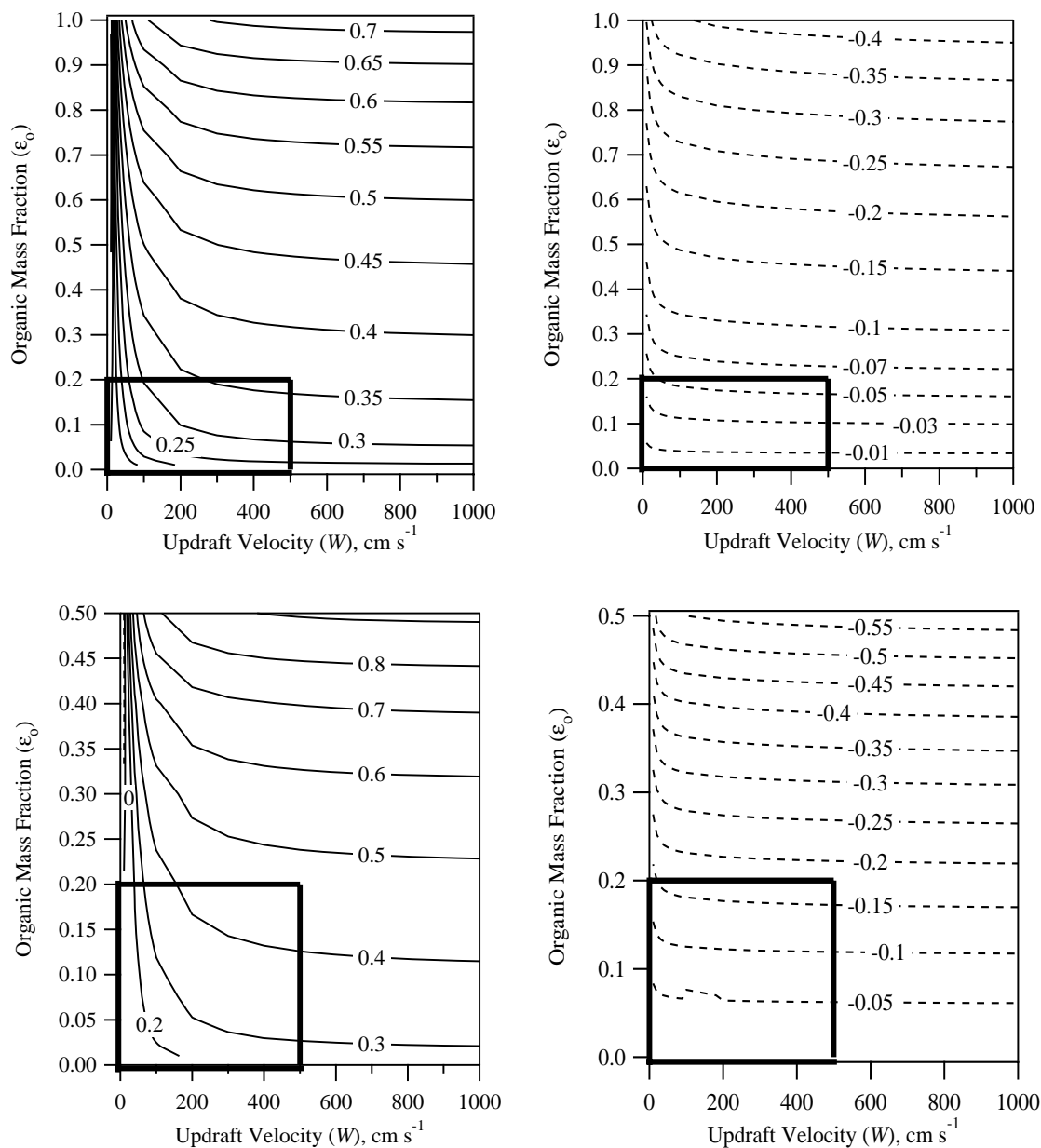


Figure 2.3. Sensitivity ratio $\phi(\epsilon_o)$ for a marine aerosol size distribution with (left) surface tension effects and without (right) surface tension effects. The aerosol consists of $(\text{NH}_4)_2\text{SO}_4$ and dissolved organics with no insoluble species present (top) and 50% insoluble species (bottom). The inner rectangles represent typical organic mass fraction and updraft velocity ranges for marine, stratocumulus conditions. Solid lines represent positive $\phi(\epsilon_o)$ values; dashed lines represent negative $\phi(\epsilon_o)$ values.

spectrum. The latter can be seen in Figure 2.3, where the lack of surfactant behavior yields an almost constant $\phi(\varepsilon_o)$ for all updraft velocities. Once a surfactant is placed in the CCN, $\phi(\varepsilon_o)$ is variable for a large range of updraft velocities, certainly under the range expected for marine stratocumulus. In the absence of insoluble species, $\phi(\varepsilon_o)$ ranges from 0.1 to 0.35 for typical marine conditions; with an insoluble mass fraction of 0.5, the sensitivity ratio ranges from 0 to 0.45. These values are consistent with the simulations of a detailed, numerical parcel model [Nenes *et al.*, 2002a]. Although $\phi(\varepsilon_o)$ (in the presence of surfactant species) is positive for most cases, negative values of $\phi(\varepsilon_o)$ occur in the lower panel of Figure 2.3 at very low W ($< 10 \text{ cm s}^{-1}$) and high ε_o (0.20–0.5). This means that an increase in ε_o would lead to a decrease in N because $\partial N/\partial W > 0$. Also, $\partial N/\partial \varepsilon_o < 0$ because, relative to the case with no soluble organic present [i.e., $\phi(0)$], more CCN activate earlier in the cloud updraft and deplete water vapor from the gas phase. As a result, the maximum supersaturation drops and, with it, the total number of activated CCN. Such dynamical readjustments are most effective under polluted conditions, such as the competition between sea salt and sulfate for CCN [Ghan *et al.*, 1998] and black carbon effects on cloud microphysics [Nenes *et al.*, 2002b]. However, for larger values of W , increases in ε_o lead to increases in the sensitivity. Although interesting, this effect occurs at values of ε_o and W that are not typically found in the marine atmosphere. Therefore, for most marine aerosols, $\phi(\varepsilon_o) > 0$. Given that $\phi(\varepsilon_o)$ has a magnitude between 0.1 and 0.5 under marine conditions, one concludes that surface tension effects can exhibit an important effect on activated droplet number concentration (when present). For a given ε_o , $\phi(\varepsilon_o)$ increases with updraft

velocity, because the maximum supersaturation increases, and, thus, the potential for CCN activation is greater (this effect is not seen when the surface tension effect is excluded). However, as smaller nuclei activate, decreases in surface tension are less effective in facilitating activation, because the concentration of soluble organics at the critical diameter drops as the particle dry diameter decreases [see equations (2.8) and (2.9)]. The latter effect leads to an “asymptotic” limit in $\phi(\varepsilon_o)$, which is generally reached, for the current set of parameters, at an updraft velocity of 5 m s^{-1} . Mathematically, this limit can be derived by $\partial^2 N / \partial \varepsilon_o^2 = \partial^2 N / \partial W^2$. At low updraft velocities (in the presence of surfactants), $\phi(\varepsilon_o) \sim 0.1$, regardless of ε_o . The maximum supersaturation for these parcels is very low, and under these conditions, perturbations in droplet number concentration result in dynamical readjustments in cloud maximum supersaturations that tend to maintain constant N . This variation in $\phi(\varepsilon_o)$ means that the importance of ε_o variability will depend on the cloud regime. The strongest surface tension effects are expected to be seen in cumulus and stratocumulus clouds, where updraft velocities are relatively high.

For the multimodal, continental aerosol shown in Figure 2.4, $\phi(\varepsilon_o)$ increases with decreasing ε_o and increasing W for most of the parameter range. The $\phi(\varepsilon_o)$ values for typical continental conditions range from 0 to 0.2 in the absence of insoluble species and from 22 to 0.5 when the insoluble mass fraction is 0.5 (both in the presence of surfactants). In the absence of surfactants, $\phi(\varepsilon_o)$ is negative and becomes larger as the organic mass fraction increases; this is expected, as the decreased hygroscopicity is most prominent when the CCN has a substantial amount of organics. Similar to what is seen

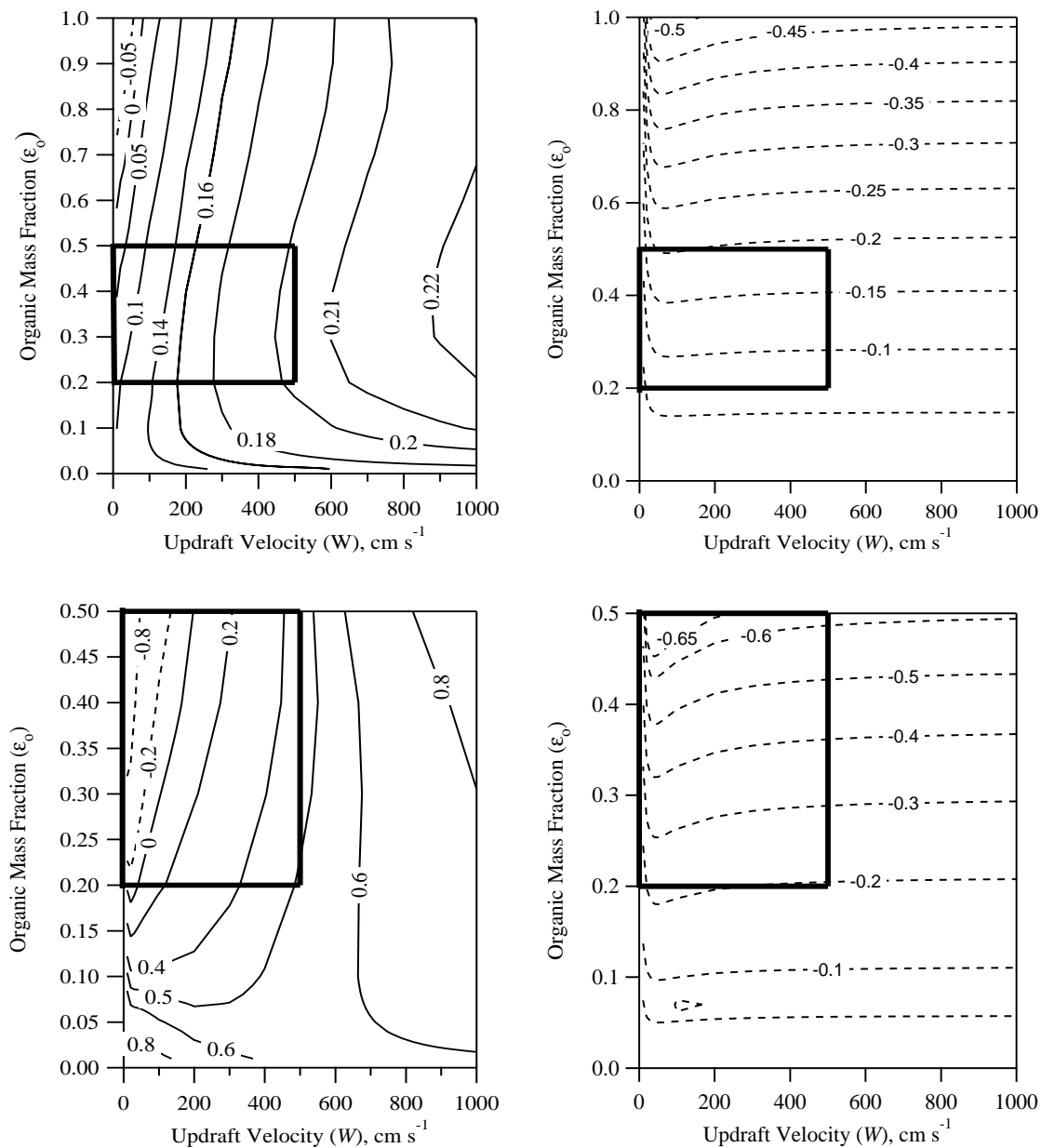


Figure 2.4. Sensitivity ratio $\phi(\varepsilon_o)$ for a continental aerosol size distribution with (left) surface tension effects and without (right) surface tension effects. The aerosol consists of $(\text{NH}_4)_2\text{SO}_4$ and dissolved organics with no insoluble species present (top) and 50% insoluble species (bottom). The inner rectangles represent typical organic mass fraction and updraft velocity ranges for stratocumulus clouds under continental conditions. Solid lines represent positive $\phi(\varepsilon_o)$ values; dashed lines represent negative $\phi(\varepsilon_o)$ values.

under marine conditions, $\phi(\varepsilon_o)$ exhibits negative values at low W and high ε_o , which become larger in the presence of surfactants. Negative $\phi(\varepsilon_o)$ values are more prevalent for continental conditions as compared to marine conditions, because the higher concentration of aerosol decreases the maximum supersaturation even further for the same change in ε_o .

Note from Figure 2.4 that there are areas of atmospheric relevance where $\phi(\varepsilon_o) \sim 0$, which generally occurs for low W and high ε_o (in the presence of surfactants) and low ε_o (in the absence of surfactant species). In these regions, the sensitivity of N to W is much greater than that of N to ε_o , and chemical effects can be negligible, or cancel out, particularly if the updraft velocity distribution is centered on a W for which $\phi(\varepsilon_o) \sim 0$.

For a given ε_o , $\phi(\varepsilon_o)$ increases with updraft velocity, as was seen under marine conditions in Figure 2.3. However, under continental conditions, the asymptotic limit occurs for small updraft velocities ($W < 50 \text{ cm s}^{-1}$) and the transition to the asymptotic regime is not as sharp as for marine conditions. For $W < 700 \text{ cm s}^{-1}$, increases in ε_o lead to decreases in $\phi(\varepsilon_o)$; for $W > 700 \text{ cm s}^{-1}$, increases in ε_o lead to increases in $\phi(\varepsilon_o)$. Again, the variation in the behavior of $\phi(\varepsilon_o)$ at constant W indicates that the importance of changes in ε_o depends on the cloud regime. As was seen under marine conditions, the strongest positive effects (in the presence of surfactants) are expected when updraft velocities are high.

A comparison between the $\phi(\varepsilon_o)$ values of Figures 2.3 and 2.4 at particular values of W and ε_o further exemplifies this trend. For $W = 200 \text{ cm s}^{-1}$ and $\varepsilon_o = 0.3$, $\phi(\varepsilon_o)$ for marine conditions is about 0.38 in the absence of insoluble species and about 0.53 with

an insoluble mass fraction of 0.5 (both in the presence of surfactants). For continental conditions, $\phi(\varepsilon_o)$ is about 0.16 in the absence of insoluble species and about 0.19 for an insoluble mass fraction of 0.5. Under these conditions, the presence of an insoluble species seems to have a small effect on droplet activation, which is consistent with a full activation model [Nenes *et al.*, 2002a].

Figure 2.5 shows that $\phi(a_m)$ is largest for low W and a_m for a unimodal aerosol population, representative of a continental accumulation mode aerosol. The inner rectangle represents the ambient range of unimodal mean radius and organic mass fractions. Values of $\phi(a_m)$ in Figure 2.5 vary from 0.01 to 1.5. The positive values of $\phi(a_m)$ result because the droplet number concentration is positively correlated with both updraft velocity and the geometric mean radius. The sensitivity of N with respect to a_m , although positive, decreases as a_m becomes larger. Thus, as a_m increases, $\phi(a_m) \rightarrow 0$. The high sensitivity of N to a_m results because a_m exerts a strong effect on the shape of the CCN spectrum, which controls both the time at which the CCN start to absorb water as well as the maximum supersaturation achieved in the rising air parcel. In addition, N is less sensitive to large a_m than to small a_m . Particles with large radii activate for lower updraft velocities than those with small a_m . Whereas the activation fraction is relatively large with a large value for a_m , the differential change in N is small. With small a_m , the droplet number concentration tends to be smaller, and changes in the number activated will have a larger effect on total N .

Figure 2.6 shows $\phi(a_{mA})$, where the subscript A refers to the accumulation mode, for marine (top panel) and continental (bottom panel) aerosol size distributions. The inner rectangles represent the range of accumulation mode radius and organic mass

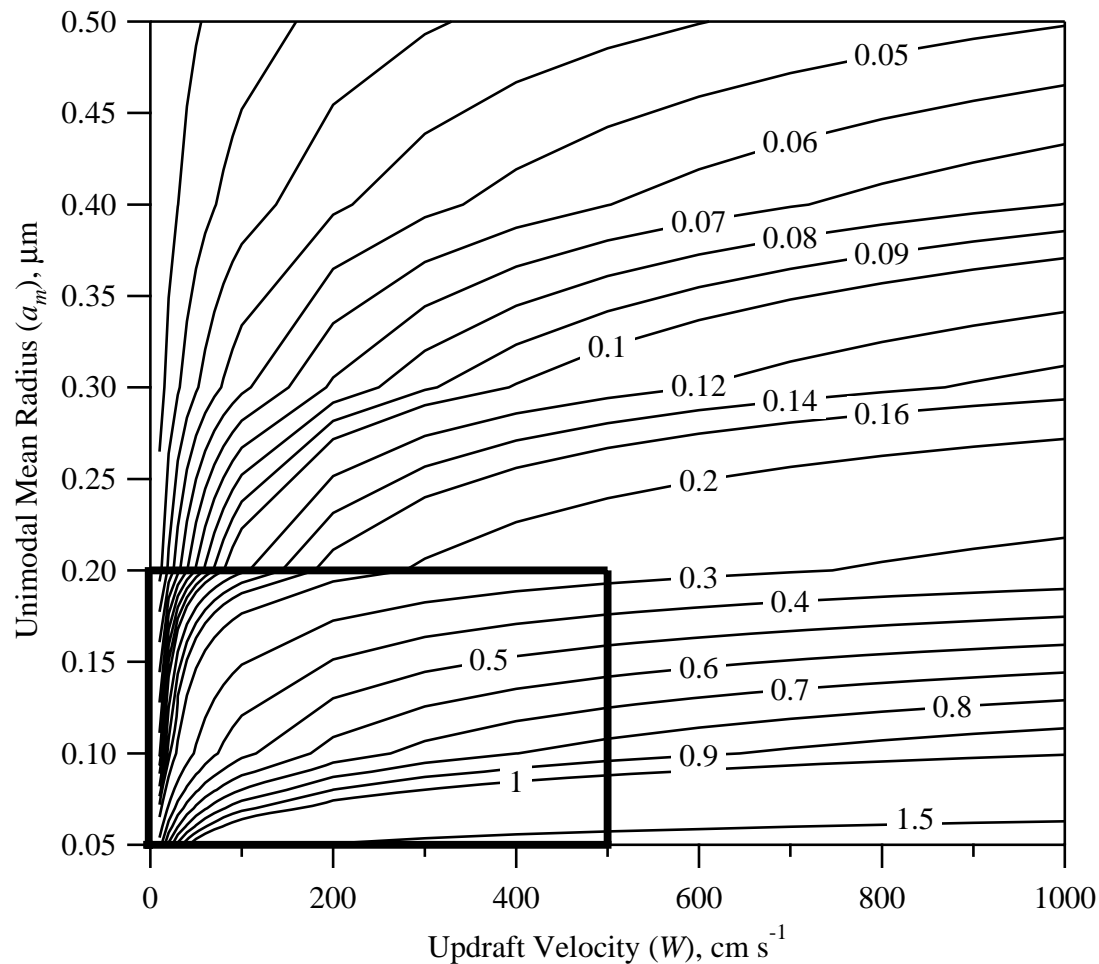


Figure 2.5. Sensitivity ratio $\phi(a_m)$ for single-mode aerosol with $N_{ap} = 1000 \text{ cm}^{-3}$ and $\sigma = 2$. The aerosol is assumed to be composed of pure $(\text{NH}_4)_2\text{SO}_4$. The inner rectangle represents the typical unimodal mean radius and updraft velocity ranges for stratocumulus clouds under continental conditions. Solid lines represent positive $\phi(a_m)$ values.

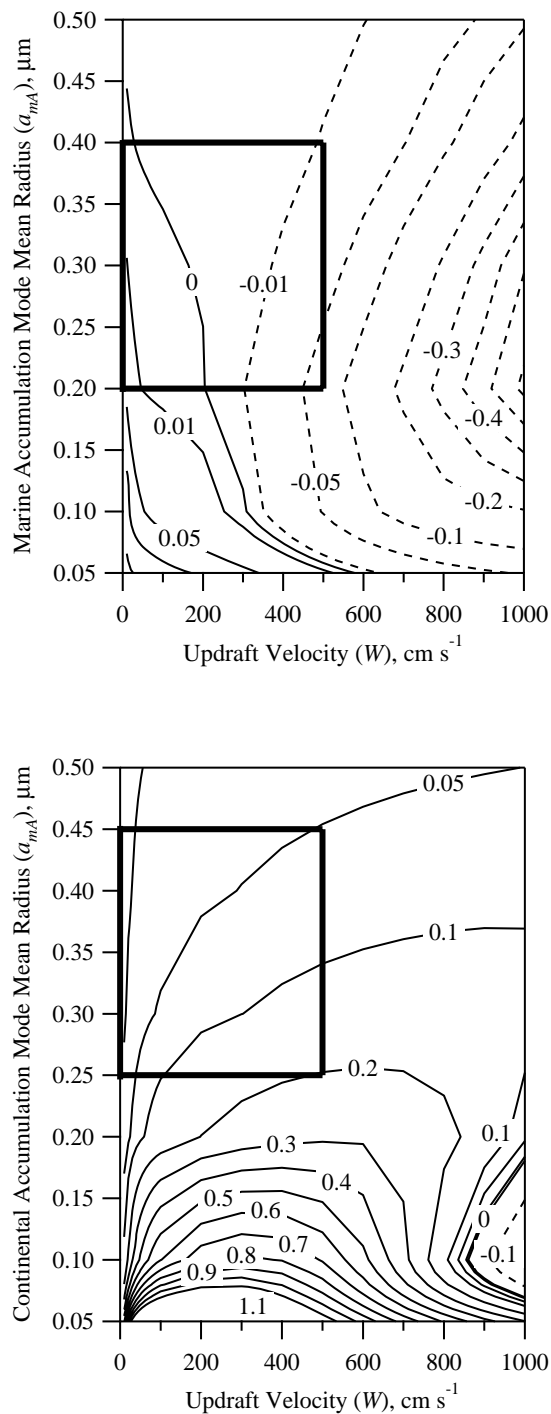


Figure 2.6. Sensitivity ratio $\phi(a_{mA})$: marine (top) and continental (bottom) aerosol size distributions. The aerosol is assumed to be composed of pure $(\text{NH}_4)_2\text{SO}_4$. The inner boxes represent typical accumulation mode mean radius and updraft velocity ranges for stratocumulus clouds under marine and continental conditions. Solid lines represent positive $\phi(a_{mA})$ values; dashed lines represent negative $\phi(a_{mA})$ values.

fractions found in the atmosphere for marine and continental conditions, as reflected by measurements (e.g., *Whitby*, 1978). The values for $\phi(a_{mA})$ vary from -0.6 to 0.3 for marine conditions and from -0.2 to 3.6 for continental conditions. When the aerosol size distribution is shifted toward smaller sizes, fewer CCN become activated in the initial stages of the cloud, and more water vapor is available for subsequent activation. By contrast, with a greater number of large particles present, the water vapor is absorbed earlier in the cloud resulting in less water vapor being available for subsequent particle growth. For this reason, $\phi(a_{mA})$ becomes negative for large a_{mA} and large updraft velocities. These results are consistent with those of *Cohard et al.* [1998, 2000].

For $W = 200 \text{ cm s}^{-1}$ and $a_{mA} = 0.1 \text{ }\mu\text{m}$, $\phi(a_{mA})$ is about 0.02 for marine conditions and about 0.8 for continental conditions. Generally, cloud droplet formation is more sensitive to the geometric mean radius under continental conditions than under marine conditions. Since the total aerosol number concentration is larger for continental conditions than for marine conditions, the absolute number of activated droplets is also larger for continental conditions, and thus there is greater competition for water vapor among the particles.

2.5 Conclusions

The conditions under which chemical effects can either amplify or dampen the Twomey effect are assessed by determining relative sensitivities of different parameters, χ to that of updraft velocity, W : $\phi(\chi) = (\chi/W)(\partial N/\partial\chi)/(\partial N/\partial W)$. Expressions for the sensitivity of N with respect to updraft velocity (W), aerosol number concentration (N_{ap}), organic mass fraction (ε_o), and geometric standard deviation (σ) and geometric mean

radius (a_m) of the aerosol size distribution are derived for both unimodal and multimodal size distributions based on an extension of Köhler theory and the parameterization of *Abdul-Razzak et al.* [1998] and *Abdul-Razzak and Ghan* [2000] (Table 2.4). Both marine and continental conditions are studied.

Although an increase in anthropogenic pollution (N_{ap}) leads to an increase in the number of cloud droplets formed, negative $\phi(\varepsilon_o)$ values are found for high ε_o , which is reflective of increasingly polluted conditions. Therefore, an increase in anthropogenic pollution can have two competing effects on cloud formation: (i) an increased number of CCN activated by increased N_{ap} and (ii), a decreased number of CCN activated by a greater presence of soluble organics. Consequently, regimes exist in which an increase in anthropogenic aerosol can actually lead to a decrease in cloud droplet number. The direction in which the presence of a soluble organic affects CCN activation will depend on the chemical characteristics of the aerosol, including its size distribution.

Chemical effects on cloud droplet number are complex, but not intractable. A range of computed sensitivity ratios show that chemical effects can, in some instances, be as influential as (or more influential than) variations in updraft velocity. Depending on atmospheric conditions, chemical effects can either enhance or weaken the activation process. An important finding is that, adding surfactants to the CCN drastically changes the character of the activation process; $\phi(\varepsilon_o)$ becomes a strong function of updraft velocity (this is not seen for the same aerosol in the absence of surfactants). This implies that, when studying aerosol-cloud interactions, the most influential (in terms of droplet number) updraft may not be in the peak of the probability distribution. Such insight is critical for understanding the aerosol indirect effect in both modeling studies and field

experiments. Future work should focus on determining the range of solubility, hygroscopicity, and surfactant properties necessary to have an important effect on droplet number.

The results of the current study provide insight into the role of surface tension lowering organics on cloud properties on a global and single-cloud scale. On a global scale, the variability of both updraft velocities and soluble aerosol organic content can be used to identify regions for which organics can have the strongest influence on cloud properties (both positive or negative). On the scale of a single cloud, since one would not expect to see the variability in organic mass fraction that is seen on global scales, N is controlled primarily by dynamical conditions. The conditions for which variations in ε_o either magnify, diminish, or do not affect the variability of cloud droplet number concentration can be isolated from the variations caused by other quantities, such as aerosol number concentration and W .

One exception to this is in ship tracks. On the boundaries of such cloud systems, large variability in chemical composition can be seen. One can envision transitioning between a region where the additional CCN have no effect on cloud properties, $\phi(\varepsilon_o) \sim 0$; to a region where cloud droplet number concentration decreases, $\phi(\varepsilon_o) < 0$; to a region where cloud droplet number concentration increases, $\phi(\varepsilon_o) > 0$. Given that the meteorological conditions across ship track boundaries (i.e., updraft velocity distribution) are not expected to change appreciably, it is possible that changes can be primarily controlled by chemical effects, such as are illustrated here. The large variation in sign predicted for $\phi(\varepsilon_o)$ for polluted conditions may help explain why cloud droplet number concentration is not always strongly correlated with CCN number in ship tracks.

Acknowledgements. This work was supported by Office of Naval Research Grant N-00014-96-1-0119. An anonymous reviewer is also thanked for helpful suggestions.

2.6 References

- Abdul-Razzak, H., and S.J. Ghan (2000), A parameterization of aerosol activation: 2. Multiple aerosol types, *J. Geophys. Res.*, *105*(D5), 6837 – 6844.
- Abdul-Razzak, H., S.J. Ghan, and C. Rivera-Carpio (1998), A parameterization of aerosol activation: 1. Single aerosol type, *J. Geophys. Res.*, *103*(D6), 6123 – 6131.
- Cohard, J.-M., J.-P. Pinty, and C. Bedos (1998), Extending Twomey's analytical estimate of nucleated cloud droplet concentrations from CCN spectra, *J. Atmos. Sci.*, *55*(22), 3348 – 3357.
- Cohard, J.-M., J.-P. Pinty, and K. Suhre (2000), On the parameterization of activation spectra from cloud condensation nuclei microphysical properties, *J. Geophys. Res.*, *105*(D9), 11,753 – 11,766.
- Facchini, M. C., M. Mircea, S. Fuzzi, and R. J. Charlson (1999), Cloud albedo enhancement by surface-active organic solutes in growing droplets, *Nature*, *401*(6750), 257 – 259.
- Ghan, S. J., G. Guzman, and H. Abdul-Razzak (1998), Competition between sea-salt and sulfate particles as cloud condensation nuclei, *J. Atmos. Sci.*, *55*(22), 3340 – 3347.
- Houghton, J. T., Y. Ding, D. J. Griggs, M. Noguer, P. J. van der Linden, and D. Xiaosu, Eds., (2001), *Climate Change 2001: The Scientific Basis*, 944 pp., Cambridge University Press, Cambridge, U.K.
- Junge, C. E. (1952): Die Konstitution der atmosphärischen aerosols, *Ann. Meteorol.*, *1*(55), 128 – 135.
- Khvorostyanov, V. I. and J. A. Curry (1999), A simple analytical model of aerosol properties with account for hygroscopic growth 1. Equilibrium size spectra and cloud condensation nuclei activity spectra, *J. Geophys. Res.*, *104*(D2), 2175 – 2184.
- Nenes, A. and J. H. Seinfeld (2003), Parameterization of cloud droplet formation in global climate models, *J. Geophys. Res.*, *108*(D14), 4415, doi:10.1029/2002JD002911.
- Nenes, A., S. Ghan, H. Abdul-Razzak, P. Y. Chuang, and J. H. Seinfeld (2001), Kinetic limitations on cloud droplet formation and impact on cloud albedo, *Tellus*, *53*(2), 133 – 149.
- Nenes, A., R. J. Charlson, M. C. Facchini, M. Kulmala, A. Laaksonen, and J. H. Seinfeld (2002a), Can chemical effects on cloud droplet number rival the first indirect effect? *Geophys. Res. Lett.*, *29*(17), 1848, doi: 10.1029/2002GL015295.

Nenes, A., W. C. Conant, and J. H. Seinfeld (2002b), Black carbon radiative effect on cloud microphysics and implications for the aerosol indirect effect 2. Cloud microphysics, *J. Geophys. Res.*, *107*(D21), 4605, doi:10.1029/2002JD002101.

Pruppacher, H. R. and J. D. Klett (1997), *Microphysics of Clouds and Precipitation: Second Revised and Enlarged Edition With an Introduction to Cloud Chemistry and Cloud Electricity*, 954 pp., Springer, New York City, NY.

Seinfeld, J. H. and S. N. Pandis (1998), *Atmospheric Chemistry: From Air Pollution to Climate Change*, 1326 pp., John Wiley & Sons, Inc., New York, NY.

Twomey, S. (1977), *Atmospheric Aerosols*, 302 pp., Elsevier, St. Louis, MO.

Whitby, K. T., (1978), The physical characteristics of sulfur aerosols, *Atmos. Environ.*, *12*(1-3), 135 – 159.

Chapter 3

CHARACTERIZATION OF AMBIENT AEROSOL FROM MEASUREMENTS OF
CLOUD CONDENSATION NUCLEI DURING THE 2003 ATMOSPHERIC
RADIATION MEASUREMENT AEROSOL INTENSIVE OBSERVATIONAL
PERIOD AT THE SOUTHERN GREAT PLAINS SITE IN OKLAHOMA*

* Full Citation: Rissman, T. A., T. M. VanReken, J. Wang, R. Gasparini, D. R. Collins, H. H. Jonsson, F. J. Brechtel, R. C. Flagan, and J. H. Seinfeld (2006), Characterization of ambient aerosol from measurements of cloud condensation nuclei during the 2003 Atmospheric Radiation Measurement Aerosol Intensive Observational Period at the Southern Great Plains site in Oklahoma, *Journal of Geophysical Research*, 111(D5), D05S11, doi: 10.1029/2004JD005695.

© 2006 American Geophysical Union (AGU). This chapter is reprinted with permission from the American Geophysical Union.

3.1 Abstract

Measurements were made by a new cloud condensation nuclei (CCN) instrument (CCNC3) during the Atmospheric Radiation Measurement (ARM) Program's aerosol intensive observational period (IOP) in May 2003 in Lamont, Oklahoma. An inverse aerosol/CCN closure study is undertaken, in which the predicted number concentration of particles available for activation (N_P) at the CCNC3 operating supersaturations is compared to that observed (N_O). N_P is based on Köhler theory, with assumed and inferred aerosol composition and mixing state, and the airborne aerosol size distribution measured by the Caltech dual automatic classified aerosol detector (DACAD). An initial comparison of N_O and N_P , assuming the ambient aerosol is pure ammonium sulfate ((NH₄)₂SO₄), results in closure ratios (N_P/N_O) ranging from 1.18 to 3.68 over the duration of the IOP, indicating that the aerosol is less hygroscopic than (NH₄)₂SO₄. N_P and N_O are found to agree when the modeled aerosol population has characteristics of an external mixture of particles, in which insoluble material is preferentially distributed among particles with small diameters (< 50 nm) and purely insoluble particles are present over a range of diameters. The classification of sampled air masses by closure ratio and aerosol size distribution is discussed in depth. Inverse aerosol/CCN closure analysis can be a valuable means of inferring aerosol composition and mixing state when direct measurements are not available, especially when surface measurements of aerosol composition and mixing state are not sufficient to predict CCN concentrations at altitude, as was the case under the stratified aerosol layer conditions encountered during the IOP.

3.2 Introduction

One of the largest uncertainties in aerosol radiative forcing is associated with the indirect effect, which results from the relationship between atmospheric aerosols and cloud formation, properties, and lifetime [Houghton *et al.*, 2001]. Twomey [1974, 1977] postulated that an increase in the number concentration of atmospheric aerosol particles would increase the number of cloud droplets formed for a given air mass. For fixed liquid water content, the cloud droplets would also be smaller than those formed under conditions with lower particle concentrations. This increase in number and decrease in mean diameter of cloud droplets would have two indirect effects on climate. Cloud albedo is greater for clouds with more numerous, smaller droplets; this has been termed the first indirect climatic effect of aerosols. Also, the lifetime of a cloud with smaller cloud droplets is greater than that of a cloud with larger droplets because the rain forming mechanisms are less efficient [Warner, 1968; Albrecht, 1989]. This is referred to as the second indirect climatic effect of aerosols. Both effects create clouds that are more reflective and more persistent, leading to the cooling of the earth's surface [Twomey, 1977].

The relationship between atmospheric particles that are capable of activating into cloud droplets, known as cloud condensation nuclei (CCN), and aerosol size distribution and composition, in addition to meteorological conditions, are central to the indirect climatic effect of aerosols. For a given particle composition and size, the supersaturation above which the particle undergoes spontaneous condensational growth (activation) into a cloud droplet, the so-called critical supersaturation, is described by Köhler theory. The activation diameter, the dry diameter at which a particle of known or assumed

composition will activate, can also be calculated for a given supersaturation. Prediction of aerosol activation from Köhler theory is very successful for aerosols composed of soluble, inorganic salts, such as ammonium sulfate ((NH₄)₂SO₄), sodium chloride (NaCl), and ammonium bisulfate (NH₄HSO₄). However, Köhler theory needs to be augmented when considering chemical components, such as organic compounds, that are partially soluble, insoluble, or affect the surface tension of the aqueous solution. The chemical composition of atmospheric aerosol can be complex and include many different chemical species, which may affect aerosol activation in competing ways.

The ability of Köhler theory to predict ambient CCN concentrations can be studied by comparing atmospheric CCN measurements at a given supersaturation with CCN concentrations calculated using aerosol size distribution and composition measurements. This type of study, called an aerosol/CCN closure, compares the observed CCN concentration (N_O) at the operating supersaturation of the CCN instrument to that predicted from the aerosol size distribution and composition (N_P) in a closure ratio, defined here as N_P/N_O . N_P is determined from the aerosol size distribution by summing the concentration of particles with diameters greater than the activation diameter calculated from Köhler theory [VanReken *et al.*, 2003]. When direct measurements of aerosol composition are unavailable, N_P can be calculated using an assumed aerosol composition or one that is inferred from other available measurements. An “inverse” aerosol/CCN closure study (explained further in section 3.6) can be undertaken to determine aerosol composition and mixing states that are most consistent with CCN observations when direct measurements of these aerosol characteristics are unavailable.

In this chapter, data measured by a new CCN instrument (CCNC3) during the Atmospheric Radiation Measurement (ARM) aerosol intensive observational period (IOP) in May 2003 are used in an inverse aerosol/CCN closure study of the mid-continental aerosol sampled near the southern great plains (SGP) central facility (CF) to determine aerosol composition and mixing states consistent with the CCN measurements at the operating supersaturations of the instrument. The Texas A&M differential mobility analyzer/tandem differential mobility analyzer (DMA/TDMA) data from the surface are used to infer the mixing state and insoluble fraction of the aerosol population as a function of dry diameter. This information is used with the airborne CCN and aerosol size distribution measurements to determine conditions under which aerosol composition and mixing states inferred from surface measurements are able to reproduce CCNC3 measurements at altitude. Aerosol properties, categorized by closure ratio and aerosol size distribution shape, during pollution and smoke events are also discussed.

3.3 ARM Aerosol IOP

The ARM Aerosol IOP occurred from 5 to 31 May 2003 at the Department of Energy's (DOE's) ARM SGP CF in Lamont, Oklahoma. There were a total of 16 science flights, with a total of 60.6 flight hours, conducted by the Center for Interdisciplinary Remotely-Piloted Aircraft Studies' (CIRPAS) Twin Otter aircraft on 15 days during this period. The ARM Aerosol IOP flight tracks for flights 6–10 and 12–17 (the flights for which there are CCN data) are shown in Figure 3.1, which illustrates that most flights took place over or near the SGP CF. The last flight, flight 17, was coordinated with the

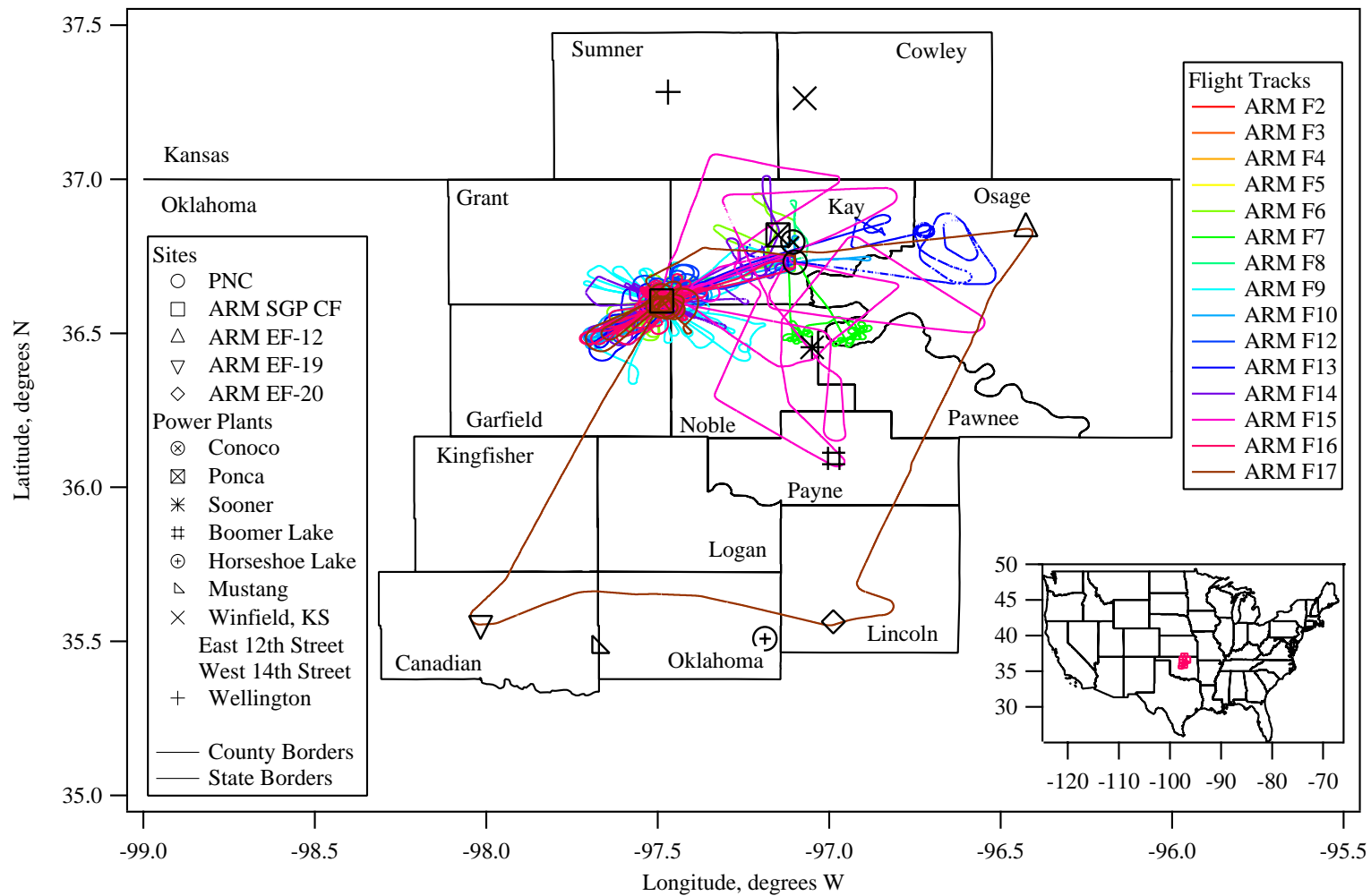


Figure 3.1. ARM Aerosol IOP flight paths for flights with CCN data. PNC is the Ponca City, Oklahoma, airport, where the Twin Otter was based. The other sites are ARM ground measurement sites. The insert shows the position of the counties (in pink) within the continental United States. The axes of the insert are in the same units as those in the main plot.

moderate resolution imaging spectroradiometer (MODIS) overpasses of four ARM sites (SGP CF, Extended Facility (EF)-12, EF-20, and EF-19 in Figure 3.1).

The ARM SGP site is located in a mid-latitude, continental area, surrounded by agricultural land and dirt roads. The site is influenced by local emissions from nearby industrial and power plants and local aerosol sources, such as vehicle and agricultural aerosols. Sulfur dioxide (SO₂) emissions from nearby oil refineries and power plants, such as the Conoco and Ponca City power plants, are major local sources of sulfate aerosols over the SGP site. Anthropogenic, agriculture-related aerosol sources include local fertilizer application and production, field burning, and animal byproducts. Local biomass burning is greatest from May through July [*Iziomon and Lohmann, 2003*]. The particles that are commonly found at the ARM SGP site are a complex mix of these aerosol types, with smoke- and dust-dominated events, which are commonly characterized by decreased aerosol hygroscopicity, occurring occasionally [*Sheridan et al., 2001*]. Routine condensation particle counter (CPC) measurements from the SGP site generally show a strong, diurnal cycle of aerosol number concentration, with peak concentrations in the afternoon and early evening. Over the 4-year period from July 1996 to June 2000, the daily average condensation nuclei (CN) concentration ranged from less than 1000 cm⁻³ to about 20,000 cm⁻³, with a mean around 5000 cm⁻³. The hourly average CN concentration ranged from about 4000 cm⁻³ from 1100 to 1500 UTC (Universal Time Coordinated) to about 18,000 cm⁻³ from 1800 to 2000 UTC [*Sheridan et al., 2001*]. (The difference between local time (LT) at the ARM site and UTC is 5–6 hours, depending on daylight savings. During the ARM Aerosol IOP, LT was 5 hours behind UTC, so that 1200 LT corresponds to 1700 UTC in this paper.) These high CN concentrations could

result from buildup and advection of pollutant aerosols from local sources, photochemical particle production [Sheridan *et al.*, 2001], coagulation, or the evolution of the boundary layer [Iziomon and Lohmann, 2003].

Most of the Twin Otter flights during the ARM Aerosol IOP were conducted under clear or partly cloudy skies to assess aerosol impacts on solar radiation. Additional flights targeted mostly cloudy conditions to assess aerosol/cloud interactions, test theoretical understanding of aerosol activation, and to test surface remote sensing of the indirect effect. Ground and airborne measurements, which included aerosol absorption, scattering, extinction, size distribution, and CCN concentration, are compared in a variety of closure studies to help resolve differences in measurements and models. Routine ARM SGP aerosol measurements (absorption, total scattering and hemispheric backscattering, light scattering as a function of relative humidity, total condensation particle concentration, number concentration of particles with diameters from 0.1 to 10 μm , vertical aerosol optical thickness, etc.) continued throughout the IOP.

3.4 Instrument Descriptions

3.4.1 Twin Otter Inlet System

In order to minimize sampling losses, the aerosol inlet on the CIRPAS Twin Otter is designed to admit the air sample prior to any bending of flow lines and slow the sample down before transport to the instruments. The intake extends forward from the roof of the cabin to a position 1.2 m directly above the aircraft's nose. The sampled air is initially slowed down by a factor of 5 by means of an aerodynamically lipped diffuser. A second diffuser, positioned at the centerline of the first diffuser, reduces the flow speed

by another factor of 2, while excess flow from the first diffuser exits along the sides of the second diffuser. The sample then flows down a 7.62 cm diameter duct and enters the cabin after a 45° bend. Inside the cabin the duct is straightened out again with another 45° bend, and samples are drawn to the various instruments from ports mounted on the side of the duct. The ports are flush inside the duct, but extend outward at 45° angle to the flow. At an aircraft speed of 50 m s⁻¹, approximately 1000 liters per minute (lpm) flow down the duct. Air not siphoned off to the instruments is dumped out of the cabin.

3.4.2 CCN Instrument (CCNC3)

The CCN instrument (CCNC3) deployed on the Twin Otter consists of three columns, each of which is physically modeled after a previous CCN instrument column design [Chuang *et al.*, 2000] with some changes to the physical design. Three temperature-controlled sections are used to create the desired temperature gradient, instead of fourteen sections, as in the work by Chuang *et al.* [2000]. The instrument was designed to be fully automated and software controllable in normal operation and to operate with a different supersaturation in each column. CCNC3 operating conditions, some aspects of which differ from those given by Chuang *et al.* [2000], are discussed in the following paragraphs. Only column 1 operated properly during the ARM Aerosol IOP, the first field mission in which the CCNC3 was deployed; thus CCN data were obtained at one supersaturation per flight.

Each CCNC3 column (Figure 3.2) consists of a stainless steel growth tube 0.4 m in length with a 1.9 cm outer diameter and a 1.6 mm wall thickness. The inner wall of the growth tube is lined with filter paper, which is rewetted by a small peristaltic pump

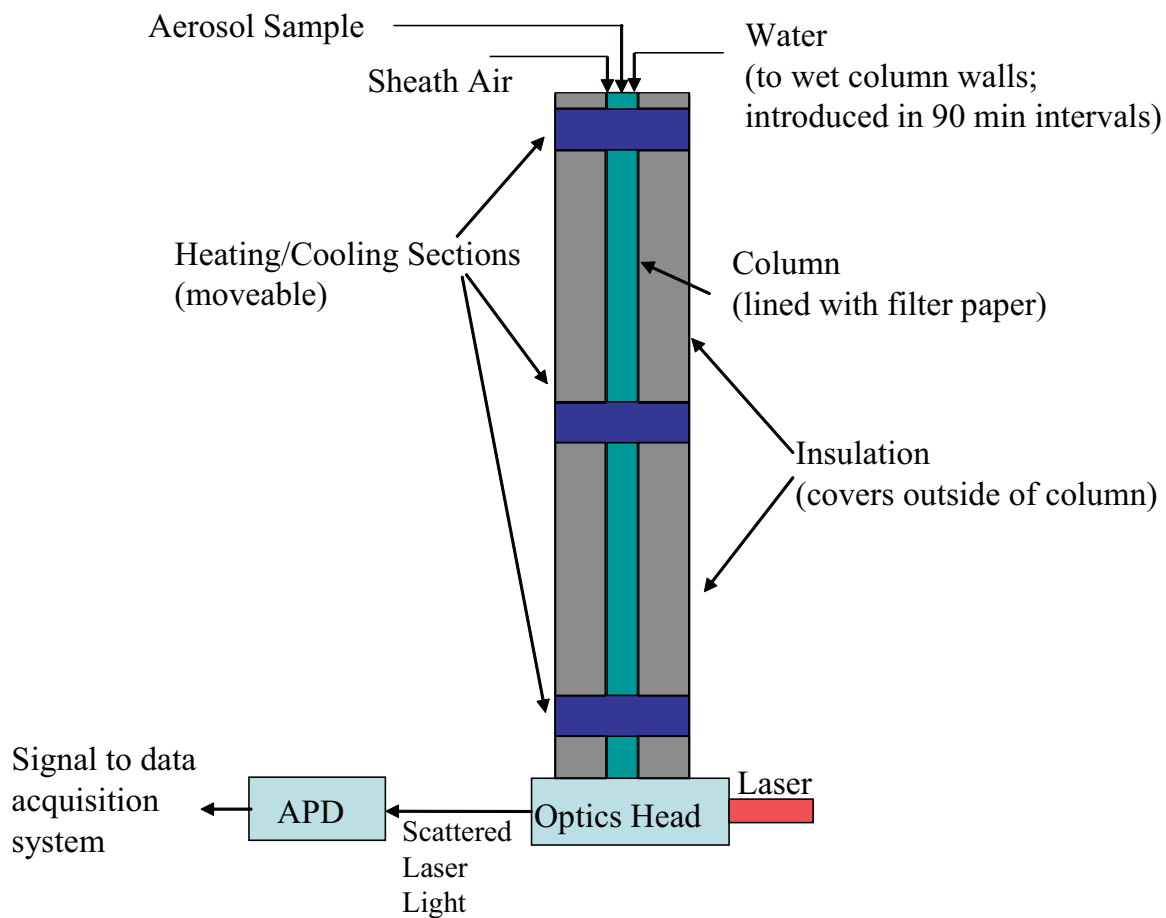


Figure 3.2. A schematic of a CCNC3 column. A second layer of insulation covers the growth tube and heating/cooling sections (to prevent temperature transfer to the outside air) and the detector (to prevent condensation within the optics tube).

every 90 min. Three temperature-controlled, moveable sections are in contact with the outer wall of the growth tube to create the desired temperature gradient, and, thus, the desired operating supersaturation, inside the growth tube. For the ARM Aerosol IOP, a linear temperature profile was used to develop a constant supersaturation at the centerline of the growth tube [*Rogers and Squires, 1977; Roberts and Nenes, 2005*]. (A linear temperature gradient was also used in the airborne CCN instruments during the Cirrus Regional Study of Tropical Anvils and Cirrus Layers—Florida Area Cirrus Experiment (CRYSTAL-FACE) [*VanReken et al., 2003; Roberts and Nenes, 2005*].) The sampled aerosol is focused onto the centerline of the growth tube and introduced to the column with filtered sheath air; the droplets that form within the growth tube are then counted by a detector.

The CCNC3 detector consists of a laser, an optics tube, and an avalanche photodiode (APD) module, and was designed on the basis of that of laser particle counter (LPC) model 3755 (TSI, Incorporated), scaled down for CCN application. A 670 nm, 10 mW Lasiris MFL Micro-Focus Laser is positioned at one end of an optics tube, so that the droplet inlet to the optics tube is at the 30 mm working distance of the laser. When a droplet falls through the laser beam, the laser light is scattered in the forward direction, and a pair of aspherical condenser lenses collects the scattered light and focuses it into a fiber optic at the other end of the optics tube. The signal from the scattered laser light is sent to a Hamamatsu Photonics C5460-01 APD module, which sends the resulting digital pulse to the data acquisition system.

During the IOP, the column operated at three different linear temperature gradients, with one temperature gradient per flight. The total flow rate of the column was

about 0.56 lpm with a sheath to sample ratio around 10. $(\text{NH}_4)_2\text{SO}_4$ calibrations for column 1 at its different linear temperature gradients are shown in Figure 3.3. The activation diameters and supersaturations associated with each linear temperature gradient are given in Figure 3.3. For each linear temperature gradient calibration, a solution of $(\text{NH}_4)_2\text{SO}_4$ was atomized to create droplets that were then dried and introduced into a differential mobility analyzer (DMA). Certain dry diameters were selected using the DMA and then split to the CCNC3 inlet and the inlet to a CPC (TSI, Inc., Model 3010). The activated ratio (AR) was calculated as the ratio of the number concentration of CCN measured by the CCNC3 (N_{CCN}) to the number concentration of total particles measured by the CPC (N_{CPC}). The activation diameter (d_{act}) is the dry diameter at which 50% of the particles are activated ($AR = 0.5$). The uncertainty limits given on the calibration curves in Figure 3.3 result from the uncertainty in the diameter produced by the DMA (generally taken to be $\pm 5\%$) and the combined uncertainties associated with the concentrations measured by the CPC and the CCNC3. These uncertainties associated with the column calibrations are folded into the overall measurement uncertainty, which is estimated for each flight on the basis of criteria explained in section 3.5.3.

The supersaturation corresponding to dry $(\text{NH}_4)_2\text{SO}_4$ particles with diameter d_{act} , and thus the operating supersaturation of the column, was calculated theoretically by Köhler theory. Droplet density is calculated from data of *Tang and Munkelwitz* [1994]; the full Pitzer model [*Pitzer*, 1973; *Pitzer and Mayorga*, 1973] is used to calculate the osmotic coefficient; and values from *Pruppacher and Klett* [1997] are used for surface tension. The model calculates the critical supersaturation for particles that contain certain

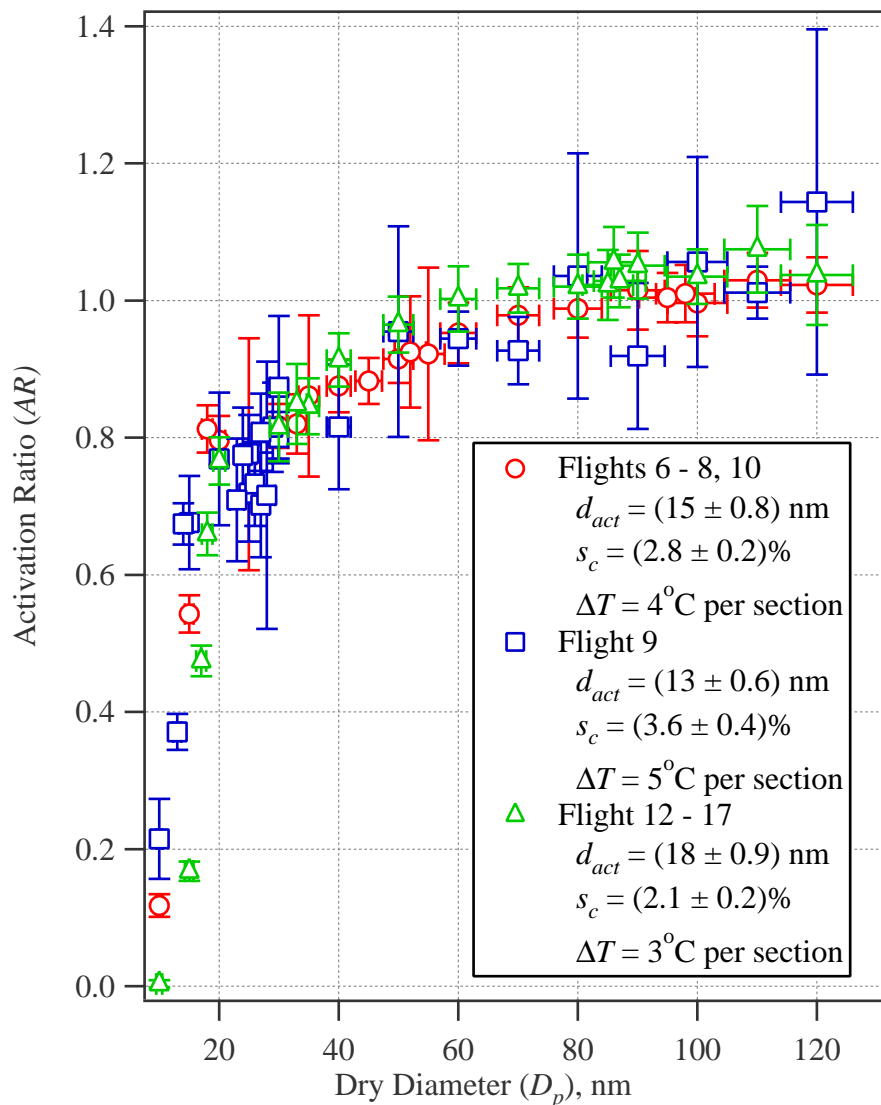


Figure 3.3. $(\text{NH}_4)_2\text{SO}_4$ calibration curves for column 1 of the CCNC3 at the temperature gradients used during the ARM Aerosol IOP. The column was not functioning properly for flights 1–5 and 11. The activation ratio is defined as the ratio of the number concentration of CCN measured by the CCNC3 to the number concentration of particles measured by the CPC.

soluble salts, certain organics, and generalized insoluble material [*Brechtel and Kreidenweis*, 2000a, 2000b].

The calibrated activation diameters and the operating supersaturations for column 1 during the ARM Aerosol IOP are given in the legend in Figure 3.3 and in Table 3.1. The instrument did not operate as expected from available instrument models and previous CCN instrument experience. Thermal contact between the temperature control sections and the growth column was improved in the design of the CCNC3. Therefore the CCNC3 requires a smaller temperature gradient than that required in previous CCN instruments to develop a similar supersaturation within the growth column. In-field calibrations were not available because the calibration CPC had been flooded with water. Therefore the operating supersaturations of the CCNC3 during the ARM Aerosol IOP were higher than would usually be desired for ambient aerosol studies. The consequences of these high supersaturations are further discussed in the Conclusion (section 3.8).

3.4.3 Dual Automatic Classified Aerosol Detectors (DACAD)

The Caltech dual automatic classified aerosol detectors (DACAD) have been deployed in several previous airborne experiments, and their characteristics are well documented [*Wang et al.*, 2002, 2003; *VanReken et al.*, 2003]. The DACAD consists of two DMA systems operated in parallel. One of the DMA systems measures the dry aerosol size distribution, while the other measures the aerosol size distribution at ambient relative humidity (*RH*) by using an active *RH* controller [*Wang et al.*, 2003]. The aerosol wet and dry size distributions are obtained separately and independent of each other;

Table 3.1. Flight Summary with Operating Conditions and Uncertainty Limits for CCNC3 Column 1

Flight	Day in May	Flight Begin Time ^a , UTC	Flight End Time ^a , UTC	Flight Length, Hours	Activation Diameter, nm	Operating Supersaturation, %	Upper Limit ^b , %	Lower Limit ^b , %
6		15:53	20:19	4.4			5	10
7	14	21:24	22:48	1.4	15 ± 0.8	2.8 ± 0.2	20	5
8	15	16:34	19:09	2.6			10	40
9	17	14:02	18:05	4.0	13 ± 0.6	3.6 ± 0.4	10	N/A
10	18	15:43	17:45	2.0	15 ± 0.8	2.8 ± 0.2	10	N/A
12	21	15:51	18:47	2.9			20	20
13	22	13:25	18:13	4.8			10	20
14	25	18:52	22:12	3.3			10	10
15	27	14:20	19:29	5.2	18 ± 0.9	2.1 ± 0.2	30	10
16	28	18:24	22:05	3.7			20	10
17	29	14:11	17:51	3.7			20	10

^aThe difference between local time (LT) and UTC was 5 hours during the ARM Aerosol IOP, so that 1200 LT corresponds to 1700 UTC.

^bUncertainty limits are reported as a percent of the measured concentration.

therefore no size-resolved information is obtained. The main components of each measurement system are a cylindrical DMA (TSI Inc., Model 3081) and a CPC (TSI Inc., Model 3010), which has a 50% counting efficiency at 10 nm. Using the scanning mobility technique, each DMA system generates a size distribution for particle diameters from ~ 17 to ~ 720 nm every 72.5 s [Wang and Flagan., 1990]. (This scanning time was reduced from 103 s [VanReken *et al.*, 2003] prior to the ARM Aerosol IOP.)

3.4.4 Tandem Differential Mobility Analyzer (DMA/TDMA)

The Texas A&M DMA/TDMA measured aerosol size distributions and size-resolved hygroscopic growth at the SGP cloud and radiation testbed (CART) trailer at the CF during the IOP [Gasparini *et al.*, 2006]. The main measurement section of the DMA/TDMA consists of two Aerosol Dynamics, Inc., high-flow DMAs (HF-DMAs; [Stolzenburg *et al.*, 1998]), a charger, two Nafion tubes, and a CPC. One DMA/TDMA measurement sequence (~ 1 hour) consists of two different operational modes to obtain both the aerosol size distribution and the size-resolved hygroscopic growth. For both modes, the sample air is first dried in a Nafion tube and then introduced to a charger before entering the first DMA. During the single DMA mode (~ 5 min), the aerosol size distribution is measured by scanning the voltage applied to the first DMA [Wang and Flagan, 1990] and counting the size-selected aerosol particle concentration with the CPC. In TDMA mode, the voltage supplied to the first DMA is fixed to produce a monodisperse aerosol of known particle size. The monodisperse aerosol is exposed to a controlled, elevated relative humidity (85% in this IOP) before entering the second DMA. The humidified aerosol is classified by scanning the voltage applied to the second DMA

and the size- and hygroscopicity-resolved aerosol particle concentration is observed with the CPC. The second mode sequence is repeated for other particle dry diameters by changing the voltage applied to the first DMA [Gasparini *et al.*, 2004]. A third mode was implemented during the IOP, in which the dry monodisperse aerosol was exposed to a wide range of *RH* to determine the deliquescence properties of the aerosol [Gasparini *et al.*, 2006].

The aerosol particle soluble fraction and mixing state is inferred by comparing the dry diameter separated by the first DMA with the hydrated size distribution measured with the second DMA. The comparison results in a normalized distribution expressed in terms of the hygroscopic growth factor ($G(RH)$), which is defined as the ratio of the hydrated particle diameter to that of the dry particle. The aerosol is then divided into four hygroscopicity-based categories: pure insoluble, pure soluble, mixed insoluble, and mixed soluble. The full technique used to determine the relative contribution of soluble and insoluble components to the dry particle composition is described by Gasparini *et al.* [2004].

3.4.5 PILS-IC, TEOM, and Integrating Nephelometer

At the SGP site, the aerosol ionic composition (species: NH_4^+ , SO_4^{2-} , NO_3^- , K^+ , Ca^{2+} , Mg^{2+} , Na^+ , and Cl^-) was measured using the particle-into-liquid sampler–ion chromatography (PILS-IC) technique [Weber *et al.*, 2001], and the aerosol total mass concentration was measured using the tapered element oscillating microbalance (TEOM) technique [Patashnick and Rupprecht, 1986]. The PILS-IC technique has a $\sim 0.05 \mu\text{g m}^{-3}$ limit of detection for all of the ions. The TEOM exhibited a temperature-related

oscillation behavior during the IOP that resulted in an uncertainty of $\pm 40\%$. The time resolution of the PILS-IC and TEOM were 8 min and 30 min, respectively, during the IOP. A sharp cut cyclone and two glass honeycomb denuders in series remove particles greater than 1 μm diameter and water-soluble vapor phase species, respectively, from the sample flow to both the PILS-IC and the TEOM. To prevent condensation of water within the tapered element, the TEOM inlet was maintained at 35°C [Pahlow *et al.*, 2006].

Routine aerosol light scattering coefficient (σ_{sp}) and light scattering hygroscopic growth factor ($f(RH)$) measurements for total and fine (submicron) mode aerosol continued at the ground site during the IOP. Measurements of σ_{sp} and $f(RH)$ complement those from the PILS-IC and TEOM. Total scattering and backscattering were measured with a three-wavelength integrating nephelometer (TSI Inc., Model 3563) [Sheridan *et al.*, 2001]. The light scattering hygroscopic growth factor, $f(RH)$, is different from the hygroscopic growth factor ($G(RH)$) determined from DMA/TDMA data. $G(RH)$ is based on the increase in particle diameter with increasing RH (see section 3.4.4), whereas $f(RH)$ is defined as the change in aerosol light scattering with changing RH [Covert *et al.*, 1972; Rood *et al.*, 1987] and is determined as the ratio of σ_{sp} at 80% to that at 40% RH . $f(RH)$ was measured using a humidograph [Carrico *et al.*, 1998], which consists of two nephelometers separated by a humidity control system that ramps up the RH in the second nephelometer. Data from the humidograph are used to relate σ_{sp} at any RH to that at 40% RH with a three-parameter curve-fitting model [Sheridan *et al.*, 2001].

3.5 Data Trends During the ARM Aerosol IOP

3.5.1 Particle Composition (PILS-IC, TEOM, and DMA/TDMA) and Aerosol Mixing State (DMA/TDMA)

Of the major inorganic ionic species (NH_4^+ , SO_4^{2-} , NO_3^- , K^+ , Ca^{2+} , Mg^{2+} , Na^+ , Cl^-) measured at the SGP site during the IOP, NH_4^+ and SO_4^{2-} were dominant. NO_3^- was observed in $\sim 10\%$ of the samples and only when SO_4^{2-} was completely neutralized by NH_4^+ . K^+ , a tracer for biomass burning, and Ca^{2+} , a tracer for dust, were occasionally observed in appreciable levels. On average, the ratio of NH_4^+ to SO_4^{2-} was 2, with ratios significantly greater than 2 observed on 20 May (no flight) and 22 May (flight 13) and less than 2 observed on 21 May (flight 12) [Pahlow *et al.*, 2006].

Aerosol organic fraction increased continuously during the daytime hours, while the inorganic concentration remained fairly constant. Overall, the aerosol organic content, which is estimated as the difference between total mass (TEOM) and total inorganic mass (PILS-IC), accounted for $> 40\%$ of the aerosol mass. Increases in organic fraction, values of which were as high as 80%, were accompanied by a lowering of $f(RH)$, suggesting that the particulate organic fraction had a lower hygroscopicity than the inorganic fraction. Also, the amount of aerosol organic mass correlated strongly with the amount of black carbon inferred from the aerosol absorption coefficient [Pahlow *et al.*, 2006], which was measured using a filter-based light absorption photometer [Sheridan *et al.*, 2001].

Gasparini *et al.* [2006] inferred size-resolved aerosol particle composition and hygroscopic growth properties from data collected by the Texas A&M DMA/TDMA at the SGP site using the technique from Gasparini *et al.* [2004]. The $G(RH)$ of the observed aerosol during the IOP was found to increase with increasing dry diameter, and

the average median $G(RH)$ at 85% RH was 1.20 at 12 nm and 1.37 at 300 nm, which indicates that the smallest analyzed particles were largely composed of carbonaceous compounds. The largest particles were either very hygroscopic or slightly hygroscopic, but rarely exhibited hygroscopicity in between these extremes. At times during the IOP, a nonhygroscopic mode with median $G(RH)$ less than 1.10 was observed at 450 and 600 nm and, more rarely, at 200 and 300 nm [Gasparini *et al.*, 2006].

3.5.2 Aerosol Size Distribution (DACAD - Airborne)

The aerosol size distributions measured by the DACAD were analyzed for flights 6–10 and 12–17, for which CCN data were collected. Aerosol size distributions differed greatly between flights, as well as at different altitudes within a single flight. For example, Figure 3.4 shows DACAD aerosol size distributions from six level legs and five different altitudes from flight 16. At the lower altitudes, 351 m and 720 m AGL (above ground level; all reported altitudes are AGL), the aerosol size distributions are multimodal with median diameters less than the cutoff diameter of the DACAD (~ 17 nm), which may indicate that the sampled aerosols are freshly emitted or formed locally in the atmosphere. The aerosol populations at 1028 m and 1337 m have similar size distributions that are multimodal with median diameters that may be smaller than the cutoff diameter of the DACAD, which may indicate mixed aerosol layers that are a combination between fresh and aged aerosol populations. The aerosol population at 2281 m during flight 16 is multimodal but with a less pronounced second mode at larger diameters, which is indicative of background aerosol. Also note that the $dN/d\log D_p$ values are greater for lower-altitude level legs than higher legs, which is a typical feature

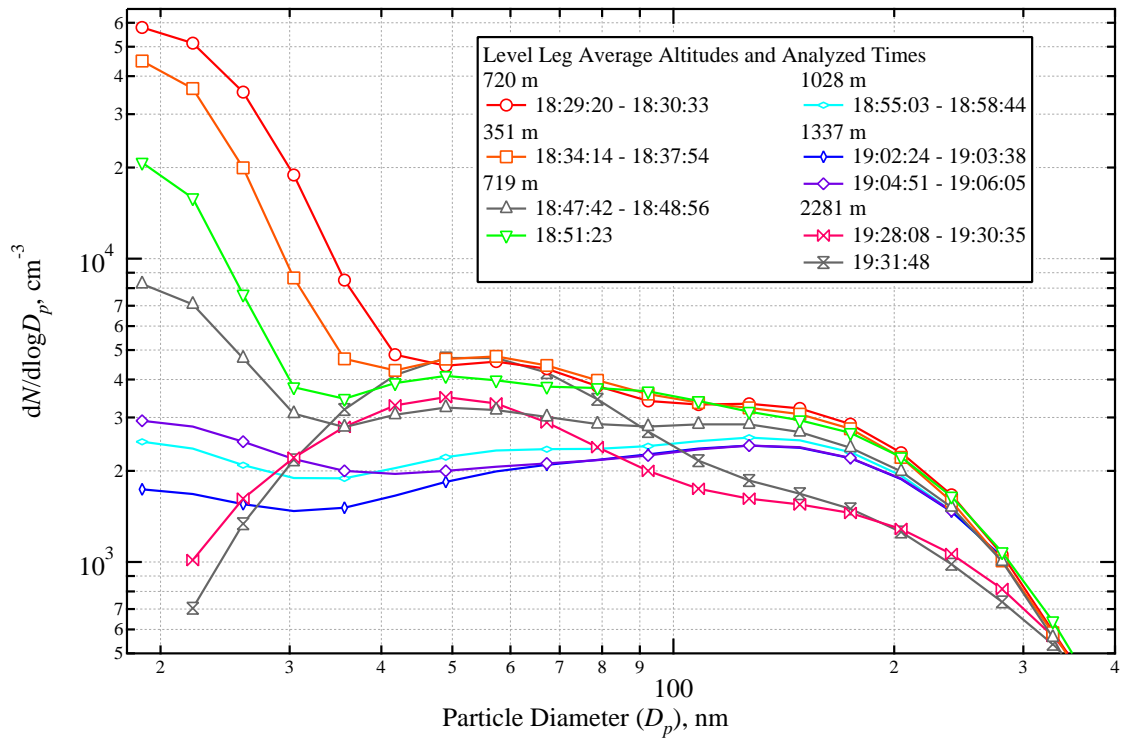


Figure 3.4. Aerosol size distributions from different level legs during flight 16. The legend gives the average altitudes (AGL) and times analyzed for each level leg. The times given are UTC; 1700 UTC corresponds to 1200 LT.

of ambient aerosol. Aerosol size distributions such as those shown in Figure 3.4 were seen throughout the IOP flights, along with some simple unimodal distributions. The differences in aerosol size distributions are consistent with sampled aerosol layers that had different sources and/or were of different ages.

Rapidly changing aerosol size distributions were observed frequently during the IOP. Since the DACAD size distribution scan time is 72.5 s, some characteristics of a rapidly changing aerosol size distribution may not have been resolved. The CCNC3 has a sampling rate of 1 s and, therefore, is capable of observing rapid changes in the aerosol size distribution. For this reason, predicted and observed CCN concentrations may not agree well during times of rapidly changing aerosol characteristics. This will be discussed further in section 3.6.

3.5.3 CCN Concentration (CCNC3-Airborne)

The trends in the CCN concentration data follow those seen in both the airborne CPC and airborne DACAD data. When present, homogeneous boundary layers are easily discerned from plots of CCNC3, CPC, and DACAD data, e.g., Figure 3.5 for flight 14. A more specific CCN trend analysis is discussed in section 3.7.

The airborne CPC had a cutoff diameter of 13 nm, and the DACAD scanned particle sizes down to ~ 17 nm. The CCN number concentrations are always less than the total particle number concentrations measured by the CPC or the DACAD in any of the eleven flights, even though the activation diameters for pure $(\text{NH}_4)_2\text{SO}_4$ particles at the operating supersaturations of the CCNC3 are similar to the cutoff diameters for the

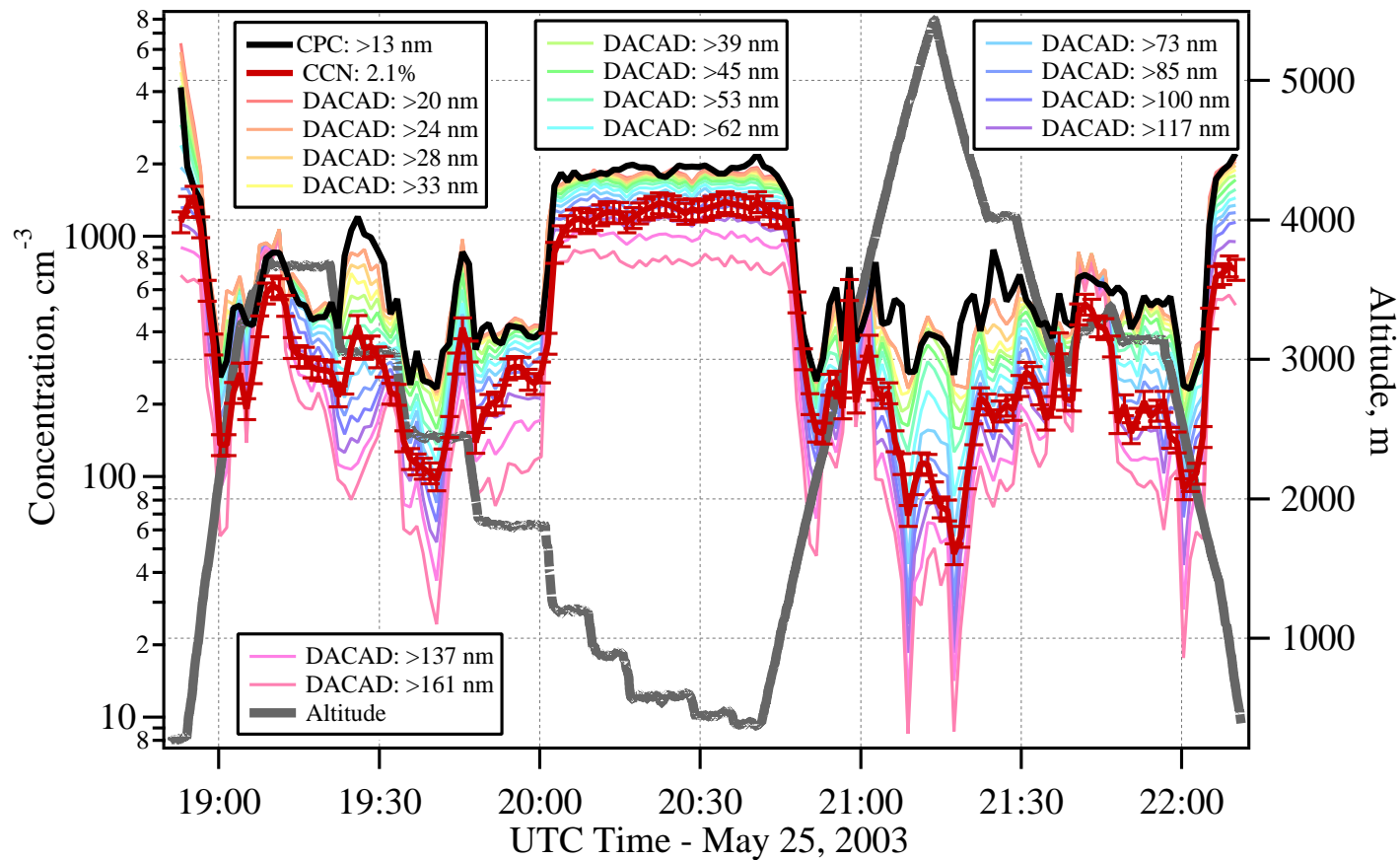


Figure 3.5. Flight traces of CPC, CCNC3, and DACAD data for flight 14. The DACAD traces give the total concentrations of particles with diameters greater than those noted in the legend. A well-mixed boundary layer is clearly shown from about 2010 to 2045. The times given are UTC; 1700 UTC corresponds to 1200 LT.

CPC and DACAD. To determine the uncertainty in the CCN measurements, the CPC concentration was used as a high-end limit for CCN concentration on all flights. The concentration measured by the CCNC3 column 2, when operating, was used as the lower limit for the column 1 CCN concentration. The operating supersaturation of column 2 was unable to be determined with any certainty, but it was always operating at some supersaturation lower than that of column 1. Therefore measurements by column 2 are used as estimates of the lower uncertainty limit for the measurements of column 1, when both columns were operating, but are not used in any other part of the analysis. Table 3.1 gives the uncertainty limits for column 1.

3.6 Inverse Aerosol/CCN Closure Study: Results and Discussion

Comparison of the CCN data to the aerosol size distribution data allows certain conclusions to be drawn about the characteristics of the measured CCN and the aerosol population. Certain aerosol population properties, such as particle insoluble fraction or mixing state, can be estimated as those that lead to closer agreement between predicted and observed CCN concentrations at the operating supersaturations of the CCN instrument. These estimated properties can be compared with those inferred from or measured by other instruments to determine whether the estimates are reasonable.

For this study, the CCN datasets were averaged over the scan time of the DACAD (72.5 s) to correspond with a single aerosol size distribution. Scans during which the standard deviation of the CCN data exceeded 15% of the mean of the CCN data were removed from the inverse closure analysis. This helps to remove intervals during which the aerosol size distribution may be changing sufficiently rapidly during the 72.5 s scan

time of the DACAD that the changes are not resolved in aerosol size distribution measurements. One further constraint: Only data measured during level legs of flight patterns were included to ensure that the CCNC3 inlet pressure was steady and did not cause any rapid changes or instability in the CCN sample flow rate, although this artifact was not observed even during rapid ascents and descents. Data measured within clouds were also removed from the inverse aerosol/CCN closure analysis to exclude the potential influence of artifact particles resulting from cloud droplet shattering in the Twin Otter inlet. The DACAD did not operate at altitudes above about ~ 3000 m (except during flight 14), so the inverse aerosol/CCN closure analysis generally does not include data above this altitude.

3.6.1 Inverse Aerosol/CCN Closure: Initial Comparison, Assuming 100% $(\text{NH}_4)_2\text{SO}_4$

Figure 3.6 shows an initial comparison of the predicted CCN number concentrations (N_P) to those observed by the CCNC3 instrument (N_O) for all eleven flights and includes all the data points from each flight that fit the criteria outlined in section 3.6. For this initial comparison, N_P is determined as the sum of the number concentration of particles in the DACAD size distributions with diameters greater than the activation diameter of an aerosol consisting of pure $(\text{NH}_4)_2\text{SO}_4$ for the operating supersaturation of the CCN instrument. Pure $(\text{NH}_4)_2\text{SO}_4$ is assumed as a starting point because PILS-IC data from the ground indicated that NH_4^+ and SO_4^{2-} were dominant species and that the average ratio of NH_4^+ to SO_4^{2-} was near 2 during the ARM Aerosol IOP. For flight 9, N_P is determined from the CPC total particle concentration, since the activation diameter of the CCNC3 column is about the same as the cutoff diameter for the

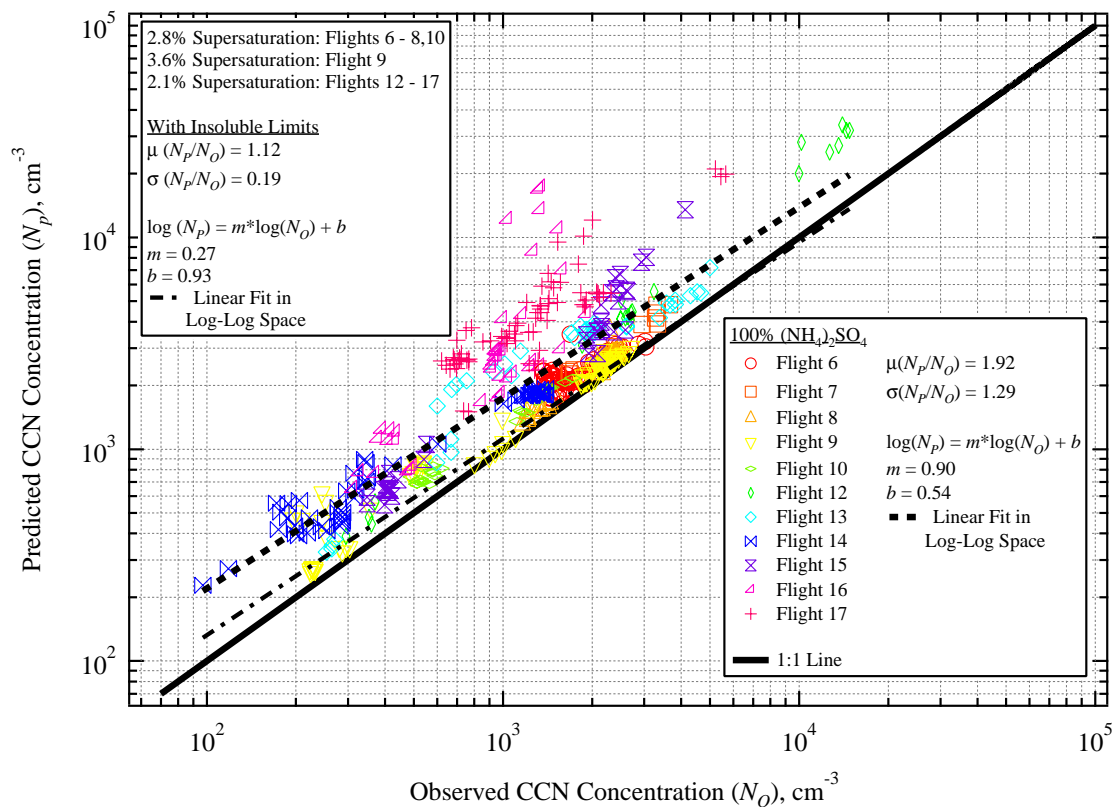


Figure 3.6. Predicted CCN concentration (N_p ; assuming pure $(\text{NH}_4)_2\text{SO}_4$) versus observed CCN concentration (N_o) for ARM Aerosol IOP. Only flights for which CCN data are available are shown. N_p is determined from the DACAD size distribution for all flights except flight 9, for which N_p is determined from the CPC total particle (> 13 nm) concentration. The linear fit in log-log space for all flight closure data is shown, and corresponding fit parameters are given. The mean and standard deviation of the ratio of N_p to N_o averaged over all flights are also given. The fit parameters and mean and standard deviation of the ratio of N_p to N_o are also shown for the “Insoluble Limit” case, for which N_p is calculated using the insoluble fractions calculated in section 3.6.2.1.

CPC. The average value of N_P/N_O ($\mu(N_P/N_O)$) for all flights is 1.92, with a standard deviation ($\sigma(N_P/N_O)$) of 1.29, and Table 3.2 shows this ratio for each flight. ($\mu(N_P/N_O)$ is used when values of the ratio, N_P/N_O , have been averaged over more than one DACAD scan.) The average value of N_P/N_O for each flight, and thus for all flights averaged together, is greater than unity. This indicates that fewer particles activated than would be expected if the particles were composed of pure $(\text{NH}_4)_2\text{SO}_4$. The average N_P/N_O also differs from flight to flight, which indicates that the aerosol CCN activity properties changed from flight to flight.

The N_P versus N_O data for each flight were fit to a straight line in log-log space, and the results for the slope and intercept of those fits are given in Table 3.2. The fit for all data is shown in Figure 3.6, and Figure 3.7 shows the fit for flights 8, 12, 14, and 17. Non-unity slopes and nonzero intercepts of these linear fits in log-log space offer some insight as to the characteristics of the ambient aerosol population through its deviation from the activation properties of pure $(\text{NH}_4)_2\text{SO}_4$ particles.

The slopes of the log-log fit of N_P versus N_O for the IOP flights are generally not unity, which indicates that the chemistry and mixing state of the aerosol population does not affect the CCN ability at all concentrations equally. This imbalance results from sampling different air masses with different aerosol properties, which lead to different N_P to N_O ratios, during the same flight. Aerosol populations with low CCN concentration, which often result from those with low total particle concentration (N_{Total}), tend to have “clean” aerosol sources or be well-aged aerosols, in which particle coagulation has decreased N_{Total} and cloud processing has likely increased soluble fractions. These types of air masses with low CCN concentrations would have N_P to N_O ratios nearer to unity.

Table 3.2. Average ($\mu(N_P/N_O)$) and Standard Deviation ($\sigma(N_P/N_O)$) of the Ratios of Predicted CCN Concentration to Observed CCN Concentration for All Flights for Which There Were CCN Data^a

Flight	Day in May	$\mu(N_P/N_O)^b$	$\sigma(N_P/N_O)^b$	m	b	R^2	Number of Data Points
6		1.30	0.18	0.63	1.32	0.63	80
7	14	1.29	0.13	0.81	0.77	0.96	11
8	15	1.18	0.07	1.05	-0.10	0.96	55
9	17	1.29	0.35	0.85	0.54	0.96	78
10	18	1.34	0.08	0.97	0.21	0.98	27
12	21	1.79	0.36	1.13	-0.22	0.99	23
13	22	1.78	0.51	0.91	0.51	0.90	38
14	25	1.84	0.48	0.77	0.88	0.96	54
15	27	1.87	0.45	1.14	-0.18	0.97	38
16	28	3.68	2.96	1.40	-0.68	0.65	42
17	29	3.45	0.86	0.93	0.74	0.77	71
	All	1.92	1.29	0.90	0.54	0.74	517

^aSlope (m) and intercept (b) values for linear fits of N_P to N_O in log-log space are also given.

^bAssumes pure $(\text{NH}_4)_2\text{SO}_4$ in the calculation of N_P .

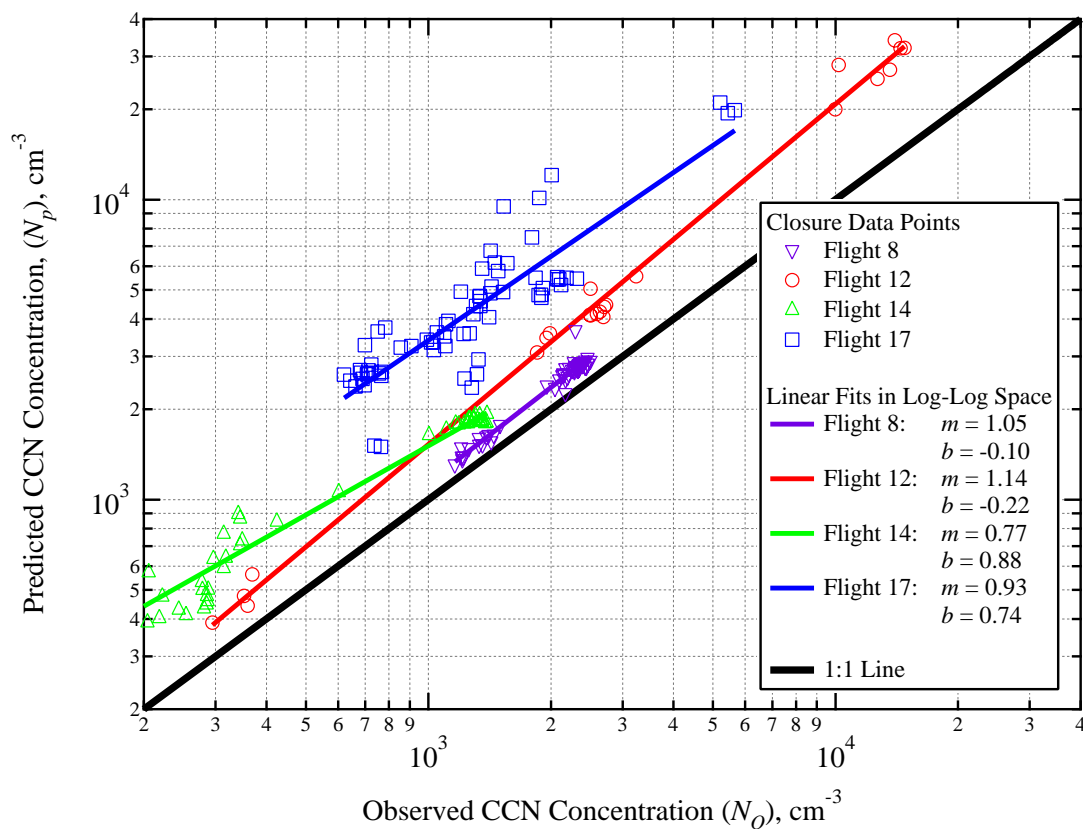


Figure 3.7. N_p (assuming pure $(\text{NH}_4)_2\text{SO}_4$) versus N_o and linear fits in log-log space for flights 8, 12, 14, and 17. High aerosol concentrations (from the CPC) were $10,400 \text{ cm}^{-3}$, $37,000 \text{ cm}^{-3}$, 3550 cm^{-3} , and 2890 cm^{-3} for flights 8, 12, 14, and 17, respectively. High CCN concentrations were 2882 cm^{-3} , $16,941 \text{ cm}^{-3}$, 2143 cm^{-3} , and 7454 cm^{-3} for flights 8, 12, 14, and 17, respectively. High concentration values were determined as the maximum concentrations measured after the Twin Otter had achieved sampling altitude after takeoff, regardless of whether the data were obtained during constant altitude legs.

High N_{Total} , on the other hand, is often indicative of fresh, polluted aerosol sources, possibly with high levels of insoluble material and a greater degree of external mixing, which could lead to higher values (greater than unity) of N_P/N_O . In Figure 3.7, the clustering of flight 12's closure data points at low, medium, and high CCN concentrations could indicate that three different air masses were sampled. The air mass with mid-level CCN concentrations could be a mixture of the air masses with high- and low-level CCN concentrations, instead of a distinct air mass. Figure 3.8 illustrates trends of N_P/N_O with altitude as a function of longitude for flights 12 (Figure 3.8a) and 14 (Figure 3.8b). The high CCN concentration data points (Figure 3.7) for flight 12 correspond to the N_P/N_O points (Figure 3.8) at altitudes of about 600 m ($N_P/N_O = 2.77$), 850 m ($N_P/N_O = 1.99$ – 2.42), and 1380 m ($N_P/N_O = 2.00$); the mid CCN concentration data points correspond to the N_P to N_O ratios at about 550 m ($N_P/N_O = 1.51$ – 2.02), 600 m ($N_P/N_O = 1.77, 1.80$), and 1380 m ($N_P/N_O = 1.67$); and the low CCN concentration points correspond to the N_P to N_O ratios at about 2100 m ($N_P/N_O = 1.23$ – 1.53).

The situation is quite different for flight 14 (see Figures 3.7 and 3.8), for which the generalized high and low N_{Total} classifications do not hold. All of the closure data points from flight 14 are clustered at CCN concentrations less than 2000 cm^{-3} , and the slope is less than unity. Contrary to what was observed in flight 12, the sampled aerosol with lower N_{Total} has a greater deviation from idealized, pure $(\text{NH}_4)_2\text{SO}_4$ particles than those with higher N_{Total} . As will be discussed later in section 3.7, flight 14 was apparently influenced by a Siberian smoke event [*Schmid et al.*, 2004]. Smoke aerosols that have been transported a long distance are likely to have low particle concentrations through particle coagulation and cloud processing. However, the aged smoke particles at

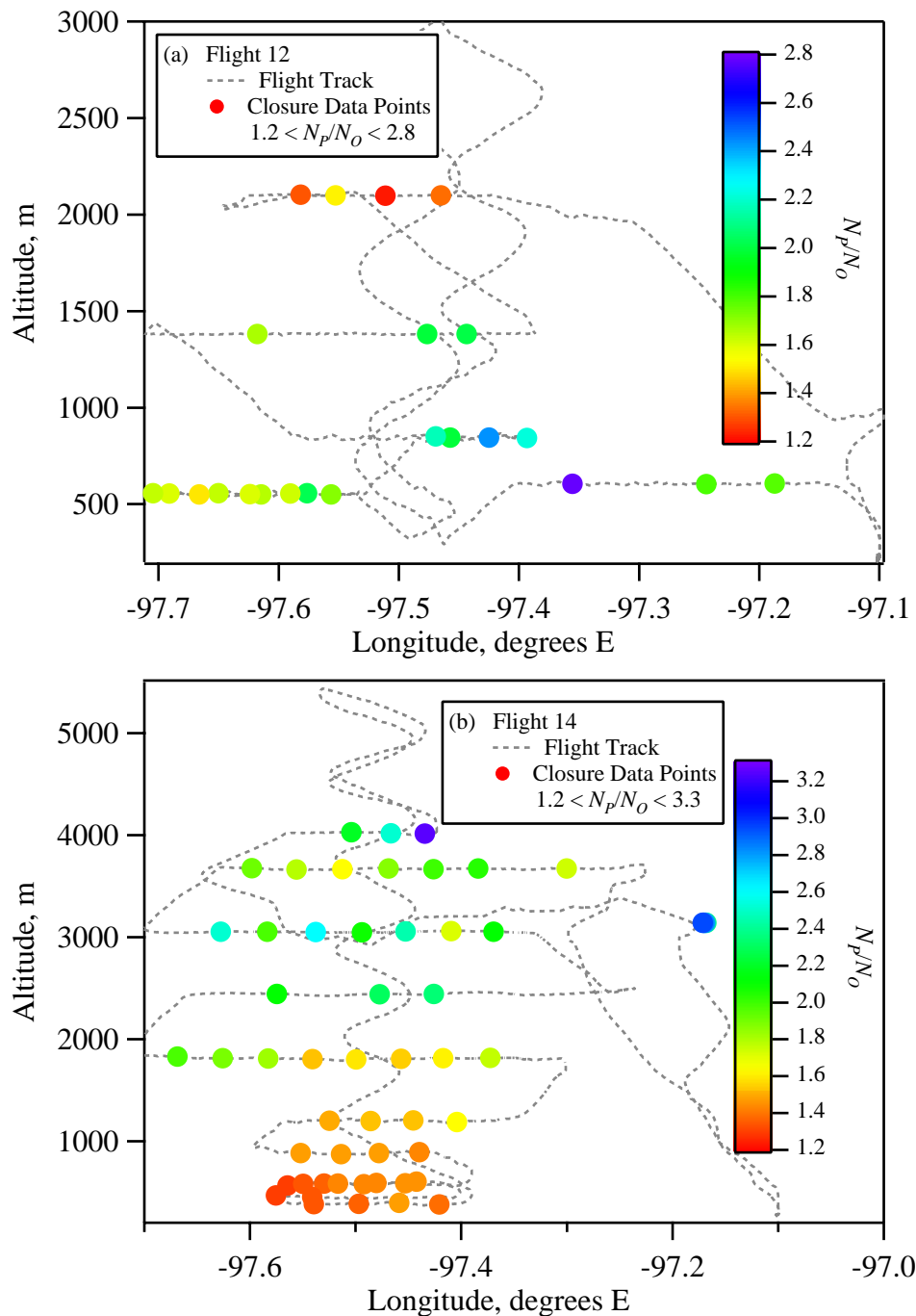


Figure 3.8. Altitude versus longitude trace for flights (a) 12 and (b) 14. Closure data points are indicated by the solid circles. The color of the closure data points indicates the magnitude of N_p/N_o , assuming pure $(\text{NH}_4)_2\text{SO}_4$, for the corresponding DACAD scan.

low N_{Total} in flight 14 did not become more CCN active than the background aerosol, which is probably the type of aerosol sampled under about 1400 m (see Figure 3.8).

An intercept that deviates from zero indicates that some fraction of the aerosol population is unavailable for activation at the measurement supersaturation, although this fraction would activate under the assumption of pure $(\text{NH}_4)_2\text{SO}_4$ particles. This non-active fraction could consist of particles from an internal or external mixture that have some fraction of insoluble, hydrophobic material that prevents activation. Even if the slope were near unity, the intercept can, as explained above, deviate from zero if particles exist that do not exhibit predicted CCN activity characteristics. Flights 8 and 17 (Figure 3.7) have slopes near unity but have very different intercepts, even though their observed CCN concentrations are within a similar range. HYSPLIT [Draxler and Rolph, 2003; Rolph, 2003] 3-day back trajectories for flights 8 and 17 (Figures 3.9 and 3.10, respectively) show that the sampled air masses from flights 8 and 17 originated in different areas, with those from flight 8 being more influenced by marine conditions in the Gulf of Mexico and those from flight 17 being more influenced by inland continental conditions. DACAD size distributions from the analyzed times during flight 8 are bimodal, with no indication of sampled pollution events, and $dN/d\log D_p$ values were less than 5000 cm^{-3} . Flight 17, however, was dominated by pollution events, as is indicated by its primarily multimodal size distributions that are dominated by particles with diameters smaller than 50 nm. Measured $dN/d\log D_p$ values for flight 17 were as high as $60,000 \text{ cm}^{-3}$, but most were under $10,000 \text{ cm}^{-3}$. It makes sense, then, that the deviation of flight 17's intercept from zero is greater than that of flight 8 because fewer particles are available for activation under polluted than clean conditions. When the slope is not near

NOAA HYSPLIT MODEL
 Backward trajectories ending at 19 UTC 15 May 03
 EDAS Meteorological Data

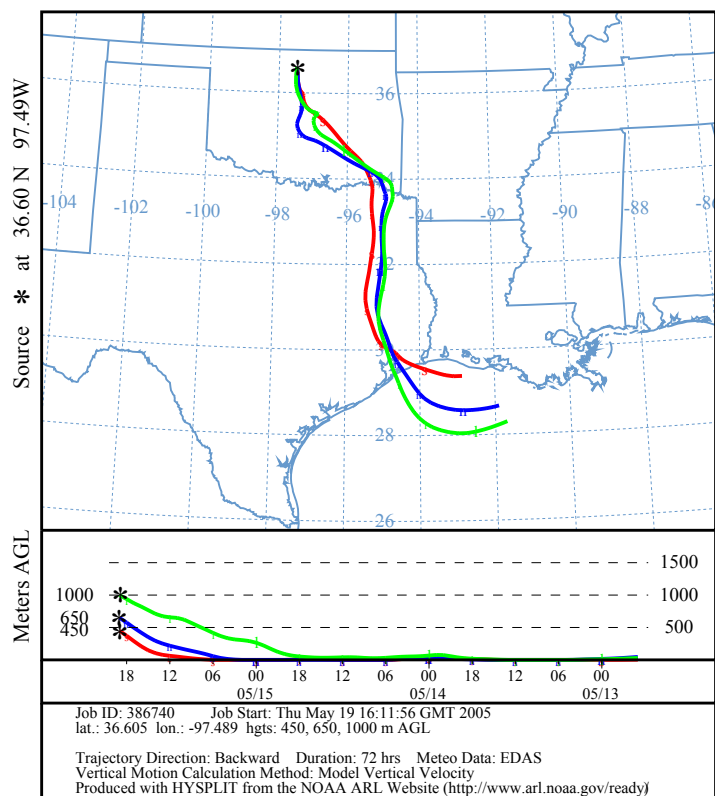


Figure 3.9. Three-day HYSPLIT back trajectories for 15 May 2003 (flight 8) at the SGP site at altitudes of 450, 650, and 1000 m. The times given are UTC; 1700 UTC corresponds to 1200 LT.

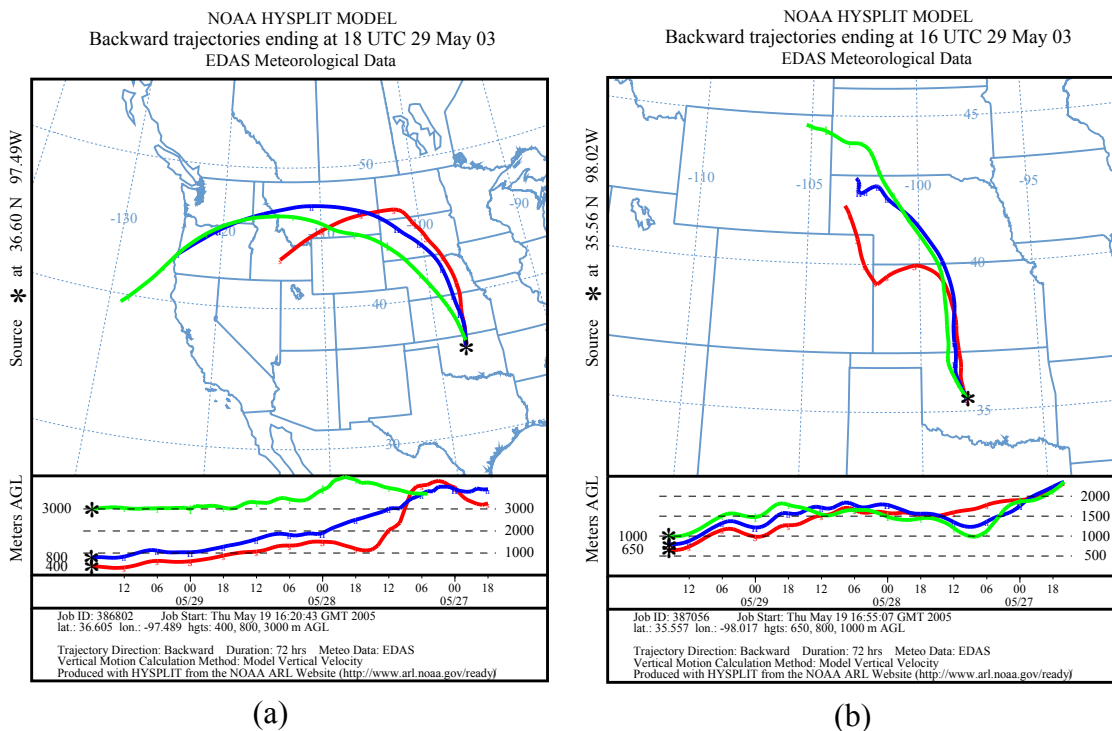


Figure 3.10. Three-day HYSPLIT back trajectories for 29 May 2003 (flight 17) (a) at the SGP site at altitudes of 400, 800, and 3000 m and (b) at site EF-19 at altitudes of 650, 800, and 1000 m. The times given are UTC; 1700 UTC corresponds to 1200 LT.

unity, the intercept can be affected by differences in CCN activities among the sampled air masses and may not have a simple interpretation.

On the basis of this initial comparison of N_O and N_P determined from DACAD size distributions with the assumption of 100% $(\text{NH}_4)_2\text{SO}_4$, it is apparent that more detailed aerosol properties, such as chemical composition and the mixing state, are needed to predict the CCN measurements at the operating supersaturations of the CCNC3. Because such composition and mixing data were, however, unavailable on the Twin Otter during the IOP, an inverse closure study is performed, in which the comparison of N_O and N_P based on the assumption of pure $(\text{NH}_4)_2\text{SO}_4$ is used to infer the aerosol composition and mixing state that are consistent with CCN observations.

3.6.2 Inverse Aerosol/CCN Closure: Inferring Deviations from 100% $(\text{NH}_4)_2\text{SO}_4$

An inverse aerosol/CCN closure evaluates the extent to which particle composition alone can explain the discrepancy between N_P and N_O . Particle composition can be modeled as an internal or an external mixture and can consist of completely soluble and insoluble material or include partially soluble material, as well. For the purposes of the study presented here, particle components are considered to be either completely soluble or completely insoluble, and both internally and externally mixed aerosol populations are considered. Although the customary definition of an internal mixture is that all particles of the same size have the same chemical composition, a more simplified, size-independent internal mixture is used here in the absence of airborne measurements of size-resolved chemistry. Thus, under the assumption of a size-independent internally mixed aerosol population, all particles of all diameters have the

same fractional insoluble/soluble composition in this analysis. An external mixture can include purely soluble particles, purely insoluble particles, and particles composed of both insoluble and soluble material.

3.6.2.1 Estimating Aerosol Particle Composition From CCNC3 and DACAD

Measurements

The initial comparison of N_P and N_O (from section 3.6.1) can be used to determine the particle volumetric fraction of insoluble material (ϵ_{ins}) that would be necessary for $\mu(N_P/N_O)$ to approach unity, assuming that the ambient aerosol is a size-independent internal mixture, with particles of all sizes having insoluble fraction ϵ_{ins} . In order to calculate ϵ_{ins} for each flight, the cumulative aerosol size distribution is determined, with each size bin containing the concentration of all particles with diameters greater than the bin diameter. For each analysis period, the DACAD mid-bin diameter for which the cumulative aerosol concentration approaches the measured CCN concentration is chosen as the cutoff diameter, defined as the dry diameter above which sampled ambient particles would be able to activate under the assumption of size-independent internal mixing. A value for ϵ_{ins} is determined by inputting the cutoff diameter and different values of ϵ_{ins} (with the balance $(\text{NH}_4)_2\text{SO}_4$) into the Köhler theory model, until the particle's calculated critical supersaturation approaches the operating supersaturation of the CCNC3.

Since the sampled air mass properties typically varied widely during a flight, this analysis is carried out for each level leg during each flight. A level leg is defined as one for which consecutive static pressure measurements are constant within ± 3 mbar. Some

level legs are further divided if it appears that drastically different air masses were sampled during the same level leg. This usually occurs for level legs that cover long distances but was observed even during some shorter-distance legs. Table 3.3 gives the range and mean of ε_{ins} values for each flight. Most of the values of ε_{ins} that are required for $\mu(N_P/N_O)$ to approach unity exceed 0.90, with only 14 out of the 113 analyzed level legs having ε_{ins} values less than 0.90. While insoluble mass fractions in aerosol particles in continental areas have been found as high as 0.98, values less than 0.6 are more common [Pruppacher and Klett, 1997]. Lower insoluble fractions would be expected in the ambient aerosol, especially if the aerosol were truly internally mixed independently of particle size. Under the assumption of a size-independent internal mixture of particles, the values of ε_{ins} that would be required to achieve agreement between N_P and N_O exceed the average fraction of insoluble material commonly found in continental aerosols. Other aerosol properties likely contributed to the discrepancy between N_P and N_O .

3.6.2.2 CCN and DACAD Derived Insoluble Fraction (Flight 10)

During the IOP, there was one flight (flight 10) during which CCN concentrations and DACAD wet and dry aerosol size distributions were all measured. From the wet and dry aerosol size distributions and assuming a size-independent internally mixed aerosol population, an estimate of ε_{ins} can be obtained by comparing the cumulative particle concentrations of the wet and dry size distributions at each diameter. The average difference in wet and dry diameter between the wet and dry cumulative concentration curves can give an estimate of the hygroscopic growth factor ($G(RH)_{Total}$) of the aerosol population during the scan in question. $G(RH)_{Total}$ is used instead of the hygroscopic

Table 3.3. Insoluble Volumetric Fractions (ϵ_{ins}) and Fraction of Particles Unavailable for Activation (f_{NA}) for Which $\mu(N_p/N_O) \approx 1$

$s, \%$	d_{act}, nm	Flight	ϵ_{ins}^a (Range ^b)	ϵ_{ins}^a (Mean ^c)	f_{NA}^d (Range ^b)	f_{NA}^d (Mean ^c)
2.8	15	6	0.66 – 0.96	0.90	0 – 0.39	0.22
		7	0.93 – 0.96	0.94	0 – 0.27	0.21
		8	0.97 – >0.99	0.98	0.13 – 0.37	0.15
		10	>0.99 (all)	>0.99	0.24 – 0.26	0.25
3.6	13	9	0.91 – >0.99	0.98	0.04 – 0.61	0.22
		12	0.78 – 0.96	0.92	0.26 – 0.64	0.42
		13	0.95 – 0.98	0.96	0.17 – 0.61	0.40
2.1	18	14	0.98 – >0.99	>0.99	0.24 – 0.63	0.42
		15	0.92 – >0.99	0.98	0.36 – 0.70	0.44
		16	>0.99 (all)	>0.99	0.40 – 0.91	0.63
		17	0.87 – >0.99	0.98	0.50 – 0.76	0.69

^aSize-independent internal mixing is assumed in the determination of ϵ_{ins} .

^bThe ranges of values for ϵ_{ins} and f_{NA} are determined from those averaged over each of the level legs during a flight.

^cThe mean values of ϵ_{ins} and f_{NA} are averaged over all analysis points.

^d N_p is determined under the assumption of pure $(\text{NH}_4)_2\text{SO}_4$ in the determination of f_{NA} .

growth factor, $f(RH)$, because $G(RH)_{Total}$ is based on the difference between the wet and dry diameters of the particle, which is directly related to the water uptake by the particle and is more directly applicable to CCN activity. The total growth factor can be used to estimate ε_{ins} from

$$G(RH)_{Total}^3 = \varepsilon_{ins} + \varepsilon_{org} G(RH)_{org}^3 + \varepsilon_{sol} G(RH)_{sol}^3 \quad (3.1)$$

where ε_{org} is the volumetric fraction of organic material, $G(RH)_{org}$ is the growth factor of organic material, ε_{sol} is the volumetric fraction of soluble material, and $G(RH)_{sol}$ is the growth factor of soluble material. If it is assumed that no soluble organic material is present in the aerosol particles, then the calculated value of ε_{ins} will be the maximum fraction of insoluble material possible for the determined value of $G(RH)_{Total}$. Then, equation (3.1) can be solved for $\varepsilon_{ins,DACAD}$, the insoluble fraction estimated from the DACAD wet and dry aerosol size distributions,

$$\varepsilon_{ins,DACAD} = \frac{G(RH)_{Total}^3 - G(RH)_{sol}^3}{1 - G(RH)_{sol}^3} \quad (3.2)$$

The soluble particle fraction is assumed to be composed of deliquesced $(\text{NH}_4)_2\text{SO}_4$, for which the value of $G(RH)_{sol}$ is 1.35 at the approximate DACAD operating RH of 70%.

The average value of the growth factor for the aerosol populations during flight 10, $G(RH)_{ave}$, is 1.05, and the average $\varepsilon_{ins,DACAD}$ is 0.78. The $G(RH)_{Total}$ and $\varepsilon_{ins,DACAD}$ values for each DACAD scan, and the resulting $\mu(N_P/N_O)$, are given in Table 3.4. N_P is

Table 3.4. Flight 10 Analysis Using $\varepsilon_{ins} = \varepsilon_{ins,DACAD}$ as Determined from DACAD Wet and Dry Cumulative Size Distributions

DACAD Midscan Time	$\varepsilon_{ins,DACAD}$	D_c^a ($\varepsilon_{ins,DACAD}$), nm	$N_P(D_c)$, cm^{-3}	N_{O_3} , cm^{-3}	N_P/N_O	f_{NA}^b
16:30:11	0.88	30	769	618	1.24	0.20
16:32:28	0.71	22	797	530	1.50	0.34
16:33:51	0.85	26	743	579	1.28	0.22
16:35:05	0.76	22	743	588	1.26	0.21
16:37:32	0.75	22	759	578	1.31	0.24
16:38:45	0.74	22	665	564	1.18	0.15
16:42:26	0.94	36	655	490	1.34	0.25
16:43:39	0.92	30	620	512	1.21	0.18
16:57:07	0.84	26	2093	1720	1.22	0.18
16:58:20	0.89	30	1915	1621	1.18	0.15
16:59:34	0.78	26	1858	1454	1.28	0.22
17:00:47	0.86	26	1728	1331	1.30	0.23
17:02:01	0.83	26	1586	1292	1.23	0.19
17:03:14	0.75	22	1483	1162	1.28	0.22
17:04:28	0.72	22	1475	1204	1.22	0.18
17:05:41	0.80	26	1334	1116	1.20	0.16
17:11:49	0.72	22	1505	1148	1.31	0.24
17:13:02	0.77	26	1740	1288	1.35	0.26
17:14:16	0.83	26	1874	1404	1.33	0.25
17:15:29	0.72	22	1895	1422	1.33	0.25
17:25:17	0.69	22	700	538	1.30	0.23
17:26:31	0.36	19	707	535	1.32	0.24
17:30:11	0.73	22	697	526	1.32	0.25

^a D_c is the cutoff diameter of a particle with insoluble fraction $\varepsilon_{ins,DACAD}$ and the balance $(\text{NH}_4)_2\text{SO}_4$ at 2.8% supersaturation.

^b f_{NA} values are determined using $\varepsilon_{ins} = \varepsilon_{ins,DACAD}$.

the summation of particles from the DACAD size distribution that have diameters greater than a cutoff diameter, D_C , which is the activation diameter (at 2.8% supersaturation) of a particle with an insoluble fraction equal to $\varepsilon_{ins,DACAD}$ and with the balance $(\text{NH}_4)_2\text{SO}_4$. DACAD scans with $G(RH)_{Total}$ less than unity, and thus $\varepsilon_{ins,DACAD}$ values greater than unity were eliminated from this analysis. A value of $G(RH)_{Total}$ less than unity could result when the assumption of size-independent internal mixing is invalid or for scan times during which the aerosol population is changing rapidly and the DACAD is unable to resolve these changes.

The values of $\varepsilon_{ins,DACAD}$ derived from the DACAD size distributions for flight 10 still result in $\mu(N_P/N_O)$ values greater than unity, which indicates, in accord with the previous analysis, that even a maximum estimate of ε_{ins} is not sufficient to obtain agreement between N_P and N_O in this continental environment. Other properties of the aerosol population need to be considered when attempting to obtain satisfactory agreement between N_P and N_O . The next property to consider is the mixing state of the aerosol population.

3.6.3 Inverse Aerosol/CCN Closure: Inferring Aerosol Mixing State

3.6.3.1 Aerosol Mixing State Inferred from Initial Comparison of N_P to N_O

The aerosol mixing state can be inferred from the initial comparison of N_P and N_O (section 3.6.1) in an inverse analysis similar to that carried out for the insoluble volume fraction. In this mixing state analysis, N_P is calculated by assuming pure $(\text{NH}_4)_2\text{SO}_4$ particles. The fraction of particles that is unavailable for activation (f_{NA}) could consist of

purely insoluble particles or particles with an insoluble fraction that is large enough to prevent activation. The f_{NA} such that $\mu(N_P/N_O) \approx 1$ is calculated from the following equation:

$$f_{NA} = \frac{N_{PExt}}{N_P} = \frac{N_P - N_O}{N_P} = 1 - \frac{N_O}{N_P} \quad (3.3)$$

where N_{PExt} is the number concentration of the externally mixed particles that are unavailable for activation. The statement that $N_{PExt} = N_P - N_O$ assumes that the CCNC3 was able to count all particles that were capable of activating at the operating supersaturations, which is likely at such high supersaturations where kinetic effects would not be dominant. Table 3.3 gives the average f_{NA} for each flight and the results are discussed further in section 3.6.3.3.

3.6.3.2 Aerosol Mixing State Inferred With DACAD Derived Insoluble Fraction (Flight 10)

Along with the $\varepsilon_{ins,DACAD}$ estimates, which were not sufficient to obtain agreement between N_P and N_O , an additional estimate of the extent of external mixing of the aerosol population can be calculated for flight 10. For this analysis, the f_{NA} that leads to $\mu(N_P/N_O) \approx 1$ is calculated by considering $\varepsilon_{ins,DACAD}$ (constant for particles of all diameters) with the balance $(NH_4)_2SO_4$ in the calculation of N_P . Table 3.4 shows the values of f_{NA} that satisfy $\mu(N_P/N_O) \approx 1$ for each DACAD scan during flight 10. The average value of f_{NA} in Table 3.4 is 0.22, which is close to the average value of f_{NA} (0.25) for flight 10 with $\varepsilon_{ins} = 0$. The similar values of f_{NA} calculated with and without the maximum value of ε_{ins} for a

size-independent internal mixture of particles ($\epsilon_{ins,DACAD}$) indicates that the aerosol was an external mixture that included some purely insoluble particles. Particles with an insoluble fraction of $\epsilon_{ins,DACAD}$ that were unable to activate at the operating supersaturations of the CCNC3 made up only 3% of the total aerosol population; 22% were purely insoluble particles (that did not activate), and 78% of the particles were able to activate.

3.6.3.3 Aerosol Mixing State Discussion

The values of f_{NA} follow a similar trend to that seen for $\mu(N_P/N_O)$ in section 3.6.1, with more particles unavailable for activation during flights that encountered polluted conditions. The aerosol size distribution feature that distinguishes between polluted and clean conditions is the predominance of small particles with diameters less than 30 nm under polluted conditions. The increase in f_{NA} values with increasing polluted conditions, therefore, indicates that the particles that are unavailable for activation at the operating supersaturations of the CCNC3 are predominantly those with diameters less than 30 nm.

This is consistent with the findings of *Gasparini et al.* [2006], that the smallest analyzed particles were largely composed of nonhygroscopic compounds (see section 3.5.1). At the relatively high operating supersaturations of the CCNC3, these small (< 30 nm), largely nonhygroscopic particles would make up the majority of the particles that remained unactivated. Considering that the insoluble fractions in a size-independent internal mixture required for N_P and N_O agreement in section 3.6.2 exceed 0.90 for 99 out of the 113 level legs analyzed, f_{NA} probably consists of some pure insoluble particles, with a range of diameters. An internal mixture of particles with an even distribution of

insoluble material across particle diameters is not expected, especially at the location of the SGP site, where sampled aerosol varies in both source and age.

3.6.4 CCN and DMA/TDMA-Derived Mixing State and Particle Composition

Size-resolved particle composition and mixing state of ambient aerosol were derived from the Texas A&M DMA/TDMA ground data from the IOP [Gasparini *et al.*, 2006]. For each size bin, the DMA/TDMA measurements can be used to calculate the fraction of the particles in that size bin that are purely soluble material, purely insoluble material, and a mixture of soluble and insoluble material. The fraction of insoluble material in the mixed particles is also calculated. It was assumed that the purely insoluble particles did not activate at the operating supersaturations of the instrument. The purely soluble particles were assumed to activate if the size bin diameter was greater than the critical diameter of $(\text{NH}_4)_2\text{SO}_4$ at the operating supersaturation of the CCNC3 instrument. The mixed particle soluble and insoluble fractions were input into the Köhler model to determine whether particles with this chemical composition and diameters equal to the mid-diameter of the size bin were able to activate at the operating supersaturation of the CCNC3 instrument.

The flights for which there were simultaneous CCN measurements, DACAD size distributions, and DMA/TDMA-derived aerosol population properties were flights 8, 9, and 16. For this analysis, included level legs were limited to being within 8047 m (5 miles; horizontal distance) of the SGP CART site and within the boundary layer, where the ground DMA/TDMA-derived aerosol properties are more likely to be valid for flight data. The boundary layer height was calculated using the procedure described by *Delle*

Monache et al. [2004], which uses balloon-borne sounding system data. The boundary layer height is defined as the lowest altitude within a potential temperature inversion at which a critical lapse rate and threshold potential temperature are exceeded. The following thresholds were determined by *Delle Monache et al.* [2004] to apply at the SGP CF: $\theta_{Top} - \theta_{Bottom} = 2 \text{ K}$ and $\Delta\theta/\Delta z = 0.001 \text{ K m}^{-1}$, where θ_{Top} is the potential temperature at the top of the boundary layer in Kelvin (K), θ_{Bottom} is the potential temperature at the bottom of the boundary layer in K, θ is the potential temperature in K, and z is the altitude in m. DMA/TDMA data were used to classify aerosol particle components as externally mixed insoluble, externally mixed soluble, internally mixed insoluble, and internally mixed soluble, and these aerosol properties were averaged over the diameter ranges of the DACAD. DACAD scan times within the DMA/TDMA size distribution scan times ($\sim 5 \text{ min}$) were used.

The $\mu(N_P/N_O)$ values resulting from the DMA/TDMA-derived properties are given in Table 3.5. For flights 8 and 9, the $\mu(N_P/N_O)$ values are within instrument uncertainty, but they are still significantly greater than unity for flight 16, even though using the DMA/TDMA-derived aerosol properties decreased the $\mu(N_P/N_O)$ value significantly, by about 73%. The flight traces for flights 8 and 9 (Figures 3.11 and 3.12) show well-mixed boundary layers for the time periods during which the Twin Otter was sampling within the boundary layer and within 8 km of the ground site. The boundary layer during the time period studied for flight 16 is less well mixed, as is illustrated by its flight trace in Figure 3.13. The time period within which the Twin Otter was sampling within the boundary layer and within 8 km of the ground site was near the beginning of flight 16, from about 1849 to 1851 UTC. Considering that the DMA/TDMA data were

Table 3.5. $\mu(N_P/N_O)$ and $\sigma(N_P/N_O)$ Values for Flights 8, 9, and 16 Using ε_{ins} and External Mixing Properties Derived from DMA/TDMA Data^a

s , %	d_{act} , nm	Flight	Number of DACAD Scans Included	Without DMA/TDMA Derived Properties ($\varepsilon_{ins} = 0, f_{NA} = 0$)		With DMA/TDMA Derived Properties	
				$\mu(N_P/N_O)$	$\sigma(N_P/N_O)$	$\mu(N_P/N_O)$	$\sigma(N_P/N_O)$
2.8	15	8	4	1.18	0.02	1.00	0.02
3.6	13	9	1	1.14	One Scan	1.10	One Scan
2.1	18	16	3	5.38	2.26	1.47	0.15

^aThe results without DMA/TDMA derived properties are also given for the same DACAD scans. This table only includes times during which the Twin Otter was within 5 miles of the SGP CART site and within the boundary layer.

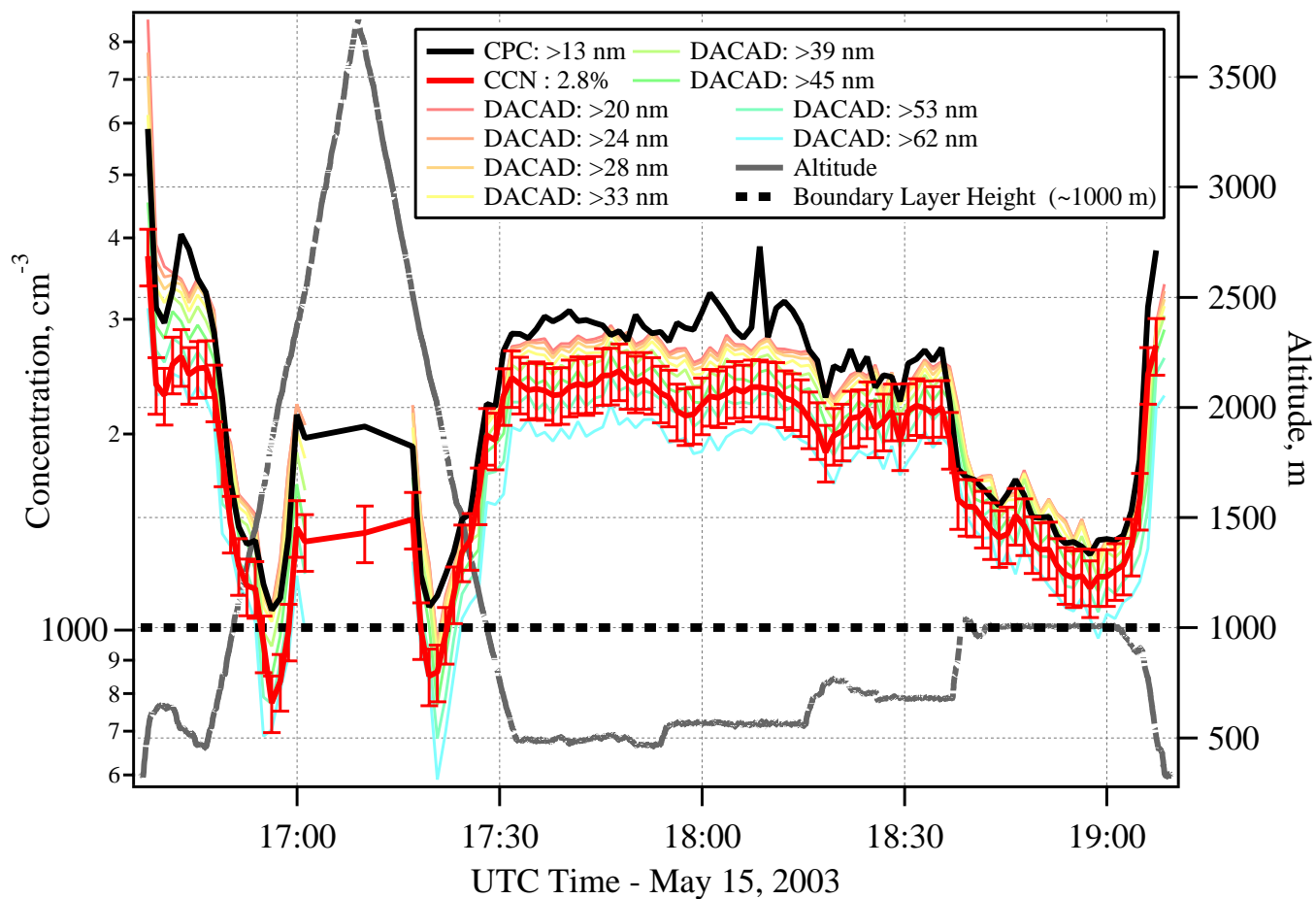


Figure 3.11. Flight trace for flight 8, showing a well-mixed boundary layer between approximately 1730 and 1840 UTC when the Twin Otter was sampling beneath ~ 1000 m. The error bars on the CCN trace indicate the 10% uncertainty level. The times given are UTC; 1700 UTC corresponds to 1200 LT.

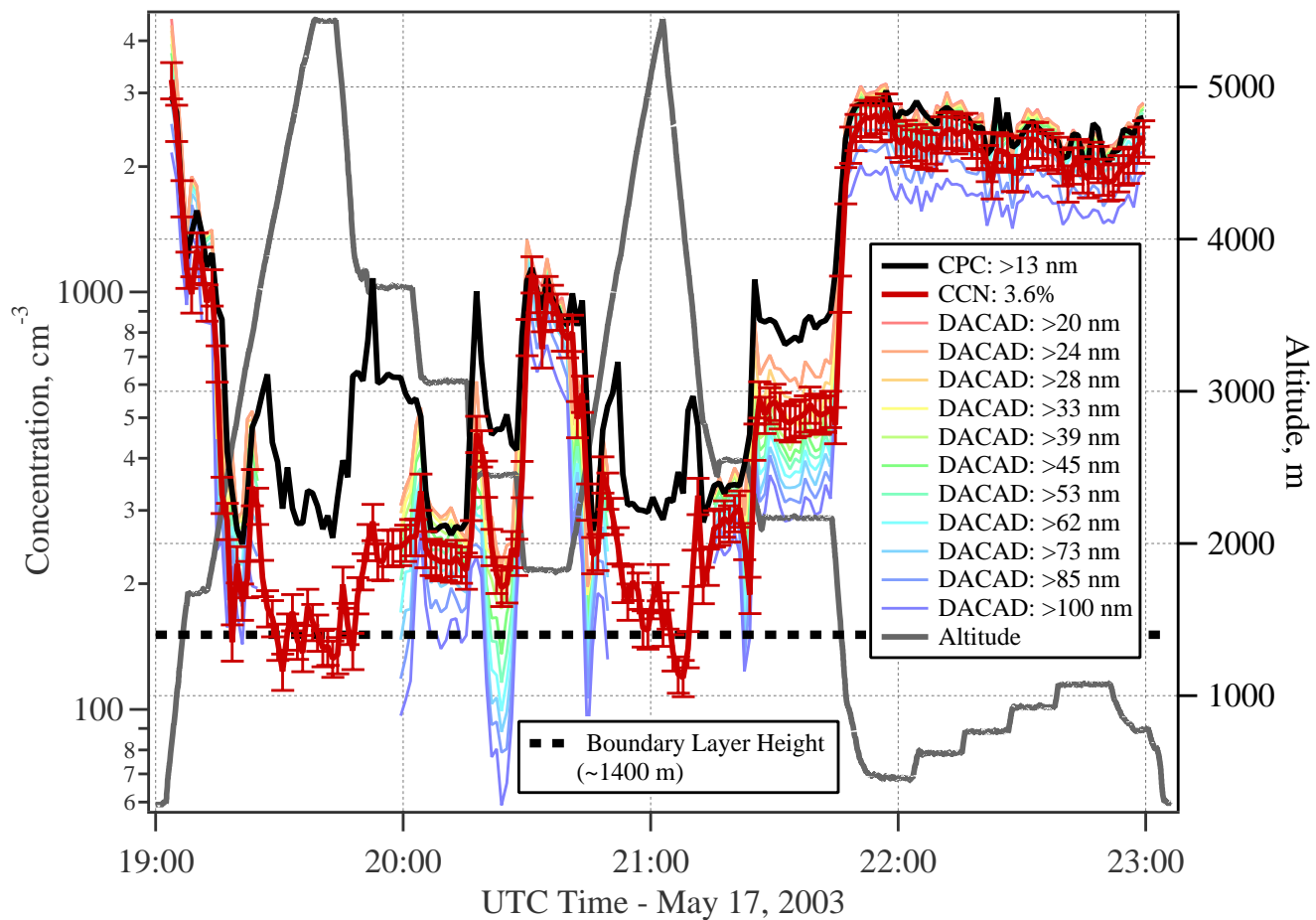


Figure 3.12. Flight trace for flight 9, showing a well-mixed boundary layer between approximately 2200 and 2300 UTC when the Twin Otter was sampling beneath ~ 1400 m. The error bars on the CCN trace indicate the 10% uncertainty level. The times given are UTC; 1700 UTC corresponds to 1200 LT.

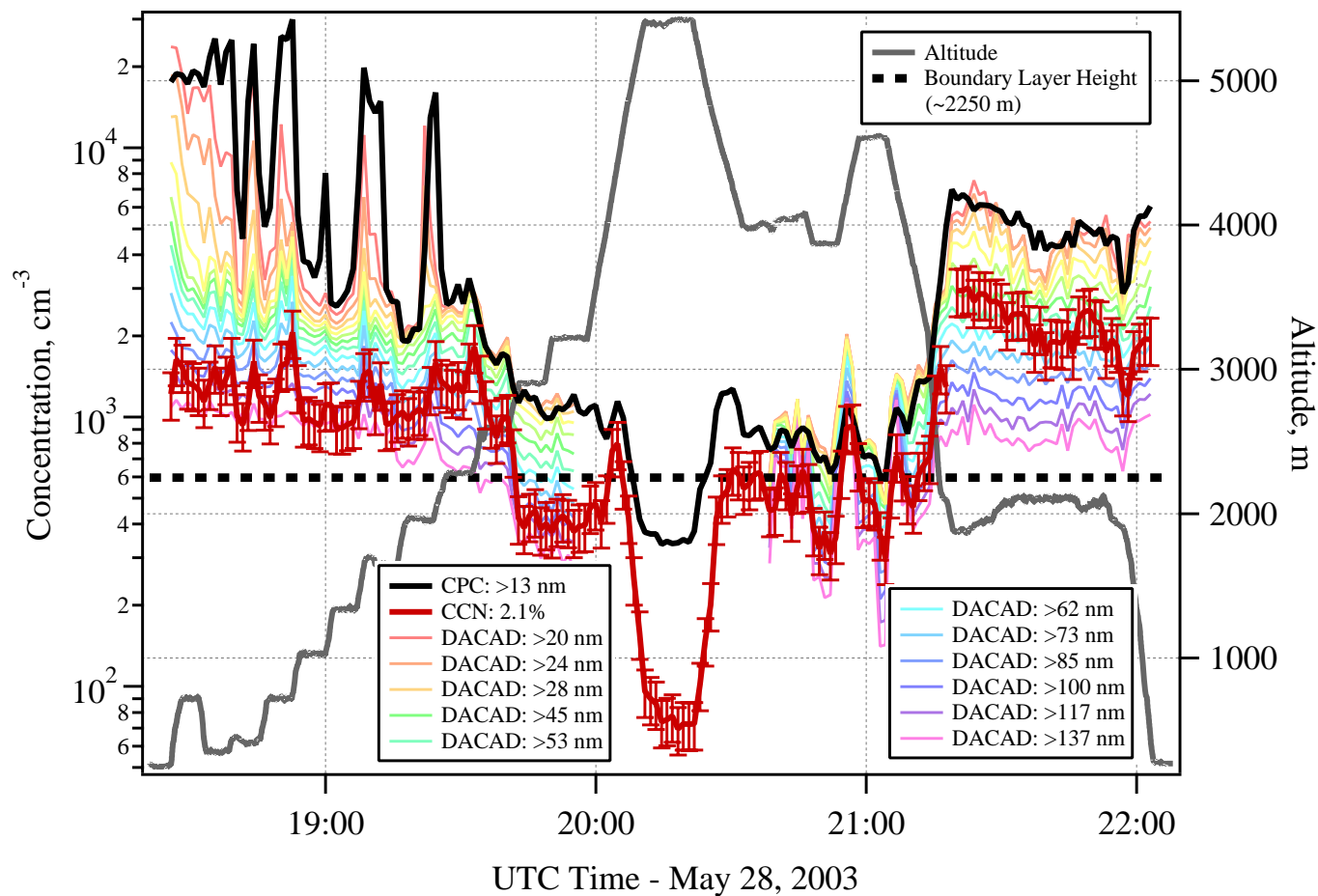


Figure 3.13. Flight trace for flight 16, showing the lack of a well-mixed boundary layer from approximately 1820 to 1940 UTC when the Twin Otter was sampling beneath ~ 2250 m. The error bars on the CCN trace indicate 20% uncertainty level. The times given are UTC; 1700 UTC corresponds to 1200 LT.

measured at the ground, it is not unexpected that the agreement between N_P and N_O is more satisfactory for well-mixed boundary layers than non-well-mixed boundary layers.

A comparison of the DMA/TDMA and DACAD aerosol size distributions illustrates this point further. Figure 3.14 compares the DMA/TDMA and DACAD aerosol and predicted CCN size distributions for flights 8 and 9; Figure 3.15 illustrates the same for flight 16. Both of the CCN size distributions (DMA/TDMA and DACAD) are calculated using the size-resolved chemistry derived from the DMA/TDMA measurements. For the DACAD CCN size distributions, the DMA/TDMA size-resolved chemistry is applied to the DACAD aerosol size distributions, which assumes that the DMA/TDMA-derived chemistry applies at the sampling altitude of the DACAD. As can be seen, this assumption seems to hold for flights 8 and 9 but not flight 16.

During the sampling period 1849 to 1851 UTC during flight 16, the CPC and DACAD exhibit sharp peaks in number concentration. The DACAD aerosol size distribution shows that these peaks are caused by increases in small particles that do not show up in the DMA/TDMA size distribution for the same time period. This indicates that the layers that were sampled by the Twin Otter did not necessarily reach the ground and that the aerosol layers within the boundary layer were stratified. The DELTA (Detection and Evaluation of the Long-Range Transport of Aerosols) rotating drum impactor aerosol composition results from the SGP site measurements also indicate that the layers sampled aloft on 25–29 May did not reach the ground [Cahill *et al.*, 2004]. Another possibility is that the DMA/TDMA, which has a longer total sequence scan time (~ 1 hour) than the DACAD (72.5 s), was unable to resolve rapid changes in the aerosol size distribution, which may have occurred during the time period of interest. The

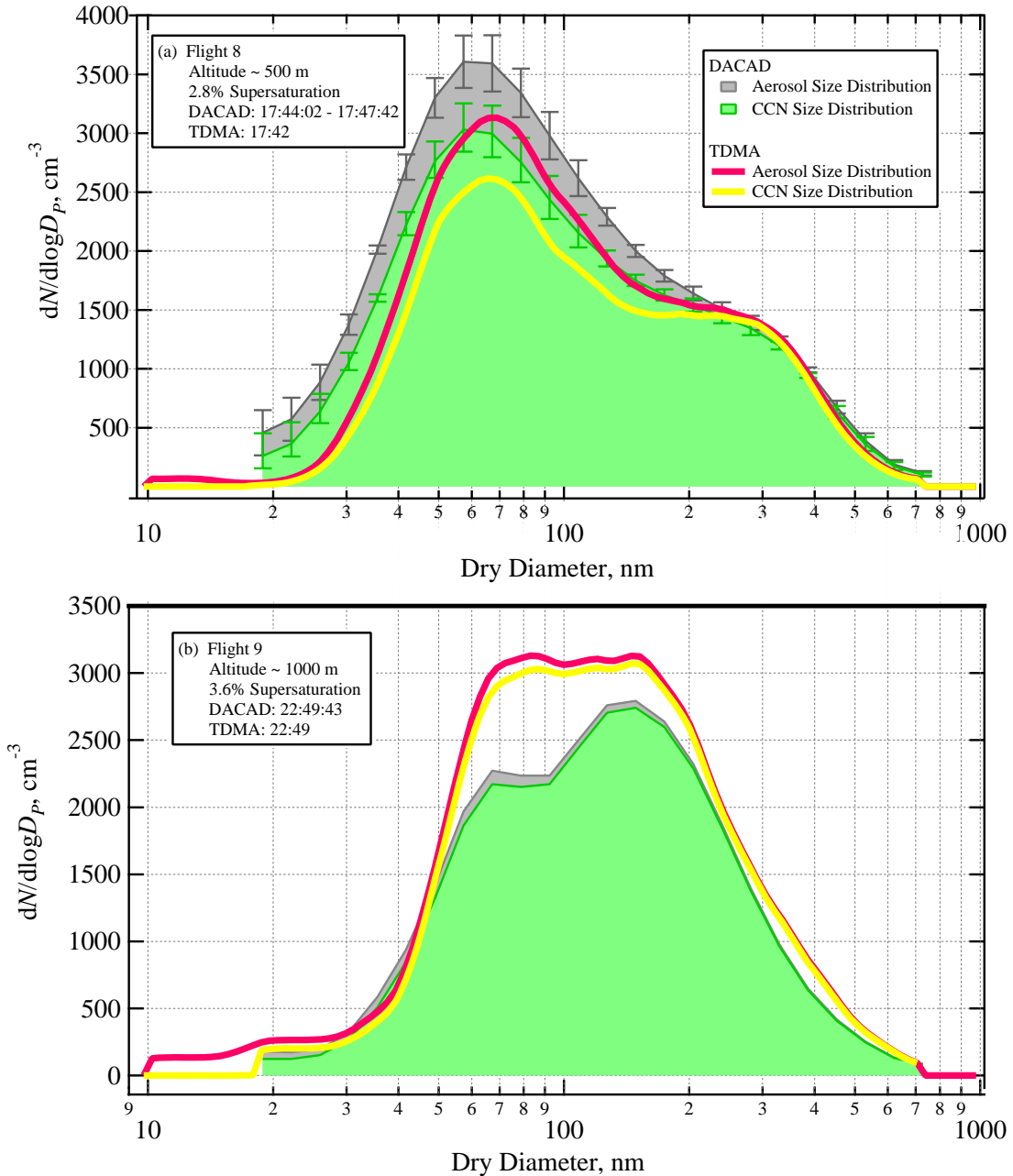


Figure 3.14. Comparison of DMA/TDMA and DACAD size distributions for flights (a) 8 and (b) 9. The error bars give the standard deviation of the DACAD aerosol size distributions averaged over the DMA/TDMA scan times. The times given are DACAD mid scan times in UTC; 1700 UTC corresponds to 1200 LT. The area under the aerosol size distribution curve gives the total aerosol number concentration, and the area under the CCN size distribution curve gives the predicted CCN number concentration. Both DACAD and DMA/TDMA predicted CCN distributions were calculated using the insoluble fraction and external mixing properties determined from the DMA/TDMA data.

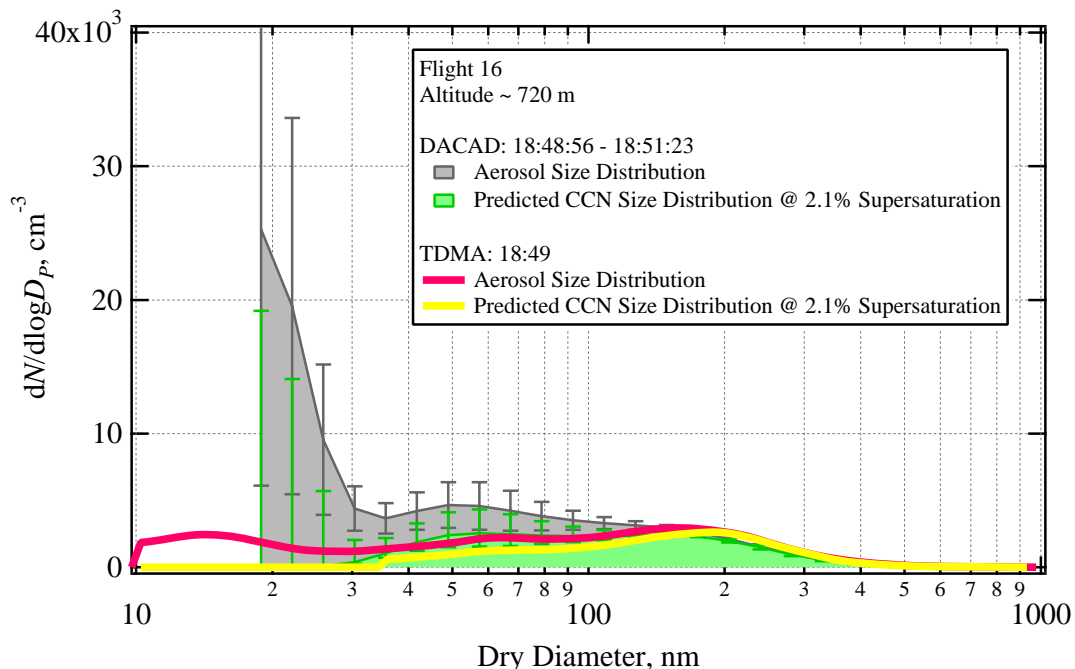


Figure 3.15. Comparison of DMA/TDMA and DACAD size distributions for flight 16. The error bars give the standard deviation of the DACAD aerosol size distributions averaged over the DMA/TDMA scan times. The times given are the DACAD midscan times in UTC; 1700 UTC corresponds to 1200 LT. The area under the aerosol size distribution curve gives the total aerosol number concentration, and the area under the CCN size distribution curve gives the predicted CCN number concentration. Both DMA/TDMA and DACAD predicted CCN distributions were calculated using the insoluble fraction and external mixing properties determined from the DMA/TDMA data.

DMA/TDMA size-resolved composition does not apply to the air masses sampled by the Twin Otter for flight 16 because the shape of the DMA/TDMA and DACAD sampled aerosol size distributions are not similar. If the DMA/TDMA and DACAD size distribution shapes are similar, as is true for flights 8 and 9, then the DMA/TDMA composition results can be coupled with airborne aerosol size distribution measurements to predict CCN concentrations within the boundary layer and within a reasonable horizontal distance from the ground measurement site.

3.7 Case Studies: “Clean” Conditions, Local Pollution, and Siberian Smoke Events

The inverse aerosol/CCN closure study (assuming 100% $(\text{NH}_4)_2\text{SO}_4$) indicates a division of the flights into three groups, based on the value of the closure ratio of N_P to N_O . Flights 6 through 10 (14–18 May) have $\mu(N_P/N_O)$ values between 1.18 and 1.34, while values for flights 12 through 15 (21–27 May) are between 1.78 and 1.87, and values for flights 16 and 17 (28 and 29 May) are 3.68 and 3.45, respectively. This division seems independent of the instrument operating supersaturation. Operating supersaturations of 2.8% and 3.6% are included in flights 6 through 10, which have similar $\mu(N_P/N_O)$ values. The operating supersaturation (2.1%) is the same for flights 12 through 17, although each flight has different $\mu(N_P/N_O)$ values. ARM Aerosol IOP flights fall into categories consistent with relatively clean conditions with intermittent pollution events (flights 6–10), conditions influenced by local pollution and/or smoke events (flights 12–15), and conditions dominated by local pollution events (flights 16–17) [*Schmid et al.*, 2004]. Aerosol size distributions from the DACAD are especially illustrative of the different categories of sampled air masses. In the following

discussions, only DACAD scan times that were used in the inverse closure analysis are considered and presented.

During the first 2 weeks of the ARM Aerosol IOP (5–18 May, flights 6–10), relatively clean atmospheric conditions were noted. Also during this time, severe weather moved through north-central Oklahoma, including a “thunderstorm and high wind” event on 16 May (NOAA National Climatic Data Center (NCDC) access via Department of Commerce (DOC) NOAA National Environmental Satellite, Data, and Information Service (NESDIS) NCDC website, <http://lwf.ncdc.noaa.gov/oa/ncdc.html>). This may be one reason that the atmosphere was relatively clean. DACAD size distributions early in flights 6–10 (14–18 May) have unimodal or bimodal distributions with median diameters between about 40 and 160 nm and peak $dN/d\log D_p$ values less than 5000 cm^{-3} . Aerosol size distributions for flight 6 begin to deviate from these characteristics about 45 min after takeoff and continue to deviate until landing. Aerosol size distributions exhibit these “clean” characteristics throughout the analyzed times during flights 7, 8 and 10. For flight 9, aerosol size distributions exhibit these “clean” characteristics near the end, as well as early in, the flight, but deviate for mid-flight times. The $\mu(N_p/N_o)$ values for these clean background periods are 1.19, 1.33, 1.18, 1.21, and 1.34 for flights 6–10, respectively.

Background closure ratios for flights 9 and 10 (1.21 and 1.34, respectively) on 17 and 18 May may include data points related to a sulfur event in the SGP area. Around 17 May, *Cahill et al.* [2004] noted, on the basis of their ground site data, an aerosol sulfur episode caused by an air mass that they predict was over Ohio 2 days earlier. Most of the aerosol size distributions from flights 9 and 10 are unimodal with median diameters

greater than 100 nm, which could be indicative of an aged aerosol population and which is consistent with the findings of *Cahill et al.* [2004]. Some aerosol size distributions from flight 9 indicate the influence of local aerosol sources, as will be discussed.

After 18 May, the aerosol size distributions are unimodal or bimodal with median diameters between 40 and 80 nm and peak $dN/d\log D_p$ values less than $10,000 \text{ cm}^{-3}$. Aerosol size distributions with these “dirtier” background aerosol characteristics were found during flights 12–17 (21–29 May). The $\mu(N_p/N_o)$ values for background conditions during flights 12–17 are 1.36, 1.28, 1.70, 1.54, 2.30, and 2.30, respectively.

At later times during flight 6, mid-times during flight 9, and times throughout flights 12–17, measured aerosol size distributions indicated the presence of local pollution sources. Elevated aerosol layers were visually observed at altitudes of ~ 3700 m during flight 6, ~ 2500 m during flight 9, ~ 3000 and 3700 m during flight 14, and ~ 2000 , 3000 , 3700 , and 5000 m during flight 15. Some DACAD size distributions from flights 6, 7, 9, and 12–17 have characteristically low median diameters (sometimes less than the cutoff diameter of the DACAD, ~ 17 nm) and particularly large concentrations of particles with diameters less than 30 nm. These aerosol size distributions are consistent with those from locations that are downwind of a fresh pollution source, such as a coal-fired power plant [*Brock et al.*, 2002]. Ground-based PILS-IC results show that for flights 12, 14, and 15 (21, 25, and 27 May) NH_4^+ to SO_4^{2-} molar ratios much less than 2 were observed [*Pahlow et al.*, 2006], which could indicate addition of sulfate to particles through vapor and aqueous phase reactions. The SGP site is near two power plants: the Ponca City and Conoco power plants, and IOP flight patterns passed near at least four other industrial and/or power plants, as well. Figure 3.1 shows the locations of

these plants. The $\mu(N_P/N_O)$ values for these periods that seem to be influenced by local pollution are 1.35 and 1.26 for flights 6 and 9, respectively and 1.89, 1.85, 2.41, 2.73, 6.83, 3.75 for flights 12–17, respectively.

Table 3.6 summarizes the $\mu(N_P/N_O)$ values for all flights when divided into categories based on the shape and magnitude of the DACAD aerosol size distribution. In general, the $\mu(N_P/N_O)$ values are lower for the clean conditions than the more obviously polluted conditions.

Siberian smoke layers were observed in the SGP CF area during the period 25–28 May, 2003 (flights 14–17) [Schmid *et al.*, 2004]. DACAD aerosol size distributions indicate that smoke layers were sampled at altitudes of ~ 3700 m on flight 14 and ~ 3100 m on flight 15. The Siberian fires were detected in April but escalated greatly in May. In transport simulations beginning on 10 May 2003, the smoke plume from Siberia reached Canada in about 11 days, with a smoke maximum on 23 May in Manitoba, Canada [Damoah *et al.*, 2004]. HYSPLIT [Draxler and Rolph, 2003; Rolph, 2003] back trajectories for flight 14 on 25 May 2003 show that air masses 3000 and 4000 m over the ARM SGP site were over Canada 2 days prior to sampling, which corresponds with the smoke maximum in Manitoba on 23 May.

On 25 May 2003 (flight 14), the observed elevated layers were characterized by large values of dry extinction and backscatter, which are consistent with aged smoke particles [Ghan *et al.*, 2006]. The DACAD size distributions from these smoke events tend to have a large accumulation mode, with median diameters greater than 100 nm. This is consistent with aged aerosol populations originating from biomass burning, in which processes such as particle coagulation and cloud processing have occurred and

Table 3. 6. Summary of the Values of $\mu(N_P/N_O)$ for Each Flight, Divided into Categories Determined from DACAD Size Distributions^a

$s, \%$	d_{act}, nm	Flight	$\mu(N_P/N_O)$		
			Background	Polluted	Smoke
2.8	15	6	1.19	1.35	NE
		7	1.33	NE	NE
		8	1.18	NE	NE
		10	1.34	NE	NE
3.6	13	9	1.21	1.26	NE
		12	1.36	1.89	NE
		13	1.28	1.85	NE
2.1	18	14	1.70	2.41	2.28
		15	1.54	2.73	1.61
		16	2.30	6.83	NE
		17	2.30	3.75	NE

^a“NE” indicates that the condition was “Not Encountered” during the DACAD scan times used in the closure analysis.

have decreased the peak concentration and increased the median diameter of the size distribution [Radke *et al.*, 1995].

The ability of smoke particles to act as CCN has been shown to increase with smoke plume age [Andreae and Merlet, 2001]. The critical supersaturation of smoke particles is reduced, and thus their CCN ability increased, through cloud processing, in which condensational uptake of water-soluble material is possible. Past studies have found that the ratio of CN to CCN at 1% supersaturation is about 1.7 in a slightly aged (1–2 hours) smoke plume [Andreae and Merlet, 2001]. The Siberian smoke aerosols were transported over a large distance, which included time spent over industrial and desert regions. Therefore, along with aged smoke particles, it is likely that industrial pollutants and some mineral dust were present in these smoke layers [Jaffe *et al.*, 2004]. This may explain why the $\mu(N_p/N_o)$ values, given in Table 3.6, differ from those of other studies of aged smoke plumes.

The layers that were analyzed in the closure analysis for flights 16 and 17 have aerosol size distributions that are more consistent with local pollution sources than with aged smoke particles. Flight 17 was a MODIS overpass flight, which sampled above three ARM ground sites, in addition to the SGP CF. During flight 17, the Twin Otter flew near five power plants, so the aerosol size distribution characteristics are not unexpected

3.8 Conclusions

The inverse aerosol/CCN closure study has revealed possible features of the aerosol sampled during the ARM Aerosol IOP in the absence of direct airborne aerosol

composition measurements. The ARM SGP site is greatly influenced by local aerosol sources, as well as long-range sources, and the aerosol CCN activity at high supersaturations was greatly influenced by the chemical characteristics and mixing state of the aerosols in the sampled air masses. The characteristics of air masses sampled during the ARM Aerosol IOP ranged from those of relatively clean air masses to those of air masses influenced by local and long-range pollution events to those of aged smoke plumes. These air masses can be categorized by aerosol size distribution, as well as by CCN behavior as indicated in the ratio of N_P to N_O . It has been shown that the general low aerosol CCN activity that was observed in this inverse aerosol/CCN study is consistent with other measurements from the IOP.

The DACAD aerosol size distributions measured during the ARM Aerosol IOP were highly variable, even on level legs of approximately constant altitude. This could account for some of the disagreement between N_P and N_O because the DACAD is not able to resolve rapid changes in aerosol size distributions because of its longer measurement time compared to that of the CCNC3.

If the CCNC3 instrument had operated at lower supersaturations that are more representative of those found in the atmosphere, the inverse aerosol/CCN closure study may have resulted in significantly different N_P to N_O ratios. The only indication that we have of the size-resolved aerosol composition in this area is the DMA/TDMA derived results. These results indicate that, in general, material of low hygroscopicity was preferentially distributed among the smallest measured particles. This is consistent with in-cloud aerosol processing and/or fresh pollution sources, and it is likely that both of these scenarios were encountered during the ARM Aerosol IOP because of the close

proximity of power and industrial plants and the verified Siberian smoke events near the end of the month.

Although some of the chemistry effects may not have been captured at smaller supersaturations, future measurements should be made at lower operating supersaturations to better determine the ability to predict CCN concentration using surface data. However, for a continental location such as the ARM SGP site that is influenced by many different aerosol sources, ranging from local to international, predicting CCN concentrations from aerosol size distributions and surface aerosol composition measurements alone is probably not adequate. Future studies should also include airborne aerosol composition measurements to allow more complete aerosol/CCN closure studies.

Acknowledgements. The authors wish to acknowledge Z. Song, L. Bowerman, and Y.-N. Lee for providing results from the PILS-IC. Data were obtained from the Atmospheric Radiation Measurement (ARM) Program sponsored by the U.S. Department of Energy, Office of Science, Office of Biological and Environmental Research, Environmental Sciences Division.

3.9 References

- Albrecht, B. A. (1989), Aerosols, cloud microphysics, and fractional cloudiness, *Science*, 245(4923), 1227 – 1230.
- Andreae, M. O., and P. Merlet (2001), Emission of trace gases and aerosols from biomass burning, *Global Biogeochem. Cycles*, 15(4), 955 – 966.
- Brechtel, F. J., and S. M. Kreidenweis (2000a), Predicting particle critical supersaturation from hygroscopic growth measurements in the humidified TDMA. Part I: Theory and sensitivity studies, *J. Atmos. Sci.*, 57(12), 1854 – 1871.
- Brechtel, F. J., and S. M. Kreidenweis (2000b), Predicting particle critical supersaturation from hygroscopic growth measurements in the humidified TDMA. Part II: Laboratory and ambient studies, *J. Atmos. Sci.*, 57(12), 1872 – 1887.
- Brock, C. A., et al. (2002), Particle growth in the plumes of coal-fired power plants, *J. Geophys. Res.*, 107(D12), 4155, doi:10.1029/2001JD001062.
- Cahill, T. A., L. Portnoff, and R. A. Reck (2004), Impact of long-range aerosol transport in Oklahoma, May 2003, paper presented at Fourteenth ARM Science Team Meeting, U.S. Dep. of Energy, Albuquerque, NM.
- Carrico, C. M., M. J. Rood, and J. A. Ogren (1998), Aerosol light scattering properties at Cape Grim, Tasmania, during the first Aerosol Characterization Experiment (ACE 1), *J. Geophys. Res.*, 103(D13), 16,565 – 16,574.
- Chuang, P. Y., A. Nenes, J. N. Smith, R. C. Flagan, and J. H. Seinfeld (2000), Design of a CCN instrument for airborne measurement, *J. Atmos. Oceanic Technol.*, 17(8), 1005 – 1019.
- Covert, D. S., R. J. Charlson, and N. C. Ahlquist (1972), A study of the relationship of chemical composition and humidity to light scattering by aerosols, *J. Appl. Meteorol.*, 11(6), 968 – 976.
- Damoah, R., N. Spichtinger, C. Forster, P. James, I. Mattis, U. Wandinger, S. Beirle, T. Wagner, and A. Stohl (2004), Around the world in 17 days—Hemispheric-scale transport of forest fire smoke from Russia in May 2003, *Atmos. Chem. Phys.*, 4, 1311 – 1321.
- Delle Monache, L., K. D. Perry, R. T. Cederwall, and J. A. Ogren (2004), In situ aerosol profiles over the Southern Great Plains cloud and radiation test bed site: 2. Effects of mixing height on aerosol properties, *J. Geophys. Res.*, 109(D6), D06209, doi:10.1029/2003JD004024.

- Draxler, R. R., and G. D. Rolph (2003), HYSPLIT (HYbrid Single-Particle Lagrangian Integrated Trajectory) Model, NOAA Air Resour. Lab., Silver Spring, MD. (Available at <http://www.arl.noaa.gov/ready/hysplit4.html>)
- Gasparini, R., R. J. Li, and D. R. Collins (2004), Integration of size distributions and size-resolved hygroscopicity measured during the Houston Supersite for compositional categorization of the aerosol, *Atmos. Environ.*, *38*(20), 3285 – 3303.
- Gasparini, R., D. R. Collins, E. Andrews, P. J. Sheridan, J. A. Ogren, and J. G. Hudson (2006), Coupling aerosol size distributions and size-resolved hygroscopicity to predict humidity-dependent optical properties and cloud condensation nuclei spectra, *J. Geophys. Res.*, *111*(D5), D05S13, doi:10.1029/2005JD006092.
- Ghan, S. J., T. A. Rissman, R. Elleman, R. A. Ferrare, D. Turner, C. Flynn, J. Wang, J. Ogren, J. Hudson, H. H. Jonsson, T. M. VanReken, R. C. Flagan, and J. H. Seinfeld (2006), Use of in situ cloud condensation nuclei, extinction, and aerosol size distribution measurements to test a method for retrieving cloud condensation nuclei profiles from surface measurements, *J. Geophys. Res.*, *111*(D5), D05S10, doi:10.1029/2004JD005752.
- Houghton, J. T., Y. Ding, D. J. Griggs, M. Noguer, P. J. van der Linden, and D. Xiaosu, Eds., (2001), *Climate Change 2001: The Scientific Basis*, 944 pp., Cambridge University Press, Cambridge, U.K.
- Iziomon, M. G., and U. Lohmann (2003), Characteristics and direct radiative effect of mid-latitude continental aerosols: The ARM case, *Atmos. Chem. Phys.*, *3*, 1903 – 1917.
- Jaffe, D., I. Bertschi, L. Jaegle, P. Novelli, J. S. Reid, H. Tanimoto, R. Vingarzan, and D. L. Westphal (2004), Long-range transport of Siberian biomass burning emissions and impact on surface ozone in western North America, *Geophys. Res. Lett.*, *31*(16), L16106, doi:10.1029/2004GL020093.
- Pahlow, M., G. Feingold, A. Jefferson, E. Andrews, J. A. Ogren, J. Wang, Y.-N. Lee, R. A. Ferrare, and D. D. Turner (2006), Comparison between lidar and nephelometer measurements of aerosol hygroscopicity at the Southern Great Plains Atmospheric Radiation Measurement site, *J. Geophys. Res.*, *111*(D5), D05S15, doi:10.1029/2004JD005646.
- Patashnick, H., and G. Rupprecht (1986), Microweighing goes on-line in real time, *Ind. Res. Dev.*, *28*(6), 74 – 78.
- Pitzer, K. S. (1973), Thermodynamics of electrolytes. I. Theoretical basis and general equations, *J. Phys. Chem.*, *77*(2), 268 – 277.

- Pitzer, K. S., and G. Mayorga (1973), Thermodynamics of electrolytes. II. Activity and osmotic coefficients for strong electrolytes with one or both ions univalent, *J. Phys. Chem.*, 77(19), 2300 – 2308.
- Pruppacher, H. R., and J. D. Klett (1997), *Microphysics of Clouds and Precipitation: Second Revised and Enlarged Edition with an Introduction to Cloud Chemistry and Cloud Electricity*, 954 pp., Springer, New York.
- Radke, L. F., A. S. Hegg, P.V. Hobbs, and J. E. Penner (1995), Effects of aging on the smoke from a large forest fire, *Atmos. Res.*, 38(1 – 4), 315 – 332.
- Roberts, G. C., and A. Nenes (2005), A continuous-flow streamwise thermal-gradient CCN chamber for atmospheric measurements, *Aerosol Sci. Technol.*, 39(3), 206 – 221.
- Rogers, C., and P. Squires (1977), A new device for studies of cloud condensation nuclei active at low supersaturations, in *Ninth International Conference on Atmospheric Aerosols, Condensation, and Ice Nuclei*, edited by A. Roddy and T. O’Conner, pp. 9 – 100, Galway Univ., Galway, Ireland.
- Rolph, G. D. (2003), Real-time Environmental Applications and Display sYstem (READY), NOAA Air Resour. Lab., Silver Spring, MD. (Available at <http://www.arl.noaa.gov/ready/hysplit4.html>)
- Rood, M. J., D. S. Covert, and T. V. Larson (1987), Hygroscopic properties of atmospheric aerosols in Riverside, California, *Tellus, Ser. B*, 39, 383 – 397.
- Schmid, B., J. Redemann, W. P. Arnott, A. Bucholtz, J. Reid, P. Colcarco, D. Covert, E. Elleman, P. Pilewskie, A. Strawa, R. A. Ferrare, B. N. Holben, E. J. Welton, H. H. Jonsson, K. Ricci, J. H. Seinfeld, D. D. Turner, and J. Wang (2004), Measurement and modeling of vertically resolved aerosol optical properties and radiative fluxes over the ARM SGP site during the May 2003 Aerosol IOP, paper presented at Fourteenth ARM Science Team Meeting, U.S. Dep. of Energy, Albuquerque, NM.
- Sheridan, P. J., D. J. Delene, and J. A. Ogren (2001), Four years of continuous surface aerosol measurements from the Department of Energy’s Atmospheric Radiation Measurement Program Southern Great Plains Cloud and Radiation Testbed site, *J. Geophys. Res.*, 106(D18), 20,735 – 20,747.
- Stolzenburg, M., N. Kreisberg, and S. Hering (1998), Atmospheric size distributions measured by differential mobility particle size spectrometry, *Aerosol Sci. Technol.*, 29(5), 402 – 418.
- Tang, I. N., and H. R. Munkelwitz (1994), Water activities, densities, and refractive indices of aqueous sulfates and sodium nitrate droplets of atmospheric importance, *J. Geophys. Res.*, 99(D9), 18,801 – 18,808.

- Twomey, S. (1974), Pollution and the planetary albedo, *Atmos. Env.*, 8(12), 1251 – 1256 .
- Twomey, S. (1977), *Atmospheric Aerosols*, 302 pp., Elsevier, New York City, NY.
- VanReken, T. M., T. A. Rissman, G. C. Roberts, V. Varutbangkul, H. H. Jonsson, R. C. Flagan, and J. H. Seinfeld (2003), Toward aerosol/cloud condensation nuclei (CCN) closure during CRYSTAL-FACE, *J. Geophys. Res.*, 108(D20), 4633, doi:10.1029/2003JD003582.
- Wang, J., R. C. Flagan, J. H. Seinfeld, H. H. Jonsson, D. R. Collins, P. B. Russell, B. Schmid, J. Redemann, J. M. Livingston, S. Gao, D. A. Hegg, E. J. Welton, and D. Bates (2002), Clear-column radiative closure during ACE-Asia: Comparison of multiwavelength extinction derived from particle size and composition with results from Sun photometry, *J. Geophys. Res.*, 107(D23), 4688, doi:10.1029/2002JD002465.
- Wang, J., R. C. Flagan, and J. H. Seinfeld (2003), A Differential Mobility Analyzer (DMA) system for submicron aerosol measurements at ambient relative humidity, *Aerosol Sci. Technol.*, 37(1), 46 – 52.
- Wang, S. C., and R. C. Flagan (1990), Scanning electrical mobility spectrometer, *Aerosol Sci. Technol.*, 13(2), 230 – 240.
- Warner, J. (1968), A reduction in rainfall associated with smoke from sugar-cane fires – An inadvertent weather modification?, *J. Appl. Meteor.*, 7(2), 247 – 251.
- Weber, R. J., D. Orsini, Y. Daun, Y.-N. Lee, P. J. Klotz, and F. Brechtel (2001), A particle-into-liquid collector for rapid measurement of aerosol bulk composition, *Aerosol Sci. Technol.*, 35(3), 718 – 727.

Chapter 4

CLOUD CONDENSATION NUCLEUS PROPERTIES OF ORGANIC COMPOUNDS:
EXPERIMENTAL RESULTS AND THEORETICAL PREDICTIONS

4.1 Abstract

The cloud condensation nucleation properties of a suite of organic compounds were studied in laboratory experiments at three operating supersaturations (0.11%, 0.21%, and 0.32%), and predictions of CCN behavior of a subset of these compounds were made using the Aerosol Diameter Dependent Equilibrium Model (ADDEM). Experimental activation diameters for these compounds ranged from 121 – 254 nm, 77 – 185 nm, and 51 – 125 nm for supersaturations of 0.11, 0.21, and 0.32%, respectively. These activation diameters indicate that some organic compounds were as CCN active as inorganic salts. In general, dicarboxylic acids and functionalized dicarboxylic acids were found to be the most active as cloud condensation nuclei (CCN), followed by amino acids, alcohols, glycolaldehyde dimer, and sinapic acid. The fatty acids and cholesterol did not activate at the experimental supersaturations. Compounds that were not expected to be very CCN active, based on aqueous solubility, were found to be fairly CCN active if they had high dissociation constants. The ADDEM predictions and the experimental results agreed well for DL-malic acid, adipic acid, glutaric acid, malonic acid, and succinic acid. Oxalic acid exhibited less CCN activity than was predicted by the ADDEM. The experiments presented here expose the laboratory complications associated with the investigation of the CCN properties of organic compounds due to the nature of the organic particles themselves. Careful consideration of these properties is necessary for successful experimental design and interpretation of experimental results.

4.2 Introduction

The complex relationship between atmospheric aerosols and cloud formation, properties, and lifetime represent one of the largest uncertainties in aerosol radiative forcing and, thus, climate change [Houghton *et al.*, 2001]. The climatic influence of aerosols caused by their effects on clouds is referred to as indirect effect, of which there are two major effects. Twomey [1974, 1977] stated that anthropogenic sources could increase the number concentration of atmospheric aerosol and, thus, cloud condensation nuclei (CCN), the aerosol particles upon which cloud droplets grow. An increase in CCN reduces the size of cloud droplets because the same amount of liquid water is distributed among more particles, and this leads to higher cloud albedo. This increase in cloud albedo, and the associated radiative cooling, is referred to as the first indirect climatic effect of aerosols [Houghton *et al.*, 2001]. The reduced size of the cloud droplets also inhibits rain-forming mechanisms, and the lifetime of the cloud is extended beyond that of a cloud with larger droplets [Warner, 1968; Albrecht, 1989]. This increase in cloud lifetime is referred to as the second indirect climatic effect of aerosols. Both effects result in clouds that are more reflective and more persistent, which cools the earth's surface [Twomey, 1977].

Aerosol particles are central to the formation of clouds because, as stated above, they act as CCN. More specifically, CCN are those aerosol particles that possess physical and chemical properties favorable to the condensation of water and subsequent cloud droplet growth under atmospheric conditions [Seinfeld and Pandis, 1998; Cruz and Pandis, 1997]. The ability of an aerosol particle of known size and composition to act as a CCN is described by Köhler theory, which incorporates the effects of particle curvature,

the so-called Kelvin effect, and particle dissolution into the droplet, referred to as the Raoult effect. Particle size and chemical properties, such as aqueous solubility, molecular weight, density, and extent of dissociation in solution, are very important factors in the ability of an aerosol particle to act as a CCN [Rudich, 2003; Sun and Ariya, 2006]. The formation of cloud droplets from inorganic salts, such as ammonium sulfate ((NH₄)₂SO₄), ammonium bisulfate (NH₄HSO₄), and sodium chloride (NaCl) is well understood, and predictions of the CCN behavior of salts have been successful. After sulfate, organic material has been found to be the second most abundant aerosol component in fine aerosols [Heintzenberg, 1989; Novakov and Penner, 1993; Saxena and Hildemann, 1996; Rudich, 2003; Sun and Ariya, 2006]. Properties, such as solubility, extent of dissociation, and surface activity, of the organic compounds found in atmospheric aerosol vary widely and can have complex, and sometimes conflicting, effects on the ability of these particles to act as CCN. Whether the presence of an organic enhances or limits CCN activation depends on the chemical characteristics of the aerosol, as well as the size distribution [Rissman *et al.*, 2004].

Laboratory studies of the CCN activation of organic aerosol particles are an important element in understanding the aerosol-cloud relationship, and many such studies exist in the literature. Dicarboxylic acids have been studied extensively, and their CCN abilities have been found to vary widely, with some compounds exhibiting CCN activity near that of (NH₄)₂SO₄. The CCN behaviors of some compounds were successfully predicted from Köhler theory modified to include solubility and/or surface tension effects [Cruz and Pandis, 1997; Corrigan and Novakov, 1999; Prenni *et al.*, 2001; Giebl *et al.*, 2002; Kumar *et al.*, 2003; Broekhuizen *et al.*, 2004].

Some studies have discussed the complications inherent to laboratory experiments concerning the CCN activity of organic compounds. *Raymond and Pandis* [2002] found that some compounds were much more CCN active than their solubilities would suggest and attributed this to the ability of water to wet these compounds. *Huff Hartz et al.* [2006] atomized some compounds from both water and alcohol solutions, and concluded that the CCN activity of some of the compounds was reduced if the aerosol particles were atomized from a non-aqueous solution. They also concluded that the ability of a compound to act as a CCN beyond what would be predicted based on solubility was a result of the existence of particles in a metastable state at low relative humidity (*RH*). *Hori et al.* [2003] found that particulate drying, solute vaporization, morphology and hydrophobicity of particles were key factors in theoretical prediction and experimental interpretation.

In the CCN laboratory study presented here, many of these experimental considerations were taken into account and corrections were made when possible. A suite of organic compounds (see Table 4.1) was chosen based on atmospheric relevance and/or use as surrogates in the chemical analysis and component identification of secondary organic aerosol samples. Some of these compounds have been studied previously, and those studies are compared to the present results. The Aerosol Diameter Dependent Equilibrium Model [*Topping et al.*, 2005a; 2005b] was used to predict the CCN behavior of a subset of these compounds, for which experimental surface tension data are available.

Table 4.1 Chemical Properties of Compounds Studied

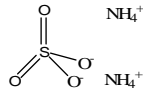
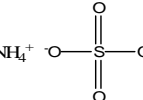
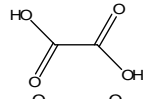
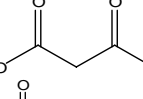
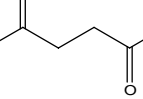
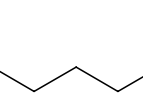
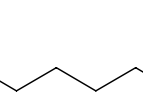
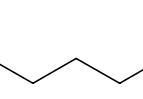
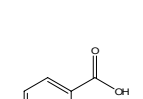
Class	Compound (# on Plots)	Chemical Formula	Chemical Structure	Molecular Weight ^a , g mol ⁻¹	Density ^a , g cm ⁻³	Solubility, g solute cm ⁻³ H ₂ O	pKa ^{c,j}	Vapor Pressure ^e , Torr
Inorganic Salts	Ammonium Sulfate (1)	(NH ₄) ₂ SO ₄		132.14	1.770	0.757 ⁱ		
	Ammonium Bisulfate (2)	NH ₄ HSO ₄		115.11	1.170	0.359 ⁱ		
	Sodium Chloride (3)	NaCl	Na ⁺ Cl ⁻	58.44	2.170	0.30 ^c		
Dicarboxylic Acids	Oxalic Acid (22)	C ₂ H ₂ O ₄		90.04	1.900	0.0951 ^b	1.23 ^d	2.51 x 10 ⁻⁶ 3.5 x 10 ^{-5k}
	Malonic Acid (4)	C ₃ H ₄ O ₄		104.06	1.619	0.424 ^b	2.83 ^d	1.0 x 10 ^{-5k} 3.6 x 10 ^{-4l}
	Succinic Acid (10)	C ₄ H ₆ O ₄		118.09	1.572	0.0835 ^b (25°C)	4.22	6.9 x 10 ^{-7k} 3.9 x 10 ^{-5l}
	Glutaric Acid (8)	C ₅ H ₈ O ₄		132.12	1.429	0.583 ^b (25°C)	4.35	2.23 x 10 ⁻⁴ 4.1 x 10 ^{-6k} 6.7 x 10 ^{-4l} 7.7 x 10 ^{-4m}
	Adipic Acid (20)	C ₆ H ₁₀ O ₄		146.14	1.360	0.015 ^b (15°C)	4.44	1.81 x 10 ⁻⁵ 1.5 x 10 ^{-7k} 9.8 x 10 ^{-6l} 1.0 x 10 ^{-5m}
	Pimelic Acid (18)	C ₈ H ₆ O ₄		160.17	1.329	0.058 ^e	4.46	5.92 x 10 ⁻⁶
	Phthalic Acid (14)	C ₈ H ₆ O ₄		166.17	2.180	0.00697 ^b (25°C)	2.95	2.14 x 10 ⁻⁶

Table 4.1 Continued...

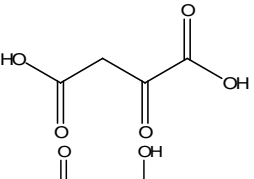
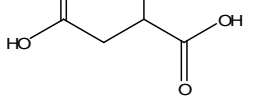
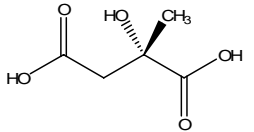
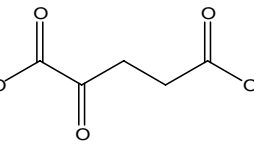
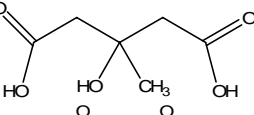
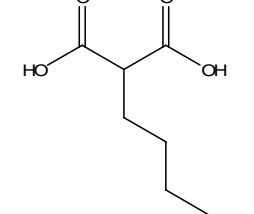
Class	Compound (# on Plots)	Chemical Formula	Chemical Structure	Molecular Weight ^a , g mol ⁻¹	Density ^a , g cm ⁻³	Solubility, g solute cm ⁻³ H ₂ O	pKa ^{c,j}	Vapor Pressure ^e , Torr
Functionalized Dicarboxylic Acids	Oxalacetic Acid (7)	C ₄ H ₄ O ₅		132.07	1.631 ^h	0.882 ^e	2.22 ^d	1.41 x 10 ⁻⁵
	DL-Malic Acid (6)	C ₄ H ₆ O ₅		134.09	1.601 ^d	1.44 ^b	3.40 ^d	7.19 x 10 ⁻⁵
	(S)-(+)- Citramalic Acid (15)	C ₅ H ₈ O ₅		148.12	1.513 ^e	0.727 ^e	3.65 ^e	1.61 x 10 ⁻⁴
	2-Ketoglutaric Acid (5)	C ₅ H ₆ O ₅		146.10	1.499 ^e	0.1 ^f	2.47 ^d	1.08 x 10 ⁻⁵
	3-Hydroxy-3- Methylglutaric Acid (12)	C ₆ H ₁₀ O ₅		162.14	1.417 ^e	1.0 ^e	3.95 ^e	1.95 x 10 ⁻⁶
	Butylmalonic Acid (17)	C ₇ H ₁₂ O ₄		160.17	1.197 ^e	0.019 ^e	2.99	2.69 x 10 ⁻⁵

Table 4.1 Continued...

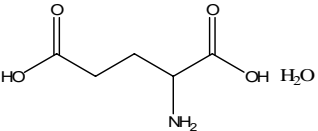
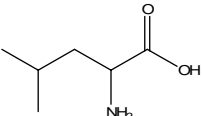
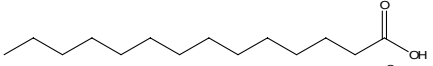
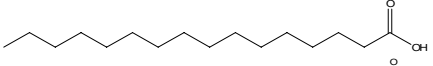
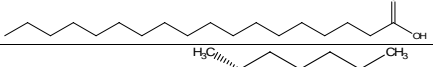
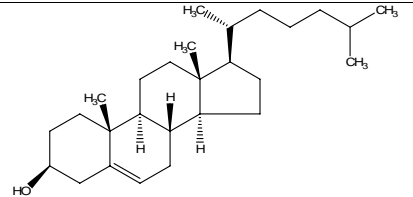
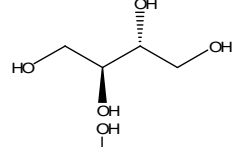
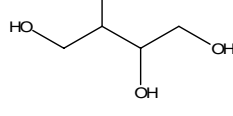
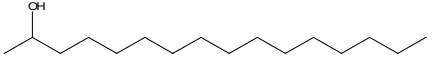
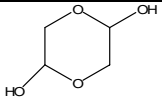
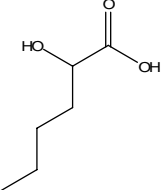
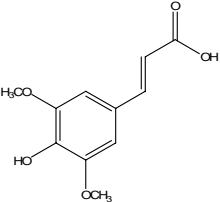
Class	Compound (# on Plots)	Chemical Formula	Chemical Structure	Molecular Weight ^a , g mol ⁻¹	Density ^a , g cm ⁻³	Solubility, g solute cm ⁻³ H ₂ O	pKa ^{c,j}	Vapor Pressure ^e , Torr
Amino Acids	DL-Glutamic Acid Monohydrate (9)	C ₅ H ₉ NO ₄ •H ₂ O		165.15	1.409 ^e	0.0235 ^b (25°C)	9.66 ^a	
	DL-Leucine (16)	C ₆ H ₁₃ NO ₂		131.17	1.293	0.022 ^b	2.328 ^d	0.0309
Fatty Acids	Myristic Acid (26)	C ₁₄ H ₂₈ O ₂		228.38	0.862	2.0 x 10 ⁻⁵ ^b	4.78 ^e	1.39 x 10 ⁻⁴
	Palmitic Acid (27)	C ₁₆ H ₃₂ O ₂		256.43	0.853	7.2 x 10 ⁻⁶ ^b	4.78	3.28 x 10 ⁻⁵
	Stearic Acid (28)	C ₁₈ H ₃₆ O ₂		284.48	0.941	2.9 x 10 ⁻⁶ ^b	4.78	8.58 x 10 ⁻⁶
Steroid	Cholesterol (25)	C ₂₇ H ₄₆ O		386.66	1.067	<3.87 x 10 ⁻⁷ _b	15.03 ^e	2.95 x 10 ⁻¹¹
Alcohols	<i>meso</i> - Erythritol (13)	C ₄ H ₁₀ O ₄		122.12	1.451	0.60 ^b	13.9 ^a	1.26 x 10 ⁻⁵
	DL-Threitol (11)	C ₄ H ₁₀ O ₄		122.12	1.451	0.38 ^b	13.9 ^a	1.25 x 10 ⁻⁵
	2- Hexadecanol (21)	C ₁₆ H ₃₄ O		242.45	0.834 ^e	3.0 x 10 ⁻⁸ ^h	15.26	4.14 x 10 ⁻⁵

Table 4.1 Continued...

Class	Compound (# on Plots)	Chemical Formula	Chemical Structure	Molecular Weight ^a , g mol ⁻¹	Density ^a , g cm ⁻³	Solubility, g solute cm ⁻³ H ₂ O	pKa ^{c,j}	Vapor Pressure ^e , Torr
Acetaldehyde	Glycolaldehyde Dimer (23)	C ₄ H ₈ O ₄		120.10	1.455 ^e	0.1 ^f		
	2- Hydroxycaproic Acid (19)	C ₆ H ₁₂ O ₃		132.16	1.100 ^e	0.032 ^e	3.86 ^e	9.28 x 10 ⁻⁴
Multifunctional	Sinapic Acid (24)	C ₁₁ H ₁₂ O ₅		224.21	1.307 ^e	0.0038 ^e	3.98 ^e	3.12 x 10 ⁻⁷

^aFrom *CRC Handbook*, unless specified otherwise

^bFrom *CRC Handbook of Data on Organic Compounds*; solubility at $T = 20^\circ\text{C}$, unless specified otherwise

^cFrom *Dictionary of Organic Compound*; values are at $T = 25^\circ\text{C}$ for water solutions; solubility is given at $T = 100^\circ\text{C}$
^dFrom *Properties of Organic Compounds* CRC online data base (<http://www.chemnetbase.com/scripts/pocweb.exe>); values are at $T = 25^\circ\text{C}$
^eCalculated using Advanced Chemistry (ACD/Labs) Software V8.14 for Solaris (© 1994-2006 ACD/Labs) by SciFinder; $T = 25^\circ\text{C}$
^fFrom MSDS, Sigma-Aldrich Co.

^gFrom *Raymond and Pandis* [2002]

^hFrom *The Merck Index*
ⁱFrom *Saxena and Hildemann* [1996]

^jValues are for the first dissociation constant.

^kFrom *Prenni et al.* [2001]

^lFrom *Bilde et al.* [2003]

^mFrom *Tao and McMurray* [1989]

4.3. The Aerosol Diameter Dependent Equilibrium Model (ADDEM)

4.3.1 Köhler Theory

When studying the hygroscopicity of aerosols, theoretical modeling techniques can often be divided into categories based on whether predictions are in the sub- or super-saturated humid environment. However, these techniques are largely based on a general equilibrium relation that can be derived by modifying the Clausius-Clapeyron equation [Köhler, 1936; McFiggans et al., 2005],

$$\begin{aligned}
 S = s + 1 &= \frac{p_w}{p_{w,sat}^o} = a_w K_e \\
 &= a_w \exp\left(\frac{4\sigma_{sol}M_w}{RT\rho_w D_{drop}}\right)
 \end{aligned}
 \tag{4.1}$$

where S is the saturation ratio, s is the supersaturation, p_w is the vapor pressure of water, $p_{w,sat}^o$ is the saturation vapor pressure of water, a_w is the water activity of the solution droplet, K_e is the Kelvin term $\{K_e = \exp[4\sigma_{sol}M_w/(RT\rho_w D_{drop})]\}$, σ_{sol} is the surface tension of the solution, M_w is the molecular weight of water, R is the universal gas constant, T is the temperature, ρ_w is the density of water, and D_{drop} is the droplet diameter [Koehler et al., 2005]. The water activity, a_w , of the solution droplet is given by

$$a_w^{-1} = 1 + v\Phi \frac{n_s}{n_w}
 \tag{4.2}$$

where ν is the number of ions into which a solute molecule dissociates, Φ is the osmotic coefficient, n_s is the number of moles of solute, and n_w is the number of moles of water [Koehler *et al.*, 2005]. Equation (4.2) can be simplified using the Taylor series expansion of the exponential ($e^x = 1 + x/1! + x^2/2! + \dots$) [McFiggans *et al.*, 2005]:

$$a_w = \exp\left(-\frac{\nu n_s}{n_w} \Phi\right) \quad (4.3)$$

The number of moles of water in solution is related to the diameter of the droplet, and the number of moles of solute in the droplet is related to the number of moles originally present in the dry solute particle. If the dry solute particle is assumed to be completely dissolved in the aqueous droplet, then equation (4.3) becomes

$$a_w = \exp\left(-\frac{\nu \rho_s M_w d_s^3}{\rho_w M_s D_{drop}^3} \Phi\right) \quad (4.4)$$

where ρ_s is the density of the solute, d_s is the diameter of the dry solute particle, and M_s is the molecular weight of the solute. Substitution of equation (4.4) into equation (4.1) and again using the Taylor series expansion for the exponential results in the following equation:

$$\begin{aligned} s &= \frac{4\sigma_{sol} M_w}{RT\rho_w D_{drop}} - \frac{\nu \rho_s M_w d_s^3}{\rho_w M_s D_{drop}^3} \Phi \\ &= \frac{A}{D_{drop}} - \frac{B}{D_{drop}^3} \end{aligned} \quad (4.5)$$

where $A = 4\sigma_{sol}M_w/(RT\rho_w)$ and $B = v\rho_sM_wd_s^3\Phi/(\rho_wM_s)$ [Seinfeld and Pandis, 1998].

Direct use of the fundamental Köhler (equation (4.5)) for predicting behavior in the subsaturated humid regime is prohibitive because it does not easily allow treatment of solid precipitation and requires modifications to be more applicable to such regions. Equilibrium models analyze the problem on a more fundamental level, using the theoretical basis on which the Köhler equation has been derived. This usually involves iterative models combined with equilibrium constants or a direct minimization of the Gibbs free energy for relating the equilibrium water activity to the composition. However, most equilibrium models do not consider the influence of curvature and, thus, cannot be used above 100% RH (or below about 100 nm radius). In other words, they analyze only the Raoult term of the Köhler equation, which is the second term of equation (4.5). An equilibrium model can evaluate a_w directly by using the original Köhler equation (equation (4.1)) and combining it with a method for including the influence of curvature, either by including a surface free energy term within the Gibbs energy summation or by using an iterative loop to solve for the Kelvin term. In this way, the entire Köhler curve can be constructed for a given particle or aerosol population.

Details about the Aerosol Diameter Dependent Equilibrium Model (ADDEM) and its use in the subsaturated humid regime are given in detail in *Topping et al.* [2005a, 2005b]. Essentially, it combines a direct minimization of the Gibbs free energy within an iterative loop that solves the original Köhler equation and allows for diameter-dependent growth factor calculations. For treating non-ideality, both the Pitzer-Simonson-Clegg [Pitzer and Simonson, 1986; Clegg et al., 1992] and UNIFAC (universal quasichemical

functional group activity coefficients) models [Fredenslund *et al.*, 1975] are employed in an additive approach for treating mixed inorganic/organic systems. The advantages and caveats of such an approach are discussed in Topping *et al.* [2005a,2005b], and the complexities in treating mixed inorganic/organic systems are treated extensively in the literature.

The ADDEM is expanded to the supersaturated regime by applying model adjustments and extensions which allow activation predictions, as well as growth factor calculations, above 100% *RH*. It should be noted that the original form of the Köhler equation given by equation (4.1) is for a purely aqueous droplet and does not treat the influence of the crystal-air interface on the deliquescence process.

4.3.2 Input Parameters

For the organic compounds, three different surface tension models (S1, S2, and S3) were employed in ADDEM calculations, as well as one model that assumes the surface tension of pure water (at 298.15 K). Surface tension model S1 employs the Tamura mixing rule [Tamura *et al.*, 1955]. Both models S1 and S2 are solved using the Brent method (see section 4.3.3) [Brent *et al.*, 1973], and the S2 model uses the Suarez thermodynamic method [Suarez *et al.*, 1989] and assumes constant molar surface area. Activities are calculated using UNIFAC with published parameters from Peng *et al.* [2001] for both the S2 and S3 models. The Li and Lu thermodynamic model [Li and Lu, 2001] is used in model S1 to fit experimental surface tension data, and saturated surface excess and adsorption constant parameters are also fit to experimental data in model S3. Hence, it is expected that model S3 is the most accurate surface tension model. For the

inorganic compounds, three different models were also used. The first model, S'1, is that of *Chen* [1994]; model S'2 uses the *Hu and Lee* [2004] mixing rule; and model S'3 is the *Li and Lu* [2001] model. *Topping et al.* [2005a, 2005b] found that growth factor calculations were particularly sensitive to the density, so the dry density is assumed in the ADDEM calculations presented here. The physical parameters used for the ADDEM calculations are given in Table 4.2.

4.3.3 Calculations for Supersaturated Conditions

For calculations above 100% *RH*, the surface energy associated with the aqueous-air interface is included within the Gibbs energy summation. As shown in Figure 4.1, the Raoult term divided by a_w converges to unity as the water content divided by D_{drop} increases and when the surface energy is not included. Also, in the atmosphere at equilibrium, a_w in the aerosol is equal to the ambient *RH* when curvature is neglected, and the ambient *RH* is restricted to values below 100%. Using rudimentary thermodynamics, it is possible to establish constraints for the final water activity as calculated by the model. The difference between the energies of formation for water in the gaseous and aqueous phase dictates this condition, and the chemical potentials of water must be equal in each phase, as is required for equilibrium:

$$\mu_{H_2O}^o + RT \ln(p_w) = \mu_{H_2O}^* + RT \ln(a_w) \quad (4.6)$$

Table 4.2 Physical Parameters for the ADDEM Calculations

Compound	Molecular Weight (M_s), g mol ⁻¹	Dry Density (ρ_s), g cm ⁻³	Super Cooled Density (ρ_{sc}), g cm ⁻³	Molar Volume ^a (v), cm ³ mol ⁻¹	Critical Molar Volume ^b (v_c), cm ³ mol ⁻¹	Surface Tension of Pure Component ^b (σ_s), dyn cm ⁻¹
Adipic Acid	146.14	1.360	1.250	149.02	422.65	40.70
Glutaric Acid	132.11	1.429	1.410	109.97	366.85	38.88
Malic Acid	134.09	1.595	1.595	100.57	325.75	37.51
Malonic Acid	104.06	1.619	1.619	77.47	255.25	40.70
Succinic Acid	118.09	1.572	1.572	93.27	311.05	40.16

^a Model S1, S2^b Model S1

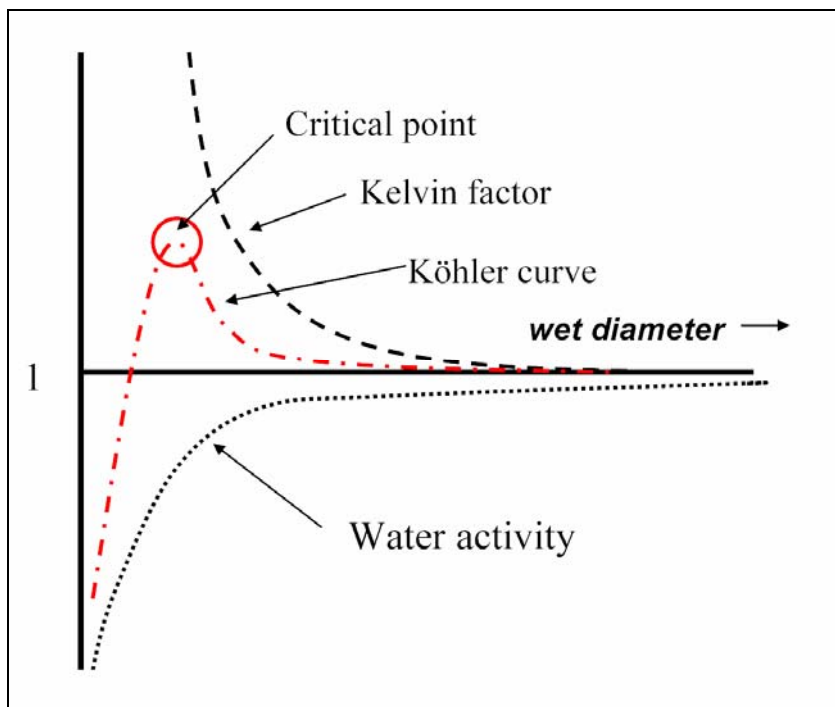


Figure 4.1. Hypothetical Köhler curve highlighting the contributions from the Raoult term (water activity, a_w) and the Kelvin factor. The critical point, the point at which the aerosol particle is said to be activated, is also highlighted.

where $\mu_{H_2O}^o$ is the energy of formation of water in the gas phase, p_w is the vapor pressure of water, and $\mu_{H_2O}^*$ is the energy of formation in the liquid phase. Rearranging to get an expression for $\mu_{H_2O}^o$ gives

$$\mu_{H_2O}^o = \mu_{H_2O}^* + RT \ln(a_w) - RT \ln(p_w) \quad (4.7)$$

Within this computation, $\mu_{H_2O}^o$ can be changed to obtain a different a_w , and vice versa. In this instance, a lower a_w (RH_{lower}) is required, and the new energy of formation for liquid water, $\mu_{H_2O,new}^o$, is given as

$$\mu_{H_2O,new}^o = \mu_{H_2O}^* + RT \ln(RH_{lower}) - RT \ln(p_w) \quad (4.8)$$

Using equation (4.6), and noting that $a_w = RH$ for this case:

$$\begin{aligned} \mu_{H_2O,new}^o &= RT \ln(RH_{lower}) + \mu_{H_2O}^o - RT \ln(RH) \\ &= \mu_{H_2O}^o + RT \ln\left(\frac{RH_{lower}}{RH}\right) \end{aligned} \quad (4.9)$$

Since the ratio of RH_{lower} to RH is less than 1, $\mu_{H_2O,new}^o$ is less than $\mu_{H_2O}^o$, and the magnitude is defined by the choice of RH_{lower} [Topping *et al.*, 2005a; 2005b]. Boundary conditions can be placed on the Raoult curve and used to encompass the root of the difference relationship given as

$$\frac{RH}{\exp\left(\frac{4\nu\sigma}{RTD_{drop}}\right)} - a_w = 0 \quad (4.10)$$

For systems where curvature can be neglected, the Kelvin factor is unity and equation (4.10) reduces to

$$RH - a_w = 0 \quad (4.11)$$

To calculate the growth factor at 1% supersaturation, an upper bound on the Raoult curve multiplied by the associated Kelvin factor may give an equilibrium RH greater than the ambient level. In other words, equation (4.10) is negative. Also, a lower bound on the Raoult curve multiplied by the associated Kelvin factor could give an equilibrium RH lower than the ambient levels. In this case, equation (4.10) is positive. Figure 4.2 shows how equation (4.10) varies by altering the water activity, adjusting $\mu_{H_2O, new}^0$, and varying ambient RH for a given dry size. Next, the Brent method [Brent *et al.*, 1973], which combines bisection, secant method, and inverse quadratic interpolation, can be employed to find the root of the difference relationship. The secant method, which assumes approximate linear behavior in the region of interest, is used for all calculations; the quadratic inverse interpolation is used where possible, and bisection is used as a backup method. Brent's method takes advantage of the largely linear behavior of the difference relationship when plotted as a function of a_w .

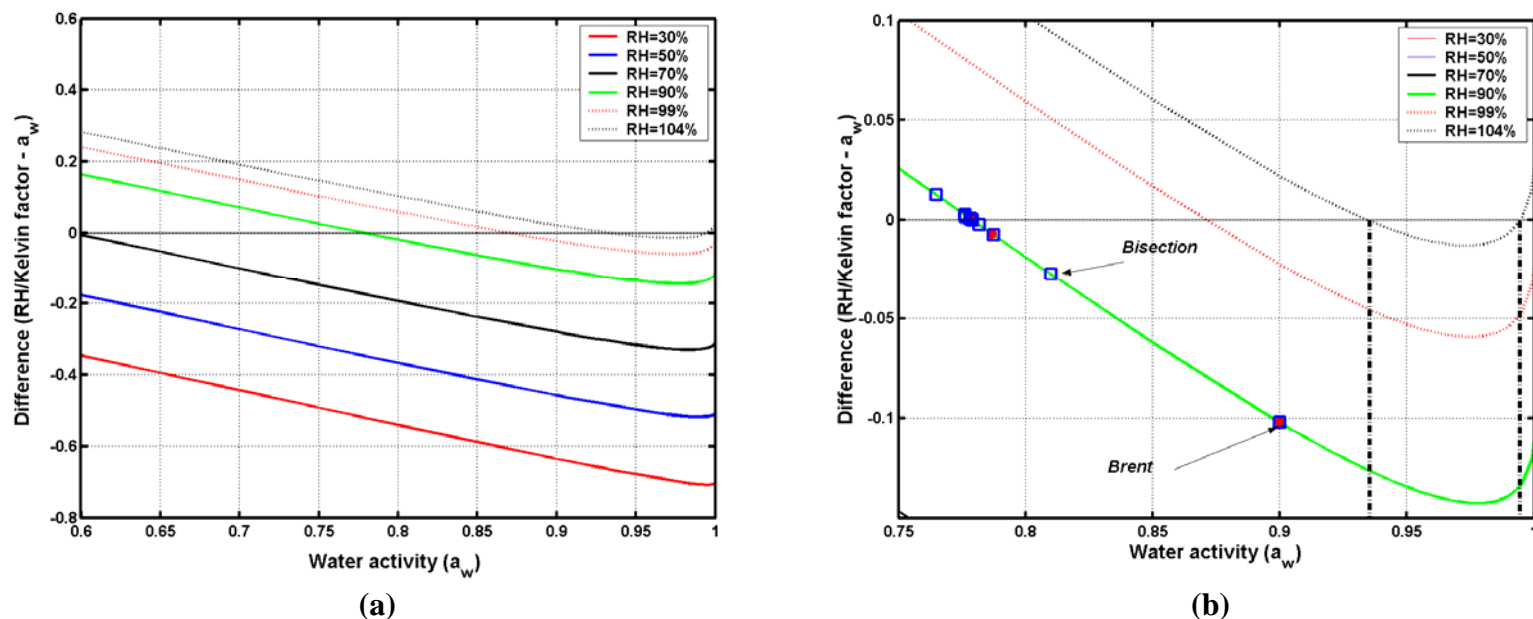


Figure 4.2. (a) Difference in RH divided by the Kelvin factor and water activity (a_w) as a function of water activity for a 10 nm dry diameter $(\text{NH}_4)_2\text{SO}_4$ aerosol at six different ambient RH values (given in the legend). At 90% RH , a water activity of 0.9 corresponds to a negative difference and only upon lowering the water activity to around 0.78 does the difference value approach zero. Hence, a 10 nm aerosol has an equilibrium water activity of around 0.78 at 90% RH and has a growth factor equivalent to a bulk solution at 78% RH . (b) Magnification of panel (a) for three ambient RH values for a 10 nm diameter $(\text{NH}_4)_2\text{SO}_4$ aerosol at water activities greater than 0.75. Below a water activity of 0.9 the difference relationship is fairly linear, but at higher water activities the relationship becomes parabolic near the critical point. At high RH (104%; $S = 1.04$; $s = 4\%$) there are two roots of the difference relationship for this size and composition (black dashed lines). The blue squares indicate iterations carried out using a bisection approach. The red circles indicate the much more efficient Brent's method for converging on solution (see section 4.3.3).

For these calculations, the algorithm provided by *Press et al.* [1992] is used. The difference between this scheme and that used for subsaturated regimes is that an initial nudge must be given before the energy minimization is run. In other words, the “flat” model must be kept at a water activity less than 1. The shape of the Köhler curve above 100% *RH* dictates that there are two possible solutions, and the history of the aerosol needs to be known before appropriate boundary conditions, defined by the maximum point, can be used to refine the calculation. As shown in Figure 4.2, there are two roots to equation (4.10) at an ambient *RH* of 104% ($S = 1.04$; $s = 4\%$) and for the specified size and composition. The a_w associated with the minimum point, which is equivalent to the critical point on the Köhler curve, would be used as the upper boundary on the Raoult curve for points prior to activation and as a lower boundary for points after activation. For the former case, a lower boundary of 50% of the ambient *RH* should bracket the root, using an overly cautious maximum Kelvin factor of 2. For the latter scenario, a maximum water activity of 0.9999, for example, should again be sufficient, and this is easily altered in the algorithm. An example of a full Köhler curve constructed using ADDEM is given in Figure 4.3.

4.3.4 Critical Points

For each growth factor calculation an ambient *RH* is set, and an iterative loop may ensue, such that the difference between the calculated wet diameters is minimized or instability in the growth calculations is sought (i.e., an overshoot of the critical point). A much more reliable technique is to minimize the Köhler curve directly. The required one-dimensional search uses the control of a_w through equation (4.9) to define upper and

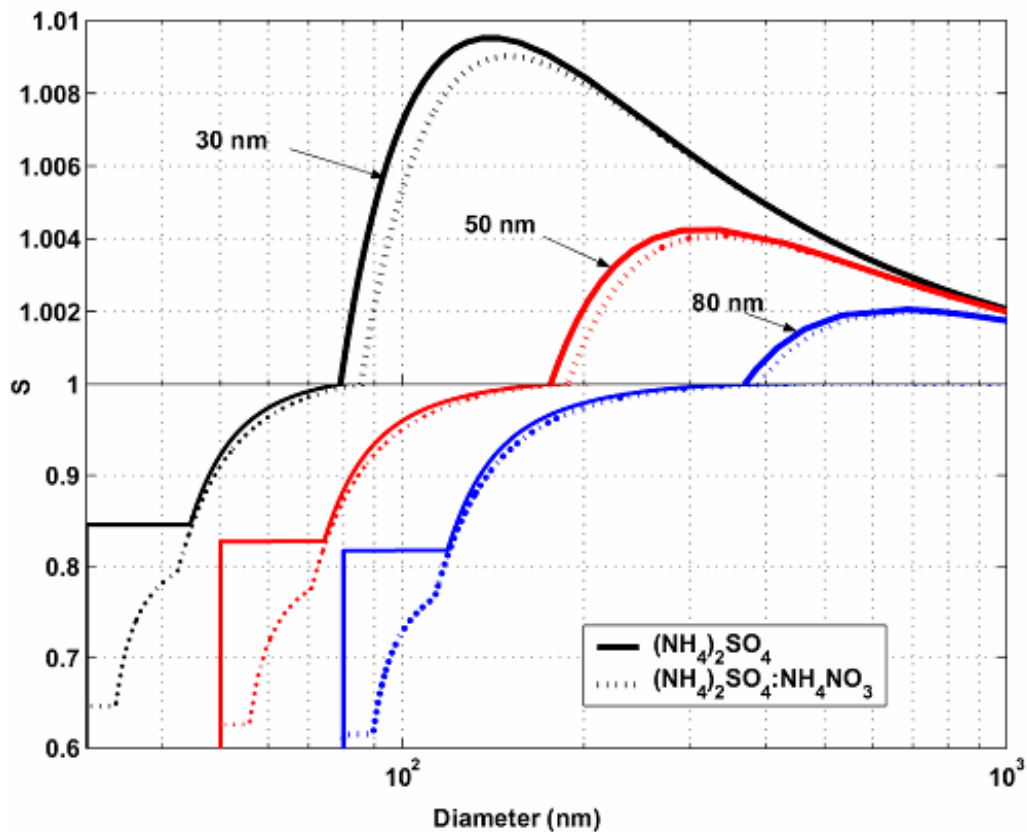


Figure 4.3. Predicted Köhler curves for $(\text{NH}_4)_2\text{SO}_4$ and mixed $(\text{NH}_4)_2\text{SO}_4:\text{NH}_4\text{NO}_3$ aerosols at 30, 50, and 80 nm dry diameters and 298.15 K using ADDEM. The top half of the plot is magnified to clearly show the critical points. The effect of solid precipitation can be clearly seen on each curve.

lower boundaries that bracket the critical point. Once the model is run with a given a_w , the appropriate physical information such as surface tension and density can be calculated and the point on the Köhler curve determined. Unfortunately derivative information cannot be attained easily. As a_w varies, so do the terms that define the Kelvin factor. The use of complex thermodynamic activity coefficient models and surface tension rules would require complicated derivative information. Fortunately there is no need to derive such relationships and methods can be used that need only evaluations of the function, such as a basic bisection approach or Brent's method for function minimization. The latter is likely to be particularly useful since it will exploit the parabolic nature of the Köhler curve near the critical point (see Figure 4.4). Figure 4.5 shows an example of the minimization function converging on the critical point. Since the function needs to be minimized, the negative equilibrium saturation ratio is plotted. The point labeled "1" is the first calculated value of the iteration halfway between the upper and lower boundaries set here as 0.9999 and 0.9. The successive iterations are also highlighted.

4.4 Experimental Setup

4.4.1 General Setup

The experimental setup (diagramed in Figure 4.6) includes: (a) an aerosol generation system to create aerosol particles; (b) a differential mobility analyzer (DMA) classification system to classify the aerosol particles; (c) a condensation particle counter (CPC; TSI, Inc., Model 3010) to count the total number of aerosol particles at a certain classified diameter; (d) the Caltech three-columned CCN counter (CCNC3) to count the number of aerosol particles that grow into droplets at the operating supersaturations of

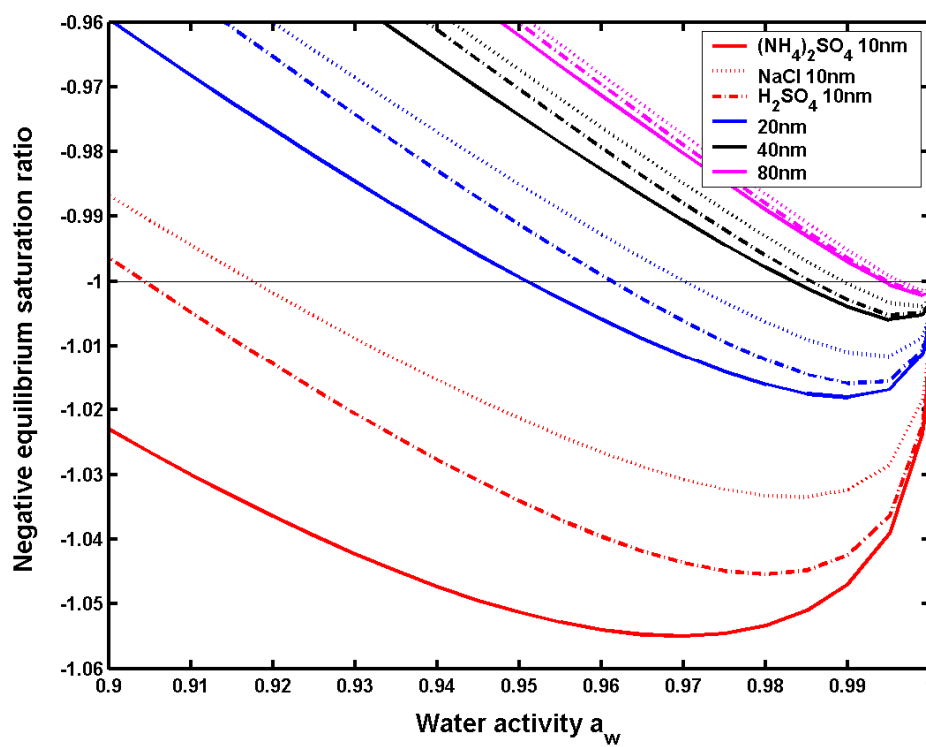


Figure 4.4. Negative equilibrium saturation ratio (S) as a function of water activity (a_w) for $(\text{NH}_4)_2\text{SO}_4$, NaCl and H_2SO_4 aerosol at 10, 20, 40, and 80 nm. The negative value is shown because the function is minimized when finding the critical point.

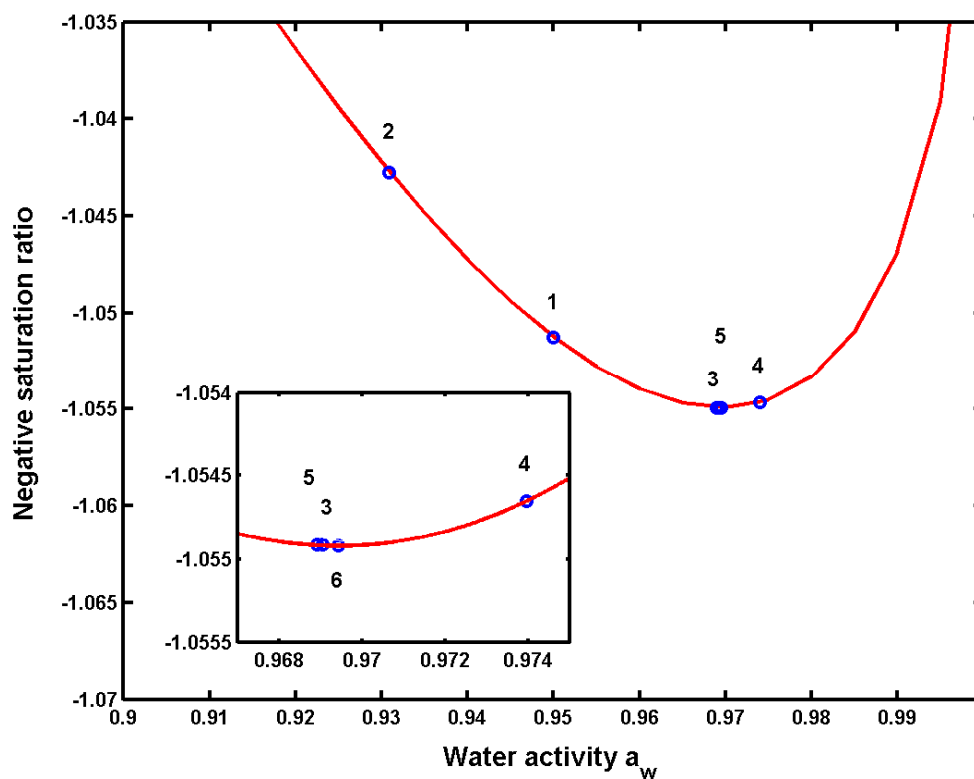


Figure 4.5. Negative saturation ratio (S) for a 10 nm $(\text{NH}_4)_2\text{SO}_4$ aerosol as a function of water activity (a_w). The blue circles highlight the iterations carried out by Brent's minimization scheme, and the iteration number is given above the blue circle. The subplot magnifies the region around the minimum point, clearly showing its parabolic nature.

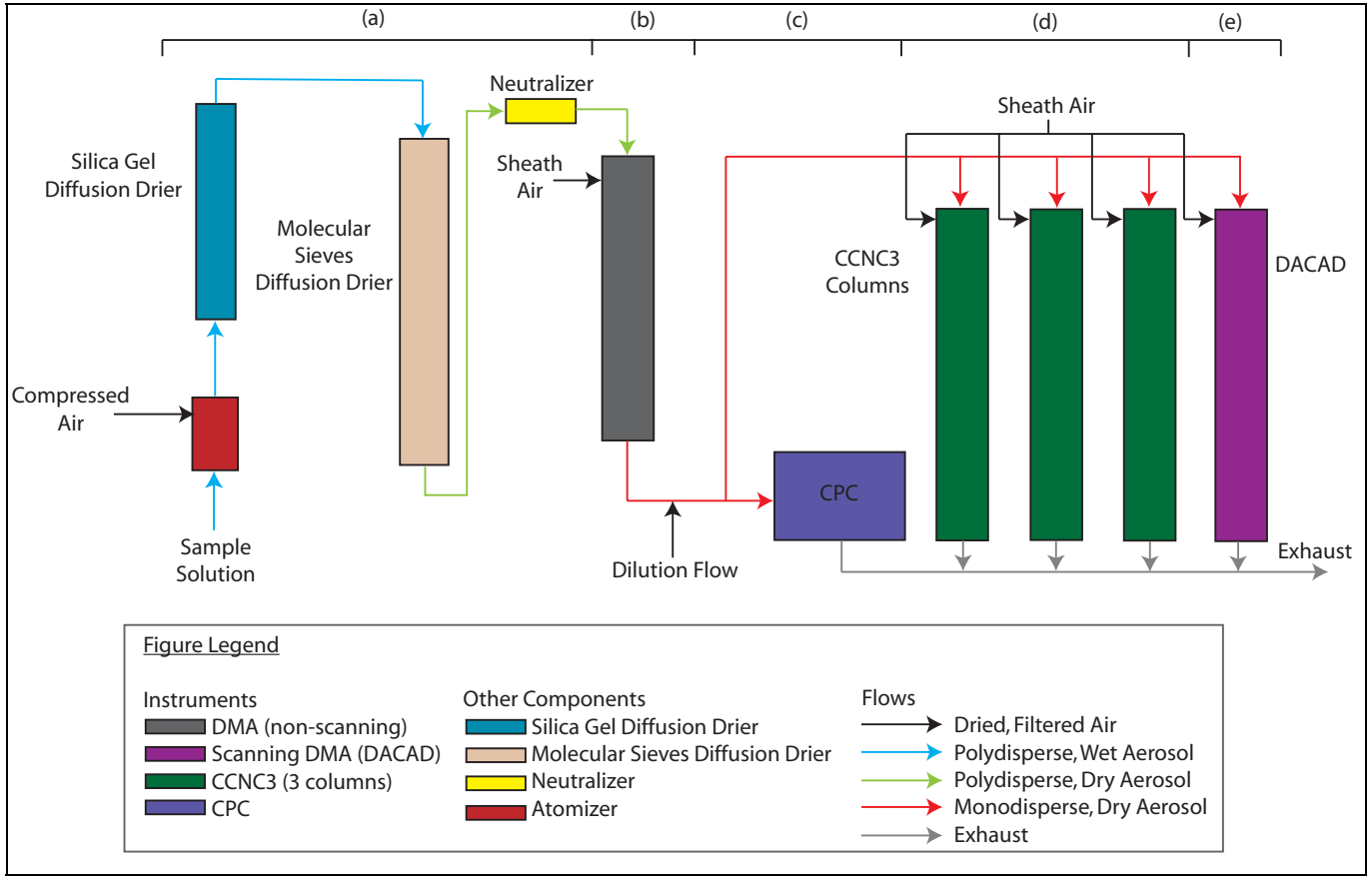


Figure 4.6. Experimental Setup. Includes: (a) an aerosol generation system to create aerosol particles; (b) a classification DMA to classify the aerosol particles (c) a CPC to count the total number of aerosol particles at a certain classified diameter; (d) the CCNC3 to count the number of aerosol particles that grow into droplets at the operating supersaturations of the instrument (see Table 4.3); (e) the DACAD to determine the size distribution of the aerosol particles entering the CCNC3.

the instrument; and (e) the Caltech dual automatic classified aerosol detectors (DACAD) to determine the size distribution of the aerosol particles entering the CCNC3.

The aerosol generation and classification system consists of an atomizer, diffusion driers, a neutralizer, and a DMA. (“DMA” will be used to signify parameters associated with the DMA from the classification system; “DACAD” will be used for the DMA from the DACAD system.) The DMA has Caltech geometry, with an outer radius ($R1$) of 0.0192 m, an inner radius ($R2$) of 0.00945 m, and a length (L) of 0.4119 m, and operated with an aerosol sample flow rate (Q_{aero}) of 0.33 lpm and a sheath-to-aerosol ratio of 10.

For each calibration and experiment, a solution of the compound of interest was atomized to create droplets that were then dried in two diffusion driers, one filled with silica and the other with molecular sieves (type 5A, 4-8 mesh). After drying, the aerosol particles were charged using a Po-210 bipolar ion source (neutralizer) and introduced into the classification DMA, which selected particles with the desired dry diameters ($D_{p,DMA}$). The resulting monodisperse aerosol sample was then split to the CCNC3, DACAD, and CPC.

4.4.2 Three-Column CCN Counter (CCNC3)

The CCNC3 (described in-depth in Chapter 3 [Rissman *et al.*, 2006]) consists of three columns that operate in parallel. In this study, each column operated at a different supersaturation, which was determined by calibrations with ammonium sulfate ($(\text{NH}_4)_2\text{SO}_4$), ammonium bisulfate (NH_4HSO_4), and sodium chloride (NaCl). For each calibration, an aqueous solution of the inorganic salt was atomized to create droplets that were then dried and introduced into the classification system. Certain dry diameters were

selected using the DMA, and the resulting monodisperse aerosol sample was split to the CCNC3 and CPC. The activated ratio (AR) is the ratio of the number concentration of CCN measured by the CCNC3 (N_{CCN}) to the number concentration of total particles measured by the CPC (N_{CPC}), and the activation diameter (d_{act}) is the dry diameter at which 50% of the particles grow into droplets ($AR = 0.5$). A shape factor of 0.08 was used for NaCl. The critical supersaturations (s_c) corresponding to dry salt particles with the classified diameters, $D_{p,dry}$, were calculated using an average of the ADDEM surface tension models (S'1, S'2, S'3; not including the water surface tension model). Calibrations were performed before and after the organic experiments, and the operating supersaturation (s_o) of each column was taken as the sigmoid fit to the plot of all AR (from all three calibration salts and from both pre- and post-experiment calibrations) versus the s_c corresponding to $D_{p,DMA}$. The columns operated at supersaturations of $(0.11 \pm 0.03) \%$, $(0.21 \pm 0.03) \%$, and $(0.32 \pm 0.06) \%$. The calibrated d_{act} and the s_o values for all three columns are given in the legends in Figure 4.7 and in Table 4.3. The error bars on the calibration curves result from the uncertainty in the diameter selected by the DMA (horizontal, $D_{p,dry}$ error bars; generally taken to be $\pm 5\%$, although calibrations indicated it to be less than $\pm 2\%$) and the combined uncertainties associated with the concentrations measured by the CPC and the CCNC3 (vertical, AR error bars).

4.4.3 Dual Automatic Classified Aerosol Detectors (DACAD)

The Caltech DACAD has been deployed in several airborne experiments, and its characteristics are well documented [*Wang et al.*, 2002, 2003; *VanReken et al.*, 2003]. The DACAD consists of two DMA systems operated in parallel. One of the DMA

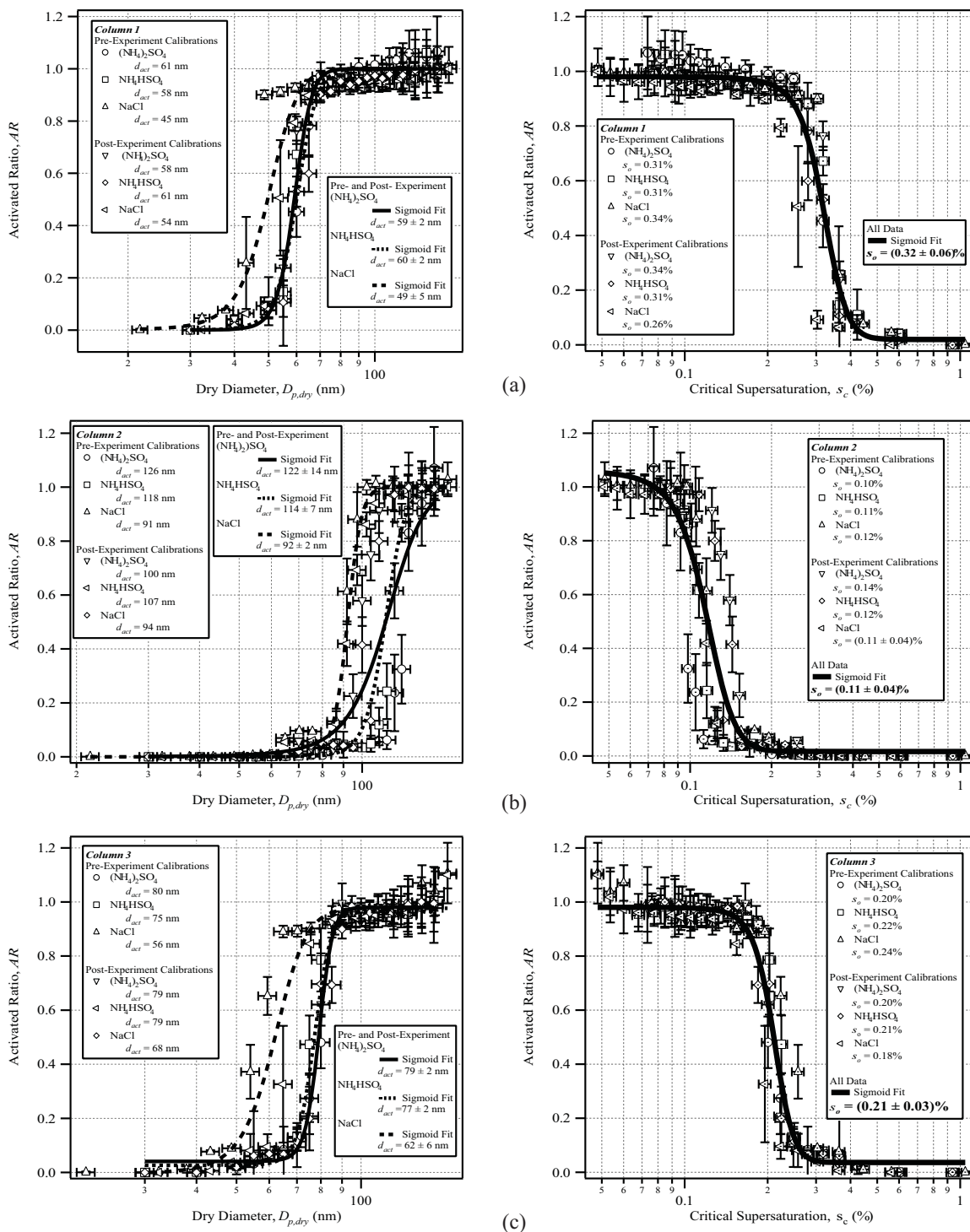


Figure 4.7. Calibration curves for (a) column 1, (b) column 2, and (c) column 3 using $(\text{NH}_4)_2\text{SO}_4$, NH_4HSO_4 , and NaCl as calibration salts.

Table 4.3 CCNC3 Calibration Summary^a

Column	d_{act} , nm			s_c , %			s_o , %
	(NH ₄) ₂ SO ₄	NH ₄ HSO ₄	NaCl	(NH ₄) ₂ SO ₄	NH ₄ HSO ₄	NaCl	
1	59 ± 2	60 ± 2	49 ± 5	0.32 ± 0.02	0.32 ± 0.01	0.30 ± 0.04	0.32 ± 0.06
2	122 ± 14	114 ± 7	92 ± 3	0.12 ± 0.02	0.12 ± 0.01	0.11 ± 0.01	0.11 ± 0.03
3	79 ± 3	77 ± 3	62 ± 6	0.20 ± 0.01	0.22 ± 0.01	0.21 ± 0.03	0.21 ± 0.03

^a d_{act} and s_c values are determined from both pre- and post-experimental calibrations for each inorganic salt. s_o is determined from the combined calibrations for all of the inorganic salts both before and after experiments.

systems measures the dry aerosol size distribution, while the other measures the aerosol size distribution at ambient *RH* by using an active *RH* controller [Wang *et al.*, 2003]. The main components of each measurement system are a cylindrical DMA (TSI Inc., Model 3081) and a CPC (TSI Inc., Model 3010), which has a 50% counting efficiency at 10 nm. Using the scanning mobility technique [Wang and Flagan., 1990], each DMA system generates a size distribution for particle diameters from ~ 12 to ~ 730 nm every 73.5 s. In this study, only the dry DMA system operated in the DACAD.

4.4.4 Organic Compounds and Experimental Issues

The organic compounds studied here and some of their chemical properties are given in Table 4.1. The organic compounds were selected for their atmospheric relevance or because they have similar structural features to secondary organic aerosol (SOA). The CCN properties of many of these compounds have been studied before, but published CCN studies were not found for the following compounds: *meso*-erythritol, sinapic acid, 2-hydroxycaproic acid, 2-ketoglutaric acid, (S)-(+)-citramalic acid, 3-hydroxy-3-methylglutaric acid, butylmalonic acid, glycolaldehyde dimer, DL-threitol, and oxalacetic acid. Many of these compounds are surrogate standards used in chemical analyses to identify species in SOA particles formed in Caltech chamber studies or collected from field experiments. Surrogate standards usually have similar masses, retention times (in gas or liquid chromatography methods), and functional groups as the species present in the SOA. These compounds were chosen based on their usefulness as SOA surrogates, as well as for their various functional groups.

DL-threitol and *meso*-erythritol are polyols and are good surrogate standards for the 2-methyltetrol species, which act as good tracer compounds in ambient aerosol formed from oxidation of isoprene. *Claeys et al.* [2004] and *Edney et al.* [2005] have detected 2-methyltetrols in ambient aerosol, as well as in chamber studies. (S)-(+)-citramalic acid is also used as a surrogate for isoprene SOA because it has a C5 backbone like isoprene and is essentially the oxidized form of isoprene. Sinapic acid was used as a surrogate standard for an SOA product from α -pinene oxidation in the presence of NO_x because it is a biogenic compound and had a retention time on the liquid chromatograph close to that of the SOA species, which had an elemental composition of $\text{C}_{10}\text{H}_{16}\text{NO}_7\text{S}$ (sinapic acid is $\text{C}_{11}\text{H}_{12}\text{O}_5$). This $\text{C}_{10}\text{H}_{16}\text{NO}_7\text{S}$ compound was the most abundant species detected in SOA sampled in the southeast United States [*Gao et al.*, 2006]. Glycolaldehyde dimer is a surrogate standard for glyoxal polymerization in SOA. *Kalberer et al.* [2004] showed that glyoxal results from 1,3,5-trimethylbenzene oxidation. 2-hydroxycaproic acid is used to quantify SOA due to its acid and hydroxyl groups. 2-ketoglutaric acid, 3-hydroxy-3-methylglutaric acid, and butylmalonic acid have been used to quantify cycloalkene ozonolysis SOA products. Oxalacetic acid is good diacid standard and has been detected in cycloalkene ozonolysis experiments [*Gao et al.*, 2004].

Evidence has been found that organic aerosols created by atomization from water solutions may retain water from the solution, even after drying to low relative humidity before size selection, and that the phase state of the aerosol particles is an important factor in their CCN activity [*Hori et al.*, 2003; *Bilde and Svenningsson*, 2004; *Henning et al.*, 2005]. This complicates CCN activation experiments in two different ways: (1) incorrect size selection in the DMA (the wet particle is a different size than the dry

particle would be); and (2) activation properties of the compound are masked by the presence of water. *Henning et al.* [2005] showed that dry particles require higher supersaturations to activate than wet particles of the same compound. To ensure that the particles did not contain water, aerosol particles were created from a methanol solution for the experiments presented here.

Some of the organic particles shrank in the system plumbing, perhaps due to the evaporation of organic material from the particles into the air stream or from the release of trapped solvent from the particles after size selection. The evaporation, and consequent shrinking, of the organic particles after size selection by the DMA but before being counted by the CCNC3 would cause the d_{act} to appear artificially large if the actual size of the particle entering the CCNC3 was unknown. The DACAD was included in the experimental setup to measure the size distribution of the particles that actually entered the CCNC3. At least six up- and down-scans were measured by the DACAD for each diameter selected by the DMA during the experiments. Calibrations were performed for the both the DMA and DACAD using polystyrene latex (PSL) spheres and showed that diameters classified by the two systems agreed within 1.8% and 3.2% for the DACAD up- and down-scans, respectively. The sizes of the particles may have been changing inside the DMA and/or DACAD, while the particles were being size classified. For this reason, errors in selected diameter for the DMA have been increased to $\pm 5\%$, which is about twice as large as the error determined from calibrations with PSL spheres.

Size distribution changes were also observed after size selection in the classification DMA, with distributions becoming broadened or multi-peaked by the time they were measured in the DACAD. DMA and DACAD PSL calibrations indicate that

size classification resulted in very sharp peaks, defined here as having a standard deviation (σ) less than 0.10. Size distribution changes, including both broadening and the appearance of multiple peaks, were observed for 8 out of the 27 organic compounds studied. If the only process occurring were evaporation of organic material from the aerosol particles, the DACAD size distribution would still show only one, sharp peak but at a smaller diameter (as it did for most compounds) because the same-sized particles would evaporate at the same rate. A hypothesis for the formation of the multi-peaked size distributions is that solvent was trapped in some of the particles and subsequently “escaped” from those particles between the DMA and DACAD/CCN instruments, effectively causing those particles to “shrink” more than the particles that did not contain solvent at the point of classification. This occurred for myristic acid in methanol and for oxalic acid particles created from both methanol and water solutions, although a full experiment was not run from the aqueous solution for oxalic acid.

Figure 4.8 shows examples of shrinking and size distribution changes for the given diameter particle, size-selected by the DMA, for three different compounds: oxalic acid, malonic acid, and pimelic acid. The pimelic acid size distribution shown is indicative of a “sharp” size distribution, with $\sigma < 0.10$. The size distribution information from the DACAD allowed corrections to be made in the calculation of AR and, therefore, in the determination of d_{act} . For compounds for which DACAD size distributions have a standard deviation less than or equal to 0.10, the DMA selected $D_{p,DMA}$ was replaced with the DACAD measured diameter ($D_{p,DACAD}$) in the analysis. (In some plots and tables, the dry diameter is shown as a generic $D_{p,dry}$. For inorganic compounds, $D_{p,dry}$ is $D_{p,DMA}$; for organic compounds, $D_{p,DACAD}$.) When size distributions were broadened or became

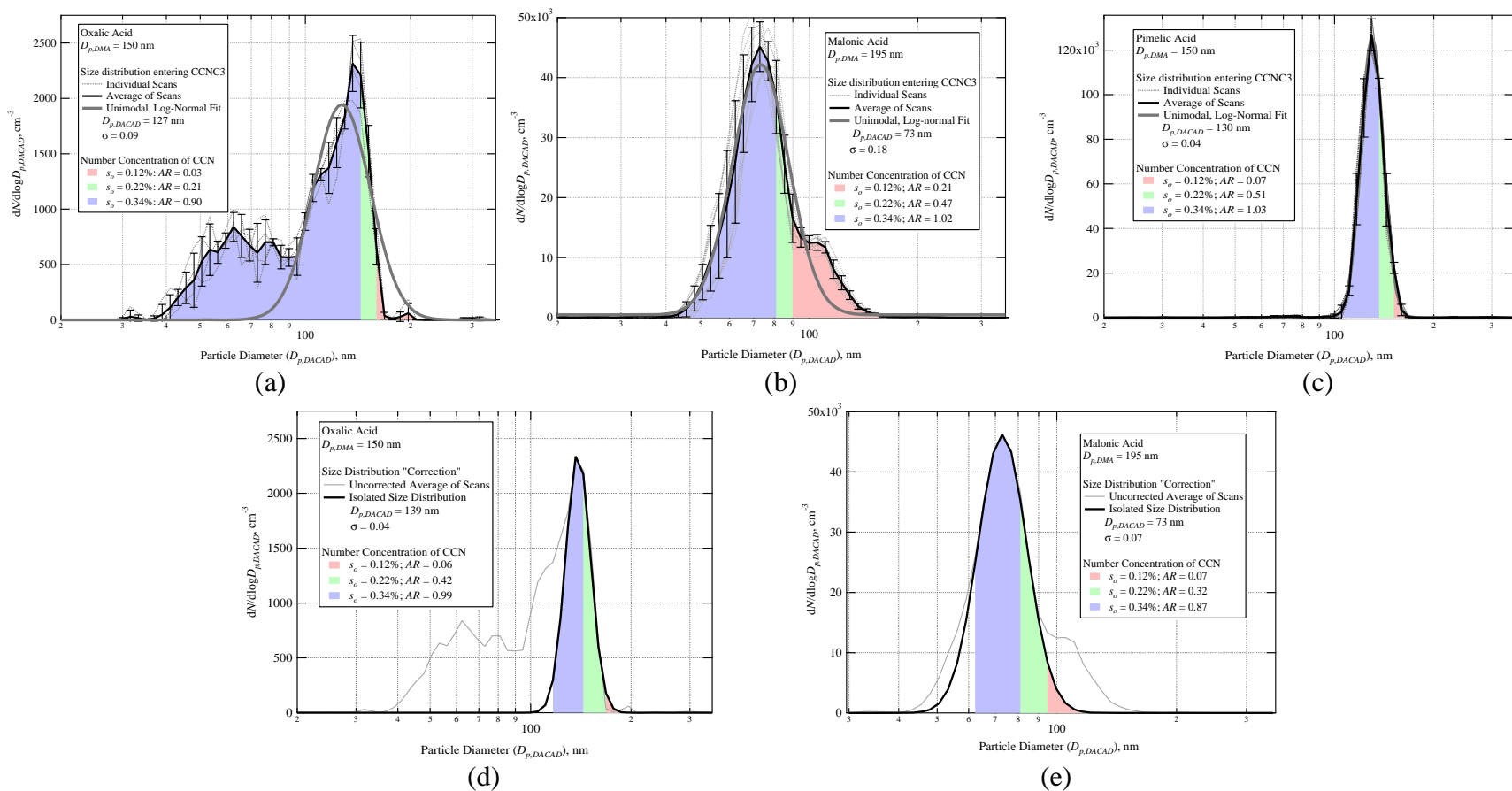


Figure 4.8. DACAD size distributions for the given DMA-selected sized particles of (a) oxalic acid ($D_{p,DMA} = 150$ nm), (b) malonic acid ($D_{p,DMA} = 195$ nm), and (c) pimelic acid ($D_{p,DMA} = 150$ nm). The CCN number concentrations (the shaded areas) are shown for each operating supersaturation. The bottom panels show the “corrected”, $\sigma < 0.10$, size distributions and CCN number concentrations for DMA-selected particles of (d) oxalic acid, and (e) malonic acid. No correction was necessary for pimelic acid because its size distribution had a σ less than 0.10.

multipeaked due to particle evaporation, the AR value did not necessarily correspond to the peak $D_{p,DACAD}$ determined by a unimodal, lognormal fit to the size distribution. A new, sharp size distribution was determined by fitting a lognormal distribution to the main peak of the measured size distribution. A cutoff diameter, the DACAD bin diameter at which the cumulative summation of particles with diameters greater than the cutoff diameter was closest to the measured CCN concentration, was determined for each operating supersaturation. The difference between the original size distribution and the new, sharp distribution was then used to adjust the AR values. This method is illustrated in Figure 4.8, where the CCN number concentration is the area under the curve (the shaded areas).

Figure 4.9 shows the experimental CCN activation curves for malonic acid, atomized from both methanol and aqueous solutions. For all three operating supersaturations, AR shows a slight increase at lower dry diameters after AR decreases below 0.2, 0.3, and 0.4 for s_o of 0.11, 0.21, and 0.32%, respectively. These features are the result of multiply charged particles, which are actually larger than the size selected in the DMA and are able to activate in the CCNC3. AR values were adjusted to account for the multiply charged particles, but the adjustment usually did not affect d_{act} ($AR = 0.5$) values by more than 1 or 2 nm, except in the extreme case of malonic acid at $s_o = 0.11\%$. After the multiply charged particles are removed, d_{act} decreases from 138 to 121 nm for malonic acid at $s_o = 0.11\%$. This decrease was simply caused by the shifting of the sigmoid fits and not by a shifting of the data around $AR = 0.50$.

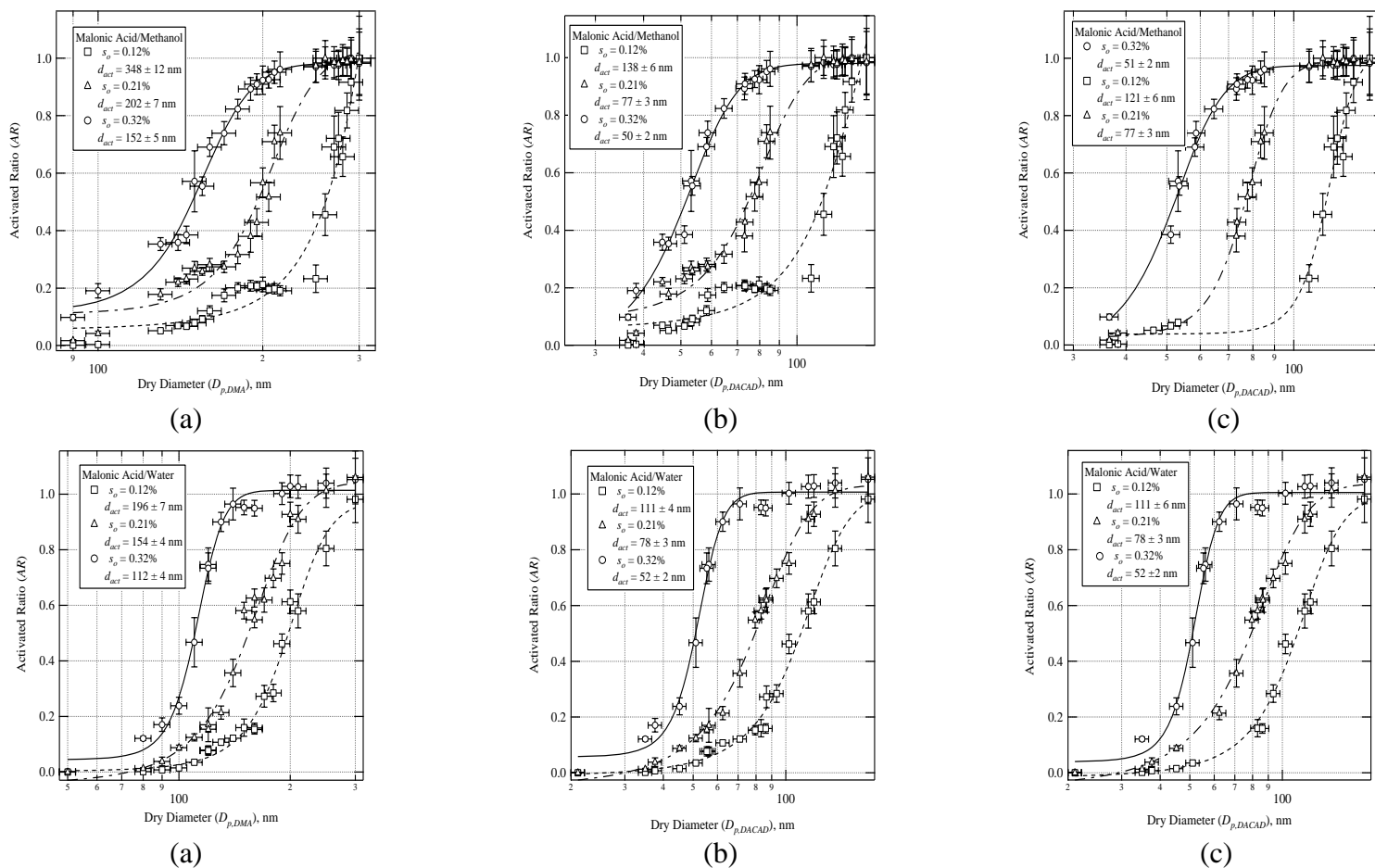


Figure 4.9. Experimental CCN activation curves for malonic acid in methanol (panels (a), (b), and (c)) and water (panels (d), (e), and (f)). Panels (a) and (d) show data versus the uncorrected diameter selected with the classification DMA. Panels (b) and (e) show experimental data with dry diameter corrected to the DACAD diameter, and panels (c) and (f) show experimental data with doubly charged particles removed.

4.4.5 Solvent Comparison

A comparison between water and methanol as atomization solvents was undertaken, with adipic acid, succinic acid, DL-malic acid, and malonic acid as the solutes. The d_{act} values for water and methanol solutions for these compounds are given in Table 4.4. As an example, the experimental CCN activation curves for malonic acid in water and methanol are shown in Figure 4.9, and the experimentally determined values for d_{act} (corrected for DACAD values) are given in the legend. The d_{act} values are close and often within the measurement errors for these compounds, except for adipic acid (see section 4.5.4.1), which does not allow a definite conclusion about a difference in the d_{act} values for particles atomized from aqueous and methanol solutions. It would seem that the CCN activity of a species depends on the solution from which particles are atomized if the dry diameters had not been corrected to the DACAD values. Figure 4.9 also shows the results for malonic acid particles atomized from both aqueous and methanol solutions before DACAD correction. There is a greater difference in the experimentally determined d_{act} values when the shrinking of the particles is not taken into account and the diameters are not DACAD corrected. The shrinking of particles after classification but before detection in the CCN instrument, which would lead to an overestimation of d_{act} , might make it seem that the CCN activity of the species depends on the solution from which it is atomized. However, CCN activity is a property of the pure compound (not the compound and solvent) and most discrepancies can be attributed to experimental design.

Table 4.4 Comparison between Methanol and Aqueous Solution Experiments

Compound (# on plots)	Methanol Solution			Aqueous Solution		
	d_{act} , nm at $s_o = 0.11\%$	d_{act} , nm at $s_o = 0.21\%$	d_{act} , nm at $s_o = 0.32\%$	d_{act} , nm at $s_o = 0.11\%$	d_{act} , nm at $s_o = 0.21\%$	d_{act} , nm at $s_o = 0.32\%$
Succinic Acid (9)	142 ± 7	105 ± 5	73 ± 4	133 ± 9	93 ± 9	66 ± 5
Malonic Acid (4)	121 ± 6	77 ± 4	51 ± 3	111 ± 6	78 ± 4	52 ± 3
DL-Malic Acid (6)	128 ± 6	89 ± 4	62 ± 4	140 ± 7	102 ± 5	73 ± 4

4.5 Results and Discussion

4.5.1 Experimental Results

Table 4.5 gives the experimental d_{act} results for each compound as a ratio (ψ) of d_{act} for the compound divided by d_{act} for $(\text{NH}_4)_2\text{SO}_4$ at the same s_o ,

$$\psi(s_o) = \frac{d_{act,compound}(s_o)}{d_{act,(NH_4)_2SO_4}(s_o)} \quad (4.12)$$

and Table 4.6 gives the actual experimental d_{act} . In these tables, the numbers in parentheses give reference numbers that identify the compounds on comparison plots. These numbers roughly rank the compounds by their ψ values at $s_o = 0.11\%$, with malonic acid, which exhibited activation properties similar to the inorganic salts, numbered 4, and cholesterol and the fatty acids, which did not activate at any of the operating supersaturations, numbered 25 through 28. Values for ψ range from 0.99 – 2.08 (121 – 254 nm) for $s_o = 0.11\%$, 0.97 - 2.34 (77 – 85 nm) for $s_o = 0.21\%$, and 0.86 - 2.12 (51 – 125 nm) for $s_o = 0.32\%$, which indicates that some of the organic compounds were as CCN active as the inorganic salts.

ADDEM predictions were performed for those systems for which experimental surface tension data was available for model S3 (see section 4.3.2). The model predictions of d_{act} for $(\text{NH}_4)_2\text{SO}_4$, NH_4HSO_4 , NaCl , succinic acid, malonic acid, adipic acid, glutaric acid, malic acid, and oxalic acid are also included in Tables 4.5 and 4.6. These systems have also been validated for calculations of a_w , which results in a direct comparison with the fundamental Köhler equation without being subject to too many

Table 4.5 Experimental and ADDEM Results, as the Ratio of the Activation Diameters to Those of Ammonium Sulfate^a

Compound (# on Plots)	ψ for $s_o = 0.11\%$					ψ for $s_o = 0.21\%$					ψ for $s_o = 0.32\%$				
	Experimental ^b	ADDEM ^c				Experimental ^b	ADDEM ^c				Experimental ^b	ADDEM ^c			
		S1	S2	S3	Water		S1	S2	S3	Water		S1	S2	S3	Water
Ammonium Sulfate (1)	1.00	0.96	0.95	0.96	0.98	1.00	0.98	0.98	0.98	1.00	1.00	1.01	1.01	1.01	1.02
Ammonium Bisulfate(2)	1.02 ± 0.17	0.97	0.97	0.99	0.98	0.93 ± 0.05	0.99	0.99	0.99	1.00	0.97 ± 0.07	1.01	0.97	1.01	1.02
Sodium Chloride (3)	0.83 ± 0.10	0.77	0.77	0.78	0.78	0.75 ± 0.07	0.78	0.78	0.78	0.79	0.78 ± 0.11	0.79	0.80	0.79	0.80
Oxalic Acid (22)	>1.06	1.24	1.19	1.22	1.21	>1.63	1.21	1.13	1.20	1.20	1.69 ± 0.34	1.20	1.11	1.20	1.20
Malonic Acid (4)	0.99 ± 0.17	1.36	1.27	1.36	1.35	0.97 ± 0.07	1.31	1.21	1.34	1.34	0.86 ± 0.04	1.29	1.18	1.34	1.34
Succinic Acid (10)	1.16 ± 0.17	1.35	1.30	1.46	1.73	1.33 ± 0.09	1.29	1.23	1.42	1.41	1.23 ± 0.08	1.26	1.20	1.41	1.41
Glutaric Acid (8)	1.12 ± 0.16	1.32	1.32	1.51		1.33 ± 0.08	1.26	1.26	1.51		1.51 ± 0.08	1.24	1.24	1.52	
Adipic Acid (20)	1.43 ± 0.23	1.32	1.20	1.40	1.53	1.62 ± 0.11	1.29	1.18	1.36	1.54	1.86 ± 0.16	1.28	1.18	1.34	1.57
Phthalic Acid (14)	1.19 ± 0.18					1.30 ± 0.09					1.25 ± 0.11				
Pimelic Acid (18)	1.40 ± 0.18					1.64 ± 0.08					1.34 ± 0.09				
Oxalacetic Acid (7)	1.11 ± 0.14					1.20 ± 0.06					1.27 ± 0.10				
DL-Malic Acid (6)	1.05 ± 0.16	1.39	1.32	1.50	1.50	1.13 ± 0.06	1.32	1.24	1.48	1.47	1.05 ± 0.08	1.29	1.21	1.47	1.47
(S)-(+)-Citramalic Acid (15)	1.20 ± 0.17					1.39 ± 0.05					1.19 ± 0.09				
2-Ketoglutaric Acid (5)	1.02 ± 0.16					1.28 ± 0.05					1.14 ± 0.09				
3-Hydroxy-3-Methylglutaric Acid (12)	1.18 ± 0.17					1.67 ± 0.10					1.22 ± 0.09				
Butylmalonic Acid (17)	1.27 ± 0.20					1.53 ± 0.07					1.24 ± 0.063				
DL-Glutamic Acid Monohydrate (9)	1.12 ± 0.14					1.22 ± 0.09					1.08 ± 0.09				
DL-Leucine (16)	1.24 ± 0.20					1.33 ± 0.10					1.20 ± 0.06				
Myristic Acid (26)	>4.71					>7.28					>9.74				
Palmitic Acid (27)	>4.71					>7.28					>9.74				
Stearic Acid (28)	>4.71					>7.28					>9.74				

Table 4.5 Continued...

Compound (# on Plots)	ψ for $s_o = 0.11\%$					ψ for $s_o = 0.21\%$					ψ for $s_o = 0.32\%$									
	Experimental ^b	ADDEM ^c				Experimental ^b	ADDEM ^c				Experimental ^b	ADDEM ^c								
		S1	S2	S3	Water		S1	S2	S3	Water		S1	S2	S3	Water					
Cholesterol (25)	>4.66					>7.20									>9.64					
<i>meso</i> -Erythritol (13)	1.19 ± 0.18					1.28 ± 0.08									1.28 ± 0.07					
DL-Threitol (11)	1.16 ± 0.17					1.39 ± 0.09									1.41 ± 0.10					
2-Hexadecanol (21)	>1.06					1.42 ± 0.10									1.69 ± 0.13					
Glycolaldehyde Dimer (23)	1.46 ± 0.22					1.70 ± 0.14									1.76 ± 0.14					
2-Hydroxycaproic Acid (19)	1.42 ± 0.23					1.68 ± 0.11									1.64 ± 0.13					
Sinapic Acid (24)	2.08 ± 0.32					2.34 ± 0.09									2.12 ± 0.17					

^aResults are presented as the ratio of the modeled or experimental d_{act} divided by the d_{act} for $(\text{NH}_4)_2\text{SO}_4$.

^bExperimental results are for atomization from methanol solutions, except for the inorganic salts, which were atomized from aqueous solutions.

^cModels are S'1, S'2, and S'3 for inorganic species. The "Water" model assumes the surface tension of pure water in the calculations (see section 2.1).

Table 4.6 Experimental and ADDEM Results, Given as Activation Diameters

Compound (# on Plots)	d_{act} , nm for $s_o = 0.11\%$					d_{act} , nm for $s_o = 0.21\%$					d_{act} , nm for $s_o = 0.32\%$				
	Experimental ^a	ADDEM ^b				Experimental ^a	ADDEM ^b				Experimental ^a	ADDEM ^b			
		S1	S2	S3	Water		S1	S2	S3	Water		S1	S2	S3	Water
Ammonium Sulfate (1)	122 ± 14	120	121	120	121	79 ± 3	77	78	78	79	59 ± 2	60	60	60	60
Ammonium Bisulfate(2)	114 ± 7	118	118	118	118	77 ± 3	78	78	78	79	60 ± 2	60	60	60	60
Sodium Chloride (3)	92 ± 3	94	94	95	95	62 ± 6	62	62	62	62	49 ± 5	47	47	47	47
Oxalic Acid (22)	>128	151	145	149	148	>128	95	90	95	95	100 ± 17	71	65	71	71
Malonic Acid (4)	121 ± 6	166	155	166	165	77 ± 3	104	96	106	106	51 ± 2	76	70	79	79
Succinic Acid (10)	142 ± 5	164	158	178	173	105 ± 4	102	97	112	111	73 ± 3	74	71	83	83
Glutaric Acid (8)	137 ± 5	160	161	184		105 ± 4	100	100	119		89 ± 3	73	73	89	
Adipic Acid (20)	174 ± 8	161	147	170	184	128 ± 5	102	93	107	120	110 ± 6	75	70	79	91
Phthalic Acid (14)	145 ± 5					103 ± 4					74 ± 4				
Pimelic Acid (18)	171 ± 6					130 ± 4					79 ± 3				
Oxalacetic Acid (7)	135 ± 5					95 ± 3					75 ± 4				
DL-Malic Acid (6)	128 ± 4	170	161	183	183	89 ± 3	104	98	116	116	62 ± 3	76	71	87	87
(S)-(+)-Citramalic Acid (15)	146 ± 5					110 ± 4					70 ± 3				
2-Ketoglutaric Acid (5)	124 ± 5					101 ± 2					67 ± 3				
3-Hydroxy-3-Methylglutaric Acid (12)	144 ± 5					132 ± 5					72 ± 3				
2-Hydroxycaproic Acid (19)	173 ± 8					133 ± 5					97 ± 4				
Butylmalonic Acid (17)	155 ± 6					121 ± 4					73 ± 3				
DL-Glutamic Acid Monohydrate (9)	137 ± 5					96 ± 5					64 ± 3				
DL-Leucine (16)	152 ± 7					105 ± 5					71 ± 2				
Myristic Acid (26)	>575					>575					>575				
Palmitic Acid (27)	>575					>575					>575				
Stearic Acid (28)	>575					>575					>575				

Table 4.6 Continued...

Compound (# on Plots)	d_{act} , nm for $s_o = 0.11\%$					d_{act} , nm for $s_o = 0.21\%$					d_{act} , nm for $s_o = 0.32\%$				
	Experimental ^a	ADDEM ^b				Experimental ^a	ADDEM ^b				Experimental ^a	ADDEM ^b			
		S1	S2	S3	Water		S1	S2	S3	Water		S1	S2	S3	Water
Cholesterol (25)	>569					>569					>569				
<i>meso</i> -Erythritol (13)	145 ± 5					101 ± 4					76 ± 3				
DL-Threitol (11)	142 ± 5					110 ± 4					83 ± 4				
2-Hexadecanol (21)	>127					112 ± 5					100 ± 4				
Glycolaldehyde Dimer (23)	178 ± 6					134 ± 7					104 ± 4				
2-Hydroxycaproic Acid (19)	173 ± 8					133 ± 5					97 ± 5				
Sinapic Acid (24)	254 ± 9					185 ± 6					125 ± 6				

^aExperimental results are for atomization from methanol solutions, except for the inorganic salts, which were atomized from aqueous solutions.

^bModels are S'1, S'2, and S'3 for inorganic species. The "Water" model assumes the surface tension of pure water in the calculations (see section 4.3.1).

unknowns. Models S1 and S2 require variables that have to be calculated for most systems of atmospheric interest. The ADDEM and experimental results for adipic acid, glutaric acid, malic acid, malonic acid, oxalic acid, and succinic acid from this study, as well as data from previous studies (previous studies are from aqueous solutions unless otherwise noted), are discussed in section 4.5.4. From the ADDEM results, ψ values range from 1.19 – 1.73 (145 – 2.11) for $s_o = 0.11\%$, 1.13 – 1.54 (89 – 122 nm) for $s_o = 0.21\%$, and 1.11 – 1.57 (65 – 93 nm) for $s_o = 0.32\%$.

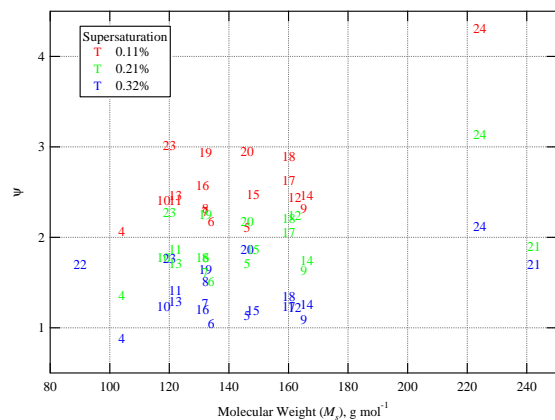
4.5.2 Trends with Chemical Properties

Figure 4.10 shows ψ plotted versus (a) M_s , (b) aqueous solubility, (c) the negative logarithm of the first dissociation constant (pKa), and (d) $M_s/(\rho_s\nu)$ (assuming that $\nu = 1$) for each compound. The results are plotted against $M_s/(\rho_s\nu)$ because it contains the solute information found in the simplified Köhler equation (equation (4.5)). When equation (4.5) is solved for the dry diameter (d_s) and then d_s , the droplet diameter (D_{drop}), and the supersaturation (s) are replaced with their critical values (d_{act} , $D_{drop,c}$, and s_c), the result is the following:

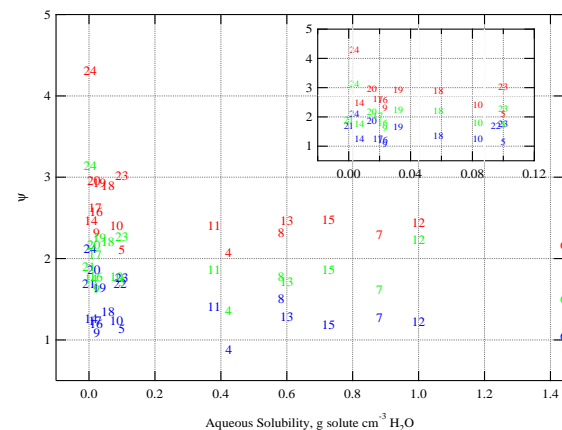
$$d_{act} = \left[\left(\frac{A}{D_{drop,c}} - s_c \right) \frac{D_{drop,c}^3 M_s}{B' \rho_s \nu} \right]^{1/3} \quad (4.13)$$

$$= C_1 \left(\frac{M_s}{\rho_s \nu} \right)^{1/3}$$

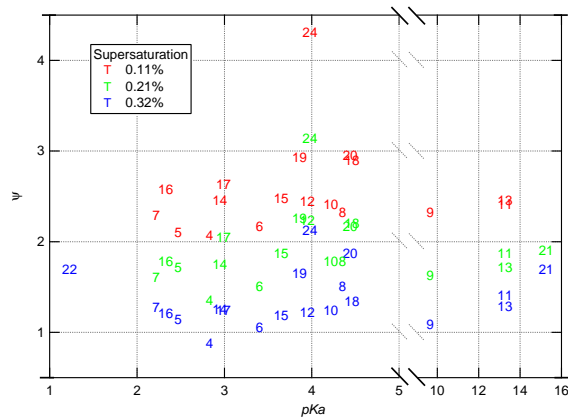
where $C_1 = \{[(A/D_{drop,c}) - s_c](D_{drop,c}^3/B')\}^{1/3}$ and $B' = \pi M_w$. Therefore, a plot of d_{act} versus $M_s/(\rho_s\nu)$ in log-log space should yield a straight line, especially if the assumption that $\nu =$



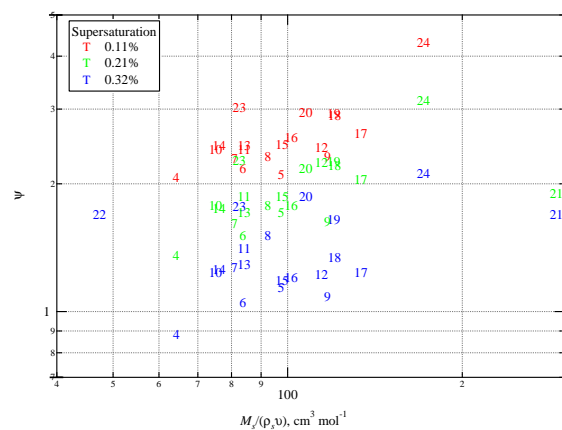
(a)



(b)



(a)



(b)

Figure 4.10. Ψ as a function of (a) M_s , (b) aqueous solubility, (c) pK_a , and (d) $M_s/(\rho_s\nu)$. It is assumed that $\nu = 1$ in panel (d). The inset for panel (b) zooms in on the compounds with aqueous solubilities less than $0.12 \text{ g cm}^{-3} \text{ H}_2\text{O}$. The units for inset axes (panel (d)) are the same as those on the main plot. Major outliers in panels (a), (c), and (d) are DL-threitol (11), *meso*-erythritol (13), 2-hexadecanol (21), oxalic acid (22), and sinapic acid (24).

1 is valid. The value of ν for complete dissociation in a dilute solution is determined by the molecular structure of the compound in question. Most of the organics studied here do not dissociate much in solution, and the first dissociation constant, K_a , can be used as an approximation of ν [Koehler *et al.*, 2005]. The K_a is a measure of the ability of a compound to deprotonate in solution and is given by

$$K_a = \frac{\lambda^2}{m_o - \lambda} \quad (4.14)$$

$$= \frac{m_o(\nu - 1)^2}{2 - \nu}$$

where λ is the extent of dissociation, m_o is the solution molality, and $\nu = (m_o + \lambda)/m_o$ [Koehler *et al.* 2005]. The dissociation constant, K_a , is usually expressed as the negative of its logarithm, $pKa = -\log(K_a)$. Low pKa values indicate a high degree of dissociation, while high pKa values indicate low dissociation. Solubility is the actual amount of solid that is able to dissolve per volume of solvent [Wade, 1995].

In general, ψ increases as M_s , pKa_1 , and $M_s/(\rho_s\nu)$ increase. This is expected, as Köhler theory predicts that CCN activity is lower for compounds that exhibit larger M_s and decreased dissociation in water (represented by higher pKa values). Köhler theory also predicts that CCN activity decreases for compounds that are less soluble in water. Values of ψ are high at very low aqueous solubilities, indicating that these compounds have low CCN activity, but ψ values seem to level off for aqueous solubilities greater than about 0.04 g solute cm⁻³ H₂O. Koehler *et al.* [2005] state that the assumption of $\nu =$

1 is probably reasonable for glutaric and malonic acids but not oxalic acid, and panel (d) in Figure 4.10 reinforces this claim.

The outliers in the plots in Figure 4.10 include DL-threitol (11), *meso*-erythritol (13), 2-hexadecanol (21), and oxalic acid (22). DL-threitol activates at moderate diameters, 83, 110, and 142 nm ($\psi = 1.16, 1.39, \text{ and } 1.41$) for $s_o = 0.11, 0.21, \text{ and } 0.32\%$, respectively, even though it has a very large pK_{a1} value, indicating that it does not dissociate much in solution. Although DL-threitol does not dissociate much in solution, it is soluble in aqueous solution ($0.38 \text{ g cm}^{-3} \text{ H}_2\text{O}$, similar to NH_4HSO_4 and NaCl). *Meso*-erythritol, which is simply a stereoisomer of DL-threitol, exhibits this same behavior. Oxalic acid shows the opposite behavior, with lower CCN activity than would be expected from its pK_a value (1.93) or molecular weight (90 g mol^{-1}) alone. Oxalic acid has low solubility, which limits the amount of solid that can actually be solvated and, therefore, limits its CCN activity.

2-hexadecanol requires special attention because it has very low solubility ($3 \times 10^{-8} \text{ g solute cm}^{-3} \text{ H}_2\text{O}$) and a very high pK_a (15.26) yet it exhibits unexpectedly moderate CCN activity with d_{act} values of 112 and 100 nm at $s_o = 0.21$ and 0.32% , respectively. 2-hexadecanol particles shrank to a large degree after being size-selected in the classification DMA and being measured in the DACAD, which could have resulted from residual methanol escaping from the particles between the classification DMA and the DACAD. 2-hexadecanol is very soluble in methanol, due to the similar nature of the compounds. If residual methanol remained in the particles, its presence could have facilitated the apparent aqueous solubility or dissociation of 2-hexadecanol in the solution droplets by helping to dissolve the particles. In this case, the choice of methanol as the

atomization solvent could have introduced uncertainty in the CCN activity if the methanol were not completely removed from the 2-hexadecanol aerosol particles before entering the CCNC3.

4.5.3 Compound Comparisons

Many of the compounds are related by their functional groups or only differ by one functional group, and comparisons between compounds allow insights into CCN activation. In general, the dicarboxylic acids and functionalized dicarboxylic acids exhibited the greatest CCN activity, followed by the amino acids, the alcohols, the acetaldehyde, sinapic acid, and finally by the fatty acids and cholesterol. The fatty acids and cholesterol did not activate for diameters less than 575 nm at any of the operating supersaturations, probably due to their very low solubilities (all $< 2.0 \times 10^{-5}$ g solute cm^{-3} H_2O).

The dicarboxylic acids exhibit increasing CCN activity in the following order: malonic acid, glutaric acid, succinic acid, phthalic acid, pimelic acid, adipic acid, and oxalic acid. There is an odd-even affect with the carbon number for these compounds, with compounds with an odd number of carbons having greater aqueous solubility and CCN activity, and those with an even number of carbons having lower solubility and CCN activity. Phthalic acid and pimelic acid have the same chemical formula ($\text{C}_8\text{H}_6\text{O}_4$) but very different structures and properties. The aqueous solubility of phthalic acid (6.97×10^{-3} g solute cm^{-3} H_2O) is about 8 times less than that of pimelic acid (0.058 g solute cm^{-3} H_2O), but its K_a value is about 32 times greater than that of pimelic acid, which may explain the difference in their abilities to act as CCN.

Oxalacetic acid, DL-malic acid, and (S)-(+)-citramalic acid are functionalized versions of succinic acid, with a ketone group, a hydroxyl group, and a methyl and hydroxyl group, respectively. DL-malic acid is the most CCN active of the four compounds, followed by oxalacetic acid, and then succinic acid and (S)-(+)-citramalic acid. The differences in d_{act} values between succinic acid and (S)-(+)-citramalic acid are within experimental error. This order follows the order of their aqueous solubilities, with DL-malic acid also being the most soluble.

Two functionalized versions of glutaric acid, 2-ketoglutaric acid and 3-hydroxy-3-methylglutaric acid, were also studied. Values of ψ ranged from 1.02 – 1.28, 1.12 – 1.51, and 1.1.18 – 1.67 for 2-ketoglutaric acid, glutaric acid, and 3-hydroxy-3-methylglutaric acid, respectively. Based on solubility alone, this order would not be predicted; however, 2-keotglutaric has the lowest pKa . A comparison of d_{act} values between glutaric acid and 3-hydroxy-3-methylglutaric for each operating supersaturation shows that d_{act} for glutaric acid is less than that of 3-hydroxy-3-methylglutaric acid at $s_o = 0.21\%$ but is within experimental error for $s_o = 0.11$ and 0.32% .

Butylmalonic acid, which is essentially malonic acid with a butyl group on the second carbon, was also studied and was found to be much less CCN active than malonic acid. Although its pKa value is near to that of malonic acid, butylmalonic acid is less soluble in aqueous solution, which probably leads to its lower CCN activity.

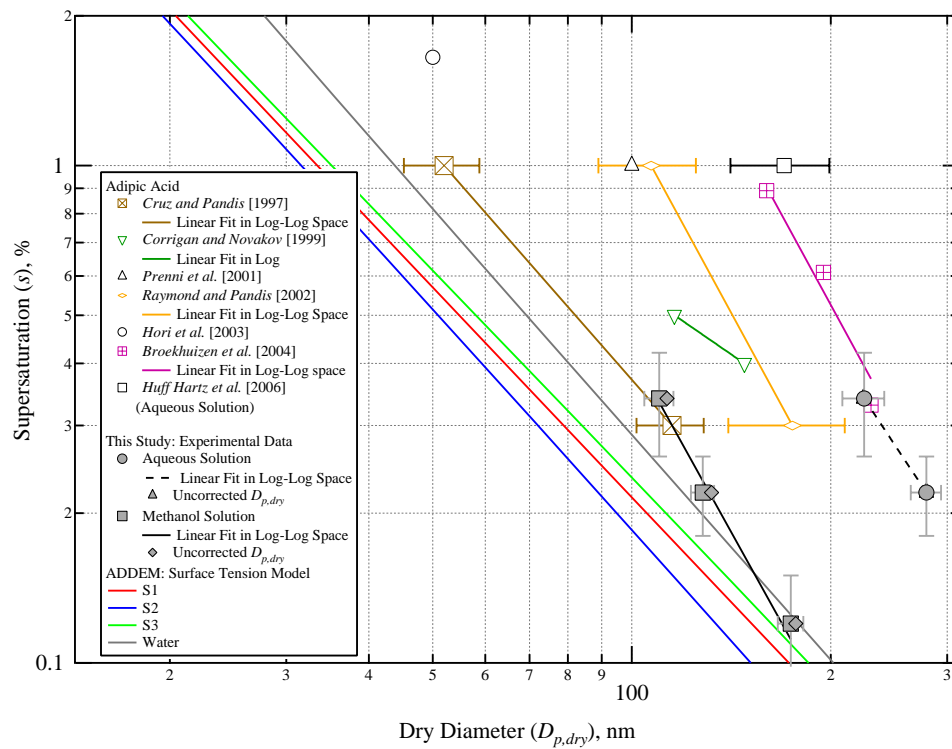
For the amino acids, DL-glutamic acid monohydrate activated at smaller diameters (64, 96, and 137 nm) than DL-leucine (71, 105, and 152 nm), but the values at $s_o = 0.21$ and 0.11% are within experimental error. DL-glutamic acid monohydrate and DL-leucine have similar solubilities, but DL-leucine has a much lower pKa . However,

the fact that DL-glutamic acid monohydrate is hydrated might increase its CCN activity above that expected for the non-hydrated compound.

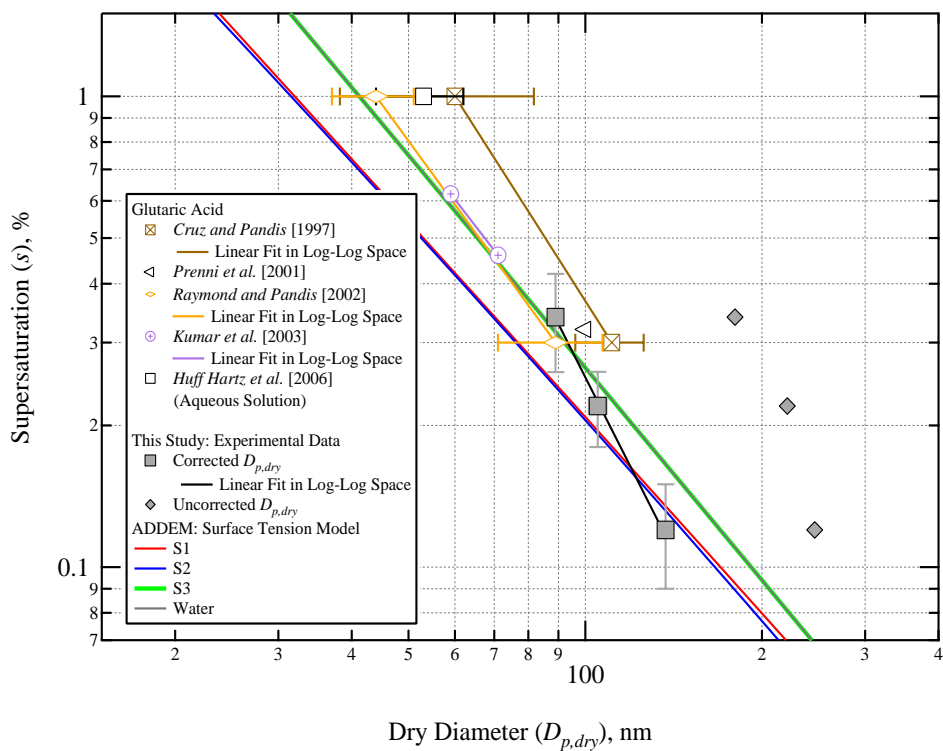
The alcohols, *meso*-erythritol, DL-threitol, and 2-hexadecanol, all exhibited similar CCN activity, even though 2-hexadecanol is much less soluble in aqueous solution than the other two alcohols. A possible experimental reason for this unexpected result was discussed in section 4.5.2.

4.5.4 ADDEM Modeling

Figures 4.11 – 4.13 show the ADDEM and experimental results for adipic acid, glutaric acid, malic acid, malonic acid, oxalic acid, and succinic acid from this study, as well as data from previous studies (previous studies results are from aqueous solutions unless otherwise noted). Experimental data for particles atomized from both methanol and aqueous solutions are shown, when available. Also shown on each plot are the uncorrected d_{act} values, which means that these d_{act} were determined from sigmoid fits to AR versus $D_{p,DMA}$ data. The uncorrected d_{act} give an idea of how much the particles changed size between the classification DMA and the DACAD. Note that the results are given on log-log plots, which results in a linear relationship between s_c and d_{act} . The slopes and intercepts for the linear fits (in log-log) space to the data are given in Tables 4.7 through 4.11.



(a)



(b)

Figure 4.11. ADDEM and experimental results for (a) adipic acid and (b) glutaric acid.

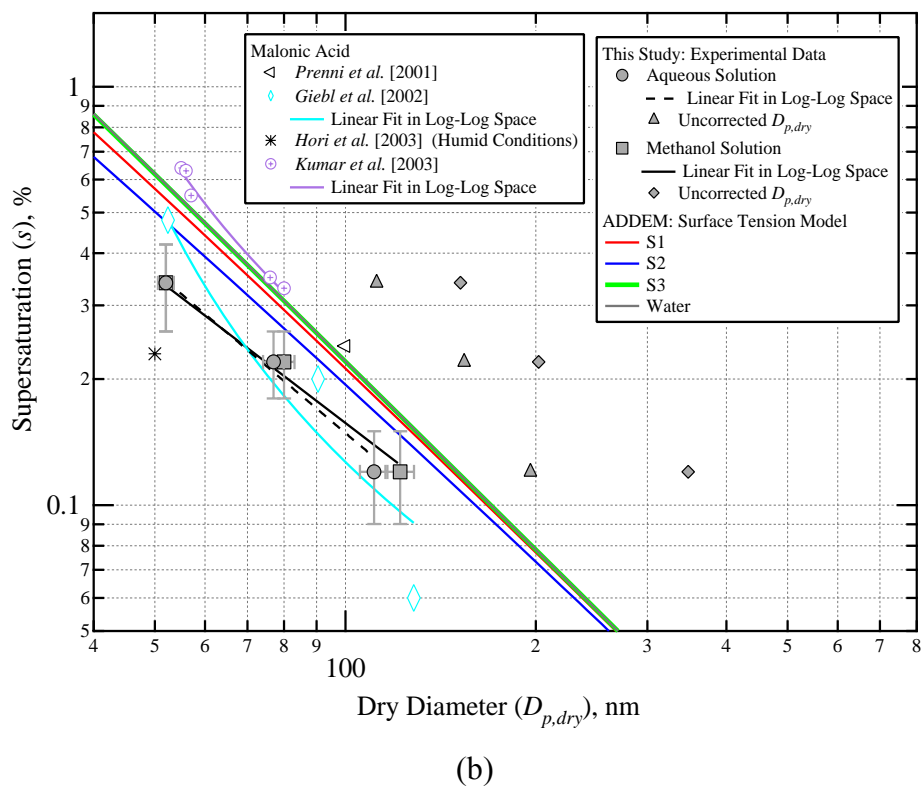
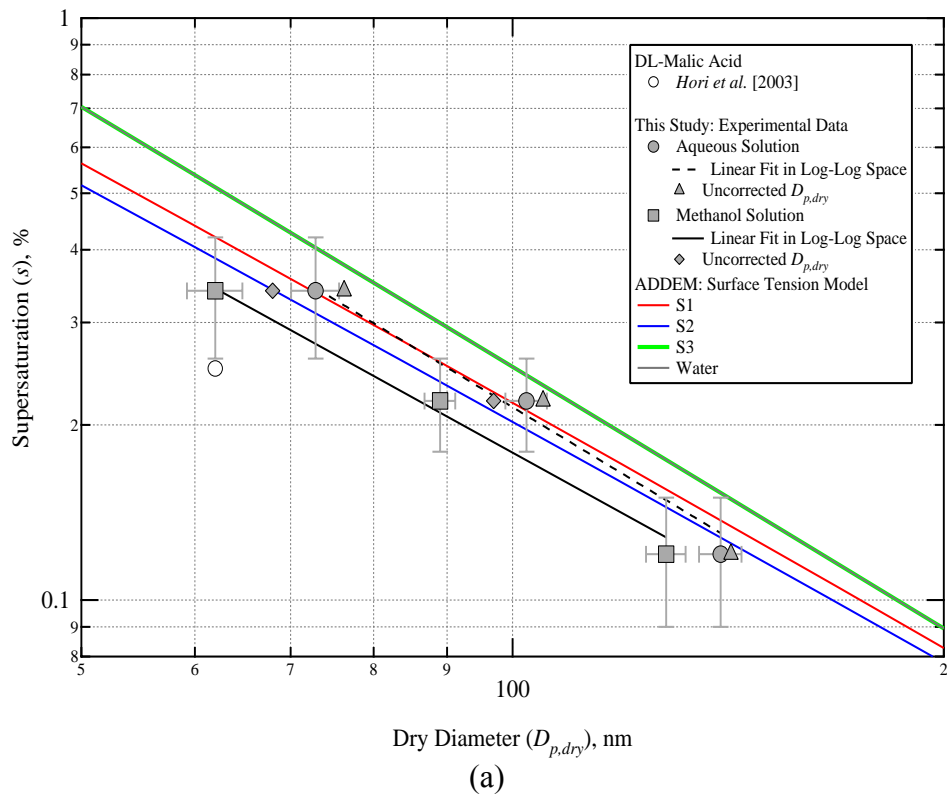
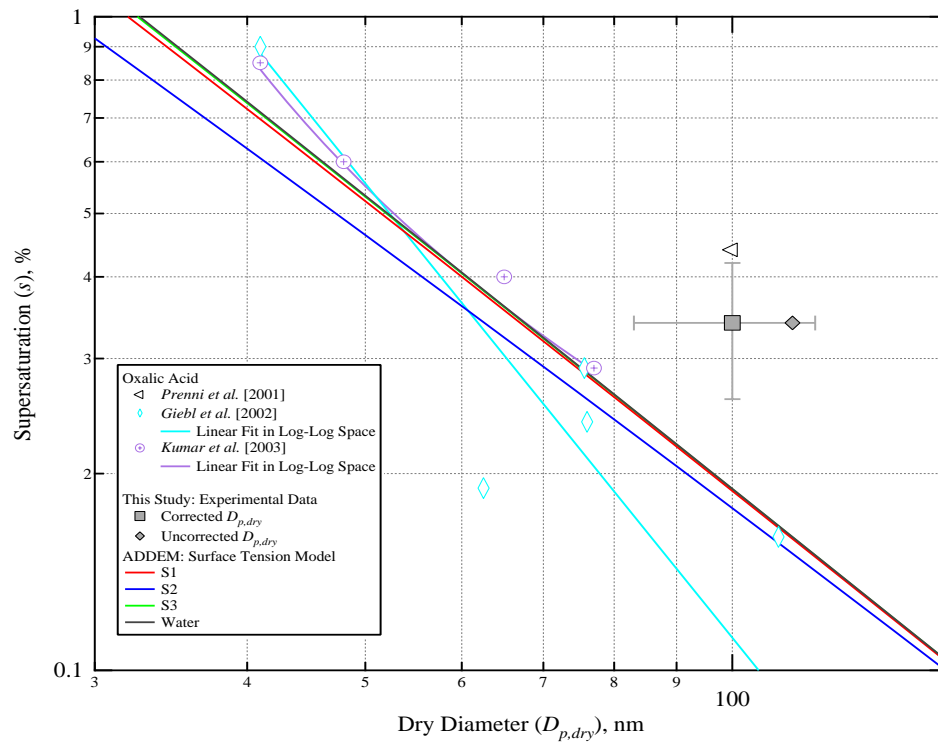
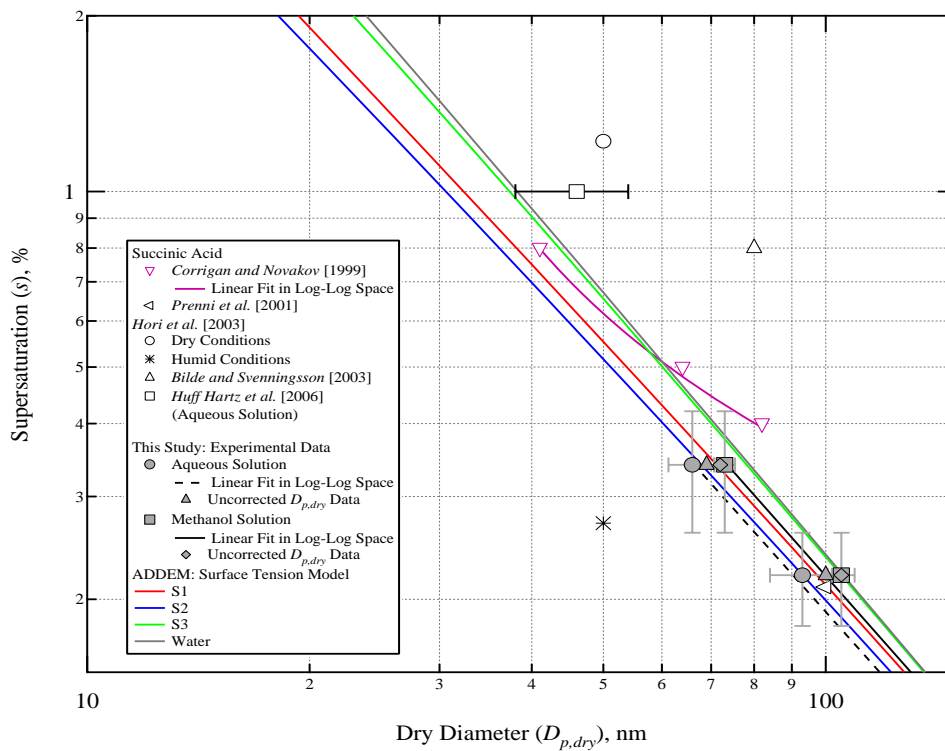


Figure 4.12. ADDEM and experimental results for (a) DL-malic acid and (b) malonic acid.



(a)



(b)

Figure 4.13. ADDEM and experimental results for (a) oxalic acid and (b) succinic acid.

Table 4.7 Slopes and Intercepts for Linear Fits of s_c and d_{act} in Log-Log Space for Experimental Data and ADDEM Predictions for Adipic Acid

Organic Compound	Study or Model	s_o , %	d_{act} , nm	Linear Fit Parameters		
				Slope, nm	Intercept, %	
Adipic Acid	ADDEM		S1		-1.40	2.14
			S2		-1.43	2.14
			S3		-1.40	2.16
			Water		-1.53	2.51
	Experimental ^a	Methanol	0.11	174 ± 8		
			0.21	128 ± 5	-2.40	4.41
			0.32	110 ± 6		
		Aqueous	0.11			
			0.21	279 ± 15	-2.00	4.24
			0.32	224 ± 16		
		<i>Cruz and Pandis</i> [1997]	0.30	115 ± 13.4	-1.52	2.60
	1.00		52 ± 6.8			
	<i>Corrigan and Novakov</i> [1999]	0.40	148	-0.92	1.59	
		0.50	116			
	<i>Prenni et al.</i> [2001]	1.00	100			
	<i>Raymond and Pandis</i> [2002]	0.30	175 ± 35	-2.45	4.97	
1.00		107 ± 18				
<i>Hori et al.</i> [2003] ^b	1.65	50				
<i>Broekhuizen et al.</i> [2004]	0.33	230	-2.44	5.34		
	0.61	195				
	0.89	160				
<i>Huff Hartz et al.</i> [2006]	1.00	170 ± 29				

^a“Experimental” refers to results from this study and for particles atomized from a methanol solution, unless otherwise specified.

^b*Hori et al.* [2003] results are for “humid conditions,” unless otherwise specified.

Table 4.8 Slopes and Intercepts for Linear Fits of s_c and d_{act} in Log-Log Space for Experimental Data and ADDEM Predictions for Glutaric Acid and DL-Malic Acid

Organic Compound	Study or Model	s_o , %	d_{act} , nm	Linear Fit Parameters		
				Slope, nm	Intercept, %	
Glutaric Acid	ADDEM	S1		-1.36	2.05	
		S2		-1.34	2.01	
		S3		-1.48	2.38	
		Water		-.148	2.38	
	Experimental		0.11	137 ± 5		
			0.21	105 ± 4	-2.45	4.34
			0.32	89 ± 3		
	<i>Cruz and Pandis</i> [1997]		0.30	111 ± 14.8		
			1.00	60 ± 21.8	-1.96	3.48
	<i>Prenni et al.</i> [2001]		0.32	100		
	<i>Raymond and Pandis</i> [2002]		0.30	89 ± 18		
			1.00	44 ± 7	-1.71	2.81
	<i>Kumar et al.</i> [2003]		0.46	71		
		0.62	59	-1.61	2.65	
<i>Huff Hartz et al.</i> [2006]		1.00	53 ± 9			
DL-Malic Acid	ADDEM	S1		-1.33	2.00	
		S2		-1.32	1.95	
		S3		-1.43	2.28	
		Water		-1.43	2.29	
	Experimental	Methanol	0.11	128 ± 4		
			0.21	89 ± 3	-1.35	1.97
			0.32	62 ± 3		
	Experimental	Aqueous	0.11	140 ± 5		
			0.21	102 ± 4	-1.50	2.30
			0.32	73 ± 3		
	<i>Hori et al.</i> [2003] ^b		0.25	50		

^a“Experimental” refers to results from this study and for particles atomized from a methanol solution, unless otherwise specified.

^b*Hori et al.* [2003] results are for “humid conditions,” unless otherwise specified.

Table 4.9 Slopes and Intercepts for Linear Fits of s_c and d_{act} in Log-Log Space for Experimental Data and ADDEM Predictions for Malonic Acid

Organic Compound	Study or Model	s_o , %	d_{act} , nm	Linear Fit Parameters		
				Slope, nm	Intercept, %	
Malonic Acid	ADDEM	S1		-1.36	2.07	
		S2		-1.33	1.96	
		S3		-1.44	2.24	
		Water		-1.45	2.26	
	Experimental	Methanol	0.11	122 ± 6		
			0.21	80 ± 3	-1.15	1.51
		Aqueous	0.32	52 ± 2		
			0.11	111 ± 6		
		Aqueous	0.21	77 ± 4	-1.28	1.73
			0.32	52 ± 3		
		<i>Prezzi et al.</i> [2001]	0.24	100		
		<i>Geibl et al.</i> [2002]	0.06	128		
	0.20		90	-1.87	2.90	
	<i>Hori et al.</i> [2003] ^b	0.48	52			
		0.23	50			
	<i>Kumar et al.</i> [2003]	0.33	80			
0.35		76				
0.55		57	-1.78	2.89		
0.63		56				
		0.64	55			

^a“Experimental” refers to results from this study and for particles atomized from a methanol solution, unless otherwise specified.

^b*Hori et al.* [2003] results are for “humid conditions,” unless otherwise specified.

Table 4.10 Slopes and Intercepts for Linear Fits of s_c and d_{act} in Log-Log Space for Experimental Data and ADDEM Predictions for Oxalic Acid

Organic Compound	Study or Model	s_o , %	d_{act} , nm	Linear Fit Parameters		
				Slope, nm	Intercept, %	
Oxalic Acid	ADDEM	S1		-1.41	2.12	
		S2		-1.34	1.94	
		S3		-1.44	2.18	
		Water		-1.46	2.20	
	Experimental		0.11			
			0.21			
			0.32	100 ± 17		
	<i>Prenni et al.</i> [2001]	0.44	100			
	<i>Geibl et al.</i> [2002]		0.16	109		
			0.19	62		
			0.24	76	-2.31	3.67
			0.29	76		
			0.90	41		
	<i>Kumar et al.</i> [2003]		0.29	77		
			0.40	65		
		0.60	48	-1.69	2.64	
		0.85	41			

^a“Experimental” refers to results from this study and for particles atomized from a methanol solution, unless otherwise specified.

Table 4.11 Slopes and Intercepts for Linear Fits of s_c and d_{act} in Log-Log Space for Experimental Data and ADDEM Predictions for Succinic Acid

Organic Compound	Study or Model	s_o , %	d_{act} , nm	Linear Fit Parameters		
				Slope, nm	Intercept, %	
Succinic Acid	ADDEM			-1.35	2.035	
		S1		-1.34	1.98	
		S2		-1.41	2.21	
		S3		-1.46	2.30	
	Experimental	Water				
			0.11	142 ± 5		
		Methanol	0.21	105 ± 4	-1.43	2.20
			0.32	73 ± 3		
			0.11	133 ± 9		
		Aqueous	0.21	93 ± 9	-1.41	2.11
			0.32	66 ± 5		
			0.40	82		
		<i>Corrigan and Novakov</i> [1999]	0.50	64	-1.02	1.54
			0.80	41		
	<i>Prenni et al.</i> [2001]	0.21	100			
<i>Hori et al.</i> [2003] ^b	Dry Conditions	1.22	50			
	Humid Conditions	0.27	50			
<i>Bilde and Svenningsson</i> [2003]		0.80	80			
<i>Huff Hartz et al.</i> [2006]		1.00	46 ± 8			

^a“Experimental” refers to results from this study and for particles atomized from a methanol solution, unless otherwise specified.

^b*Hori et al.* [2003] results are for “humid conditions”, unless otherwise specified.

4.5.4.1 Adipic Acid

Panel (a) in Figure 4.11 summarizes the ADDEM predictions and experimental results, for both methanol and aqueous solutions, for adipic acid. The uncorrected and corrected d_{act} values were within experimental error for adipic acid. The values of d_{act} for particles created from a methanol solution are near those of the ADDEM predictions, within experimental error, and are nearest to the model “Water,” which uses the surface tension of pure water in calculations. The methanol results are near to those measurements made by *Cruz and Pandis* [1997]. From other past studies, most results for d_{act} are larger than those observed here for particles atomized from methanol solution. However, experimental results for particles created from aqueous solution are more similar to measurements made in past studies, especially those from *Broekhuizen et al.* [2004].

Adipic acid is more soluble in methanol than water. As in the case of 2-hexadecanol, residual methanol in the particles could have facilitated the apparent aqueous solubility or dissociation of adipic acid in the solution droplets by helping to dissolve the particles. However, the size distribution changes observed for adipic acid were much less dramatic than those seen for 2-hexadecanol. The size distributions for adipic acid remained sharp ($\sigma < 0.10$) and particle size reduction was less than 20%, so it is likely that the amount of residual methanol in the particles was lower than that in the 2-hexadecanol particles.

4.5.4.2 Glutaric Acid

The results for glutaric acid are given in Figure 4.11, panel (b). The ADDEM predictions for model S1 and the “Water” model are basically identical (the green and gray traces). The experimental results for particles atomized from methanol solution fall within the ADDEM predictions but with a different slope. In the case of glutaric acid, the corrected d_{act} values are much less than the uncorrected values because glutaric acid particles shrank significantly between the classification DMA and the DACAD. The present study results compare quite well with those of past studies.

4.5.4.3 DL-Malic Acid

As seen in Figure 4.12, panel (a), the experimental results compare well with the ADDEM predictions, but are closest in magnitude to model S2. The slope of the experimental data also compares well with the ADDEM predictions, and DL-malic acid exhibited moderate size change between the classification DMA and the DACAD. Note that the results for DL-malic acid particles created from an aqueous solution are actually closer to the “Water” model predictions than the results for particles created from a methanol solution. The *Hori et al.* [2003] results indicate that DL-malic acid is somewhat more CCN active than the results of this study would imply but are almost within the experimental error of this study.

4.5.4.4 Malonic Acid

For malonic acid (panel (b) in Figure 4.12), the experimental results for particles atomized from methanol and aqueous solutions are very similar and are similar to the results from *Giebl et al.* [2002]. The ADDEM predicts that malonic acid is less CCN

active than the experimental results indicate but are almost within experimental error. However, experimental results from *Prenni et al.* [2001] and *Kumar et al.* [2003] fall on the opposite side of the ADDEM predictions than the experimental results from this study and the studies of *Giebl et al.* [2002] and *Hori et al.* [2003].

4.5.4.5 Oxalic Acid

Only one experimental data point (shown in panel (a) of Figure 4.13) was measured for oxalic acid because of limitations in the size of particles that could be selected by the classified DMA and the large degree of size distribution changes that were observed. The experimental d_{act} (100 nm at $s_o = 0.32\%$) which has a large degree of uncertainty, is much larger than the ADDEM predictions, but agrees well with the experimental data of *Prenni et al.* [2001]. The experimental data of *Giebl et al.* [2002] and *Kumar et al.* [2003] agree well with the ADDEM predictions.

4.5.4.6 Succinic Acid

The experimental results for succinic acid, for particles created from both methanol and aqueous solutions, agree well with ADDEM predictions and are closest to models S3 and “Water.” *Hori et al.* [2003] give results for a 50 nm particle under dry and humid conditions and found that the dry particle required a much greater supersaturation for activation ($> 1\%$) than the wet particle ($\sim 0.28\%$), and these results fall on either side of the ADDEM predictions. The d_{act} determined from methanol and aqueous solutions in this study are similar (within experimental error) and only a small size change is observed between the classification DMA and the DACAD.

4.6 Conclusions

4.6.1 *Experimental Conclusions*

The molecular structure of an organic compound can affect properties that, in turn, affect CCN activation. These properties include, but are not exclusive to, the pK_a , solubility, and molecular weight. A compound that has low solubility can still act as a CCN if its pK_a value is low, meaning that it dissociates to a large extent in solution. On the other hand, a compound that does not dissociate in solution can act as a CCN if it is highly soluble. CCN activity generally decreases with increases in molecular weight and pK_a and decreases in solubility. However, the actual extent to which each of these factors affects CCN activity can be difficult to determine, which can complicate predictions of CCN activity.

In general, the dicarboxylic acids and functionalized dicarboxylic acids were found to be the most CCN active, followed by the amino acids, the alcohols, glycolaldehyde dimer, sinapic acid, and finally by the fatty acids and cholesterol. The fatty acids and cholesterol did not activate at the experimental supersaturations. As functional groups are added, CCN activity can increase or decrease, depending not only on the nature of the added functional group, but also on the original structure of the compound. For both succinic and glutaric acid, addition of a ketone group on the second carbon in the chain increased CCN activity, apparently by increasing the dissociation constant (decreasing the pK_a) over that of the unsubstituted compounds.

4.6.2 *Experiment and Model Comparisons*

For the most part, the ADDEM predictions and the experimental results were successful for DL-malic acid and the dicarboxylic acids presented here. The compound for which the comparison was fairly poor was oxalic acid. The experimental activation diameter was 100 nm at a supersaturation of 0.32%, but the error in this measurement was relatively large due to experimental complications, such as particle shrinking and size distribution broadening.

Comparisons of experimental results with past studies were less successful, and values for activation diameters varied greatly among the studies. The activation diameters from this study agreed well with *Cruz and Pandis* [1997] for adipic acid, *Raymond and Pandis* [2002] for glutaric acid, *Giebl et al.* [2002] for malonic acid, and *Prezzi et al.* [2001] for succinic acid. Most of these experimental studies used aqueous solutions in the atomization of their organic particles, and agreement between this study and past studies improved only for adipic acid when an aqueous solution was used for atomization. DL-malic acid, malonic acid, and succinic acid did not show much of a difference in the experimentally determined activation diameters when atomized from aqueous solution rather than methanol. The addition of the DACAD to the measurement system was an invaluable tool in that the size of the particle entering the CCNC3 could be determined. Many of the organic particles became smaller between the classification DMA and the DACAD. If the DACAD had not been present and the dry diameter been corrected, many of these compounds would have appeared to be much less CCN active because their activation diameters would have seemed larger, as much as 75% larger for some compounds. It was not clear that any of the past studies sampled with a scanning

DMA in parallel with the CCN instrument, so that changes in size distribution and diameter may not have been accounted for, as they were in this study.

4.6.3 Experimental Design Considerations

Measurements of CCN activity are complicated by experimental design flaws, which can cause large discrepancies in experimental results. The process by which the organic aerosol particles are formed, such as atomization, needs to be carefully considered. Atomization of the organic aerosol particles from different solutions (i.e., alcohol versus aqueous solution) can affect the experimental results, not because the solvent changes the actual CCN properties of the compound but because residual solvent on the particles can affect the ability of water to condense upon the particles. Complete drying, while somewhat difficult to obtain, is essential in order to determine the CCN activation properties of the pure organic compound. In the studies presented here, organic particles were atomized from a methanol solution because methanol is more volatile than water and would be easier to remove from the particles. As has been presented, though, there were issues even with methanol as the solvent. There is evidence that methanol solvent may have been trapped in some particles and subsequently escaped after size-selection in the classification DMA, causing some particles to “collapse” into smaller particles before entering the CCN instrument. Also, some of the organic compounds (2-hexadecanol and adipic acid) were more soluble in methanol than in water, and the presence of methanol may have facilitated dissolution into the water droplets, thus increasing the apparent CCN activity of the particles. Other solvents, such as acetone or dichloromethane, could also be used in place of methanol

and water for preparation of atomization solutions. Acetone and dichloromethane are more volatile than methanol and less polar, so they would not be expected to facilitate CCN activity by solvating the organic compounds.

In future experiments, Nafion driers, in addition to diffusion driers, could be included in the drying system to help remove solvent from the particles after atomization. Preliminary tests have indicated that the amount of methanol in the sample air stream can be reduced significantly by using the Nafion drier (with dry, clean purged air). This may or may not affect the CCN experiments. Over the course of a CCN experiment, the amount of methanol, as indicated by a Vaisala Humitter (which is sensitive to methanol, as well as water vapor), in the sample air stream increased from less than 5% to over 15%. However, no differences were observed between the results at the beginning and the end of the CCN experiments. If the methanol had been affecting the CCN results, the effect would have been evident in the activation curves because the diameters were chosen at random (not in order) to avoid experimental bias.

In the atmosphere, these organic compounds would most likely be present in mixed particles with inorganic compounds, especially after undergoing cloud processing. Future CCN studies should carefully consider the CCN activity of mixed particles. In an attempt to make mixed inorganic/organic aerosol particles, a methanol solution of *cis*-pinonic acid and ammonium bisulfate was atomized. The CCN activation curve was very broad and the activation diameter was much lower than that of pure ammonium bisulfate. Although this might be expected simply from the increased amount of ions and solute present, the solution was atomized into an aerosol mass spectrometer (AMS) in an attempt to look at the composition of the particles. The AMS showed that atomization of

the *cis*-pinonic/ammonium bisulfate methanol solution created some pure ammonium sulfate particles, some mixed particles, and some pure *cis*-pinonic particles. This indicates that atomization of mixed particles should be carefully planned and tested. Also, future studies could humidify the sample after size selection (when there is no water present) but before the CCN instrument to look at how CCN activity is affected by initial *RH*. However, it must be kept in mind that laboratory experiments of the CCN properties of organic compounds are complicated by the properties of the organic particles themselves and careful consideration of these properties are necessary to successful experimental design and interpretation of experimental results.

Acknowledgements. The authors would like to thank J. H. Kroll and J. D. Surratt for helpful suggestions and comments. The authors would also like to thank M. C. Facchini, G. Kiss, and S. Decesari for experimental surface tension data.

4.7 References

- Bilde, M. and B. Svenningsson (2004), CCN activation of slightly soluble organics: The importance of small amounts of inorganic salt and particle phase, *Tellus*, 56B(2), 128 – 134.
- Bilde, M., B. Svenningsson, J. Mønster, and T. Rosenørn (2003), Even-odd alternation of evaporation rates and vapor pressures of C3-C9 dicarboxylic acid aerosols, *Environ. Sci. Technol.*, 37(7), 1371 – 1378.
- Brent, R., S. Winograd, and P. Wolfe (1973), Optimal iterative processes for root-finding, *Numer. Mathe.*, 20(5), 327 – 341.
- Broekhuizen, K., P. P. Kumar, and J. P. D. Abbatt (2004), Partially soluble organics as cloud condensation nuclei: Role of trace soluble and surface active species, *Geophys. Res. Lett.*, 31(1), L01107, doi:10.1029/2003GL018203.
- Chen, J. P. (1994), Theory of deliquescence and modified Köhler Curves, *J. Atmos. Sci.*, 51(23), 3505 – 3516.
- Claeys, M., B. Graham, G. Vas, W. Wang, R. Vermeylen, V. Pashynska, J. Cafmeyer, P. Guyon, M. O. Andreae, P. Arataxo, and W. Maenhaut (2004), Formation of secondary organic aerosols through photooxidation of isoprene, *Science*, 303(5661), 1173 – 1176.
- Clegg, S. L., K. S. Pitzer, and P. Brimblecombe (1992), Thermodynamics of Multicomponent, Miscible, Ionic Solutions. 2. Mixtures including unsymmetrical electrolytes, *J. Phys. Chem.*, 96(23), 9470 – 9479.
- Corrigan, C. E. and T. Novakov (1999), Cloud condensation nucleus activity of organic compounds: a laboratory study, *Atmos. Env.*, 33(17), 2661 – 2668.
- Cruz, C. N. and S. N. Pandis (1997), A study of the ability of pure secondary organic aerosol to act as cloud condensation nuclei, *Atmos. Env.*, 31(15), 2205 – 2214.
- Edney, E. O., T. E. Kleindienst, M. Jaoui, M. Lewandowski, J. H. Offenberg, W. Wang, and M. Claeys (2005), Formation of 2-methyl tetrols and 2-methylglyceric acid in secondary organic aerosol from laboratory irradiated isoprene/NO_x/SO₂/air mixtures and their detection in ambient PM_{2.5} samples collected in the eastern United States, *Atmos. Env.*, 39(29), 5281 – 5289.
- Fredenslund, A., R. L. Jones, and J. M. Prausnitz (1975), Group-contribution estimation of activity-coefficients in nonideal liquid-mixtures, *AIChE J.*, 21(6), 1086 – 1099.

- Gao, S., M. Keywood, N. L. Ng, J. Surratt, V. Varutbangkul, R. Bahreini, R. C. Flagan, and J. H. Seinfeld (2004), Low – molecular weight and oligomeric components in secondary organic aerosol from the ozonolysis of cycloalkenes and α -pinene, *J. Phys. Chem.*, 108(46), 10,147 – 10,164.
- Gao, S., J. D. Surratt, E. M. Knipping, E. S. Edgerton, M. Shahgholi, and J. H. Seinfeld (2006), Characterization of polar organic components in fine aerosols in the Southeastern United States: Identity, origin, and evolution, *J. Geophys. Res.*, *in press*.
- Giebl, H., A. Berner, G. Reischl, H. Puxbaum, A. Kasber-Giebl, and R. Hitzenberger (2002), CCN activation of oxalic and malonic test aerosols with the University of Vienna cloud condensation nuclei counter, *J. Aerosol Sci.*, 33(12), 1623 – 1634.
- Heintzenberg, J. (1989), Fine particles in the global troposphere, A review, *Tellus*, 41B, 149 – 160.
- Henning, S., T. Rosenørn, B. D'Anna, A. A. Gola, B. Svenningsson, and M. Bilde (2005), Cloud droplet activation and surface tension of mixtures of slightly soluble organics and inorganic salt, *Atmos. Chem. Phys.*, 5, 575 – 582.
- Hori, M., S. Ohta, N. Murao, and S. Yamagata (2003), Activation capability of water soluble organic substances as CCN, *J. Aerosol Sci.*, 34(4), 419 – 448.
- Houghton, J. T., Y. Ding, D. J. Griggs, M. Noguera, P. J. van der Linden, and D. Xiaosu, Eds., (2001), *Climate Change 2001: The Scientific Basis*, 944 pp., Cambridge University Press, Cambridge, U.K.
- Hu, Y. F. and H. Lee (2004), Prediction of the surface tension of mixed electrolyte solutions based on the equation of Patwardhan and Kumar and the fundamental Butler equations, *J. Coll. Inter. Sci.*, 269(2), 442 – 448.
- Huff Hartz, K. E., J. E. Tischuk, M. N. Chan, C. K. Chan, N. M. Donahue, and S. N. Pandis (2006), Cloud condensation nuclei activation of limited solubility organic aerosol, *Atmos. Env.*, 40(4), 605 – 617.
- Kalberer, M., D. Paulsen, M. Sax, M. Steinbacher, J. Dommen, A. S. H. Prevot, R. Fisseha, E. Weingartner, V. Frankevich, R. Zenobi, and U. Baltensperger (2004), Identification of polymers as major components of atmospheric organic aerosols, *Science*, 303(5664), 1659 – 1662.
- Koehler, K. A., S. M. Kreidenweis, P. J. DeMott, A. J. Prenni, C. M. Carrico, B. Ervens, and G. Feingold (2005), Water activity and activation diameters from hygroscopicity data—Part II: Application to organic species, *Atmos. Chem. Phys.*, 5, 10,881 – 10,924.

- Köhler, H. (1936), The nucleus in and the growth of hygroscopic droplets, *Trans. Far. Soc.*, 32(2), 1152 – 1161.
- Kumar, P. P., K. Broekhuizen, and J. P. D. Abbatt (2003), Organic acids as cloud condensation nuclei: Laboratory studies of highly soluble and insoluble species, *Atmos. Chem. Phys.*, 3, 509 – 520.
- Lide, D. R., Ed., (2003), *CRC Handbook of Chemistry and Physics, 84th Edition*, 2576 pp., CRC Press, FL.
- Li, Z. B. and B. C. Y. Lu (2001), Surface tension of aqueous electrolyte solutions at high concentrations—representation and prediction, *Chem. Eng. Sci.*, 56(8), 2879 – 2888.
- McFiggans, G., P. Artaxo, U. Baltensperger, H. Coe, M. C. Facchini, G. Feingold, S. Fuzzi, M. Gysel, A. Laaksonen, U. Lohmann, T. F. Mentel, D. M. Murphy, C. D. O’Dowd, J. R. Snider, and E. Weingartner (2005), The effect of physical and chemical aerosol properties on warm cloud droplet activation, *Atmos. Chem. Phys. Discuss.*, 5, 8507 – 8646.
- Ming, Y. and L. M. Russell (2004), Organic aerosol effects on fog droplet spectra, *J. Geophys. Res.*, 109(D10), D10206, doi:10.1029/2003JD004427.
- Novakov, T. and J. E. Penner (1993), Large contributions of organic aerosols to cloud-condensation nuclei concentrations, *Nature*, 365(6449), 823 – 825.
- O’Neil, M. J., A. Smith, and P. E. Heckelman (Eds.) (2001), *The Merck Index—An Encyclopedia of Chemicals, Drugs, and Biologicals. 13th Edition*, 289 pp., Merck & Co., Inc., New Jersey.
- Peng, C., M. N. Chan, and C. K. Chan (2001), The hygroscopic properties of dicarboxylic acids: Measurements and UNIFAC predictions, *Env. Sci. Tech.*, 35(22), 4495 – 4501.
- Pitzer, K. S. and J. M. Simonson (1986), Thermodynamics of multicomponent, miscible, ionic systems: Theory and equations, *J. Phys. Chem.*, 90(13), 3005 – 3009.
- Prenni, A. J., P. J. DeMott, S. M. Kreidenweis, D. E. Sherman, L. M. Russell, and Y. Ming (2001), The effects of low molecular weight dicarboxylic acids on cloud formation, *J. Phys. Chem.*, 105(50), 11,240 – 11,248.
- Press, W. H., S. A. Teukolsky, W. T. Vetterling, and B. P. Flannery (1992), *Numerical Recipes in Fortran 77: The Art of Scientific Computing*, 915pp., Cambridge University Press, Cambridge, U.K.
- Raymond, T. M., and S. N. Pandis (2002), Cloud activation of single-component organic aerosol particles, *J. Geophys. Res.*, 107(D24), 4787, doi:10.1029/2002JD002159.

- Rissman, T. A., A. Nenes, and J. H. Seinfeld (2004), Chemical amplification (or dampening) of the Twomey Effect: Conditions derived from droplet activation theory, *J. Atmos. Sci.*, *61*(8), 919 – 930.
- Rissman, T. A., T. M. VanReken, J. Wang, R. Gasparini, D. R. Collins, H. H. Jonsson, F. J. Brechtel, R. C. Flagan, and J. H. Seinfeld (2006), Characterization of ambient aerosol from measurements of cloud condensation nuclei during the 2003 Atmospheric Radiation Measurement Aerosol Intensive Observational Period at the Southern Great Plains site in Oklahoma, *J. Geophys. Res.*, *111*(D5), D05S11, doi:10.1029/2004JD005695.
- Rudich, Y. (2003), Laboratory perspectives on the chemical transformations of organic matter in atmospheric particles, *Chem. Rev.*, *103*(12), 5097 – 5124.
- Saxena, P. and L. M. Hildeman (1996), Water-soluble organics in atmospheric particles: a critical review of the literature and application of thermodynamics to identify candidate compounds, *J. Atmos. Chem.*, *24*(1), 57 – 109.
- Seinfeld, J. H. and S. N. Pandis (1998), *Atmospheric Chemistry: From Air Pollution to Climate Change*, 1326 pp., John Wiley & Sons, Inc., New York City, NY.
- Suarez, J. T., C. Torresmarchal, and P. Rasmussen (1989), Prediction of surface tensions of nonelectrolyte solutions, *Chem. Eng. Sci.*, *44*(3), 782 – 786.
- Sun, J. and P. A. Ariya (2006), Atmospheric organic and bio-aerosols as cloud condensation nuclei (CCN): A review, *Atmos. Env.*, *40*(5), 795 – 820.
- Tamura, M., M. Kurata, and H. Odani (1955), Practical method for estimating surface tensions of solutions, *Bull. Chem. Soc. Japan*, *28*(1), 83 – 88.
- Tao, Y. and P. H. McMurry (1989), Vapor-pressures and surface free-energies of C14-C18 monocarboxylic acids and C5-dicarboxylic and C6-dicarboxylic acids, *Environ. Sci. Technol.*, *23*(12), 1519 – 1523.
- Topping, D. O., G. B. McFiggans, and H. Coe (2005a), A curved multi-component aerosol hygroscopicity model framework: Part 1—Inorganic compounds, *Atmos. Chem. Phys.*, *5*(5), 1205 – 1222.
- Topping, D. O., G. B. McFiggans, and H. Coe (2005b), A curved multi-component aerosol hygroscopicity model framework: Part 2—Including organic compounds, *Atmos. Chem. Phys.*, *5*(5), 1223 – 1242.
- Twomey, S. (1974), Pollution and the planetary albedo, *Atmos. Env.*, *8*(12), 1251 – 1256.
- Twomey, S. (1977), *Atmospheric Aerosols*, 302 pp., Elsevier, New York City, NY.

- VanReken, T. M., T. A. Rissman, G. C. Roberts, V. Varutbangkul, H. H. Jonsson, R. C. Flagan, and J. H. Seinfeld (2003), Toward aerosol/cloud condensation nuclei (CCN) closure during CRYSTAL-FACE, *J. Geophys. Res.*, *108*(D20), 4633, doi:10.1029/2003JD003582.
- Wade, L. G. (1995), *Organic Chemistry*, 1269 pp., Prentice Hall, NJ.
- Wang, J., R. C. Flagan, J. H. Seinfeld, H. H. Jonsson, D. R. Collins, P. B. Russell, B. Schmid, J. Redemann, J. M. Livingston, S. Gao, D. A. Hegg, E. J. Welton, and D. Bates (2002), Clear-column radiative closure during ACE-Asia: Comparison of multiwavelength extinction derived from particle size and composition with results from Sun photometry, *J. Geophys. Res.*, *107*(D23), 4688, doi:10.1029/2002JD002465.
- Wang, J., R. C. Flagan, and J. H. Seinfeld (2003), A Differential Mobility Analyzer (DMA) system for submicron aerosol measurements at ambient relative humidity, *Aerosol Sci. Technol.*, *37*(1), 46 – 52.
- Wang, S. C., and R. C. Flagan (1990), Scanning electrical mobility spectrometer, *Aerosol Sci. Technol.*, *35*(3), 718 – 727.
- Warner, J. (1968), A reduction in rainfall associated with smoke from sugar-cane fires – An inadvertent weather modification?, *J. Appl. Meteor.*, *7*(2), 247 – 251.
- Weast, R. C. and M. J. Astle, Eds. (1985), *CRC Handbook of Data on Organic Compounds*, 1936 pp., CRC Press, FL.
- Yalkowsky, S. H. and Y. He (2003), *Handbook of Aqueous Solubility Data*, 1496 pp., CRC Press, FL.

Chapter 5

CONCLUSIONS AND FUTURE WORK

The results presented in this thesis reinforce the importance of atmospheric aerosol chemical composition in cloud droplet activation processes through theoretical, field, and laboratory investigations. Including surface tension and limited solubility effects, especially of organic compounds, in parameterizations of cloud formation indicate that these chemical effects can rival those of the physical properties of the aerosol population, as well as the meteorological environment. Assumptions of simple chemistry and mixing state in the interpretation and analysis of field cloud condensation nuclei (CCN) measurements may not necessarily be sufficient and/or realistic, depending heavily on the location of the field study. The determination of the CCN properties of pure organic compounds in a controlled, laboratory environment is very important in the understanding the effects of organics on cloud formation and determining parameters to be included in aerosol activation theory and parameterizations. However, these experiments must be carefully planned and the results carefully interpreted to avoid experimental bias in the conclusions.

5.1 CCN Activation Theory (Chapter 2)

The conditions under which chemical effects can either amplify or dampen the Twomey effect are assessed by determining relative sensitivities of chemical and size distribution parameters to that of updraft velocity. Depending on atmospheric conditions, chemical effects can either enhance or weaken the activation process. An important finding is that, adding surfactants to the CCN drastically changes the character of the activation process; and the sensitivity of the droplet number concentration to organic mass fraction becomes a strong function of updraft velocity (this is not seen for the same

aerosol in the absence of surfactants). This implies that, when studying aerosol–cloud interactions, the most influential (in terms of droplet number) updraft may not be in the peak of the probability distribution. Such insight is critical for understanding the aerosol indirect effect in both modeling studies and field experiments.

An increase in anthropogenic pollution can have two competing effects on cloud formation: (i) an increased number of CCN activated by increased aerosol number concentration (the Twomey Effect) and (ii) a decreased number of CCN activated by a greater presence of soluble, surface active organics. Consequently, regimes exist in which an increase in anthropogenic aerosol can actually lead to a decrease in cloud droplet number. The direction in which the presence of a soluble organic affects CCN activation will depend on the chemical characteristics of the aerosol, including its size distribution. Future work should focus on determining the range of solubility, hygroscopicity, and surfactant properties necessary to have an important effect on droplet number.

5.2 CCN Field Measurements (Chapter 3)

The inverse aerosol/CCN closure study from Chapter 3 reveals possible features of ambient aerosol sampled during the Atmospheric Radiation Measurement (ARM) Aerosol Intensive Observational Period (IOP) in the absence of direct airborne aerosol composition measurements. The ARM Southern Great Plains (SGP) site is greatly influenced by local aerosol sources, as well as long-range sources, and the aerosol CCN activity at high supersaturations was greatly influenced by the chemical characteristics and mixing state of the aerosols in the sampled air masses. The characteristics of air

masses sampled during the ARM Aerosol IOP ranged from those of relatively clean air masses to those of air masses influenced by local and long-range pollution events to those of aged smoke plumes. These air masses can be categorized by aerosol size distribution, as well as by CCN behavior. The general low aerosol CCN activity that was observed in the inverse aerosol/CCN study is consistent with other measurements from the IOP.

Although some of the chemistry effects may not have been captured at smaller supersaturations, future measurements should be made at lower operating supersaturations to better determine the ability to predict CCN concentration using surface data. However, for a continental location such as the ARM SGP site that is influenced by many different aerosol sources, ranging from local to international, predicting CCN concentrations from aerosol size distributions and surface aerosol composition measurements alone is probably not adequate. Future studies should also include airborne aerosol composition measurements to allow more complete aerosol/CCN closure studies.

5.3 Laboratory CCN Studies of Pure Organic Compounds (Chapter 4)

The molecular structure of an organic compound can affect properties that, in turn, affect CCN activation. These properties include, but are not exclusive to, the pK_a , solubility, and molecular weight. A compound that has low solubility can still act as a CCN if its pK_a value is low, meaning that it dissociates to a large extent in solution. On the other hand, a compound that does not dissociate in solution can act as a CCN if it is highly soluble. CCN activity generally decreases with increases in molecular weight and pK_a and decreases in solubility. However, the actual extent to which each of these

factors affects CCN activity can be difficult to determine, which can complicate predictions of CCN activity.

In general, the dicarboxylic acids and functionalized dicarboxylic acids were found to be the most CCN active, followed by the amino acids, the alcohols, glycolaldehyde dimer, sinapic acid, and finally by the fatty acids and cholesterol. The fatty acids and cholesterol did not activate at the experimental supersaturations. As functional groups are added, CCN activity can increase or decrease, depending not only on the nature of the added functional group, but also on the original structure of the compound. For both succinic and glutaric acid, addition of a ketone group on the second carbon in the chain increased CCN activity, apparently by increasing the dissociation constant (decreasing the pK_a) over that of the unsubstituted compounds.

For the most part, the Aerosol Diameter Dependent Equilibrium Model (ADDEM) predictions and the experimental results were successful for DL-malic acid and the dicarboxylic acids presented here. The compound for which the comparison was fairly poor was oxalic acid, but the error in the activation diameter measurement was relatively large due to experimental complications, such as particle shrinking and size distribution broadening.

Comparisons of experimental results with past studies were less successful, and values for activation diameters varied greatly among the studies. Measurements of CCN activity are complicated by experimental design flaws, which can cause large discrepancies in experimental results. The process by which the organic aerosol particles are formed, such as atomization, needs to be carefully considered. Atomization of the organic aerosol particles from different solutions (i.e., alcohol versus aqueous solution)

can affect the experimental results, not because the solvent changes the actual CCN properties of the compound but because residual solvent on the particles can affect the ability of water to condense upon the particles. Complete drying, while somewhat difficult to obtain, is essential in order to determine the CCN activation properties of the pure organic compound. In future experiments, Nafion driers, in addition to diffusion driers, could be included in the drying system to help remove solvent from the particles after atomization. Preliminary tests have indicated that the amount of methanol in the sample air stream can be reduced significantly by using the Nafion drier (with dry, clean purge air).

In the studies presented in Chapter 4, organic particles were atomized from a methanol solution because methanol is more volatile than water and would be easier to remove from the particles. As has been presented, though, there were issues even with methanol as the solvent. There is evidence that methanol solvent may have been trapped in some particles and subsequently escaped after size-selection in the classification DMA, causing some particles to “collapse” into smaller particles before entering the CCN instrument. Also, some of the organic compounds (2-hexadecanol and adipic acid) were more soluble in methanol than in water, and the presence of methanol may have facilitated dissolution into the water droplets, thus increasing the apparent CCN activity of the particles. Other solvents, such as acetone or dichloromethane, could also be used in place of methanol and water for preparation of atomization solutions. Acetone and dichloromethane are more volatile than methanol and less polar, so they would not be expected to facilitate CCN activity by solvating the organic compounds.

In the atmosphere, these organic compounds would most likely be present in mixed particles with inorganic compounds, especially after undergoing cloud processing. Future CCN studies should carefully consider the CCN activity of mixed particles. Also, future studies could humidify the sample after size selection (when there is no water present) but before the CCN instrument to look at how CCN activity is affected by initial *RH*. However, it must be kept in mind that laboratory experiments of the CCN properties of organic compounds are complicated by the properties of the organic particles themselves and careful consideration of these properties are necessary to successful experimental design and interpretation of experimental results.

Appendix A

BLACK AND WHITE FIGURES FOR CHAPTER 3

* Full Citation: Rissman, T. A., T. M. VanReken, J. Wang, R. Gasparini, D. R. Collins, H. H. Jonsson, F. J. Brechtel, R. C. Flagan, and J. H. Seinfeld (2006), Characterization of ambient aerosol from measurements of cloud condensation nuclei during the 2003 Atmospheric Radiation Measurement Aerosol Intensive Observational Period at the Southern Great Plains site in Oklahoma, *Journal of Geophysical Research*, 111(D5), D05S11, doi: 10.1029/2004JD005695.

© 2006 American Geophysical Union (AGU). This chapter is reprinted with permission from the American Geophysical Union.

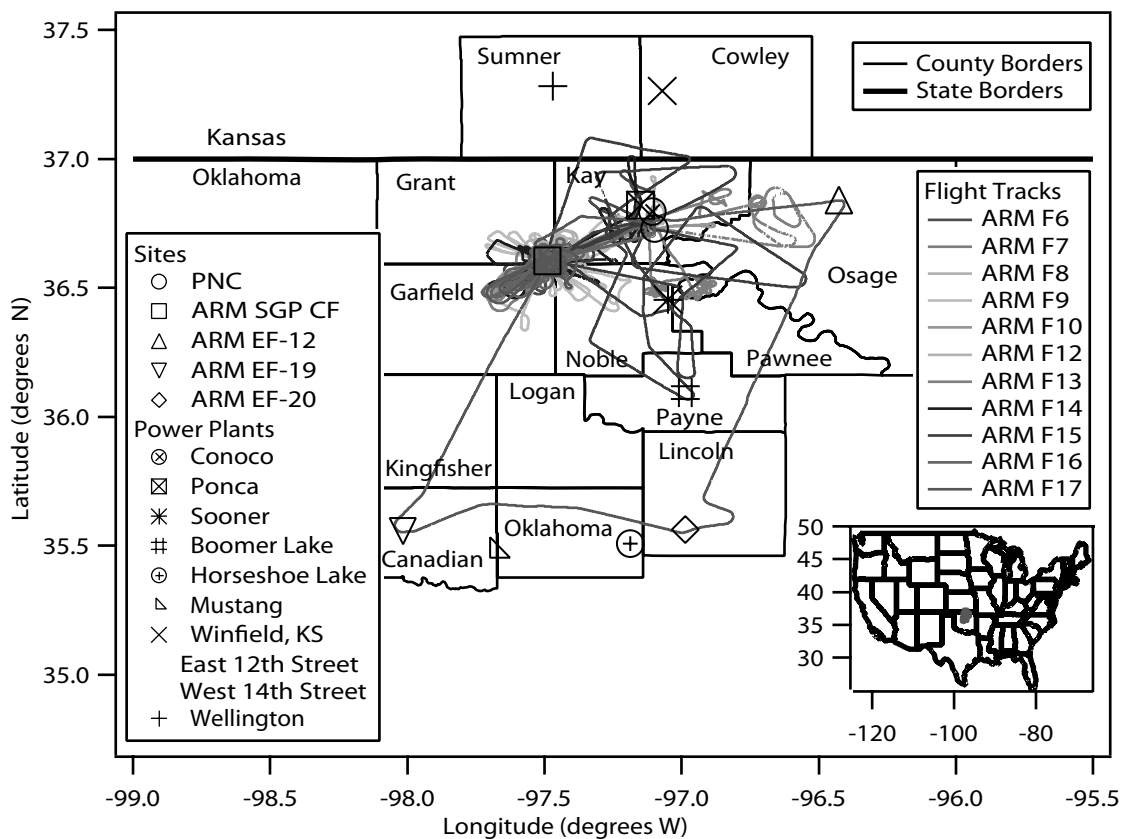


Figure 3.1. ARM Aerosol IOP flight paths for flights with CCN data. PNC is the Ponca City, Oklahoma, airport, where the Twin Otter was based. The other sites are ARM ground measurement sites. The insert shows the position of the counties (in pink) within the continental United States. The axes of the insert are in the same units as those in the main plot.

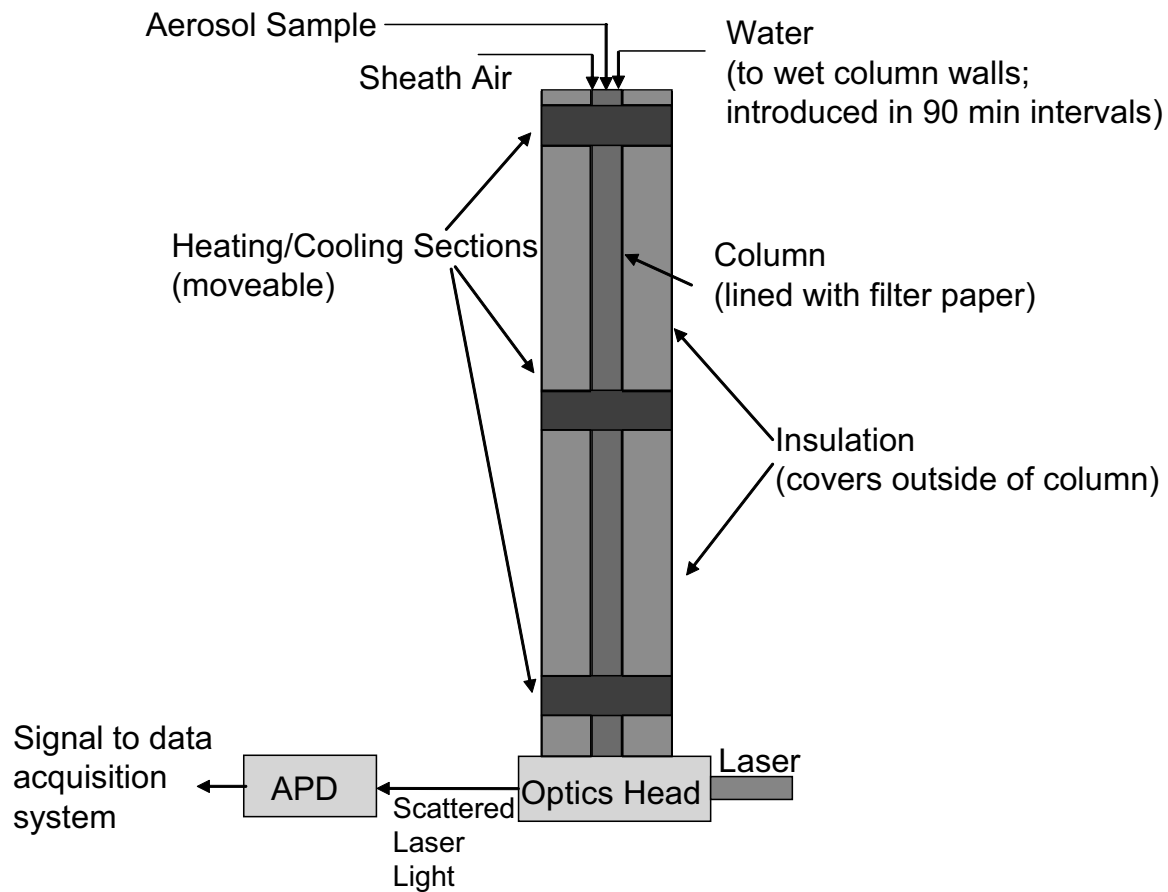


Figure 3.2. A schematic of a CCNC3 column. A second layer of insulation covers the growth tube and heating/cooling sections (to prevent temperature transfer to the outside air) and the detector (to prevent condensation within the optics tube).

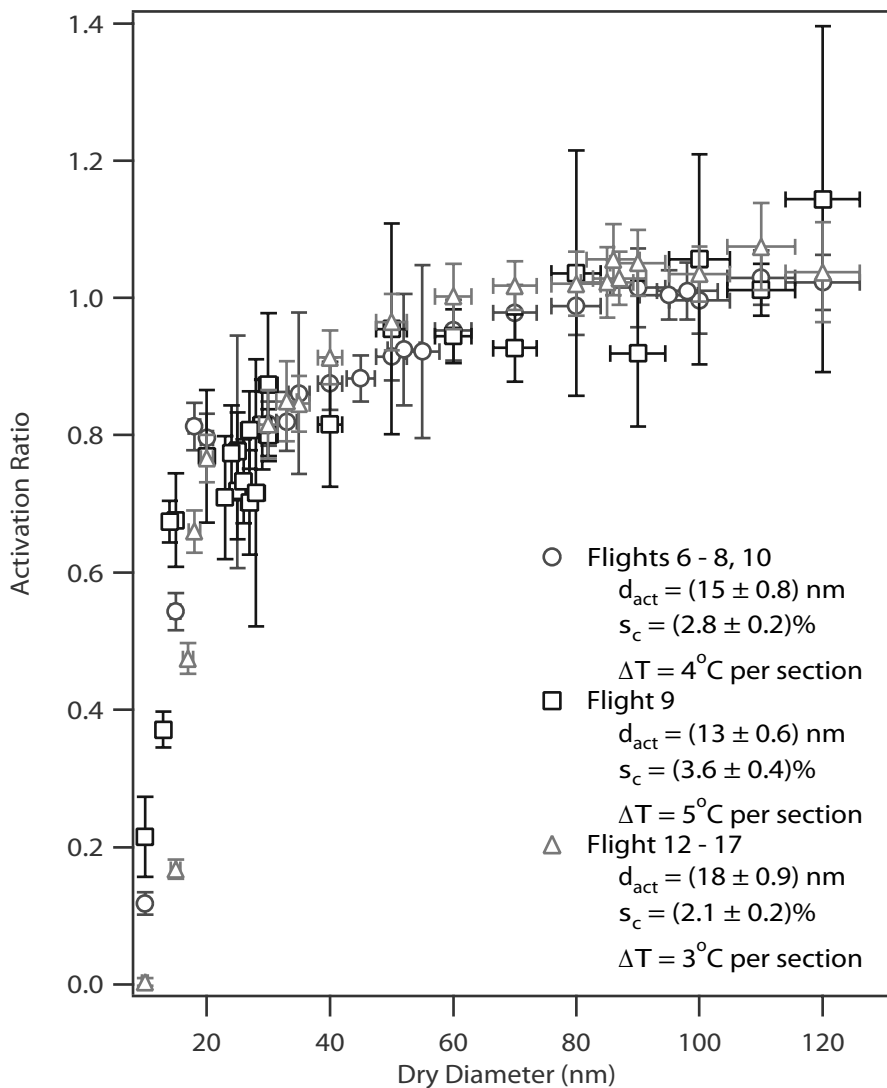


Figure 3.3. $(\text{NH}_4)_2\text{SO}_4$ calibration curves for column 1 of the CCNC3 at the temperature gradients used during the ARM Aerosol IOP. The column was not functioning properly for flights 1–5 and 11. The activation ratio is defined as the ratio of the number concentration of CCN measured by the CCNC3 to the number concentration of particles measured by the CPC.

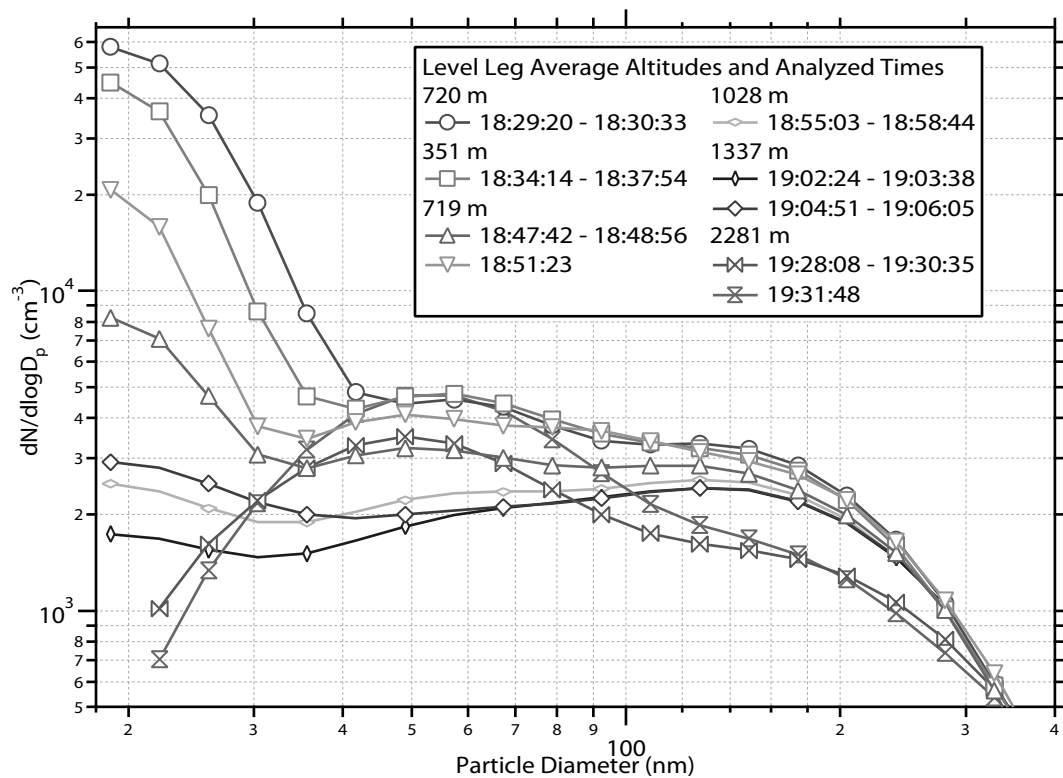


Figure 3.4. Aerosol size distributions from different level legs during flight 16. The legend gives the average altitudes (AGL) and times analyzed for each level leg. The times given are UTC; 1700 UTC corresponds to 1200 LT.

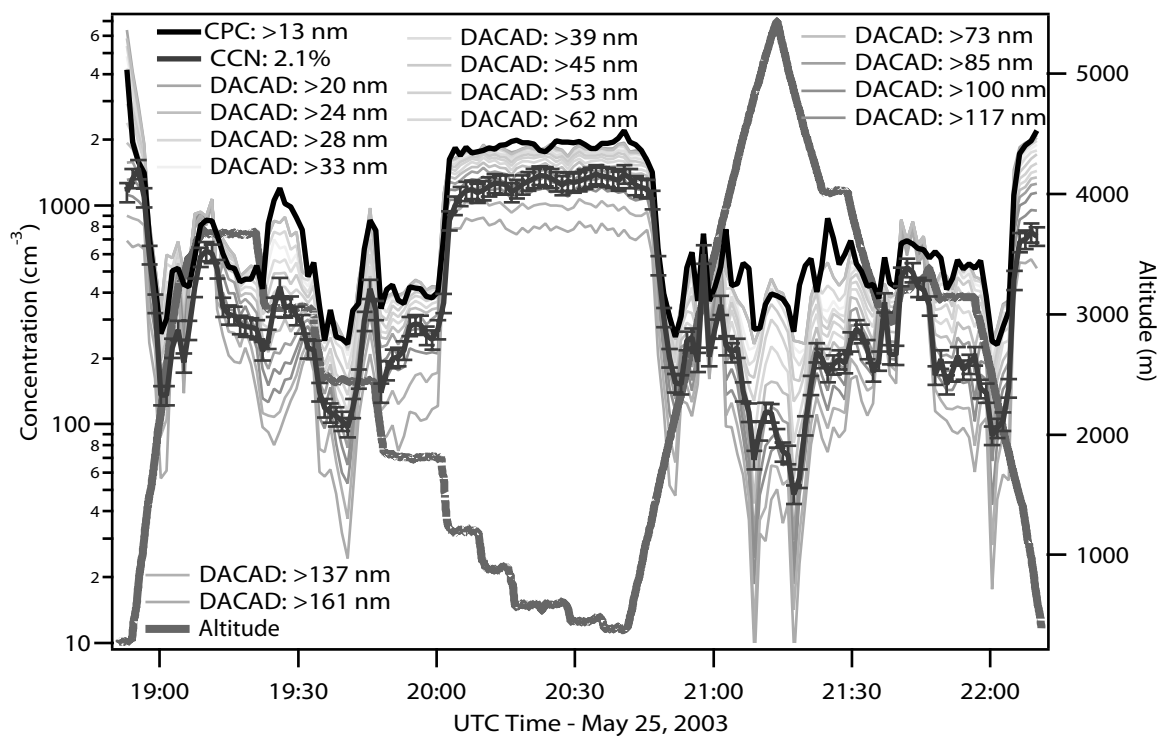


Figure 3.5. Flight traces of CPC, CCNC3, and DACAD data for flight 14. The DACAD traces give the total concentrations of particles with diameters greater than those noted in the legend. A well-mixed boundary layer is clearly shown from about 2010 to 2045. The times given are UTC; 1700 UTC corresponds to 1200 LT.

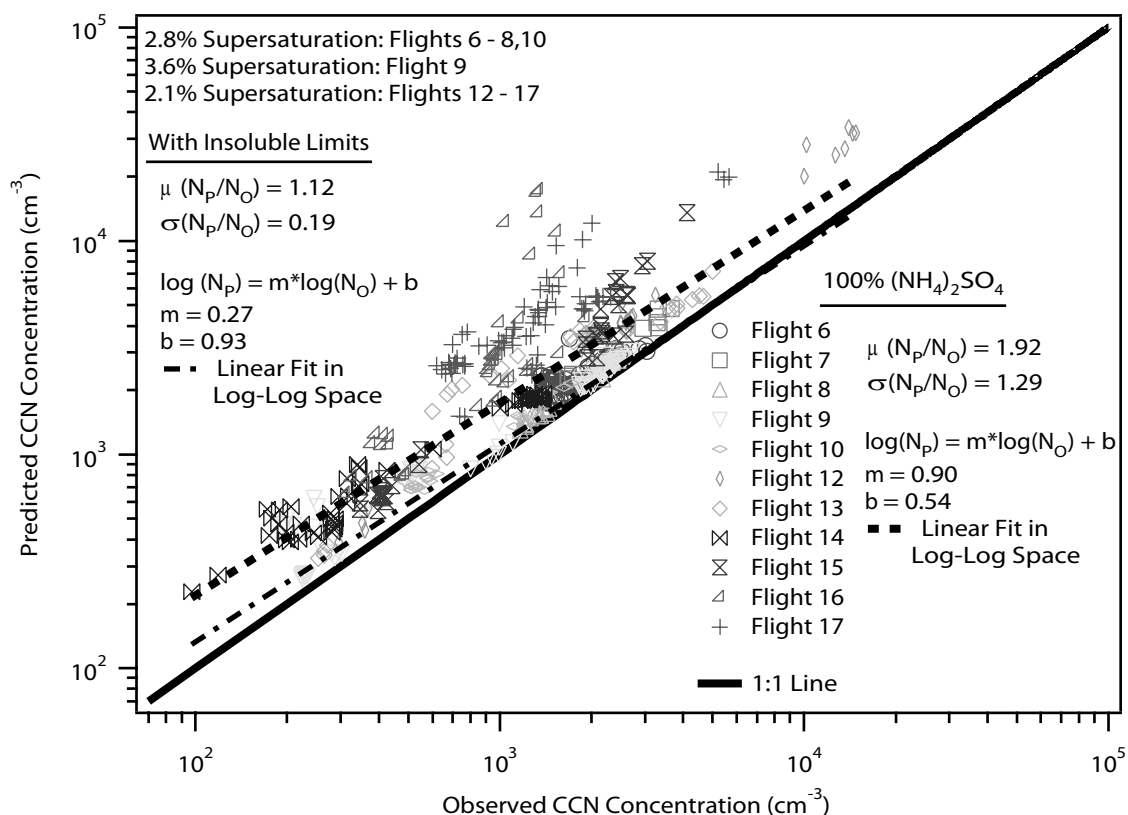


Figure 3.6. Predicted CCN concentration (N_P ; assuming pure $(\text{NH}_4)_2\text{SO}_4$) versus observed CCN concentration (N_O) for ARM Aerosol IOP. Only flights for which CCN data are available are shown. N_P is determined from the DACAD size distribution for all flights except flight 9, for which N_P is determined from the CPC total particle (> 13 nm) concentration. The linear fit in log-log space for all flight closure data is shown, and corresponding fit parameters are given. The mean and standard deviation of the ratio of N_P to N_O averaged over all flights are also given. The fit parameters and mean and standard deviation of the ratio of N_P to N_O are also shown for the ‘‘Insoluble Limit’’ case, for which N_P is calculated using the insoluble fractions calculated in section 3.6.2.1.

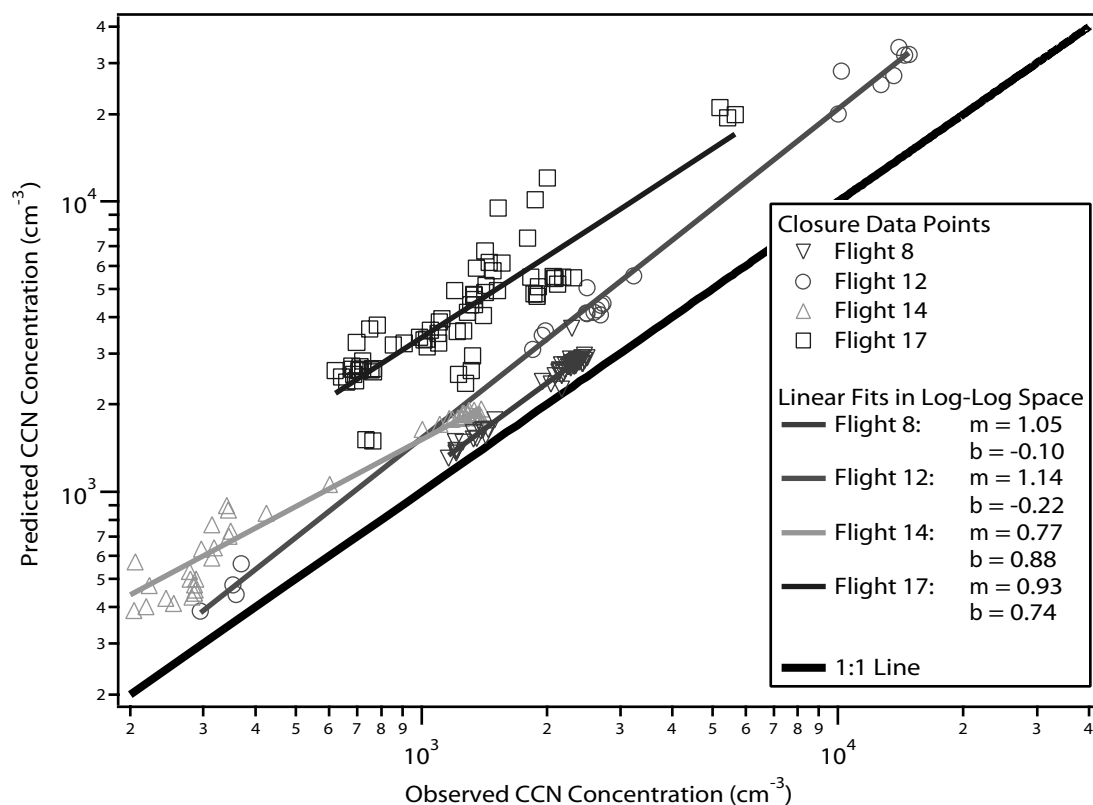


Figure 3.7. N_P (assuming pure $(\text{NH}_4)_2\text{SO}_4$) versus N_O and linear fits in log-log space for flights 8, 12, 14, and 17. High aerosol concentrations (from the CPC) were $10,400 \text{ cm}^{-3}$, $37,000 \text{ cm}^{-3}$, 3550 cm^{-3} , and 2890 cm^{-3} for flights 8, 12, 14, and 17, respectively. High CCN concentrations were 2882 cm^{-3} , $16,941 \text{ cm}^{-3}$, 2143 cm^{-3} , and 7454 cm^{-3} for flights 8, 12, 14, and 17, respectively. High concentration values were determined as the maximum concentrations measured after the Twin Otter had achieved sampling altitude after takeoff, regardless of whether the data were obtained during constant altitude legs.

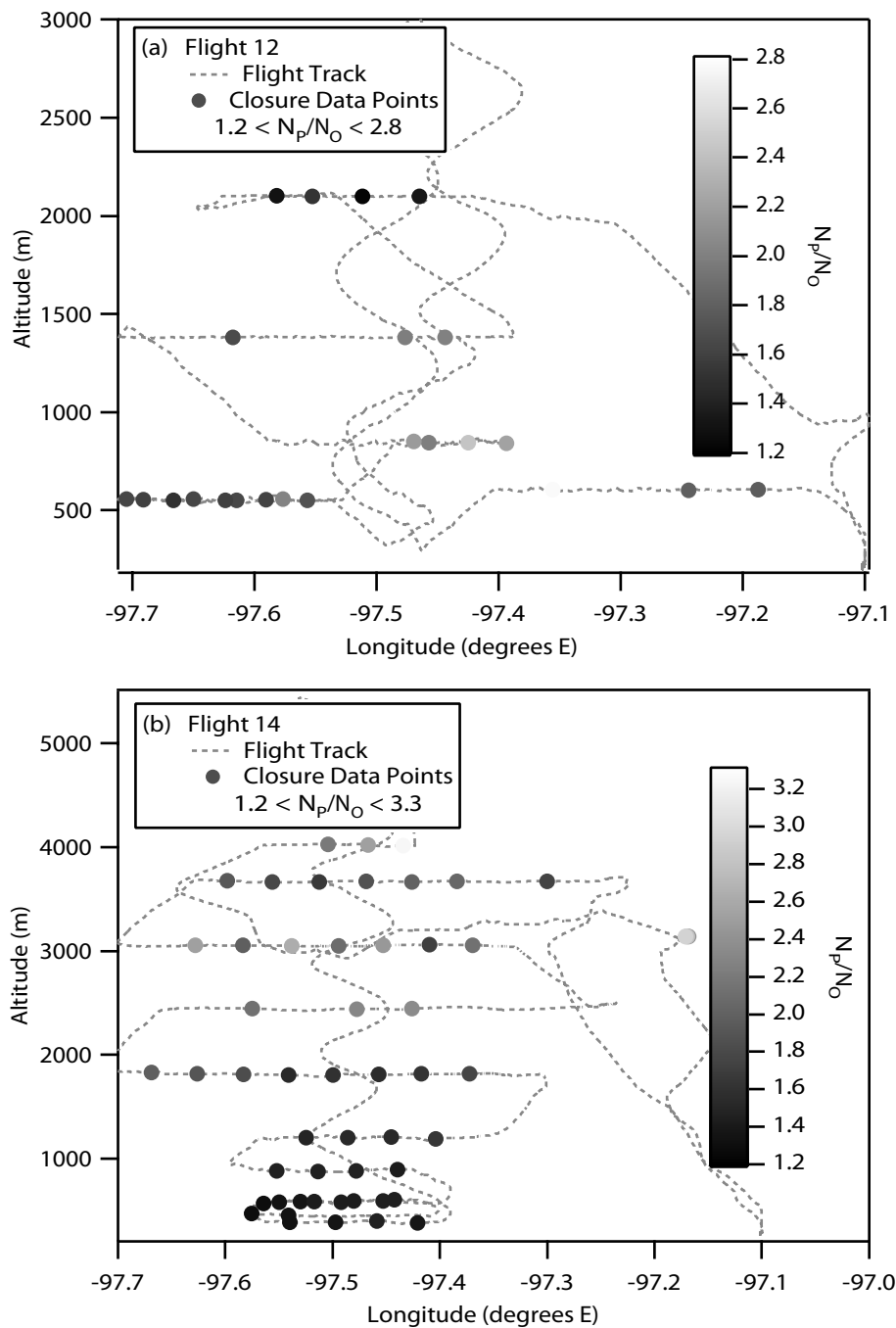


Figure 3.8. Altitude versus longitude trace for flights (a) 12 and (b) 14. Closure data points are indicated by the solid circles. The color of the closure data points indicates the magnitude of N_p/N_0 , assuming pure $(\text{NH}_4)_2\text{SO}_4$, for the corresponding DACAD scan.

NOAA HYSPLIT MODEL
 Backward trajectories ending at 19 UTC 15 May 03
 EDAS Meteorological Data

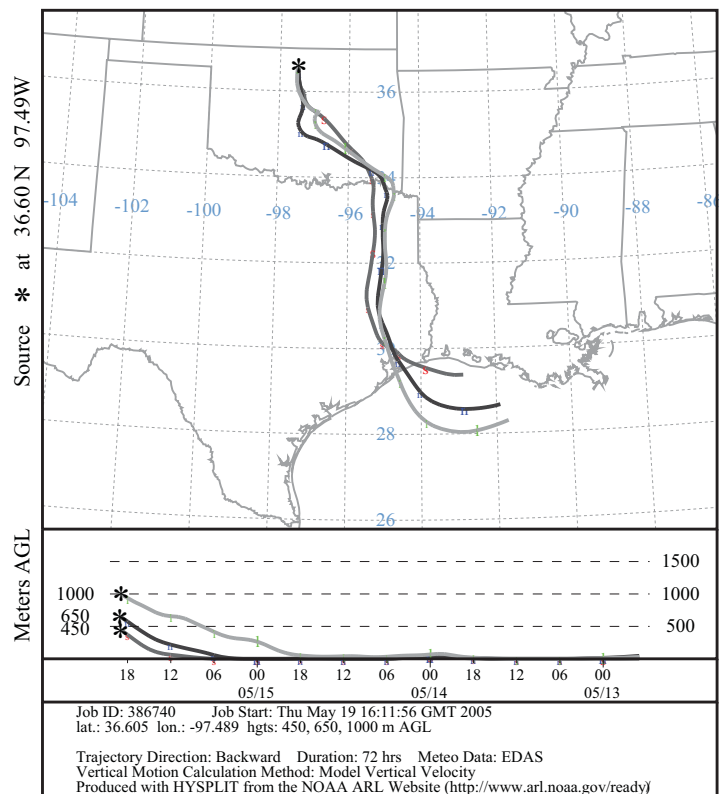


Figure 3.9. Three-day HYSPLIT back trajectories for 15 May 2003 (flight 8) at the SGP site at altitudes of 450, 650, and 1000 m. The times given are UTC; 1700 UTC corresponds to 1200 LT.

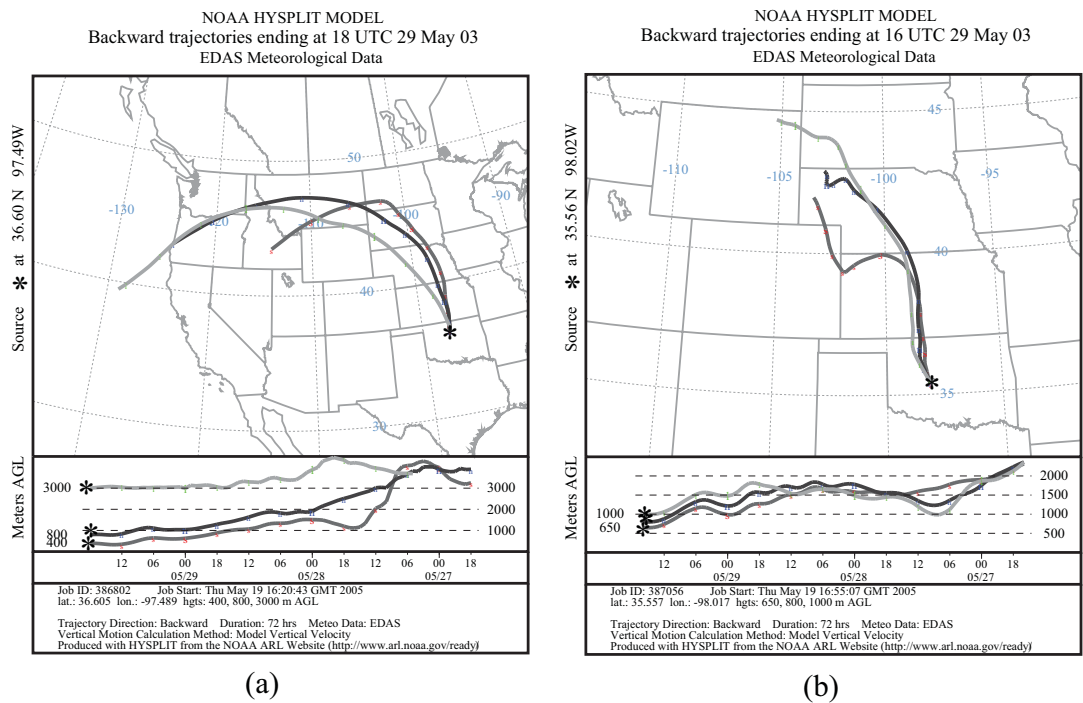


Figure 3.10. Three-day HYSPLIT back trajectories for 29 May 2003 (flight 17) (a) at the SGP site at altitudes of 400, 800, and 3000 m and (b) at site EF-19 at altitudes of 650, 800, and 1000 m. The times given are UTC; 1700 UTC corresponds to 1200 LT.

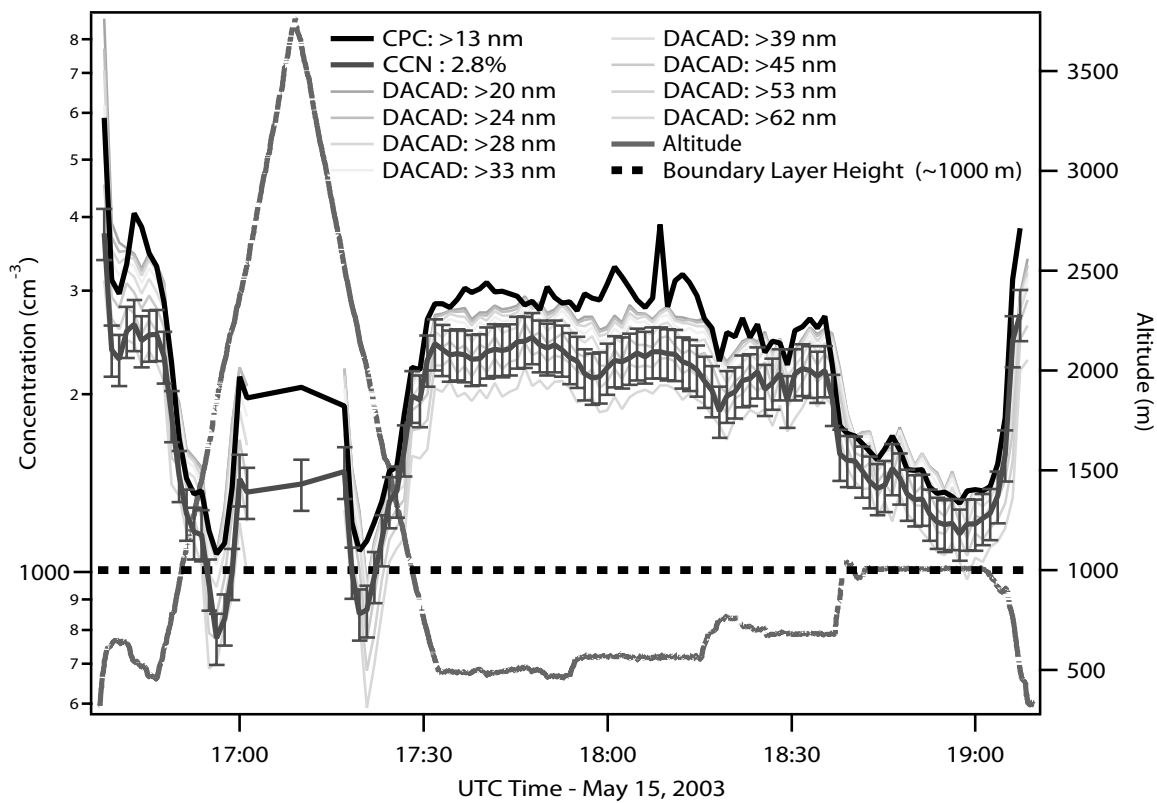


Figure 3.11. Flight trace for flight 8, showing a well-mixed boundary layer between approximately 1730 and 1840 UTC when the Twin Otter was sampling beneath ~ 1000 m. The error bars on the CCN trace indicate the 10% uncertainty level. The times given are UTC; 1700 UTC corresponds to 1200 LT.

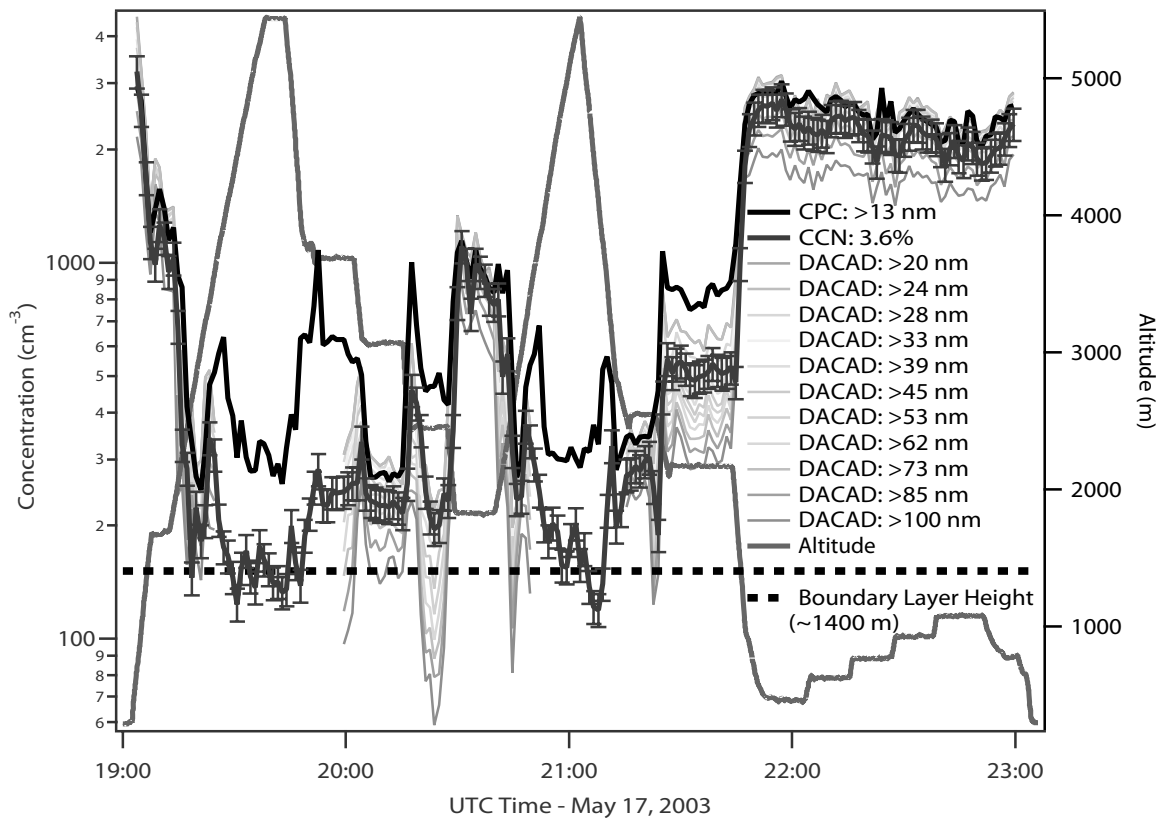


Figure 3.12. Flight trace for flight 9, showing a well-mixed boundary layer between approximately 2200 and 2300 UTC when the Twin Otter was sampling beneath ~1400 m. The error bars on the CCN trace indicate the 10% uncertainty level. The times given are UTC; 1700 UTC corresponds to 1200 LT.

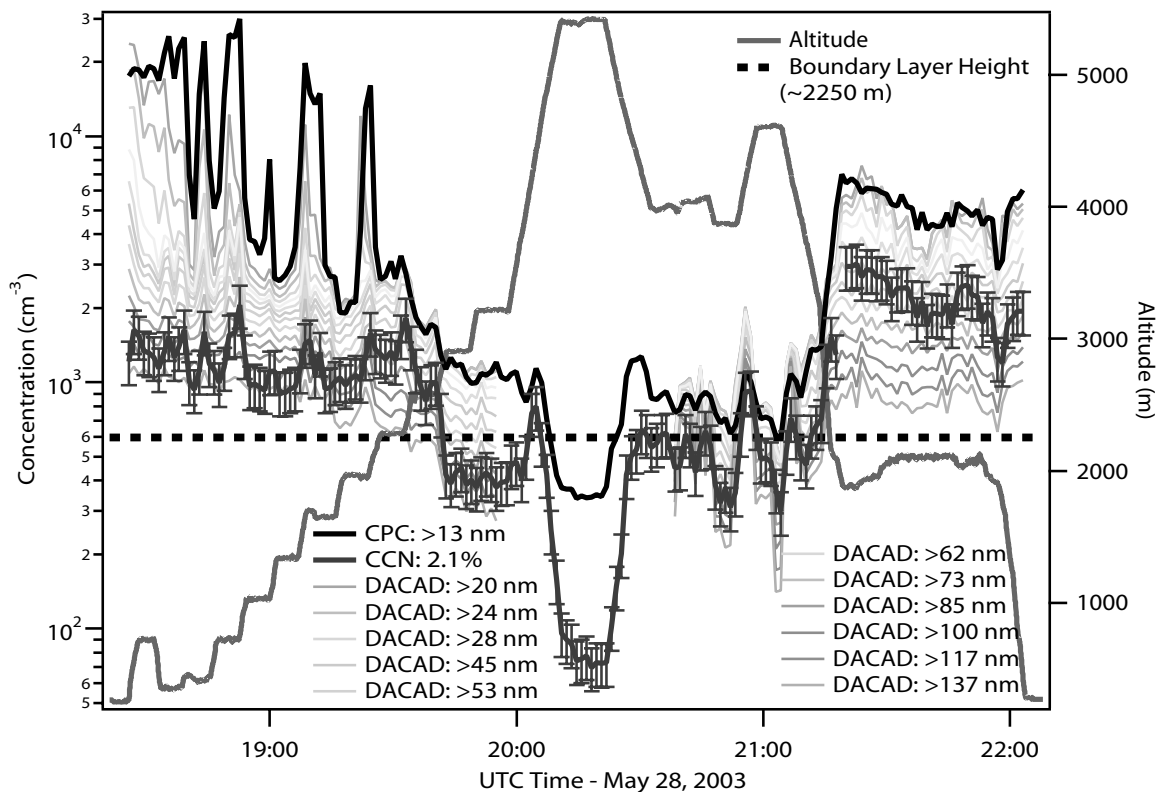


Figure 3.13. Flight trace for flight 16, showing the lack of a well-mixed boundary layer from approximately 1820 to 1940 UTC when the Twin Otter was sampling beneath ~2250 m. The error bars on the CCN trace indicate 20% uncertainty level. The times given are UTC; 1700 UTC corresponds to 1200 LT.

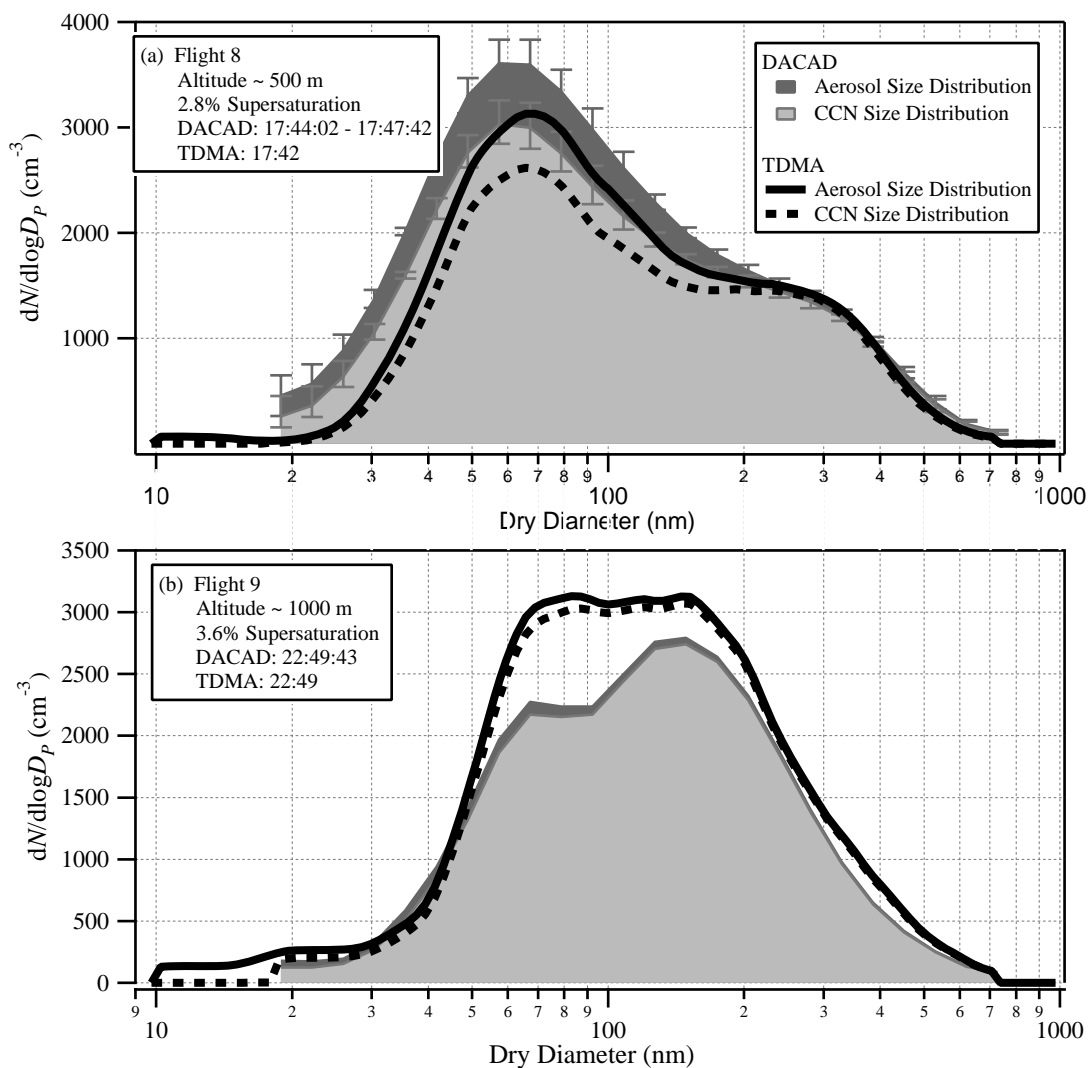


Figure 3.14. Comparison of DMA/TDMA and DACAD size distributions for flights (a) 8 and (b) 9. The error bars give the standard deviation of the DACAD aerosol size distributions averaged over the DMA/TDMA scan times. The times given are DACAD mid scan times in UTC; 1700 UTC corresponds to 1200 LT. The area under the aerosol size distribution curve gives the total aerosol number concentration, and the area under the CCN size distribution curve gives the predicted CCN number concentration. Both DACAD and DMA/TDMA predicted CCN distributions were calculated using the insoluble fraction and external mixing properties determined from the DMA/TDMA data.

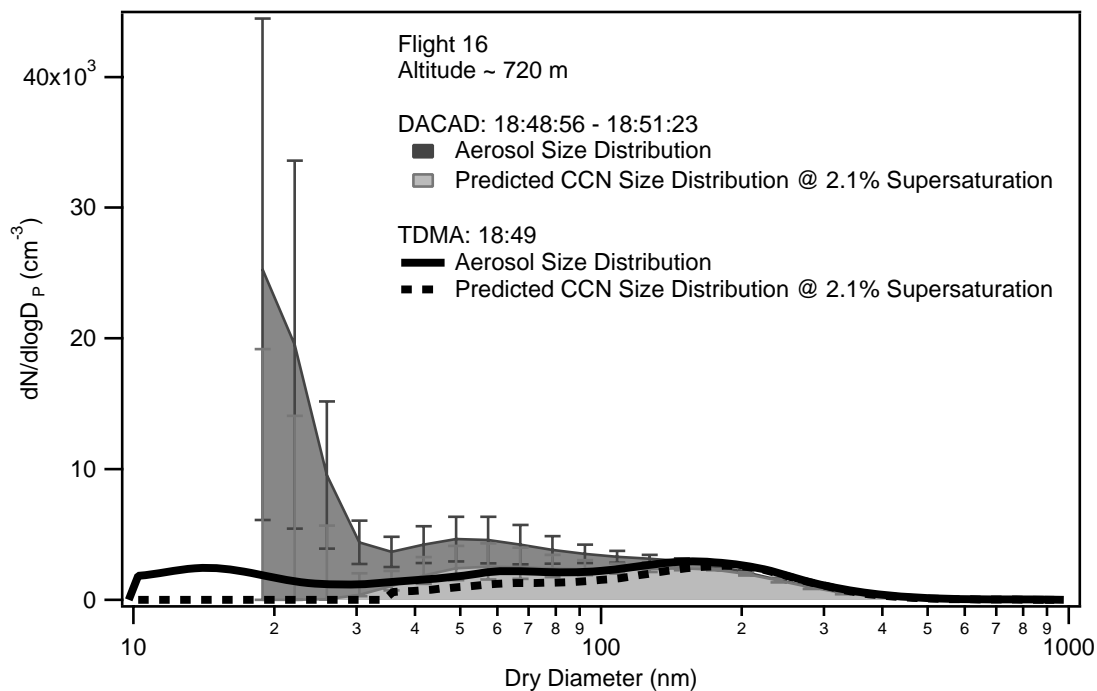


Figure 3.15. Comparison of DMA/TDMA and DACAD size distributions for flight 16. The error bars give the standard deviation of the DACAD aerosol size distributions averaged over the DMA/TDMA scan times. The times given are the DACAD midscan times in UTC; 1700 UTC corresponds to 1200 LT. The area under the aerosol size distribution curve gives the total aerosol number concentration, and the area under the CCN size distribution curve gives the predicted CCN number concentration. Both DMA/TDMA and DACAD predicted CCN distributions were calculated using the insoluble fraction and external mixing properties determined from the DMA/TDMA data.

Appendix B

BLACK AND WHITE FIGURES FOR CHAPTER 4

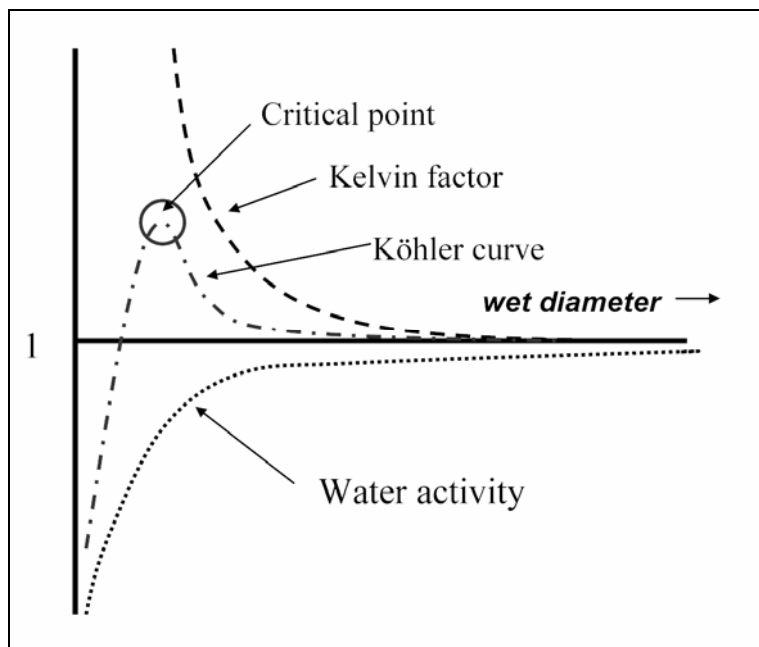
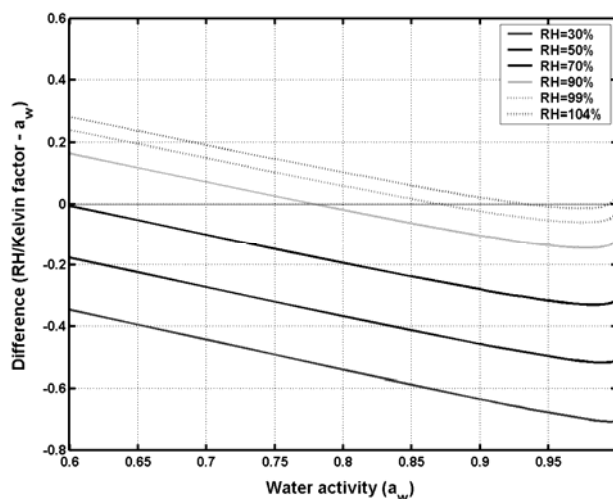
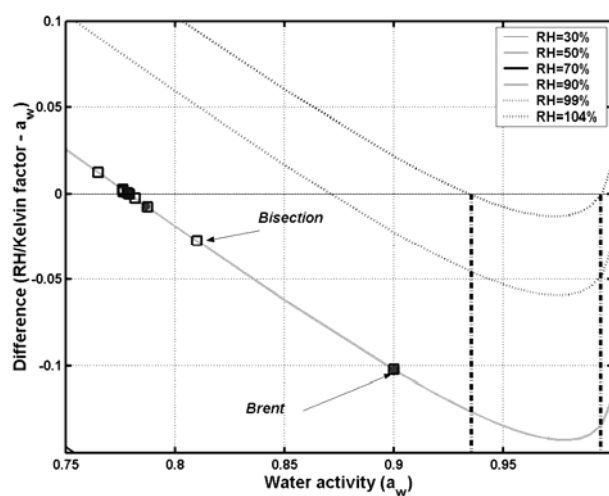


Figure 4.1. Hypothetical Köhler curve highlighting the contributions from the Raoult term (water activity, a_w) and the Kelvin factor. The critical point, the point at which the aerosol particle is said to be activated, is also highlighted.



(a)



(b)

Figure 4.2. (a) Difference in RH divided by the Kelvin factor and water activity (a_w) as a function of water activity for a 10 nm dry diameter $(\text{NH}_4)_2\text{SO}_4$ aerosol at six different ambient RH values (given in the legend). At 90% RH , a water activity of 0.9 corresponds to a negative difference and only upon lowering the water activity to around 0.78 does the difference value approach zero. Hence, a 10 nm aerosol has an equilibrium water activity of around 0.78 at 90% RH and has a growth factor equivalent to a bulk solution at 78% RH . (b) Magnification of panel (a) for three ambient RH values for a 10 nm diameter $(\text{NH}_4)_2\text{SO}_4$ aerosol at water activities greater than 0.75. Below a water activity of 0.9 the difference relationship is fairly linear, but at higher water activities the relationship becomes parabolic near the critical point. At high RH (104%; $S = 1.04$; $s = 4\%$) there are two roots of the difference relationship for this size and composition (black dashed lines). The blue squares indicate iterations carried out using a bisection approach. The red circles indicate the much more efficient Brent's method for converging on solution (see section 4.3.3).

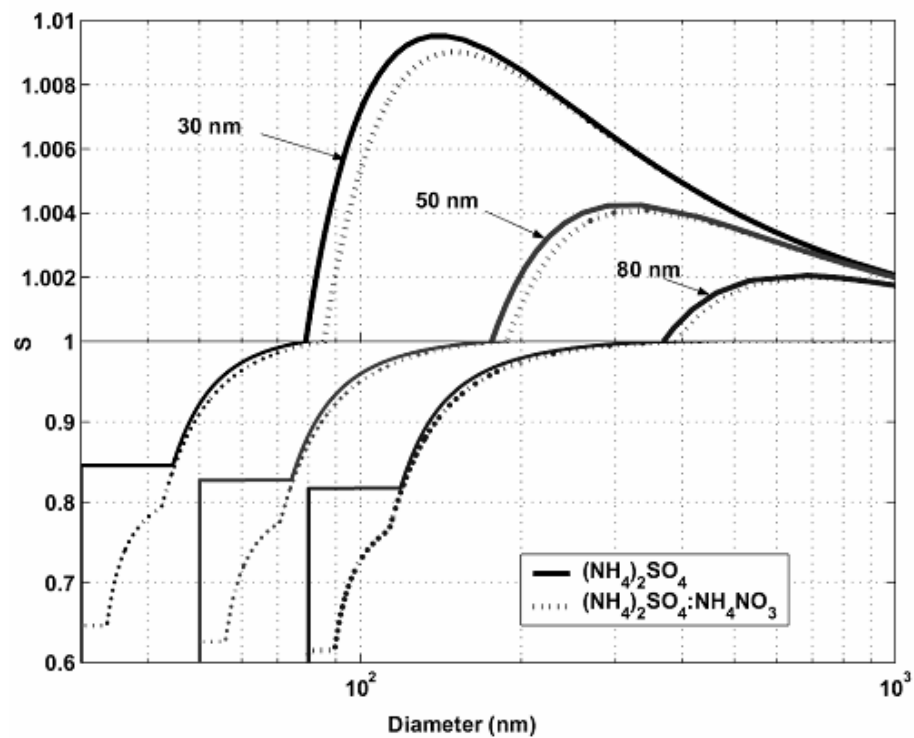


Figure 4.3. Predicted Köhler curves for $(\text{NH}_4)_2\text{SO}_4$ and mixed $(\text{NH}_4)_2\text{SO}_4:\text{NH}_4\text{NO}_3$ aerosols at 30, 50, and 80 nm dry diameters and 298.15 K using ADDEM. The top half of the plot is magnified to clearly show the critical points. The effect of solid precipitation can be clearly seen on each curve.

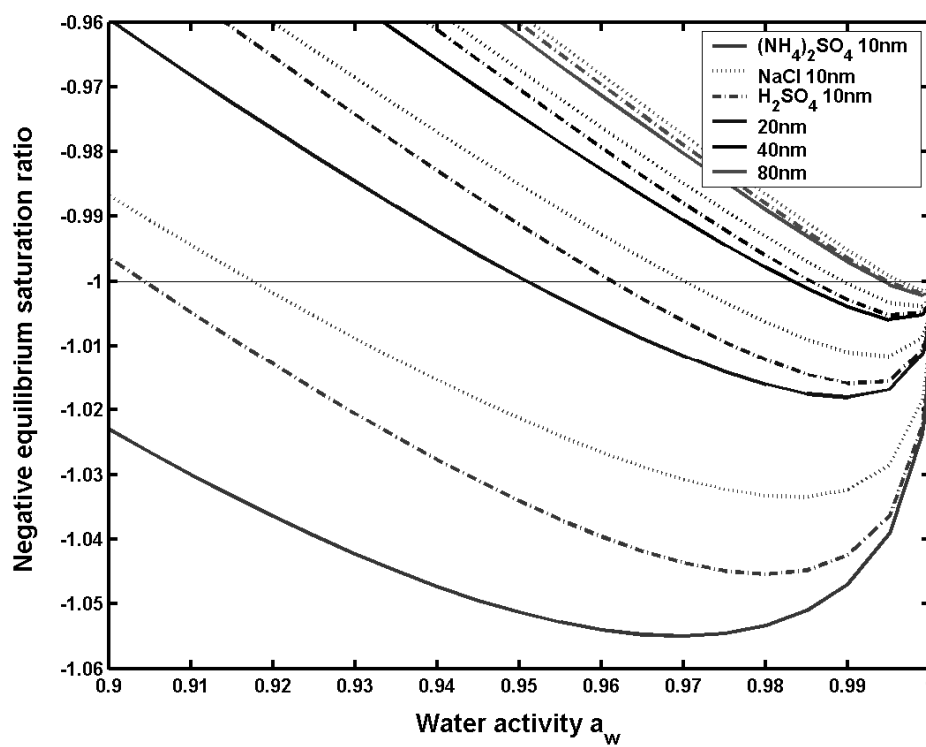


Figure 4.4. Negative equilibrium saturation ratio (S) as a function of water activity (a_w) for $(\text{NH}_4)_2\text{SO}_4$, NaCl and H_2SO_4 aerosol at 10, 20, 40, and 80 nm. The negative value is shown because the function is minimized when finding the critical point.

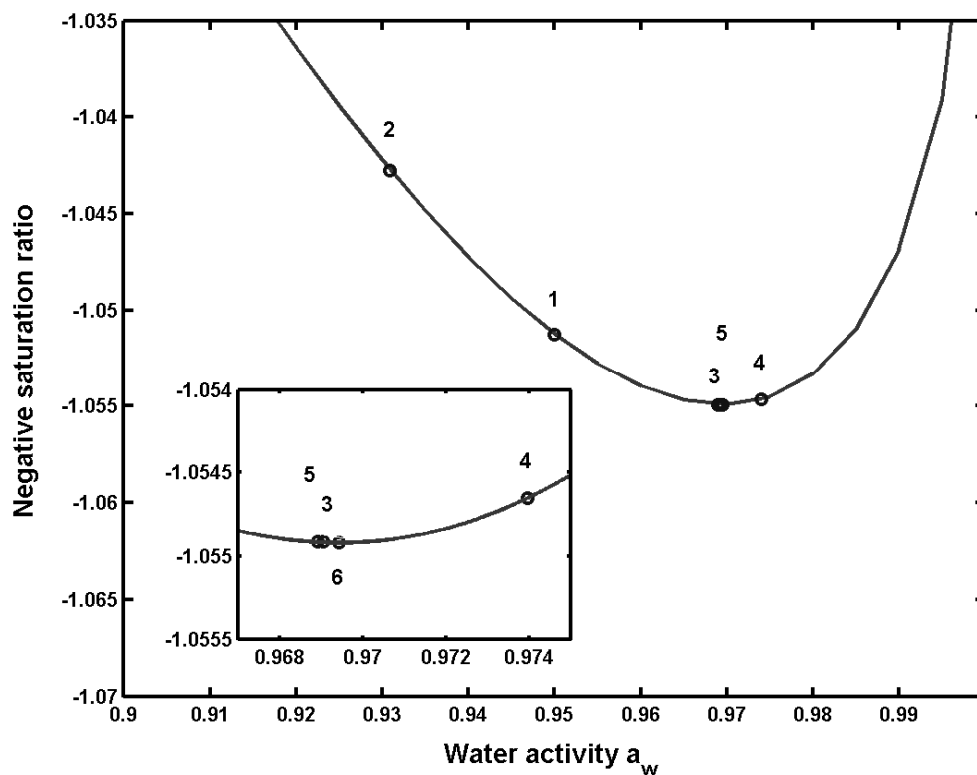


Figure 4.5. Negative saturation ratio (S) for a 10 nm $(\text{NH}_4)_2\text{SO}_4$ aerosol as a function of water activity (a_w). The blue circles highlight the iterations carried out by Brent's minimization scheme, and the iteration number is given above the blue circle. The subplot magnifies the region around the minimum point, clearly showing its parabolic nature.

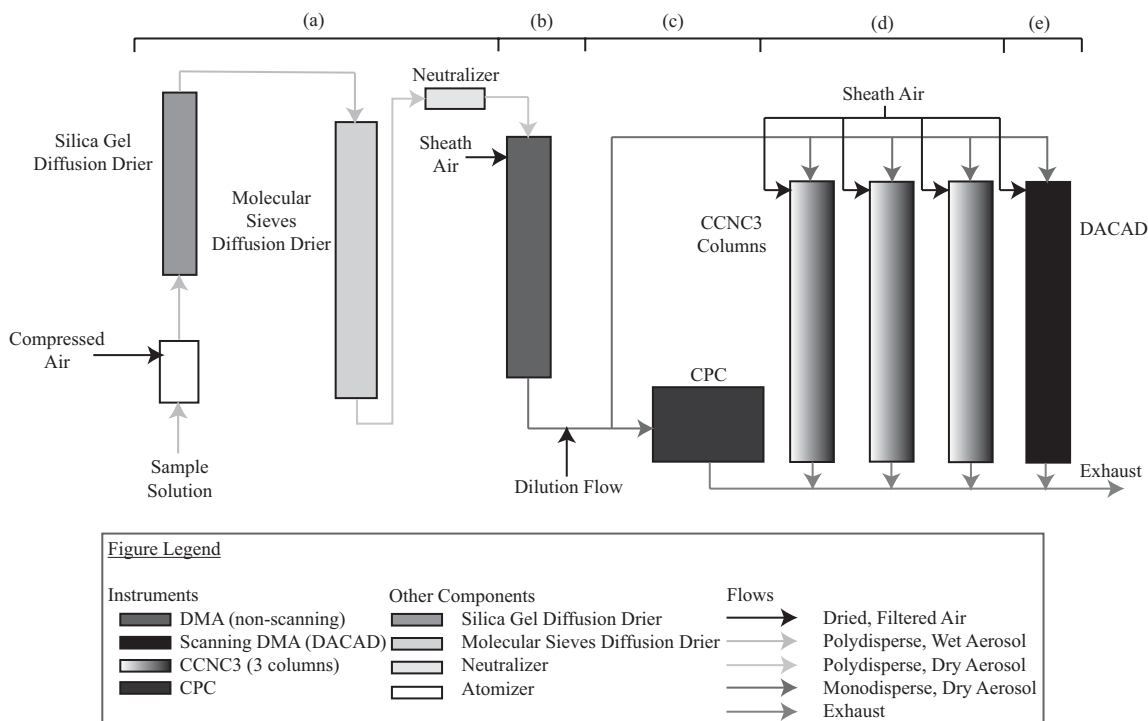


Figure 4.6. Experimental Setup. Includes: (a) an aerosol generation system to create aerosol particles; (b) a classification DMA to classify the aerosol particles (c) a CPC to count the total number of aerosol particles at a certain classified diameter; (d) the CCNC3 to count the number of aerosol particles that grow into droplets at the operating supersaturations of the instrument (see Table 4.3); (e) the DACAD to determine the size distribution of the aerosol particles entering the CCNC3.

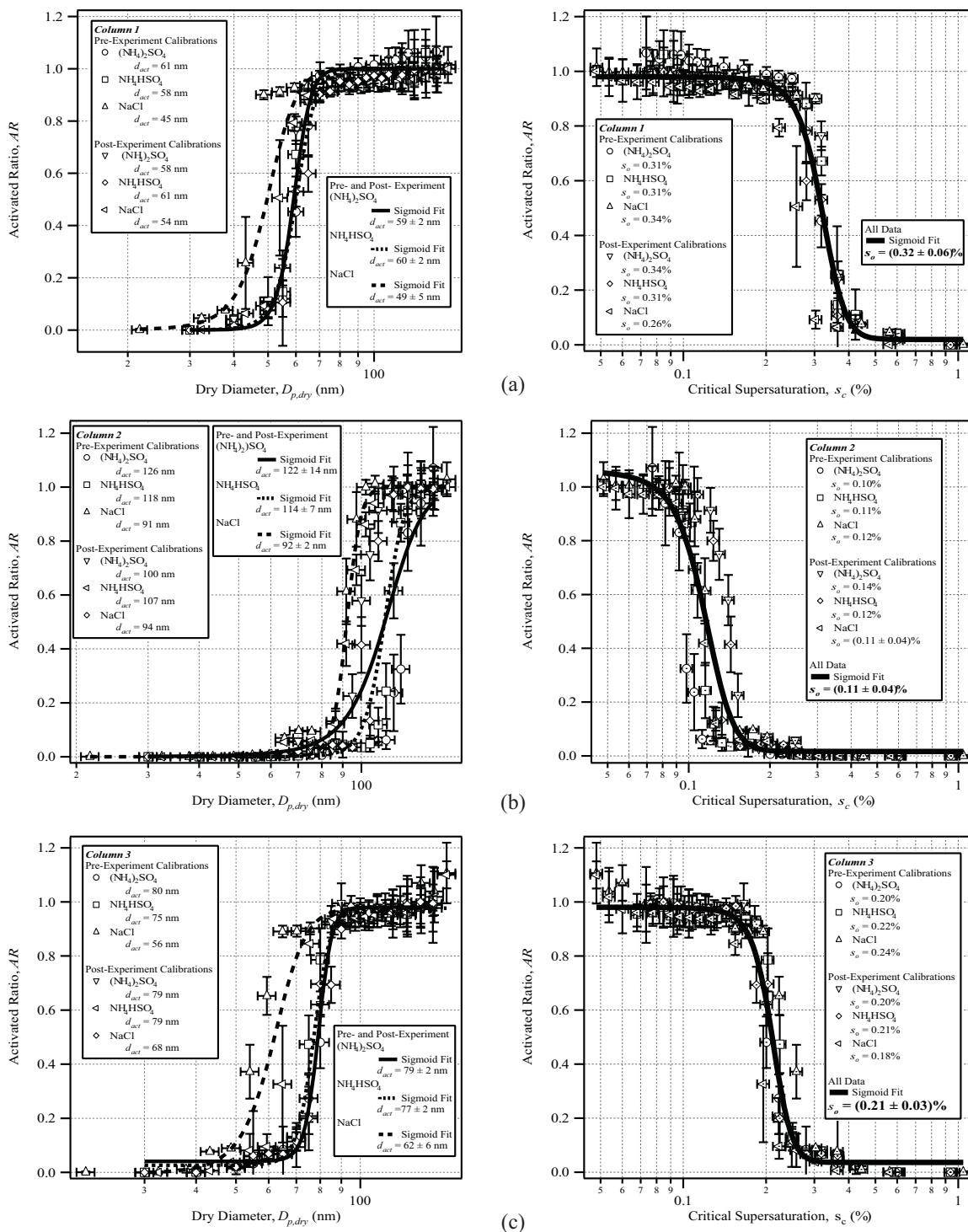


Figure 4.7. Calibration curves for (a) column 1, (b) column 2, and (c) column 3 using $(\text{NH}_4)_2\text{SO}_4$, NH_4HSO_4 , and NaCl as calibration salts.

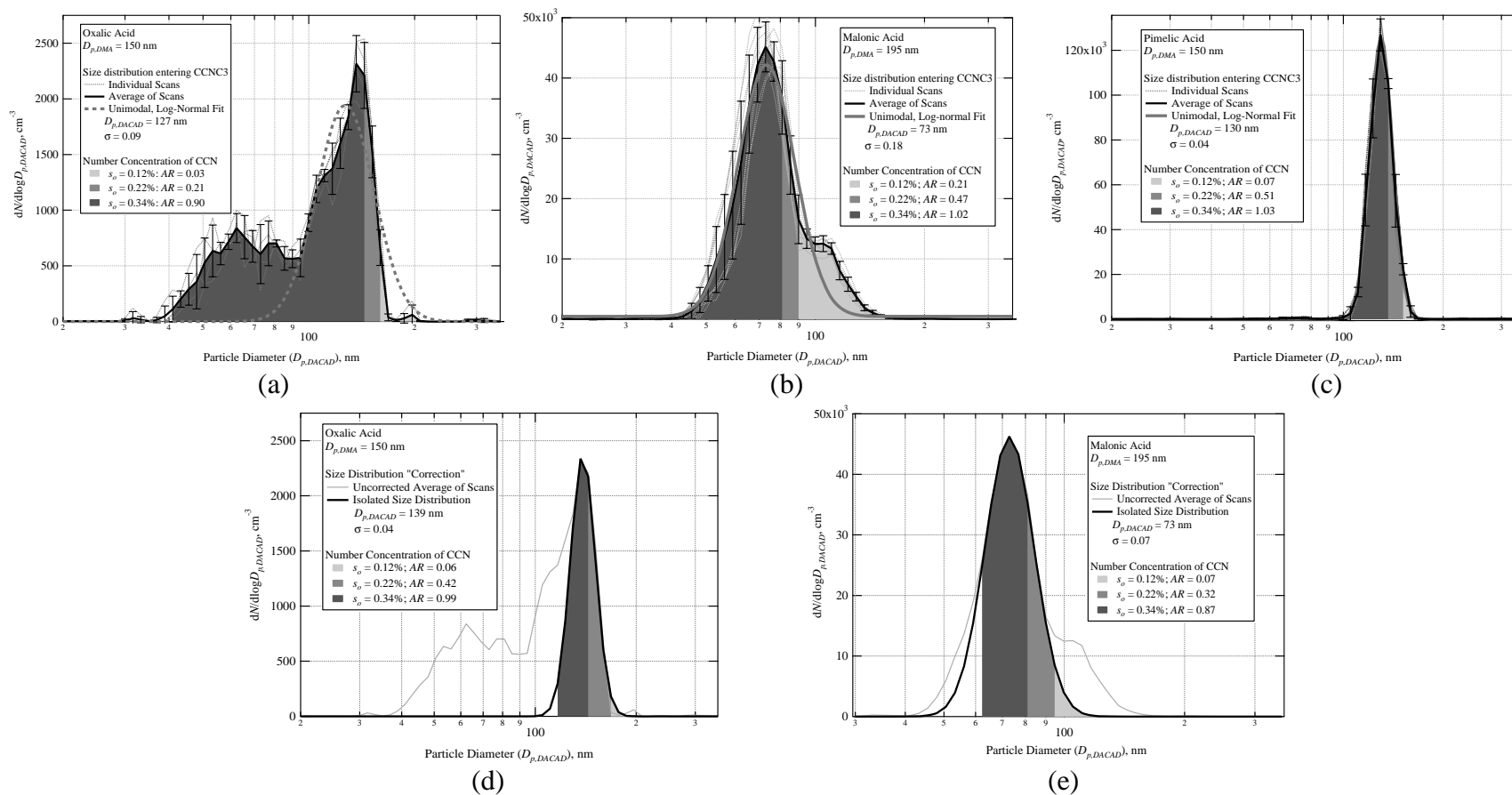


Figure 4.8. DACAD size distributions for the given DMA-selected sized particles of (a) oxalic acid ($D_{p,DMA} = 150$ nm), (b) malonic acid ($D_{p,DMA} = 195$ nm), and (c) pimelic acid ($D_{p,DMA} = 150$ nm). The CCN number concentrations (the shaded areas) are shown for each operating supersaturation. The bottom panels show the “corrected”, $\sigma < 0.10$, size distributions and CCN number concentrations for DMA-selected particles of (d) oxalic acid, and (e) malonic acid. No correction was necessary for pimelic acid because its size distribution had a σ less than 0.10.

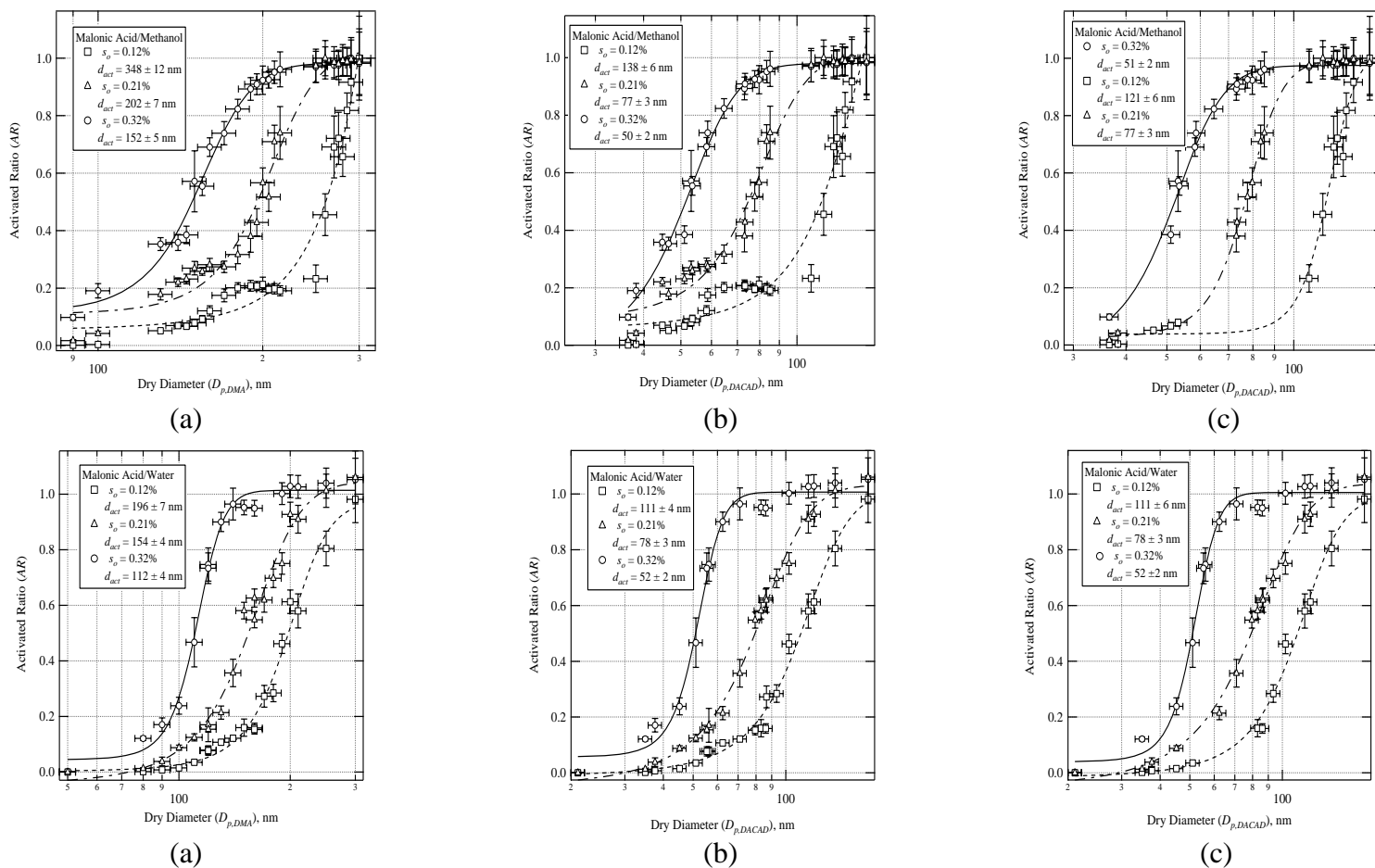
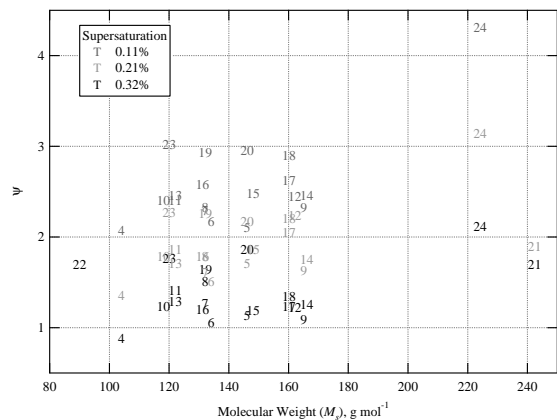
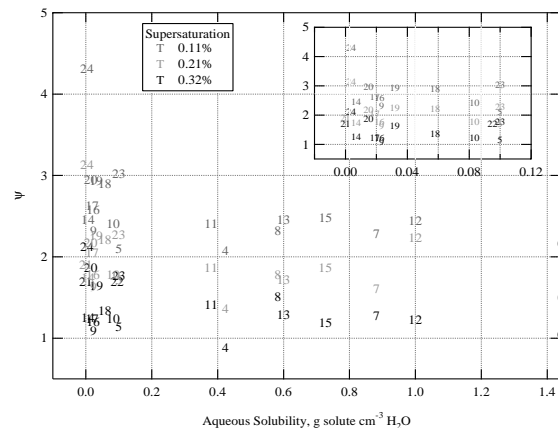


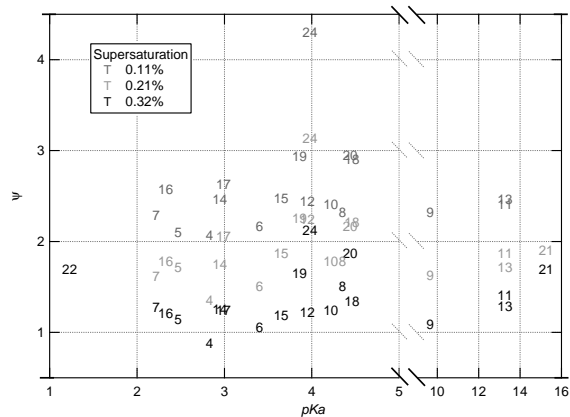
Figure 4.9. Experimental CCN activation curves for malonic acid in methanol (panels (a), (b), and (c)) and water (panels (d), (e), and (f)). Panels (a) and (d) show data versus the uncorrected diameter selected with the classification DMA. Panels (b) and (e) show experimental data with dry diameter corrected to the DACAD diameter, and panels (c) and (f) show experimental data with doubly charged particles removed.



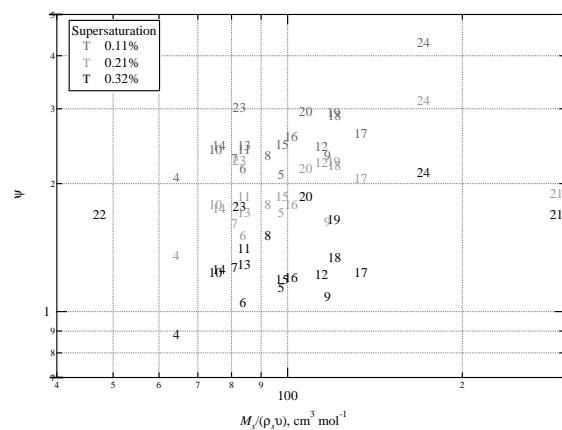
(a)



(b)



(a)



(b)

Figure 4.10. Ψ as a function of (a) M_s , (b) aqueous solubility, (c) pK_a , and (d) $M_s/(\rho_s v)$. It is assumed that $v = 1$ in panel (d). The inset for panel (b) zooms in on the compounds with aqueous solubilities less than $0.12 \text{ g cm}^{-3} \text{ H}_2\text{O}$. The units for inset axes (panel (d)) are the same as those on the main plot. Major outliers in panels (a), (c), and (d) are DL-threitol (11), *meso*-erythritol (13), 2-hexadecanol (21), oxalic acid (22), and sinapic acid (24).

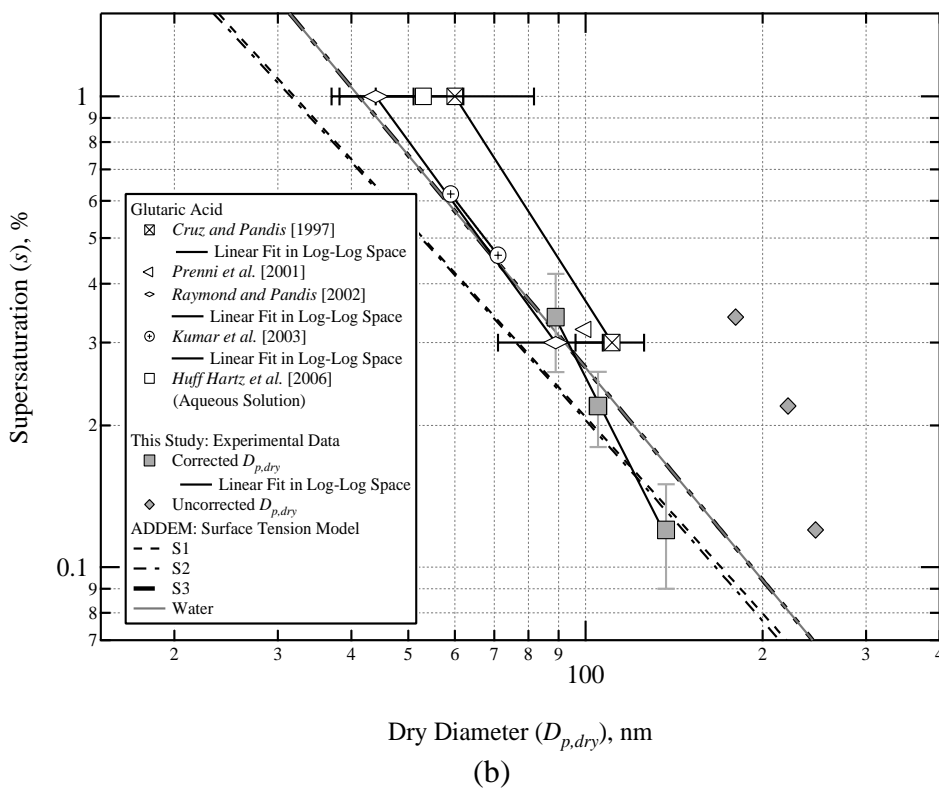
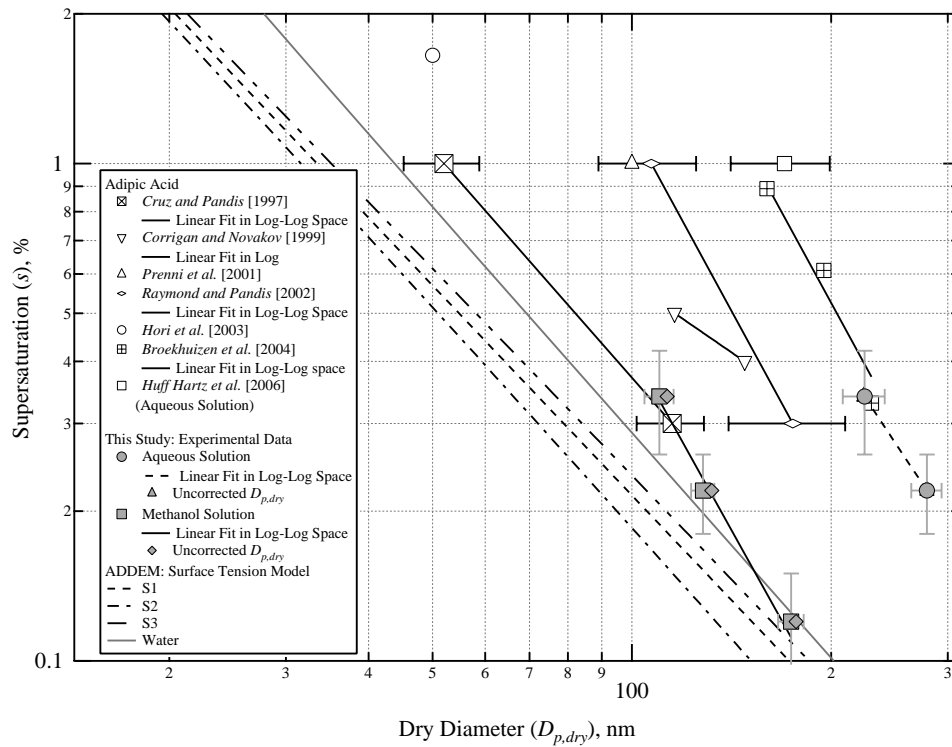


Figure 4.11. ADDEM and experimental results for (a) adipic acid and (b) glutaric acid.

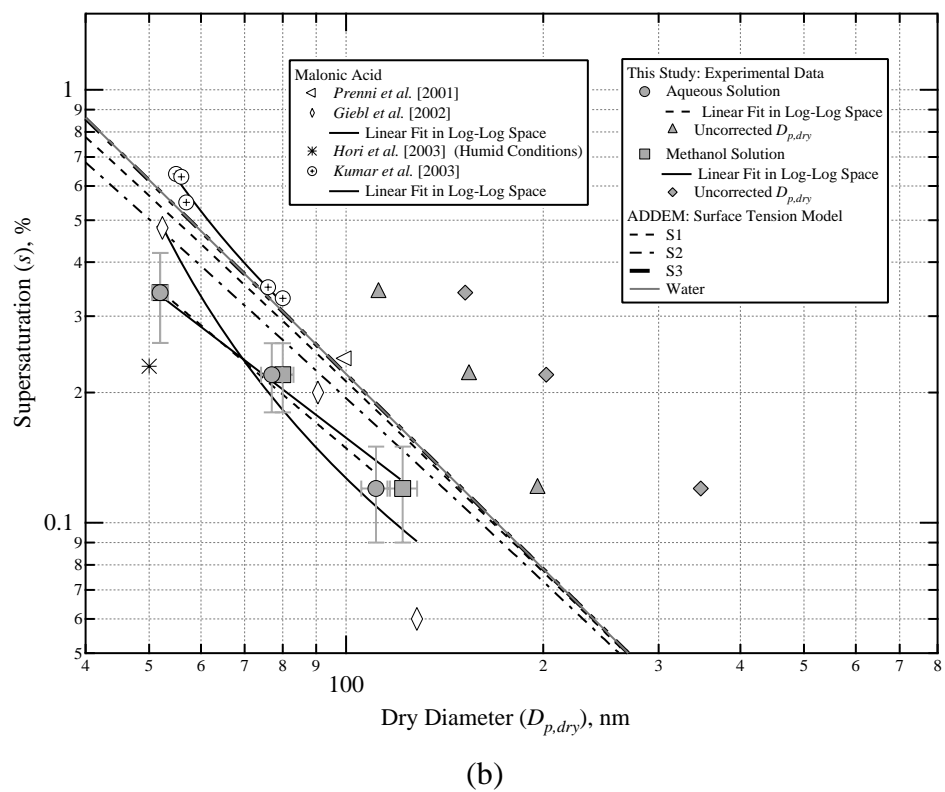
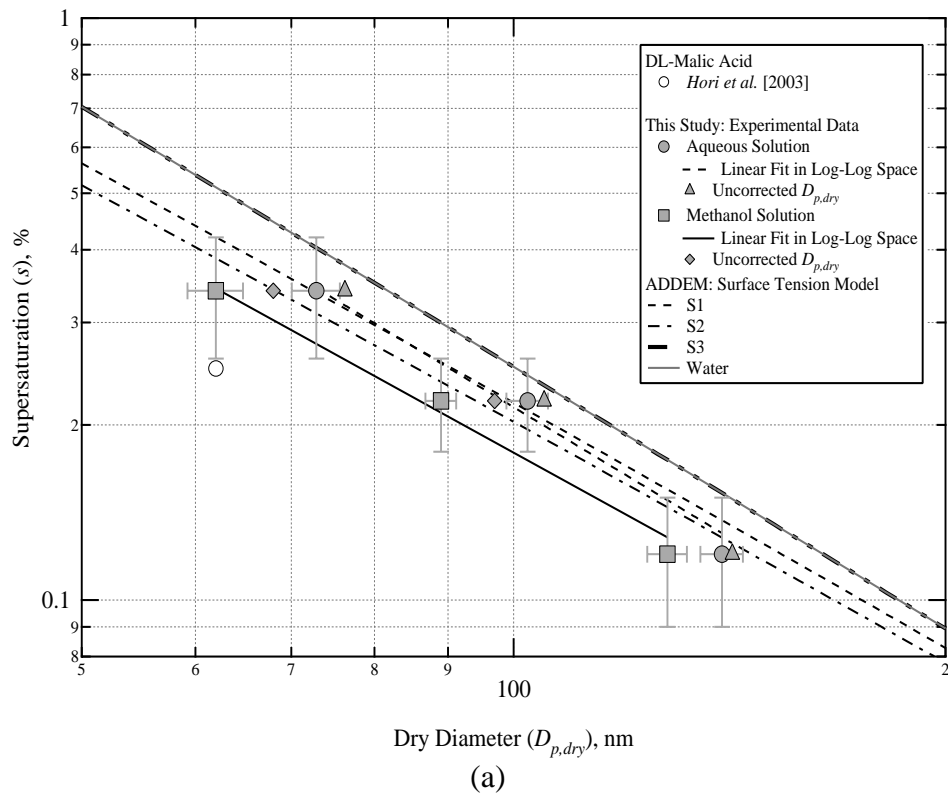
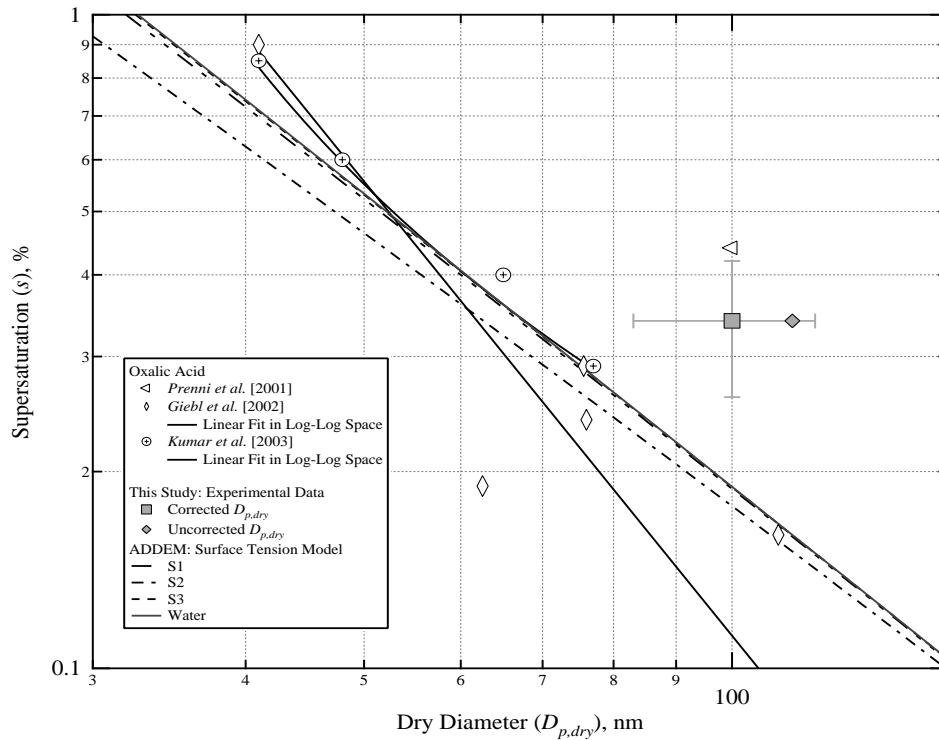
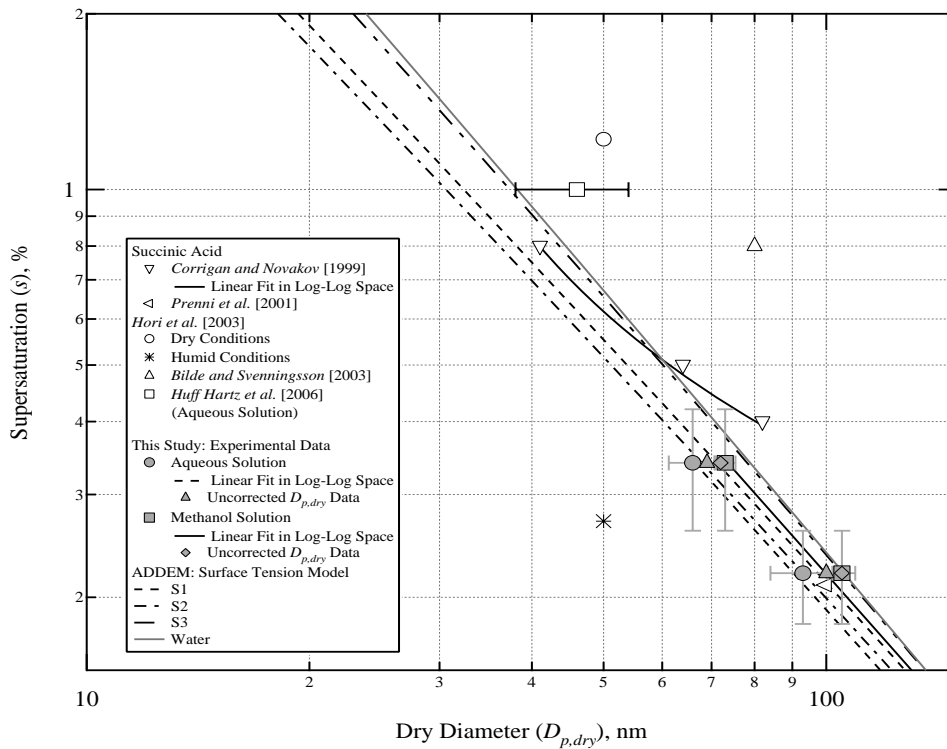


Figure 4.12. ADDEM and experimental results for (a) DL-malic acid and (b) malonic acid.



(a)



(b)

Figure 4.13. ADDEM and experimental results for (a) oxalic acid and (b) succinic acid.

Appendix C

TOWARD AEROSOL/CLOUD CONDENSATION NUCLEI (CCN)

CLOSURE DURING CRYSTAL-FACE*

*Full Citation: VanReken, T. M., T. A. Rissman, G. C. Roberts, V. Varutbangkul, H. H. Jonsson, R. C. Flagan, and J. H. Seinfeld (2003), Toward aerosol/cloud condensation nuclei (CCN) closure during CRYSTAL-FACE, *Journal of Geophysical Research*, 108(D20), 4633, doi: 10.1029/2002JD002465.

© 2003 American Geophysical Union (AGU). This appendix is reprinted with permission from the American Geophysical Union.

Toward aerosol/cloud condensation nuclei (CCN) closure during CRYSTAL-FACE

Timothy M. VanReken,¹ Tracey A. Rissman,¹ Gregory C. Roberts,²
Varuntida Varutbangkul,¹ Haflidi H. Jonsson,³ Richard C. Flagan,¹ and John H. Seinfeld¹

Received 10 March 2003; revised 1 July 2003; accepted 15 July 2003; published 18 October 2003.

[1] During July 2002, measurements of cloud condensation nuclei were made in the vicinity of southwest Florida as part of the Cirrus Regional Study of Tropical Anvils and Cirrus Layers-Florida Area Cirrus Experiment (CRYSTAL-FACE) field campaign. These observations, at supersaturations of 0.2 and 0.85%, are presented here. The performance of each of the two CCN counters was validated through laboratory calibration and an in situ intercomparison. The measurements indicate that the aerosol sampled during the campaign was predominantly marine in character: the median concentrations were 233 cm^{-3} (at $S = 0.2\%$) and 371 cm^{-3} (at $S = 0.85\%$). Three flights during the experiment differed from this general trend; the aerosol sampled during the two flights on 18 July was more continental in character, and the observations on 28 July indicate high spatial variability and periods of very high aerosol concentrations. This study also includes a simplified aerosol/CCN closure analysis. Aerosol size distributions were measured simultaneously with the CCN observations, and these data are used to predict a CCN concentration using Köhler theory. For the purpose of this analysis, an idealized composition of pure ammonium sulfate was assumed. The analysis indicates that in this case, there was good general agreement between the predicted and observed CCN concentrations: at $S = 0.2\%$, $N_{\text{predicted}}/N_{\text{observed}} = 1.047$ ($R^2 = 0.911$); at $S = 0.85\%$, $N_{\text{predicted}}/N_{\text{observed}} = 1.201$ ($R^2 = 0.835$). The impacts of the compositional assumption and of including in-cloud data in the analysis are addressed. The effect of removing the data from the 28 July flight is also examined; doing so improves the result of the closure analysis at $S = 0.85\%$. When omitting that atypical flight, $N_{\text{predicted}}/N_{\text{observed}} = 1.085$ ($R^2 = 0.770$) at $S = 0.85\%$. **INDEX TERMS:** 0305 Atmospheric Composition and Structure: Aerosols and particles (0345, 4801); 0320 Atmospheric Composition and Structure: Cloud physics and chemistry; 1610 Global Change: Atmosphere (0315, 0325); **KEYWORDS:** CCN closure, CCN instrumentation, CRYSTAL-FACE, aircraft measurements, cloud

Citation: VanReken, T. M., T. A. Rissman, G. C. Roberts, V. Varutbangkul, H. H. Jonsson, R. C. Flagan, and J. H. Seinfeld, Toward aerosol/cloud condensation nuclei (CCN) closure during CRYSTAL-FACE, *J. Geophys. Res.*, 108(D20), 4633, doi:10.1029/2003JD003582, 2003.

1. Introduction

[2] The importance of clouds in the climate system is well established; clouds play a vital role in the global radiation budget and hydrological cycle. Clouds form when a parcel of air becomes supersaturated with respect to water vapor and the excess water condenses rapidly on ambient particles to form droplets. For this rapid condensation (termed activation) to occur at a given supersaturation, the particle must have sufficient soluble mass; this subset of the

aerosol population is called cloud condensation nuclei, denoted CCN. The atmospheric concentration of CCN is often substantially enhanced by human activities, and the various ways that this enhancement affects the radiative properties of clouds are collectively known as indirect aerosol forcing (the inclusion of the word “indirect” differentiates these effects from the direct aerosol effect, which describes the radiative interactions of the particles themselves). Cloud processes are complex by nature and heavily dependent on purely dynamical factors, but in general terms indirect aerosol effects can be split into two categories. For a given supersaturation, an air mass with a higher CCN concentration would produce a cloud with a higher droplet concentration, but a smaller mean droplet diameter; this often results in a more reflective cloud and is known as the first indirect effect or Twomey effect [Twomey, 1977]. The second indirect effect, identified by Albrecht [1989], also stems from the smaller average droplet diameter in polluted clouds; a smaller mean droplet size inhibits the processes

¹Department of Chemical Engineering, California Institute of Technology, Pasadena, California, USA.

²Center for Atmospheric Sciences, Scripps Institution of Oceanography, San Diego, California, USA.

³Center for Interdisciplinary Remotely Piloted Aircraft Studies, United States Naval Postgraduate School, Marina, California, USA.

that lead to precipitation, thereby increasing cloud lifetime and therefore cloud coverage.

[3] While observations support the existence of indirect aerosol effects on a local scale [Johnson *et al.*, 1996; Rosenfeld, 1999, 2000; Durkee *et al.*, 2000; Garrett *et al.*, 2002], current understanding of the processes involved is insufficient to accurately predict the global importance of indirect aerosol forcing. The *Intergovernmental Panel on Climate Change (IPCC)* [2001] estimates that the first indirect effect results in a global mean forcing of between 0 and -2 W m^{-2} and does not give an estimate for the second indirect effect, which is also expected to be one of cooling. Reliable predictions regarding climate forcing await more detailed understanding of the dependence of cloud properties on aerosol properties.

[4] The first step in understanding the relationship between the ambient aerosol and the cloud that forms therefrom is to know the activation properties of the atmospheric aerosol. In theory, if a particle's size and chemical composition were precisely known, the supersaturation at which activation occurs could be calculated using Köhler theory [Seinfeld and Pandis, 1998]. However, ambient aerosol populations can contain myriad chemical species, the activation properties of most of which have not been established. Furthermore, recent studies have demonstrated that simply categorizing aerosol species into soluble and insoluble fractions is sometimes insufficient [Cruz and Pandis, 1998; Hegg *et al.*, 2001; Raymond and Pandis, 2002]; slightly soluble species, surfactants, and soluble gases can affect activation either thermodynamically or kinetically [Charlson *et al.*, 2001; Nenes *et al.*, 2002]. To establish the connection between theory and the actual atmosphere, it is desirable to directly measure the portion of the aerosol population that activates at a given supersaturation. Such a measurement generally involves exposing an aerosol sample to a known supersaturation; the CCN active at that supersaturation rapidly grow to a size at which they can be counted by standard techniques. In the laboratory, instruments using such measurement strategies can be tested using aerosols whose size and chemical properties are carefully controlled. Then, the activation behavior of an ambient aerosol can be measured, giving rise to a so-called closure experiment, whereby measured CCN concentrations are compared against predictions based on simultaneously measured aerosol size and composition data. A successful closure study serves to validate both the performance of the CCN instrument itself and the theoretical basis for the prediction of the activation properties of the aerosol.

[5] The Cirrus Regional Study of Tropical Anvils and Cirrus Layers-Florida Area Cirrus Experiment (CRYSTAL-FACE) field campaign in the Florida Keys during July 2002 had as its goal the investigation of the properties of tropical convective systems and the resultant cirrus layers. These cirrus layers, known as anvils, affect the radiative balance [Ramanathan *et al.*, 1989], and a detailed understanding of the physical processes involved in their formation would enhance the ability to predict their occurrence and lifetime. As part of the CRYSTAL-FACE campaign, the Center for Interdisciplinary Remotely Piloted Aircraft Studies (CIRPAS) Twin Otter aircraft flew 20 research missions, focused on characterizing the ambient aerosol in the vicinity of the convective systems, measuring cloud properties, and

on making radiation measurements below the cirrus anvils. Data were collected both over land and water along the southwest coast of Florida; Figure 1 shows the flight tracks for the missions for which CCN data are available. Table 1 provides details on each research flight, and Table 2 lists the aerosol and gas-phase instrumentation on board the Twin Otter.

[6] This study presents the airborne CCN measurements from CRYSTAL-FACE and examines the extent to which it is possible to predict CCN concentrations from size distribution data in the absence of a detailed knowledge of the aerosol composition. Two CCN counters were on board the Twin Otter (Table 2). One instrument, operating at a supersaturation of approximately 0.85%, provided useful data for all but three flights, when electrical noise from another instrument caused the CCN counter to malfunction. The second CCN counter, with an effective supersaturation of approximately 0.2%, was operated for all but one flight from CF-8 through the end of the campaign; no data are available from CF-16 due to an instrument malfunction. The reliability of these measurements is verified by laboratory experiments, by a field intercomparison of the two instruments, and by comparison with other instruments measuring aerosol concentration. After establishing the validity of the data, the observations are described in more detail in order to provide a comprehensive picture of the typical summertime CCN population over southwest Florida. A simplified closure analysis follows, comparing the CCN data set at both measured supersaturations to size spectral data from the Caltech differential mobility analyzer (DMA, described by Wang *et al.* [2003]), assuming an idealized (ammonium sulfate) composition. The study concludes by discussing the sensitivity of the results to assumptions made in the analysis.

2. Background

[7] Previous attempts to match predicted CCN concentrations with those directly observed have met with mixed success. The methods by which these studies were conducted vary considerably, and by examining the details of these methodologies one can determine those elements required for a successful experiment.

[8] Only three studies in the literature present results that can be considered successful in terms of aerosol/CCN closure. All were ground-based studies: Liu *et al.* [1996] made measurements in Nova Scotia as part of the North Atlantic Regional Experiment (NARE), Cantrell *et al.* [2001] used measurements made in the Maldives during the Indian Ocean Experiment (INDOEX), and Roberts *et al.* [2002] collected data in the Amazon Basin during the Cooperative Large-Scale Biosphere-Atmosphere (LBA) Airborne Regional Experiment 1998 (CLAIRE-98). In the first two studies, the aerosol was split into soluble and insoluble fractions based on filter samples and the soluble fraction was assumed to be ammonium sulfate. Roberts *et al.* further split the soluble fraction into organic and inorganic components. All three studies averaged the CCN and size spectral data over a substantial period of time to match the filter sampling time. Liu *et al.* used an isothermal haze chamber to obtain CCN concentrations at a supersaturation,

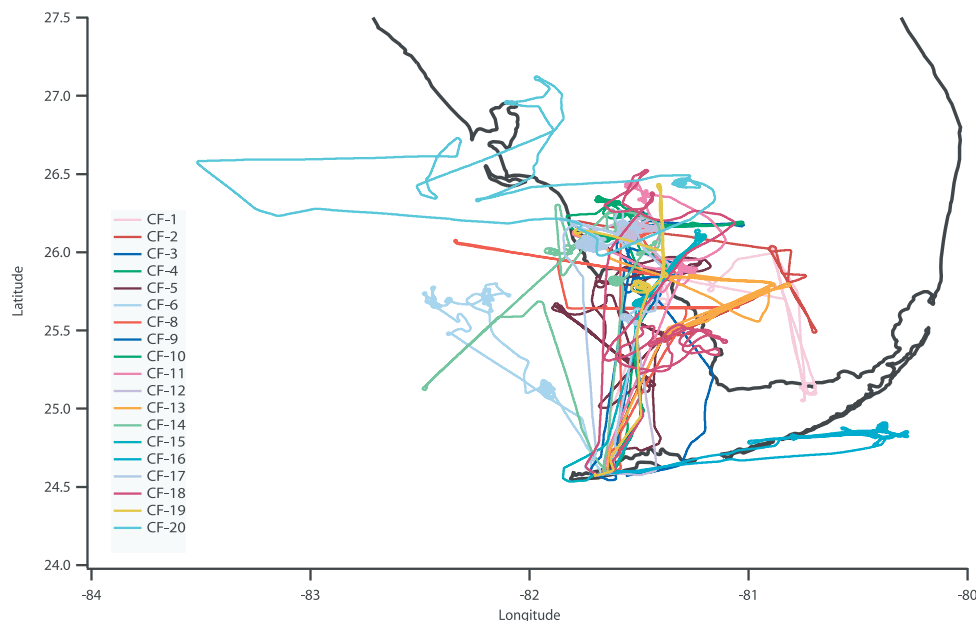


Figure 1. Flight tracks for the CRYSTAL-FACE flights for which CCN data are available.

$S = 0.06\%$; these data were compared against integrated size distributions from an optical particle counter (Particle Measurement Systems model PCASP-100X). For each of the 12 samples in the closure analysis, data were averaged for a period of 2–5 hours. In 10 of the 12 sampling intervals, the predicted concentration agreed with the measurement within the uncertainty limits; of the other two samples, in one case the measurement was overpredicted, and in one case it was underpredicted. Cantrell et al. measured CCN spectra for supersaturations between 0.1 and 1% using the CCN Remover described by Ji et al. [1998]; in this case, the aerosol-size distribution was measured using a scanning mobility particle sizer (SMPS) (TSI, Inc.). The average measured spectra from three dates were compared to predicted concentrations based on the filter cut sizes. Eight of the 10 data points matched within experimental uncertainties; in the other two cases, the predicted CCN spectra exceeded the measurements. In the Roberts et al. study, CCN measurements were made at several supersaturations using a static thermal-gradient chamber. These data were averaged over 48–72 hour periods to match the sampling time for the microorifice uniform deposit impactor (MOUDI) cascade impactors that were the source of the compositional data in the analysis. As in the Cantrell et al. study, aerosol-size spectra were measured with a differential mobility analyzer. For each of the four sampling periods, the calculated CCN spectrum agreed with the observation to within measurement uncertainties. Although these studies were limited in scope, the measured and predicted CCN concentrations agreed well enough to indicate that closure had been achieved.

[9] Other ground-based studies of CCN closure have been less successful. A common characteristic is that measured CCN concentrations were less than would be predicted based on available size and composition information. In measure-

ments carried out at Cape Grim, Australia, Bigg [1986] used measured size distributions and assumed that the aerosol was composed of either sodium chloride or ammonium sulfate; this produced reasonable results at low CCN concentrations, but there were large discrepancies at higher CCN concentrations. Studies by Covert et al. [1998] and Zhou et al. [2001] (a ship-based study) each compared two methods for predicting CCN concentrations. Both studies used data from tandem differential mobility analyzers to infer an insoluble fraction using hygroscopic growth information and assumed that the soluble fraction was ammonium sulfate. In the Covert

Table 1. Summary of Twin Otter Missions for the CRYSTAL-FACE Campaign

Flight Number	Date	Launch Time, UT	Flight Duration, hours	Mission Type	CCN Data	
					0.2%	0.85%
CF-1	3 July	1159	4.01	radiation	no	yes
CF-2	3 July	1750	3.03	radiation	no	yes
CF-3	6 July	1234	3.13	radiation	no	yes
CF-4	7 July	1223	3.14	cloud	no	yes
CF-5	7 July	1723	4.44	radiation	no	yes
CF-6	10 July	1404	3.41	cloud	no	yes
CF-7	11 July	1525	4.44	radiation	no	no
CF-8	13 July	1725	4.54	cloud, radiation	yes	no
CF-9	16 July	1752	2.16	clear air	yes	no
CF-10	18 July	1424	2.30	cloud	yes	yes
CF-11	18 July	1800	2.59	radiation	yes	yes
CF-12	19 July	1458	2.50	cloud	yes	yes
CF-13	19 July	1901	4.06	radiation	yes	yes
CF-14	21 July	1713	4.21	radiation	yes	yes
CF-15	23 July	1929	4.24	radiation	yes	yes
CF-16	25 July	1400	2.09	cloud	no	yes
CF-17	26 July	1556	4.03	cloud	yes	yes
CF-18	28 July	1831	4.03	radiation	yes	yes
CF-19	29 July	1328	1.27	clear air	yes	yes
CF-20	29 July	1700	4.10	radiation	yes	yes

Table 2. Twin Otter Aerosol and Trace Gas Payload During CRYSTAL-FACE

Instrument	Measurement	Sampling Interval, s
Aerosol mass spectrometer (AMS)	particle size and composition: 50 nm to 1.0 μm	60
Aerodynamic Particle Sizer (APS)	size distribution: 0.37–2.0 μm	27
Carbon monoxide (CO)	carbon monoxide concentration	1
Cloud condensation nucleus counter (Caltech)	CCN at $S_c = 0.85\%$	2
Cloud condensation nucleus counter (Scripps)	CCN at $S_c = 0.2\%$	1
Condensation particle counters (CPCs)	particle concentration: cut sizes at 3, 7, and 12 nm	1
Differential mobility analyzer (DMA)	aerosol size distribution: 10–900 nm	103
Multisample aerosol collection system (MACS)	aerosol samples for transmission electron microscopy (TEM) analysis	variable (min)
Water Vapor (NOAA)	water vapor concentration	1
Cloud, Aerosol, Precipitation Spectrometer (CAPS)	size distribution: 0.3 μm to 1.6 mm	1
Forward Scattering Spectrometer Probe (FSSP-100)	size distribution: 0.5–47 μm	1
Passive cavity aerosol spectrometer probe (PCASP)	size distribution: 0.1–3.0 μm	1
Microorifice uniform deposit impactor (MOUDI)	size-classified filter sampling	variable (hours)

et al. study, the correlation between measured and predicted CCN improved when particle solubility was taken into account. Zhou et al., following the same procedure, did not see an improved correlation, and concluded that this was due to a very low insoluble fraction. In both cases, the measured CCN concentration was, on average, 20–30% lower than that predicted; while this error is, perhaps, not excessive, a consistent overprediction is indicative of either a problem with the measurement or an incomplete understanding of the processes affecting activation.

[10] Airborne closure studies are inherently more difficult than those that are ground-based, and the results of the few available airborne closure studies reflect this difficulty. A moving platform greatly increases the variability in the aerosol population sampled, making rapid measurements necessary. Space considerations on the aircraft often limit the instrumentation available; the resulting sacrifices in the data set add further uncertainty to an already demanding measurement. In short, aerosol/CCN closure has not yet been demonstrated from an airborne platform. An attempt by Martin et al. [1994] consisted of only two data points, one maritime and one polluted. The authors assumed a pure ammonium sulfate aerosol and compared the CCN measurement with an integrated spectrum from an optical particle counter. There was reasonable agreement in the maritime case but not in the polluted case. In the second Aerosol Characterization Experiment (ACE-2), Snider and Brenguier [2000], using data from the Météo-France Merlin aircraft, compared measured CCN with size spectra from an optical particle sizing instrument (passive cavity aerosol spectrometer probe (PCASP)), assuming a pure ammonium sulfate composition. The measured CCN concentration (at $S = 0.2\%$) was roughly half that expected from the PCASP data; the difference was attributed to an incomplete understanding of the aerosol composition. Wood et al. [2000] undertook a similar analysis during ACE-2, using data from the UK Meteorological Office C-130 aircraft, and attempted to improve the agreement by varying the assumed soluble aerosol fraction. At high supersaturations ($S > 0.5\%$), the CCN concentrations were overpredicted by more than 50%; no explanation was offered for this disagreement. Also, during ACE-2, Chuang et al. [2000a] measured CCN at $S \approx 0.1\%$ from the CIRPAS Pelican and predicted CCN concentrations based on airborne size distributions and aerosol composition measurements from ground-based filter samples. Measurements were roughly an order of magnitude

lower than predictions; the authors surmised that instrumentation problems were the source of most of the discrepancy.

[11] In summary, in most of the published closure studies, measured CCN concentrations are significantly lower than expected based on theoretical activation of the measured aerosol-size distributions. This disagreement has usually been attributed to an incomplete understanding of the activation processes, even when sampling relatively clean air masses. However, in three cases, closure was generally achieved despite the use of a relatively simple compositional model: Liu et al. [1996], Cantrell et al. [2001], and Roberts et al. [2002]. While in some cases a lack of closure may be due to measurement errors, this still leaves open the basic question of whether it is possible to achieve an aerosol/CCN closure.

3. CCN Instrument Descriptions

[12] Both CCN counters deployed during CRYSTAL-FACE are based on the instrument described by Chuang et al. [2000b], using an improved temperature configuration first identified by Rogers and Squires [1981] and brought to fruition by G. C. Roberts and A. Nenes (manuscript in preparation, 2003, hereinafter referred to as Roberts and Nenes, manuscript in preparation, 2003). The instrument described by Chuang et al. [2000b] was intended to function as a CCN spectrometer, where the supersaturation at which particles activated could be inferred from the droplet diameter at the outlet. However, during the ACE-2 campaign, in which that instrument flew aboard the CIRPAS Pelican, stability and resolution issues limited its usefulness, and data were reported only for a single supersaturation [Chuang et al., 2000a]. Later work also discussed by Chuang et al. [2000b] indicated that those resolution issues were characteristic of the temperature configuration employed during ACE-2, a result that was later verified theoretically by Nenes et al. [2001].

[13] Recent work by Roberts and Nenes (manuscript in preparation, 2003) indicates that the cylindrical CCN design could be significantly improved by incorporating a different control strategy, where the temperature of the column wall is increased axially to asymptotically approach a constant supersaturation. Because water vapor diffuses more rapidly than heat, the constant streamwise temperature gradient leads to a nearly constant supersaturation on the instrument centerline. The simulated supersaturation profile arising

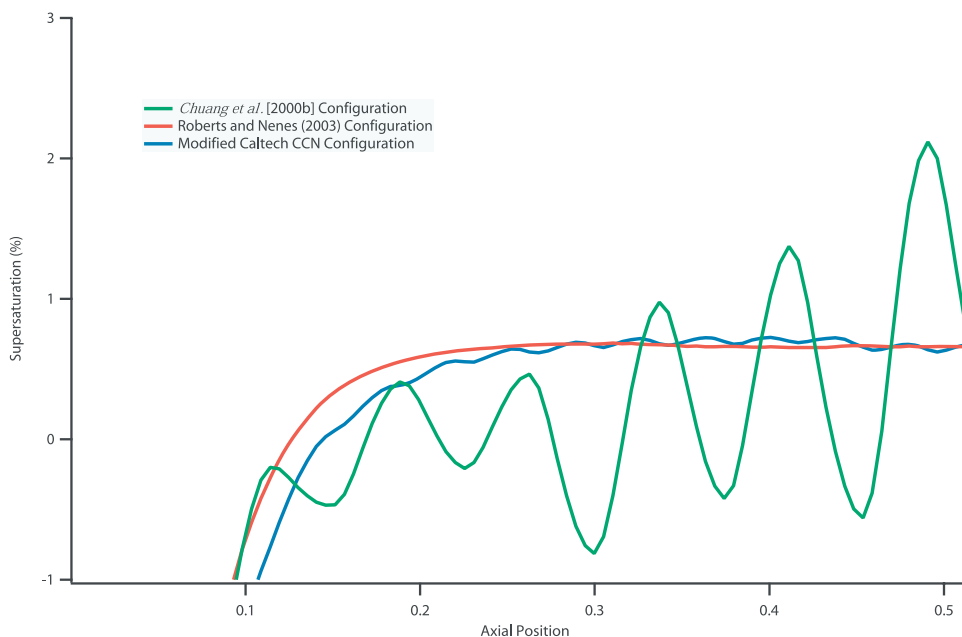


Figure 2. Simulated saturation profiles for various configurations for cylindrical CCN instruments. Both the Roberts and Nenes (manuscript in preparation, 2003) configuration and the current configuration of the Caltech instrument are substantial improvements over the design described by *Chuang et al.* [2000b].

from this new temperature configuration is compared to that of the *Chuang et al.* [2000b] configuration in Figure 2. The constant temperature increase clearly creates a more stable saturation profile. The new configuration also significantly simplifies the instrument, since ideally it requires active temperature control only at the beginning and end of the growth chamber, compared to the numerous independently controlled segments in the original configuration.

[14] For the CRYSTAL-FACE campaign, both the instrument described by Roberts and Nenes (manuscript in preparation, 2003) (the Scripps CCN counter) and the Caltech CCN counter were on board the Twin Otter. The Caltech counter, described by *Chuang et al.* [2000b], was modified to incorporate a variation on the improved temperature profile developed by Roberts and Nenes (manuscript in preparation, 2003). Instead of controlling actively only at the top and bottom of the growth chamber, 14 independent sections are maintained, with a constant temperature increase in each section. The temperatures in the first and last sections are controlled with thermoelectric coolers, and resistive heaters are used to maintain the temperature in the intermediate sections (see Figure 3). Using the model described by *Nenes et al.* [2001], the saturation profile for this configuration was simulated and is presented along with the others in Figure 2; the result is close to that of the idealized linear profile. The Caltech instrument was originally designed for stepwise variation in the wall temperature, leading to the slight oscillations in the temperature profile when operated in this mode.

[15] Other technical improvements were made to the Caltech CCN Counter prior to its use in the CRYSTAL-

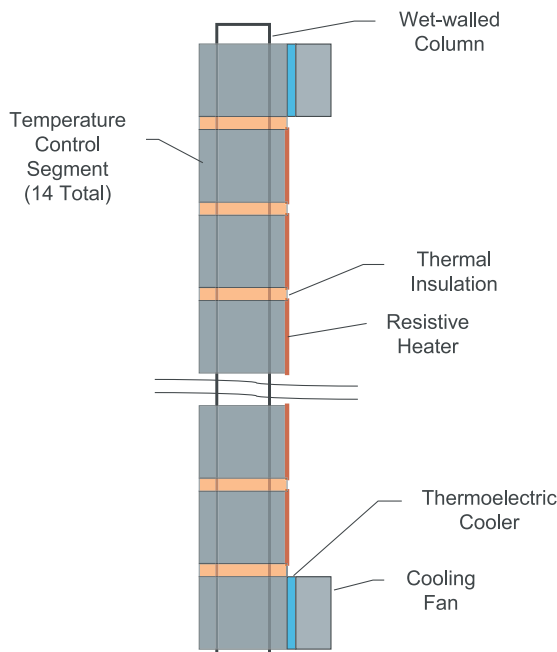


Figure 3. Schematic of the Caltech CCN counter as configured during CRYSTAL-FACE.

FACE campaign (see *Chuang et al.* [2000b] for details on the original instrument configuration). The sheath flow is controlled on a volumetric rather than on a mass basis, using volumetric flow controllers from Alicat Scientific Instruments. The humidification of the sheath air is now accomplished using Nafion humidifiers from Perma-Pure, Inc. The computer has been upgraded and data acquisition is managed with National Instruments LabView software; a separate multichannel analyzer card is no longer used since only the number of activated particles must be determined. The thermoelectric coolers are now driven with Wavelength Electronics MPT-5000 temperature controllers, while the resistive heaters are still driven by RHM-4000 units. Controlled resistive heaters have been added to the sheath and sample inlets and to the optical particle counter to prevent instantaneous supersaturations at the inlet and water condensation at the outlet. Finally, the wetted filter paper on the internal walls of the growth column is periodically resaturated using a peristaltic pump; while this made the instrument unavailable for data collection approximately 5% of the time, it prevented the more serious flooding and drying problems experienced in the past. These technical improvements all contributed to substantial gains in instrument stability and reliability.

4. Instrument Verification

4.1. Scripps CCN Counter

[16] The principle of the Scripps CCN instrument has been validated in controlled laboratory experiments using aerosol with known activation properties. (A detailed description of the calibration and results is presented by Roberts and Nenes (manuscript in preparation, 2003).) Monodisperse aerosol of a known composition (i.e., ammonium sulfate) and size was generated by a DMA (TSI Model 3081). Particle diameters between 0.01 and 0.6 μm were chosen to observe various degrees of activation at a particular supersaturation. The aerosol at a selected size was simultaneously sampled at the outlet of the DMA by an SMPS (TSI Model 3081), a condensation particle counter (CPC) (TSI Model 3010), and the CCN instrument. The SMPS verified the monodisperse output of the first DMA and quantified the amount of multiply charged particles. The scans were averaged, and the median diameter of the distribution was used as the calibration size for the CCN counter. The integrated droplet distribution from the SMPS yielded the total aerosol concentration and was normalized to the average number concentrations recorded by the CPC for the same SMPS scan period. Number and droplet concentrations were recorded every second by the CPC and CCN, respectively, and ranged between 0 and 10^4 cm^{-3} . The CPC has detection efficiency near 100% for particles with diameters larger than 0.018 μm and was used as a reference for comparing the activated fraction of CCN to total aerosol concentration. The median diameter of the selected monodisperse size distribution that activated 50% of the aerosol to CCN was used to calculate the corresponding supersaturation using Köhler theory.

[17] The calibration of the instrument yielded sharp activation curves, presented by Roberts and Nenes (manuscript in preparation, 2003), and verified the novel technique of generating a supersaturation profile. At a flow rate of

$500 \text{ cm}^3 \text{ min}^{-1}$ and temperature difference between the ends of the column of 5°C , a sharp rise in the activated droplet concentration occurred at a median diameter of 72 nm. Theory predicts that, for ammonium sulfate aerosol, the corresponding critical supersaturation of 72-nm diameter particles is 0.24%. These calibrations were performed at ambient pressure (ca. 1000 mbar) and need to be corrected for airborne measurements at higher altitudes. The flights during CRYSTAL-FACE occurred mostly in the boundary layer around 900 mbar, which slightly lowers the supersaturation to 0.2%.

4.2. Caltech CCN Counter

[18] To verify the effective supersaturation of the Caltech CCN instrument in its new configuration, a laboratory calibration was carried out. In this experiment, the instrument was set up in the laboratory in parallel with a CPC and either ammonium sulfate or sodium chloride particles of known size were fed simultaneously to both instruments. Laboratory pressure and temperature were approximately 980 hPa and 293 K, respectively. The activation properties of these particles were calculated using Köhler theory as it is presented by *Seinfeld and Pandis* [1998]; constant van't Hoff factors ($\nu = 2$ for sodium chloride and $\nu = 3$ for ammonium sulfate) were used. Polydisperse aerosol distributions of each composition were generated with a nebulizer and passed through a diffusion dryer before being classified with a cylindrical DMA. The resulting monodisperse aerosol was then sampled by both the Caltech CCN counter and a TSI 3010 CPC. The sample concentrations were kept between 800 and 1500 particles cm^{-3} , somewhat above what were commonly observed during the CRYSTAL-FACE campaign.

[19] The results of the verification experiments are given in Figures 4 and 5. Figure 4 shows the CCN ratio (measured CCN concentration/particle concentration as measured by the TSI 3010) as a function of dry particle size. For both ammonium sulfate and sodium chloride, the data indicate a sharp activation transition. Vertical lines indicate the smallest dry diameters that activate in the column for each species, as predicted by the instrument model developed by *Nenes et al.* [2001]. As expected, the size at which this transition takes place is smaller for NaCl than for $(\text{NH}_4)_2\text{SO}_4$. When the CCN ratio is plotted as a function of critical supersaturation (Figure 5), the instrument's response for each species is found to be nearly identical, with the transition occurring at approximately 0.85%. During CRYSTAL-FACE, housekeeping data from the CCN counter for level legs were frequently inserted in the instrument model to determine the effective supersaturation in the instrument during that period; the results indicate that the supersaturation over the course of the campaign was typically within 5% of the value determined by the laboratory experiments.

4.3. Field Instrument Intercomparison

[20] Making airborne aerosol measurements is inherently difficult, and it is impossible to completely mimic flight conditions in the laboratory. A well-characterized instrument in the laboratory is necessary but not sufficient for a well-characterized flight instrument. As a means of verifying the in situ performance of both CCN counters,

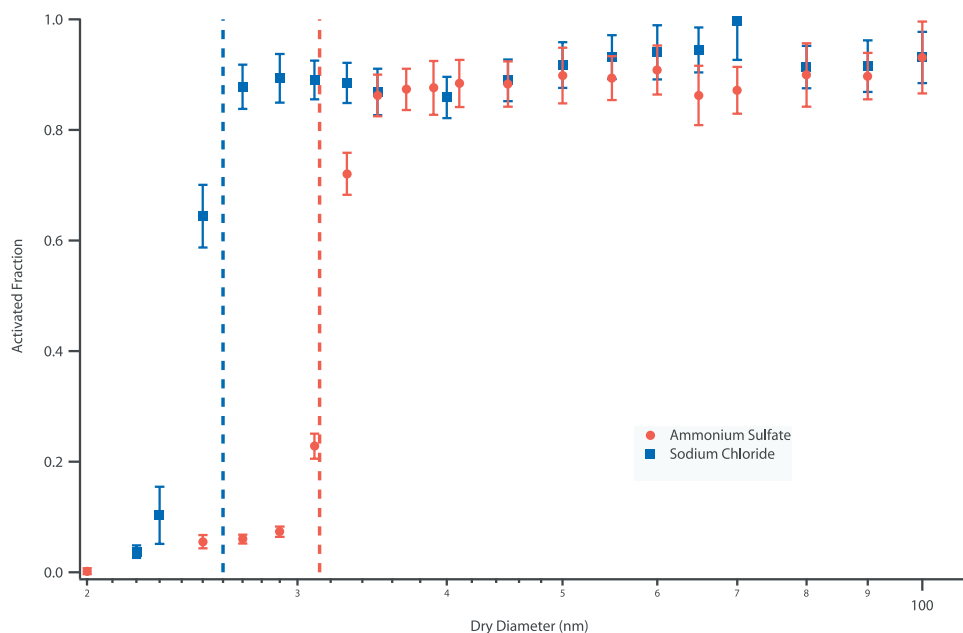


Figure 4. Activated fraction versus dry diameter from the laboratory verification experiments for the Caltech CCN instrument. The dashed lines represent the cut size predicted from the instrument model described by *Nenes et al.* [2001].

the temperature gradient of the Scripps counter was temporarily adjusted so that each had an effective supersaturation of $\sim 0.85\%$. The comparison took place during CF-11, from 1914 to 1932 UTC; this time period included samples in and out of cloud and at several altitudes between 1000 and

1700 m. The time series for this period is presented in Figure 6; for easier comparison, the data from the Scripps counter are given as 2-s averages to match the slower sampling rate of the Caltech instrument. Brief gaps in the data from the Scripps instrument occur during altitude

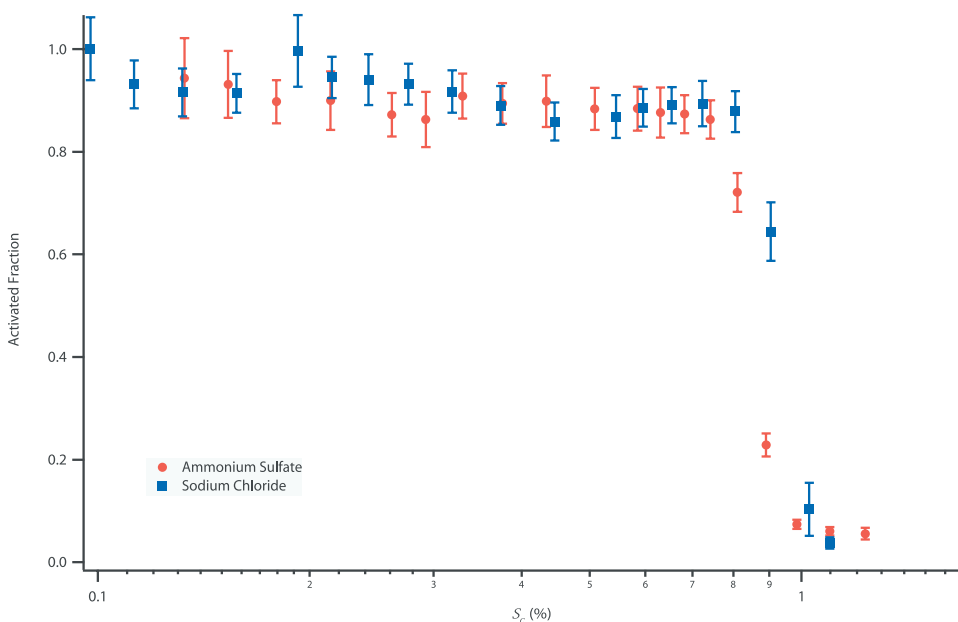


Figure 5. The data from Figure 4 plotted versus particle critical supersaturation.

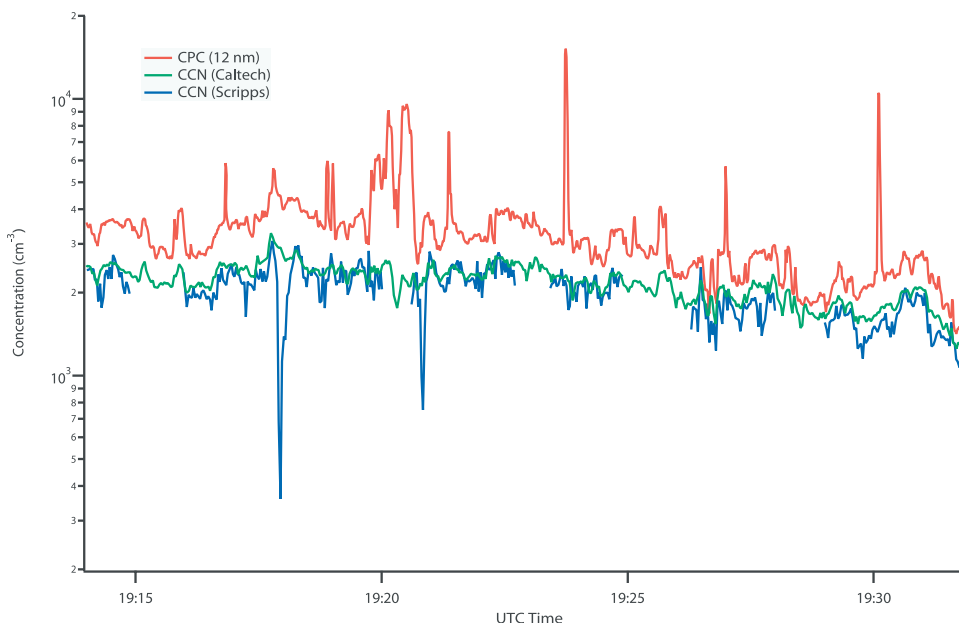


Figure 6. Time series from the in situ intercomparison of CCN instruments conducted during flight CF-11. The brief gaps in the data from the Scripps instrument occurred during altitude changes.

changes. For the purposes of the statistical comparison, these time periods are also removed from the Caltech CCN data set.

[21] The two instruments agree quite closely over the course of the comparison, except for two brief periods, each less than 20 s, where the concentration indicated by the Scripps counter decreased significantly relative to data from both instruments over the rest of the time period. Overall, agreement was excellent: the mean ratio ($N_{\text{Scripps}}/N_{\text{Caltech}}$) was 0.917, with a standard deviation of 0.115. When the two brief periods of large disagreement are omitted, the mean increases to 0.929, with a standard deviation of 0.086. In either case, the data indicate agreement between the instruments to within the standard deviation, indicating that both instruments work reliably on board the aircraft and the slightly different configurations produced similar results.

4.4. Instrument Response

[22] Another test of the validity of the CCN measurements in the field is to examine the instrument response to rapid changes in atmospheric concentrations, which can occur frequently on airborne platforms. During CRYSTAL-FACE, three TSI condensation particle counters were on board the Twin Otter and sampled from the same inlet as the CCN counters. Figure 7 displays a 30-min time series from CF-20 for one of these particle counters (operating at a nominal cut size of 12 nm), along with the corresponding data from both CCN counters. The gaps in the time series for $S = 0.2\%$ are the result of the removal of data during altitude changes. The CCN counters record several rapid changes in concentration that correspond closely with concurrent transitions in the total particle concentration measured by the CPC. For example, several sharp transitions occur between 1732 and 1735 UT that are seen clearly in the time series for all three

instruments, indicating that the response times of the CCN counters to changes in the sample concentration are similar to that of the CPC. However, there are also several instances where a pulse is seen by the CPC that is not seen by one or both of the CCN counters (e.g., at 1749, 1752, and 1754 UT). This does not necessarily indicate a problem with the CCN instruments: the CPC has a smaller cut size and these pulses in the time series probably correspond to particles too small or too insoluble to activate. The time series data confirm that changes in the observed CCN concentration in situ correspond to actual changes in the aerosol population.

5. Trends in CCN During CRYSTAL-FACE

[23] Previous studies have shown that CCN concentrations, like all aerosol properties, vary substantially in space and time; therefore when comparing CCN concentrations with those of previous surface and airborne studies, the conditions of the measurements must be considered. CCN concentrations are typically lowest ($N_{\text{CCN}} < 250 \text{ cm}^{-3}$ for $S > 0.5\%$) under remote marine conditions in either hemisphere [Hegg *et al.*, 1991, 1995; Hudson, 1993; Covert *et al.*, 1998; Cantrell *et al.*, 2000]. In contrast, concentrations can be on the order of several thousand cm^{-3} where a heavy anthropogenic influence exists [Hudson and Frisbie, 1991; Hüttenberger *et al.*, 1999; Cantrell *et al.*, 2000].

[24] Earlier published measurements of CCN concentrations in eastern and southern Florida indicate substantial variation depending on the recent history of the air mass. Hudson and Yum [2001] described measurements made along the eastern coast of Florida; these data were classified based on the origin of the air mass, each flight designated either maritime or continental. Over 28,000 separate measurements were included in the analysis, with an average

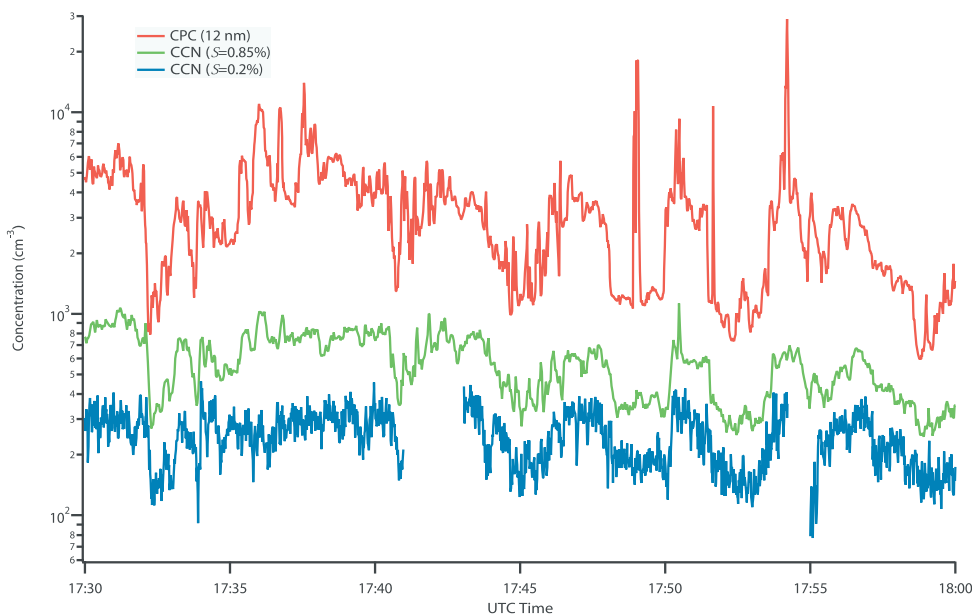


Figure 7. Time series data from flight CF-20. The altitude of the aircraft was ~ 1000 m until 1742 UT and ~ 1500 m thereafter. The gaps in the data at $S = 0.2\%$ are due to occasional instabilities in the instrument.

duration of 3.5 s. At a supersaturation of 1%, the average concentration was 359 cm^{-3} for the maritime flights and 1411 cm^{-3} for the continental flights. Concentrations were slightly lower at $S = 0.85\%$ (320 and 1300 cm^{-3} , respectively) and significantly lower at $S = 0.2\%$ (~ 200 and 500 cm^{-3} , respectively). An earlier study by *Sax and Hudson* [1981] presented ground measurements of CCN in south central Florida and airborne measurements from east-west transects of the southern Florida peninsula. For the airborne measurements ($S = 0.75\%$), concentrations peaked at 2500 cm^{-3} over the east coast, but dropped to between 250 and 500 cm^{-3} over the center of the peninsula. Ground measurements from the following year supported these data and demonstrated that the local concentrations in the boundary layer were dependent on wind speed and direction. Such a result is intuitive, given the nature of the Florida peninsula: large population centers along both coasts surround a rural interior. Off the eastern coast is the open Atlantic Ocean, where maritime conditions are the norm, while off the western coast lies the Gulf of Mexico, where there is often more recent continental influence.

[25] The range of CCN concentrations observed during the CRYSTAL-FACE campaign is in general agreement with these earlier studies. During CRYSTAL-FACE, data were collected both over land and the Gulf of Mexico near the southwestern coast of Florida (Figure 1). For this description of the general trends in CCN concentrations and the closure analysis that follows, the data from both CCN counters were averaged over 103 s to match the timescale of the individual size distributions from the DMA. Only data from level legs were included in the analysis. In this presentation, in-cloud data are included; cloud passes were brief relative to the averaging time, and it will be

demonstrated in a later section that removing in-cloud data has a negligible impact on the results. As mentioned previously, the 0.85% S counter required periodic resaturation and was out of service $\sim 5\%$ of the time. The 0.2% S counter experienced temperature and pressure stability problems throughout the campaign that required some data filtering; these problems were usually seen at high altitudes and during changes in altitude.

[26] Table 3 summarizes the data from the Caltech CCN counter during the CRYSTAL-FACE campaign. For this instrument, operating at $S = 0.85\%$, there are 868 measurements collected during 17 flights. Figure 8 shows a histogram of these data. The concentrations ranged from a low of 70 cm^{-3} (during CF-5) up to 5999 cm^{-3} (during CF-18); the average over the entire duration of the campaign was 533 cm^{-3} . However, Figure 8 indicates that the mean is skewed by a small number of data points at the upper end of the range; the vast majority of measured concentrations were below 1000 cm^{-3} , and the peak in the histogram lies between 250 and 300 cm^{-3} ; the median is at 371 cm^{-3} . Almost all of the very high concentration measurements ($>2000 \text{ cm}^{-3}$) are from CF-18 on 28 July. The final line on Table 3 indicates that if the data from CF-18 are omitted, the mean falls to 447 cm^{-3} and the upper boundary of the remaining data is 2332 cm^{-3} .

[27] The summary data for the Scripps CCN instrument, operating at $S = 0.2\%$, are presented in Table 4. Over 12 flights, there were 353 sampling intervals, with measured concentrations ranging from 33 cm^{-3} (during CF-15) to 1553 cm^{-3} (during CF-10). The mean of these measurements is 306 cm^{-3} , but the histogram in Figure 9 shows that, as is the case for the higher supersaturation measurements, the mean is skewed by a proportionally small

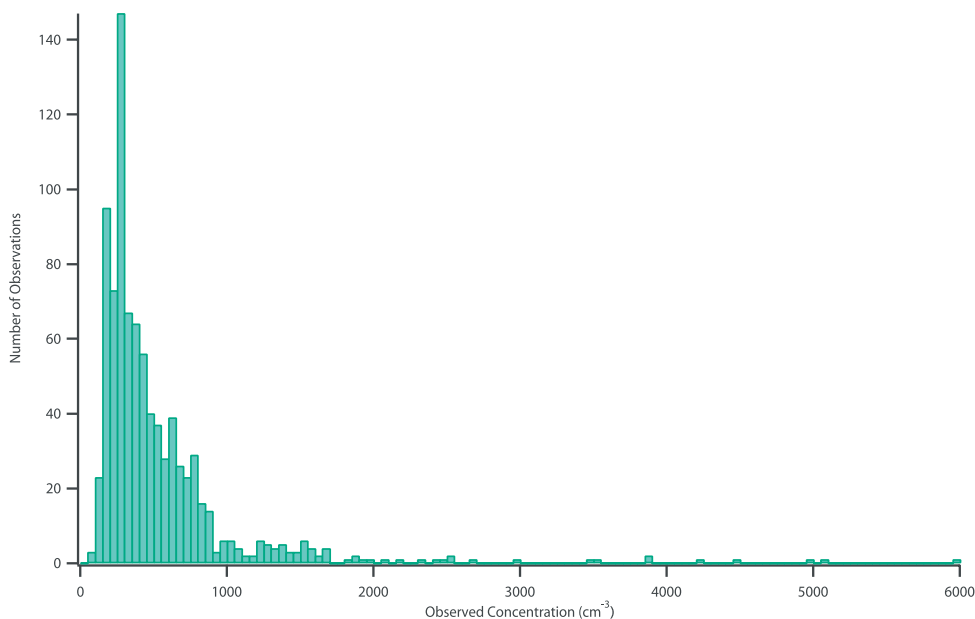


Figure 8. Histogram of CCN observations at $S = 0.85\%$.

number of high-concentration measurements. The median concentration is 233 cm^{-3} , and the peak in the histogram lies between 50 and 150 cm^{-3} .

[28] The histogram data at both supersaturations indicate that the air sampled during the campaign was typically marine and modified marine in character; air masses with more distinct continental and anthropogenic influence were encountered, but infrequently. At both $S = 0.2\%$ and $S = 0.85\%$, the peak in the histogram is below the mean reported by *Hudson and Yum* [2001] for marine aerosol, and the median concentrations from CRYSTAL-FACE are only slightly larger. The data ranges in Tables 3 and 4 may

lead to the conclusion that the continental samples were spread over numerous flights; only during CF-10 was the continental influence obvious throughout the flight.

[29] The flight path of the Twin Otter during a CRYSTAL-FACE mission usually involved multiple altitudes with different patterns on each flight; much of the intraflight variability indicated in Tables 3 and 4 is a result of these complex flight patterns. Figures 10 and 11 show the relationship between CCN concentration and altitude. For clarity, the data from CF-18 are omitted from Figure 11 and from the present discussion; the very high concentrations at $S = 0.85\%$ during that flight all occurred at altitudes

Table 3. CCN Data Summary at $S = 0.85\%$ ^a

Flight Number	Date	Number of Observations	Measured Concentration, cm^{-3}		Coefficient of Variation	
			Range	Mean	Range	Mean
CF-1	3 July	45	324–1040	660	0.03–0.20	0.07
CF-2	3 July	57	288–801	514	0.03–0.99	0.09
CF-3	6 July	44	155–872	606	0.03–0.19	0.07
CF-4	7 July	29	399–935	554	0.03–0.41	0.22
CF-5	7 July	93	70–391	185	0.04–1.44	0.20
CF-6	10 July	14	427–851	614	0.04–0.23	0.08
CF-10	18 July	18	1138–2332	1413	0.03–0.19	0.07
CF-11	18 July	34	407–1661	1052	0.03–0.31	0.09
CF-12	19 July	20	287–640	456	0.04–0.20	0.08
CF-13	19 July	96	195–515	313	0.04–0.67	0.13
CF-14	21 July	52	225–1105	615	0.03–0.32	0.09
CF-15	23 July	84	218–720	326	0.04–1.28	0.13
CF-16	25 July	60	199–774	305	0.04–0.38	0.10
CF-17	26 July	27	261–402	314	0.03–0.53	0.09
CF-18	28 July	89	286–5999	1283	0.03–0.90	0.22
CF-19	29 July	38	84–436	215	0.04–0.50	0.16
CF-20	29 July	68	151–1193	385	0.05–0.56	0.15
Overall		868	70–5999	533	0.03–1.44	0.13
Omitting CF-18		779	70–2332	447	0.03–1.44	0.12

^aEach observation is averaged over 103 s. The coefficient of variation is the ratio of the standard deviation of each observation to the observed concentration.

Table 4. CCN Data Summary at $S = 0.2\%$ ^a

Flight Number	Date	Number of Observations	Measured Concentration, cm ⁻³		Coefficient of Variation	
			Range	Mean	Range	Mean
CF-08	13 July	9	269–702	501	0.12–0.25	0.17
CF-09	16 July	36	129–582	391	0.07–0.27	0.13
CF-10	18 July	18	679–1553	850	0.10–0.49	0.22
CF-11	18 July	26	106–1310	649	0.10–0.76	0.36
CF-12	19 July	18	120–347	225	0.12–0.31	0.18
CF-13	19 July	25	39–80	55	0.25–0.76	0.46
CF-14	21 July	7	281–641	475	0.13–0.33	0.20
CF-15	23 July	55	33–304	141	0.12–0.68	0.28
CF-17	26 July	15	163–263	211	0.10–0.23	0.15
CF-18	28 July	52	219–1275	447	0.10–0.82	0.24
CF-19	29 July	28	50–261	109	0.13–0.43	0.25
CF-20	29 July	64	94–462	175	0.12–0.44	0.21
Overall		353	33–1553	306	0.07–0.82	0.24

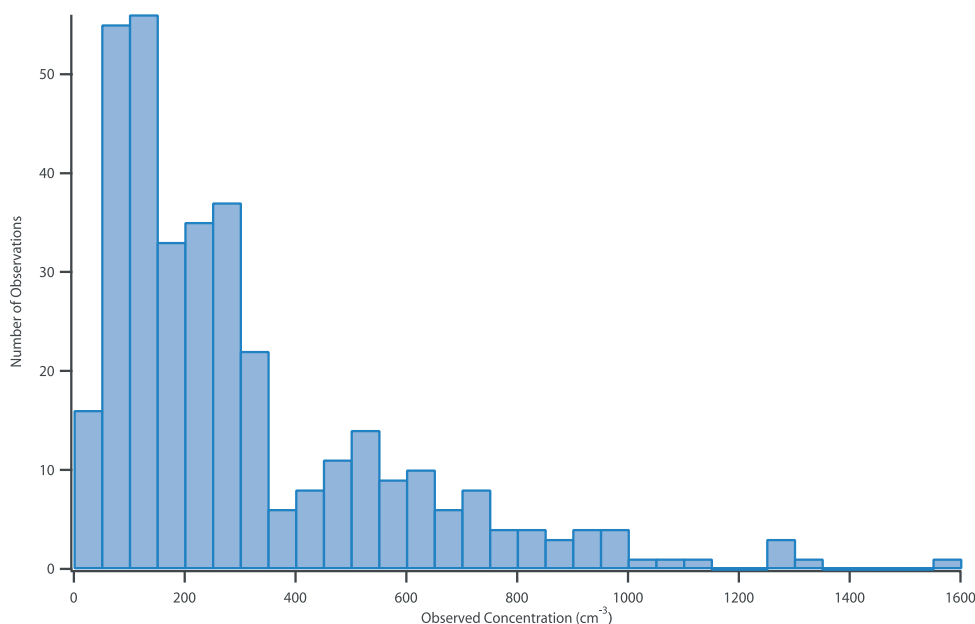
^aEach observation is averaged over 103 s. The coefficient of variation is the ratio of the standard deviation of each observation to the observed concentration.

between 700 and 1500 m. The outstanding feature in both figures is the group of high-concentration observations at about 1600 m. Although concentrations sufficiently high to be considered continental were seen on several flights, only during CF-10 and CF-11, the two flights on 18 July, was an air mass of apparent continental origin sampled for an extended time period. The lower concentrations also observed during CF-11 were from another flight leg at a higher altitude; the variation of concentration with altitude is much stronger than during other flights. The difference is explained by examining the back trajectory of the air mass for that day, using the National Oceanic and Atmospheric Administration's (NOAA) Hybrid Single-Particle Lagrangian Integrated Trajectory (HYSPLIT) model (available at <http://www.arl.noaa.gov/ready/hysplit4.html>, NOAA Air Resources Laboratory, Silver Spring, Maryland). For most

of the mission, the air mass sampled by the Twin Otter had been aloft and/or over water for several days prior to being sampled. Figure 12 indicates a different history for 18 July: the air had been over the land for several days and the air at 1600 m had been at ground level 48 hours before. This air mass history explains the elevated concentrations seen on that day. For the rest of the data set, there appears to be some altitudinal dependence in CCN concentrations, but the temporal and local spatial variation appears to be more important.

6. Comparison of CCN Data With Aerosol-Size Distributions

[30] The importance of aerosol/CCN closure, and the difficulty in achieving it, is the primary motivation for this

**Figure 9.** Histogram of CCN observations at $S = 0.2\%$.

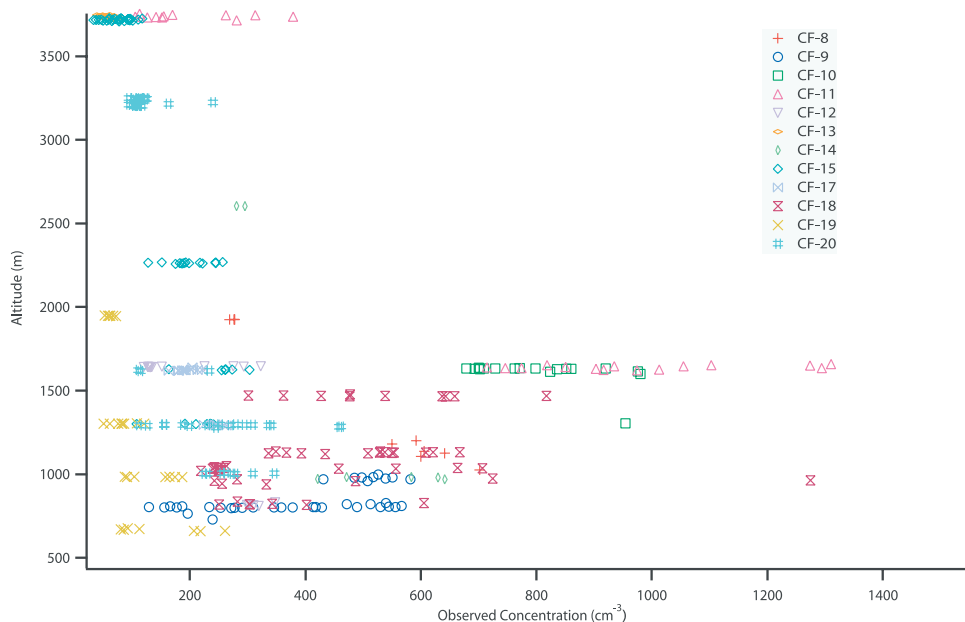


Figure 10. Altitude versus observed CCN concentration at $S = 0.2\%$.

work. The activation properties of the atmospheric aerosol determine in large part the extent of cloud formation and propagation, but our understanding of the processes involved is incomplete. Comparing measurements of CCN concentrations to predictions based on activation theory serves to validate both the measurement and the theory.

During the CRYSTAL-FACE campaign, the DMA measured aerosol number size distributions, with an operating range of 10–900 nm. The scans from this DMA system last 103 s, and the instrument sampled from the same inlet as the CPC and CCN instruments; the data from both CCN counters were averaged to match the sampling interval of

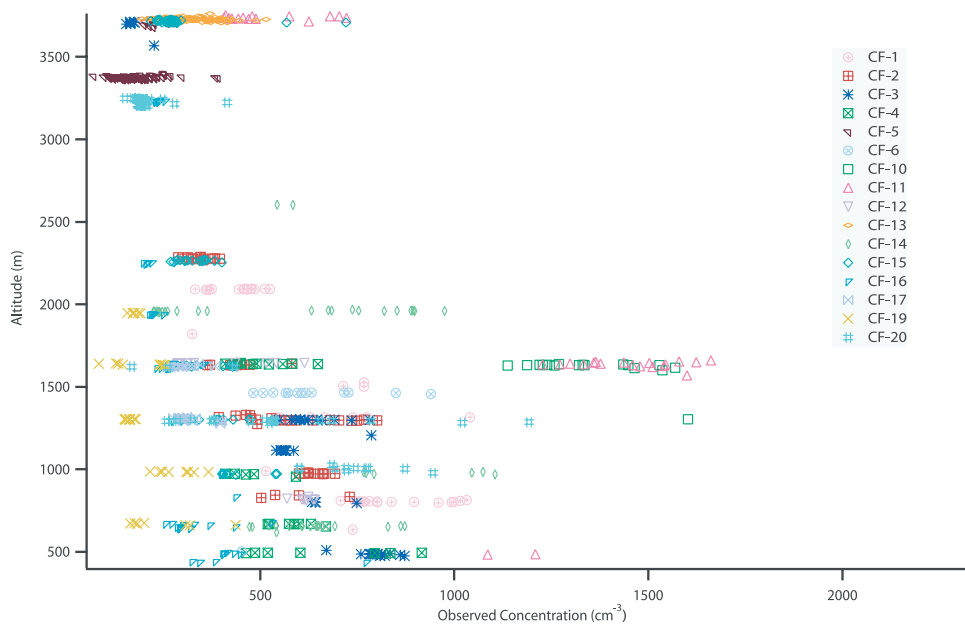


Figure 11. Altitude versus observed CCN concentration at $S = 0.85\%$. The observations from CF-18 are omitted for clarity.

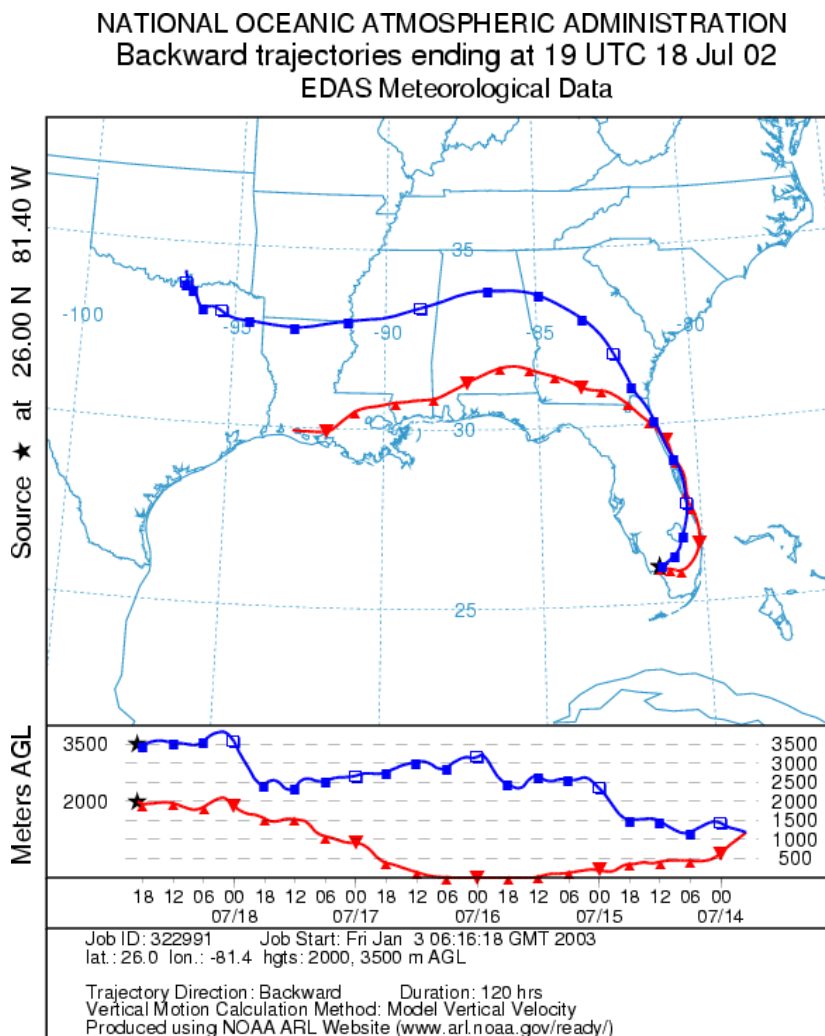


Figure 12. Simulated 120-hour back trajectories for the air mass sampled during flights CF-10 and CF-11. The plot is a product of the NOAA Air Resources Laboratory HYSPLIT model.

these size distributions. The operating range of the DMA includes the vast majority of the particles in the atmosphere, thus the CCN population can be effectively assumed to be a subset of the measured size distribution.

[31] For this analysis, the entire aerosol population was assumed to be pure ammonium sulfate. This is clearly a simplification, but it can be considered an obvious first step in estimating CCN concentrations from aerosol-size distributions, and the same assumption has been used in similar analyses previously [e.g., *Bigg*, 1986; *Martin et al.*, 1994; *Snider and Brenguier*, 2000]. Furthermore, the choice is supported, in general, by unpublished data obtained during CRYSTAL-FACE using the aerosol mass spectrometer (AMS) (R. Bahreini, personal communication, 2003). The assumed composition leads directly to a predicted cut size corresponding to the effective supersaturation in each CCN counter, calculated using Köhler theory where the van't

Hoff factor for ammonium sulfate is held constant at three [cf. *Seinfeld and Pandis*, 1998]. For the counter operating at $S = 0.2\%$, this calculated cut size was 79 nm; for the Caltech instrument, which operated at $S = 0.85\%$, the cut size was 32 nm. The predicted CCN concentration is calculated by integrating upward from the cut size to the upper boundary of the size distribution.

[32] The long sampling time of the DMA system relative to other aerosol instruments limits its resolution during airborne measurements. During CRYSTAL-FACE, the nominal airspeed of the Twin Otter was 50 m s^{-1} ; thus the spatial resolution of the DMA was approximately 5 km. The concentration at a given size is only measured at one point during each scan, and the data analysis implicitly assumes that the aerosol-size distribution is uniform over this spatial scale. In reality, the aerosol population frequently varies on scales shorter than 5 km. For this reason, it is not

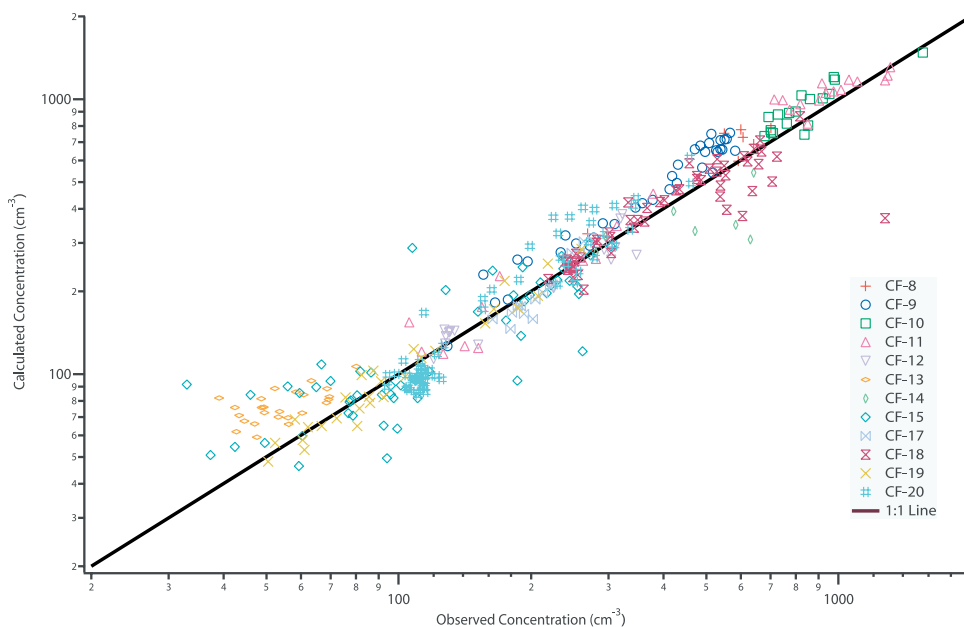


Figure 13. Scatterplot of the simplified closure analysis at $S = 0.2\%$.

necessarily expected that any individual comparison in the simplified closure analysis would indicate good agreement, but the uncertainties would presumably average to zero over the course of many measurements.

[33] The results of this simplified closure analysis are shown in scatterplot form in Figures 13 and 14. At $S = 0.2\%$, the agreement is excellent throughout the entire data set. A linear regression of predicted versus observed concentrations produces a slope of 1.026 and an intercept of 11.1 cm^{-3} , with an R^2 value of 0.912. If the intercept is forced to zero, the slope increases only slightly, to 1.047 ($R^2 = 0.911$). The overall correlation at $S = 0.85\%$ indicates some moderate overprediction: a slope of 1.264, with an intercept of -70.5 cm^{-3} ($R^2 = 0.840$); forcing a zero intercept reduces the slope to 1.201 ($R^2 = 0.835$). However, as was noted earlier, during portions of CF-18, both the CN and CCN (at $S = 0.85\%$) concentrations were much higher than were seen at any other point during the campaign. Omitting this flight from the regression reduces the slope to 1.093, with an intercept of -5.2 cm^{-3} ($R^2 = 0.770$); with a forced zero intercept, the slope is 1.085 ($R^2 = 0.770$).

[34] On the basis of these linear regressions, the overprediction of CCN at $S = 0.2\%$ is on average only 5% when assuming the idealized composition. At $S = 0.85\%$, the predicted concentration is 9% greater than the observation when omitting CF-18. These overestimates are very small, compared to the earlier studies discussed in section 2, and are within estimated measurement uncertainties (note that in the verification study for the Caltech instrument, Figure 4, the counting efficiency appears to be near 90%). Obviously, the compositional assumption is not strictly correct. The present analysis is as much a test of the assumption as of anything else, and the results support its use in cases like this one. The sensitivity of the results to the compositional

assumption is examined further in the next section. In summary, the overpredictions are small, and the analysis validates the CCN measurements and the theory upon which the predicted concentrations are based.

7. Discussion

[35] The CCN population over southwest Florida and the surrounding waters during CRYSTAL-FACE is primarily marine in character and can be accurately calculated using the aerosol-size distribution. However, some assumptions used in the analysis can be scrutinized, particularly the inclusion of in-cloud data in the analysis and the assumption of a pure ammonium sulfate aerosol. Also, at several points in the analysis, the CCN observations at $S = 0.85\%$ from CF-18 have been omitted. The reasoning behind these decisions and the impact they have on the analysis are discussed below.

7.1. In-Cloud Sampling

[36] The decision to include in-cloud observations in the analysis was primarily one of convenience. Cloud passes were usually very brief, and it was assumed that the impact of including these data would be negligible. To confirm this, the CCN data at $S = 0.85\%$ were filtered to remove data collected in-cloud, and the results were compared to the unfiltered data. The filter removed observations where the average liquid water content (over the 103-s sampling period), as measured by a Forward Scattering Spectrometer Probe (FSSP, from PMS, Inc.), was greater than $500 \mu\text{g cm}^{-3}$. This effectively removed all data points wherein a portion of the sample time was in-cloud, 17% of the data set. The average CCN concentration of the filtered data set is 518 cm^{-3} , a decrease of 3%. The effect on the closure analysis was

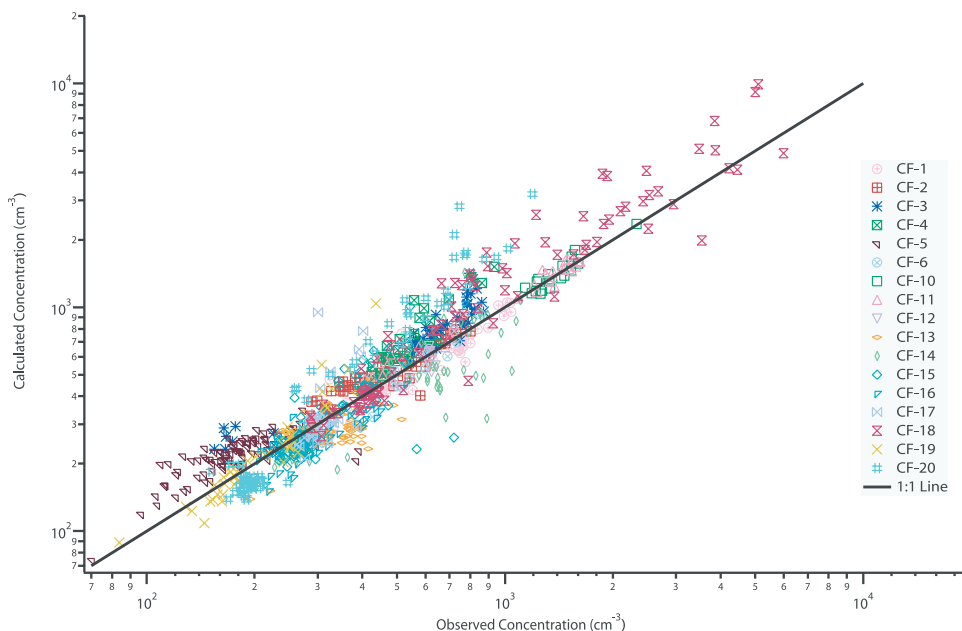


Figure 14. Scatterplot of the simplified closure analysis at $S = 0.85\%$.

even smaller: after removing the in-cloud samples, the slope of the curve fit (predicted versus observed concentration) increases to 1.240 ($R^2 = 0.826$, intercept forced to zero), a 1% difference. This confirms that the inclusion of in-cloud samples has a negligible impact on the overall analysis.

7.2. Aerosol Composition

[37] For the simplified closure analysis in section 6, the aerosol was assumed to be composed entirely of ammonium sulfate. The results indicate that this was a viable procedure in this case, even though the assumption could not have been strictly true. Each of the successful closure analyses discussed in section 2 relied on more detailed compositional assumptions, as did nearly all of the studies where closure was not achieved. Incomplete understanding of the role of composition in establishing the aerosol/CCN relationship was cited in many cases as a primary reason why the closure analysis was unsuccessful.

[38] One reason the idealized ammonium sulfate compositional assumption works so well here may lie in the mixing state of the aerosol. The viability of the assumption provides strong evidence of an internally mixed aerosol. Substantial external mixing of the population would mean that some fraction of the aerosol would have little or no ammonium sulfate. Whatever their actual composition, these particles (at equivalent diameters) would almost certainly activate at higher critical supersaturations; sodium chloride is the only common atmospheric species that activates more readily than ammonium sulfate, and *Twomey* [1971] determined that most atmospheric CCN are not NaCl. Explaining the results in section 6 using an externally mixed aerosol requires that the concentration of smaller NaCl particles that activate at 0.85% (or 0.2%) supersaturation

be consistently offset by an equivalent number of larger, less readily activated particles; this result is highly unlikely.

[39] However, if the aerosol is internally mixed, it is expected that the population, as a whole, would be relatively insensitive to the presence of insoluble species. *Roberts et al.* [2002] demonstrated using a prescribed size distribution that replacing half of the soluble mass (in this case, ammonium bisulfate) with insoluble organic material throughout the entire aerosol population reduced the activated fraction by only about 10% (at $S = 0.85\%$). The effect is somewhat more pronounced at lower supersaturations; the same replacement of soluble mass with insoluble mass leads to a drop in activated fraction on the order of 35% at $S = 0.2\%$. This result is not surprising; although the replacement of soluble mass with insoluble mass can have a large effect on activation properties for particles whose critical supersaturations are near the effective supersaturation of the instrument, the integral nature of the measurement means that the overall impact will be substantially less important. In practical terms, substituting insoluble mass for soluble mass would cause the activation cut size to shift by some undetermined number of channels. This relative insensitivity to the presence of insoluble compounds lends credence to the idealized ammonium sulfate composition used in this analysis.

[40] The selection of ammonium sulfate as opposed to other species also impacts the analysis. The choice reflects the predominance of ammonium and sulfate in the atmospheric aerosol particles smaller than $1 \mu\text{m}$, as a result of cloud processing [*Seinfeld and Pandis*, 1998]. However, the composition of the resultant particle is influenced by the relative abundance of ammonia and sulfur dioxide at the time of processing. Ammonium sulfate production

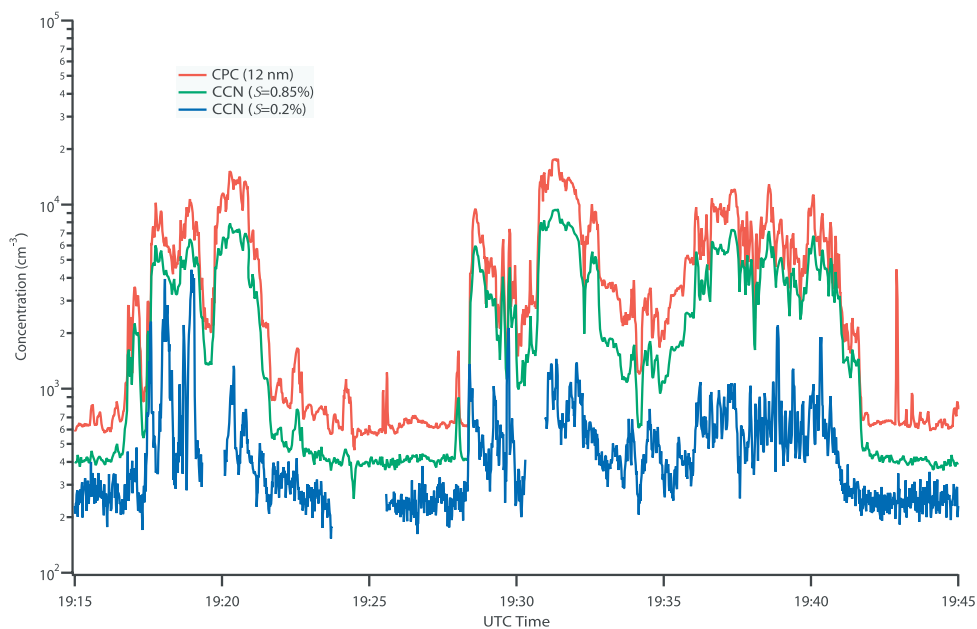


Figure 15. Time series for a portion of flight CF-18. Note how the aerosol concentrations measured by the CPC change rapidly by more than an order of magnitude. The high concentrations were atypical of the conditions normally encountered during CRYSTAL-FACE.

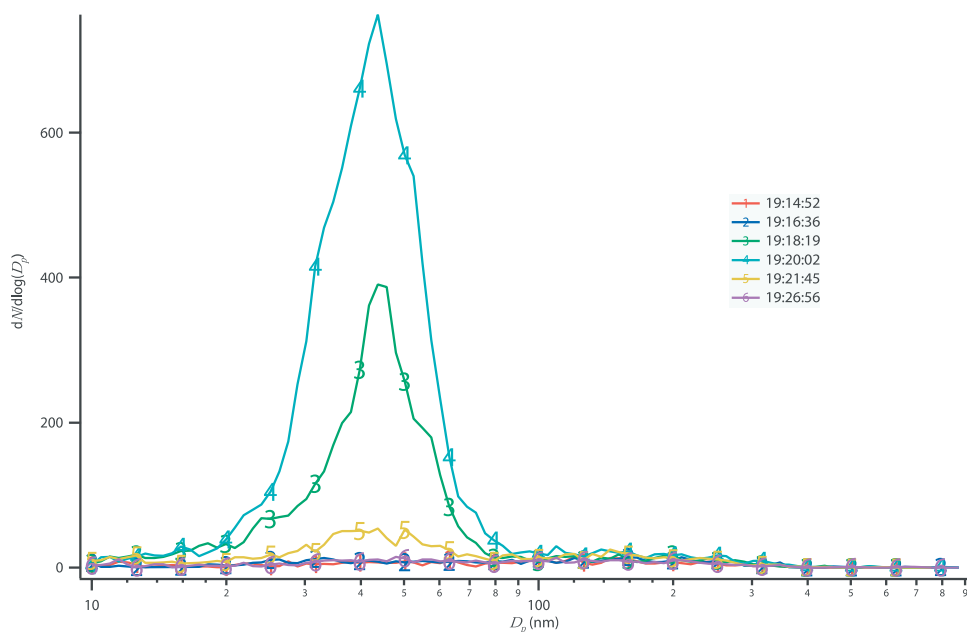


Figure 16. Consecutive size distributions from the DMA for the first half of the time series in Figure 15. The large peak that dominates the spectrum at 1920:02 UT disappears almost completely in the next scan. Nearly all of the particles in the scans showing elevated concentrations are below the size at which ammonium sulfate particles would activate at $S = 0.2\%$ (i.e., 80 nm).

dominates at high ammonia concentrations; at lower ammonia concentrations, ammonium bisulfate is the more common product. To determine the sensitivity of the closure analysis to the particular species chosen as the solute, the statistics were recalculated using a different composition, ammonium bisulfate. In practical terms, this means increasing the cut size from 79 to 87 nm for the comparison at $S = 0.2\%$ and from 32 to 35 nm for the analysis at $S = 0.85\%$. At $S = 0.2\%$, the adjustment resulted in a decrease in the slope of the fitted line from 1.047 to 0.939; the R^2 is nearly unchanged (0.911 and 0.909, respectively). At $S = 0.85\%$, the reanalysis results in the slope of the fitted line dropping from 1.234 ($R^2 = 0.822$) to 1.201 ($R^2 = 0.835$). If the data from flight CF-18 are omitted, the slope drops to 1.085 ($R^2 = 0.770$). Thus if the aerosol is assumed to be ammonium bisulfate rather than ammonium sulfate, the size distribution underpredicts the CCN concentration somewhat at $S = 0.2\%$ and overpredicts the CCN concentration somewhat at 0.85% . This confirms that the success of the analysis is not entirely dependent on the precise soluble species used to define the aerosol composition.

7.3. Flight CF-18

[41] During the 28 July flight, CF-18, several instruments on the CIRPAS Twin Otter measured particle concentrations far greater than at any other time during the CRYSTAL-FACE campaign. The source or sources of these particles is not immediately clear, but the result was that aerosol (and CCN) concentrations rapidly changed by more than an order of magnitude, as can be seen in Figure 15. The CCN concentration at $S = 0.85\%$ tracks closely with the total aerosol concentration, while CCN at $S = 0.2\%$ appear to correlate less well; this is an indication that the particles were too small to be activated at the lower supersaturation. The size distribution data corroborate this (Figure 16); the vast majority of particles are smaller than 80 nm, the nominal cut size at which ammonium sulfate particles activate when $S = 0.2\%$. This explains why the concentrations at the lower supersaturation are not atypically high. Figure 16 also provides some explanation as to why the closure analysis from CF-18 involved large underpredictions as well as overpredictions. The consecutive size distributions show how rapid the transitions were between elevated and normal particle concentrations. As was discussed in the previous section, the scan time for the DMA was sufficiently long that it could miss these particles: if the transition occurs while the DMA is scanning at the upper end of the size range, the huge numbers of small particles would not be observed. This is true at all times, but usually the atmospheric particle concentrations are spatially stable enough that the scan rate is not an issue; that does not appear to be the case here. The extremely high concentrations and large spatial variation for the small particles on this flight are very interesting and worthy of further study. However, the atypical concentrations on this day justify omitting them from the closure analysis and from the description of the CCN trends for the region.

8. Conclusions

[42] Information gathered from the CIRPAS Twin Otter during the July 2002 CRYSTAL-FACE campaign provides

a clear picture of the character of the atmospheric aerosol along the coast of southwest Florida. Included in the Twin Otter payload were two cloud condensation nucleus counters that employed a recently developed technique for maintaining a stable constant supersaturation in order to make continuous real-time measurements of CCN. These instruments, operating at supersaturations of 0.2 and 0.85%, were well characterized in the laboratory and in the field, and their performance was consistent with those of other aerosol counters on board the aircraft.

[43] The CCN concentrations measured over the course of the campaign by the two instruments were in general agreement with those from earlier studies in the region. At $S = 0.2\%$, the mean concentration over the course of the campaign was 306 cm^{-3} , while the median was 233 cm^{-3} . At $S = 0.85\%$, the mean and median were 533 and 371 cm^{-3} , respectively. These data indicate that the majority of observations are best described as marine in character. Of the 19 flights for which data are available, only two air masses were sampled that had a distinct continental influence.

[44] The extensive data set from the CRYSTAL-FACE campaign was used as the basis for a simplified closure analysis to determine whether the CCN concentration could be accurately predicted by assigning an assumed composition to a measured aerosol-size distribution. The analysis proved successful: at $S = 0.2\%$ the calculated concentration was on average 3% greater than the prediction, with an R^2 value of 0.91. At $S = 0.85\%$, the overall ratio of calculated to measured concentrations was 1.09 ($R^2 = 0.77$), when the atypical data from CF-18 are excluded. The analysis indicates that for conditions like those encountered during the CRYSTAL-FACE campaign it may be possible to accurately calculate the concentrations of CCN over a range of supersaturations from the aerosol-size distribution by assuming a pure ammonium sulfate composition.

[45] More study is required in order to determine whether it is a generally applicable practice to predict CCN concentrations from the aerosol-size distribution using an idealized composition. There are certainly conditions, like the elevated concentrations encountered during CF-18, where assuming a pure composition is not sufficient for characterizing the CCN population. The measurements made during the CRYSTAL-FACE campaign establish new instrumentation for accurate in situ CCN measurements for use in future campaigns.

[46] **Acknowledgments.** The authors acknowledge Athanasios Nenes for assistance with simulating the performance of the CCN instruments. This work was supported by National Aeronautics and Space Administration grant NAG5-11549 and the Office of Naval Research.

References

- Albrecht, B., Aerosols, cloud microphysics and fractional cloudiness, *Science*, 245, 1227–1230, 1989.
- Bigg, E. K., Discrepancy between observation and prediction of concentrations of cloud condensation nuclei, *Atmos. Res.*, 20, 82–86, 1986.
- Cantrell, W., G. Shaw, C. Leck, L. Granat, and H. Cachier, Relationships between cloud condensation nuclei spectra and aerosol particles on a south-north transect of the Indian Ocean, *J. Geophys. Res.*, 105, 15,313–15,320, 2000.
- Cantrell, W., G. Shaw, G. R. Cass, Z. Chowdhury, L. S. Hughes, K. A. Prather, S. A. Guazzotti, and K. R. Coffee, Closure between aerosol particles and cloud condensation nuclei at Kaashidhoo Climate Observatory, *J. Geophys. Res.*, 106, 28,711–28,718, 2001.

- Charlson, R. J., J. H. Seinfeld, A. Nenes, M. Kulmala, A. Laaksonen, and M. C. Facchini, Reshaping the theory of cloud formation, *Science*, 292, 2025–2026, 2001.
- Chuang, P. Y., D. R. Collins, H. Pawlowska, J. R. Snider, H. H. Jonsson, J.-L. Brenguier, R. C. Flagan, and J. H. Seinfeld, CCN measurements during ACE-2 and their relationship to cloud microphysical properties, *Tellus, Ser. B*, 52, 843–867, 2000a.
- Chuang, P. Y., A. Nenes, J. N. Smith, R. C. Flagan, and J. H. Seinfeld, Design of a CCN instrument for airborne measurement, *J. Atmos. Oceanic Technol.*, 17, 1005–1019, 2000b.
- Covert, D. S., J. L. Gras, A. Wiedensohler, and F. Stratmann, Comparison of directly measured CCN with CCN modeled from the number-size distribution in the marine boundary layer during ACE I at Cape Grim, Tasmania, *J. Geophys. Res.*, 103, 16,597–16,608, 1998.
- Cruz, C. N., and S. N. Pandis, The effect of organic coatings on the cloud condensation nuclei activation of inorganic atmospheric aerosol, *J. Geophys. Res.*, 103, 13,111–13,123, 1998.
- Durkee, P. A., et al., The impact of ship-produced aerosols on the microstructure and albedo of warm marine stratocumulus clouds: A test of MAST hypotheses Ii and Iii, *J. Atmos. Sci.*, 57, 2554–2569, 2000.
- Garrett, T. J., L. F. Radke, and P. V. Hobbs, Aerosol effects on cloud emissivity and surface longwave heating in the arctic, *J. Atmos. Sci.*, 59, 769–778, 2002.
- Hegg, D. A., L. F. Radke, and P. V. Hobbs, Measurements of Aitken nuclei and cloud condensation nuclei in the marine atmosphere and their relation to the DMS-cloud-climate hypothesis, *J. Geophys. Res.*, 96, 18,727–18,733, 1991.
- Hegg, D. A., R. J. Ferek, and P. V. Hobbs, Cloud condensation nuclei over the Arctic Ocean in early spring, *J. Appl. Meteorol.*, 34, 2076–2082, 1995.
- Hegg, D. A., S. Gao, W. Hoppel, G. Frick, P. Caffrey, W. R. Leaitch, N. Shantz, J. Ambrusko, and T. Albrechtski, Laboratory studies of the efficiency of selected organic aerosols as CCN, *Atmos. Res.*, 58, 155–166, 2001.
- Hitzenberger, R., A. Berner, H. Giebl, R. Kromp, S. M. Larson, A. Rouc, A. Koch, S. Marischka, and H. Puxbaum, Contribution of carbonaceous material to cloud condensation nuclei concentrations in European background (Mt. Sonnblick) and urban (Vienna) aerosols, *Atmos. Environ.*, 33, 2647–2659, 1999.
- Hudson, J. G., Cloud condensation nuclei near marine cumulus, *J. Geophys. Res.*, 98, 2693–2702, 1993.
- Hudson, J. G., and P. R. Frisbie, Surface cloud condensation nuclei and condensation nuclei measurements at Reno, Nevada, *Atmos. Environ., Part A*, 25, 2285–2299, 1991.
- Hudson, J. G., and S. S. Yum, Maritime-continental drizzle contrasts in small cumuli, *J. Atmos. Sci.*, 58, 915–926, 2001.
- Intergovernmental Panel on Climate Change (IPCC), *Climate Change 2001: The Scientific Basis*, edited by J. T. Houghton et al., Cambridge Univ. Press, New York, 2001.
- Ji, Q., G. E. Shaw, and W. Cantrell, A new instrument for measuring cloud condensation nuclei: Cloud condensation nucleus “remover”, *J. Geophys. Res.*, 103, 28,013–28,019, 1998.
- Johnson, D. W., S. R. Osborne, and J. P. Taylor, The effects of a localized aerosol perturbation on the microphysics of a stratocumulus cloud layer, in *Nucleation and Atmospheric Aerosols 1996*, edited by M. Kulmala and P. E. Wagner, Elsevier Sci., New York, 1996.
- Liu, P. S. K., W. R. Leaitch, C. M. Banic, S.-M. Li, D. Ngo, and W. J. Megaw, Aerosol observations at Chebogue Point during the 1993 North Atlantic Regional Experiment: Relationships among cloud condensation nuclei, size distribution, and chemistry, *J. Geophys. Res.*, 101, 28,971–28,990, 1996.
- Martin, G. M., D. W. Johnson, and A. Spice, The measurement and parameterization of effective radius of droplets in warm stratocumulus clouds, *J. Atmos. Sci.*, 51, 1823–1842, 1994.
- Nenes, A., P. Y. Chuang, R. C. Flagan, and J. H. Seinfeld, A theoretical analysis of cloud condensation nucleus (CCN) instruments, *J. Geophys. Res.*, 106, 3449–3474, 2001.
- Nenes, A., R. J. Charlson, M. C. Facchini, M. Kulmala, A. Laaksonen, and J. H. Seinfeld, Can chemical effects on cloud droplet number rival the first indirect effect?, *Geophys. Res. Lett.*, 29(17), 1848, doi:10.1029/2002GL015295, 2002.
- Ramanathan, V., R. D. Cess, E. F. Harrison, P. Minnis, B. R. Barkstrom, E. Ahmad, and D. Hartmann, Cloud-radiative forcing and climate: Results from the Earth Radiation Budget Experiment, *Science*, 243, 57–63, 1989.
- Raymond, T. M., and S. N. Pandis, Cloud activation of single-component organic aerosol particles, *J. Geophys. Res.*, 107(D24), 4787, doi:10.1029/2002JD002159, 2002.
- Roberts, G. C., P. Artaxo, J. Zhou, E. Swietlicki, and M. O. Andreae, Sensitivity of CCN spectra on chemical and physical properties of aerosol: A case study from the Amazon Basin, *J. Geophys. Res.*, 107(D20), 8070, doi:10.1029/2001JD00583, 2002.
- Rogers, C. F., and P. Squires, A new device for studies of cloud condensation nuclei active at low supersaturations, in *Atmospheric Aerosols and Nuclei: Proceedings of the Ninth International Conference on Atmospheric Aerosols, Condensation, and Ice Nuclei Held at University College, Galway, Ireland, 21–27 September, 1977*, edited by A. F. Roddy and T. C. O’Connor, Galway Univ. Press, Ireland, 1981.
- Rosenfeld, D., TRMM observed first direct evidence of smoke from forest fires inhibiting rainfall, *Geophys. Res. Lett.*, 26, 3105–3108, 1999.
- Rosenfeld, D., Suppression of rain and snow by urban and industrial air pollution, *Science*, 287, 1793–1796, 2000.
- Sax, R. I., and J. G. Hudson, Continentality of the south Florida summer-time CCN aerosol, *J. Atmos. Sci.*, 38, 1467–1479, 1981.
- Seinfeld, J. H., and S. N. Pandis, *Atmospheric Chemistry and Physics: From Air Pollution to Climate Change*, 1326 pp., John Wiley, Hoboken, N. J., 1998.
- Snider, J. R., and J.-L. Brenguier, Cloud condensation nuclei and cloud droplet measurements during ACE-2, *Tellus, Ser. B*, 52, 828–842, 2000.
- Twomey, S., The composition of cloud nuclei, *J. Atmos. Sci.*, 28, 377–381, 1971.
- Twomey, S., Influence of pollution on the short-wave albedo of clouds, *J. Atmos. Sci.*, 34, 1149–1152, 1977.
- Wang, J., R. C. Flagan, and J. H. Seinfeld, A differential mobility analyzer (DMA) system for submicron aerosol measurements at ambient relative humidity, *Aerosol Sci. Technol.*, 37, 46–52, 2003.
- Wood, R., et al., Boundary layer and aerosol evolution during the 3rd Lagrangian experiment of ACE-2, *Tellus, Ser. B*, 52, 401–422, 2000.
- Zhou, J., E. Swietlicki, O. H. Berg, P. P. Aalto, K. Hämeri, E. D. Nilsson, and C. Leck, Hygroscopic properties of aerosol particles over the central Arctic Ocean during summer, *J. Geophys. Res.*, 106, 32,111–32,123, 2001.

R. C. Flagan, T. A. Rissman, J. H. Seinfeld, T. M. VanReken, and V. Varutbangkul, Department of Chemical Engineering, California Institute of Technology, Mail Code 210-41, 1200 East California Boulevard, Pasadena, CA 91125, USA. (flagan@caltech.edu; rissman@its.caltech.edu; seinfeld@caltech.edu; vanreken@its.caltech.edu; tomtor@its.caltech.edu)

H. H. Jonsson, Center for Interdisciplinary Remotely Piloted Aircraft Studies, United States Naval Postgraduate School, 3240 Imjin Road, range #510, Marina, CA 93633, USA. (hjonsson@nps.navy.mil)

G. C. Roberts, Center for Atmospheric Sciences, Scripps Institution of Oceanography, 9500 Gilman Drive #0239, San Diego, CA 92093, USA. (greg@hji.ucsd.edu)

Appendix D

USE OF IN SITU CLOUD CONDENSATION NUCLEI, EXTINCTION,
AND AEROSOL SIZE DISTRIBUTION MEASUREMENTS
TO TEST A METHOD FOR RETRIEVING CLOUD CONDENSATION NUCLEI
PROFILES FROM SURFACE MEASUREMENTS*

*Full Citation: Ghan, S. J., T. A. Rissman, R. Elleman, R. A. Ferrare, D. Turner, C. Flynn, J. Wang, J. Ogren, J. Hudson, H. H. Jonsson, T. VanReken, R. C. Flagan, and J. H. Seinfeld (2006), Use of in situ cloud condensation nuclei, extinction, and aerosol size distribution measurements to test a method for retrieving cloud condensation nuclei profiles from surface measurements, *Journal of Geophysical Research*, 111(D5), D05S10, doi: 10.1029/2004JD005752.

© 2006 American Geophysical Union (AGU). This appendix is reprinted with permission from the American Geophysical Union.

Use of in situ cloud condensation nuclei, extinction, and aerosol size distribution measurements to test a method for retrieving cloud condensation nuclei profiles from surface measurements

Steven J. Ghan,¹ Tracey A. Rissman,² Robert Elleman,³ Richard A. Ferrare,⁴
David Turner,¹ Connor Flynn,¹ Jian Wang,⁵ John Ogren,⁶ James Hudson,⁷
Hafliði H. Jonsson,⁸ Timothy VanReken,² Richard C. Flagan,² and John H. Seinfeld²

Received 28 December 2004; revised 21 April 2005; accepted 19 July 2005; published 19 January 2006.

[1] If the aerosol composition and size distribution below cloud are uniform, the vertical profile of cloud condensation nuclei concentration can be retrieved entirely from surface measurements of CCN concentration and particle humidification function and surface-based retrievals of relative humidity and aerosol extinction or backscatter. This provides the potential for long-term measurements of CCN concentrations near cloud base. We have used a combination of aircraft, surface in situ, and surface remote sensing measurements to test various aspects of the retrieval scheme. Our analysis leads us to the following conclusions. The retrieval works better for supersaturations of 0.1% than for 1% because CCN concentrations at 0.1% are controlled by the same particles that control extinction and backscatter. If in situ measurements of extinction are used, the retrieval explains a majority of the CCN variance at high supersaturation for at least two and perhaps five of the eight flights examined. The retrieval of the vertical profile of the humidification factor is not the major limitation of the CCN retrieval scheme. Vertical structure in the aerosol size distribution and composition is the dominant source of error in the CCN retrieval, but this vertical structure is difficult to measure from remote sensing at visible wavelengths.

Citation: Ghan, S. J., et al. (2006), Use of in situ cloud condensation nuclei, extinction, and aerosol size distribution measurements to test a method for retrieving cloud condensation nuclei profiles from surface measurements, *J. Geophys. Res.*, *111*, D05S10, doi:10.1029/2004JD005752.

1. Introduction

[2] One of the greatest sources of uncertainty in estimates of global climate change by climate models is in the treatment of indirect effects of aerosols on cloud optical depth through the role of aerosols as cloud condensation nuclei (CCN). All cloud droplets form on aerosol particles, so the CCN concentration has a powerful influence on droplet number concentration. However, the maximum supersaturation (which largely determines the number of CCN activated) in updrafts depends on the updraft velocity, which is highly variable within the droplet nucleation zone of clouds. Furthermore, droplet number is reduced by

evaporation, by droplet collision and coalescence with other droplets and with precipitating drops, and the precipitation process (which reduces the liquid water path of the cloud) which depends on both the mean and the dispersion of the droplet number size distribution [Liu and Daum, 2002].

[3] These complicating factors make it very difficult to represent aerosol indirect effects in climate models, to evaluate that representation, and to isolate the aerosol indirect effect from field measurements. Aircraft measurements have been used to evaluate droplet nucleation models [Lin and Leaitch, 1997; Gultepe et al., 1998; Yum and Hudson, 2002; Hudson and Yum, 2002; Snider et al., 2003; Conant et al., 2004; Peng et al., 2005], but such high-quality measurements are too costly to permit the collection of the thousands of independent samples needed to isolate the indirect effect in models and observations. Moreover, they do not permit the simultaneous measurement of cloud base properties (updraft velocity and CCN concentration) and column integrated properties (liquid water path and optical depth). Satellite retrievals provide a large sample size of measurements of column integrated properties [Han et al., 1998], but cannot provide estimates of updraft velocity and CCN concentration at cloud base. Surface in situ measurements on mountaintops [Hallberg et al., 1997; Menon and Saxena, 1998; Menon et al., 2002] provide an

¹Pacific Northwest National Laboratory, Richland, Washington, USA.

²California Institute of Technology, Pasadena, California, USA.

³Department of Atmospheric Science, University of Washington, Seattle, Washington, USA.

⁴NASA Langley Research Center, Hampton, Virginia, USA.

⁵Brookhaven National Laboratory, Upton, New York, USA.

⁶NOAA Climate Monitoring and Diagnostics Laboratory, Boulder, Colorado, USA.

⁷Desert Research Institute, Reno, Nevada, USA.

⁸Naval Postgraduate School, Monterey, California, USA.

economical source of measurements but are only useful when cloud base is near the elevation of the site. Consequently, there have been few attempts to use measured CCN concentration to evaluate the treatment of indirect effects in climate models [Menon *et al.*, 2003; Ovtchinnikov and Ghan, 2005].

[4] Surface-based remote sensing offers some appealing advantages to these other measurement strategies. By looking upward from the surface, profilers can provide useful information about the aerosol up to cloud base, about updrafts within the cloud, and about column-integrated cloud properties such as liquid water path and cloud optical depth. This permits long-term collection of data that can be used to isolate the aerosol indirect effect and evaluate the treatment of it in single column versions of global climate models.

[5] Kim *et al.* [2003] and Penner *et al.* [2004] used surface-based remote sensing of cloud optical depth and liquid water path to demonstrate how the dependence of optical depth on liquid water path (i.e., the droplet effective radius) varies from day to day, but only used a surface measure of the aerosol to relate to this dependence. Feingold *et al.* [2003] extended this method by relating the droplet effective radius to the aerosol extinction near cloud base.

[6] Although aerosol extinction might serve as a first approximation to CCN concentration, further improvements are possible by (1) accounting for the influence of water uptake on extinction and (2) using the resulting dry extinction to scale surface measurements of CCN concentration. This provides the ability to estimate the full CCN spectrum at cloud base, if the spectrum is measured at the surface.

[7] This method for estimating CCN concentration near cloud base was suggested by Ghan and Collins [2004, hereinafter referred to as GC]. In this retrieval, surface measurements of the CCN concentration $CCN(S, z_0)$ at supersaturation S are scaled by the ratio of the dry extinction (or 180° backscatter) profile $\sigma_{de}(z)$ to the dry extinction (or 180° backscatter) at or near the surface, $\sigma_{de}(z_0)$:

$$CCN(S, z) = CCN(S, z_0) \sigma_{de}(z) / \sigma_{de}(z_0) \quad (1)$$

The dry extinction (or 180° backscatter) profile $\sigma_{de}(z)$ is determined from the extinction (or 180° backscatter) profile at ambient humidity $\sigma_e(z)$ and the dependence of extinction (or 180° backscatter) on relative humidity, $f(RH(z))$:

$$\sigma_{de}(z) = \sigma_e(z) / f(RH(z)) \quad (2)$$

The aerosol particle humidification factor $f(RH)$ is measured at the surface and is assumed to apply at all levels up to cloud base using the retrieved relative humidity profile. GC describe the instruments that can be used to provide the necessary measurements for this retrieval. Anderson *et al.* [2000] and GC show that for RH up to 80%, $f(RH)$ for extinction is indistinguishable from $f(RH)$ for 180° backscatter. We will therefore use the same expression for both.

[8] The method assumes the humidification factor measured at the surface is representative of the humidification factor at altitude, and it assumes that the vertical structure of CCN concentration is identical to the vertical structure of dry extinction or backscatter. Since both extinction/

backscatter and CCN concentration are determined entirely by the size distribution of aerosol number, composition, and geometric shape, both of these assumptions are valid if (1) the aerosol size distribution (but not necessarily the total aerosol number) is independent of altitude, and (2) the aerosol composition and particle shape are independent of altitude. GC used in situ aerosol size distribution measurements, Mie theory, and Köhler theory to examine the vertical variability of the size distribution, but did not have the CCN or aerosol composition measurements needed to investigate the vertical variability of aerosol composition and shape. Clearly the impact of this variability on the retrieval also needs to be tested.

[9] In May 2003 the Atmospheric Radiation Measurement (ARM) program conducted an aerosol intensive observation period (IOP) that provides the data needed to test assumptions A and B. The goal of this study is to evaluate the GC CCN retrieval and to understand what is limiting its performance. In section 2 we describe the design of the ARM experiment, and in section 3 we describe the use of the measurements to evaluate the performance of the retrieval scheme. Conclusions are summarized in section 4.

2. Experiment Design

2.1. Instruments and Measurements

[10] To distinguish between different sources of error in the retrieval scheme, a variety of measurements were collected. These include both in situ and remote sensing measurements. In situ measurements were collected both from aircraft and at the surface.

2.1.1. Measurements From Aircraft

[11] In situ measurements include (1) CCN concentration, (2) aerosol size distribution, (3) relative humidity, (4) aerosol scattering and absorption, and (5) aerosol particle humidification factor. Although in situ measurements of aerosol composition and shape are not available (except for composition at the ground), the measurements of CCN concentration, aerosol scattering and absorption, and humidification provide the opportunity to test the influence of variability in aerosol composition and shape on the CCN retrieval because each of these fields depend on aerosol composition and shape.

[12] The CCN concentrations were measured from the Center for Interdisciplinary Remotely Piloted Aircraft Studies (CIRPAS) Twin Otter aircraft every second by the California Institute of Technology (Caltech) CCN counter. The CCN counter has three columns, each operating with a linear axial temperature gradient, allowing each column to achieve one supersaturation. Only two of the columns operated during the IOP. Because of undetected problems with the detector on column 2, the supersaturation for column 2 could not be determined for any of the flights, so the CCN concentrations for column 2 will not be considered here. The operating supersaturation of column 1 was determined from the critical supersaturation of $(\text{NH}_4)_2\text{SO}_4$ particles with dry size such that 50% of a controlled size are able to activate in the CCN counter. The Köhler theory [Brechtel and Kreidenweis, 2000a, 2000b] is used to determine the critical supersaturation as a function of dry size (activation diameter d_{pc}), and a differential mobility analyzer (DMA) is used to select a

Table 1. Flight Summary With Operating Conditions for CCNC3 Column 1

Flight Number	Date	Flight Begin Time, UTC	Flight End Time, UTC	Flight Length, hours	Activation Diameter, nm	Operating Supersaturation, %
6	14 May	1553	2019	4.4	15 ± 0.8	2.8 ± 0.2
7	14 May	2124	2248	1.4	15 ± 0.8	2.8 ± 0.2
8	15 May	1634	1909	2.6	15 ± 0.8	2.8 ± 0.2
9	17 May	1402	1805	4.0	13 ± 0.6	3.6 ± 0.4
10	18 May	1543	1745	2.0	15 ± 0.8	2.8 ± 0.2
12	21 May	1551	1847	2.9	18 ± 0.9	2.1 ± 0.2
13	22 May	1325	1813	4.8	18 ± 0.9	2.1 ± 0.2
14	25 May	1852	2212	3.3	18 ± 0.9	2.1 ± 0.2
15	27 May	1420	1929	5.2	18 ± 0.9	2.1 ± 0.2
16	28 May	1824	2205	3.7	18 ± 0.9	2.1 ± 0.2
17	29 May	1411	1751	3.7	18 ± 0.9	2.1 ± 0.2

variety of dry diameters which are then split to the CCN counter and a TSI Model 3010 condensation particle counter. Droplet density is calculated from Tang's polynomials [Tang and Munkelwitz, 1994]; the full Pitzer model [Pitzer, 1973; Pitzer and Mayorga, 1973] is used to calculate the osmotic coefficient; surface tension values from Pruppacher and Klett [1997] are used for surface tension. The calibrated activation diameters and the operating supersaturations for Column 1 are given in the legend in Table 1.

[13] The supersaturations listed in Table 1 are quite high, all above 2%. Such high supersaturations are typically expected only for strong updrafts and clean conditions. Moreover, unless particles have high insoluble contents, most of the particles that can be activated at such high supersaturations are usually quite small, with radius between 20 and 100 nm (although larger particles are also activated, their number concentrations are usually much smaller than those of particles smaller than 100 nm radius). These particles have little impact on extinction or backscatter, which are most sensitive to particles with radius between 100 and 600 nm [Ghan and Collins, 2004]. Thus extinction and backscatter will be well correlated with CCN concentration at such supersaturations only if the particles have high insoluble contents or if the aerosol size distribution varies little with altitude so that the concentration of particles with radii between 20 and 100 nm varies in concert with the concentration of particles with radii between 100 and 600 nm. These in situ CCN measurements therefore provide a difficult test of the CCN retrieval scheme. CCN concentration at lower supersaturations, which is dominated by larger particles that produce stronger extinction and backscatter signatures, should be more accurately retrieved by the scheme.

[14] The aerosol size distribution was measured at 72.5 s intervals at ambient relative humidity by a Caltech DMA [Wang et al., 2003]. Particles were dried to below 25% RH prior to measurements. The sizes are centered at 23 diameters ranging from 19 to 620 nm.

[15] Relative humidity is calculated from the ambient temperature (calculated from Rosemount total temperature and true airspeed) and dew point temperature (measured by Edgetech EG&G chilled mirror).

[16] Aerosol scattering at wavelengths of 450, 550, and 700 nm was measured every 8 s by a TSI model 3563 nephelometer for dry conditions. The data have been corrected for nonidealities and corrected to ambient temperature and pressure [Anderson and Ogren, 1998]. Aerosol absorption at wavelengths of 467, 530, and 660 nm is

measured by a Particle Soot Absorption Photometer (PSAP). The scattering data have been adjusted to the PSAP wavelengths using the Ångström exponent. Unrealistic data points due to instrument malfunction, adjustment in flight, and data acquisition problems have been removed from all data sets.

[17] The humidification factor at a wavelength of 540 nm is approximated by

$$f(RH) = \left(\frac{1 - RH_{lo}}{1 - RH} \right)^\gamma \quad (3)$$

where γ is determined from a fit to humidigraph scattering measurements at two different humidities:

$$\gamma = \frac{\ln(\sigma_{hi}/\sigma_{lo})}{\ln[(1 - RH_{lo})/(1 - RH_{hi})]} \quad (4)$$

where RH_{lo} and RH_{hi} are typically 30% and 80%, respectively.

2.1.2. Surface Measurements

[18] At the surface, both in situ and remote sensing measurements were collected at the ARM Climate Research Facility (CRF) central site near Lamont Oklahoma. Remote sensing measurements were provided by the CRF Raman lidar (CARL) and the micropulse lidar (MPL). CARL provides retrievals of both aerosol extinction and 180° backscatter at a wavelength of 355 nm [Ferrare et al., 2001; Turner et al., 2002], and relative humidity is estimated from the Raman lidar retrieval of absolute humidity and from a retrieval of temperature from an Atmospheric Emitted Radiance Interferometer (AERI). The Raman lidar retrievals are performed every 10 min and interpolated to a vertical resolution of 39 m. Comparisons of the CARL aerosol and water vapor profiles with these additional data sets acquired during the IOP as well as trends derived from long-term CARL measurements revealed several issues with the CARL data that adversely impacted retrievals of both aerosol and water vapor profiles. The sensitivity of the CARL had significantly declined since the end of 2001. This loss of sensitivity has greatly impacted the quality of the CARL aerosol backscattering and extinction profiles derived since this time and during the Aerosol IOP. Therefore the automated algorithms used to derive aerosol and water vapor profiles from the CARL data were modified in an attempt to reduce or remove these adverse effects. The extensive modifications made to the CARL automated

algorithms reduced but could not eliminate these adverse effects [Ferrare *et al.*, 2004, 2006]. Modifications and upgrades performed during 2004 have dramatically enhanced the sensitivity of CARL to surpass all previous performance levels [Turner and Goldsmith, 2005].

[19] The MPL provides vertical profiles of attenuated 180° backscatter every 30 s with 30 m vertical resolution. Current processing yields 10-min averaged profiles of aerosol extinction and 180° backscatter. However, in contrast to the Raman lidar technique, the MPL retrievals of extinction and backscatter are not truly independent, but are in fact related through an assumed constant extinction to backscatter ratio. This assumption will not always be valid, particularly in the case of separated aerosol layers. However, under well-mixed conditions the assumption typically has reasonable local validity.

[20] Schmid *et al.* [2006] compare in detail the Raman lidar and MPL retrievals of extinction with the in situ measurements collected during this IOP. We therefore will not compare the estimates here.

[21] Surface in situ measurements consisted of aerosol humidification and CCN spectra. Surface humidification measurements were provided by the Aerosol Observing System (AOS) humidograph system at the ARM Climate Research Facility [Sheridan *et al.*, 2001]. The same parametric representation for $f(RH)$, given by equation (3), is used. For consistency with the aircraft measurements, the humidification at 550 nm wavelength is used.

[22] CCN spectral measurements at the surface were provided by two Desert Research Institute CCN spectrometers [Hudson, 1989], which were operated over two different but overlapping supersaturation ranges. Concentrations at supersaturations between 0.03% and 1% are considered most accurate. The CCN concentrations were averaged over the period spanning the aircraft overflights. The time means will be used to scale the vertical distribution profile provided by dry extinction.

2.2. Platforms and Flight Patterns

[23] All airborne in situ measurements used in this study were collected from the CIRPAS Twin Otter, which has a cruising speed of about 50 m s⁻¹.

[24] The 2003 ARM aerosol IOP had a variety of objectives, but most required coincident in situ and remote sensing measurements of vertical profiles of aerosol and its microphysical and radiative properties. Thus, although a variety of aircraft flight patterns were employed on different days, useful data for testing the CCN retrieval scheme were collected on most flight days. Two flight patterns were most common: the spiral and the level legs. Spirals were typically performed with a 1 km diameter centered over the central site, with ascent/descent speeds of 2–3 m s⁻¹. Level legs were typically 15–30 km in length crossing over the central site, spaced every 500–1000 ft in altitude, with 180° turns between legs. All flight patterns were designed to prevent sampling of the aircraft's own exhaust.

2.3. Sampling

[25] Critical to the success of this study is the collocation of the aircraft and remote sensing measurements, both in space and time. To ensure this, samples were discarded unless all of the following conditions were met: (1) Aircraft

is within 30 km of SGP CF (36°N 37° 97° W 30'), (2) lidar samples at the same altitude as the aircraft and within 60 min of aircraft flyover, (3) cloud-free (number concentration of particles with diameter larger than 2.5 μm < 10 cm⁻³), (4) relative humidity <95%, and (5) estimated error in extinction retrieved from Raman lidar <50% of extinction. The 30 km and 60 min proximity criterion were determined from a compromise between the need to accumulate a sufficient number of samples and the need for collocation of in situ and remote sensing samples. We have found results to be insensitive to the spatial and temporal range of the sampling filter for distances between 5 and 30 km and time differences between 15 and 60 min. To permit comparison on a point-by-point basis, for each day the aircraft data were averaged over all the resulting samples within the 40 m thick lidar layers. This produces a single vertical profile of all fields for each day. However, values for many layers may not be defined, particularly for days without spiral flight patterns.

[26] To ensure a comparable evaluation of different retrievals, all quantities were sampled only when all sampling criteria were met. Although reliable in situ data were discarded, we felt it was more important to ensure a comparable evaluation than to have the most extensive sampling for each retrieval.

3. Analysis

[27] To evaluate the performance of the CCN retrieval scheme, we look at the data in three different ways. First we look at vertical profiles of normalized quantities to identify the vertical structure in the data and to see the relationships between different quantities. Then we use the full scheme to retrieve vertical profiles of CCN concentration. Finally, we look at vertical profiles of quantities that are sensitive to the size distribution and composition and hence can be used to determine whether the assumptions of the retrieval are valid.

3.1. Vertical Structure and Relationships

[28] The objective of this study is to determine how well the CCN retrieval scheme can determine the vertical profile of CCN concentration below cloud, and to understand what is limiting its performance. The measure of performance will be the agreement with in situ measurements of CCN concentration. To isolate errors due to differences between the CCN instruments on the ground and in the aircraft, we will compare vertical profiles of CCN concentration and dry extinction normalized by values at the lowest altitude available for all profiles. This still tests the validity of equation (1), but removes errors due to the very different designs and calibration procedures for the CCN instruments [Nenes *et al.*, 2001]. Errors in the measured variability of CCN (the gain) are not removed by normalization.

[29] Given the anchor point of the retrieval scheme at the surface, it is likely to perform well at altitudes near the surface. Such agreement is neither useful nor indicative of the performance of the retrieval scheme, because surface measurements without the scaling by dry extinction should provide close approximations to the CCN concentrations near the surface. We therefore have extended our evaluation up to 5 km above the surface. Although the performance of the scheme is likely to be worse far from the surface, such

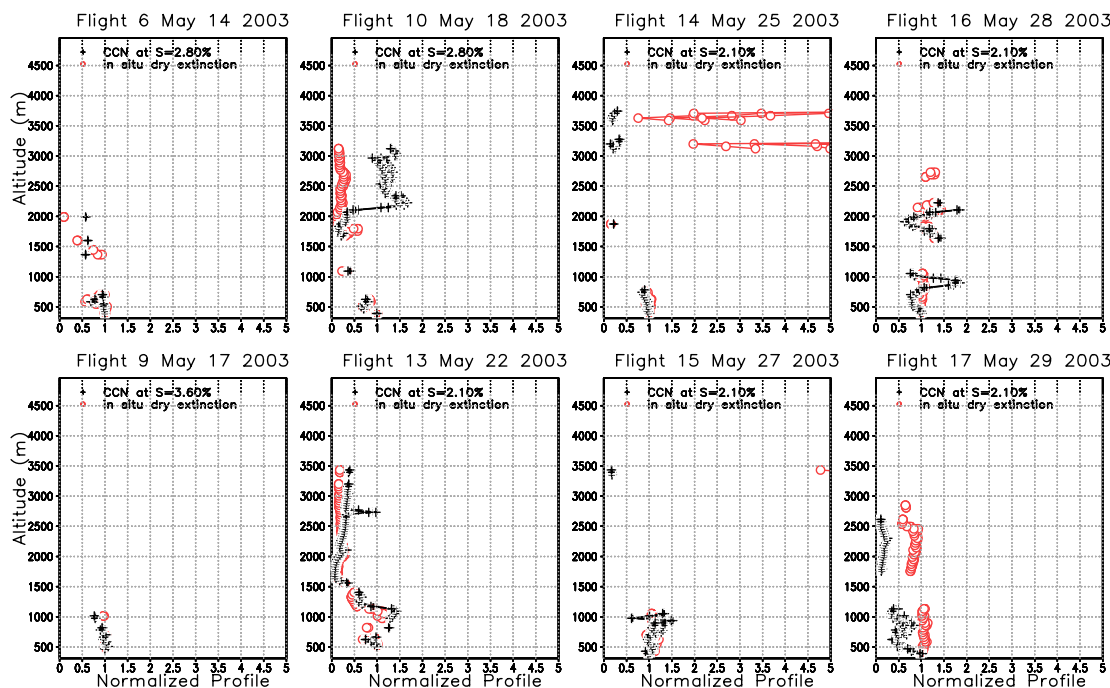


Figure 1. Vertical distribution of in situ measurements of the mean, mean plus standard error, and mean minus standard error of dry extinction (467 nm) and CCN concentration measured over the ARM site from the aircraft, at the supersaturation S indicated, on each of eight flights. Values have been normalized by the value at the lowest level with valid data for both profiles.

an evaluation tells us much more about the conditions that degrade the performance.

[30] Although normalization removes the absolute concentration from the evaluation and hence prevents examination of the skill in retrieving CCN variability from day to day, if much of that variability is captured by surface CCN measurements then there is little additional information for the retrieval to provide. Normalization focuses the evaluation on the additional information provided by the retrieval. We assume that surface CCN measurements provide reliable measurements of the variability of CCN concentrations near the surface.

[31] The retrievals of dry extinction and backscatter from surface instruments are subject to both retrieval error and sampling error. Before testing the validity of equation (1) using the retrieved dry extinction and backscatter, it is worth first testing using the in situ measurements of dry extinction. Figure 1 compares the vertical profile of the normalized in situ measurements of dry extinction (at 467 nm wavelength) with normalized in situ measurements of CCN for eight flights. The CCN concentration has considerable vertical structure, with concentrations varying by a factor of at least two and in most cases five. The vertical profile of normalized dry extinction closely follows that of CCN concentration on most flights, particularly within the lowest km above the surface. This agreement is surprising, considering the high supersaturation and hence (assuming the particles are hygroscopic) small characteristic size of the CCN measurements. Consistent with this finding, *Rissman et al.* [2006]

show that most CCN on these flights are highly insoluble and hence have lower hygroscopicity and larger sizes than highly soluble particles would have at that supersaturation. The larger size is consistent with the particles influencing extinction as well as CCN concentration.

[32] On some flights the vertical profile of normalized dry extinction does not follow that of CCN concentration. On flight 10 the normalized dry extinction significantly underestimates the normalized CCN concentration at altitudes between 2 and 3 km, suggesting a higher proportion of small particles (diameters less than 0.1 micron) there than near the surface; independent measurements of the particle size distribution confirm this. On flights 14 and 15 the normalized dry extinction increases dramatically above 3 km, while the normalized CCN concentration does not. This is due to the presence of an elevated plume of aged particles, most likely from forest fires in Siberia [*Damoah et al.*, 2004; *Jaffe et al.*, 2004]. DMA measurements show a large increase in the concentration of accumulation mode particles in the layer, which increases the extinction but not the CCN concentration. On flight 17, the normalized dry extinction overestimates the normalized CCN concentration at almost all levels, suggesting a greater presence of small particles near the surface.

[33] Table 2 lists 95% confidence limits of the square of the correlation between CCN concentration and in situ dry extinction for each flight. The confidence limits were determined using Fisher's Z transformation with the number of samples assumed to be the number of matching points in

Table 2. Ninety-Five Percent Confidence Intervals of Square of Correlation Between x and y for Eight Flights^a

x	y	Flight							
		6	9	10	13	14	15	16	17
CCN1	in situ ext	0.13–0.87	0.08–0.93	–0.19–0.02	0.75–0.90	–0.62 to –0.02	–0.92 to –0.57	0.12–0.64	0.41–0.78
CCN1	RL ext	–0.84 to –0.01	–0.38–0.60	–0.37 to –0.01	0.19–0.56	–0.90 to –0.52	–0.26–0.12	–0.01–0.32	0.59–0.86
CCN1	RL bscat	–0.70–0.07	–0.01–0.86	–0.37 to –0.01	0.39–0.71	–0.90 to –0.52	–0.23–0.14	0.00–0.38	0.59–0.86
CCN1	MPL ext	–0.88 to –0.06	0.82–0.99	–0.99–0.00	0.00–0.96	–0.26–0.60	–0.48–0.52
CCN1	MPL bscat	–0.87 to –0.04	0.17–0.93	–0.99 to –0.17	–0.10–0.92	–0.25–0.61	–0.69–0.26
in situ ext	RL ext	–0.86 to –0.02	–0.66–0.30	0.36–0.74	0.25–0.62	0.12–0.74	–0.20–0.17	0.07–0.56	0.56–0.84
in situ ext	MPL ext	–0.17–0.61	0.92–0.99	0.02–0.99	–0.03–0.94	–0.54–0.34	–0.41–0.58
CCN	in situ ext	–0.17–0.90	0.04–0.97	0.00–0.59	0.92–0.99	–0.79–0.00	–0.76–0.54	–0.40–0.09	0.38–0.87
@ S = 0.1%									
CCN	in situ ext	–0.41–0.82	0.08–0.97	–0.51–0.00	0.63–0.93	–0.84 to –0.03	–0.67–0.65	–0.06–0.43	0.46–0.90
@ S = 1%									
CCN	CCN1	–0.31–0.86	0.02–0.94	0.00–0.57	0.77–0.96	0.89–0.99	–0.82–0.40	–0.21–0.36	0.60–0.93
@ S = 0.1%									
CCN	CCN1	–0.52–0.76	0.14–0.96	0.31–0.84	0.77–0.96	0.92–0.99	–0.78–0.49	0.00–0.71	0.28–0.84
@ S = 1%									

^aNegative values denote negative correlations. Ext denotes extinction, and bscat denotes 180° backscatter.

Figure 1. In situ dry extinction explains 75–90% of the variance of CCN concentration on flight 13 and 41–78% of the variance on flight 17. The correlation might also be high on flights 6, 9, and 16, but the sample size is too small to permit a reliable estimate of the correlation. The high correlation on flight 15 is a negative correlation due to the elevated plume at 3400 m, the negative correlation indicating a failure of the retrieval scheme. The poor correlation on

two of the other three flights reflects deviations in the upper troposphere; dry extinction is highly correlated with CCN concentration in the lowest 1–2 km on those flights.

[34] The Raman lidar (RL) is one potential aerosol remote sensing tool for scaling surface CCN measurements. It provides retrievals of both extinction and backscatter at 355 nm wavelength. Figure 2 compares vertical profiles of the dry extinction and backscatter, normalized by the value

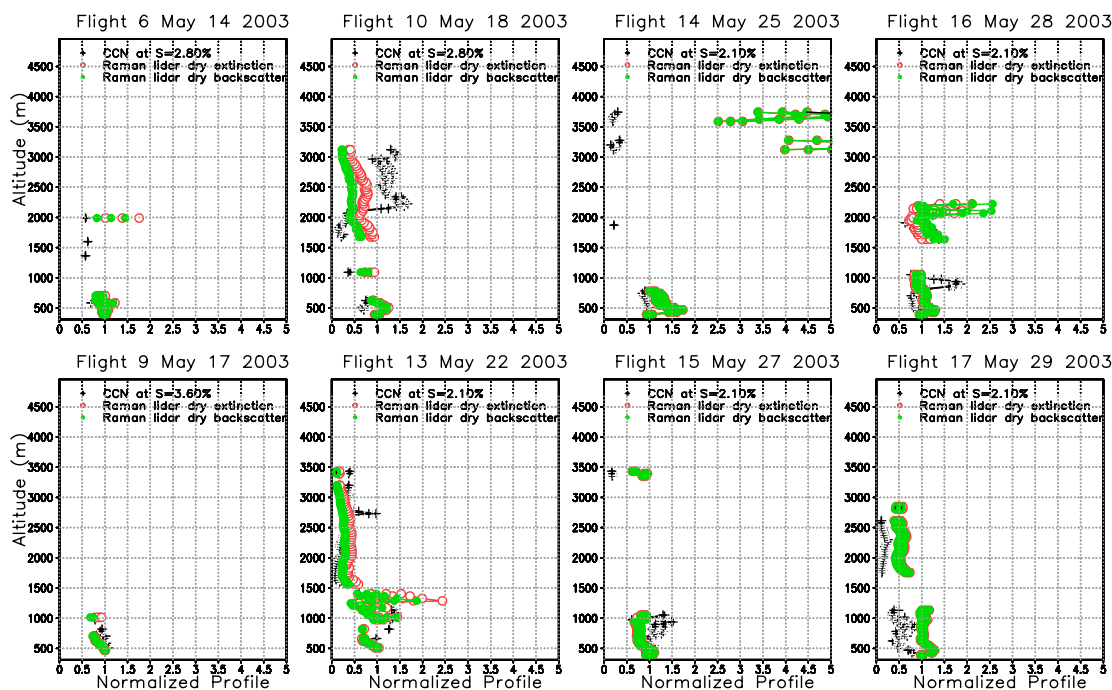


Figure 2. Vertical distribution of the mean, mean plus standard error, and mean minus standard error of CCN concentration measured over the ARM site from the aircraft and Raman lidar retrievals of extinction and backscatter, adjusted to dry conditions using the humidification factor measured on the aircraft, on each of eight flights. Values have been normalized by the value at the lowest level with valid data for all profiles.

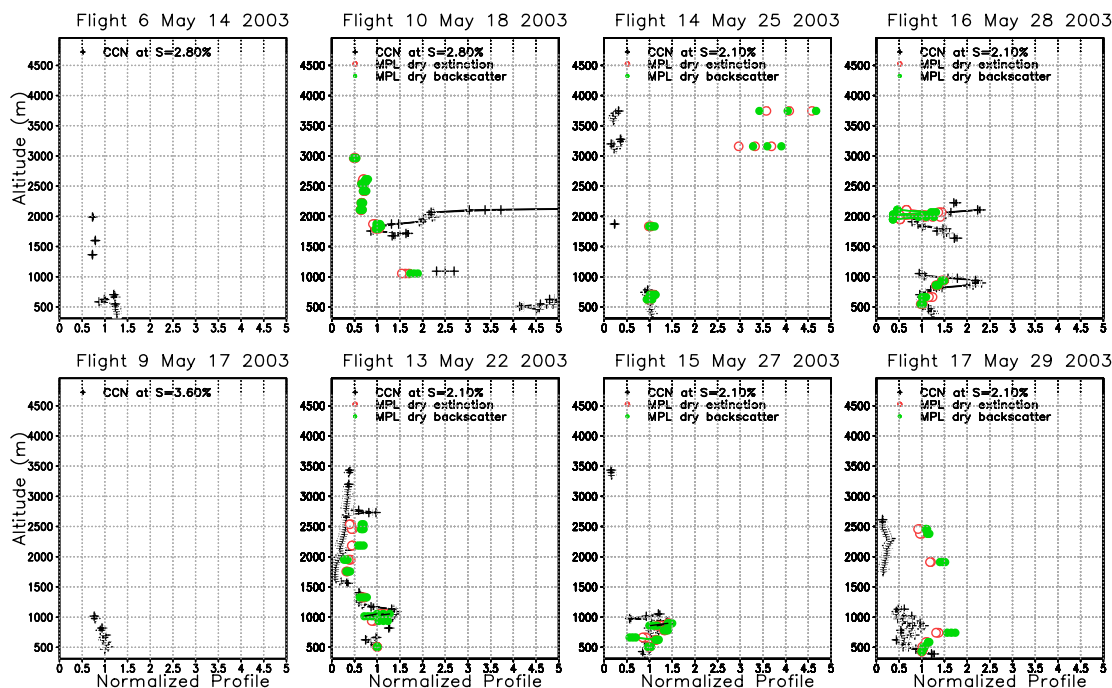


Figure 3. Vertical distribution of the mean, mean plus standard error, and mean minus standard error of CCN concentration measured over the ARM site from the aircraft and micropulse lidar retrievals of extinction and backscatter, adjusted to dry conditions using the humidification factor measured on the aircraft, on each of eight flights. Values have been normalized by the value at the lowest level with valid data for all profiles.

at the lowest level, with the vertical profile of the normalized CCN concentration. To separate errors due to remote sensing of relative humidity and the use of surface humidification measurements, the extinction and backscatter retrieved at ambient humidity have been adjusted to dry conditions using the humidification factor measured on aircraft instead of at the surface (retrievals adjusted using surface measurements of humidification and remote sensing of relative humidity will be considered later in this section).

[35] In general the Raman lidar retrievals of vertical profiles of normalized dry extinction and backscatter exhibit similar vertical structure and are comparably but somewhat more weakly correlated with CCN concentration compared with the in situ measurements of dry extinction. Many of the same profile differences evident for in situ measurements in Figure 1 are also evident for the Raman lidar retrievals shown in Figure 2. On flights 10 and 14 the same differences between normalized CCN concentration and normalized dry extinction above 2 km are evident for both the in situ and remote measurements of dry extinction, producing negative correlations between extinction and CCN concentration. The Raman lidar is clearly showing that dry extinction should not be used to scale CCN concentration for those conditions. On two other flights (13 and 17) the normalized dry extinction and backscatter follow the normalized CCN concentration rather well, with correlations (Table 2) comparable to those for in situ measurements of

dry extinction. On flights 10 and 16 the retrieved dry extinction and backscatter both correlate poorly with CCN concentration, as is the case for the in situ measurement of dry extinction. On flights 6, 9 and 15 the CCN concentration is correlated much less with the Raman lidar retrievals than the in situ extinction, but for all three flights there is very little vertical structure in CCN concentration.

[36] There is little difference between the normalized dry extinction and backscatter profiles on most days, suggesting that the extinction/backscatter ratio profile is nearly uniform on those days.

[37] The micropulse lidar (MPL) is another potential aerosol remote sensing tool for scaling surface CCN measurements. It provides retrievals of both extinction and backscatter at 523 nm wavelength, but assumes a constant extinction/backscatter ratio. Figure 3 compares vertical profiles of the dry extinction and backscatter, normalized by the value at the lowest level, with the vertical profile of the normalized CCN concentration. The extinction and backscatter retrieved at ambient humidity have been adjusted to dry conditions using the humidification factor measured on aircraft instead of at the surface.

[38] The normalized dry extinction and backscatter retrieved by the MPL do not appear to explain much of the variance of normalized CCN concentration on all flights except flight 13. The square of the correlation (Table 2) is at least 80% for flight 13, but the sample size is so low for the

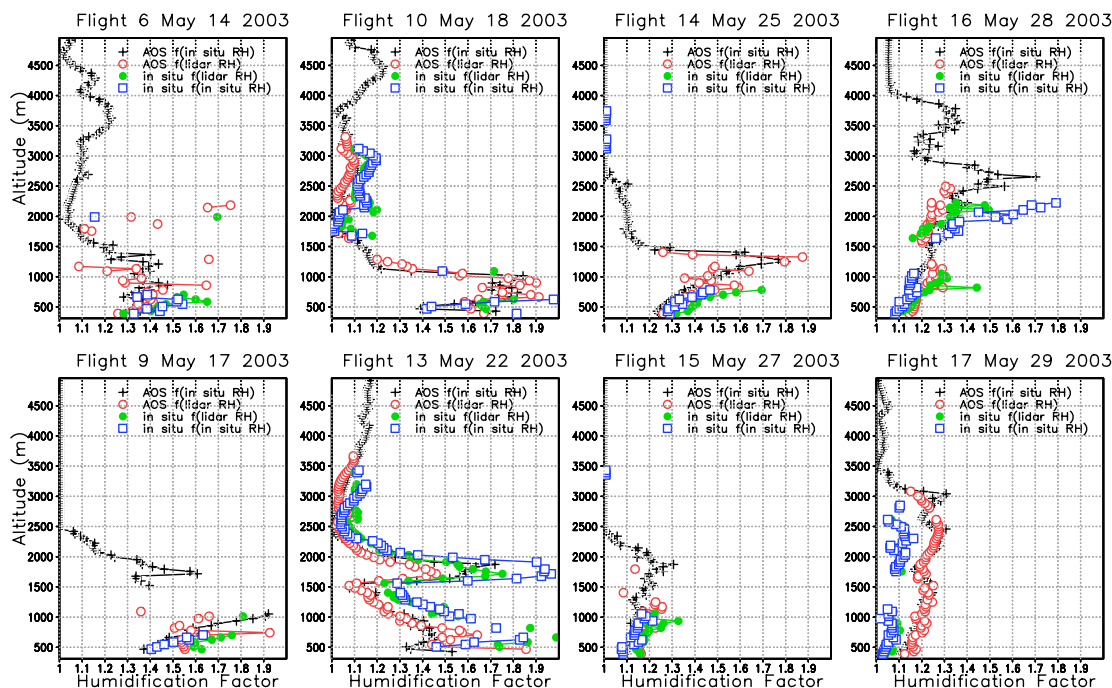


Figure 4. Vertical profiles of the humidification factor determined from the parameters of the humidification factor measured either from aircraft (in situ) or from the surface (AOS) and using relative humidity measured either from aircraft or from the Raman lidar retrieval of water vapor.

other flights that the uncertainty in the correlation is too large to draw conclusions. On most days there is little difference between the normalized extinction and backscatter because the MPL retrieval uses a single value for the extinction/backscatter ratio for each retrieval, but there are differences on some days because different retrievals (and different extinction/backscatter ratios) are used for different altitudes because the aircraft sampled the altitudes over the site at different times during its typical 4-hour flight.

[39] Given the high correlation between CCN concentration and in situ dry extinction, it is not surprising that the correlation between CCN concentration and remote sensing estimates of dry extinction is related to how well the remote sensing estimates correlate with the in situ measurement (Table 2). The correlations between CCN concentration and remote sensing estimates of dry extinction are only high if the correlations between CCN concentration and in situ dry extinction are high and the correlation between in situ dry extinction and estimates from remote sensing are also high. The former is true if the aerosol size distribution and composition are uniform or if the supersaturation is below 0.1% (GC), and latter is true only if the remote sensing estimates are not degraded by retrieval limitations or sampling errors. Both conditions must be satisfied before the remote sensing estimates are highly correlated with CCN concentration.

[40] How important is humidification in the retrieval, and how great is the uncertainty in its retrieval? Figure 4 shows vertical profiles of the humidification factor determined four

ways, using the parameters of the humidification factor measured either from aircraft or from the surface, and using relative humidity measured either from aircraft or from the Raman lidar retrieval of water vapor. The humidification factor varies widely, as much as a factor of two, in the vertical on some days. Clearly this vertical structure must be accounted for in the retrieval. On most days all four vertical profiles agree remarkably well, to within 20%, suggesting that retrieval of the vertical distribution of the humidification factor will not be a significant error source in the retrieval. The consistency of the humidification factor determined using in situ and remote sensing of relative humidity suggest that the retrieval of relative humidity is not a significant source of uncertainty, except as demonstrated on flight 13 when relative humidity approaches 100% and the humidification factor becomes large. The difference on flight 17 is clearly due to different values of the humidification exponent γ . The difference is evident even near the surface. It is not clear why the exponent is different on flight 17 but not on other flights.

[41] As stated previously, we would expect the CCN retrieval scheme to perform better at lower supersaturations. Although in situ CCN measurements on the Twin Otter are not available at supersaturations less than 2%, CCN concentrations at lower supersaturations can be estimated from Köhler theory using the measured size distribution and an assumed composition. We assume all particles are composed of ammonium sulfate. Although *Rissman et al.* [2006] conclude that a significant fraction of particles with

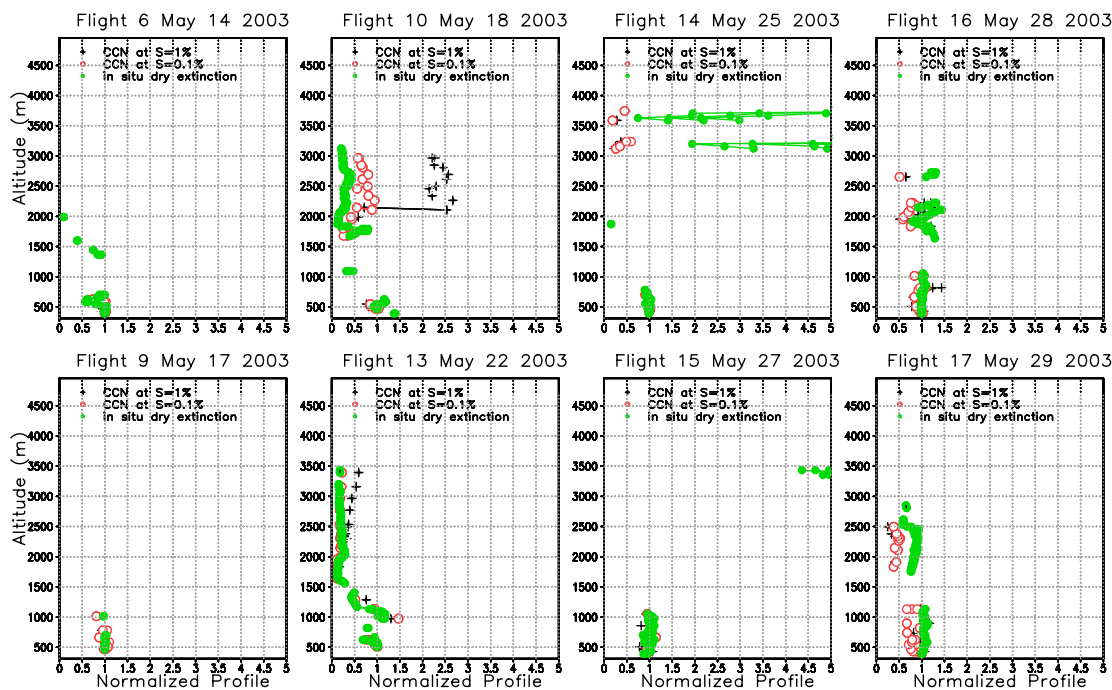


Figure 5. Vertical distribution of the mean, mean plus standard error, and mean minus standard error of in situ measurements of dry extinction and CCN concentration calculated from Köhler theory using aircraft measurements of aerosol size distribution at supersaturations of 0.1% and 1% on each of eight flights. Values have been normalized by the value at the lowest level with valid data.

diameter < 50 nm are dominated by insoluble material, we assume pure ammonium sulfate here simply to illustrate the dependence of the retrieval performance on particle size. Extinction depends much less on composition than on particle size at low relative humidity. We could easily choose a smaller hygroscopicity for the particles and a smaller critical supersaturation to focus on the same size range of particles. Figure 5 shows vertical profiles of the in situ measurement of dry extinction and the CCN concentration estimated at 0.1% and 1% supersaturation, all normalized by their values at the lowest available level. The vertical profile of the normalized CCN concentration estimated at 1% supersaturation is very similar to the CCN measurements shown in Figure 1. Indeed, as listed in Table 2 the squared correlation between the CCN measurement and that estimated at 1% is at least 0.6 on all but three flights. As expected, the agreement between the dry extinction and estimated CCN concentration is clearly better for the CCN concentration at 0.1% than at 1%, particularly above the boundary layer for flights 10 and 13. This visual interpretation is confirmed by the higher squared correlation with dry extinction for CCN concentration estimated at 0.1% than at 1%, as listed in Table 2, for those flights. The better agreement at 0.1% is encouraging, because such a supersaturation is considered to be more typical of boundary layer clouds under continental conditions [Hudson and Yum, 2001, 2002; Yum and Hudson, 2002]. On flight 14 dry extinction above 3 km does not correlate well with the estimated CCN concentration at either supersaturation,

which suggests that the elevated plume there has a different size distribution or composition than in the boundary layer. For almost all flights correlations are higher if the soluble fraction of the particles is assumed to be 0.2 rather than 1.0, which shifts the mean size of CCN closer to the accumulation mode size of the particles that dominate extinction.

[42] Could sampling errors due to spatial/temporal variability explain the weaker relationship between CCN concentration and remote retrievals of dry extinction and backscatter than between CCN concentration and in situ measurements of dry extinction? We have found the relationship to be insensitive to the spatial and temporal range of the sampling filter for distances between 5 and 30 km and time differences between 15 and 60 min. Figure 6 provides further evidence that sampling errors for RH profiles are small. The relative humidity retrieved from Raman lidar measurements agrees remarkably well with in situ measurements. This suggests that spatial/temporal sampling error does not contribute much to the differences between the CCN profiles and the retrieved profiles of extinction and backscatter.

[43] We have noted that the presence of elevated layers of aerosol with very different size distributions or compositions can degrade the performance of the retrieval scheme. Della Monache *et al.* [2004] conclude that aerosol properties above the mixed layer are poorly correlated with those within the boundary layer. To further test this hypothesis, we have recalculated the correlations of Table 2 for only levels within the mixed layer. We use Heffter's [1980]

D05S10

GHAN ET AL.: CCN RETRIEVAL EVALUATION

D05S10

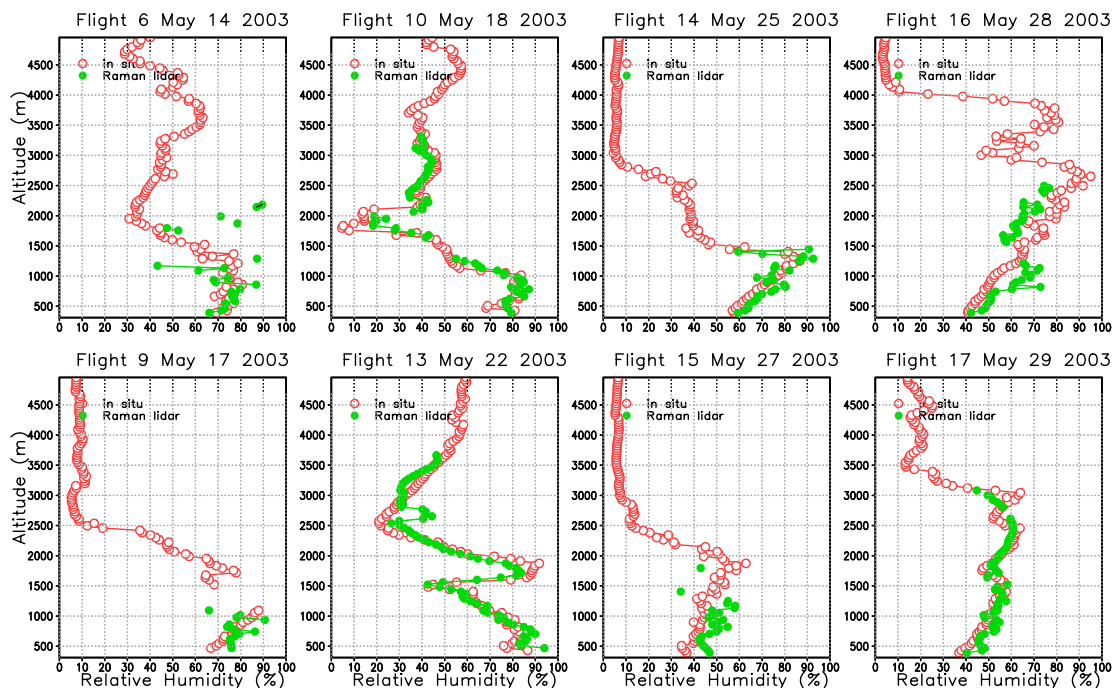


Figure 6. Vertical profile of relative humidity retrieved by Raman lidar and measured by aircraft for eight flights. Raman lidar retrievals are only if estimated error <25%.

definition of the mixed layer height, which is the lowest level in the inversion layer where the difference between the potential temperature at that level and at the base of the inversion layer exceeds 2°C , where the inversion layer is defined by the condition that potential temperature increases with altitude at a rate exceeding $0.005^{\circ}\text{C m}^{-1}$. Table 3 lists the same correlations as those in Table 2, except that it is only over levels within the mixed layer. As expected, the large negative correlations associated with elevated plumes have been eliminated, particularly on flights 14 and 15. However, the positive correlations on other flights, such as 13 and 17, have been reduced because variance above the mixed layer that had been explained in Table 2 has now been filtered out. By limiting the retrieval to the mixed layer, which is highly correlated with the surface [della Monache et al., 2004], little improvement over surface

values is permitted. If cloud base is above the mixed layer much more can be gained by extending the retrieval above the mixed layer, provided the accuracy of the retrieval there can be estimated independently. Doing so will not affect the retrieval for the boundary layer. Estimating the accuracy is addressed in section 3.3.

3.2. Evaluation of Full Retrieval

[44] As a final test combining all sources of uncertainty, Figure 7 compares vertical profiles of retrieved and estimated (from DMA size distribution) CCN concentrations at 0.1% and 2% supersaturation and measured CCN concentration at the indicated supersaturation. The retrieval scales the surface measurement of CCN concentration by the Raman lidar retrieval of ambient extinction divided by the humidification factor at the retrieved relative humidity using

Table 3. As in Table 2, but Only for Points Within the Mixed Layer

x	y	Flight							
		6	9	10	13	14	15	16	17
CCN1	in situ ext	0.47–0.97	0.08–0.93	0.65–0.99	0.00–0.83	0.00–0.80	–0.36–0.09	0.00–0.51	–0.31–0.11
CCN1	RL ext	–0.45–0.43	–0.38–0.60	–0.90–0.16	–0.05–0.77	–0.12–0.60	–0.46–0.03	–0.56–0.00	–0.07–0.36
CCN1	RL bscat	–0.36–0.52	–0.01–0.86	–0.89–0.22	–0.11–0.72	–0.11–0.60	–0.54–0.01	–0.34–0.06	–0.08–0.35
CCN1	MPL ext	0.00–0.96	–0.21–0.99	–0.92–0.45
CCN1	MPL bscat	–0.10–0.92	0.22–0.99	–0.92–0.47
in situ ext	RL ext	–0.25–0.61	–0.66–0.30	–0.94–0.02	0.00–0.84	–0.09–0.63	–0.37–0.09	–0.34–0.06	–0.33–0.10
in situ ext	MPL ext	–0.03–0.94	–0.71–0.98	–0.76–0.79
CCN @ S = 0.1%	in situ ext	–0.17–0.90	0.04–0.97	–0.65–0.99	–0.44–0.99	–0.12–0.92	–0.76–0.54	–0.56–0.43	–0.83–0.00
CCN @ S = 1%	in situ ext	–0.41–0.82	0.08–0.98	–0.73–0.98	–0.28–0.99	–0.50–0.78	–0.67–0.65	–0.15–0.76	–0.12–0.71
CCN @ S = 0.1%	CCN1	–0.31–0.86	0.02–0.94	–0.69–0.98	0.04–0.99	–0.03–0.94	–0.82–0.40	0.48–0.98	–0.01–0.82
CCN @ S = 1%	CCN1	–0.52–0.76	0.14–0.96	–0.75–0.98	0.45–0.99	–0.40–0.82	–0.78–0.49	0.47–0.98	–0.32–0.55

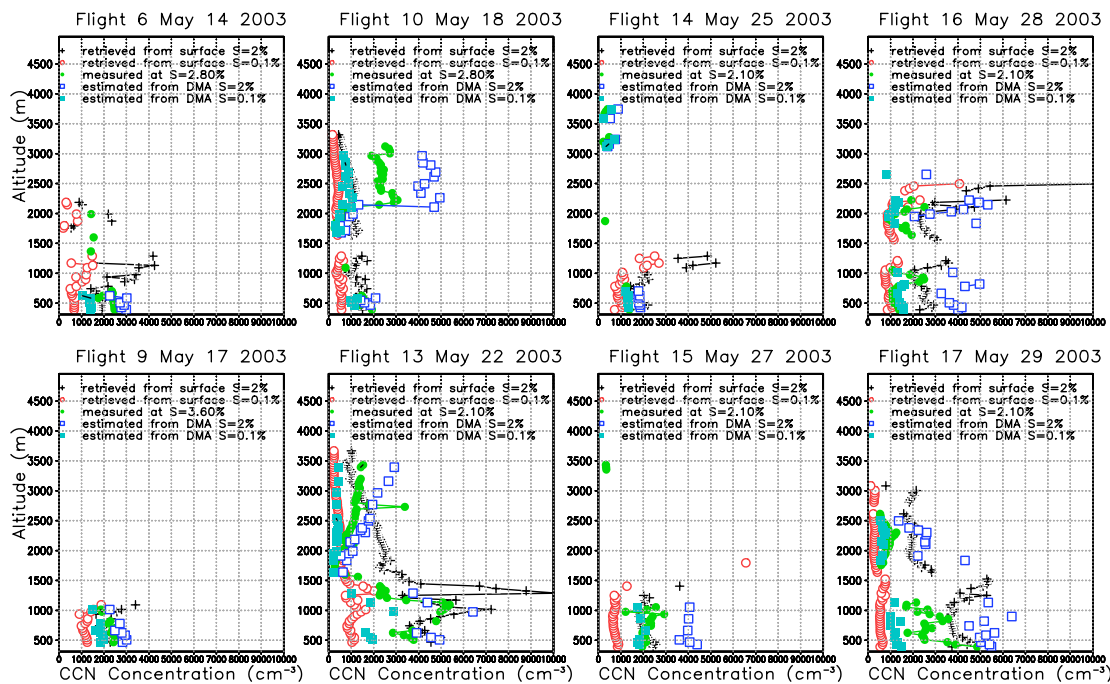


Figure 7. Vertical profiles of retrieved and estimated (from DMA size distribution) CCN concentrations at 0.1% and 1% supersaturation and measured CCN concentration at the indicated supersaturation for each flight. The retrieval scales the surface measurement of CCN concentration by the Raman lidar retrieval of ambient extinction divided by the humidification factor at the retrieved relative humidity using the surface measurement of the humidification function.

the surface measurement of the humidification function. The same scaling profile is therefore applied to the surface CCN measurements at both supersaturations. This is an especially difficult test because even if the retrieval were perfect it would still differ from the in situ measurements because of differences between the surface CCN instrument, the aircraft CCN instrument, and the estimate using the measured size distribution and an assumed ammonium sulfate composition.

[45] Yet some skill (relative to surface values) is evident in the retrieval when the vertical structure in the CCN profile is not dominated by variations in aerosol composition or in the aerosol size distribution. On the flight with the best performance of the CCN retrieval scheme (13), the retrieval of CCN at $S = 2\%$ captures the increase with altitude up to 1000 m and then the decrease with altitude up to 1600 m. Although the agreement is not as good as the agreement between the in situ CCN measurement and CCN estimated from the measured size distribution, useful skill is clearly evident. At $S = 0.1\%$ the agreement is also quite good, not only up to 1600 but up to at least 3500 m. On other days the performance is marginal with skill generally limited to the boundary layer. As we have already seen, the performance above the boundary layer is on some flights (14, 15, and 16) limited by the presence of an aerosol layer aloft with very different microphysical characteristics. Identifying such conditions is therefore important for determining when CCN concentrations can

be retrieved with confidence. This question is addressed in the next section.

3.3. Estimating Retrieval From the Surface

[46] Given the variable performance of the CCN retrieval scheme, its value would be greatly enhanced if there was some independent way to estimate its accuracy. GC suggested that Raman lidar retrievals of the extinction to backscatter ratio, which depends on particle size, could be used to distinguish conditions in which the particle size distribution and composition are uniform (when one would expect the CCN retrieval scheme to work best) or stratified (when the CCN retrieval scheme should perform poorly unless the CCN concentration is dominated by the same particles that control extinction). We have looked at the vertical structure of the extinction to backscatter ratio for the flights during this experiment, and conclude that the degraded sensitivity of the Raman lidar during the experiment limited the accuracy and hence the utility of the ratio as an indicator of vertical structure in the aerosol size distribution and composition.

[47] To assess the potential value of extinction/backscatter retrievals from a healthy Raman lidar, we can look at vertical profiles of the dry hemispheric backscatter fraction and of the Ångström exponent determined from in situ measurements. The hemispheric backscatter fraction b is defined as the ratio of the dry hemispheric backscattering to the dry total scattering. Larger values of b indicate particles

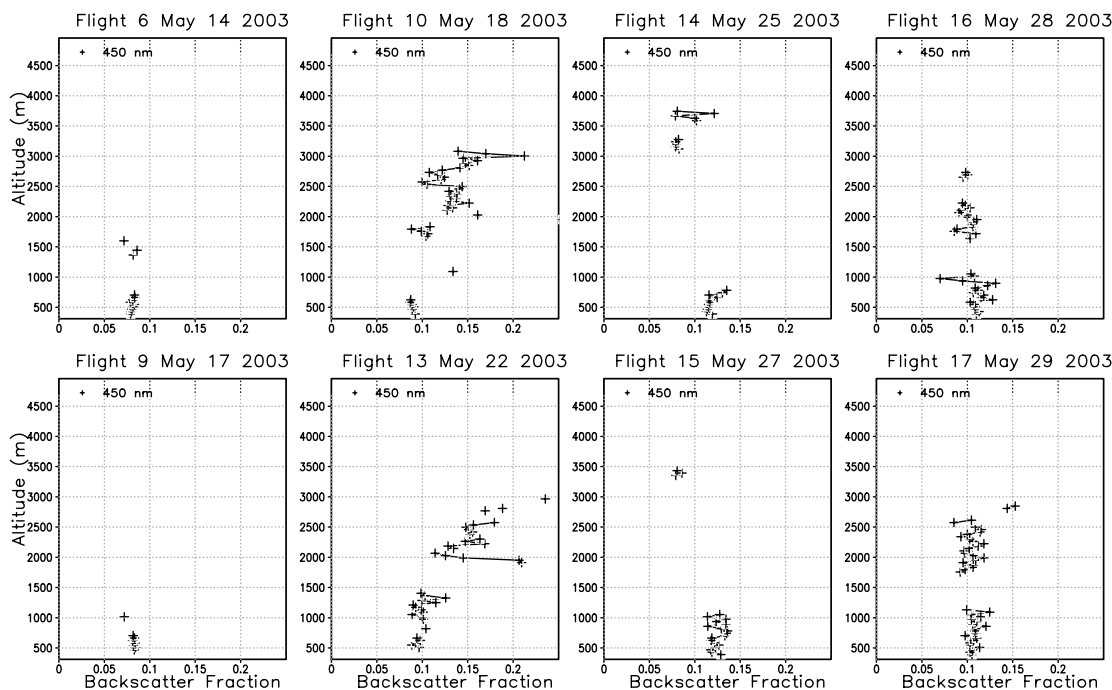


Figure 8. Vertical profile of dry hemispheric backscatter fraction at 450 nm for eight flights.

in the optical range 100–500 nm are shifted toward the smaller end of the range. The Ångström exponent, which is the exponent in a power law approximation for the wavelength-dependence of scattering, $\sigma_s \sim \lambda^{-\hat{a}}$, is determined from the dry scattering measured at two different wavelengths: $\hat{a}(\lambda_1, \lambda_2) = \ln(\sigma_2/\sigma_1)/\ln(\lambda_1/\lambda_2)$ where σ_1 and σ_2 are the dry scattering at wavelengths λ_1 and λ_2 . The Ångström exponent is near zero in the geometric optics limit of particles much larger than the wavelength, and near four in the Rayleigh limit of particles much smaller than the wavelength. Hence larger values of \hat{a} indicate a larger proportion of scattering contributed by particles smaller than the wavelength, i.e., with radius less than 80 nm.

[48] Figure 8 shows vertical profiles of the hemispheric backscatter fraction at 450 nm. One might expect the backscatter fraction to be most uniform on flight 13, which is when the CCN retrieval scheme performs best. Contrary to this expectation, the vertical profile of backscatter fraction is least uniform on flight 13, increasing more than twofold between the surface and 3000 m. On flights that we might expect vertical structure in the backscatter fraction, we find that the vertical structure is consistent with expectations. On flight 10, which according to the DMA measurements has an elevated plume of ultrafine particles (diameter less than 100 nm) that produce higher CCN concentrations at altitudes between 2000 and 3000 m, the backscatter fraction increases with altitude, which also indicates a shift toward smaller particles within the optical size range. In the elevated plume on flights 14 and 15, which according to the DMA measurements has reduced ultrafine particle concentrations and higher accumulation mode particles (diameters between 100 and 500 nm), the backscatter fraction is lower

than in the mixed layer, which as expected implies a shift toward larger particles within the optical size range.

[49] Somewhat different conclusions follow from the vertical profile of Ångström exponent, shown in Figure 9. The exponent is lower in the elevated plume than in the mixed layer for flights 14 and 15, which suggests larger particles and hence is consistent with the DMA measurements and the bias in the retrieval. However, on flight 10 the exponent is lower in the plume than in the mixed layer (at least for 550–700 nm), which also suggests larger particles but is inconsistent with the higher concentration of ultrafine particles measured in the plume by the DMA. On flight 13 the moderate decrease in exponent with height is inconsistent with the increase in backscatter fraction and with the strong performance of the CCN retrieval scheme for that flight.

[50] These inconsistencies suggest that any reliability metrics based on measurements at visible wavelengths are of questionable value in predicting the performance of the retrieval scheme for the high supersaturations for which we have CCN measurements. At such high supersaturations the CCN concentration is often controlled by particles that are simply too small to influence optical measurements. At lower supersaturations the CCN concentration is more sensitive to the same particles that influence the aerosol optical properties, and hence we can expect higher performance of both the retrieval and optical metrics that might assess reliability. A reliability metric based on the Raman lidar, which operates at 355 nm, might be more useful than metrics based on visible wavelengths, but the degraded sensitivity of the Raman lidar prevented a direct evaluation of its potential for providing a useful reliability.

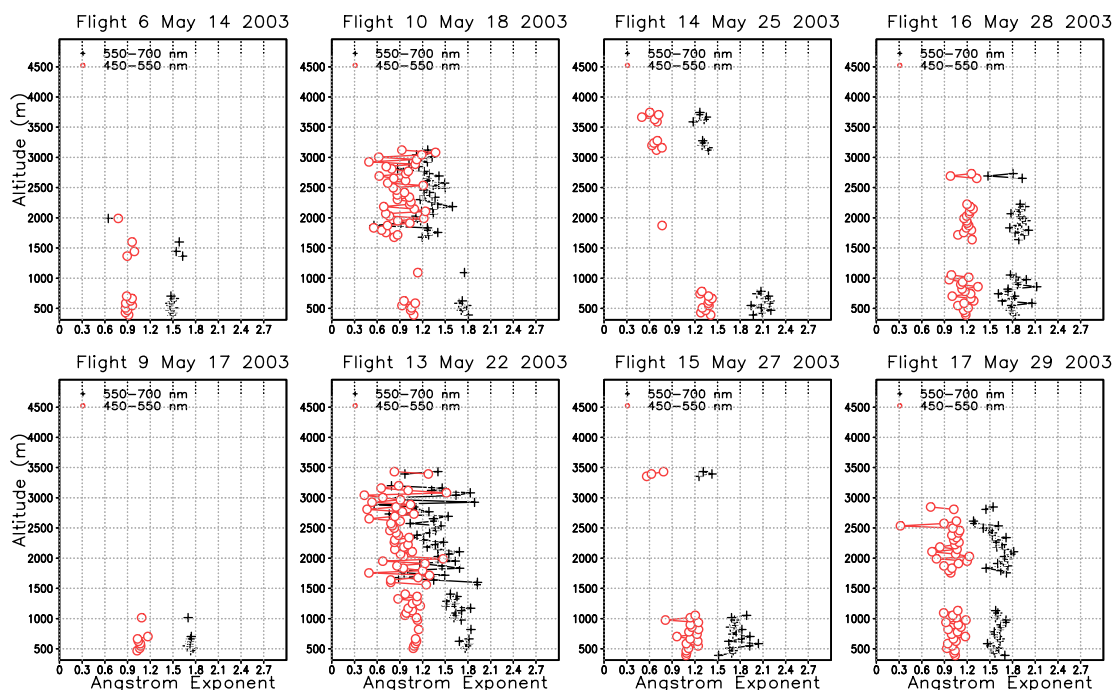


Figure 9. Vertical profile of Ångström exponent between 450 and 550 nm and between 550 and 700 nm for eight flights.

[51] Finally, one final metric from this IOP deserves some attention. The single-scattering albedo (the ratio of absorption to extinction) is controlled by the size distribution and chemical composition of the aerosol, and thus changes in the single-scattering albedo with altitude indicate conditions where the assumptions of the retrieval algorithm may not be valid. Although remote sensing of the vertical profile of single-scattering albedo is not currently feasible and hence we cannot expect single-scattering albedo to be a useful surface-based predictor of the performance of the CCN retrieval, we examine the vertical structure of the single-scattering albedo for evidence of vertical structure in aerosol composition as an explanation for biases in the CCN retrieval. Figure 10 shows vertical profiles of the single-scattering coalbedo (1- single-scattering albedo) for each flight. Higher coalbedo indicates more absorption. The largest variance is for flights 10 and 13, with somewhat higher coalbedo at higher altitudes. On flights 14 and 15 there is little difference between the albedo of the plume and mixed layers. It would appear that the particles controlling single-scattering albedo are not well correlated with the particles controlling the CCN number concentration, as the vertical profile of single-scattering albedo does not appear to explain much of the differences in performance of the CCN retrieval scheme on the flights studied here.

4. Conclusions

[52] We have used a combination of aircraft, surface in situ, and surface remote sensing measurements to test various aspects of the GC scheme for retrieving CCN

concentration. Our analysis leads us to the following conclusions.

[53] 1. If in situ measurements of extinction are used, the performance of the CCN retrieval for the high supersaturations (>2%) of the in situ CCN measurements can be quite high, with r^2 exceeding at least 0.4 on two and perhaps five of the eight flights examined, but can be negligible on other flights. GC arrived at a similar conclusion for pure ammonium sulfate particles and for supersaturations exceeding 1%, explaining the poor performance on some flights because CCN concentration at high supersaturations is dominated by particles too small to influence extinction or backscatter. Independent evidence [Rissman *et al.*, 2006] suggests a high insoluble content and hence low hygroscopicity and high critical supersaturation for particles large enough to influence extinction and backscatter as well as CCN concentration. The significant skill on such a large fraction of the flights suggests that degradation of the retrieval performance by stratification of the size distribution and composition is uncommon. It is worth noting that the poor performance on two of the flights was caused by a highly unusual elevated plume of large particles.

[54] 2. On some flights, correlations are significantly higher for supersaturations of 0.1% than for 1% because CCN concentrations at 0.1% are more likely to be controlled by the same particles that control extinction and backscatter. This conclusion is compromised by the absence of CCN measurements at these supersaturations and the need to assume a uniform composition when using Köhler theory to estimate CCN concentration from the measured aerosol size distribution.

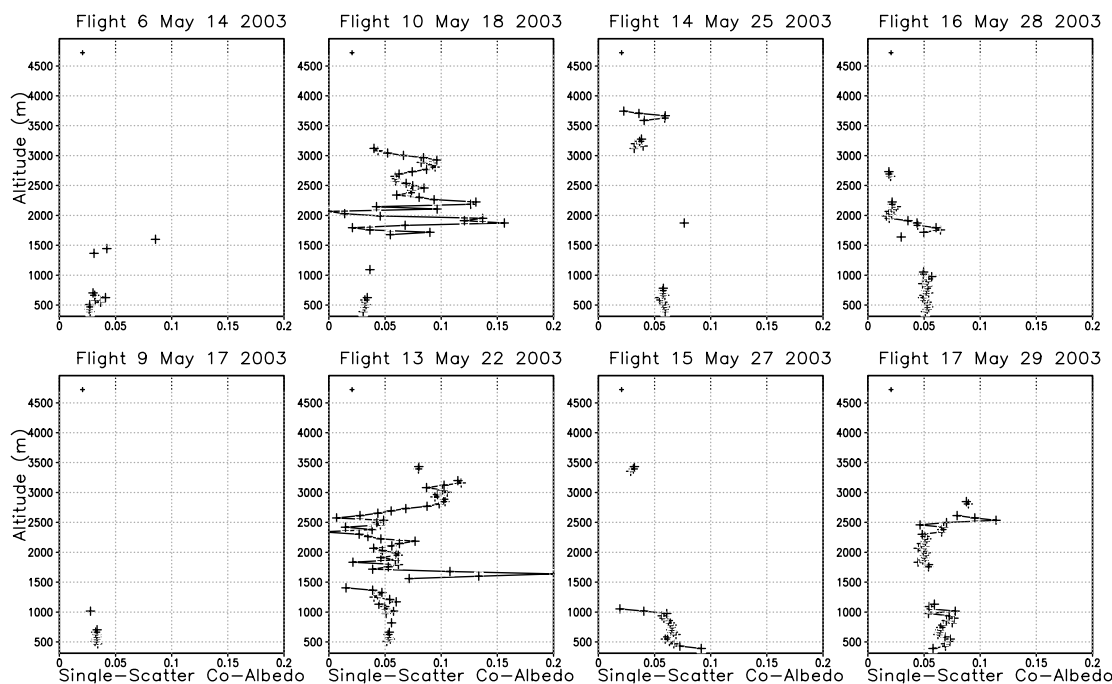


Figure 10. Vertical profile of single-scattering coalbedo for eight flights.

[55] 3. The retrieval of the vertical profile of the humidification factor is not the major limitation of the CCN retrieval scheme.

[56] 4. The performance of the retrieval varies significantly from day to day, particularly at supersaturations of 1% and higher, with higher correlations on days with uniform vertical profiles of size distribution.

[57] 5. Vertical inhomogeneity in the size distribution and presumably composition and particle shape are the dominant sources of error in the CCN retrieval.

[58] 6. Measurements of optical parameters that depend on the aerosol composition, shape and size distribution are not reliable predictors of the performance of the retrieval at high supersaturations because such measurements are based on visible wavelengths, which are insensitive to the particles that control CCN concentration at high supersaturations. A reliability metric based on the Raman lidar, which operates at 355 nm, might be more useful than metrics based on visible wavelengths, but the degraded sensitivity of the Raman lidar prevented a direct evaluation of its potential for providing a useful reliability.

[59] The evaluation of the retrieval scheme was compromised by three limitations. First, the Raman lidar was not performing up to its capability. This limited our interpretation of the full retrieval scheme. Second, the lack of in situ measurements of CCN concentration at supersaturations less than 2% limited our ability to evaluate the performance at low supersaturation. Estimating the CCN concentration at lower supersaturations using the measured size distribution and an assumed ammonium sulfate composition was clearly a significant compromise. Yet it served to illustrate important aspects of the retrieval performance. Third, the in situ CCN

measurements were not strictly collocated in time and space with the lidar retrievals. We did not find much sensitivity of the correlations to the collocation requirements, but this limitation still needs to be considered as a source of error.

[60] Further evaluation of the retrieval would therefore benefit from more reliable retrievals by ambient extinction and backscatter, and from in situ measurements of the full CCN spectrum. The sensitivity of the Raman lidar at the ARM CRF has been restored recently, and instruments to measure the full CCN spectrum are available and could be deployed in an experiment more focused on CCN.

[61] **Acknowledgments.** This study and the May 2003 Aerosol IOP were supported by the U.S. Department of Energy Atmospheric Radiation Measurement Program and Atmospheric Science Program, which are part of the DOE Biological and Environmental Research Program. The Pacific Northwest National Laboratory is operated for the DOE by Battelle Memorial Institute under contract DE-AC06-76RLO 1830.

References

- Anderson, T. L., and J. A. Ogren (1998), Determining aerosol radiative properties using the TSI 3563 integrating nephelometer, *Aerosol Sci. Technol.*, *29*, 57–69.
- Anderson, T. L., S. J. Masonis, D. S. Covert, R. J. Charlson, and M. J. Rood (2000), In situ measurement of the aerosol extinction-to-backscatter ratio at a polluted, continental site, *J. Geophys. Res.*, *105*, 26,907–26,915.
- Brechtel, F. J., and S. M. Kreidenweis (2000a), Predicting particle critical supersaturation from hygroscopic growth measurements in the humidified TDMA. Part I: Theory and sensitivity studies, *J. Atmos. Sci.*, *57*, 1854–1871.
- Brechtel, F. J., and S. M. Kreidenweis (2000b), Predicting particle critical supersaturation from hygroscopic growth measurements in the humidified TDMA. Part II: Laboratory and ambient studies, *J. Atmos. Sci.*, *57*, 1872–1887.
- Conant, W. C., et al. (2004), Aerosol-cloud drop concentration closure in warm cumulus, *J. Geophys. Res.*, *109*, D13204, doi:10.1029/2003JD004324.

- Damoah, R., N. Spichtinger, C. Forster, P. James, I. Mattis, U. Wandinger, S. Beirle, T. Wagner, and A. Stohl (2004), Around the world in 17 days—Hemispheric-scale transport of forest fire smoke from Russia in May 2003, *Atmos. Chem. Phys. Discuss.*, *4*, 1449–1471.
- della Monache, L. D., K. D. Perry, R. T. Cederwall, and J. A. Ogren (2004), In situ aerosol profiles over the Southern Great Plains cloud and radiation test bed site: 2. Effects of mixing height on aerosol properties, *J. Geophys. Res.*, *109*, D06209, doi:10.1029/2003JD004024.
- Feingold, G., W. L. Eberhard, D. E. Veron, and M. Previdi (2003), First measurements of the Twomey indirect effect using ground-based remote sensors, *Geophys. Res. Lett.*, *30*(6), 1287, doi:10.1029/2002GL016633.
- Ferrare, R. A., D. D. Turner, L. H. Brasseur, W. F. Feltz, O. Dubovik, and T. P. Tooman (2001), Raman lidar measurements of the aerosol extinction-to-backscatter ratio over the Southern Great Plains, *J. Geophys. Res.*, *106*, 20,333–20,348.
- Ferrare, R., et al. (2004), Raman lidar measurements of aerosols and water vapor over the Southern Great Plains, *22nd International Laser Radar Conference*, edited by G. Pappalardo and A. Amodio, *Eur. Space Agency Spec. Publ., ESA SP-561*, 333–336.
- Ferrare, R., D. Turner, M. Clayton, V. Brackett, B. Schmid, J. Redemann, D. Covert, R. Elleman, J. Ogren, E. Andrews, J. Goldsmith, and H. Jonsson (2006), Evaluation of daytime measurements of aerosols and water vapor made by an operational Raman lidar over the Southern Great Plains, *J. Geophys. Res.*, doi:10.1029/2005JD005836, in press.
- Ghan, S. J., and D. R. Collins (2004), Use of in situ data to test a Raman lidar-based cloud condensation nuclei remote sensing method, *J. Atmos. Oceanic Technol.*, *21*, 387–394.
- Gultepe, I., G. A. Isaac, and W. R. Leaitch (1998), Parameterizations of marine stratus microphysics based on in situ observations: Implications for GCMs, *J. Clim.*, *9*, 345–357.
- Hallberg, A., et al. (1997), Microphysics of clouds: Model vs measurements, *Atmos. Environ.*, *31*, 2453–2462.
- Han, Q., W. B. Rossow, J. Chou, and R. Welch (1998), Global variation in column droplet concentration in low-level clouds, *Geophys. Res. Lett.*, *25*, 1419–1422.
- Heffter, J. L. (1980), Transport layer depth calculations, paper presented at Second Joint Conference on Applications of Air Pollution Meteorology, Am. Meteorol. Soc., New Orleans, La., 24–28 March.
- Hudson, J. G. (1989), An instantaneous CCN spectrometer, *J. Atmos. Oceanic Technol.*, *6*, 1055–1065.
- Hudson, J. G., and S. S. Yum (2001), Maritime-continental drizzle contrasts in small cumuli, *J. Atmos. Sci.*, *58*, 915–926.
- Hudson, J. G., and S. S. Yum (2002), Cloud condensation nuclei spectra and polluted and clean clouds over the Indian Ocean, *J. Geophys. Res.*, *107*(D19), 8022, doi:10.1029/2001JD000829.
- Jaffe, D., I. Bertschi, L. Jaegle, P. Novelli, J. S. Reid, H. Tanimoto, R. Vingarzan, and D. L. Westphal (2004), Long-range transport of Siberian biomass burning emissions and impact on surface ozone in western North America, *Geophys. Res. Lett.*, *31*, L16106, doi:10.1029/2004GL020093.
- Kim, B.-G., S. E. Schwartz, M. A. Miller, and Q. Min (2003), Effective radius of cloud droplets by ground-based remote sensing: Relationship to aerosol, *J. Geophys. Res.*, *108*(D23), 4740, doi:10.1029/2003JD003721.
- Lin, H., and R. Leaitch (1997), Development of an in-cloud aerosol activation parameterization for climate modeling, paper presented at Workshop on Measurements of Cloud Properties for Forecasts of Weather, Air Quality, and Climate, World Meteorol. Organ., Geneva, Switzerland.
- Liu, Y., and P. H. Daum (2002), Indirect warming effect from dispersion forcing, *Nature*, *419*, 580–581.
- Menon, S., and V. K. Saxena (1998), Role of sulfates in regional cloud-climate interactions, *Atmos. Res.*, *47–48*, 299–315.
- Menon, S., V. K. Saxena, P. Durkee, B. N. Wenny, and K. Nielsen (2002), Role of sulfate aerosols in modifying the cloud albedo: A closure experiment, *Atmos. Res.*, *61*, 169–187.
- Menon, S., et al. (2003), Evaluating aerosol/cloud/radiation process parameterizations with single column models and ACE-2 cloudy column observations, *J. Geophys. Res.*, *108*(D24), 4762, doi:10.1029/2003JD003902.
- Nenes, A., P. Y. Chuang, R. C. Flagan, and J. H. Seinfeld (2001), A theoretical analysis of cloud condensation nucleus (CCN) instruments, *J. Geophys. Res.*, *106*, 3449–3474.
- Ovtchinnikov, M., and S. J. Ghan (2005), Parallel simulations of aerosol influence on clouds using cloud-resolving and single-column models, *J. Geophys. Res.*, *110*, D15S10, doi:10.1029/2004JD005088.
- Peng, Y., U. Lohmann, and R. Leaitch (2005), Importance of vertical velocity variations in the cloud droplet nucleation process of marine stratus clouds, *J. Geophys. Res.*, *110*, D21213, doi:10.1029/2004JD004922.
- Penner, J. E., X. Dong, and Y. Chen (2004), Observational evidence of a change in radiative forcing due to the indirect aerosol effect, *Nature*, *427*, 231–233.
- Pitzer, K. S. (1973), Thermodynamics of electrolytes. I. Theoretical basis and general equations, *J. Phys. Chem.*, *77*, 268–277.
- Pitzer, K. S., and G. Mayorga (1973), Thermodynamics of electrolytes. II. Activity and osmotic coefficients for strong electrolytes with one or both ions univalent, *J. Phys. Chem.*, *77*, 2300–2308.
- Pruppacher, H. R., and J. D. Klett (1997), *Microphysics of Clouds and Precipitation*, Springer, New York.
- Rissman, T. A., T. M. VanReken, J. Wang, R. Gasparini, D. R. Collins, Y.-N. Lee, H. Jonsson, F. J. Brechtel, R. C. Flagan, and J. H. Seinfeld (2006), Characterization of cloud condensation nuclei (CCN) during the 2003 Atmospheric Radiation Measurement aerosol intensive operational period at the Southern Great Plains site in Oklahoma, *J. Geophys. Res.*, doi:10.1029/2004JD005695, in press.
- Schmid, B., et al. (2006), How well can we measure the vertical profile of aerosol extinction?, *J. Geophys. Res.*, doi:10.1029/2005JD005837, in press.
- Sheridan, P. J., D. J. Delene, and J. A. Ogren (2001), Four years of continuous surface aerosol measurements from the Department of Energy's Atmospheric Radiation Measurement Program Southern Great Plains Cloud and Radiation Testbed site, *J. Geophys. Res.*, *106*, 20,735–20,747.
- Snider, J. R., S. Guibert, J.-L. Brenguier, and J.-P. Putaud (2003), Aerosol activation in marine stratocumulus clouds: 2. Kohler and parcel theory closure studies, *J. Geophys. Res.*, *108*(D15), 8629, doi:10.1029/2002JD002692.
- Tang, I. N., and H. R. Munkelwitz (1994), Water activities, densities, and refractive indices of aqueous sulfates and sodium nitrate droplets of atmospheric importance, *J. Geophys. Res.*, *99*, 18,801–18,808.
- Turner, D. D., and J. Goldsmith (2005), The refurbishment and upgrade of the ARM Raman Lidar, paper presented at 15th ARM Science Team Meeting, U.S. Dep. of Energy, Daytona Beach, Fla. (Available at http://www.arm.gov/publications/proceedings/conf15/extended_abs/turner_dd1.pdf)
- Turner, D. D., R. A. Ferrare, L. A. Heilman, W. F. Feltz, and T. P. Tooman (2002), Automated retrievals of aerosol extinction coefficient from a Raman lidar, *J. Atmos. Oceanic Technol.*, *19*, 37–50.
- Wang, J., R. C. Flagan, and J. H. Seinfeld (2003), A differential mobility analyzer (DMA) system for submicron aerosol measurements at ambient relative humidity, *Aerosol Sci. Technol.*, *37*, 46–52.
- Yum, S. S., and J. G. Hudson (2002), Maritime/continental microphysical contrasts in stratus, *Tellus, Ser. B*, *54*, 61–73.

R. Elleman, Department of Atmospheric Science, University of Washington, Seattle, WA 98195, USA.

R. A. Ferrare, NASA Langley Research Center, Hampton, VA 23681-0001, USA.

R. C. Flagan, T. A. Rissman, J. H. Seinfeld, and T. VanReken, California Institute of Technology, Pasadena, CA 91125, USA.

C. Flynn, S. J. Ghan, and D. Turner, Pacific Northwest National Laboratory, Richland, WA 99352, USA. (steve.ghan@arm.gov)

J. Hudson, Desert Research Institute, Reno, NV 89512, USA.

H. H. Jonsson, Naval Postgraduate School, Monterey, CA 93943, USA.

J. Ogren, NOAA Climate Monitoring and Diagnostics Laboratory,

Boulder, CO 80303, USA.

J. Wang, Brookhaven National Laboratory, Upton, NY 11973, USA.

Appendix E

CHEMICAL AND DYNAMICAL EFFECTS ON CLOUD DROPLET NUMBER:
IMPLICATIONS FOR ESTIMATES OF THE AEROSOL INDIRECT EFFECT*

*Full Citation: Lance, S., A. Nenes, and T. A. Rissman (2004), Chemical and dynamical effects on cloud droplet number: Implications for estimates of the aerosol indirect effect, *Journal of Geophysical Research*, 109(D22), D22208, doi: 10.1029/2004JD004596.

© 2004 American Geophysical Union (AGU). This appendix is reprinted with permission from the American Geophysical Union.

Chemical and dynamical effects on cloud droplet number: Implications for estimates of the aerosol indirect effect

Sara Lance

School of Earth and Atmospheric Sciences, Georgia Institute of Technology, Atlanta, Georgia, USA

Athanasios Nenes

School of Earth and Atmospheric Sciences and School of Chemical and Biomolecular Engineering, Georgia Institute of Technology, Atlanta, Georgia, USA

Tracey A. Rissman

Department of Chemical Engineering, California Institute of Technology, Pasadena, California, USA

Received 2 February 2004; revised 11 August 2004; accepted 15 August 2004; published 27 November 2004.

[1] Most aerosol-cloud-climate assessment studies use empirical aerosol number/droplet number relationships, which are subject to large variability. Historically, this variability has been attributed to unresolved variations in updraft velocity. We revisit this postulation and assess the effects of both updraft velocity and chemical composition on this variability. In doing so we utilize an inverse modeling approach. Using a detailed numerical cloud parcel model and published aerosol characteristics, with published correlations of cloud droplet versus sulfate and cloud droplet versus aerosol number as constraints, we determine a most probable size distribution and updraft velocity for polluted and clean conditions of cloud formation. A sensitivity analysis is then performed to study the variation in cloud droplet number with changes in aerosol chemistry and updraft velocities. This addresses the need to estimate the importance of chemical effects on spatial scales relevant for global climate models. Our analysis suggests that the effect of organic surfactants can introduce as much variability in cloud droplet number as the effect of expected variations in updraft velocity. In addition, the presence of organics seems to further enhance the sensitivity of droplet concentration to vertical velocity variability. The variability from organic surfactants is seen to be insensitive to variations in aerosol number concentration, implying that such effects can affect cloud droplet number consistently over large spatial scales. Our findings suggest that organics can be as important to the aerosol indirect effect as the effect of unresolved cloud dynamics, and they illustrate the potential and complex role of chemical effects on aerosol-cloud interactions. *INDEX TERMS*: 0305 Atmospheric Composition and Structure: Aerosols and particles (0345, 4801); 0320 Atmospheric Composition and Structure: Cloud physics and chemistry; 0345 Atmospheric Composition and Structure: Pollution—urban and regional (0305); 1610 Global Change: Atmosphere (0315, 0325); 3314 Meteorology and Atmospheric Dynamics: Convective processes; *KEYWORDS*: aerosol, clouds, indirect effect

Citation: Lance, S., A. Nenes, and T. A. Rissman (2004), Chemical and dynamical effects on cloud droplet number: Implications for estimates of the aerosol indirect effect, *J. Geophys. Res.*, *109*, D22208, doi:10.1029/2004JD004596.

1. Introduction

[2] The largest uncertainty in prediction of anthropogenic influences on climate change involves the details of the hydrological cycle [Houghton *et al.*, 2001]. Water in the atmosphere has three major, competing effects on climate. Water vapor is the primary greenhouse gas in the Earth's atmosphere. Conversely, liquid water in the form of suspended cloud droplets accounts for ~30% of the Earth's albedo [Charlson *et al.*, 1987]. Water ice in the upper

troposphere absorbs infrared radiation emitted by the Earth. The mechanisms for distribution of each phase are therefore important for determining the overall effect of atmospheric water on climate. This study focuses on the formation of liquid water clouds.

[3] Cloud droplets in the atmosphere are formed from condensation of water vapor upon cloud condensation nuclei (CCN). Both the physical and chemical characteristics of a CCN population influence the number and size of cloud droplets that form. However, the physical and chemical properties of CCN vary significantly with space and time, since the sources and sinks of CCN are localized and since CCN have short atmospheric lifetimes (as compared

to the mixing timescale of the atmosphere). In addition, the cloud updraft velocity, which is highly variable within a cloud and difficult to measure [Mason, 1971], has a strong influence on the number and size of cloud droplets formed; a higher updraft provides a higher water vapor supersaturation, which is the driving force for condensational growth. The wide variability in these parameters, to which cloud droplet formation is highly sensitive, causes much of the uncertainty in cloud modeling.

[4] Most of the radiative properties of liquid water clouds can be inferred from knowledge of the cloud liquid water content and cloud droplet number concentration. Twomey [1974] suggested that increasing the number of aerosol particles increases the number of CCN, which increases the number of cloud droplets and leads to a higher cloud albedo. The increased cloud reflectivity and the associated radiative cooling are referred to as the “first indirect climate effect” of aerosols. Global climate models (GCMs) are currently incapable of providing the resolution necessary for explicitly addressing the scales involved in aerosol-cloud interactions; instead, empirical correlations between cloud droplet number and one aerosol characteristic (e.g., number concentration [Gultepe and Isaac, 1999] or sulfate mass [Boucher and Lohmann, 1995]) are often used to quantify aerosol-cloud interactions. The variability inherent in such relationships translates to a large predictive uncertainty of the indirect effect, potentially as large as the greenhouse gas radiative forcing [Houghton et al., 2001]. For example, in the Boucher and Lohmann [1995] observations the cloud droplet number concentration ranges from 60 to 600 cm^{-3} for an aerosol non-sea-salt (nss) sulfate mass of 1 $\mu\text{g m}^{-3}$. For the same liquid water path this variability in cloud droplet concentration could lead to a change in cloud reflectivity of up to $\sim 60\%$ [Seinfeld and Pandis, 1998]. This large variability shows that cloud droplet number is strongly influenced by factors other than sulfate mass but does not indicate to what the variability can be attributed.

[5] The variability in the Boucher and Lohmann [1995] and Gultepe and Isaac [1999] observations is historically attributed to variations in cloud updraft velocity [Houghton et al., 2001]. Although updraft variations may produce an order-of-magnitude range in droplet number, recent work has suggested that a variety of organic chemical effects, including reduction in surface tension and modified growth kinetics, can potentially contribute as much to the variability in cloud droplet number as updraft velocity.

[6] Several studies have shown that organic compounds can reduce the surface tension of droplets. Facchini et al. [2000] observed a decrease of up to 25% in the surface tension of polluted fog water samples as compared to the surface tension of water. The surface tension depression was shown to be a function of the bulk concentration of water-soluble organic compounds [Facchini et al., 1999]. Using Köhler theory and assuming a power law relationship between droplet number and supersaturation, Facchini et al. [1999] estimated that the maximum decrease in surface tension could lead to an $\sim 20\%$ increase in the number of cloud droplets. Li et al. [1998] found that laboratory-generated aerosol consisting of mixtures of sodium dodecyl sulfate and NaCl can lower the surface tension by up to 20% compared to the same size dry particle composed of pure

NaCl. Shulman et al. [1996] measured the solubility and surface tension of laboratory-generated aerosols, which consisted of two-component mixtures of ammonium sulfate and various difunctional organic oxygenates that have significant concentrations in the atmosphere (e.g., *cis*-pinonic acid and glutaric acid). The observed surface tension decreased by as much as 20% compared to water. It was also found that higher concentrations of ammonium sulfate actually enhanced the surface tension depression for *cis*-pinonic acid. This relatively high molecular weight organic compound is the least soluble of the model compounds studied; however, the addition of 0.5 M ammonium sulfate (which is ubiquitous in the atmosphere) allowed for the same $\sim 20\%$ reduction in surface tension at half the *cis*-pinonic acid concentration (0.02 M rather than 0.04 M).

[7] Numerous modeling studies have been performed to estimate the effect of the observed surface tension depression and gradual dissolution of organic compounds. These studies illustrate that the response in CCN concentrations to the presence of organic surfactants is often important and strongly depends on the size distribution of chemical composition and aerosol number and the local dynamical conditions of cloud formation. Nenes et al. [2002] used a numerical cloud parcel model to show that for polluted aerosol at high updraft velocities the reduction in surface tension due to organic surfactants can have a greater effect on droplet number than doubling aerosol number. For marine aerosol at low updraft the enhancement in droplet number from surfactants can be 50% of the enhancement from doubling aerosol number. Rissman et al. [2004] modified an existing parameterization by Abdul-Razzak et al. [1998] and Abdul-Razzak and Ghan [2000] to explicitly account for the effect of surface active organics on droplet number. Rissman et al. [2004] conclude that the normalized cloud droplet number sensitivity to aerosol organic mass fraction is usually between 10 and 50% of the sensitivity to updraft velocity, with the strongest relative sensitivity at higher updraft velocity. For marine aerosol, as updraft velocity increases above $\sim 0.4 \text{ m s}^{-1}$, the relative sensitivity becomes nearly constant. For continental aerosol the relative sensitivity can be negative at low updraft velocities, implying that an increase in aerosol organic mass fraction increases CCN concentration but decreases the number of cloud droplets (by decreasing the maximum supersaturation). Mircea et al. [2002] estimated that including the surface tension effects of water soluble organic compounds may increase the CCN number concentration by up to 13% for a marine aerosol, by up to 97% for a rural aerosol, and by up to 110% for an urban aerosol, under typical atmospheric supersaturations.

[8] The presence of organic film-forming compounds (FFCs), which form a thin film over a partially deliquesced aerosol particle (with the hydrophobic side of the molecules facing outward and the hydrophilic side facing inward), has the potential to inhibit the rate of droplet growth. The condensation coefficient, which is the probability of a water vapor molecule “sticking” upon collision with an aerosol particle, may be considerably reduced when FFCs are present on the particle surface. A condensation coefficient of 0.045 is widely recognized by the cloud physics community as the typical value for atmospheric droplets (e.g., Feingold and Chuang [2002] used a value of 0.042 to

represent typical FFC-free cloud droplets), although the value varies significantly between studies [Mozurkewich, 1986; Pruppacher and Klett, 2000]. Pruppacher and Klett [2000] summarize that an aged atmospheric drop will have a condensation coefficient of ~ 0.01 , while a clean drop will have a value closer to unity. Two recent studies indicate that the condensation coefficient of pure water is even smaller than previously estimated; Shaw and Lamb [1999] estimate a value of 0.04–0.1, and Li *et al.* [2001] estimate a value of 0.17 ± 0.03 at 280 K and 0.32 ± 0.04 at 258 K.

[9] There is evidence for the existence of FFC compounds in ambient aerosol that lower the condensation coefficient to as low as 10^{-5} [Chuang, 2003]. This lower condensation coefficient indicates that at least 99.98% fewer collisions result in “capture” of a water molecule from the gas as compared to an uncoated cloud drop. The chemical composition of FFC-coated particles and the corresponding condensation coefficients are issues that need to be addressed in future studies. In addition, the distribution of FFCs within the aerosol population must be looked at carefully. The modeling study of Feingold and Chuang [2002] shows that when a minor fraction (5–10% mass) of polluted aerosol is composed of FFCs and the FFC is distributed according to surface area, modified growth kinetics can suppress the number of cloud droplets by as much as 90%. When Nenes *et al.* [2002] distributed the same organic FFC by aerosol mass, a decrease in the initial rate of condensation led to a large enough increase in cloud parcel supersaturation that the result was an increase (by 50–100%) in cloud droplet number. For marine aerosols both studies found that cloud droplet number was modestly affected by the presence of FFCs. Feingold and Chuang [2002] also did simulations in which the FFC was distributed by mass, which resulted in nearly the same droplet number as when FFCs were not present. However, Feingold and Chuang [2002] used a unimodal lognormal size distribution, whereas Nenes *et al.* [2002] used a trimodal lognormal distribution. Distributing the FFC by mass reduces the growth of larger aerosol particles, which can increase the cloud supersaturation and allow more of the smaller particles to activate. The greater number of larger aerosol in the Nenes *et al.* [2002] study may have been a significant factor enabling greater droplet activation when the condensation coefficient was decreased to 10^{-5} .

[10] These and many other studies have shown that considerable variability in cloud droplet number may be induced by different chemical effects, but the studies do not assess the potential significance of the chemical effects on scales larger than individual updrafts. The current study attempts to address the cloud system scale by using an inverse modeling approach based on an observational data set that includes cumuliform and stratiform clouds and CCN originating from both clean and polluted conditions. This unique approach uses empirical correlations of droplet number versus aerosol number and sulfate mass, observed ranges of chemical composition, cloud dynamics, and aerosol size distribution to constrain the chemical effects on cloud droplet number. We use a numerical adiabatic cloud parcel model with explicit microphysics [Nenes *et al.*, 2001] to determine the minimum updraft velocity required to produce the number of droplets described by the Boucher and Lohmann [1995] and Gultepe and Isaac [1999] corre-

lations. This representative base case updraft velocity is then used with the parcel model to estimate the sensitivity of cloud droplet number to organic chemical effects. For comparison, cloud droplet number sensitivity to updraft velocity is also evaluated.

2. Methods

[11] Not all the factors affecting the number of cloud droplets are available from the published data. To overcome this lack of information, we adopt an inverse modeling analysis to constrain key unresolved parameters. The procedure is illustrated in Figure 1. For a given aerosol number the Gultepe and Isaac [1999] correlations provide the cloud droplet number, and the Boucher and Lohmann [1995] correlations provide the aerosol sulfate mass. With information about the aerosol size distribution an updraft velocity can be determined that is consistent with the observations; these conditions are used as a “base case.” Organic mass fraction, condensation coefficient, updraft velocity, and aerosol number concentration are then varied to assess their effects on cloud droplet number. The aerosol physical characteristics (Table 1) and chemical composition (Table 2) used in the analysis are obtained from published literature.

[12] The exact procedure (Figure 1) is as follows: (1) Specify the average aerosol physical and chemical characteristic for three typical environments (polluted, continental, and marine) on the basis of published observations, (2) determine a likely droplet number concentration on the basis of the empirical correlations of Gultepe and Isaac [1999], (3) using the Boucher and Lohmann [1995] correlations, determine a representative sulfate mass concentration that corresponds to the cloud droplet concentration determined from the Gultepe and Isaac [1999] correlations, (4) determine the coarse mode sulfate mass fraction or coarse mode number concentration needed to provide this total sulfate mass, and (5) determine an updraft velocity that can produce the droplet concentration from step 2 using the numerical cloud parcel model of Nenes *et al.* [2001]. These representative updraft velocities and aerosol characteristics are referred to as the base case values. The sensitivity of cloud droplet number to chemical effects is assessed by introducing a reasonable variability in organic mass fraction and condensation coefficient. The sensitivity of cloud droplet number to updraft velocity is also computed for comparison. When varying the cloud updraft velocity, the organic mass fraction is maintained at the base case value, with a condensation coefficient of 0.045. When varying the organic mass fraction, the base case updraft velocity is maintained, with a condensation coefficient of 0.045. When varying the condensation coefficient, the base case updraft velocity and organic mass fraction are assumed.

2.1. Aerosol

[13] Aerosols are diverse in their size distribution, number concentration, and chemical composition, and they exhibit significant spatiotemporal variability. As changes in aerosol physical characteristics are known to have a significant effect on the resulting cloud droplet number, the aerosol characteristics used in this analysis must encompass this diversity.

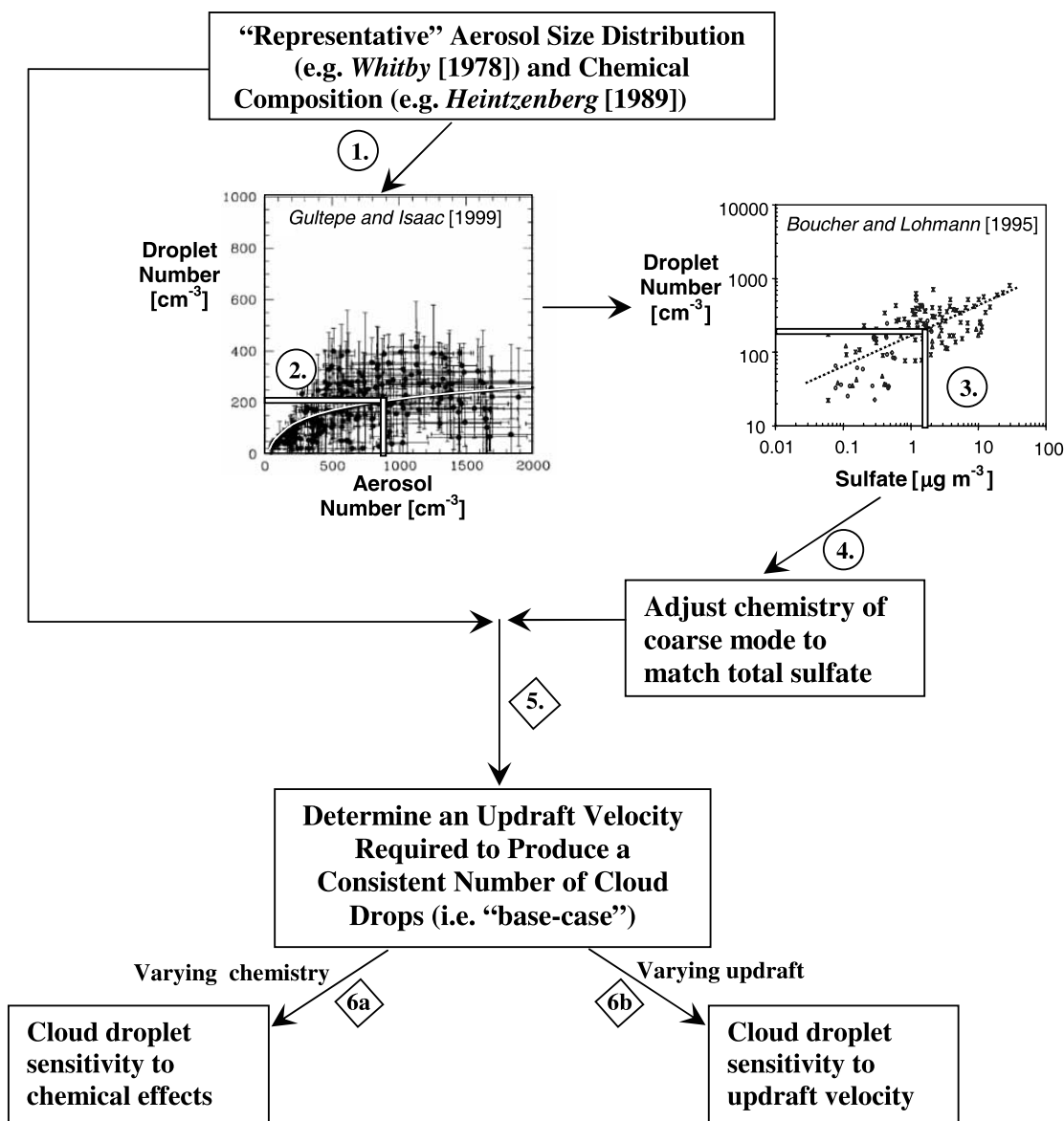


Figure 1. Flow diagram illustrating the “inverse modeling” analysis methodology used for determining cloud droplet number concentration sensitivities. Steps 1–4 (numbers in circles) involve manipulation of observational data, while the remaining steps (numbers in diamonds) employ the cloud parcel model.

[14] Regardless of the origin of the air mass, often, three distinct modes are observed in the aerosol size distribution (nuclei, accumulation, and coarse modes). The nuclei and accumulation modes together represent what are often referred to as “fine particles” (with geometric mean diameters $<0.1 \mu\text{m}$). *Whitby* [1978] characterized sulfur-containing aerosols by averaging multiple size distribution measurements made at several sites over a decade. These measurements were fit to trimodal lognormal distributions, as shown for marine, continental, and polluted aerosol in Table 1.

[15] Fine particle chemical compositions have been analyzed by *Heintzenberg* [1989], using data from 21 cities in the United States, China, Europe, and Japan; 15 nonurban continental sites in Sweden, Brazil, the United States, and the United Kingdom; and 13 locations in remote marine regions (Table 2). The fine particles mainly consist of sulfate, carbonaceous material (including elemental and organic carbon), ammonia, and nitrate. While inorganic compounds are easily resolved by chemical analysis, a substantial portion of organic matter in atmospheric aerosols has remained uncharacterized because of the wide range of

Table 1. Average Modal Size Distribution Parameters^a

Aerosol Type	Nuclei Mode			Accumulation Mode			Coarse Mode		
	\overline{D}_{g1}	σ_{g1}	N_1	\overline{D}_{g2}	σ_{g2}	N_2	\overline{D}_{g3}	σ_{g3}	N_3
Remote marine	0.01	1.6	340	0.071	2.0	60	0.62	2.7	3.1
Latitudes 60°–75°S ^b	0.018	1.4	310	0.075	1.6	70	0.58	2.49	3.1
Latitudes 15°–60°N ^b	0.020	1.47	230	0.092	1.47	176.7	0.58	2.49	3.1
Clean continental	0.016	1.6	1,000	0.067	2.1	800	0.93	2.2	0.72
Polluted	0.014	1.8	106,000	0.054	2.16	32,000	0.86	2.21	5.4

^a \overline{D}_g is given in μm , and N_i is given in cm^{-3} . Parameters are from *Whitby* [1978].

^bAverage fine marine parameters over the latitude range are from *Heintzenberg et al.* [2000], and coarse mode parameters are from *Jaenicke* [1993].

carbon numbers, functional groups, and solubilities in extraction media [*Saxena and Hildemann*, 1996]. The organic mass fraction in polluted and continental aerosol often comprises an estimated 20% of fine particle mass [*Heintzenberg*, 1989; *Ramanathan et al.*, 2001; *Neusiß et al.*, 2002]. However, the organic mass fraction may potentially be as high as 70% for a highly polluted aerosol [*Saxena and Hildemann*, 1996]. It is estimated that organic carbon (OC) can represent up to 50% of the mass of particulate matter <10 μm in diameter (PM₁₀) over the continental United States [*Saxena and Hildemann*, 1996; *Seinfeld and Pandis*, 1998]. Given that the total organic mass can be up to 2.1 times the OC mass for nonurban aerosol [*Turpin and Lim*, 2001], organic compounds may represent up to 100% of the aerosol mass in continental aerosol. For marine aerosol the organic mass fraction may be as high as 41–67% [*Heintzenberg*, 1989].

2.2. Aerosol Used in This Study

[16] Three different aerosol (marine, continental, and polluted) are represented in this study. The trimodal log-normal size distributions used in this analysis are based on the distributions of *Whitby* [1978], scaling the modal aerosol number concentrations to be within the range of the *Gultepe and Isaac* [1999] observations (Table 3). *Heintzenberg's* [1989] observed sulfate and organic mass fractions represent the fine particle composition for these cases (Table 2). The polluted coarse mode aerosol composition is estimated by averaging mass fraction observations reported by *Ramanathan et al.* [2001], *Neusiß et al.* [2002], and *Finlayson-Pitts and Pitts* [1986]. The marine coarse mode aerosol composition estimated by *Fitzgerald* [1991] is used, and the continental coarse mode composition is assumed to be 90% insoluble and 10% ammonium sulfate. We vary the fine particle organic mass fractions from 0 to 0.41 (marine), from 0 to 0.45 (continental), and from 0 to 0.61 (polluted), which are below the ranges noted in previous studies. When the organic mass fraction is increased, the sulfate mass fraction remains as specified by *Heintzenberg* [1989], and the insoluble mass fraction is adjusted. This is an important difference from many studies [e.g., *Li et al.*, 1998], in which highly hygroscopic inorganic salts are replaced with partially soluble organic compounds.

[17] The water-soluble organic component (by a simplification of chemical composition observed in Po Valley, Italy) is assumed to be composed of (by mass) 18% levoglucosan (C₆H₁₀O₅, density of 1600 kg m⁻³, and van't Hoff factor of 1), 41% succinic acid (C₆O₄H₆, density of 1572 kg m⁻³, and van't Hoff factor of 3), and 41% fulvic acid (C₃₃H₃₂O₁₉, density of 1500 kg m⁻³, and van't Hoff

factor of 5) [*Nenes et al.*, 2002]. The average solubility is assumed to be 0.02 kg (kg H₂O)⁻¹ (or 0.1 moles C L⁻¹).

2.3. Aerosol Number/Droplet Number Correlations

[18] The data represented by the *Boucher and Lohmann* [1995] and *Gultepe and Isaac* [1999] correlations cover a wide range of conditions of cloud formation. The *Boucher and Lohmann* [1995] correlations are based on four data sets, which include 85 observations of cloud droplet number and cloud water sulfate within stratiform and cumuliform clouds over North America [*Leaitch et al.*, 1992]; 15 observations of nss sulfate and CCN active at 0.3% supersaturation at Cheeka Peak, Washington [*Berresheim et al.*, 1993; *Quinn et al.*, 1993]; 12 observations of dimethylsulfide, nss sulfate mass, and CCN active over the northeast Atlantic [*Hegg et al.*, 1993]; and 14 observations of accumulation mode particle concentrations and sulfate mass concentrations over the North Atlantic [*Van Dingenen et al.*, 1995].

[19] The *Gultepe and Isaac* [1999] plots of cloud droplet number concentration versus aerosol number concentration is based on five data sets, which include observations in Syracuse, New York, Ontario (Eulerian Model Evaluation Field Study (EMEFS) I and II), Nova Scotia (North Atlantic Regional Experiment (NARE)), Bay of Fundy, and central Ontario (Radiation, Aerosol, and Cloud Experiment (RACE)). There were more than 10,000 observations collected over a period of 11 years. The cloud types observed were primarily stratus and stratocumulus.

[20] These observations exhibit a high degree of variability. Thus we do not use the correlations to predict the number of droplets for individual updrafts. Rather, the correlations are used to estimate a representative updraft velocity that is required to produce the typical observed droplet concentration for cloud systems in different environments (represented by average aerosol chemical and phys-

Table 2. Modal Base Case Chemical Composition for Each Aerosol Type Used in This Study^a

Aerosol Type	Fine			Coarse			
	ϵ_{SO_4}	ϵ_o	ϵ_{ins}	ϵ_{SO_4}	ϵ_{NaCl}	ϵ_o	ϵ_{ins}
Marine	0.22	0.11	0.59	0.05	0.93	-	0.05
Clean continental	0.37	0.24	0.25	0.07	-	-	0.9
Diluted polluted	0.28	0.31	0.30	0.11	-	0.2	0.644

^aThe fine particle ($\overline{D}_g < 0.1 \mu\text{m}$) mass fractions are obtained from *Heintzenberg* [1989]. Coarse mode sulfate mass fractions are calculated using the procedure outlined in the text. The other coarse mode mass fractions are estimated from *Fitzgerald* [1991], *Ramanathan et al.* [2001], *Neusiß et al.* [2002], and *Finlayson-Pitts and Pitts* [1986].

Table 3. Base Case Modal Aerosol Number Concentrations as Obtained From the Procedure Outlined in the Text^a

Aerosol Type	Modal Number Concentration, cm ⁻³				Parameters Constrained by Droplet Correlations	
	Nuclei	Accumulation	Coarse	Total N_{ap}	N_d^b	$m_{SO_4}^c$
Marine	230	177	3.1	410	150	1.75
Clean continental	555	444	4.1	1003	299	4.46
Diluted polluted	1152	348	5.4	1505	352	6.62

^aConcentrations N_i are given in cm⁻³. The other modal size distribution parameters are given in Table 1.

^bBase case droplet number N_d , given in cm⁻³, is constrained by the *Gultepe and Isaac* [1999] correlations.

^cTotal aerosol sulfate mass m_{SO_4} , given in $\mu\text{g m}^{-3}$, is constrained by the *Boucher and Lohmann* [1995] correlations.

ical characteristics and a representative base case updraft velocity). The *Gultepe and Isaac* [1999] and *Boucher and Lohmann* [1995] correlations are currently being used in GCMs, and their inherent variability contributes to the large predictive uncertainty in the models. By evaluating the sensitivities within the context of these correlations we are providing an assessment within the framework of the current methodology.

2.4. Cloud Parcel Model

[21] The cloud parcel model [*Nenes et al.*, 2001] captures the explicit aerosol microphysics of cloud droplet formation by diffusional growth. The model simulates the evolution of liquid water cloud droplet distributions in a nonprecipitating, adiabatic updraft and has been used in numerous studies, including a successful CCN/cloud droplet number closure study using in situ observations from the NASA Cirrus Regional Study of Tropical Anvils and Cirrus Layers (CRYSTAL)–Florida Area Cirrus Experiment (FACE) mission [*Conant et al.*, 2004]. The model does not include collision-coalescence processes but rather focuses on cloud droplet activation. The presence of slightly soluble and surfactant substances in CCN is treated explicitly, using the *Facchini et al.* [1999] correlation to characterize the surface tension of the growing droplets. The model computes the time-dependent particle sizes, water vapor supersaturation, pressure, and temperature. The initial assumed parcel conditions are a relative humidity of 98%, temperature of 284.2 K, and pressure of 939 mbar. The aerosol is not initially in equilibrium with the environment. The updraft is assumed constant since we are only interested in the cloud drop activation process, which generally occurs on the order of seconds; the buoyancy of the cloud parcel does not change significantly within this time. The number of droplets is computed by finding the CCN of highest critical supersaturation that activates (i.e., with a diameter larger than its critical diameter, evaluated at cloud top). Particles larger than this characteristic CCN are considered droplets. This definition of cloud droplets includes large CCN, which have not attained their critical diameter but are as large as activated drops ($\sim 1 \mu\text{m}$), and does not include CCN that deactivate and become interstitial aerosol.

[22] A film-breaking model is used to evaluate the effect of FFCs. The model assumes that the presence of FFCs on the droplet surface decreases the condensation coefficient to 10^{-5} . The FFC is distributed among the aerosol by mass, which is appropriate for primary sources, whereas a surface area-weighted distribution would be more appropriate for secondary organics that have entered the particles via condensation [*Feingold and Chuang*, 2002]. As the droplet

grows, the film thickness decreases. At the point when a monolayer of FFC (0.5 nm thick) is achieved, the film breaks, and the condensation coefficient immediately increases to 0.045. The FFC mass fraction is assumed to be equal to the base case organic mass fraction, only for determining how long it takes the film to break. When FFCs are not present, a constant condensation coefficient of 0.045 is assumed, uniform for all particles. In addition, a simulation is performed with a constant condensation coefficient of 0.005 to represent the maximum potential effect of FFCs. A thermal accommodation coefficient of unity is assumed [*Shaw and Lamb*, 1999]. It should be noted that the structure and evolution of films, in addition to the size-resolved chemical composition of the films themselves, are so uncertain that the mechanism of the film-breaking model is highly speculative.

2.5. Empirical Correlations and Model Setup

[23] The *Boucher and Lohmann* [1995] and *Gultepe and Isaac* [1999] relationships correlate cloud droplet number concentration with different aerosol characteristics. Employing both relationships consistently limits two of three key aerosol-cloud interaction parameters (sulfate mass, aerosol, and droplet number). By specifying a total aerosol number concentration (N_{ap}) for each environment (Table 3), cloud droplet number concentration (N_d) is calculated according to the empirical best fit relationships of *Gultepe and Isaac* [1999], as shown by

$$\text{Continental and polluted} \quad N_d = -595 + 298 \log(N_{ap}) \quad (1a)$$

$$\text{Marine} \quad N_d = -273 + 162 \log(N_{ap}) \quad (1b)$$

[24] The *Gultepe and Isaac* [1999] correlation (equation (1a)) can be applied for N_{ap} up to 1000 and 1500 cm⁻³ for the continental and polluted environments, respectively, since this is the range of the observations. Because of this the continental and polluted fine particle number concentrations from *Whitby* [1978] are reduced so that the total aerosol number concentrations are 1000 and 1500 cm⁻³, respectively, while the mean diameter and mean dispersion are kept constant. Reducing the particle number concentration can be justified physically as dilution of an urban plume or vertical mixing of a continental air mass. Thus the polluted case should be thought of as “diluted polluted” and the continental as “clean continental.”

[25] The cloud droplet number concentration, computed from equation (1), is introduced into the *Boucher and*

Lohmann [1995] correlation to obtain the total aerosol sulfate mass concentration (m_{SO_4}):

$$\text{Average} \quad m_{\text{SO}_4} = 10^{\left\{ \frac{\log(N_d) - 2.21}{0.41} \right\}} \quad (2a)$$

$$\text{Maritime} \quad m_{\text{SO}_4} = 10^{\left\{ \frac{\log(N_d) - 2.06}{0.48} \right\}} \quad (2b)$$

Table 3 shows the base case droplet number (N_d) and total aerosol sulfate mass (m_{SO_4}) as constrained by these correlations.

[26] Aerosol mass is often dominated by the larger particles, while number is dominated by smaller particles. Because of this we need to be careful in how the sulfate is distributed throughout the size distribution. The sulfate mass determined by the *Boucher and Lohmann* [1995] correlation (m_{SO_4}) is equal to the sum of the sulfate mass within each lognormal mode. The sulfate mass concentration of each lognormal mode ($m_{\text{SO}_{4i}}$) is calculated according to equations (3)–(5):

$$m_{\text{SO}_{4i}} = \varepsilon_{\text{SO}_{4i}} \rho_{\text{ap}_i} V_i, \quad (3)$$

where

$$\rho_{\text{ap}_i} = \frac{1}{\frac{\varepsilon_{o_i}}{\rho_{o_i}} + \frac{\varepsilon_{s_i}}{\rho_{s_i}} + \frac{\varepsilon_{\text{ins}_i}}{\rho_{\text{ins}_i}}}, \quad (4)$$

where the subscripts are as follows: s denotes properties of the soluble component, o stands for the organic component (which is slightly soluble), and ins stands for the insoluble component, with subscript i indicating the modes (nuclei, accumulation, and coarse). In the absence of other soluble compounds the sulfate mass fraction ($\varepsilon_{\text{SO}_{4i}}$) is related to the soluble mass fraction (ε_{s_i}) by the ratio of their molecular weights (M_{SO_4}/M_s), where M_s is the molecular weight of ammonium sulfate. For the marine coarse aerosol the addition of NaCl yields $\varepsilon_{s_i} = \varepsilon_{(\text{NH}_4)_2\text{SO}_{4i}} + \varepsilon_{\text{NaCl}}$, where $\varepsilon_{(\text{NH}_4)_2\text{SO}_{4i}} = \varepsilon_{\text{SO}_{4i}} (M_{(\text{NH}_4)_2\text{SO}_4}/M_{\text{SO}_4})$. The volume concentration (V_i) is calculated from the number concentration (N_i), geometric mean diameter (\bar{D}_{g_i}), and geometric standard deviation (σ_{g_i}) for each mode, according to

$$V_i = N_i \left(\frac{\pi}{6} \right) \exp \left(3 \ln \bar{D}_{g_i} + \frac{9}{2} \ln^2 \sigma_{g_i} \right). \quad (5)$$

[27] Given that a variety of combinations of $m_{\text{SO}_{4i}}$ can give m_{SO_4} , we consider values that are consistent with observations. In this study, we set the fine particle mass fractions to the values reported by *Heintzenberg* [1989] (Table 2) and then compute the coarse mode sulfate mass fraction from the constraint $\sum m_{\text{SO}_{4i}} = m_{\text{SO}_4}$. If the computed coarse mode sulfate mass fraction is not within observed values, then we instead assume an observed coarse mode sulfate fraction and adjust the coarse mode number concentration so that $\sum m_{\text{SO}_{4i}} = m_{\text{SO}_4}$.

[28] Adjustment of the chemical composition or number concentration of the coarse mode can be justified in two ways. First, coarse mode measurements are often the least certain of the three modes because of limitations in the

instrumentation [*Baron and Willeke*, 2001]. Second, the contribution of the coarse mode particles to cloud droplet number is negligible, on the order of $1 - 10 \text{ cm}^{-3}$. Therefore, given that the coarse particle sulfate mass fraction can strongly influence sulfate mass burden, it is preferable to first assign the sulfate mass for the fine particles and then to attribute the remaining sulfate mass, given by the *Boucher and Lohmann* [1995] correlations, to the coarse particles.

[29] Using the procedure outlined above, coarse mode sulfate mass fractions are calculated for the marine and polluted aerosol (keeping coarse mode number concentrations constant). The calculated coarse mode sulfate mass fraction for the polluted aerosol is 0.11, midway between the observed range, 0.02–0.25 [*Ramanathan et al.*, 2001; *Neusüß et al.*, 2002; *Finlayson-Pitts and Pitts*, 1986]. Coarse mode particles in the marine boundary layer are primarily composed of sea salt, with much smaller amounts of nitrates and mineral dust [*Fitzgerald*, 1991]. Sea salt consists of $\sim 7.68\%$ (by mass) sulfate [*Seinfeld and Pandis*, 1998], so that in the absence of other mechanisms the coarse mode mass fraction of sulfate should be < 0.08 for the marine aerosol. Our analysis yields a coarse mode sulfate mass fraction of 0.01, which is slightly lower than expected.

[30] The continental aerosol distribution used lacks sufficient coarse mode particles to yield an m_{SO_4} consistent with the *Boucher and Lohmann* [1995] correlation. Increasing the coarse mode number concentration from 0.72 to 4.1 cm^{-3} satisfies the constraint $\sum m_{\text{SO}_{4i}} = m_{\text{SO}_4}$. This change has a negligible impact on CCN and droplet number concentrations.

3. Results

3.1. Base Case Updraft Velocity

[31] Ensuring that the aerosol chemistry and size distribution are consistent with observations is a necessary but not sufficient condition for the plausibility of our analysis. The base case updraft velocity must also be consistent with observations; otherwise, the sensitivities calculated may not be representative of the ambient atmosphere, as they have been shown to be strong functions of updraft velocity and chemical composition [e.g., *Rissman et al.*, 2004]. The base case updraft velocity is inferred, rather than prescribed, because updraft is highly uncertain; it is both difficult to measure and highly variable.

[32] Coalescence and entrainment may have in reality affected observations of droplet number, although these processes are not explicitly addressed within the parcel model. However, these processes can only reduce droplet number. Thus the calculated base case updraft velocity actually represents the minimum cooling rate required to produce the number of cloud droplets that are predicted by the empirical correlations. Where entrainment does exist, this means that a greater updraft velocity is required to produce the observed number of droplets. A higher updraft is expected to enhance the relative sensitivity of cloud droplet number to surface tension effects [*Rissman et al.*, 2004].

[33] The base case updraft velocity is determined iteratively. Updraft velocity is varied until cloud droplet number calculated from the cloud parcel model matches the *Gultepe and Isaac* [1999] and *Boucher and Lohmann* [1995] corre-

lations. The resulting base case updraft velocities are ~ 0.7 – 1.5 m s^{-1} for the continental case and ~ 2 – 3.5 m s^{-1} for the polluted case, which are within the expected range (e.g., 0 – 1 m s^{-1} for stratiform and ~ 1 – 17 m s^{-1} for continental cumulus clouds [Seinfeld and Pandis, 1998]). Mason [1971] found that updrafts in nonprecipitating continental cumulus clouds are typically no greater than 5 – 7 m s^{-1} . The maximum parcel supersaturations for the continental and polluted base cases are 0.7 – 0.8% and 1.2 – 1.4% , respectively. Supersaturations in the ambient atmosphere are usually $<1\%$ and almost never exceed 2% [Seinfeld and Pandis, 1998]. Although the base case updraft velocities and maximum supersaturations are higher than average values measured in situ, this is expected. Within a single cloud the higher end of the updraft velocity spectrum is expected to control the total number of cloud droplets formed. Thus, when a single updraft is used to represent the production of cloud droplets, its intensity is expected to be larger than average but still within the observed range. Thus the base case aerosol size distribution and chemical composition are reasonable representations of the ambient aerosol for the continental and polluted cases.

[34] Surface tension depression from the presence of the organics is not considered for the base case calculations. If surfactants were considered, the base case updraft velocities would be cut in half and the maximum supersaturations would be reduced to 0.4 – 0.5% and 0.8 – 0.9% for the continental and polluted cases, respectively.

[35] If the condensation coefficient were increased from 0.045 to 1.0 , the maximum supersaturation for the base case does not change significantly, but the base case updraft velocity doubles for both the continental and polluted cases. With a higher condensation coefficient an increased rate of condensation in the initial stages of cloud formation leads to a lower cloud supersaturation and thus a lower cloud droplet number. Since the droplet number is constrained, the required updraft velocity must increase in order to provide the same driving force for condensational growth.

[36] The updraft velocity for the marine environment is expected to be lower than updraft velocities over continents. However, using the Whitby [1978] distribution, the base case updraft velocity for the marine case is $\sim 13 \text{ m s}^{-1}$ (neglecting surface tension effects), which is apparently greatly overestimated. If we use a different size distribution from Heintzenberg *et al.* [2000] and Jaenicke [1993] (Table 1), the base case updraft velocity is reduced to 0.1 – 0.35 m s^{-1} . While the total number of aerosol particles remains nearly the same as the number given by Whitby [1978] (within 2%), this alternative particle size distribution has a larger proportion of particles in the accumulation mode, where the majority of CCN are found. The maximum parcel supersaturation for this new base case is $<0.5\%$, whereas using the Whitby [1978] remote marine distribution, the maximum supersaturation was $>5\%$, which is not realistic for the atmosphere. Thus we use the Heintzenberg *et al.* [2000] and Jaenicke [1993] aerosol size distribution for the marine case in our analysis.

[37] Heintzenberg *et al.* [2000] grouped a total of 64 independent observations of marine fine aerosol size distributions from all over the world according to latitude (Table 1). Interestingly, the Whitby [1978] size distribution most closely approximates the latitude range 60° – 75°S in

terms of the proportion of aerosol in the nuclei and accumulation modes. This latitude range is very remote, and in fact, Whitby [1978] actually describes the observations as representative of a “remote marine” environment. By comparison, the 24 independent observations of fine aerosol size distribution that are listed within the latitude range 15° – 60°N by Heintzenberg *et al.* [2000] are likely influenced by anthropogenic activities. Since the Boucher and Lohmann [1995] and Gulpepe and Isaac [1999] observations are from the Northern Hemisphere, we take an average of the size distribution parameters in the latitude range 15° – 60°N from Heintzenberg *et al.* [2000] to represent the fine marine aerosol in our analysis. The Jaenicke [1993] distribution is used to represent sea salt aerosol, which closely resembles the Whitby [1978] marine coarse mode aerosol distribution. With this new marine size distribution the calculated coarse mode sulfate mass fraction increases from 0.01 to 0.05 , which is closer to the expected value of ~ 0.08 .

3.2. Sensitivity of Droplet Number to Updraft Velocity

[38] The observations covered by the correlations include both stratiform and cumuliform data sets. For this reason, we consider a range of updrafts between 0.1 and 5 m s^{-1} for the continental and polluted cases and between 0.05 and 3 m s^{-1} for the marine case to cover the expected variability of droplet number from dynamical effects in both cloud types [Mason, 1971].

[39] For the updraft velocity sensitivity analysis the cloud parcel model is run twice (first at a high updraft velocity and then at a low updraft velocity) for each of the three aerosol number concentrations (1.0 , 0.75 , and 0.50 times the base case aerosol number concentration) and for each of the three environments (marine, continental, and polluted). In these simulations the organic component of the aerosol is not considered a surfactant, meaning that the surface tension remains constant as the droplet grows.

[40] For the marine base case (using the Heintzenberg *et al.* [2000] and Jaenicke [1993] distribution), cloud droplet number varies from 91 to 336 cm^{-3} as a result of changes in updraft velocity (Figure 2). The maximum parcel supersaturation corresponding to the 3 m s^{-1} updraft velocity for this case is 1.25 – 1.5% , which is on the high end of observations. This either indicates that the high updraft is very unlikely or indicates the presence of an aerosol with a chemical composition and/or size distribution that differs significantly from the average. Increasing the condensation coefficient to 1.0 decreases the maximum supersaturation for 3 m s^{-1} updrafts to 0.9 – 1.1% . However, the number of droplets also decreases by 11 – 18% .

[41] For the continental base case, cloud droplet number varies from 112 to 510 cm^{-3} (Figure 3), and for the polluted base case, cloud droplet number varies from 91 to 495 cm^{-3} as a result of changes in updraft velocity (Figure 4). For the continental case this variability ($\sim 400 \text{ cm}^{-3}$) encompasses a majority of the scatter in the observations. However, for the polluted case a significant fraction of the observations appear to be unexplained by the very large updraft variability.

[42] The maximum parcel supersaturations within 5 m s^{-1} updrafts are 1.6 – 1.9% and 1.7 – 2.0% for the continental and polluted cases, respectively. Changing the condensation

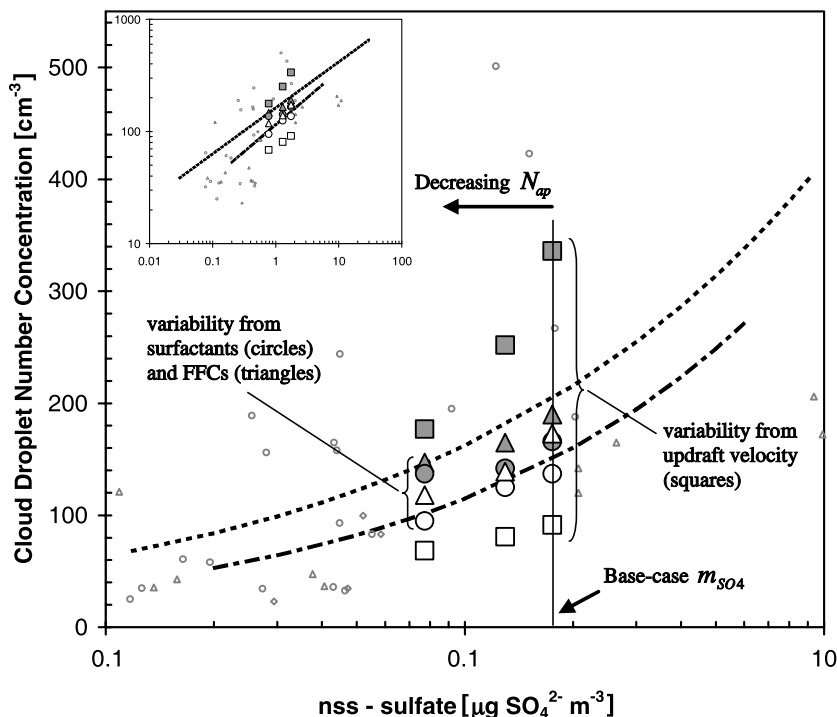


Figure 2. Marine cloud droplet number sensitivity to updraft velocity and chemical effects (using the *Heintzenberg et al.* [2000] and *Jaenicke* [1993] size distribution). Maritime observations, average correlation (dotted line), and maritime correlation (dash-dotted line) are from *Boucher and Lohmann* [1995]. Marine case cloud parcel model results for high updraft velocity (shaded squares), low updraft velocity (open squares), high organic mass fraction (shaded circles), low organic mass fraction (open circles), constant condensation coefficient (0.005, shaded triangles), and changing condensation coefficient (10^{-5} –0.045, open triangles) are overlaid on the observational data. The values of organic mass fraction and updraft velocity for each simulation point are given in Table 4. The condensation coefficient is 0.045, except where otherwise specified. The inset shows the full range of the observations on a log-log scale.

coefficient to 1.0 changes the maximum supersaturations to 1–1.4% and 1.2–1.5% for the continental and polluted cases, respectively. However, the number of droplets decreases with this higher condensation coefficient by 18–19% and 20–27% for the continental and polluted cases, respectively. Including the surface tension effect would also slightly decrease the maximum supersaturation within 5 m s^{-1} updrafts but would result in an increase in cloud droplet number by up to 39%.

3.3. Sensitivity of Droplet Number to Chemical Effects

[43] The cloud parcel model is run twice (high and low organic mass fractions specified in Table 4) for each of the three number concentrations and for each of the three aerosol types to determine the sensitivity of cloud droplet number to surfactants. Only the fine particle organic mass fractions (which contribute the most to the CCN) are manipulated. These simulations utilize a constant condensation coefficient of 0.045 under the base case updraft conditions.

[44] Two additional simulations are performed to address the sensitivity of droplet number to a delayed

condensational growth rate that may result from the presence of FFCs on the droplet surface. Surface tension effects are neglected for these simulations. First, the condensation coefficient is decreased by ~ 1 order of magnitude (from 0.045 to 0.005). Then, a nonconstant condensation coefficient is assessed using a film-breaking model, for which the lowered condensation coefficient (10^{-5}) changes to 0.045 when the film breaks. Three different aerosol number concentrations and three different aerosol types are assessed at the base case updraft velocity and base case organic mass fraction.

[45] For the marine base case, increasing the organic mass fraction from 0 to 0.41 increases the number of cloud droplets from 137 cm^{-3} (Figure 2). This increase ($\sim 30 \text{ cm}^{-3}$) is mainly due to the effect of surface tension depression by the organic species but is also influenced by the replacement of insoluble compounds with slightly soluble compounds. For the constant 0.005 condensation coefficient the number of cloud droplets for the marine base case increases further to 190 cm^{-3} . Using the film-breaking model yields a droplet number of 173 cm^{-3} . Thus the overall sensitivity of

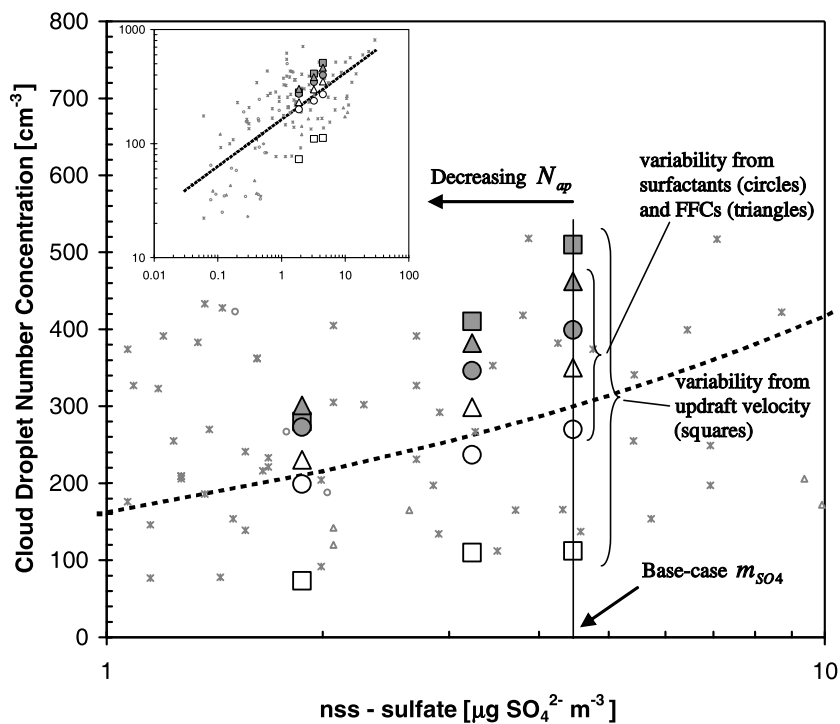


Figure 3. Same as Figure 2 but for continental aerosol with the average correlation and including all observations from *Boucher and Lohmann* [1995].

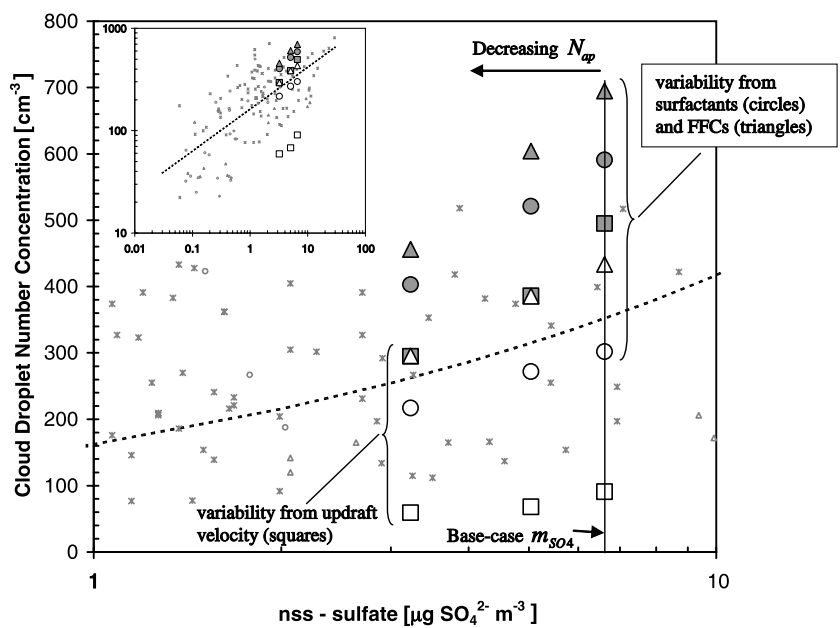


Figure 4. Same as Figure 3 but for polluted aerosol.

Table 4. Base Case, Lower, and Upper Limit Values for Updraft Velocity and Fine Particle Organic Mass Fractions Used for Assessing the Sensitivity to Dynamical and Chemical Effects, Respectively^a

Aerosol Type	Updraft Velocity, m s ⁻¹			Fine Particle Organic Mass Fraction		
	Base	Lower	Upper	Base	Lower	Upper
Marine	0.1, 0.16, 0.35	0.05	3	0.11	0	0.41
Clean continental	0.7, 1.0, 1.5	0.1	5	0.24	0	0.45
Diluted polluted	2.0, 3.0, 3.5	0.1	5	0.31	0	0.61

^aThe range of base case updraft velocities for each aerosol type is for each of the three different aerosol number concentrations (100%, 75%, and 50% of the base case N_{ap} given in Table 3). The base case fine particle organic mass fraction is from *Heintzenberg* [1989], and the upper limit in organic mass fraction is estimated from *Seinfeld and Pandis* [1998].

droplet number to chemical effects for the marine base case is ~ 50 cm⁻³. This is $\sim 20\%$ of the cloud droplet sensitivity from updraft variability.

[46] As a result of surface tension effects, increasing the organic mass fraction increases the number of droplets from 270 to 399 cm⁻³ (continental base case) and from 302 to 591 cm⁻³ (polluted base case). The constant 0.005 condensation coefficient simulation increases the number of droplets further to 462 and 695 cm⁻³ for the continental and polluted base cases, respectively. Thus the cloud droplet number sensitivity to surfactants is 32–36% (continental) and 79–96% (polluted) of the sensitivity induced by updraft variability. However, it is important to note that the number of droplets resulting from surface tension effects can be much greater than the droplet number resulting from high updraft velocity. In other words, surface tension effects shift the variability to higher droplet concentrations. This is typically the case for the polluted aerosol.

[47] Surface tension effects increased the number of cloud droplets by 9–35% (marine), 30–33% (continental), and 54–68% (polluted) from the base case. *Mircea et al.* [2002] also found that the change in droplet number resulting from replacing insoluble compounds with surfactants was greater for the urban aerosol (110% increase in droplet number from the base case) and rural aerosol (97% increase) than for marine aerosol (13% increase).

[48] The constant 0.005 condensation coefficient simulations produce the greatest number of cloud droplets resulting from chemical effects. One of the interesting results is that the highest sensitivity of cloud droplet number to condensation coefficient appears to be at or near typical observations of cloud droplet condensation coefficient (i.e., 0.045). Decreasing the condensation coefficient further (below 10⁻³) has an almost negligible effect on droplet number, as most of the aerosol particles have already activated by this point. As mentioned previously, condensation coefficients on the order of 10⁻⁵ have been suggested for atmospheric aerosol influenced by FFCs. When the film-breaking model is introduced, the effect on droplet number is less pronounced than with a constant condensation coefficient; using the film-breaking model produces 91% (marine), 76% (continental), and 62% (polluted) of the droplet number resulting from the constant condensation coefficient simulation. Nevertheless, for the polluted case the increase in droplet number using the film-breaking

model is nearly equivalent to the effect from a 5 m s⁻¹ updraft.

3.4. Chemical and Dynamical Effects for Variable Aerosol Number

[49] It is instructive to examine the variability from chemical and dynamical effects for other values of the aerosol number concentration. The striking feature for all three aerosol is the remarkable robustness of the variability; chemical effects remain significant, even when decreasing the aerosol number concentration by 25 and 50%. Since the *Gultepe and Isaac* [1999] observations of aerosol concentration only go up to 1000 cm⁻³ (for continental aerosol) and 1500 cm⁻³ (for the polluted aerosol), the correlations cannot be used to extrapolate the base case updraft velocity and we cannot assess the sensitivity for higher concentration plumes, although there are indications that the sensitivity may change under such conditions [*Rissman et al.*, 2004].

[50] In general, the relative sensitivity of cloud droplet number to surfactants increases as the aerosol number concentration decreases. This is most important for the marine case (Figure 2), while it appears negligible for the continental and polluted cases (Figures 3 and 4). For the marine case the sensitivity of droplet number to surfactants increases from 15 to 35% when the aerosol number concentration is reduced by 50% from the base case. The marine base case updraft velocities are on the most sensitive region of the relative organic surfactant sensitivity plot of *Rissman et al.* [2004]. At the lower aerosol number concentration a higher base case updraft is required. As updraft velocity increases (0.1 m s⁻¹ for the base case N_{ap} , 0.16 m s⁻¹ with 75% N_{ap} , and 0.35 m s⁻¹ with 50% N_{ap}), surface tension effects have a larger relative effect on droplet number, as expected from the results of *Rissman et al.* [2004]. Conversely, the continental base case updraft velocities are within a stable regime on the *Rissman et al.* [2004] relative sensitivity plot, and an increase in the base case updraft velocities causes only a slight increase in the relative sensitivity of droplet number to surfactants.

4. Implications for the Aerosol Indirect Effect

[51] The first indirect effect is related to changes in cloud reflectivity, which can be characterized fairly well by two of the following three parameters: cloud liquid water content, effective radius, and droplet number. By assuming a constant liquid water content (q_c) a change in droplet number (N_d) can be roughly related to a change in cloud reflectivity (R_c). The approximation $\Delta R_c \sim 0.075 \Delta \ln(N_d)$ is valid within 10% for an initial cloud reflectivity between 0.28 and 0.72 [*Seinfeld and Pandis*, 1998]. We assume an initial R_c of 0.5 and plot the average percent change in R_c resulting from changes in cloud droplet number from updraft variability and chemical effects (Figure 5). This rough approximation shows that chemical effects, which include both surface tension effects and changes in the condensation coefficient, may enhance cloud reflectivity by 4–10%, with respect to the base case cloud droplet number. Comparatively, variations in updraft velocity are expected to enhance cloud reflectivity by 2–12%.

[52] The second indirect effect, which is related to cloud lifetime, is an even greater challenge to quantify. We look at

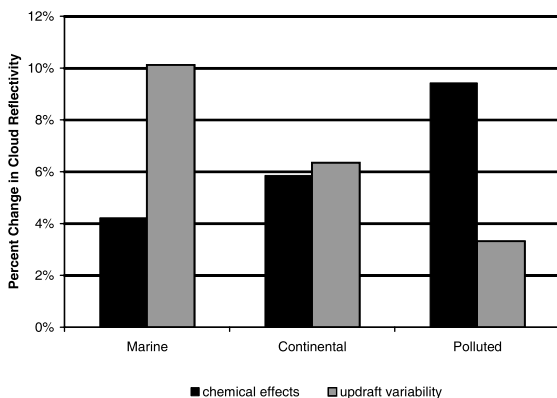


Figure 5. Estimated percent change in cloud reflectivity resulting from increases in droplet number from chemical effects and updraft variability, assuming a constant liquid water content and using a parameterization from *Seinfeld and Pandis* [1998]. An initial cloud reflectivity of 0.5 is assumed.

the rate of autoconversion (Q_{aut}) to represent the second indirect effect, since autoconversion is the rate of initial generation of rain/drizzle from cloud water, which has direct implications for cloud lifetime. The *Khairoutdinov and Kogan* [2000] parameterization describes Q_{aut} as a function of droplet number and cloud liquid water content, $Q_{\text{aut}} = 1350q_c^{2.47}N_d^{-1.79}$. Assuming constant liquid water content, the increase in droplet number resulting from chemical effects suggests that Q_{aut} may decrease by 34–63%. This is due to the smaller sizes of the droplets, which have smaller settling velocities, thereby decreasing their rate of collision. For comparison, a high updraft velocity may decrease Q_{aut} by 19–76%.

5. Conclusions

[53] This study assesses the variability in cloud droplet number that may result from the effect of organic species on surface tension and from the effect of film-forming compounds on the water vapor condensation coefficient. The cloud droplet number variability is compared to the variability caused by uncertainties in updraft velocity. An inverse modeling approach is employed for this task. Using a detailed numerical cloud parcel model, observed aerosol characteristics, and correlations of cloud droplet versus sulfate and cloud droplet versus aerosol number, a most probable size distribution and updraft velocity for polluted and clean conditions are obtained. The variation in cloud droplet number from expected variations in aerosol chemistry and updraft velocity is then compared to the observed cloud droplet number scatter in the empirical aerosol sulfate-cloud droplet number correlation.

[54] Three important results come out of this study. First, chemical effects can potentially have a significant effect on cloud droplet number concentration for conditions ranging from marine to polluted in the regions surrounding the North American continent and Atlantic Ocean. Chemical effects may account for an average of 28% (marine), 49%

(continental), and >100% (polluted) of the variability in cloud droplet number, as compared to the variability from updraft velocity. This underlines the importance of including chemical effects within GCM assessments of the aerosol indirect effect and challenges the common belief that the variability seen in empirical aerosol number/cloud droplet number relationships is primarily from the highly variable cloud dynamics.

[55] Another important finding is that surface tension effects may enhance the sensitivity of droplet number to variations in updraft velocity. Thus the microphysical characteristics of clouds originating from organic CCN are likely more sensitive to the shape of the updraft velocity spectrum than are the characteristics of clouds composed of purely inorganic CCN. Including surface tension effects increases the number of cloud droplets formed in 5 m s^{-1} updrafts by 55–63% for the polluted case and 30–39% for the continental case and increases the number of cloud droplets formed in 3 m s^{-1} updrafts by 14–16% for the marine case. Thus surface tension effects could help to explain the high end of the measured cloud droplet number variability.

[56] The other significant finding is that the relative effect of organic species on cloud droplet number appears relatively insensitive to the aerosol number concentration for a wide range of aerosol and updraft conditions typically found in GCM simulations. This suggests that the relative importance of chemical effects on cloud droplet number may not be masked by fluctuations in aerosol number concentration expected on the spatial scale of a typical GCM grid cell.

[57] **Acknowledgments.** This work was supported by a National Science Foundation CAREER award and by the NASA Earth Observing System–Interdisciplinary Science program (NASA EOS-IDS). We also acknowledge the support of a Georgia Institute of Technology Presidential Fellowship and a National Center for Atmospheric Research Advanced Study Program Fellowship.

References

- Abdul-Razzak, H., and S. J. Ghan (2000), A parameterization of aerosol activation: 2. Multiple aerosol types, *J. Geophys. Res.*, *105*, 6837–6844.
- Abdul-Razzak, H., S. J. Ghan, and C. Rivera-Carpio (1998), A parameterization of aerosol activation: 1. Single aerosol type, *J. Geophys. Res.*, *103*, 6123–6131.
- Baron, P. A., and K. Willeke (Eds.) (2001), *Aerosol Measurement: Principles, Techniques, and Applications*, 2nd ed., Wiley-Interscience, Hoboken, N. J.
- Beresheim, H., F. L. Eisele, D. J. Tanner, L. M. McInnes, D. C. Ramsey-Bell, and D. S. Covert (1993), Atmospheric sulfur chemistry and cloud condensation nuclei (CCN) concentrations over the northeastern Pacific coast, *J. Geophys. Res.*, *98*, 12,701–12,711.
- Boucher, O., and U. Lohmann (1995), The sulfate-CCN-cloud albedo effect: A sensitivity study with two general circulation models, *Tellus, Ser. B*, *47*, 291–300.
- Charlson, R. J., J. E. Lovelock, M. O. Andreae, and S. G. Warren (1987), Oceanic phytoplankton, atmospheric sulphur, cloud albedo and climate, *Nature*, *326*, 655–661.
- Chuang, P. Y. (2003), Measurement of the timescale of hygroscopic growth for atmospheric aerosols, *J. Geophys. Res.*, *108*(D9), 4282, doi:10.1029/2002JD002757.
- Conant, W. C., et al. (2004), Aerosol-cloud drop concentration closure in warm cumulus, *J. Geophys. Res.*, *109*, D13204, doi:10.1029/2003JD004324.
- Facchini, M. C., M. Mircea, S. Fuzzi, and R. J. Charlson (1999), Cloud albedo enhancement by surface-active organic solutes in growing droplets, *Nature*, *401*, 257–259.
- Facchini, M. C., S. Decesari, M. Mircea, S. Fuzzi, and G. Loglio (2000), Surface tension of atmospheric wet aerosol and cloud/fog droplets in relation to their organic carbon content and chemical composition, *Atmos. Environ.*, *34*, 4853–4857.

- Feingold, G., and P. Y. Chuang (2002), Analysis of the influence of film-forming compounds on droplet growth: Implications for cloud microphysical processes and climate, *J. Atmos. Sci.*, *59*, 2006–2018.
- Finlayson-Pitts, B. J., and J. N. Pitts (1986), *Atmospheric Chemistry: Fundamentals and Experimental Techniques*, John Wiley, Hoboken, N. J.
- Fitzgerald, J. W. (1991), Marine aerosols: A review, *Atmos. Environ., Part A*, *25*, 533–545.
- Gultepe, I., and G. A. Isaac (1999), Scale effects on averaging of cloud droplet and aerosol number concentrations: Observations and models, *J. Clim.*, *12*, 1268–1279.
- Hegg, D. A., R. J. Ferek, and P. V. Hobbs (1993), Light scattering and cloud condensation nucleus activity of sulfate aerosol measured over the northeast Atlantic Ocean, *J. Geophys. Res.*, *98*, 14,887–14,894.
- Heintzenberg, J. (1989), Fine particles in the global troposphere: A review, *Tellus, Ser. B*, *41*, 149–160.
- Heintzenberg, J., D. C. Covert, and R. Van Dingenen (2000), Size distribution and chemical composition of marine aerosols: A compilation and review, *Tellus, Ser. B*, *52*, 1104–1122.
- Houghton, J. T., Y. Ding, D. J. Griggs, M. Noguer, P. J. van der Linden, X. Dai, K. Maskell, and C. A. Johnson (Eds.) (2001), *Climate Change 2001: The Scientific Basis—Contribution of Working Group I to the Third Assessment Report of the Intergovernmental Panel on Climate Change*, Cambridge Univ. Press, New York.
- Jaenicke, R. (1993), Tropospheric aerosols, in *Aerosol-Cloud-Climate Interactions*, edited by P. V. Hobbs, pp. 1–31, Academic, San Diego, Calif.
- Khairoutdinov, M., and Y. Kogan (2000), A new cloud physics parameterization in a large-eddy simulation model of marine stratocumulus, *Mon. Weather Rev.*, *128*(1), 229–243.
- Leitch, W. R., G. A. Isaac, J. W. Strapp, C. M. Banic, and H. A. Wiebe (1992), The relationship between cloud droplet number concentrations and anthropogenic pollution: Observations and climatic implications, *J. Geophys. Res.*, *97*, 2463–2474.
- Li, Y. Q., P. Davidovits, Q. Shi, J. T. Jayne, C. E. Kolb, and D. R. Worsnop (2001), Mass and thermal accommodation coefficients of H₂O (g) on liquid water as a function of temperature, *J. Phys. Chem.*, *105*(47), 10,627–10,634.
- Li, Z., A. L. Williams, and M. J. Rood (1998), Influence of soluble surfactant properties on the activation of aerosol particles containing inorganic solute, *J. Atmos. Sci.*, *55*(10), 1859–1866.
- Mason, B. J. (1971), *The Physics of Clouds*, Oxford Univ. Press, New York.
- Mircea, M., M. C. Facchini, S. Decesari, S. Fuzzi, and R. J. Charlson (2002), The influence of the organic aerosol component on CCN supersaturation spectra for different aerosol types, *Tellus, Ser. B*, *54*, 74–81.
- Mozurkewich, M. (1986), Aerosol growth and the condensation coefficient for water: A review, *Aerosol Sci. Technol.*, *5*, 223–236.
- Nenes, A., S. Ghan, H. Abdul-Razzak, P. Y. Chuang, and J. H. Seinfeld (2001), Kinetic limitations on cloud droplet formation and impact on cloud albedo, *Tellus, Ser. B*, *53*, 133–149.
- Nenes, A., R. J. Charlson, M. C. Facchini, M. Kulmala, A. Laaksonen, and J. H. Seinfeld (2002), Can chemical effects on cloud droplet number rival the first indirect effect?, *Geophys. Res. Lett.*, *24*(17), 1848, doi:10.1029/2002GL015295.
- Neusüß, C., H. Wex, W. Birmili, A. Wiedensohler, C. Koziar, B. Busch, E. Brüggemann, T. Gnauk, M. Ebert, and D. S. Covert (2002), Characterization and parameterization of atmospheric particle number-, mass-, and chemical-size distributions in central Europe during LACE 98 and MINT, *J. Geophys. Res.*, *107*(D21), 8127, doi:10.1029/2001JD000514.
- Pruppacher, H. R., and J. D. Klett (2000), *Microphysics of Clouds and Precipitation*, Kluwer Acad., Norwell, Mass.
- Quinn, P. K., D. S. Covert, T. S. Bates, V. N. Kapustin, D. C. Ramsey-Bell, and L. M. McInnes (1993), Dimethylsulfide/cloud condensation nuclei/climate system: Relevant size-resolved measurements of the chemical and physical properties of the atmospheric aerosol particles, *J. Geophys. Res.*, *98*, 10,411–10,427.
- Ramanathan, V., et al. (2001), Indian Ocean experiment: An integrated analysis of the climate forcing and effects of the great Indo-Asian haze, *J. Geophys. Res.*, *106*, 28,371–28,398.
- Rissman, T., A. Nenes, and J. H. Seinfeld (2004), Chemical amplification (or dampening) of the Twomey effect: Conditions derived from droplet activation theory, *J. Atmos. Sci.*, *61*(8), 919–930.
- Saxena, P., and L. M. Hildemann (1996), Water-soluble organics in atmospheric particles: A critical review of the literature and application of thermodynamics to identify candidate compounds, *J. Atmos. Chem.*, *24*, 57–109.
- Seinfeld, J., and S. Pandis (1998), *Atmospheric Chemistry and Physics: From Air Pollution to Climate Change*, John Wiley, Hoboken, N. J.
- Shaw, R. A., and D. Lamb (1999), Experimental determination of the thermal accommodation and condensation coefficients of water, *J. Chem. Phys.*, *111*(23), 10,659–10,663.
- Shulman, M., M. C. Jacobson, R. J. Carlson, R. E. Synovec, and T. E. Young (1996), Dissolution behavior and surface tension effects of organic compounds in nucleating cloud droplets, *Geophys. Res. Lett.*, *23*, 277–280.
- Turpin, B. J., and H. J. Lim (2001), Species contributions to PM_{2.5} mass concentrations: Revisiting common assumptions for estimating organic mass, *Aerosol Sci. Technol.*, *35*, 602–610.
- Twomey, S. (1974), Pollution and the planetary albedo, *Atmos. Environ.*, *8*, 1251–1256.
- Van Dingenen, R., F. Raes, and N. R. Jensen (1995), Evidence for anthropogenic impact on number concentration and sulfate content of cloud-processed aerosol particles over the North Atlantic, *J. Geophys. Res.*, *100*, 21,057–21,067.
- Whitby, K. T. (1978), The physical characteristics of sulfur aerosols, *Atmos. Environ.*, *12*, 135–159.

S. Lance and A. Nenes, School of Earth and Atmospheric Sciences, Georgia Institute of Technology, 311 Ferst Drive, Atlanta, GA 30332-0340, USA. (nenes@eas.gatech.edu)

T. A. Rissman, Department of Chemical Engineering, California Institute of Technology, Mail Code 210-41, 1200 E. California Blvd., Pasadena, CA 91125, USA.

Appendix F

AEROSOL-CLOUD DROP CONCENTRATION CLOSURE IN WARM CUMULUS*

*Full Citation: Conant, W. C., T. M. VanReken, T. A. Rissman, V. Varutbangkul, H. H. Jonsson, A. Nenes, J. L. Jimenez, A. E. Delia, R. Bahreini, G. C. Roberts, R. C. Flagan, and J. H. Seinfeld (2004), Aerosol-cloud drop concentration closure in warm cumulus, *Journal of Geophysical Research*, 109(D13), D132094, doi: 10.1029/2003JD004324.

© 2004 American Geophysical Union (AGU). This appendix is reprinted with permission from the American Geophysical Union.

Aerosol–cloud drop concentration closure in warm cumulus

W. C. Conant,¹ T. M. VanReken,² T. A. Rissman,² V. Varutbangkul,² H. H. Jonsson,³ A. Nenes,⁴ J. L. Jimenez,⁵ A. E. Delia,⁶ R. Bahreini,¹ G. C. Roberts,⁷ R. C. Flagan,^{1,2} and J. H. Seinfeld^{1,2}

Received 3 November 2003; revised 29 April 2004; accepted 14 May 2004; published 14 July 2004.

[1] Our understanding of the activation of aerosol particles into cloud drops during the formation of warm cumulus clouds presently has a limited observational foundation. Detailed observations of aerosol size and composition, cloud microphysics and dynamics, and atmospheric thermodynamic state were collected in a systematic study of 21 cumulus clouds by the Center for Interdisciplinary Remotely-Piloted Aircraft Studies (CIRPAS) Twin Otter aircraft during NASA's Cirrus Regional Study of Tropical Anvils and Cirrus Layers–Florida Area Cirrus Experiment (CRYSTAL-FACE). An “aerosol–cloud” closure study was carried out in which a detailed cloud activation parcel model, which predicts cloud drop concentration using observed aerosol concentration, size distribution, cloud updraft velocity, and thermodynamic state, is evaluated against observations. On average, measured droplet concentration in adiabatic cloud regions is within 15% of the predictions. This agreement is corroborated by independent measurements of aerosol activation carried out by two cloud condensation nucleus (CCN) counters on the aircraft. Variations in aerosol concentration, which ranged from 300 to 3300 cm⁻³, drives large microphysical differences (250–2300 cm⁻³) observed among continental and maritime clouds in the South Florida region. This is the first known study in which a cloud parcel model is evaluated in a closure study using a constraining set of data collected from a single platform. Likewise, this is the first known study in which relationships among aerosol size distribution, CCN spectrum, and cloud droplet concentration are all found to be consistent with theory within experimental uncertainties much less than 50%. Vertical profiles of cloud microphysical properties (effective radius, droplet concentration, dispersion) clearly demonstrate the boundary layer aerosol's effect on cloud microphysics throughout the lowest 1 km of cloud depth. Onboard measurements of aerosol hygroscopic growth and the organic to sulfate mass ratio are related to CCN properties. These chemical data are used to quantify the range of uncertainty associated with the simplified treatment of aerosol composition assumed in the closure study. *INDEX TERMS:* 0305 Atmospheric Composition and Structure: Aerosols and particles (0345, 4801); 0320 Atmospheric Composition and Structure: Cloud physics and chemistry; 0345 Atmospheric Composition and Structure: Pollution—urban and regional (0305); 1610 Global Change: Atmosphere (0315, 0325); 3314 Meteorology and Atmospheric Dynamics: Convective processes; *KEYWORDS:* aerosol, CCN, cloud microphysics

Citation: Conant, W. C., et al. (2004), Aerosol–cloud drop concentration closure in warm cumulus, *J. Geophys. Res.*, 109, D13204, doi:10.1029/2003JD004324.

1. Introduction

[2] Satellite and aircraft observations have corroborated predictions that particulate pollution increases cloud albedo and decreases precipitation efficiency [Twomey, 1977;

Albrecht, 1989; Rosenfeld and Lensky, 1998; Ackerman et al., 2000]. Because such effects alter Earth's climate by perturbing the radiation balance and hydrological cycle, they are called indirect effects of aerosol on climate, or

¹Department of Environmental Science and Engineering, California Institute of Technology, Pasadena, California, USA.

²Department of Chemical Engineering, California Institute of Technology, Pasadena, California, USA.

³Center for Interdisciplinary Remotely-Piloted Aircraft Studies, Naval Postgraduate School, Monterey, California, USA.

⁴Schools of Earth and Atmospheric Sciences and Chemical and Biomolecular Engineering, Georgia Institute of Technology, Atlanta, Georgia, USA.

⁵Department of Chemistry and Biochemistry, Cooperative Institute for Research in Environmental Sciences, University of Colorado, Boulder, Colorado, USA.

⁶Program in Atmospheric and Oceanic Sciences, University of Colorado, Boulder, Colorado, USA.

⁷Center for Atmospheric Sciences, Scripps Institution of Oceanography, University of California, San Diego, La Jolla, California, USA.

simply “indirect effects” [Houghton *et al.*, 2001]. To have confidence in predictions of indirect effects, it is necessary to develop physically based and observationally validated models of the sensitivity of cloud microphysics to the properties of the cloud condensation nuclei (CCN) on which the cloud forms. The most fundamental of these models is the adiabatic parcel model, which predicts cloud drop concentrations within ascending air parcels by simulating the transfer of water vapor and heat between the adiabatically cooling parcel and the CCN within using a first principles treatment of chemical and thermodynamic processes. These models are used as tools to formulate and validate the relatively simpler parameterizations that are used in cloud-resolving models and global climate simulations [e.g., Nenes and Seinfeld, 2003].

[3] In an attempt to give such models a firm observational foundation, two closure studies were conducted during NASA’s Cirrus Regional Study of Tropical Anvils and Cirrus Layers–Florida Area Cirrus Experiment (CRYSTAL-FACE). The first of these studies [VanReken *et al.*, 2003] finds that measured CCN concentrations at 0.2% and 0.85% supersaturations agree to within 10–20% of that predicted by Köhler theory given measured aerosol concentration and size distribution. This is termed aerosol-CCN closure. If chemical and kinetic effects on cloud activation are relatively minor, one could proceed to predict cloud drop number concentration (CDNC) directly from the measured CCN spectrum and observed updraft velocity in a CCN-CDNC closure [e.g., Snider and Brenguier, 2000]. Studies that attempt CCN-CDNC closure have generally been successful within a factor of ~50% [Twomey and Warner, 1967; Fitzgerald and Spysers-Duran, 1973; Snider and Brenguier, 2000]. In contrast, aerosol-CCN closure attempts have met with more limited success, such that predicted CCN often exceeds measured values (see review by Chuang *et al.* [2000]). The lack of aerosol-CCN closure brings into question either (1) our fundamental understanding of the role of aerosol composition on the CCN spectrum (“chemical effects,” see Nenes *et al.* [2002]) or (2) the techniques used to determine CCN spectrum or composition and mixing state. If CCN instrument bias is the source of the problem, however, this has implications for previous studies that found CCN-CDNC closure. A different strategy is taken here, in which a cloud model that predicts cloud drop concentration directly from updraft velocity and the aerosol physicochemical properties is evaluated against observations. This is termed aerosol-CDNC closure, in which the computation of CCN spectrum as an intermediary step is implicit. Taken together, aerosol-CCN closure and aerosol-CDNC closure provide a rigorous test on our understanding of how aerosol controls cloud microphysics.

[4] CRYSTAL-FACE was conducted during July 2002 from Boca Chica Naval Air Station near Key West, Florida (Figure 1). The Center for Interdisciplinary Remotely-Piloted Aircraft Studies (CIRPAS) Twin Otter, one of six aircraft deployed during CRYSTAL-FACE, provided redundant and calibrated measurements of aerosol concentration and size distribution from 0.003 to 5 μm ; mass concentrations of sulfate, organic carbon, nitrate, and ammonium from 0.1 to 0.6 μg ; cloud condensation nucleus (CCN) concentration at 0.2% and 0.85% supersaturation; cloud drop concentration and size distribution from 1 to 1600 μm ;

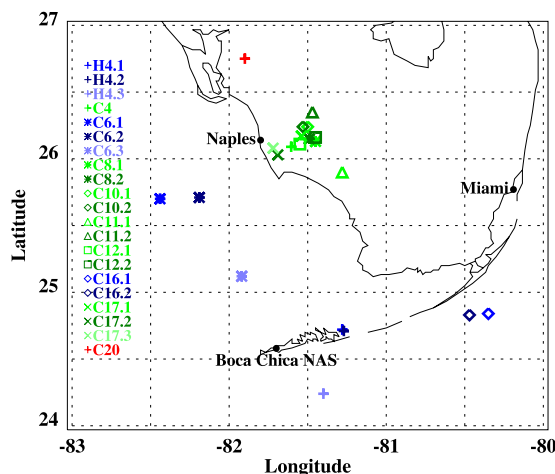


Figure 1. Map of the CRYSTAL-FACE region in South Florida. Each symbol denotes the location of a cloud characterized by the Twin Otter.

and absolute wind speed with 0.35 m s^{-1} accuracy, which is derived from a gust probe on the nose of the aircraft and internal navigation and GPS positioning systems following Lenschow [1986] (Table 1). Cumulus clouds were characterized by flying several successively higher constant altitude legs, starting with one or two legs below cloud base to obtain the aerosol properties and thermodynamic state of the air entrained through cloud base; the final legs often ended more than 2500 m above cloud base. Nine flights were dedicated to this strategy, during which 20 clouds were profiled (Table 2). These flights were conducted over land and ocean with concentrations of CCN(0.85%) ranging from 300 cm^{-3} to 3300 cm^{-3} and cloud core drop concentrations ranging from 250 cm^{-3} to 2300 cm^{-3} . These data provide a wide range of conditions necessary to evaluate models of aerosol effects on warm cumulus microphysics.

2. Aerosol-CDNC Closure

[5] The Nenes *et al.* [2002] model simulates the activation of aerosol into cloud drops by numerically integrating the equations describing the rate of transfer of heat and water vapor between the gas and particulate phases for a parcel rising at constant updraft velocity [e.g., Pruppacher and Klett, 1997]. Initial temperature, pressure, humidity, and updraft velocity are specified along with a sufficient number of lognormal modes required to describe the dry aerosol size distribution (4 modes are used here, divided into 50 size bins per mode). Dry aerosol composition (NH_4^+ , SO_4^{2-} , Na^+ Cl^-) and insoluble aerosol fraction are specified separately for each mode. It is known that soluble gases (e.g., HNO_3) and various organic species may have chemical effects (i.e., partial solubility, surface activity, film-forming tendency) that influence the CCN spectrum and the cloud activation process [Nenes *et al.*, 2002]. Although the model is designed to simulate such chemical effects, they are assumed negligible here. This model compares well with other explicit cloud activation models when standard cases are used as input [Kreidenweis *et al.*, 2003]. The conden-

Table 1. Aerosol, Cloud, and Meteorological Instrumentation for the Office of Naval Research CIRPAS Twin Otter Aircraft During CRYSTAL-FACE

Measurement	Instrument	Measurement Parameters	Measurement Principle
Aerosol concentration	condensation particle counters (3)	geometric diameter > {3 nm, 7 nm, 13 nm}	varying supersaturations of butanol
Aerosol size distribution	Dual Autostatic Classifier Detector System (DACADS)	geometric diameter: 15–800 nm	electrostatic classification; dry and ambient humidity
	Aerosol Spectrometer Probe (PCASP)	geometric diameter: 100–2500 nm	optical scattering
	Aerodynamic Particle Sizer (APS)	aerodynamic diameter: 500–10,000 nm	aerodynamic classification
Cloud and aerosol size distribution	Forward Scattering Spectrometer Probe (FSSP)	geometric diameter: 3–47 μm	optical forward scattering
	Cloud and Aerosol Particle Spectrometer (CAPS)	geometric diameter: 0.5–1600 μm	optical forward scattering and two-dimensional imaging
CCN concentration	Caltech CCN counter	$S_C < 0.85\%$	continuous flow; increasing temperature
	Scripps CCN counter	$S_C < 0.2\%$	continuous flow; increasing temperature
Aerosol composition	Aerodyne Aerosol Mass Spectrometer (AMS)	mass concentration: SO_4^{2-} , NH_4^+ , NO_3^- , OC 100–600 nm	flash ionization; quadrupole mass spectrometer
Updraft velocity and wind speed	five-hole turbulence probe, C-MIGITS inertial navigation system, and Novatel GPS	wind velocity; aircraft position and attitude	wind velocity = aircraft ground velocity (C-MIGITS INS/GPS) – aircraft air velocity (turbulence and Pitot-static probes)

sation coefficient for this study is taken to be 0.06 on the basis of the laboratory studies of *Shaw and Lamb* [1999]. (Other laboratory studies have found values ranging from 0.03 to 0.3; the standard value assumed in most cloud models is 0.042 [*Pruppacher and Klett*, 1997].) Particle surface tension is taken to be that of liquid water. Simulations are made for each cloud profiled during CRYSTAL FACE using aerosol properties and thermodynamic state measured beneath the cloud.

[6] Aerosol observations used as input to the model are obtained separately for each cloud in the following manner. Dry aerosol size measured by the Dual Autostatic Classifier Detector System (DACADS) (10–800 nm) and the Aerosol Spectrometer Probe (PCASP) optical probe (100–2500 nm) in the subcloud legs are merged into a single size distribution, averaged, and parameterized in the

form of four lognormal modes. Submicrometer modes are taken to be ammonium bisulfate, which is consistent with the observed Aerodyne Aerosol Mass Spectrometer (AMS) $\text{NH}_4^+:\text{SO}_4^{2-}$ ratios. Supermicrometer modes are presumed to be NaCl. Over land, the AMS composition (100–600 nm) often showed significant organic carbon (OC) content. OC is generally less soluble than sulfate aerosol [e.g., *Prenni et al.*, 2003; *Gysel et al.*, 2004] and may reduce aerosol surface tension [*Facchini et al.*, 1999]. These have opposite effects on the CCN spectrum, relative to sulfate aerosol. The impact of the reduced solubility on the CCN spectrum is smaller when the OC is internally mixed with sulfate. Because no comprehensive model for OC activation behavior yet exists, previous attempts at CCN prediction have typically implemented one of two assumptions: either OC is entirely insoluble and internally mixed

Table 2. Summary of Cloud Observations

Flight Number –Cloud Number	Date	Number of Passes (Below/In)	CCN 0.85%, cm^{-3}	σ CCN, cm^{-3}	N_A , cm^{-3} (35–800 nm)	OC/SO ₄ Mass Ratio (100–600 nm)	w_i m s^{-1}	N_D Predicted, cm^{-3}	N_D Observed, cm^{-3}	
									Method 1	Method 2
H4-1	27 June	2/4	764	53	811	0.16	1.4	626	769	820
H4-2	27 June	2/3	1062	97	1049	0.15	1.0	699	959	1177
H4-3	27 June	2/11	515	17	510	0.13	0.9	382	413	409
C4	7 July	3/6	860	129	1025	0.4	2.2	830	1042	1427
C6-1	10 July	1/6	343	20	294	0.3	0.9	220	216	275
C6-2	10 July	2/11	407	156	309	0.3	1.8	279	280	272
C6-3	10 July	1/7	569	103	612	0.3	1.0	400	434	392
C8-1	13 July	1/6	NA ^a	NA	1167	1.3	1.5	847	1078	1277
C8-2	13 July	1/5	NA	NA	1034	1.5	1.9	938	936	935
C10-1	18 July	1/5	2785	124	3394	2.4	1.5	2239	2285	2279
C10-2	18 July	1/5	2783	111	3350	2.5	1.2	1893	1995	2167
C11-1	18 July	1/7	1746	40	1879	1.9	2.8	1666	1717	1959
C11-2	18 July	2/5	2520	210	3007	2.5	2.4	2358	2526	2667
C12-1	19 July	1/12	561	65	478	NA	2.4	469	523	575
C12-2	19 July	2/8	450	215	410	NA	2.2	397	633	641
C16-1	25 July	1/5	316	18	348	0.6	1.1	273	360	390
C16-2	25 July	1/3	316	18	348	0.5	1.6	312	330	426
C17-1	26 July	2/6	454	43	455	0.4	1.7	384	423	419
C17-2	26 July	1/7	305	30	373	0.3	1.6	306	493	363
C17-3	26 July	1/9	NA	NA	681	0.3	2.4	614	NA	642
C20 ^b	29 July	1/1	967	387	1797	1.0	2.8	1225	1167	1167

^aNA, not applicable.

^bThis was a brief pass into the base of a larger convective system.

with sulfate [e.g., *Snider and Brenguier*, 2000] or OC is treated as equivalent to ammonium sulfate (which rapidly approaches the insoluble and internally mixed assumption in the limit of low OC fraction) [e.g., *Rivera-Carpio et al.*, 1996]. *VanReken et al.* [2003] show that the aerosol-CCN closure at 0.2% and 0.85% in CRYSTAL-FACE was accurate to within 10–20% given an ammonium sulfate assumption, in spite of wide variability in the observed AMS OC:SO₄²⁻ ratio. Given this good agreement, we initially implement the simpler assumption that OC behaves like sulfate aerosol for the purposes of cloud activation. The appropriateness of this assumption will be examined in detail in section 4. In section 5, we study the implications of varying composition through a series of sensitivity studies. Concentration measured by the DACADS is tested against that measured by a TSI 3010 condensation particle counter (CPC), which measures all aerosol particles greater than 12 nm. In clear-air cases with stable CPC concentrations (standard deviation over 100 s < 15% of the mean), the DACADS and CPC concentrations agree with a negligible mean bias and a root-mean-square deviation of 20%. The DACADS-CPC difference is not sensitive to total concentration or mean aerosol size, indicating that no significant saturation or size-dependent biases exist for the range of conditions observed here. The inlet system for the Twin Otter cabin instruments was tested in a wind tunnel experiment, in which the transmission of particles from 10 to 2500 nm was indistinguishable from unity.

[7] The measured CCN spectrum is not taken as an input to the parcel model (see methods employed by *Twomey* [1959], *Snider and Brenguier* [2000], and *Snider et al.* [2003] for examples). Instead, full Köhler theory is employed at each stage of droplet growth, using the measured aerosol properties described above. *VanReken et al.* [2003] show 10–20% agreement between calculated and measured CCN concentrations at 0.2% and 0.85% during CRYSTAL-FACE assuming the aerosol composition is ammonium sulfate, which is similar to the assumption used here of ammonium bisulfate and sodium chloride. Thus the CCN spectrum implicitly assumed here when solving the droplet growth equations is consistent with the CCN observations. Certain chemical effects on droplet activation, such as those of surface-forming organic films [*Feingold and Chuang*, 2002] and water-soluble gases [*Laaksonen et al.*, 1998], are not strictly tested in aerosol-CCN closure. These effects can contribute to a lack of aerosol-CDNC closure, even in the event that there is good aerosol-CCN closure.

[8] Observations of updraft velocity were taken from below-cloud and cloud base legs. For the remainder of this paper, “cloud base” refers to the lowest 100 m of these cumulus clouds, which extended several kilometers in height and contained coherent updrafts hundreds of meters in horizontal extent. Updraft velocity is obtained from a combination of instruments, including a five-hole gust probe on the nose of the aircraft, a Pitot-static pressure tube, a Coarse/Acquisition Code–Micro-Electro-Mechanical Systems (MEMS) Integrated GPS/INS Tactical System (C-MIGITS) GPS/inertial navigation system (INS), and the Novatel GPS system. Calibrations for all wind variables are derived using the procedures outlined by *Lenschow* [1986]. The aircraft velocity estimated by the C-MIGITS system was repro-

duced using position data from the more accurate Novatel GPS, while retaining the short-period response characteristics of the C-MIGITS INS, which is based on quartz accelerometers. Uncertainties in total air speed, INS-retrieved heading and pitch angles, GPS-retrieved aircraft velocity, and the accuracy of the gust probe differential pressure measurements combine for a total uncertainty in updraft velocity of 0.35 m s⁻¹. A number of model calculations are made for each cloud to obtain predicted CDNC(*w*) as a function of updraft velocity *w*. Then, a representative average CDNC(predicted) is obtained from

$$\text{CDNC}(\text{predicted}) = \int \text{CDNC}(w)wn(w)dw / \int wn(w)dw,$$

where *n(w)* is the observed distribution of updraft velocity below and within cloud base and the *w* weighting is introduced to account for the higher mass flux across cloud base associated with stronger updrafts. This procedure produces CDNC predictions on average 0.5% lower than simply using mass-flux-weighted mean *w*.

[9] Droplet concentrations were observed at 1-Hz (~50 m) resolution using the Cloud and Aerosol Spectrometer (CAS) optical probe on board the Cloud, Aerosol, and Precipitation Spectrometer (CAPS) integrated spectrometer system [*Baumgardner et al.*, 2001]. The CAS measures droplet size from 0.5 to 60 μm in 20 size bins using a forward scattering principle similar to that of the Forward Scattering Spectrometer Probe (FSSP-100). Relative to the FSSP-100, the CAS contains certain design improvements that have (1) obviated the need for dead-time corrections at concentrations less than 26,000 cm⁻³ (at the Twin Otter air speed of 50 m s⁻¹) because of improved electronics, (2) reduced the frequency of coincidence errors by reducing the viewing volume and refining detection techniques, and (3) allowed for spectra to be obtained at lower sizes and finer size resolution by increasing laser power. These improvements make the CAS ideal for studying cloud activation, which requires observations to be close to cloud base, where droplets are still small and have activated sufficiently recently to dramatically improve the probability of finding nearly adiabatic conditions. Coincidence errors, which are typical of single-particle optical probes [e.g., *Baumgardner et al.*, 1985; *Burnet and Brenguier*, 2002], are estimated to decrease cloud drop concentrations by 1% at 800 cm⁻³ and 10% at 7000 cm⁻³. Corrections to CDNC are applied using the principles outlined by *Burnet and Brenguier* [2002] and the CAS instrument characteristics (viewing area equals 0.112 mm²; beam width equals 0.1 mm). Because of an improved CAS detection algorithm, particles outside the depth of field (DOF) do not contribute to coincidence errors in concentration as much as in the FSSP probes (D. Baumgardner, personal communication, 2004). The CAS size measurement was calibrated before, during, and after the campaign using monodisperse polystyrene and glass beads. Viewing volume is estimated to be accurate within 15% using geometric characterization of the CAS viewing area and typical uncertainties in flow rates [e.g., *Dye and Baumgardner*, 1984]. The particular CAS flown on the Twin Otter has shown stable properties in calibration and performance over its lifetime. Observed liquid water content (LWC) is measured by integrating the CAS size distribution.

The large cumulus cloud (H4.3) sampled on 27 June provides an opportunity to test the LWC measured by the CAS probe. The core of this cloud exhibited an adiabatic profile in equivalent potential temperature θ_e and LWC for each pass from 500 m (base) to 1700 m, meaning that at the core of the cloud, θ_e was constant to within 10% of the subcloud minus out-of-cloud θ_e difference and LWC was within 10% of the adiabatic calculation. Coincidence-related sizing errors [Burnet and Brenguier, 2002] are estimated to cause a range of uncertainty in LWC from -0.5% to $+1\%$ for this cloud, whose core contained droplet concentrations of 410 cm^{-3} . Coincidence uncertainties in LWC assume that coincidence events can be caused by particles within the viewing volume outside the DOF, which is assumed to have an effective sampling volume equal to that within the DOF [Dye and Baumgardner, 1984; D. Baumgardner, personal communication, 2004]. (Although the viewing volume outside the DOF is 2–3 times that within the DOF, the signals from particles outside the DOF are significantly reduced, thus limiting their contribution to coincidence artifacts on droplet size.) Uncertainties in determining the adiabatic LWC profile are small when compared with literature uncertainty estimates [e.g., Lawson and Blyth, 1998], because cloud base itself was determined within 30 m through cloud base penetrations. This determination was made microphysically, by observing GPS altitudes at the point where a cloud drop mode emerged from the haze in the observed CAS size distribution (0.5–50- μm diameter). On the basis of this accuracy in cloud base altitude the uncertainty in adiabatic LWC is better than 10% when more than 300 m above cloud base. Because this cloud consistently exhibited core LWC values within 10% of adiabatic calculations on each pass up to 1200 m above cloud base, a 15% uncertainty in CAPS LWC is taken. This can be used to evaluate uncertainties in mean droplet volume (nominal uncertainty 33%) and number concentration (nominal uncertainty 15%), the product of which is LWC. Assuming that uncertainty estimates above are uncorrelated and normally distributed, the 15% accuracy in LWC confirms the uncertainty estimate in number concentration of 15% and increases confidence in the sizing uncertainty estimate to within 18% for mean droplet volume and 6% for volumetric average diameter.

[10] Data for the model-observation comparison in cloud drop concentration are carefully screened to avoid the influences of entrainment mixing, which is not treated in the model simulations. First, droplets below 1- μm diameter are neglected as unactivated haze. (Alternative methods to define haze based on the minimum between the haze mode and the droplet mode produced equivalent results in determining droplet concentration.) Cloud drop concentration observations are selected on the basis of the following criteria: (1) The cloud drop effective diameter is greater than 2.4 μm ($d_e = \langle d^3 \rangle / \langle d^2 \rangle$, where $\langle \rangle$ indicates an average over the size distribution $>1 \mu\text{m}$); (2) it is narrow, having geometric standard deviation, $\sigma < 1.5$; (3), it contains no droplets larger than 30- μm diameter (to eliminate precipitation); and (4) cloud edge observations are neglected (i.e., both the preceding and subsequent observations must satisfy criteria 1–3). Furthermore, only the lowest passes through the cloud are taken, which were most often within 50 m of cloud base. Two methods are used to determine mean “cloud

base droplet concentration” from the remaining data. For method 1, droplet concentration is averaged over those observations having LWC exceeding the mean adiabatic value. A range of adiabatic LWC values is determined separately for each cloud based on variability in lifting condensation level computed from subcloud measurements of pressure, water vapor mixing ratio q_g , and potential temperature θ and by assuming a moist adiabatic ascent through the cloud. Bias errors in lifting condensation level due to biases in the thermodynamic measurements are reduced through the microphysical determination of cloud base altitude discussed above. The average is obtained by weighting with updraft velocity (positive values only) to represent the mass flux through cloud base. The screening criterion that LWC exceed the mean adiabatic value minimizes the potential for including cloud regions strongly affected by entrainment, which tends to reduce droplet concentration and LWC. Method 2 screening is based on the observation that CDNC often contributes a much larger source of variability than volumetric mean diameter (d^3) to LWC (in these regions near cloud base). This is characteristic of artifacts related to averaging over cloud boundaries or including subadiabatic parcels that have been subjected to inhomogeneous mixing processes. Thus method 2 screening omits low LWC observations, so that variance in $\ln(\text{CDNC})$ is less than the variance in $\ln(d^3)$. In this manner, those observations having the maximum LWC at each pass are selected, irrespective of the adiabatic prediction.

[11] Most often, droplet concentrations derived using method 2 are larger than those derived using method 1. Two explanations are suggested below. Typically, there is a range of humidity beneath each cloud that produces variability in the adiabatic LWC profile. The source for this range is that air entering cloud base is not undiluted boundary layer air, but rather is a varying mixture of boundary layer air and lower tropospheric air that is typically drier and warmer, which often has different aerosol properties. If the subcloud measurements are somehow biased toward drier air because of limited sampling statistics, then the computed adiabatic LWC will be biased low. Because inhomogeneous mixing processes dominate over homogeneous mixing processes in these cloud regions, this bias would produce lower measured droplet concentrations. On the other hand, the range in LWC within the screened data may be a direct consequence of the variability in subcloud humidity. Higher-humidity parcels may be associated with stronger updrafts that originated closer to the surface, which is a source of moisture, buoyancy, and CCN. This may explain the strong positive correlation between updraft velocity and CDNC that was often observed near cloud bases. Because it is not clear from the present measurements whether method 1 or method 2 more accurately isolates adiabatic parcels, each method will be used, and differences will be interpreted as due to experimental uncertainty.

[12] The aerosol-CDNC closure for 20 of the clouds using method 1 screening is shown in Figure 2. A linear fit to the data (dashed line) has a slope of 1.03. The slope is statistically indistinguishable from unity, and the mean percent deviation is -12% with a standard deviation about the mean of 13%. The mean underprediction is comparable to the uncertainty in the measured number concentration. The standard deviation is comparable to the variability in

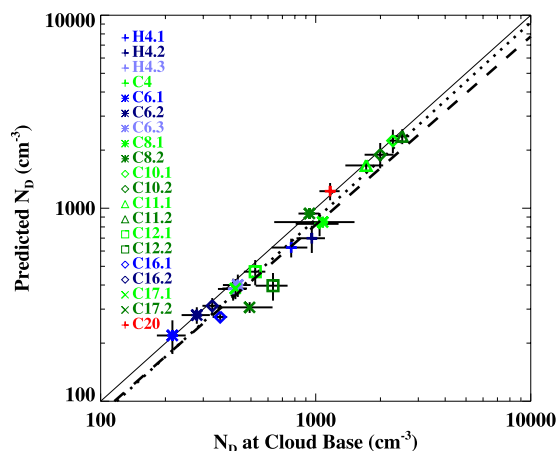


Figure 2. Aerosol-CDNC closure: predicted versus observed droplet concentration. Observed values use method 1 screening (see text) for adiabaticity. The short-dashed line represents an unweighted least squares linear fit to the data in log-log units. The long-dashed line represents a fit to the data when method 2 screening is used. The solid line represents perfect model-observation agreement. The term “cloud base” reiterates that observations used in this plot were generally taken in adiabatic regions within 100 m of cloud base.

the DACADS concentration used as input to the model. There is no statistically significant correlation between the modeled-observed CDNC difference and the following quantities: OC:SO₄²⁻ mass concentration ratio, modeled-measured CCN concentration, updraft velocity, updraft velocity variance, or total droplet concentration. While these factors may influence the model-observation difference (as discussed in sections 4 and 5), their combined effect does not exceed the experimental noise. Also shown in Figure 2 is the linear fit of the model predictions to method 2 data. This can be considered a range of uncertainty related to the method used to differentiate adiabatic parcels from sub-adiabatic parcels. The slope using method 2 is still indistinguishable from unity at 0.98. The mean deviation is larger at -16%, with a standard deviation about the mean of 15%.

[13] The difference between methods 1 and 2 of 4% combined with the 15% uncertainty in the CAS concentration measurement yields an estimated 16% uncertainty in the measured cloud base concentration. Uncertainty in modeled cloud drop concentration is 10% from a contribution of uncorrelated uncertainties: 5% from aerosol concentration, 0.5% from DACADS sizing uncertainty, 8% from updraft velocity uncertainty, and 5% from parcel modeling simplifications. Uncertainty in modeled values of CDNC is thus 11%. This yields a net experimental uncertainty of 20% in the model-observation comparison. The mean model-observation bias taking an average of methods 1 and 2 for observed concentration is -14%. This bias is within the estimated experimental uncertainty. We note that the model assumes that aerosol composition is pure ammonium bisulfate, which is not entirely consistent with the observed

composition and hygroscopic data presented in section 4. The effect of varying the ammonium bisulfate assumption on the model-observation closure is discussed in section 5.

3. Effects of Aerosol on the Vertical Profile of Cloud Microphysics

[14] A more comprehensive description of cloud microphysics must include the effects of entrainment mixing, as adiabatic parcel model predictions are only useful in regions where there is little or no mixing among parcels of differing histories. Outside of these “adiabatic cores,” entrainment mixing alters droplet concentrations, size distribution, LWC, and cloud thermodynamics via complex and unresolved mechanisms. Cloud albedo and precipitation efficiency are very sensitive to both cloud drop concentration and the shape of the size distribution; thus it will be useful to investigate the apparent relationships between aerosol, cloud drop concentration, and size distribution in sub-adiabatic cloud regions.

[15] At the core of these uncertainties is the observation that the dispersion in the cloud drop size distribution generally exceeds that of model predictions. Likewise, dispersion tends to be greater in polluted clouds than in unpolluted clouds [McFarquhar and Heymsfield, 2001]. It is not clear whether this increase is due to activation of entrained aerosol [Bower and Choulaton, 1988], activation of interstitial aerosol within vertically accelerating parcels [Segal et al., 2003], differential droplet growth rates due to chemical differences among droplets [Liu and Daum, 2002; Feingold and Chuang, 2002], or multiphase flow processes such as enhanced coalescence or supersaturation due to vortex spin-out [Shaw, 2003].

[16] To illustrate the large effect of aerosol on the vertical profile of cloud properties, two extreme examples from

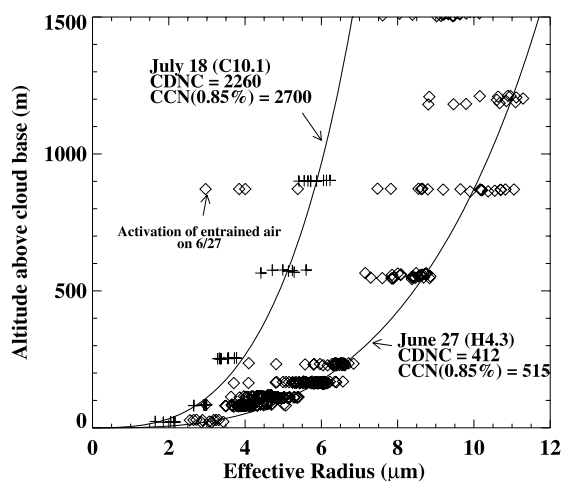


Figure 3. CCN-forced variations in CDNC and influence on the vertical profile of effective radius. The stated CCN and CDNC values for each cloud were obtained below cloud and within 100 m of cloud base, respectively. Solid lines are adiabatic predictions using observed subcloud thermodynamic properties and observed CDNC within 50 m of cloud base.

27 June (H4.3) and 18 July (C10.1) are shown in Figure 3 with their respective adiabatic calculations. For each cloud both peak effective radius and peak droplet concentrations maintained nearly adiabatic values through the lowest ~ 1 km of the cloud core. H4.3 exhibited an adiabatic core 1200 m above cloud base, whereas C10.1 appeared to be more strongly influenced by entrainment, with adiabatic LWC values only in the lowest pass.

[17] A variety of phenomena, including bimodal spectra, activation of entrained CCN, and evidence for a mixture of both homogeneous and inhomogeneous mixing processes, was observed from profiles taken in this study. For example, the points identified in Figure 3 as “activation of entrained air” in cloud H4.3 were characterized by high droplet concentrations, narrow size spectra, and small effective radii and were found within a strong updraft 900 m above cloud base. These features are identical to those of recently activated parcels found near cloud base and are inconsistent with microphysical properties found in detraining, evaporating cloud parcels, which characteristically have broad dispersions and low concentrations. Likewise, the subadiabatic profile of LWC in C10.1 was accompanied by a positive gradient in droplet dispersion strong enough to maintain nearly adiabatic profiles of effective radius and droplet concentration. An in-depth evaluation of these phenomena is beyond the scope of this work, yet deserves further study given the array of instrumentation directed toward aerosol and cloud microphysical characterization.

4. Relationships Among Hygroscopic Growth, CCN, and Organic Carbon

[18] In section 2, the model assumed that CCN are composed of simple salts. In this section, we examine this assumption using observations of organic carbon and sulfate mass concentrations, hygroscopic growth, and CCN properties. These observations were made on the Twin Otter aircraft with relatively rapid time resolution (5 min for composition) and thus can be used to capture variability in aerosol properties during a single flight.

[19] It is widely acknowledged that the hygroscopic properties of organic carbon (OC) aerosol vary among differing species and that OC aerosols generally behave differently from inorganic salts. Two important quantities relevant to OC hygroscopic properties are explored here: First is hygroscopic growth (defined below); second is critical supersaturation/CCN concentration. Compared with sulfate aerosol of the same dry diameter, OC aerosol generally produces fewer dissolved species per unit volume. This effect leads to smaller hygroscopic growth and higher critical supersaturation. Certain species of OC can even be insoluble and hydrophobic. In contrast, surface active OC species (especially humics) have been found to reduce surface tension, hence decreasing the critical supersaturation of the aerosol relative to the case in which surface tension is not reduced [Facchini *et al.*, 1999]. The effect of surface tension reduction is less apparent on hygroscopic growth, being noticeable only at small (<100 nm) sizes. When OC is found in the same aerosol population as inorganic salts, such as sulfate, the degree to which these species are internally mixed within individual particles plays an impor-

tant role in the aggregate hygroscopic properties of the aerosol population.

[20] In light of these complicated and competing effects and the currently poor ability to speciate atmospheric organics, there is a need for observations to constrain the hygroscopic properties of OC-containing aerosol populations in various regions. Some insight into this behavior for the organic species observed during CRYSTAL-FACE is obtained and presented here using three measurements: the DACADS, which measures aerosol size distribution at dry (15–20%) and moist (50–75%) relative humidities (RH); the Caltech CCN counter, measuring concentration of aerosol having critical supersaturations below 0.85%, and the AMS measurement of OC and SO_4^{2-} mass concentrations.

[21] The hygroscopic growth factor of a particle $f(\text{RH})$ is defined as the ratio of its equilibrium diameter $D(\text{RH})$ at a specified relative humidity RH to its dry diameter d : $f(\text{RH}) = D(\text{RH})/d$. In an arbitrary aerosol population, particles of a fixed dry size will have varying composition and hence varying values of $f(\text{RH})$. The ideal instrument to measure $f(\text{RH})$ as a function of d is the tandem differential mobility analyzer (DMA), in which the distribution of $f(\text{RH})$ values is obtained for each dry size d [e.g., Brechtel and Kreidenweis, 2000]. Given current instrument configurations, this measurement takes a prohibitively long time for aircraft sampling, during which aerosol properties would be varying considerably. In contrast to the tandem DMA, the DACADS used on the Twin Otter obtains size distributions from two identical DMA columns operating at different relative humidities. This method provides more limited information, in that the effect of chemical heterogeneities at each size is not obtained, but has the distinct advantage that complete size distributions are obtained every 100 s. An effective value of $f(\text{RH})$ is obtained from the DACADS data as a function of d using two methods (Figures 4a and 4b). The first method simply calculates the required (nonuniform) shift in diameter of the dry size distribution to reproduce the moist size distribution (Figure 4b). This method is subject to uncertainties related to differences in the size-dependent loss rates and calibration uncertainties between the dry and humid DMA columns. The second method takes advantage of the fact that most size distributions exhibit distinct Aitken and accumulation size modes, each of which shifts coherently with relative humidity (Figure 4a). In the second procedure both the dry and humid size distributions are represented as two or three lognormal modes using a least squares fitting technique. An effective $f(\text{RH})$ is determined for Aitken and accumulation modes separately on the basis of the shift in mode diameter. Changes in the width of the mode may be due to chemical heterogeneity within the population. This method provides less information than method 1, but does not suffer from size-dependent calibration and loss uncertainties as long as such uncertainties are slowly varying with size. To reduce sampling noise, each of the 11 days used in this study is subdivided into 2–6 periods representing distinct atmospheric conditions (altitude range, over land versus over sea, presence or lack of significant concentrations of <30 -nm particles). All DACADS size distributions made within each period

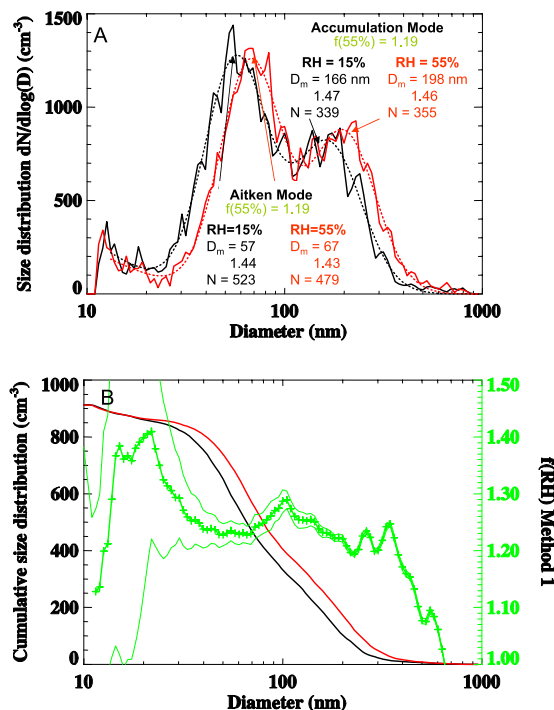


Figure 4. Illustration of methods 1 and 2 (see text) for determining hygroscopic growth factor from the DACADS data. (a) Dry and humid (55% RH) size distribution for measurements below 800-m altitude in the vicinity of clouds H4.1 and H4.2. The lognormal fitting is shown as dashed lines. The fitted parameters and method 2 $f(\text{RH} = 55\%)$ values are shown for each mode. (b) Cumulative size distributions from Figure 4a above, plotted as a function of dry diameter with the method 1 hygroscopic growth factor. Truncation in the size distribution limits accuracy beyond 300 nm.

are averaged together before being analyzed for hygroscopic growth. To minimize the occurrence of cases in which the humid column is not sufficiently moist to deliquesce particles that were dry in the atmosphere, only observations with ambient RH > 60% are considered.

[22] To relate observed hygroscopic growth factors to observed CCN concentrations, an effective cutoff diameter $D_C(0.85\%)$ is obtained from the CCN(0.85%) concentration and the dry DACADS size distribution. $D_C(0.85\%)$ is defined such that

$$\text{CCN}(0.85\%) = \int_{D_C(0.85\%)}^{800 \text{ nm}} N(d) dd,$$

where $N(d)$ is the DACADS-measured dry size distribution. For an aerosol population composed completely of ammonium sulfate, $D_C(0.85\%)$ would be approximately 32 nm. Less hygroscopic species would exhibit larger values of $D_C(0.85\%)$. For the observations presented here,

$D_C(0.85\%)$ ranges from 20 to 60 nm, which generally falls within the Aitken mode. Thus the hygroscopic properties found at Aitken mode size ranges will be most relevant to the CCN(0.85%) closure. Figure 5a illustrates the relationship between $f(\text{RH})$ of the Aitken mode to $D_C(0.85\%)$. Only cases in which method 1 and method 2 agree within 10% are included in the analysis. Variability in humid RH (which ranged from 50% to 75%) is a source of uncertainty in the following analyses (Figure 5b). The weak correlation between RH and $f(\text{RH})$ among the data used in this study indicates a small effect of RH variability relative to that of aerosol composition. The relationship between Aitken mode hygroscopic growth and $D_C(0.85\%)$ suggests that compositional variations are influencing both hygroscopic growth and critical supersaturation in a consistent manner. Data

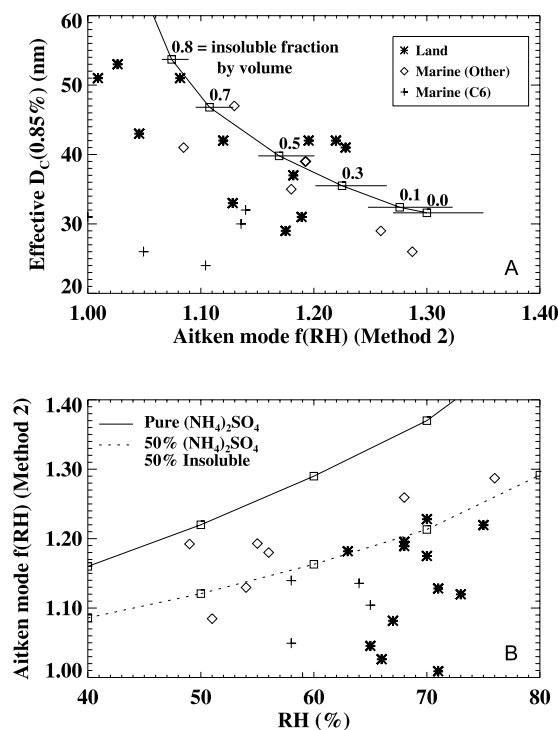


Figure 5. (a) Effective cutoff diameter for $S_C = 0.85\%$ plotted versus $f(\text{RH})$ for the Aitken mode using method 2. Diamonds are overland flights, asterisks are marine flights, and pluses are data from the marine flight C6 (discussed in text). Model simulations for $(\text{NH}_4)_2\text{SO}_4$ mixed internally with the indicated volume fraction of insoluble material are shown as connected squares. The $f(\text{RH})$ in the model calculations curve corresponds to 63% RH, and the range bars represent values from 59% to 69% (median values for ocean and land, respectively). (b) The $f(\text{RH})$ plotted versus humid DMA RH for the same points as in Figure 5a. The curves correspond to uncrystallized $(\text{NH}_4)_2\text{SO}_4$. The solid curve represents pure sulfate, and the dashed curve represents sulfate internally mixed with an equal volume of insoluble material (50% OC by volume would correspond to about 35% OC by mass).

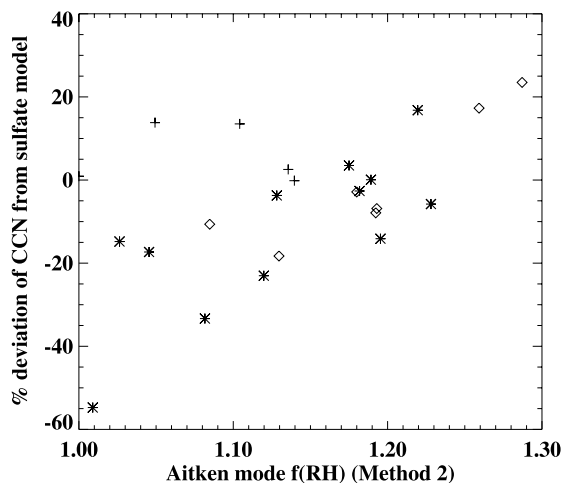


Figure 6. Percent difference between observed $CCN(0.85\%)$ and $N(d > 32 \text{ nm})$ obtained from the DMA plotted as a function of $f(RH)$ of the Aitken mode. Symbols are the same as those in Figure 5.

from marine flight C6 (10 July) are shown separately in Figures 5a and 5b, since the simultaneously low $D_C(0.85\%)$ and $f(RH)$ values are unique. Sea salt has a very low activation diameter ($D_C(0.85\%) = 25 \text{ nm}$) and may not have been deliquesced in the humid DMA, which was operating near the NaCl crystallization point of 62% RH. It is conceivable that small sea-salt particles contributed significantly to the Aitken mode concentrations on this flight (the open sea wind speed at 50-m altitude ranged from 7 to 12 m s^{-1}), although fine sea-salt concentrations in excess of 100 cm^{-3} exceed even the surf zone observations of Clarke *et al.* [2003].

[23] Overlain on Figure 5a is the relationship between $D_C(0.85\%)$ and $f(RH)$ obtained from model calculations assuming an internal mixture of ammonium sulfate solution and insoluble material. The curve corresponds to $RH = 63\%$, and the horizontal bars represent the effect of varying RH from 59% to 69% in the $f(RH)$ calculation. Two model curves are shown for Figure 5b to illustrate the expected $f(RH)$ for pure ammonium sulfate aerosol and that for a 50/50 volumetric mix of sulfate and insoluble material (e.g., 35% OC by mass).

[24] While $D_C(0.85\%)$ is more uniquely related to composition than CCN concentration, it is relevant to examine the relationships between hygroscopic growth and CCN concentration to bound the effect variations in hygroscopic growth have on $CCN(0.85\%)$. Figure 6 illustrates the percent difference between observed $CCN(0.85\%)$ to that predicted assuming the DACADS dry size distribution assuming ammonium sulfate (i.e., $D_C(0.85\%) = 32 \text{ nm}$), plotted versus $f(RH)$. The variability in CCN concentration falls within the range of -30% to $+20\%$, with one outlier approaching -60% (from C20), and this variability is clearly associated with the hygroscopic growth factor for the Aitken mode.

[25] Last, we explore the relationship between OC and hygroscopic behavior. $D_C(0.85\%)$ is plotted versus the ratio of $OC:SO_4^{2-}$ mass concentrations observed by the AMS

100–600-nm diameter particles in Figure 7. Two regimes exist. In the first regime, where $OC:SO_4^{2-}$ mass ratio is < 0.5 , a very weak relationship exists between CCN cutoff diameter and OC fraction, despite a large variability in $D_C(0.85\%)$. In the second regime, for which $OC:SO_4^{2-} > 0.5$, cutoff diameter increases with increasing OC fraction, indicative of the expected lower hygroscopicity of OC species. The majority of these high- $OC:SO_4^{2-}$ observations were made on flights C10 and C11 (18 July 2002). Backward Lagrangian trajectories computed from the National Oceanic and Atmospheric Administration (NOAA) Hybrid Single-Particle Lagrangian Integrated Trajectory (HYSPPLIT) [Draxler, 1999] model for this day estimate that the air mass below 2000 m resided over the Florida peninsula for over 48 hours in a slow, southerly flow. This contrasts with the other days studied here, in which the air masses resided over land for less than 24 hours. An interesting relationship between OC and $f(RH)$ appears for the cases when $OC:SO_4^{2-} < 0.5$ (Figure 8a). There is a general decrease in the hygroscopic behavior of the Aitken mode when OC fractions increase from 0.1 to 0.5. An interpretation of this result must take into account that the bulk of AMS mass is taken from sizes larger than those in the Aitken mode and that the accumulation mode shows a much weaker relationship between hygroscopic growth and $OC:SO_4^{2-}$ ratio relative to the Aitken mode (Figure 8b). These results imply that OC plays a strong role in Aitken mode hygroscopicity and a weaker role in accumulation mode hygroscopicity. These observations are consistent with accumulation mode particles being internal mixtures of OC and SO_4^{2-} .

[26] Despite the relationships seen among $f(RH)$, $D_C(0.85\%)$, and $OC:SO_4$ mass ratios, there is no statistically significant correspondence between each of these three observations and the degree of aerosol-CDNC closure. The first three quantities are measured in longer (6–60 min) out-of-cloud periods, which allows for much reduced sampling uncertainty, whereas CDNC and updraft velocity are taken from relatively shorter (tens of seconds) sampling periods within cloud base regions. Despite this increase in sampling uncertainty, it is notable that the standard deviation between the observations and the mod-

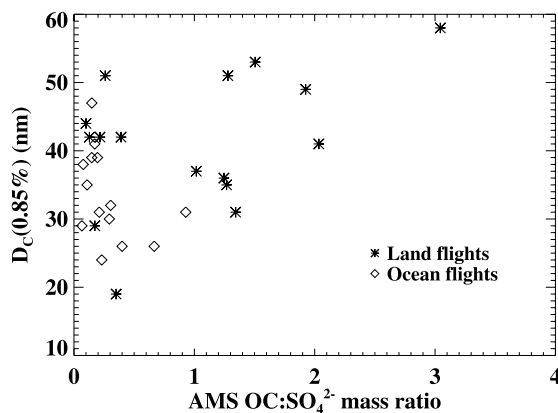


Figure 7. Relationship between $D_C(0.85\%)$ and AMS-measured organic carbon to sulfate mass ratio.

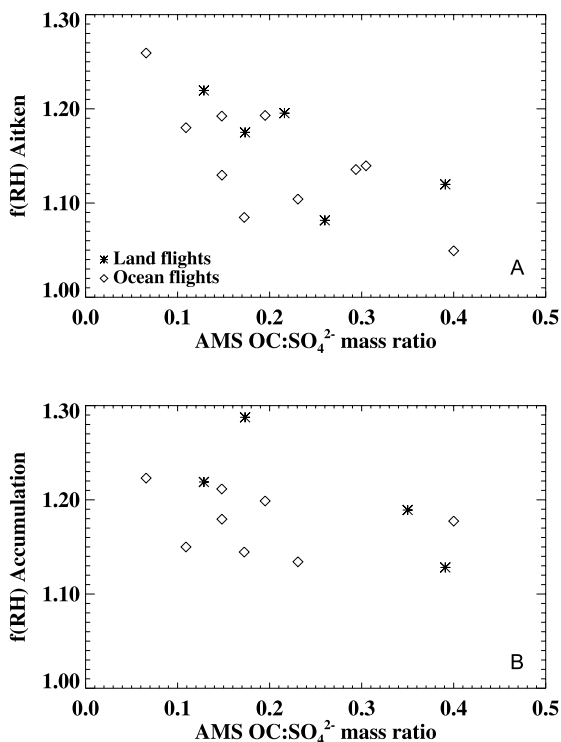


Figure 8. (a) Relationship between Aitken mode $f(\text{RH})$ and AMS-measured organic carbon to sulfate mass ratio for $\text{OC}:\text{SO}_4^{2-}$ ratios below 0.5. (b) Same as Figure 8a, but for accumulation mode $f(\text{RH})$.

els of CDNC is of order 15%. This suggests that the range of variation in CCN concentration that is related to aerosol hygroscopicity (Figure 6) is an upper limit on the influence composition has on CDNC in this study.

5. Discussion

[27] To summarize, cloud drop concentrations in Florida cumulus were observed to vary from 300 cm^{-3} to

2300 cm^{-3} , and this is driven primarily by large variations of CCN concentration in this region. The effects of the boundary layer aerosol on cloud microphysics persist through at least the lowest 1 km of the clouds. An aerosol-CDNC closure is obtained between predicted and observed CDNC with a bias within the experimental uncertainty of 20% and variability in model-observation agreement within $\sim 15\%$, which is comparable to that expected because of experimental sampling limitations. The above closures assume ammonium bisulfate aerosol composition. The CCN closure exhibits variability with a 17% standard deviation, which is found to be related to composition, as inferred from the observed hygroscopic growth and the organic carbon to sulfate mass ratio.

[28] We can now ask two questions. (1) Given the 14% model-observation agreement for aerosol-CDNC closure and the 10–20% agreement for aerosol-CCN closure found by *VanReken et al.* [2003], what constraints do these observations place on assumptions entering the models? (2) What are the most important elements for the complete aerosol-CCN-cloud closure, and are there simplifications that can be used in aerosol activation models for this region?

5.1. Question 1

[29] Table 3 illustrates the sensitivity of CCN and CDNC to variations in certain key modeling assumptions. Table 3 values are derived for two specific test cases here, but are consistent with the analyses of *Roberts et al.* [2002], *VanReken et al.* [2003], and *Rissman et al.* [2004]. Two quite different cases are chosen as examples, one from the relatively clean marine case on 10 July and the other from one of the most polluted cases on 18 July. The baseline case corresponds to ammonium bisulfate aerosol, condensation coefficient of 0.06, surface tension of water, no soluble gases, and updraft velocity of 2 m s^{-1} . The accuracy of the CDNC sensitivity tests is $\pm 2\%$ because of the size resolution used in the parcel model. The CDNC sensitivity to varying sulfate type (rows 1 and 2 in Table 3) may have somewhat larger uncertainties ($\sim 5\%$) due to simplifications in the parcel model's treatment of sulfate water activity.

[30] The effect of varying modeling assumptions on the CCN spectrum is comparable to the 17% root-mean-square variability in aerosol-CCN closure shown in section 4 and by *VanReken et al.* [2003]. Thus the CCN data do not rule out moderate variations in the chemical assumptions used.

Table 3. Effects of Changing Model Assumptions on Predicted CCN and CDNC^a

	CCN 0.2%		CCN 0.85%		CDNC	
	C10.1	C6.1	C10.1	C6.1	C10.1	C6.1
$(\text{NH}_4)_2\text{SO}_4$	-1.5%	-1.2%	-0.2%	-0.9%	+4%	+5%
H_2SO_4^b	-15%	-13%	-3%	-10%	-13%	-24%
50% insoluble (externally mixed)	-50%	-50%	-50%	-50%	-28%	-41%
50% insoluble (internally mixed)	-23%	-21%	-5%	-19%	-5%	-15%
20% surface tension reduction	+18%	+19%	+5%	+15%	+8%	+11%
50% insoluble (internal) and 20% surface tension reduction	-2%	-1%	0%	-1%	+4%	+0%
Updraft + 0.35 m s^{-1}	ND	ND	ND	ND	+8%	+5%
Condensation coeff. = 0.03	ND	ND	ND	ND	+11%	+10%
Condensation coeff. = 0.3	ND	ND	ND	ND	-9%	-10%

^aSee text. ND, not a model-dependent parameter.

^bThe sulfuric acid calculations include 35% H_2O by weight to the dry size distribution because of the fact that “dry” aerosol size distribution is measured at 15–20% RH. The other sulfate species are assumed to be crystallized below 20% RH.

The values in Table 3 should be interpreted keeping in mind that predicted CDNC using ammonium bisulfate is, on average, $\sim 15\%$ lower than the observations, which is still within the estimated experimental uncertainty of 20%. The -15% bias in the baseline model-observation difference is opposite to that expected from the neglect of species less soluble than ammonium bisulfate. For example, if one were to infer from the median value of $f(\text{RH})$ shown in Figure 5 that the insoluble fraction was $\sim 50\%$, then model observation bias would further decrease by approximately 10%. This would increase model-observation bias beyond the estimated experimental uncertainties. Note that the inference of insoluble fraction from the $f(\text{RH})$ data presented in section 4 is associated with large uncertainties, and this result should not be overinterpreted. Both the CCN and the CDNC closures suggest smaller insoluble fractions. However, it is significant that the sign of this discrepancy contrasts with some previous studies, in which a larger-than-measured insoluble fraction was needed in order to obtain closure (see review given by *VanReken et al.* [2003]). Moreover, the sign and magnitude of the model-observation discrepancy support the lower values of water condensation coefficient (~ 0.06) that have been used over the previous 50 years, as higher values (~ 0.3 or greater) would increase the model-observation difference beyond the estimated uncertainties.

5.2. Question 2

[31] *Twomey* [1959] derived a simple analytical approximation to obtain droplet concentration from updraft velocity and a two-parameter fit to the CCN spectrum, $\text{CCN}(S) = CS^k$,

$$\text{CDNC} = C^{2/(k+2)} \left[\frac{cw^{3/2}}{kB(k/2, 3/2)} \right]^{k/(k+2)}, \quad (1)$$

where w is updraft velocity, B is the beta function, and c is a constant that depends on initial parcel thermodynamic state and aerosol chemical properties. In contrast, the parcel model used in the present study performs a detailed numerical integration of the growth equation, where a 200-bin size distribution is derived from a 4-mode lognormal fit to the data, and droplet growth is derived from complete Köhler theory, as opposed to just the supersaturation spectrum. Given the wide range of conditions encountered during CRYSTAL-FACE, it is interesting to test how much added predictive ability is achieved by using the more detailed calculations. To address this, a series of calculations are made using equation (1), which are then compared to the more detailed parcel model calculations. First, the parameters C and k are taken from model-derived CCN concentrations at 0.2% and 0.85%, and w is taken from the measurements. The small, but finite, 7% standard deviation between the simple Twomey approximation and the detailed calculations is presumably caused by the simplicity of the Twomey expression. Next, the Twomey equation is used as a tool to test which parameters controlled droplet concentration during CRYSTAL-FACE. First, the simplest assumption is taken, in which CCN at 0.85% concentration is the only model input from observations; k is fixed at 0.8 (a common assumption), and updraft velocity is fixed at 2 m s^{-1} . The standard deviation between the detailed model

and this simple case is 15%. Thus CCN at 0.85% together with representative, but fixed, values of updraft velocity and spectral shape match detailed droplet concentration calculations to within 15%. Introducing observed values of k (which range from 0.32 to 0.85) drops the standard deviation only to 13%. Introducing measured updraft velocity with fixed k improves this to 8%, and introducing measured w and k improves the situation marginally to within 7%. When comparing the Twomey model to observations, considering only CCN at 0.85% leaves a variability of 18%, while the full Twomey equation leaves only 13% of the signal unexplained, which is the same as when observations are compared to the detailed model.

[32] In conclusion, this study and that of *VanReken et al.* [2003] have obtained closure among simultaneous measurements of aerosol physical properties, CCN concentrations, cloud drop concentrations, and models that use simple chemistry within the experimental accuracy of $\sim 20\%$. The degree of closure of 20% in this subtropical region with urban and maritime influences rules out any anomaly of the magnitude reported by some previous studies (see review given by *VanReken et al.* [2003]) that were conducted in different regions. Previous studies may have been influenced by differing aerosol compositions among the regions, differing cloud dynamics, and different measurement and analysis techniques. The degree of closure is not sufficiently precise to constrain certain chemical effects on cloud activation that have magnitudes less than 20% (Table 3). This study provides hope that future measurements using similar closure strategies together with improved experimental techniques will afford better accuracy in understanding aerosol-cloud interactions.

[33] **Acknowledgment.** This work was supported by National Aeronautics and Space Administration grant NAG5-11549 and the Office of Naval Research.

References

- Ackerman, A. S., O. B. Toon, J. P. Taylor, D. W. Johnson, P. V. Hobbs, and R. J. Ferek (2000), Effects of aerosols on cloud albedo: Evaluation of Twomey's parameterization of cloud susceptibility using measurements of ship tracks, *J. Atmos. Sci.*, *57*, 2684–2695.
- Albrecht, B. A. (1989), Aerosols, cloud microphysics, and fractional cloudiness, *Science*, *245*, 1227–1230.
- Baumgardner, D., W. Strapp, and J. E. Dye (1985), Evaluation of the Forward Scattering Spectrometer Probe. Part II: Corrections for coincidence and dead-time losses, *J. Atmos. Oceanic Technol.*, *2*, 626–632.
- Baumgardner, D., H. Jonsson, W. Dawson, D. O'Connor, and R. Newton (2001), The cloud, aerosol and precipitation spectrometer: A new instrument for cloud investigations, *Atmos. Res.*, *59–60*, 251–264.
- Bower, K. N., and T. W. Chouarton (1988), The effects of entrainment on the growth of droplets in continental cumulus clouds, *Q. J. R. Meteorol. Soc.*, *114*, 1411–1434.
- Brechtel, F. J., and S. M. Kreidenweis (2000), Predicting particle critical supersaturation from hygroscopic growth measurements in the humidified TDMA. Part I: Theory and sensitivity studies, *J. Atmos. Sci.*, *57*, 1854–1871.
- Burnet, F., and J.-L. Brenguier (2002), Comparison between standard and modified forward scattering spectrometer probes during the small cumulus microphysics study, *J. Atmos. Oceanic Technol.*, *19*, 1516–1531.
- Chuang, P. Y., D. R. Collins, H. Pawlowska, J. R. Snider, H. H. Jonsson, J. L. Brenguier, R. C. Flagan, and J. H. Seinfeld (2000), CCN measurements during ACE-2 and their relationship to cloud microphysical properties, *Tellus, Ser. B*, *52*, 842–866.
- Clarke, A., V. Kapustin, S. Howell, K. Moore, B. Leinert, S. Masonis, T. Anderson, and D. Covert (2003), Sea-salt size distributions from breaking waves: Implications for marine aerosol production and optical extinction measurements during SEAS, *J. Atmos. Oceanic Technol.*, *20*, 1362–1374.

- Draxler, R. R. (1999), Hybrid Single-Particle Lagrangian Integrated Trajectories (HY-SPLIT), version 4.0: Users guide, *NOAA Tech. Memo. ERL ARL-230*, 35 pp., Natl. Oceanic and Atmos. Admin., Silver Spring, Md.
- Dye, J. E., and D. Baumgardner (1984), Evaluation of the Forward Scattering Spectrometer Probe, *J. Atmos. Oceanic Technol.*, *1*, 329–344.
- Facchini, M. C., M. Mircea, S. Fuzzi, and R. J. Charlson (1999), Cloud albedo enhancement by surface-active organic solutes in growing droplets, *Nature*, *401*, 257–259.
- Feingold, G., and P. Chuang (2002), Analysis of the influence of film-forming compounds on droplet growth: Implications for cloud microphysical processes and climate, *J. Atmos. Sci.*, *59*, 2006–2018.
- Fitzgerald, J. W., and P. Spyers-Duran (1973), Changes in cloud nucleus concentration and cloud droplet size distribution associated with pollution from St. Louis, *J. Appl. Meteorol.*, *30*, 511–516.
- Gysel, M., E. Weingartner, S. Nyeki, D. Paulsen, U. Baltensperger, I. Galambos, and G. Kissn (2004), Hygroscopic properties of water-soluble matter and humic-like organics in atmospheric fine aerosol, *Atmos. Chem. Phys.*, *4*, 35–50.
- Houghton, J. T., Y. Ding, D. J. Griggs, M. Noguer, P. J. van der Linden, X. Dai, K. Maskell, and C. A. Johnson (Eds.) (2001), *Climate Change 2001: The Scientific Basis, Contribution of Working Group I to the Third Assessment Report of the Intergovernmental Panel on Climate Change*, 881 pp., Cambridge Univ. Press, New York.
- Kreidenweis, S. M., C. J. Walcek, G. Feingold, W. Gong, M. Z. Jacobson, C. H. Kim, X. Liu, J. E. Penner, A. Nenes, and J. H. Seinfeld (2003), Modification of aerosol mass and size distribution due to aqueous-phase SO₂ oxidation in clouds: Comparisons of several models, *J. Geophys. Res.*, *108*(D7), 4213, doi:10.1029/2002JD002697.
- Laaksonen, A., P. Korhonen, M. Kulmala, and R. J. Charlson (1998), Modification of the Köhler equation to include soluble trace gases and slightly soluble substances, *J. Atmos. Sci.*, *55*, 853–862.
- Lawson, R. P., and A. M. Blyth (1998), A comparison of optical measurements of liquid water content and drop size distribution in adiabatic regions of Florida cumuli, *Atmos. Res.*, *48*, 671–690.
- Lenschow, D. H. (1986), Aircraft measurements in the boundary layer, in *Probing the Atmospheric Boundary Layer*, edited by D. H. Lenschow, pp. 39–55, Am. Meteorol. Soc., Boston, Mass.
- Liu, Y. G., and P. H. Daum (2002), Anthropogenic aerosols: Indirect warming effect from dispersion forcing, *Nature*, *419*, 580–581.
- McFarquhar, G. M., and A. J. Heymsfield (2001), Parameterizations of INDOEX microphysical measurements and calculations of cloud susceptibility: Applications for climate studies, *J. Geophys. Res.*, *106*, 28,675–28,698.
- Nenes, A., and J. H. Seinfeld (2003), Parameterization of cloud droplet formation in global climate models, *J. Geophys. Res.*, *108*(D14), 4415, doi:10.1029/2002JD002911.
- Nenes, A., R. J. Charlson, M. C. Facchini, M. Kulmala, A. Laaksonen, and J. H. Seinfeld (2002), Can chemical effects on cloud droplet number rival the first indirect effect?, *Geophys. Res. Lett.*, *29*(17), 1848, doi:10.1029/2002GL015295.
- Prenni, A. J., P. J. De Mott, and S. M. Kreidenweis (2003), Water uptake of internally mixed particles containing ammonium sulfate and dicarboxylic acids, *Atmos. Environ.*, *37*, 4232–4251.
- Pruppacher, H. R., and J. D. Klett (1997), *Microphysics of Clouds and Precipitation*, 2nd rev., 954 pp., Kluwer Acad., Norwell, Mass.
- Rissman, T. A., A. Nenes, and J. H. Seinfeld (2004), Chemical amplification (or dampening) of the Twomey effect: Conditions derived from droplet activation theory, *J. Atmos. Sci.*, *61*, 919–930.
- Rivera-Carpio, C. A., C. E. Corrigan, T. Novakov, J. E. Penner, C. F. Rogers, and J. C. Chow (1996), Derivation of contributions of sulfate and carbonaceous aerosols to cloud condensation nuclei from mass size distributions, *J. Geophys. Res.*, *101*, 19,483–19,493.
- Roberts, G. C., P. Artaxo, J. Zhou, E. Swietlicki, and M. O. Andreae (2002), Sensitivity of CCN spectra on chemical and physical properties of aerosol: A case study from the Amazon Basin, *J. Geophys. Res.*, *107*(D20), 8070, doi:10.1029/2001JD000583.
- Rosenfeld, D., and I. M. Lensky (1998), Satellite-based insights into precipitation formation processes in continental and maritime convective clouds, *Bull. Am. Meteorol. Soc.*, *79*, 2457–2476.
- Segal, Y., M. Pinsky, A. Khain, and C. Erlick (2003), Thermodynamic factors influencing bimodal spectrum formation in cumulus clouds, *Atmos. Res.*, *66*, 43–64.
- Shaw, R. A. (2003), Particle-turbulence interactions in atmospheric clouds, *Annu. Rev. Fluid Mech.*, *35*, 183–227.
- Shaw, R. A., and D. Lamb (1999), Experimental determination of the thermal accommodation and condensation coefficients of water, *J. Chem. Phys.*, *111*, 10,659–10,663.
- Shulman, M. L., M. C. Jacobson, R. J. Charlson, R. E. Synovec, and T. E. Young (1996), Dissolution behaviour and surface tension effects of organic compounds in nucleating cloud droplets, *Geophys. Res. Lett.*, *23*, 277–280.
- Snider, J. R., and J.-L. Brenguier (2000), Cloud condensation nuclei and cloud droplet measurements during ACE-2, *Tellus, Ser. B*, *52*, 828–842.
- Snider, J. R., S. Guibert, J.-L. Brenguier, and J. P. Putaud (2003), Aerosol activation in marine stratocumulus clouds: 2. Köhler and parcel theory closure studies, *J. Geophys. Res.*, *108*(D15), 8629, doi:10.1029/2002JD002692.
- Twomey, S. (1959), The nuclei of natural cloud formation. Part II: The supersaturation in natural clouds and the variation of cloud droplet concentration, *Geofis. Pura Appl.*, *43*, 243–249.
- Twomey, S. (1977), The influence of pollution on the shortwave albedo of clouds, *J. Atmos. Sci.*, *34*, 1149–1152.
- Twomey, S., and J. Warner (1967), Comparison of measurements of cloud droplets and cloud nuclei, *J. Atmos. Sci.*, *24*, 702–703.
- VanReken, T. M., T. A. Rissman, G. C. Roberts, V. Varutbangkul, H. H. Jonsson, R. C. Flagan, and J. H. Seinfeld (2003), Toward aerosol/cloud condensation nuclei (CCN) closure during CRYSTAL-FACE, *J. Geophys. Res.*, *108*(D20), 4633, doi:10.1029/2003JD003582.

R. Bahreini and W. C. Conant, Department of Environmental Science and Engineering, California Institute of Technology, 1200 E. California Boulevard, Pasadena, CA 91125, USA. (broya@caltech.edu; billc@cheme.caltech.edu)

A. E. Delia, Program in Atmospheric and Oceanic Sciences, University of Colorado, UCB 311, Boulder, CO 80309-0311, USA. (alice.delia@colorado.edu)

R. C. Flagan, T. A. Rissman, J. H. Seinfeld, T. M. VanReken, and V. Varutbangkul, Chemical Engineering, California Institute of Technology, Mail Code 210-41, 1200 E. California Boulevard, Pasadena, CA 91125, USA. (flagan@caltech.edu; rissman@its.caltech.edu; seinfeld@caltech.edu; vanreken@its.caltech.edu; tomtor@its.caltech.edu)

J. L. Jimenez, Department of Chemistry and Biochemistry, Cooperative Institute for Research in Environmental Sciences, University of Colorado, UCB 216, Boulder, CO 80309-0216, USA. (jose.jimenez@colorado.edu)

H. H. Jonsson, CIRPAS, Naval Postgraduate School, 3240 Imjin Road, Range 510, Monterey, CA 93633, USA. (hjonsson@nps.navy.mil)

A. Nenes, Schools of Earth and Atmospheric Sciences and Chemical and Biomolecular Engineering, Georgia Institute of Technology, Atlanta, GA 30332, USA. (thanos.nenes@che.gatech)

G. C. Roberts, Center for Atmospheric Sciences, Scripps Institution of Oceanography, University of California, San Diego, 9500 Gilman Drive, #0239, La Jolla, CA 92093, USA. (greg@fjji.ucsd.edu)

Appendix G

EFFECT OF ANGLE OF ATTACK ON THE PERFORMANCE OF AN
AIRBORNE COUNTERFLOW VIRTUAL IMPACTOR*

*Full Citation: Chen, J., W. C. Conant, T. A. Rissman, R. C. Flagan, and J. H. Seinfeld (2005), Effect of angle of attack on the performance of an airborne counterflow virtual impactor, *Aerosol Science and Technology*, 39(6), 485 – 491.

Aerosol Science & Technology: Effect of Angle of Attack on the Performance of an Airborne Counterflow Virtual Impactor.” (39):485 – 491. Copyright 2005. Mount Laurel, NJ. Reprinted with permission.



Effect of Angle of Attack on the Performance of an Airborne Counterflow Virtual Impactor

Junhong Chen,¹ William C. Conant,² Tracey A. Rissman,² Richard C. Flagan,²
 and John H. Seinfeld²

¹*Department of Mechanical Engineering, University of Wisconsin-Milwaukee, Milwaukee, Wisconsin*

²*Department of Chemical Engineering, California Institute of Technology, Pasadena, California*

A three-dimensional model has been developed within the framework of the commercial computational fluid dynamics program, FLUENT[®], to investigate the collection efficiency of an airborne counterflow virtual impactor (CVI). The model assumes steady-state, isothermal, compressible, and turbulent flow. Particle trajectories are computed based on the Lagrangian discrete phase model (DPM). In addition to predicting the effects of flight velocity and counterflow rate on the particle collection efficiency, as do prior models, the model quantifies the effect of flight attack angle on the particle collection efficiency. With an angle of attack as small as 5°, the CVI collection efficiency drastically degrades at large particle sizes, and only particles with intermediate sizes are collected. Smaller particles do not have sufficient inertia to fight the counterflow, and larger particles tend to impact the CVI inner walls and are lost to the CVI walls. The modeling results show that the alignment between the free stream flow and the CVI inlet is critical to the performance of the CVI.

INTRODUCTION

A counterflow virtual impactor (CVI) samples droplets or particles larger than a certain size by inertially separating them from the surrounding air and the smaller interstitial aerosol particles in a cloud (Ogren et al. 1985). By analyzing the collected samples with appropriate sensors downstream, the CVI has been widely used to study the microphysics and chemistry of clouds. A CVI can be mounted on a moving aircraft to sample cloud droplets in flight (Laucks and Twohy 1998; Dhaniyala et al. 2003; Glantz et al. 2003), or in a wind tunnel to separate cloud droplets from interstitial aerosols in ground-based measurements (Noone et al. 1988; Schwarzenbock and Heintzenberg 2000).

A schematic diagram of the CVI is shown in Figure 1. Particle separation is achieved in the CVI by injecting more clean dry carrier gas through a porous wall just inside the probe inlet than

is drawn by the downstream analysis instruments. The excess carrier gas provides a counterflow through which the incoming droplets must inertially penetrate in order to be included in the sample. The counterflow is typically warmer and drier than the ambient air so that the droplets that penetrate into the sample flow are dried. Measurements then probe the nature of the cloud droplet residues thus produced. Two stagnation surfaces on which flow velocity is zero are created inside the CVI. The first stagnation surface is located near the CVI inlet, where the free stream meets the counterflow. The second stagnation surface is located further inside the CVI, where the counterflow separates from the sample flow. The shape and the position of the stagnation surface depend on the relative magnitude of the two flow rates creating the surface. Only particles with sufficient inertia or stopping distance to penetrate these two stagnation surfaces can be collected by the sampling inlet. Smaller particles escape either by following the airflow that is deflected around the CVI tip or by returning with the counterflow after passing the first stagnation surface.

The performance of a CVI is usually characterized by its collection efficiency, which is defined as the fraction of particles collected by the CVI as a function of particle size. The collection efficiency variation with droplet size depends on the geometry of the CVI, the flow field inside the CVI, and the free-stream conditions. The cut size (particle size at 50% collection efficiency) of a CVI may be estimated by a one-dimensional model based on the aerodynamic drag theory (Fuchs 1964), assuming the stopping distance of the particles to be the distance between the two stagnation surfaces (Noone et al. 1988). The approximation has been proven to successfully predict the cut size of a CVI (Schwarzenbock and Heintzenberg 2000). However, this theoretical estimate based on the simplified CVI internal and external flow fields is limited (Noone et al. 1988) because it does not account for the nonaxial velocity components that determine the cut sharpness of the collection efficiency curve (Schwarzenbock and Heintzenberg 2000) and the particle loss after the second stagnation surface.

Previous investigators have experimentally measured the collection efficiency curve using wet particles (droplets of

Received 29 October 2004; accepted 8 April 2005.

Address correspondence to Junhong Chen, Department of Mechanical Engineering, University of Wisconsin-Milwaukee, Milwaukee, WI 53211, USA. E-mail: jhchen@uwm.edu

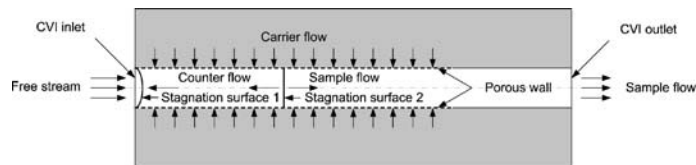


FIG. 1. Schematic diagram of a counterflow virtual impactor (CVI).

ammonium sulfate solution) to calibrate the collection efficiency of large particles, whose evaporation time is long (Noone et al. 1988), and dry particles (e.g., glass beads) to calibrate the collection efficiency at smaller particle sizes (Anderson et al. 1993). The accuracy of the experimental collection efficiency curve is limited by uncertainties in generating, transporting, and counting calibration particles. For example, use of glass beads for the calibration may overestimate the collection efficiency of small droplets, because solid particles are likely to rebound from the wall surfaces and droplets are more likely to adhere to the wall surfaces upon impact. Although the condensed water and any dissolved gases or volatile material dissolved in the adhered droplets will be sampled, the residual particles will be left behind (Noone et al. 1993). For larger droplets, the high collection efficiency assumption may not be unrealistic at large free-stream velocities due to the droplet shatter when they impact the CVI probe (Weber et al. 1998; Schwarzenbock and Heintzenberg 2000; Twohy et al. 2003).

Numerical simulations have been effectively applied to predict the CVI collection efficiency curve as a function of geometry and flow conditions and to optimize the design of a CVI. Lin and Heintzenberg (1995) simulated both a simple CVI geometry and a two-dimensional (2D) axisymmetric potential flow (Lin and Heintzenberg 1995). With a 2D axisymmetric model, the final three-dimensional (3D) flow field is approximated by rotating the computed 2D flow field around the axis of the CVI. Results from the simplified model agreed well with prior measurements of the cut size of a CVI (Anderson et al. 1993), but they predicted a much sharper cut than observed. Laucks and Twohy (1998) numerically simulated the flow field and the particle trajectories for a real CVI geometry. Their model also assumed a two-dimensional axisymmetric flow but considered the effects of compressibility and turbulence and examined the mechanisms by which large particles may be lost after they survive the counterflow.

The models described above assume perfect alignment between the free stream and the CVI inlet. In the real situation, the airflow impinging on an airborne CVI probe can easily deviate by a few degrees due to mounting uncertainties, the flow turbulence, or typical aircraft maneuvers. Deviations from perfect alignment are expected to degrade the performance of the CVI because larger particles that enter the CVI at finite attack angle may directly impact the inner wall of the CVI (Twohy 1992). Recently, a model was developed by Twohy (1998) to study the

effect of an isokinetic shroud on the flow field of the CVI. The shroud was shown to improve the alignment between the free stream flow and the CVI inlet. However, the general effect of attack angle on the collection efficiency of a CVI has not been characterized. The use of axisymmetric models precludes the study of the effect of attack angle on the collection efficiency of the CVI due to the presence of the nonaxisymmetric CVI inlet boundary condition. Since CVIs have been used in many studies without a flow-straightening shroud and continue to be so used, an understanding of the effect of finite angle of attack is needed.

In this article we describe a full 3D model of the CVI. The model allows us to study the effect of attack angle on the performance of a CVI. First, we compare the collection efficiency curve from the 3D model to those from 2D axisymmetric models. Then we present the effect of angle of attack on the collection efficiency of the CVI. Finally, we study the effect of a round nose with a diameter of 0.35 cm on the CVI performance since it is often used to reduce the turbulence (Laucks and Twohy 1998).

DESCRIPTION OF THE MODEL

The computational geometry for the CVI simulations is shown in Figure 2. The model simulates the region immediately outside the CVI and that inside the CVI inlet. The particular CVI we study is one that was designed to operate on a relatively low-speed aircraft. It has an inner radius of 0.15 cm and an outer radius of 0.5 cm. The porous tube inside the CVI is 4 cm long. Based on the previous modeling efforts (Lin and Heintzenberg 1995; Laucks and Twohy 1998), the computational domain extends a few times the CVI radius beyond the outer profile, as illustrated in Figure 2. For all cases, the free-stream flow conditions are assumed to be atmospheric pressure (1 atm) and 288 K. The free-stream velocity (flight velocity) is varied from 50 to 70 m/s. The sample flow rate (F_2) is fixed at 5 lpm and the counterflow rate (F_3) is varied from 0.1 to 1 lpm. The model assumes a 3D, steady-state, isothermal, compressible, and turbulent flow. The turbulence model employed in this study was the renormalization group (RNG) $k-\epsilon$ model, with 5% turbulence intensity and a turbulent viscosity ratio of 100 (Laucks and Twohy 1998). Boundary conditions for the external flow are also shown in Figure 2. The porous tube wall and the sample flow outlet are assumed to have uniform flow velocity. The rest of the CVI surfaces are assumed to be solid walls.

The computational domain is meshed into hexahedral cells with smaller cells close to the boundaries where the finer

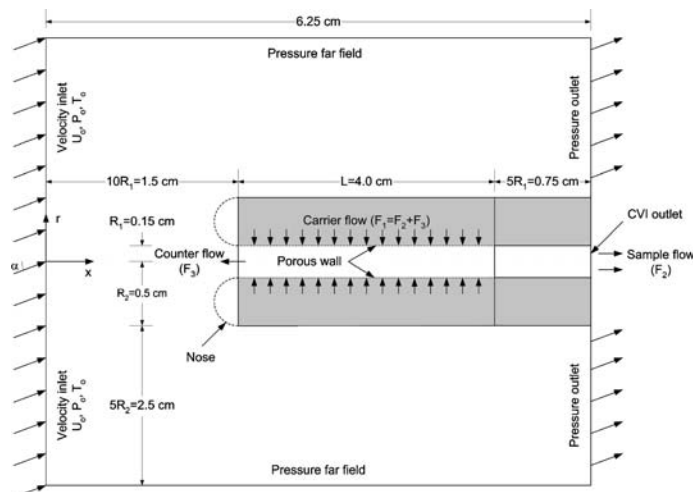


FIG. 2. Computational domain for CVI.

structure of the flow is desired than in the free-stream flow. During the solution process, cells close to the CVI wall surfaces were gradually refined to test the dependence of the results on cell volume. The adaptation process was terminated when the final results did not change with further refinement. The minimum volume of the cell was $3.0 \times 10^{-13} \text{ m}^3$, while the maximum cell volume was $9.7 \times 10^{-10} \text{ m}^3$. The total number of cells in the computational domain was on the order of 10^6 . The mass, momentum, and turbulence equations were discretized using the first-order upwind scheme, and the pressure-velocity coupling was achieved using the semi-implicit method for pressure-linked equations (SIMPLE) algorithm (Patankar 1980). The flow field was solved using the commercial computational fluid dynamics code FLUENT[®] (FLUENT Inc.). The convergence criterion for the continuity equation was 10^{-5} . The convergence criteria for the momentum, k , and ϵ equations were set at 10^{-3} . The mass flow rate of the counterflow was monitored and compared to its theoretical value to ensure convergence of solutions.

After flow field convergence was achieved, particle trajectories were computed using the Lagrangian discrete phase model (DPM) supported by FLUENT[®]. DPM applies to particles greater than $0.1 \mu\text{m}$. Particle sizes considered here range from 1 to $50 \mu\text{m}$ for the interest of ambient sampling. All particles were assumed to be spherical with unit specific gravity. The particle concentration was assumed to be sufficiently low that particle-particle interactions and the effect of the particle volume fraction on the gas flow are negligible. No heat and mass transfer between particles and the gas flow was considered. As noted by Laucks and Twohy (1998), droplet evaporation is not significant upstream of the second stagnation surface because the particles pass through that region rapidly, but it may affect

the droplet trajectories beyond the second stagnation surface due to the long droplet residence time in the latter region. Neglect of droplet evaporation is expected to lead to a slight underestimate of the collection efficiency of the CVI (Laucks and Twohy 1998). To determine the sampling efficiency, particles with a given size are released uniformly from an injection area equivalent to that of the CVI inlet on the main inlet boundary surface. The initial particle velocity is assumed to be the same as the free-stream gas velocity (flight velocity). Upon hitting the wall, the fate of droplets/particles is not well understood since they may stick, break up, or rebound (Laucks and Twohy 1998; Schwarzenbock and Heintzenberg 2000; Twohy et al. 2003). The model considers two extreme conditions with sticky or reflecting walls to show the effect of such an uncertainty on the CVI collection efficiency. For sticky walls, particles stick to the wall upon impaction. For reflecting walls, particles rebound from the wall surfaces upon impaction. The collection efficiency is defined as the ratio of the number of particles passing the CVI outlet to the total number of particles released. However, it should be noted that droplet impaction on the walls would not affect the collection efficiency for volatile nonreactive gases such as water vapor.

RESULTS AND DISCUSSION

Comparison of the Full 3D Model to Axisymmetric Models

Figure 3 compares the results from three different models for a flight velocity of 70 m/s, a counterflow of 0.1 lpm, and an attack angle of 0° . Two of the simulations are based on the axisymmetric flow, while the third simulation employs a full

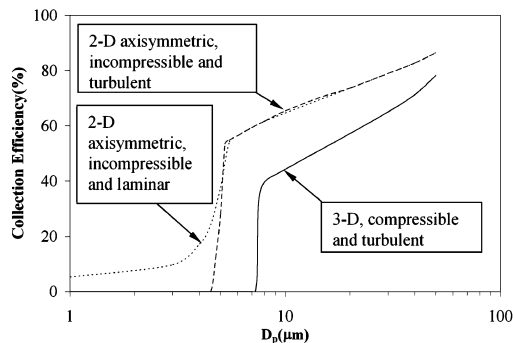


FIG. 3. Comparison of the full 3D model with axisymmetric models for a flight velocity $U_0 = 70$ m/s, a counterflow $F_3 = 0.1$ lpm, and an attack angle $\alpha = 0^\circ$.

3D model without the axisymmetric flow assumption. For the axisymmetric simulations, both the cut sharpness and the critical size (the minimum particle size that is collected by the CVI) of the collection efficiency curve increase when a turbulent-flow model was employed instead of a laminar model. The difference in the collection efficiency curve may be attributed to the effect of turbulent mixing on the shape of the first stagnation surface. With the additional mixing allowed in the turbulent model, the first stagnation surface becomes more uniform (flatter) and the distance between two stagnation surfaces is more uniform. Consequently, the required stopping distance for particles to penetrate the stagnation surfaces is more uniform, which corresponds to a sharper cutoff in the collection efficiency curve. For the particular set of operating conditions, the flow outside the CVI inlet has a Reynolds number of 4.6×10^4 based on the outer diameter of the CVI; hence, the flow is turbulent, although the flow inside the CVI is still laminar ($Re = 2,000$). For the full 3D simulations, the computed critical size increased over that predicted by the axisymmetric simulations but the collection efficiency decreased at any given particle size. The difference between the efficiency curves resulting from 2D and 3D models may be explained by the additional turbulent mixing effects along the third direction (circumferential) allowed in the 3D model, which more closely approximates the actual flow geometry.

Effect of Angle of Attack

The local flow streamlines inside and outside the CVI near the inlet and four selected particle trajectories are shown in Figure 4 for a flight velocity of 70 m/s and a counterflow rate of 0.1 lpm. Figure 4a is for an angle of attack of 0° , and Figure 4b is for an angle of attack of 5° . Based on the flow streamlines, the first stagnation surface (less visible) occurs near the CVI inlet where the free stream meets the counterflow and the second stagnation surface occurs further inside the CVI where the counterflow separates from the sample flow.

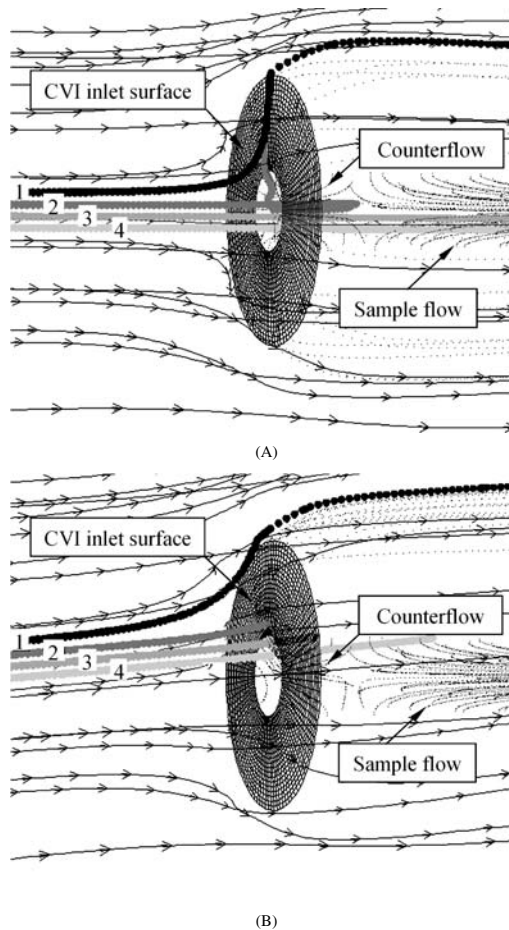


FIG. 4. Flow streamlines inside and outside the CVI near the inlet for a flight velocity $U_0 = 70$ m/s, a counterflow $F_3 = 0.1$ lpm, and two attack angles (a) $\alpha = 0^\circ$ and (b) $\alpha = 5^\circ$. Also shown are trajectories for particles 1–4 with aerodynamic diameters of 1, 7.5, 14, and $20.5 \mu\text{m}$, respectively.

The particle trajectories represented by discrete spheres are for particles 1–4 with aerodynamic diameters of 1, 7.5, 14, and $20.5 \mu\text{m}$, respectively. These particles are all released from the line intersected by the flow entrance plane in the computational domain and the vertical symmetry plane of the CVI, but with different distance from the CVI axis. Particles 1 and 2 are released from 0.06 and 0.02 cm above the CVI axis, respectively. Particles 3 and 4 are released from 0.02 and 0.06 cm below the CVI axis. Particle 1 ($1 \mu\text{m}$) has a relatively small size, so it follows the airflow in front of the CVI inlet for both attack

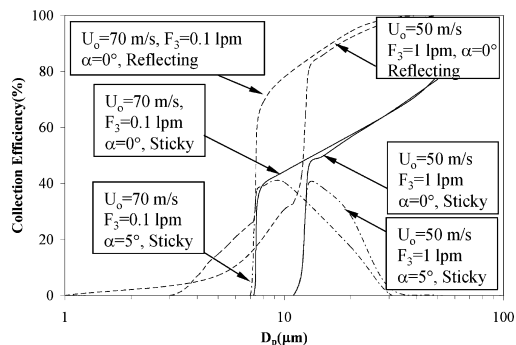


FIG. 5. Effects of attack angle on the collection efficiency of the CVI for various flow and porous wall conditions.

angles. At 0° attack angle, particle 2 ($7.5 \mu\text{m}$) can penetrate the first stagnation surface, but it does not have sufficient inertia to penetrate the second stagnation surface. As a result, particle 2 returns with the counterflow after passing the first stagnation surface and is finally trapped at the inlet wall of the CVI. With 5° attack angle, particle 2 directly impacts the CVI inlet wall and gets stuck. Particles 3 ($14 \mu\text{m}$) and 4 ($20.5 \mu\text{m}$) have sufficient inertia to penetrate both stagnation surfaces and enter the CVI when the attack angle is 0° . With an attack angle of 5° , both particles are lost by impaction on the porous wall of the CVI.

The overall collection efficiencies of the CVI for angles of attack of 0° and 5° are plotted in Figure 5, assuming both sticky and reflecting CVI inner walls. The left set of three curves shows the results for a flight velocity of 70 m/s and a counterflow rate of 0.1 lpm, while the right set of three curves is for a flight velocity of 50 m/s and a counterflow rate of 1 lpm. The solid curve in each set is for an attack angle of 0° and a sticky wall, while the dashed curve is for an attack angle of 0° and a reflecting wall. The dash-dotted curve is for an attack angle of 5° and a sticky wall. As expected, the collection efficiency of the CVI with a reflecting wall is much higher than that with a sticky wall, but the collection efficiency curves are less steep near the critical size with reflecting walls. The critical size increases with decreasing free-stream velocity and increasing counterflow rate. At a flight velocity of 70 m/s and a counterflow of 0.1 lpm, the critical size of the CVI is about $7 \mu\text{m}$. The critical size increases to about $11 \mu\text{m}$ when the flight velocity is reduced to 50 m/s and the counterflow rate is increased to 1 lpm. The increase in the critical size is explained by the increase of the distance between the two stagnation surfaces. Although it is difficult to quantitatively characterize the distance between two stagnation surfaces due to their curvatures, the qualitative increase of the separation between two stagnation surfaces with decreasing free-stream velocity and increasing counterflow rate has been observed from the modeling results. Based on the aerodynamic drag theory

(Fuchs 1964), larger particle inertia or stopping distance is required to pass the two stagnation surfaces. This result is qualitatively similar to what has been found in the earlier models (Lin and Heintzenberg 1995; Laucks and Twohy 1998). For a particle size greater than $20 \mu\text{m}$, the effects of the flight velocity and the counterflow on the collection efficiency diminish and the CVI has the same efficiency characteristics for both sets of operating conditions.

The attack angle of free-stream flow has a negligible effect on the critical size and cut sharpness of the collection efficiency curve of the CVI. However, the collection efficiency of the CVI at larger particle sizes is greatly degraded with an attack angle of 5° . Since the trend is the same for both sets of operating conditions, we discuss the left set of the curves with a sticky wall as an illustration. For an attack angle of 0° and a flight velocity of 70 m/s, the collection efficiency curve starts with a critical size of $7.25 \mu\text{m}$ and rises steeply to 40% at $8 \mu\text{m}$. The collection efficiency increases but with a slower rate with increasing particle size for particles greater than $8 \mu\text{m}$. With a particle size of $50 \mu\text{m}$, the collection efficiency reaches about 80%. With an attack angle of 5° and the same flight speed, the critical size of the CVI slightly decreases to $7 \mu\text{m}$, but the collection efficiency rises with the same rate as the case for 0° attack angle for particle sizes up to $10 \mu\text{m}$. At $10 \mu\text{m}$, the collection efficiency reaches 40%. The collection efficiency degrades drastically with increasing particle size for particles larger than $10 \mu\text{m}$. As a result, the 5° CVI can only collect particles near the transmission efficiency peak (about $10 \mu\text{m}$) and rejects all other particle sizes. Smaller particles have too little inertia to penetrate the counterflow region, while larger particles tend to maintain their direction after entering the CVI inlet but impact on the inner wall of the CVI. With a sticky wall, these particles are lost to the CVI inner wall and are not collected by the CVI.

Effect of the Nose

The significant degradation of the collection efficiency for larger particle sizes at a 5° attack angle is a problem for many applications. Rounded inlets reduce the turbulence and the sensitivity to angle of attack over sharp-edged inlets (Laucks and Twohy 1998), so we examined the influence of adding a round nose to the blunt CVI. As shown in Figure 2, the nose considered has a diameter of the thickness of the CVI wall (0.35 cm). Figure 6 shows a comparison of the streamlines near the round-nose CVI inlet and 4 particle trajectories for attack angles of 0° and 5° , and the same operating conditions as used in Figure 4. Both a reflecting nose (particles are reflected back into the flow upon impacting the nose) and a sticky nose (particles stick to the wall upon impacting the nose) are considered, but the particle trajectories shown in Figure 6 are for sticky noses only. The round nose reduces the flow separation, as can be seen from the smoother streamlines and thinner flow boundary layer shown in Figure 6 compared to Figure 4. However, the nose does not change the fate of the four particles considered.

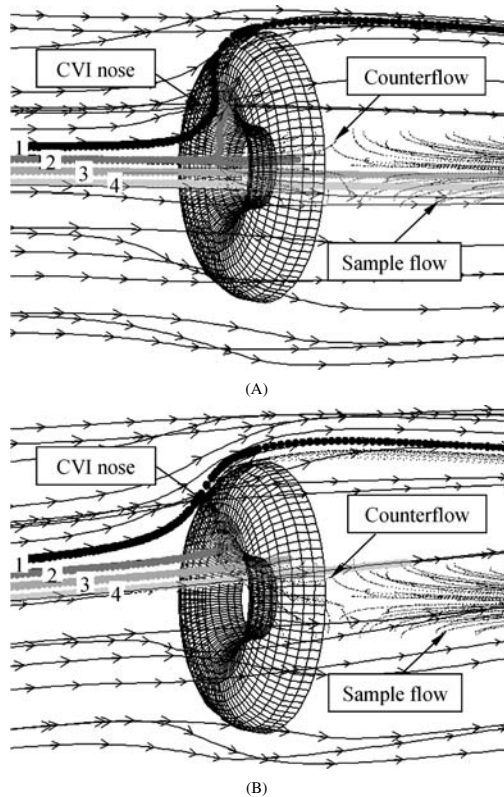


FIG. 6. Flow streamlines inside and outside the round-nose CVI near the inlet for a flight velocity $U_0 = 70$ m/s, a counterflow $F_3 = 0.1$ lpm, and two attack angles (a) $\alpha = 0^\circ$ and (b) $\alpha = 5^\circ$. Also shown are trajectories for particles 1–4 with aerodynamic diameters of 1, 7.5, 14, and 20.5 μm , respectively.

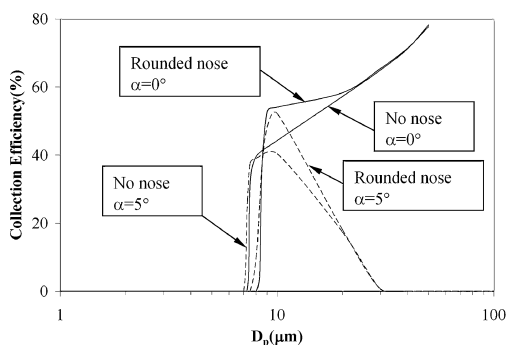


FIG. 7. Effect of a round nose on the collection efficiency of the CVI for a flight velocity $U_0 = 70$ m/s and a counterflow $F_3 = 0.1$ lpm.

The effect of the nose on the overall collection efficiency of the CVI is shown in Figure 7 for a flight velocity of 70 m/s and a counterflow rate of 0.1 lpm. Solid curves are for a 0° attack angle; the dashed curves are for an attack angle of 5° . For each attack angle, only two extreme cases (no nose and reflecting nose) are plotted. As expected based on the aerodynamic drag theory (Fuchs 1964), the presence of the nose slightly increases the critical size of the CVI due to the increase of the distance between two stagnation surfaces. For a reflecting nose, all particles hitting the nose rebound elastically, so the nose increases the collection efficiency for particles slightly larger than the critical size at both attack angles. The reflecting nose has no effect on the collection efficiency of further larger particles for both attack angles. If a sticking nose is assumed, the only effect of the nose on the collection efficiency is a small increase in the critical size. The collection efficiency curve of a CVI with a sticky nose hence follows that of a CVI without the nose for particles larger than the critical size.

CONCLUSIONS

The collection efficiency of an airborne CVI was predicted using a full 3D simulation based upon FLUENT[®]. The model predicts a larger critical size but a lower efficiency than does a 2D axisymmetric model. In agreement with the aerodynamic drag theory and prior models, the model confirms that the critical size of the collection efficiency curve increases with the increase of counterflow rate and the decrease of flight velocity. The CVI collection efficiency is very sensitive to the flight angle of attack. With an attack angle of as small as 5° , the collection efficiency for particles slightly larger than the critical size starts to degrade drastically. As a result, the CVI can only collect particles with intermediate sizes, i.e. particles near the critical size. Larger particles are lost to the CVI inner walls due to the direct impactation with a small attack angle. The addition of a round nose at the blunt CVI inlet slightly increases the critical size of the collection, but it does not improve the collection efficiency of large particles when a non-zero attack angle is present. Measures to improve the alignment between the incoming flow and the CVI inlet are critical to the performance of the CVI. Notably, use of a shroud to straighten the airflow into the CVI should alleviate the impact of the flight attack angle on the collection efficiency of the CVI.

REFERENCES

- Anderson, T. L., Charlson, R. J., and Covert, D. S. (1993). Calibration of a Counterflow Virtual Impactor at Aerodynamic Diameters from 1 to 15 μm , *Aerosol Sci. Technol.* 19(3):317–329.
- Dhaniyala, S., Flagan, R. C., McKinney, K. A., and Wennberg, P. O. (2003). Novel Aerosol/Gas Inlet for Aircraft-based Measurements, *Aerosol Sci. Technol.* 37(10):828–840.
- FLUENT Inc., <http://www.fluent.com>.
- Fuchs, N. A. (1964). *The Mechanics of Aerosols*, Dover Publications, New York.
- Glanz, P., Noone, K. J., and Osborne, S. R. (2003). Comparisons of Airborne CVI and FSSP Measurements of Cloud Droplet Number

- Concentrations in Marine Stratocumulus Clouds, *J. Atmos. Oceanic Technol.* 20(1):133–142.
- Laucks, M. L., and Twohy, C. H. (1998). Size-dependent Collection Efficiency of an Airborne Counterflow Virtual Impactor, *Aerosol Sci. Technol.* 28(1):40–61.
- Lin, H., and Heintzenberg, J. (1995). A Theoretical-Study of the Counterflow Virtual Impactor, *J. Aerosol Sci.* 26(6):903–914.
- Noone, K. B., Noone, K. J., Heintzenberg, J., Strom, J., and Ogren, J. A. (1993). In Situ Observations of Cirrus Cloud Microphysical Properties Using the Counterflow Virtual Impactor, *J. Atmos. Oceanic Technol.* 10(3):294–303.
- Noone, K. J., Ogren, J. A., Heintzenberg, J., Charlson, R. J., and Covert, D. S. (1988). Design and Calibration of a Counterflow Virtual Impactor for Sampling of Atmospheric Fog and Cloud Droplets, *Aerosol Sci. Technol.* 8(3):235–244.
- Ogren, J. A., Heintzenberg, J., and Charlson, R. J. (1985). In-Situ Sampling of Clouds with a Droplet to Aerosol Converter, *Geophys. Res. Lett.* 12(3):121–124.
- Patankar, S. V. (1980). *Numerical Heat Transfer and Fluid Flow*, Hemisphere, Washington, DC.
- Schwarzenbock, A., and Heintzenberg, J. (2000). Cut Size Minimization and Cloud Element Break-up in a Ground-based CVI, *J. Aerosol Sci.* 31(4):477–489.
- Twohy, C. H. (1992). On the Size Dependence of the Chemical Properties of Cloud Droplets: Exploratory Studies by Aircraft. Ph.D. Thesis, University of Washington, Seattle.
- Twohy, C. H. (1998). Model Calculations and Wind Tunnel Testing of an Isokinetic Shroud for High-speed Sampling, *Aerosol Sci. Technol.* 29(4):261–280.
- Twohy, C. H., Strapp, J. W., and Wendisch, M. (2003). Performance of a Counterflow Virtual Impactor in the NASA Icing Research Tunnel, *J. Atmos. Oceanic Technol.* 20(6):781–790.
- Weber, R. J., Clarke, A. D., Litchy, M., Li, J., Kok, G., Schillawski, R. D., and McMurry, P. H. (1998). Spurious Aerosol Measurements When Sampling from Aircraft in the Vicinity of Clouds, *J. Geophys. Res.—Atmos.* 103(D21):28337–28346.

Appendix H

ANVIL GLACIATION IN A DEEP CUMULUS UPDRAUGHT OVER FLORIDA
SIMULATED WITH THE EXPLICIT MICROPHYSICS MODEL.

I: IMPACT OF VARIOUS NUCLEATION PROCESSES*

*Full Citation: Phillips, V. T. J., C. Andronache, S. C. Sherwood, A. Banesmer, W. C. Conant, P. J. Demott, R. C. Flagan, A. Heymsfield, H. Jonsson, M. Poellot, T. A. Rissman, J. H. Seinfeld, T. VanReken, V. Varutbangkul, and J. C. Wilson (2005), Anvil glaciation in a deep cumulus updraught over Florida simulated with the Explicit Microphysics Model. I: Impact of various nucleation processes, *Quarterly Journal of the Royal Meteorological Society*, 131(609), 2019 – 2046.

© 2005 Royal Meteorological Society. This appendix is reprinted with permission from the Royal Meteorological Society.

Anvil glaciation in a deep cumulus updraught over Florida simulated with the Explicit Microphysics Model. I: Impact of various nucleation processes

By VAUGHAN T. J. PHILLIPS¹ †, CONSTANTIN ANDRONACHE², STEVEN C. SHERWOOD³, AARON BANSEMER⁴, WILLIAM C. CONANT⁵, PAUL J. DEMOTT⁶, RICHARD C. FLAGAN⁵, ANDY HEYMSFIELD⁴, HAFLIDI JONSSON⁷, MICHEAL POELLOT⁸, TRACEY A. RISSMAN⁵, JOHN H. SEINFELD⁵, TIM VANREKEN⁵, VARUNTIDA VARUTBANGKUL⁵ and JAMES C. WILSON⁹

¹*Atmospheric and Oceanic Sciences Program, Princeton University, New Jersey, USA*

²*Boston College, Chestnut Hill, Massachusetts, USA*

³*Department of Geology, Yale University, New Haven, USA*

⁴*National Centre for Atmospheric Research, Boulder, Colorado, USA*

⁵*Department of Environmental Science and Engineering, Caltech, Pasadena, California, USA*

⁶*Department of Atmospheric Science, Colorado State University, Fort Collins, Colorado, USA*

⁷*Center for Interdisciplinary Remotely-Piloted Aircraft Studies, Monterey, California, USA*

⁸*Department of Atmospheric Sciences, University of North Dakota, USA*

⁹*University of Denver, Colorado, USA*

(Received 1 June 2004; revised 22 December 2004)

SUMMARY

Simulations of a cumulonimbus cloud observed in the Cirrus Regional Study of Tropical Anvils and Cirrus Layers–Florida Area Cirrus Experiment (CRYSTAL-FACE) with an advanced version of the Explicit Microphysics Model (EMM) are presented. The EMM has size-resolved aerosols and predicts the time evolution of sizes, bulk densities and axial ratios of ice particles. Observations by multiple aircraft in the troposphere provide inputs to the model, including observations of the ice nuclei and of the entire size distribution of condensation nuclei.

Homogeneous droplet freezing is found to be the source of almost all of the ice crystals in the anvil updraught of this particular model cloud. Most of the simulated droplets that freeze to form anvil crystals appear to be nucleated by activation of aerosols far above cloud base in the interior of the cloud (‘secondary’ or ‘in-cloud’ droplet nucleation). This is partly because primary droplets formed at cloud base are invariably depleted by accretion before they can reach the anvil base in the updraught, which promotes an increase with height of the average supersaturation in the updraught aloft. More than half of these aerosols, activated far above cloud base, are entrained into the updraught of this model cloud from the lateral environment above about 5 km above mean sea level. This confirms the importance of remote sources of atmospheric aerosol for anvil glaciation.

Other nucleation processes impinge indirectly upon the anvil glaciation by modifying the concentration of supercooled droplets in the upper levels of the mixed-phase region. For instance, the warm-rain process produces a massive indirect impact on the anvil crystal concentration, because it determines the mass of precipitation forming in the updraught. It competes with homogeneous freezing as a sink for cloud droplets. The effects from turbulent enhancement of the warm-rain process and from other nucleation processes on the anvil ice properties are assessed.

KEYWORDS: Aerosol particles Homogeneous aerosol freezing Secondary droplet nucleation

1. INTRODUCTION

Cirrus cloud forms at temperatures colder than about -30°C . It covers about 35% of the globe and is fundamental to the radiation budget of the climate system (Ramanathan *et al.* 1983). Much tropical cirrus originates from the anvils of cumulonimbus (Cb) storms. An anvil is formed by the upwelling of condensate in the updraught of the storm. The rate of generation of crystals in Cb updraughts may affect the eventual ice concentration in this cirrus.

Cloud droplets are nucleated by activation of cloud condensation nuclei (CCN) aerosols either at cloud base (‘primary droplet nucleation’) or later in the interior of

† Corresponding author: Atmospheric and Oceanic Sciences Program (AOS), Princeton University, Princeton, New Jersey, USA. e-mail: Vaughan.Phillips@noaa.gov

© Royal Meteorological Society, 2005.

the cloud ('secondary droplet nucleation'). Spontaneous ('homogeneous') freezing of activated drops occurs at temperatures colder than a size-dependent threshold, which is usually somewhere near -36°C . Supercooled cloud-droplets and raindrops may also freeze by the activation of ice nuclei (IN; 'heterogeneous ice nucleation') at subzero temperatures. In the anvil, aerosols can persist unactivated in the supercooled state until they freeze spontaneously ('homogeneous aerosol freezing') at high supersaturations with respect to ice approaching 50% or more (Jensen *et al.* 1998; Koop *et al.* 2000).

Ovtchinnikov *et al.* (2000) found that the mixed-phase microphysics of a moderate cumulus cloud with no anvil was dominated by the Hallett–Mossop (H-M) process (Hallett and Mossop 1974) of ice particle multiplication. The H-M process involves the production of splinters during the riming of large cloud droplets of >24 microns diameter onto ice at -3 to -8°C . Such mixed-phase microphysical processes, as well as warm processes, might be expected to modify the updraught's supply of condensate, aerosols and vapour to the anvil.

Turbulence in clouds has impacts on the formation of cloud droplets, on condensation growth, and on subsequent collisions and coalescence of droplets (Jonas 1996; Smith and Jonas 1996; Khain *et al.* 2000). The evolution of the cloud-droplet distribution is influenced by turbulence due to: (i) fluctuations in the supersaturation field, affecting condensation; and (ii) increased average rates of collisions, arising from fluctuations both in the droplet concentration and the relative velocity between droplets of different sizes. Turbulence affects the cloud dynamics by mixing air from the environment into the cloud. Such entrainment reduces the cloud buoyancy and dilutes condensate.

The general importance of homogeneous freezing in ice clouds is evident from the fact that liquid water is only very rarely observed at temperatures colder than about -38°C (DeMott *et al.* 1997). Heymsfield and Sabin (1989) highlighted the potential for competition between heterogeneous and homogeneous nucleation of crystals in cirrus (see also DeMott *et al.* 1997; Spice *et al.* 1999), with homogeneous freezing favoured at stronger updraught speeds. The predominance of homogeneous freezing in observed wave-clouds with updraught speeds exceeding 1 m s^{-1} was inferred by Heymsfield and Miloshevich (1993, 1995). Updraughts extending into Cb anvils are much faster than this, which might seem to implicate homogeneous freezing as their key mechanism for glaciation. In observational studies of Cb anvils, two types of homogeneous freezing have been proposed: first, Knollenberg *et al.* (1993) speculated that homogeneous aerosol freezing might explain high concentrations, $>10\text{ cm}^{-3}$, of crystals observed in tropical Cb clouds; second, Rosenfeld and Woodley (2000) invoked massive homogeneous freezing of activated cloud-droplets to explain aircraft observations of some Texan convective storms.

In this paper we describe explicit microphysical calculations to evaluate the relative importance of these various mechanisms for the formation of anvil ice particles in a deep convective updraught. We also assess the modulation of such mechanisms by the warm- and mixed-phase microphysical processes. Relevant turbulence parameters are prescribed from aircraft observations and three-dimensional (3-D) model results. An advanced version of the Explicit Microphysics Model (EMM) developed by Phillips (2001) and Phillips *et al.* (2001, 2002, 2003) is applied to simulate a Cb case observed in the Cirrus Regional Study of Tropical Anvils and cirrus Layers—Florida Area Cirrus Experiment (CRYSTAL-FACE, Jensen *et al.* 2004). This is the first project, to our knowledge, to combine simultaneous measurements of aerosol particles in the lower and upper troposphere with *in situ* aircraft observations of Cb clouds and their anvil cirrus.

2. THE MODEL

(a) Overview

The EMM was originally developed by Phillips (2001) as an extension to the 1-D Multi-Thermal Model (MTM) of cumulus glaciation by Blyth and Latham (1997). Fully interactive components for vapour, cloud water, ice and rain were added to the model by Phillips. Precipitation ‘size-bins’ are advected in 2-D in the vertical plane on which the updraught and downdraught are located (see subsection 2(b) for a description of dynamical regions), while cloud-water size-bins and vapour are advected in 1-D. The cloud dynamics are prescribed.

Ice particles are grouped into several basic species in the model, according to their mode of formation:

- (i) Homogeneously frozen cloud droplets and aerosol particles;
- (ii) Primary ice, nucleated by condensation/deposition freezing (Meyers *et al.* 1992) between -5 and -30 °C (see subsection 3(a));
- (iii) Homogeneously frozen precipitation particles;
- (iv) H-M splinters emitted from particles in species (ii) and (iii);
- (v) Frozen raindrops formed heterogeneously and from collisions with ice in species (ii)–(iv); and finally,
- (vi) Further generations of H-M splinters and raindrops frozen in collisions with H-M splinters.

For primary nucleation of crystals, contact nucleation is omitted since thermophoretic effects tend effectively to inhibit it in the convective updraught (Phillips *et al.* 2001, 2002; see also Ovtchinnikov *et al.* 2000). The observed dependence of the H-M process (Hallett and Mossop 1974) on the riming rate, temperature and droplet size are all represented: one splinter is generated for every 200 droplets >24 μm diameter that are rimed at -5 °C. This multiplication rate is applied for all sizes of riming ice particle (see Saunders and Hosseini 2000). Homogeneous freezing of droplets of a given size occurs when the temperature falls below their size-dependent threshold (see Pruppacher and Klett 1997). The approximation is made that this freezing occurs instantaneously; the justification for this is that the time-scale for homogeneous freezing of a single cloud-droplet (~ 10 μm) is probably a few seconds (assuming a volumetric nucleation rate of 10^8 $\text{cm}^{-3}\text{s}^{-1}$ and a cooling rate of about 10 degC minute^{-1}), which is substantially less than the time taken (about 20 s) for model updraught parcels to ascend through the layer in which 99% of their cloud-water mass is homogeneously frozen. For each basic species, the evolution of its size distribution with time is predicted in all layers in the cloud.

In the EMM, a particle-growth scheme predicts the continuous evolution of the dimensions, bulk density and axial ratio of ice particles in each size-bin (see Phillips *et al.* 2001, 2002, 2003). ‘Categorization assumptions’ that prescribe the shape and bulk density of ice particles in artificial classes are not in general utilized by the EMM, in contrast with many cloud models. The *continuum* of values of shape and bulk density across the size distribution that is typically seen in a given volume of cloud in nature, is represented in the EMM. Every size-bin has a ‘memory’ of the prior history of growth of its particles; particle properties are not simply diagnosed from the current size or mass of the particle. Ice particles are represented as either cylindrical or spheroidal shapes depending on their amount of accreted rime, and have a continuously evolving axial ratio. In contrast with many microphysical models, the EMM utilizes a variable size grid

for hydrometeors: the size of each size-bin varies continuously with time, following the motion and growth of its particles.

(b) *Prescribed cloud dynamics*

A 1-D dynamical framework for the cloud is prescribed in the manner described by Phillips *et al.* (2001, 2002, 2003). Values of dynamical parameters are adjusted to match observed values from the CRYSTAL-FACE Cb case of 18 July 2002, simulated here. There is a sequence of thermals in the updraught ascending at about half the local value of the peak updraught speed (see Levine 1959), which increases linearly with height between the cloud base and 11 km above mean sea level (AMSL). These thermals lift the cloud top in stages to its maximum altitude, as in the original MTM. A downdraught 1 km deep is included adjacent to each thermal. Particles are swept into the downdraught from the tops of the thermals. Ice particles in the downdraught are evaporated at a rate that is such as to maintain exact ice saturation. A model component to represent the surrounding cloudy region (SCR), introduced by Phillips *et al.* (2003) in stratiform simulations, is retained in the current version. Particles surviving descent in the downdraught are partially recirculated back into the updraught, with the remainder being deposited in the SCR. These 1-D channels, for the updraught and SCR, are discretized as stacks of ascending horizontal layers that are each about 50 m deep. The microphysical interactions are evaluated separately in each layer, and particles may fall from one layer to the next. The slope of the channels is determined by the horizontal advection of thermals by the environmental vertical shear.

The entraining mass flux of environmental air entering the updraught per unit of altitude (z), E_z ($\text{kg s}^{-1}\text{m}^{-1}$), is related to the updraught mass flux, $F(z)$, by: $E_z = f_E^*(z)E\Phi$, with $\Phi = F(z)/H(t)$. Here $H(t)$ is the instantaneous depth of the cloud at time t . The skew factor is defined by $f_E^*(z) = f_E(z)(H(t) - z)/H(t)$. In this case $f_E(z)$ is unity except in the upper third of each thermal where it is 0.5, and in the central third of the thermal where it is interpolated from 0.5 to unity. This parametrizes the adiabatic cores seen in aircraft observations by Heymsfield *et al.* (1978). Finally, E is an entrainment parameter that is adjusted to obtain a match of the passive tracer profile between the EMM and a 3-D model at all levels (see subsection 3(b)). Details of previous versions of the EMM are provided by Phillips *et al.* (2001, 2002, 2003).

(c) *New features of model*

There are some novel features of the EMM used here. First, there is now a solution of the stochastic collection equation (SCE) for coalescence, aggregation and rain-ice collisions. This replaces the autoconversion formulae in previous model versions. The scheme proposed by Bott (1998) has been adapted for the variable size grid of the EMM. In the case of aggregation, solution of the SCE involves transferral of ice crystal properties (bulk density, shape, meltwater mass, trajectory position) between size-bins whenever ice mass is transferred. For aggregation, the bulk density of aggregates at the instant of their formation is derived from empirical relations for unrimed snow crystals, and their initial axial ratio is assigned an empirical value of 0.25 (see Pruppacher and Klett 1997). Of course, during subsequent growth, the bulk density and shape of aggregates are free to evolve as predicted by the particle-growth scheme (see subsection 2(a)). Sticking efficiencies of Mitchell (1988) are applied, as in previous model versions.

The turbulent enhancement of the collision kernel occurs by the turbulent/inertia mechanism proposed and implemented by Khain and Pinsky (1995), Pinsky and Khain

(1998, 2002), Pinsky *et al.* (2000) and Khain *et al.* (2004). By this mechanism, there is a modification of the relative velocities of drops of different masses owing to their inertia. Values of the turbulent enhancement factor for coalescence are identical to those applied in the Hebrew University Cloud Model (HUCM, Khain *et al.* 2004). This enhancement factor in a given collision is a 2-D function of the masses of collecting and collector droplets. The turbulent dissipation rate assumed for their derivation is similar to the value observed by aircraft in the deep-cumulus case being simulated for this paper (see subsection 3(a)). Similarly, for riming, a 2-D set of mass-dependent turbulent enhancement factors is applied, again using HUCM data. The same set of turbulent enhancement factors is applied for ‘collisional’ raindrop-freezing, as for riming. Values of the (non-turbulent) drop–drop collision efficiency are those utilized by Khain and Sednev (1996) and Khain *et al.* (2004), being based on data derived theoretically and numerically by Hall (1980). Raindrop break-up is also included with Bleck’s (1970) numerical method.

Explicit representation of the entire size distribution of unactivated condensation nuclei (CN) aerosols in 33 fixed doubling bins, on a grid of the dry mass of the solute, has been introduced (giant and ultra-giant aerosols are neglected—see section 6). This enhances the representation of droplet nucleation. For the j th size-bin of unactivated CN, the rate of change of the particle-number mixing ratio (number of particles per kg of air) is given by an equation similar to that for vapour and cloud water:

$$DN_j/Dt = \alpha_E(N_{\text{env},j}(z) - N_j) + S_j.$$

Here, α_E is the fractional entrainment coefficient for the updraught and is determined by E_z . Also, $N_{\text{env},j}(z)$ is the observed number mixing ratio of CN in the environment in the j th size-bin (see subsection 3(a)), while S_j is a source/sink term that accounts for losses of aerosol due to droplet nucleation. A droplet-nucleation scheme similar to that applied by Khain *et al.* (2004) has been included. For a given supersaturation, the critical CN radius is computed using Kohler theory (see Rogers and Yau 1991) assuming that the aerosols all have the same chemical composition. CN with radii exceeding this critical value are activated as cloud droplets. For an assumed chemical composition of ammonium sulphate (see subsection 3(a)), a Van’t Hoff factor of three, an average molecular weight of 132.14 and a dry density of 1.77 g cm^{-3} are utilized.

Homogeneously frozen cloud droplets are now advected in 1-D in the same manner as cloud water, CN and vapour, to improve the dynamical coupling with the vapour field. Homogeneously frozen droplets are grown as cylindrical particles, with an evolving bulk density and shape predicted by the particle-growth scheme. Homogeneous aerosol freezing as predicted by Koop *et al.* (2000) is now included. Whenever the supersaturation with respect to ice exceeds the temperature- and size-dependent critical value corresponding to a given aerosol size-bin, all the aerosols in that size-bin are instantaneously frozen. This is an approximation to reality, since it takes a finite time for real drops to freeze. It is assumed that aerosols will always freeze homogeneously before they can activate as liquid droplets, at all temperatures colder than about -40°C (see Fig. 3 of Koop *et al.* 2000; Knollenberg *et al.* 1993). Consequently, secondary droplet nucleation is only applied at temperatures warmer than about -40°C .

Collision efficiencies for the freezing of supercooled raindrops in collisions with ice crystals have been incorporated, utilizing laboratory data from Lew and Pruppacher (1983) for ice columns and from Lew *et al.* (1985) for planar crystals. The observed dependence of these collision efficiencies on ice-particle size, bulk density and axial ratio are included (by converting the published plots to multi-dimensional look-up tables). For the smaller supercooled raindrops (<0.2 and <0.6 mm for collisions with

columnar and planar particles, respectively) no empirical data are available: their drop–ice collision efficiency is approximated by the drop–drop value for a hypothetical drop of the same mass as the colliding ice particle, as in the HUCM. Finally, accretion of supercooled rain or drizzle by very large ice particles has been included. The collision efficiency for the collection of supercooled rain and droplets by larger ice particles is now dependent on the bulk density of the ice and on the masses of each colliding pair of particles, with HUCM data for the riming of graupel and hail being applied. The density of ice from accreted rain is that of pure ice.

As with previous versions of the EMM, the terminal velocity of ice is determined by relations between its Reynolds and Best numbers, and between its Best number, particle mass and size, as presented by Pruppacher and Klett (1997) for cylindrical and spheroidal shapes of particle, respectively. For graupel, a comprehensive set of relations between the Best and Reynolds numbers from Rasmussen and Heymsfield (1987) is applied.

The time step for the prescribed evolution of cloud dynamics, and for the solution of the stochastic collection equation for coagulation and collisional nucleation processes, is 2 s. The tracing of trajectories, evaluation of riming and vapour growth of particles, and solution of empirical equations for particle shape/density, are all performed on a time step of 0.1 s.

3. OBSERVED STORM CONDITIONS AND MODEL CONSTRAINTS

(a) *Case synopsis and model meteorological inputs*

The case simulated by the EMM control simulation is that of 18 July 2002 from the CRYSTAL-FACE campaign. The campaign included Twin Otter and Citation aircraft, which both flew over the peninsula on this day. The Twin Otter flew mostly in the boundary layer in the storm's environment and carried a suite of aerosol instrumentation including a Differential Mobility Analyser (DMA). The Citation spent more time at mid-levels and performed traverses of the updraughts and anvil cirrus of storm cores. The Citation was equipped with standard meteorological instrumentation and cloud microphysical sensors including a Forward Scattering Spectrometer Probe (FSSP), a Particle Measuring System two-dimensional cloud and precipitation probe, or 2-DC probe, for counting hydrometeors, the King probe for measuring liquid cloud-water, the Counterflow Virtual Impactor and the Continuous Flow Diffusion Chamber (CFDC) for measuring aerosol activation. Finally, the NASA WB-57 aircraft, also carrying several aerosol and cloud probes, observed anvil outflows and the upper-tropospheric environment during CRYSTAL-FACE.

Strong Cb storms were popping up over the southern tip and south-east coastal region of the Florida peninsula on the afternoon of 18 July, in an environment of weak low-level winds and strong upper-level north-easterly shear. The temperature and humidity structure of the environment was observed by sondes released from ground sites on the peninsula. The convective available potential energy over the South Florida region was over 2000 J kg^{-1} , among the highest values observed during the experiment, while the highest cloud tops reached about 15 km which was slightly above average (Sherwood *et al.* 2004). The cloud base sampled by the aircraft was at 0.8 km AMSL (22°C), and the freezing level was at 5.9 km AMSL. The boundary-layer aerosol content observed by the Twin Otter was more nearly continental than maritime. A CCN/aerosol closure study for CRYSTAL-FACE shows that if ammonium sulphate is assumed to be the aerosol chemical composition then there is an accurate treatment of CCN activation on this day (VanReken *et al.* 2003).

As described previously, the EMM requires several meteorological inputs, including the cloud-base and cloud-top altitudes given above. A top height of 14 km was used, since this was a more typical value, although some clouds reached higher levels. Updraught velocity was prescribed based on the penetration by the Citation after 1932 UTC, where a peak updraught speed of almost 24 m s^{-1} was measured at about 11 km AMSL ($-34 \text{ }^\circ\text{C}$) in the mixed-phase region. The turbulent dissipation rate from the Citation data had a mean value of about $700 \text{ cm}^2\text{s}^{-3}$ at about 11 km AMSL. The peak updraught speed in the model was set at 25 m s^{-1} at 11 km AMSL and 3 m s^{-1} at cloud base. The vertical wind shear between 1 and 11 km AMSL was obtained from sonde data, and was about $1.5 \text{ m s}^{-1}\text{km}^{-1}$, which was the input for the model.

A size-resolved vertical profile of aerosol-number mixing ratio ($N_{\text{env},j}(z)$) for the model was generated by combining the profiles of size distribution from the WB-57 and Twin Otter aircraft in the upper and lower troposphere, respectively. The gap between the two ranges of altitude from these aircraft was filled with an interpolation that matched the total aerosol concentration in all size-bins to that observed with the FSSP probe on the Citation aircraft at each level. The Twin Otter particle-size distribution was observed with the DMA ($<950 \text{ nm}$) and Passive Cavity aerosol Spectrometer Probe (0.1–3 microns), being normalized by the total number concentration of aerosols from the Condensation Particle Counter. The aerosol size distribution from the WB-57 was measured in the nucleation mode with the Nucleation-Mode Aerosol Size Spectrometer (data from 19 July were used because there was no WB-57 flight on 18 July).

The CFDC instrument on the Citation measured an environmental IN concentration that was up to about 1.5 times the value obtained from the Meyers *et al.* (1992) formula for condensation-deposition freezing. Consequently, in the model the environmental concentration of IN activated at each level was determined by multiplying the temperature-dependent value from Meyers *et al.* by this observed factor. The formula by Meyers *et al.* was arbitrarily extrapolated to $-30 \text{ }^\circ\text{C}$ for the lowest temperature of IN activation; a sensitivity test (see subsection 4(f)) did not reveal any appreciable sensitivity to the choice of its value.

(b) Determination of model physical parameters

Aircraft observations of convective updraughts on 18 July during CRYSTAL-FACE were analysed to estimate the contribution to the horizontally averaged (indicated by $\langle \rangle$) rate of coagulation from the correlation between spatial 3-D deviations, $\langle N'(m)N'(q) \rangle$, of the particle concentration (see the third and fourth correlation terms of Eq. (2) in Stevens *et al.* (1998)) at spatial scales $>0.1 \text{ km}$. Here, N is the particle concentration while m and q are masses of colliding particles. This correlation was observed to be at least an order of magnitude less than the product of the updraught-average concentrations, $\langle N(m) \rangle \langle N(q) \rangle$. A ‘large-scale eddy-enhancement factor’ may be defined here as the average over values of m and q at a given level of:

$$\Theta = 1 + \langle N'(m)N'(q) \rangle / (\langle N(m) \rangle \langle N(q) \rangle).$$

This eddy-enhancement factor is applied to the collision kernels for coagulation processes in the 1-D model, in order to account for the 3-D inhomogeneity of the particle concentration in the real cloud on spatial scales $>0.1 \text{ km}$. It has observed values in the range of about 1.01 to 1.1 for Citation traverses of Cb updraughts at levels in the mixed-phase region on 18 July 2002 (a value of 1.1 is applied in the model). Its proximity to unity suggests that, for the particular cloud being simulated, collision-coalescence may be adequately predicted in a 1-D framework if the average cloud-water properties are accurate.

A value of 2.7 for the entrainment parameter, E , was selected so as to match, at all levels in the updraught, the mixing ratio of a passive tracer in the EMM with that predicted in the 3-D cloud model of Fridlind *et al.* (2004). Aircraft observations analysed by Fridlind *et al.* indicate that the secondary droplet nucleation aloft occurs primarily at the edges of the updraught in regions of entrainment for Cb cells on this particular day of CRYSTAL-FACE. In such regions, the supersaturation is expected to be substantially lower than the average value for the entire width of the updraught, because values of the vertical air velocity are low and also due to dilution with dry environmental air. Hence, an 'effective supersaturation' for predicting secondary droplet nucleation was assumed to be a prescribed fraction, 0.1, of the local value of the predicted average supersaturation at a given level, at altitudes above where the average fraction of cloud-base air is 50% (4 km AMSL). This fraction was selected so as to match the predicted droplet concentration with that observed. For inputs to the droplet nucleation scheme, ammonium sulphate was assumed for the chemical composition of the aerosol (see subsection 3(a)).

(c) *Comparison of available aircraft observations with control*

The simulations were run for 75 minutes, during which time the model cloud top was lifted by a sequence of thermals from 5 km AMSL to the maximum cloud-top altitude of 14 km AMSL. The predicted vertical profiles of certain microphysical properties of the storm updraught have been averaged over the entire glaciated period of the simulation at each level, and are compared here with observed profiles (see subsection 3(b)). Figures 1 and 2 demonstrate that cloud-water properties were adequately predicted, given the spread of the observed values. (Here, as elsewhere in the present paper, 'concentration' refers to the number of particles per unit volume of air, not the mass of particles.) All the activated droplets disappear either by homogeneous freezing or by evaporation near the -36 °C level. As was found by Heymsfield and Sabin (1989), the homogeneous freezing of droplets occurs over a very narrow temperature range of about 1 degC. The predicted and observed profiles of cloud-droplet concentration tend to decrease with height throughout the entire depth of the cloud, largely due to intensification of accretional losses from riming and accretion onto rain during ascent. Secondary droplet nucleation makes an increasing contribution to the droplet concentration during ascent (see subsection 4(b)). Figure 3 shows observed and modelled total condensed-water content, and Fig. 4 shows particle concentrations from the model and filtered 2-DC aircraft observations.

In all cases, the simulated quantity is within one standard deviation of the observed mean value and is well within the observed range of raw data values. Given our inexact knowledge of the age of the cumulus turrets sampled by the Citation, and the sparseness and imperfect collocation of various observations, we believe the agreement is adequate.

The predicted liquid fraction (the fraction by mass of the total mixing ratio of cloud-water, rain and ice, that is liquid) in the updraught decreases monotonically with height from 100% at the freezing level to about 10% at 11 km AMSL just below the anvil base. It approaches zero rapidly just above 11 km AMSL, above which all remaining liquid freezes. This is consistent with aircraft observations aloft. Only about 10–15% of all particles >0.1 mm are observed to be spherical in our inspection of the 2-DC aircraft observations, for the traverse at -35 °C (11.3 km AMSL in the model) by the Citation at 1933 UTC. Similarly, the model predicts that only about 10% of particles >0.1 mm are (round) liquid raindrops at this level, while the remaining 90% of particles >0.1 mm are predicted to be ice particles that are not round, such as frozen drops (axial ratio, AR , predicted to be 0.6) and H-M splinters (AR predicted to be 0.4). The lack of sphericity

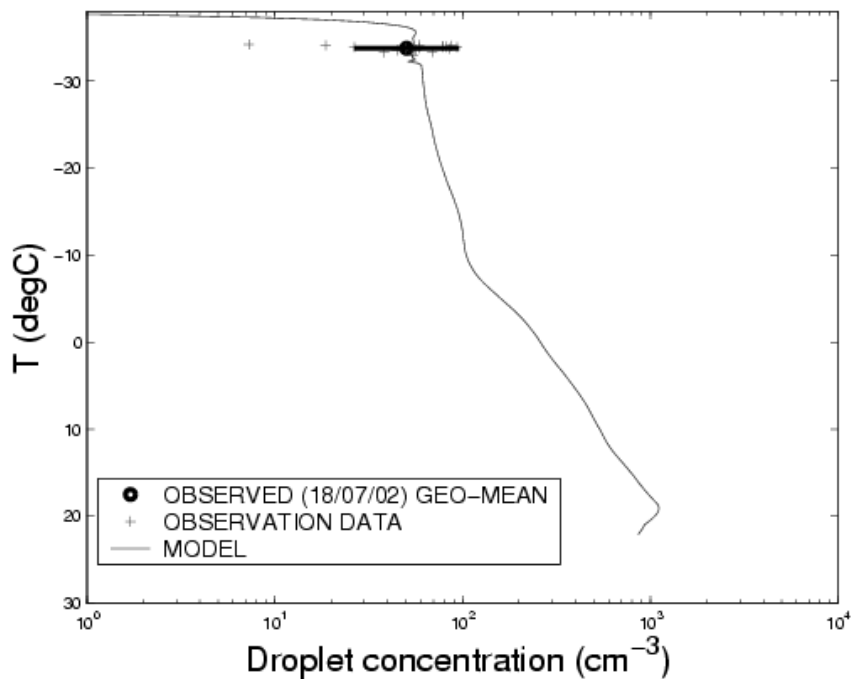


Figure 1. Mean droplet concentrations in a deep cumulus updraught observed by the Forward Scattering Spectrometer Probe and those predicted by the Explicit Microphysics Model. The horizontal bar centred on the observed mean ('o') is two standard deviations wide.

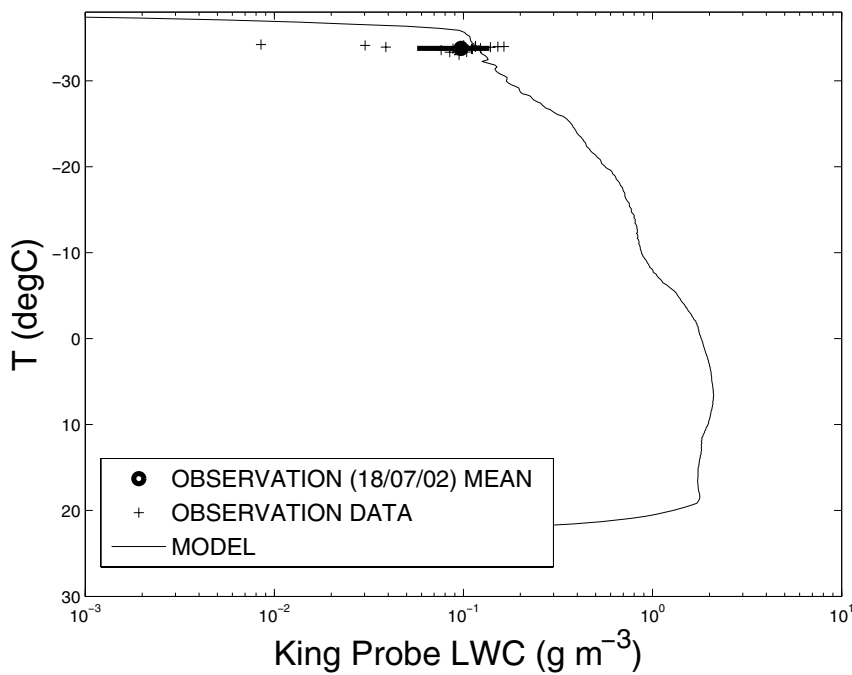


Figure 2. Mean liquid water content (LWC) in a deep cumulus updraught observed with the King probe and those predicted by the Explicit Microphysics Model. The horizontal bar centred on the observed mean ('o') is two standard deviations wide.

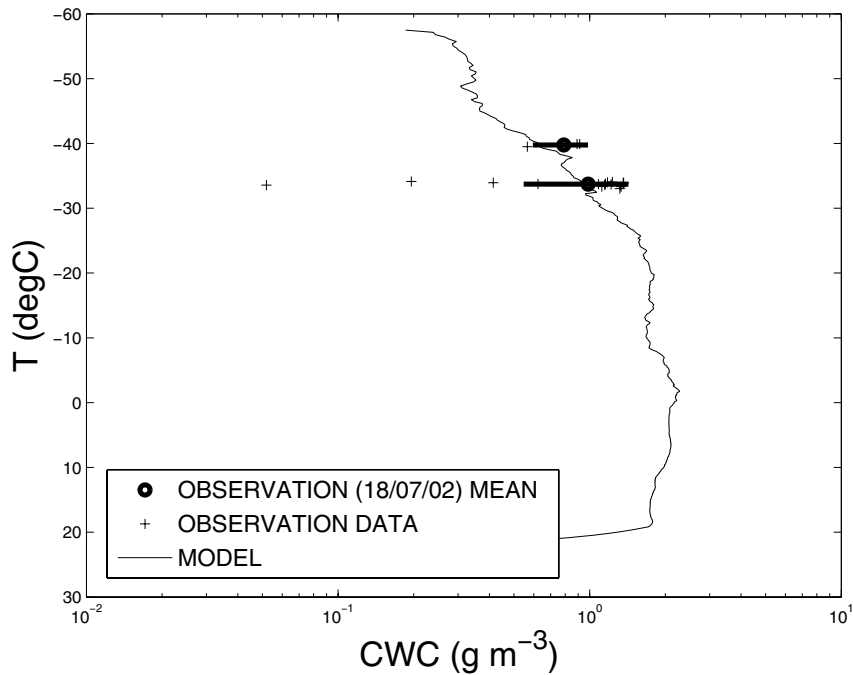


Figure 3. The measured condensed-water content observed in a deep cumulus updraught for all hydrometeors (arithmetic and geometric means are given) and that predicted by the Explicit Microphysics Model. The horizontal bars centred on the observed means ('o') are two standard deviations wide.

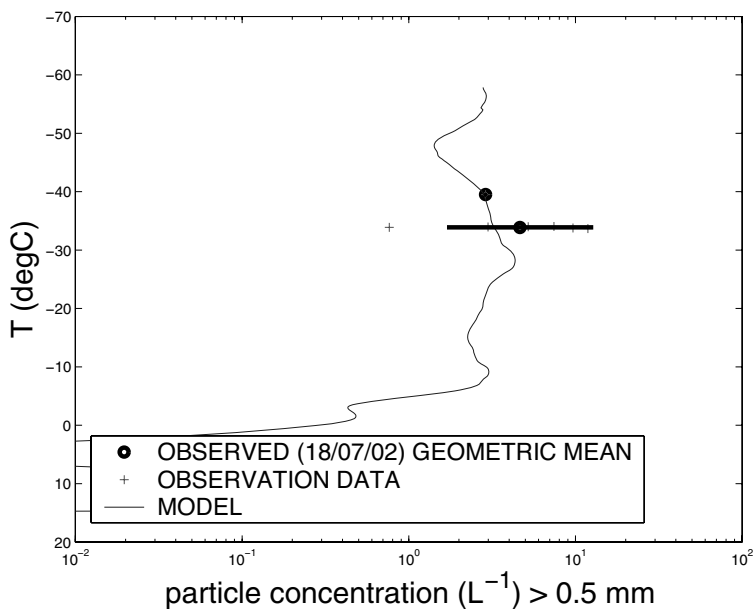


Figure 4. Filtered (>0.5mm) 2-DC (see text) particle concentrations observed in a deep cumulus updraught, and those predicted by the Explicit Microphysics Model. The increase with height towards the anvil top in the model is an artifact of the time-averaging, reflecting the fact that the ascent of thermals (with high ice concentrations) slows towards cloud top.

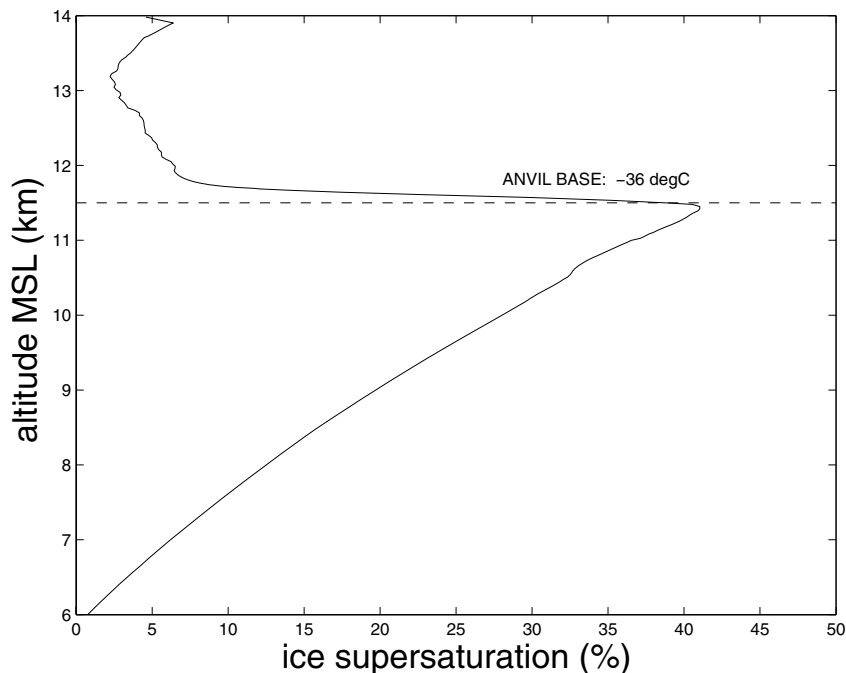


Figure 5. Vertical profile of supersaturation with respect to ice in a deep cumulus updraught in the Explicit Microphysics Model.

of frozen drops at this altitude in the control simulation is due to their vapour growth, as they are too small (0.1–0.2 mm) to rime efficiently. This validates the particle-growth scheme in the EMM.

Finally, although the ice concentration is fairly uniform with height (about 20–40 L^{-1}), the average ice-water content reduces with height from 0.9 to 0.1 $g m^{-3}$ over the entire depth of the anvil. This is at least qualitatively consistent with aircraft observations of a decrease of ice-water content with decreasing temperature in tropical convective anvil cirrus in the vicinity of Kwajelein in the west Pacific (Brown and Heymsfield 2001). In the model nearly all ice mass below the anvil resides in graupel, and ice particles are far less numerous than liquid droplets, despite contributing comparably to condensed mass at most levels. Figure 5 illustrates the vertical profile of supersaturation with respect to ice. Above the anvil base, the ice supersaturation is <10% mostly, which is well below the threshold for homogeneous aerosol freezing. Figure 6 displays the particle size distribution from the updraught at $-50^{\circ}C$ (about 13 km AMSL). Most anvil ice particles are in the size range 10–50 microns.

4. RESULTS: SENSITIVITY TO NUCLEATION PROCESSES

Results are presented here from a sequence of sensitivity studies dealing with the key nucleation processes, in order to assess the impact of various nucleation processes on the anvil.

The mixed-phase region extends from the freezing level at 5.9 km AMSL to the anvil base at about 11.5 km AMSL ($-36^{\circ}C$). Cloud droplets that reach the anvil base will freeze homogeneously there, or else simply evaporate. The anvil extends from about

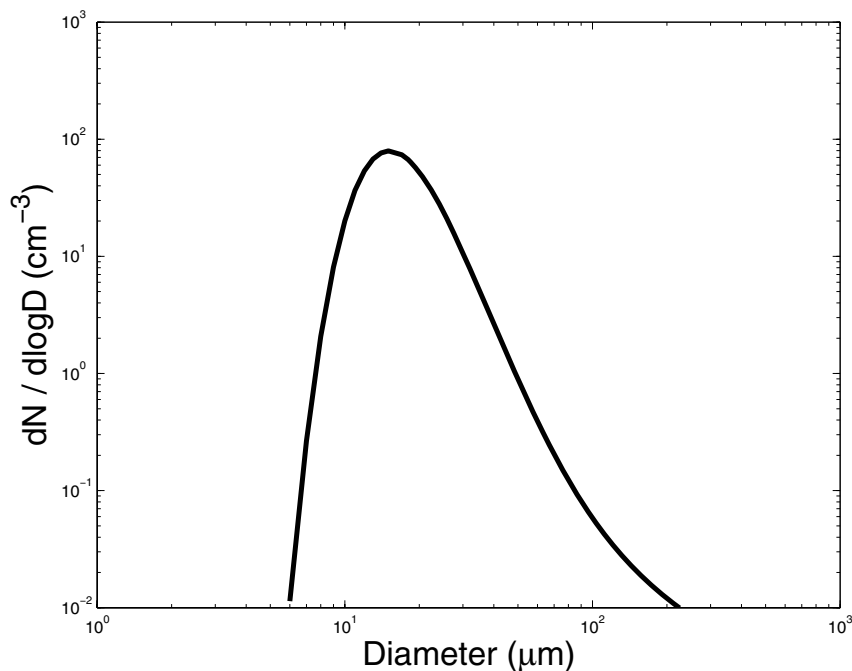


Figure 6. The particle size distribution in a deep cumulus updraught given by the Explicit Microphysics Model for ice particles at the -50°C level. Here, dN is the ice concentration (cm^{-3}) in $d(\log D)$, where D is the particle diameter.

11.5 km AMSL to the assumed maximum cloud-top level of 14 km AMSL. The H-M region is located at 6.5 to 7.4 km AMSL (-3 to -8°C). This is where the H-M process of ice multiplication is active. Unless otherwise stated, results are taken from the updraught of the storm.

(a) *No homogeneous freezing*

A model run was performed with homogeneous freezing of droplets, rain and aerosols prohibited (the case with no homogeneous freezing), so that droplets could remain as supercooled water to arbitrarily low temperatures unless frozen via activation of IN. This run was compared with the control.

Figure 7 shows that the total ice concentration at all levels in the anvil was about three orders of magnitude lower in the no-homogeneous-freezing case than in the control. The discontinuity in total ice concentration caused by the homogeneous freezing of droplets at the anvil base in the control was completely eliminated; however, the ice concentration in the mixed-phase region of the updraught remained almost unaltered. The ice mixing ratio was reduced by about 1 g kg^{-1} at most levels in the anvil in the no-homogeneous-freezing case relative to the control. The mixing ratio of supercooled cloud water was increased from zero to values of about 0.5 g kg^{-1} in the anvil when homogeneous freezing was excluded. The peak in ice crystal concentration near 7 km AMSL is due to the H-M process being active in both simulations.

Anvil crystals are about an order of magnitude larger in the case with no homogeneous freezing relative to the control. Figure 8 demonstrates that they are about 200–300 kg m^{-3} less dense. They are also slightly less columnar, with an AR that is closer to

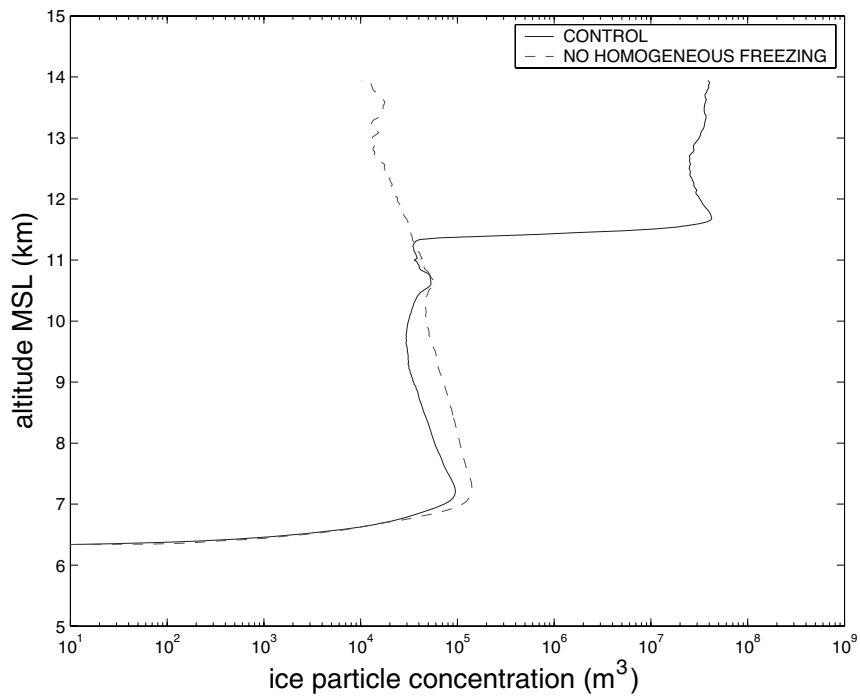


Figure 7. Comparison of the vertical profile of total ice concentration in a deep cumulus updraught predicted by the Explicit Microphysics Model with no homogenous freezing, with that from the control run.

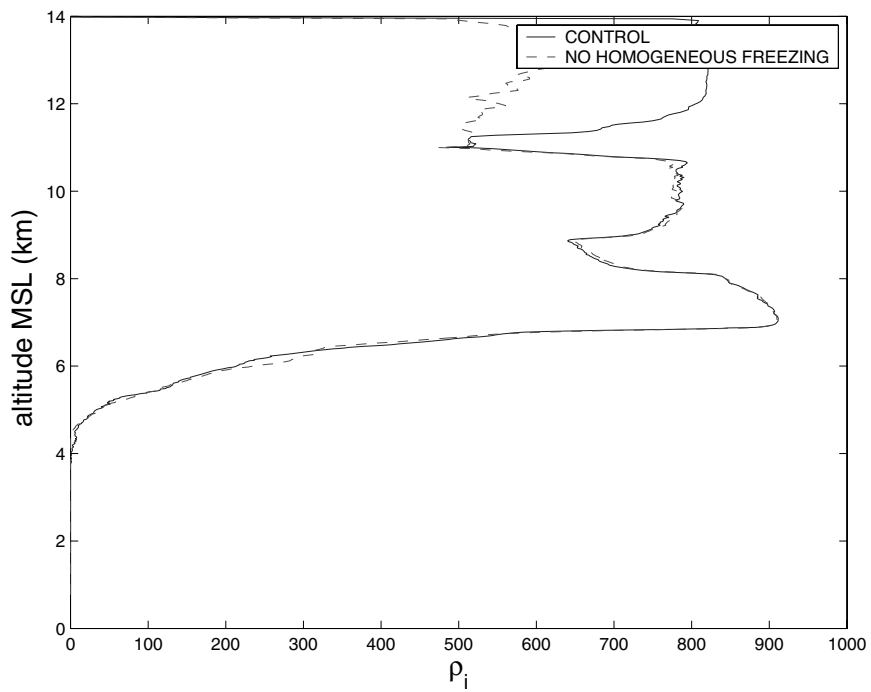


Figure 8. As Fig. 7 but for the bulk density of ice, ρ_i .

unity (lower by about 0.5). These changes arise because anvil crystals are formed by primary nucleation (i.e. condensation-freezing when IN activate) in the no-homogeneous-freezing case, and are larger (by about 0.2 mm) having experienced much vapour growth at water-saturated conditions in the mixed-phase region before entering the anvil.

In summary: about 99.9% of all anvil ice particles (representing about half of the total ice mass in the anvil) are nucleated by homogeneous freezing in the updraught of this particular model cloud, in the control simulation. This mostly involves the freezing of supercooled cloud-droplets at the anvil base. Consequently, all other nucleation processes can only significantly affect the anvil ice concentration insofar as they alter the amount of supercooled condensate available for homogeneous freezing in this model cloud.

(b) *No in-cloud CCN activation*

The next run was performed with both secondary droplet nucleation and homogeneous aerosol freezing prohibited (the primary-only case). Secondary droplet nucleation involves the activation of CCN as cloud droplets anywhere in the ‘interior’ of the cloud (i.e. at least 500 m above the cloud base), while homogeneous aerosol freezing refers to freezing of haze particles that survive the entire updraught without activating. This simulation therefore distinguishes the role of primary droplet nucleation (activation of droplets near the cloud base), traditionally viewed as the main source of droplets.

Figures 9 and 10 demonstrate the impact that secondary droplet nucleation has on the concentration of anvil ice crystals and supercooled droplets in the storm, by comparing the model run having only primary nucleation with the control run. Most of the droplets in the upper half of the mixed-phase region are clearly generated by secondary droplet nucleation in the control. The droplet concentration is reduced by about two orders of magnitude near the anvil base in the primary-only case relative to the control.

Secondary droplet nucleation is only significant at levels more than about 3 km above the cloud base, because the vertical velocity is lower and the droplet concentration higher at levels nearer the cloud base. In the upper half of the mixed-phase region, the rain mixing ratio in the primary-only case is reduced by $<0.05 \text{ g kg}^{-1}$, since the warm-rain process is less active in the absence of copious cloud-water aloft. This result is consistent with the findings of Pinsky and Khain (2002) that secondary droplet nucleation accelerates coalescence. The cloud-water mixing ratio is also reduced by about $0.5\text{--}1 \text{ g kg}^{-1}$ at those levels.

In the anvil, the ice concentration is reduced by about two orders of magnitude at most levels. The mean diameter of anvil crystals is increased by one order of magnitude (from about 0.04 to about 0.4 mm) at most levels above 11 km AMSL in the primary-only case relative to the control, due to fewer crystals competing for the available vapour. Crystals are predicted to be less columnar and less dense in the anvil of the primary-only case: their *AR* is about 0.5 lower and their bulk density is about $200\text{--}300 \text{ kg m}^{-3}$ lower, relative to the control. The bulk density is lower because the particles grow as bullets to larger sizes in the primary-only case near the anvil base, and the bulk density of bullets decreases during growth. This extra bullet growth is due to the much larger supersaturations reached aloft.

In summary: secondary droplet nucleation followed by homogeneous droplet freezing is the source of ice particles in the anvil updraught of the control simulation. This is partly because most primary droplets—nucleated near cloud base (0.8 km AMSL) in the updraught—never reach the anvil base (11.3 km AMSL), being depleted by accretion onto precipitation or detrainment in the underlying mixed-phase region. This depletion

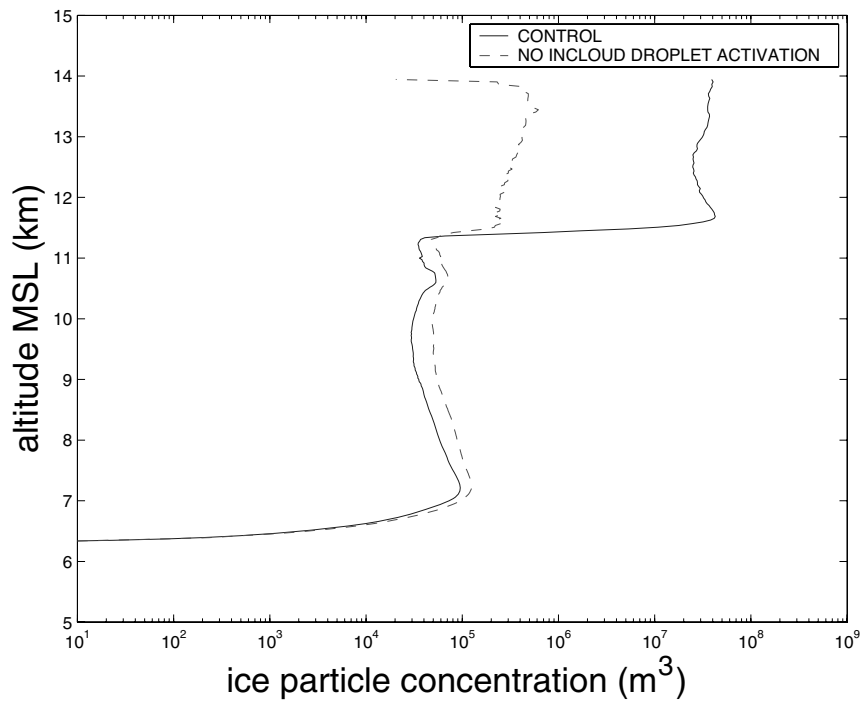


Figure 9. Comparison of the vertical profile of ice particle concentration in a deep cumulus updraught predicted by the Explicit Microphysics Model with no in-cloud droplet activation, with that from the control run.

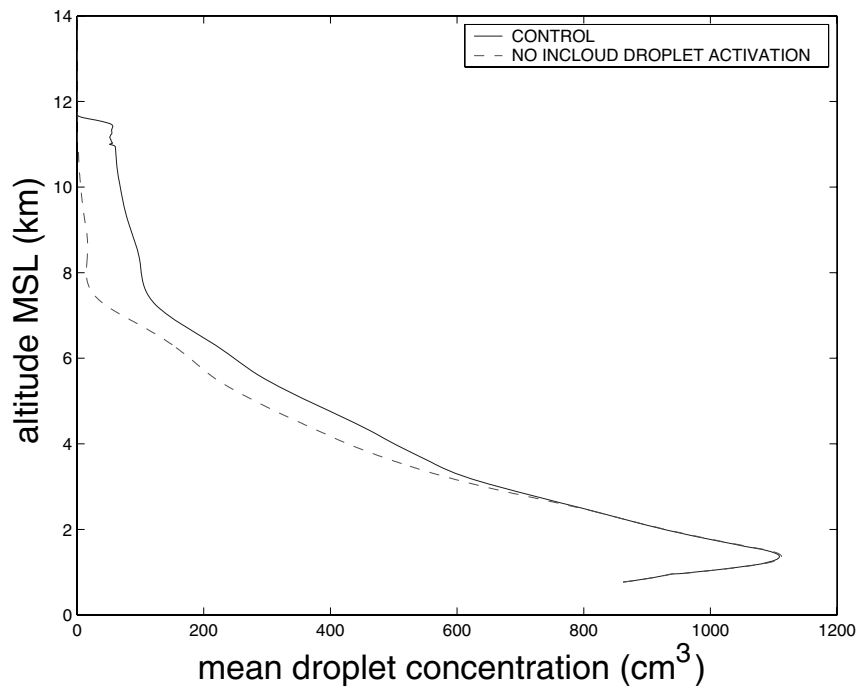


Figure 10. As Fig. 9 but for the mean predicted droplet concentration.

of primary droplets contributes to an increase of the average supersaturation with height, especially above the freezing level, which causes in-cloud activation of CCN aloft. The shape and bulk density of anvil crystals, which are explicitly predicted by the model, are appreciably sensitive to the nature of droplet nucleation in the updraught.

(c) *No warm-rain process*

A model run was performed with all coalescence prohibited (the no-coalescence case). This run was compared with the control.

Microphysical properties in, and below, the anvil were found to be radically altered by the exclusion of coalescence. The rain mixing ratio was reduced to zero throughout the updraught and at subzero levels in the SCR. The cloud-water content was increased by $<3 \text{ g kg}^{-1}$ (by up to about 200%) in the updraught above 6 km AMSL and by $<0.5 \text{ g kg}^{-1}$ (about 100%) in the SCR. In the updraught of the no-coalescence case, the average cloud-droplet diameter was found to be about 5–10 μm higher at most levels in the mixed-phase region relative to the control. This is because accretion of cloud droplets by precipitation in the control occurs preferentially at larger droplet sizes, so that coalescence tends to reduce the average droplet size in this particular model cloud.

Figures 11 and 12 depict the vertical profiles of the average number concentrations of ice particles and droplets, respectively, in the model run with all coalescence prohibited and in the control. In the anvil, the total ice concentration is at least half an order of magnitude higher in the no-coalescence case, due to more droplets being available for homogeneous freezing than in the control. The ice mixing ratio in the anvil is found to be increased by about 200% relative to the control, because there is much less precipitation and the condensed water is much less likely to fall out of the updraught. In the mixed-phase region of the updraught, the ice mixing ratio is reduced to extremely low values in the no-coalescence case; at these levels raindrop freezing dominates the ice mass budget in the control simulation. The absence of frozen rain causes the H-M process to be entirely inactive in the updraught of the no-coalescence case. H-M splinters in the control simulation account for the peak in total ice concentration at 7 km AMSL. Hence, below the anvil base the total ice concentration is reduced by at least one order of magnitude at most levels in the no-coalescence case relative to the control.

Anvil crystals are found to be less dense and less columnar in the no-coalescence case than in the control. Figures 13 and 14 show the explicitly predicted values of mean AR and bulk density, respectively, in the model run with all coalescence prohibited and the control. In the anvil, the average bulk density is reduced by about 100 kg m^{-3} while the AR is reduced from almost 2 in the control to about 1.3 in the no-coalescence case.

Both explicitly predicted profiles of AR display columnar ($AR > 1$) growth in columnar temperature regimes at 6.5–7.5 km AMSL and 9.5–11.5 km AMSL, and similarly for planar growth ($AR < 1$) at 7.5–9.5 km AMSL, as expected for vapour growth. The absence of frozen raindrops and H-M splinters in the no-coalescence case causes the average value of AR to be governed by the shape of primary crystals. The planar character of primary crystals is apparent from the low values of AR at 7.5–9.5 km AMSL in the no-coalescence case.

In summary: raindrop freezing is found to account for most of the ice mass in the mixed-phase region of the control updraught. In the anvil, however, homogeneously frozen cloud water is more important. The mass of cloud water reaching the anvil is very sensitive to whether the warm-rain process is present. Crystal properties are similarly sensitive.

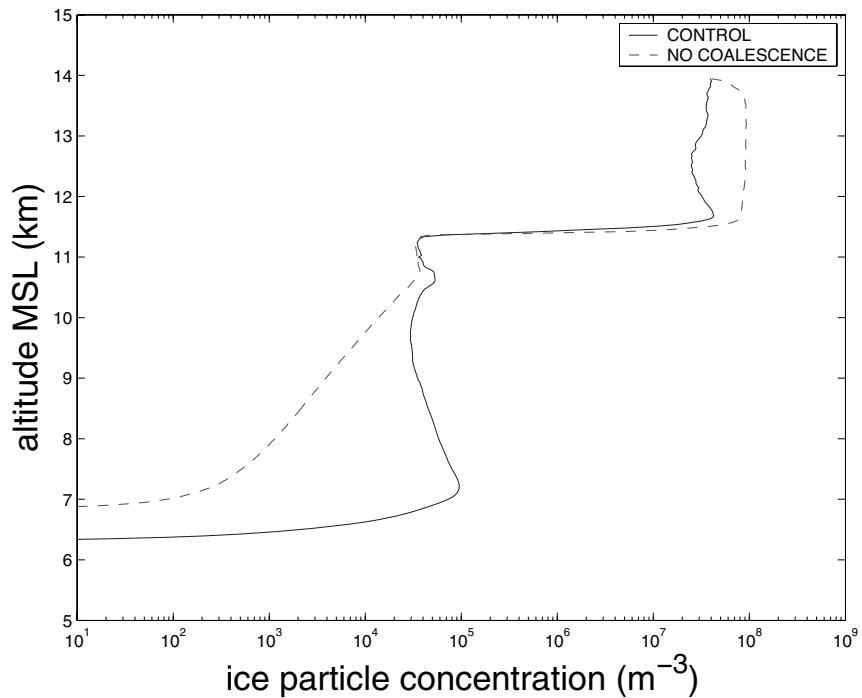


Figure 11. Comparison of the vertical profile of total ice concentration in a deep cumulus updraught predicted by the Explicit Microphysics Model having no coalescence, with that from the control run.

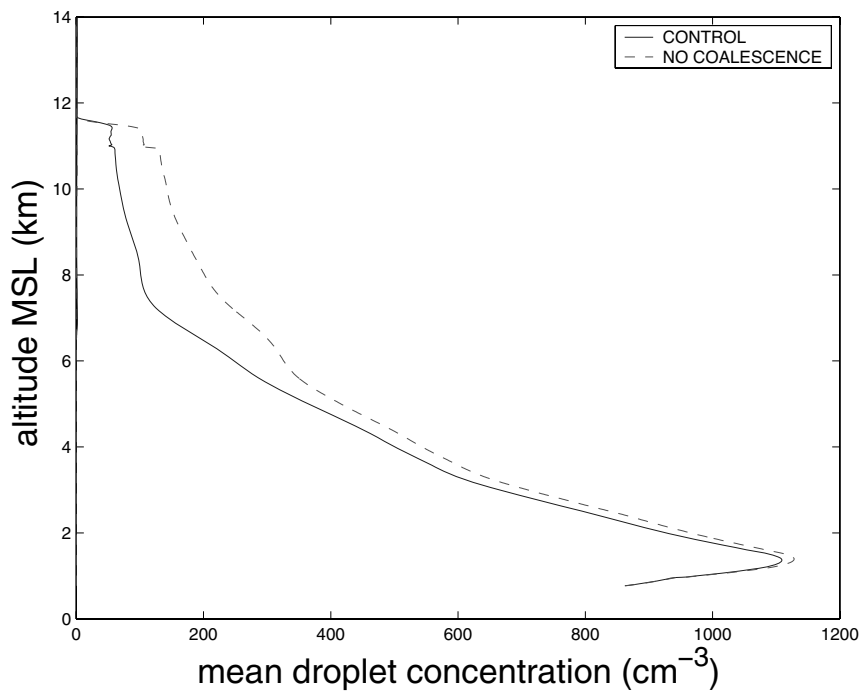


Figure 12. As Fig. 11 but for the mean droplet concentration.

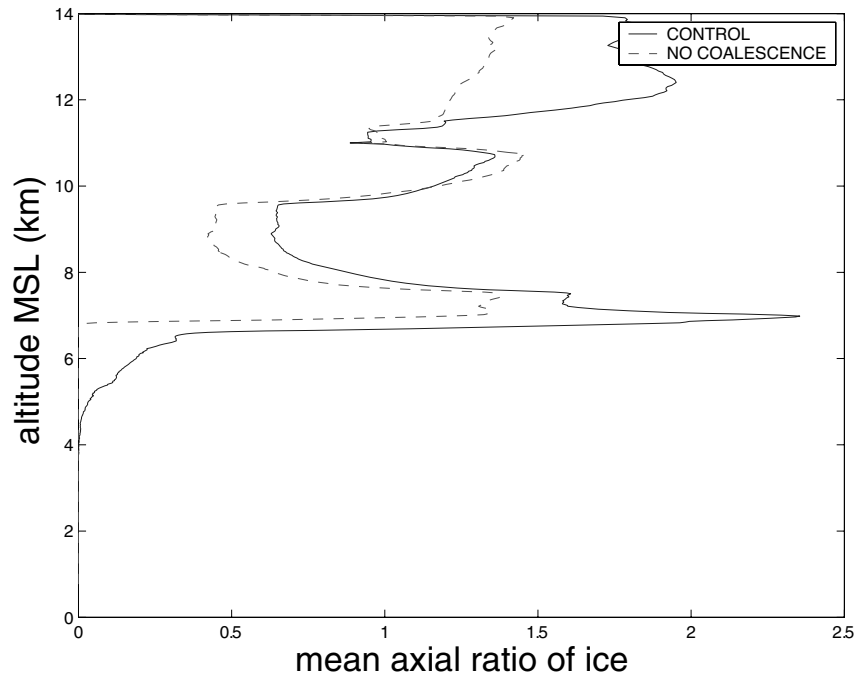


Figure 13. As Fig. 11 but for the mean axial ratio of ice.

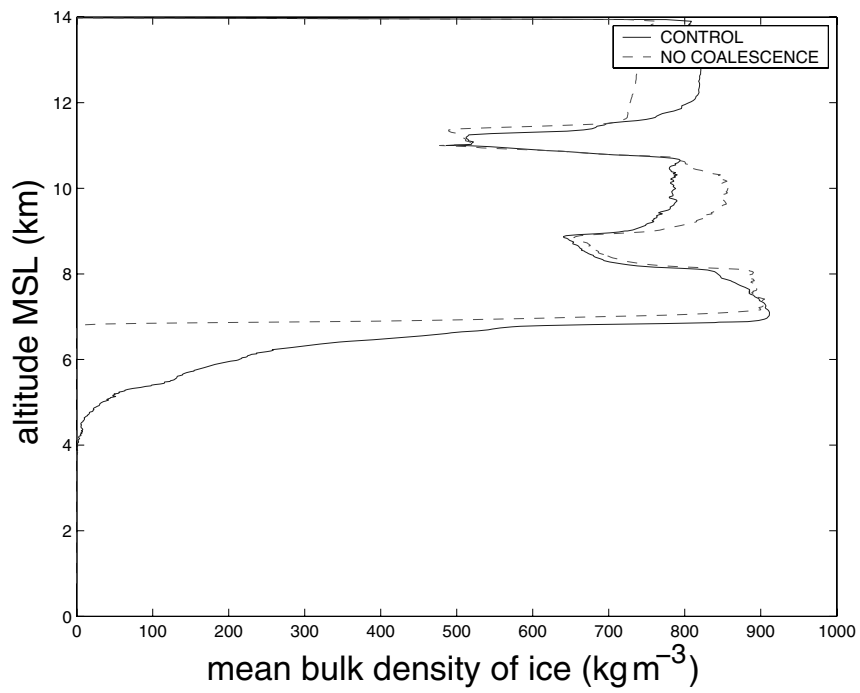


Figure 14. As Fig. 11 but for the mean bulk density of ice.

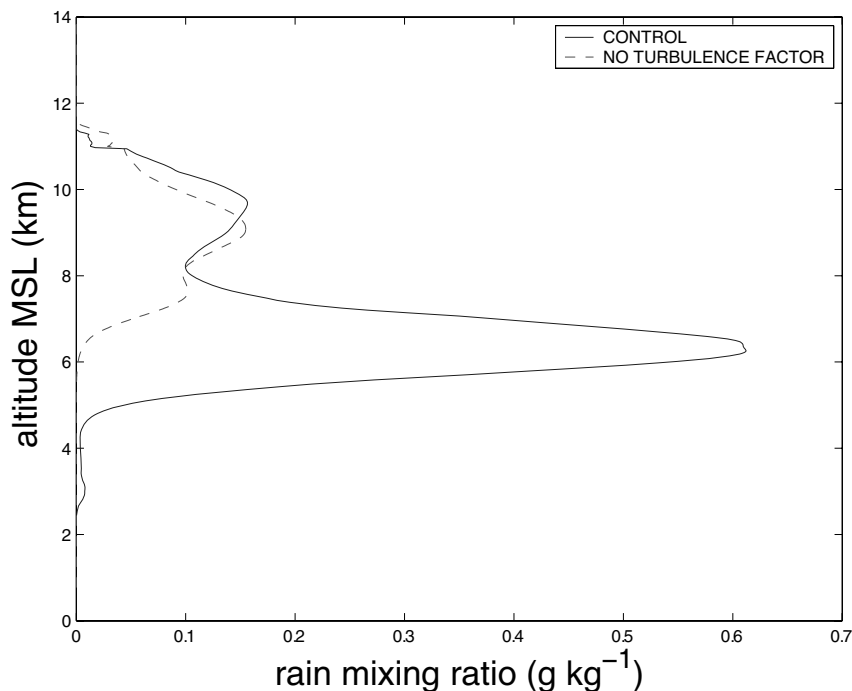


Figure 15. Comparison of the rain mixing ratio profile in a deep cumulus updraught predicted by the Explicit Microphysics Model having no turbulence in the droplet/raindrop coalescence process, with that from the control run.

(d) *No turbulence enhancement factors for coalescence*

A run was performed with the turbulence enhancement factors removed from the droplet/raindrop coalescence process (the zero-turbulence case). Turbulent enhancement of other accretional processes, such as riming, aggregation and collisional raindrop-freezing, was not altered.

Figure 15 shows that the lower of the two peaks of rain mixing ratio, which were found in the control, vanishes in the zero-turbulence case. No rain is found below the 6 km AMSL level in the zero-turbulence case. The onset of coalescence in updraught parcels is drastically delayed by the absence of turbulence effects. Figure 16 demonstrates that the average concentration of supercooled cloud-droplets is enhanced by up to about 50% in the interior of the mixed-phase region in the zero-turbulence case. This is due to lower rates of accretion of droplets by frozen and supercooled raindrops. However, the sensitivity of the supercooled droplet concentration appears to decrease with height towards the anvil base. The cloud-water content in the mixed-phase region is increased by about 1–2 g kg⁻¹. In the mixed-phase region, the peak in total ice concentration associated with H-M splinter generation in the control at about 7 km AMSL vanishes in the zero-turbulence case since frozen raindrops are scarcer.

Figure 17 shows that in the anvil the average ice concentration is enhanced by about 20% at most levels in the zero-turbulence case relative to the control, because of higher concentrations of supercooled droplets. Figure 18 illustrates that at most anvil levels there is a reduction in the mean ice diameter by a few microns relative to the control, due to increased competition between crystals for the available vapour. There are also slight reductions in the anvil crystal AR and bulk density.

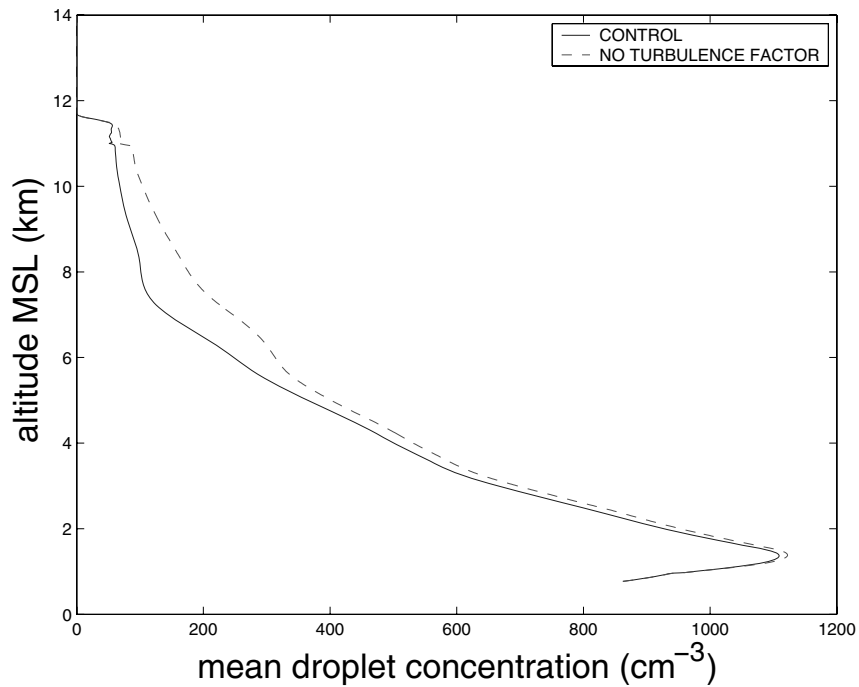


Figure 16. As Fig. 15 but for the mean droplet concentration.

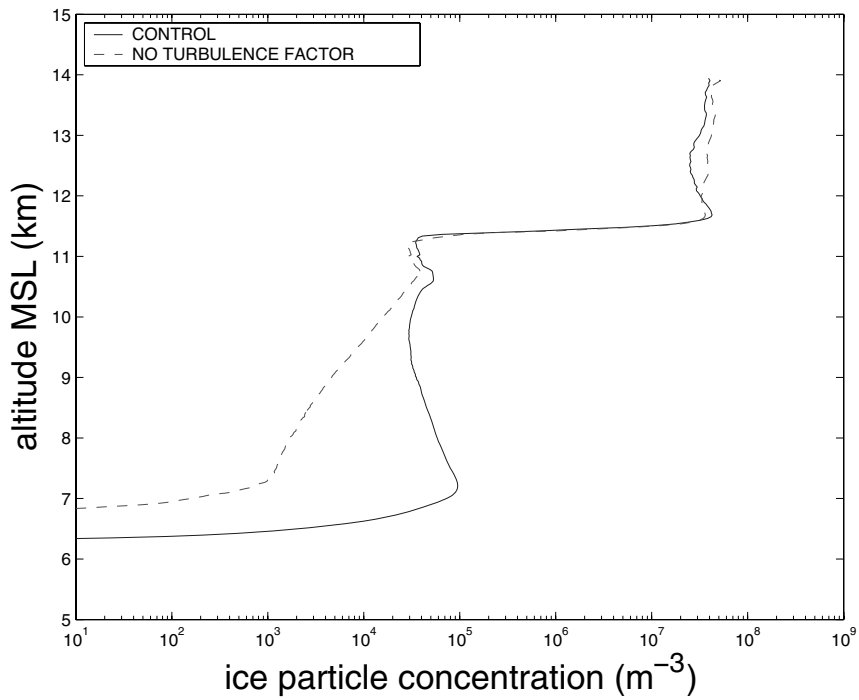


Figure 17. As Fig. 15 but for the ice particle concentration.

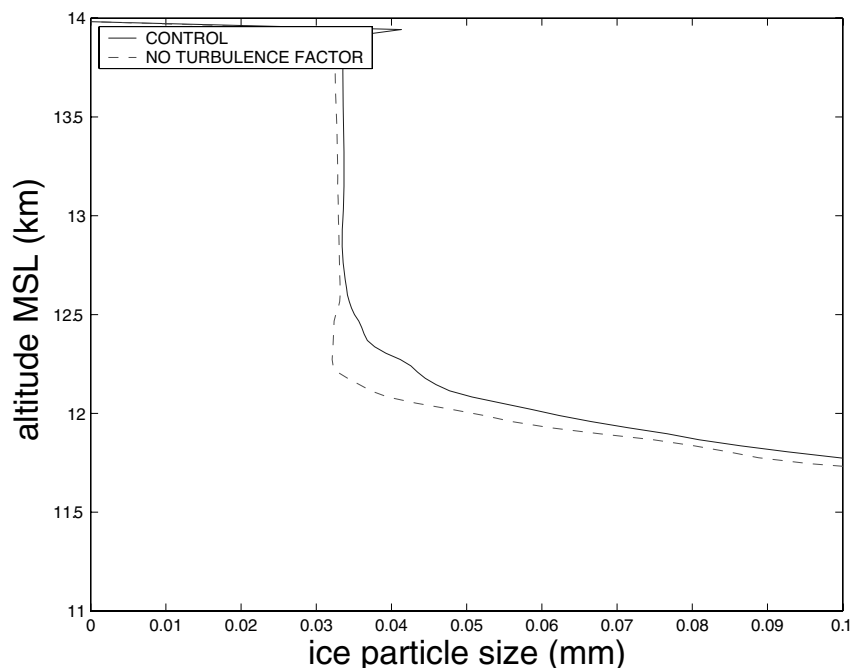


Figure 18. As Fig. 15 but for the mean ice diameter in the anvil.

Additionally, two further perturbation simulations were performed in which the difference between the turbulent enhancement factor and unity for coalescence was doubled and halved, respectively (not shown). Every doubling of this difference represents, qualitatively, the effect of increasing the turbulent dissipation rate by a few hundred percent. The altitude of warm-rain production was found to decrease steadily with increasing turbulent enhancement, and also to intensify, as expected, between the zero-turbulence case, these two extra runs and the control. This was found to reduce steadily the supercooled-droplet concentration, reducing the anvil ice concentration. However, the H-M process was only altered in a major fashion by the total removal of turbulent enhancement from the control.

(e) *No raindrop freezing*

A run was performed with heterogeneous and collisional raindrop freezing removed (the no-raindrop-freezing case). The freezing of cloud droplets and aerosols was the same as in the control run.

In the anvil, the ice concentration was found to be about 30% higher in the no-raindrop-freezing case relative to the control because of a similar fractional increase in the average droplet concentration in the mixed-phase region. The average ice diameter was lower by about 15%, while anvil crystals were less columnar (AR lower by about 0.5) and less dense by about 50 kg m^{-3} . The changes in crystal properties are qualitatively similar to those found when the warm-rain process was excluded (see subsection 4(c)). In the mixed-phase region, the number concentration of graupel particles is reduced by about two orders of magnitude, reflecting the fact that in the control run raindrop freezing, rather than the riming of primary crystals, is the main source of graupel.

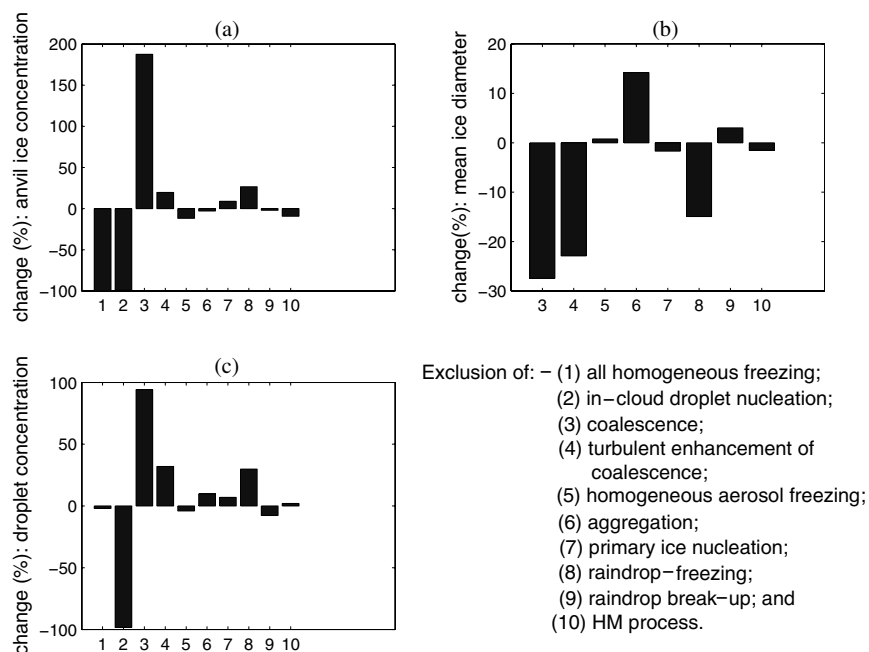


Figure 19. Percentage changes in the interior of the cloudy updraught for the ten nucleation processes studied here (see key): (a) of ice concentration in the anvil updraught, (b) of the mean diameter of ice particles in the anvil updraught; and (c) of supercooled droplet concentration changes in the 1 km layer below the anvil. The fractional changes in mean ice diameter for homogeneous freezing and in-cloud-droplet nucleation (not plotted) are about 600% and 900% respectively. HM refers to the Hallett and Mossop (1974) process of ice multiplication. See text for further details.

In summary: the higher cross-sectional area of frozen raindrops in the control run more effectively depletes droplets than in the no-raindrop-freezing case (see Johnson 1987). This means that the droplet concentration is higher in the raindrop-freezing case, with concomitant changes in the concentration and properties of anvil crystals.

(f) *Intercomparison of all nucleation processes*

The histograms in Fig. 19 show the average percentage changes in concentration and mean diameter of anvil ice particles, and in supercooled-droplet concentration below the anvil base, when ten particular processes (given in the key) are individually excluded from the model relative to the control simulation. Naturally, the greatest direct impact on the anvil ice concentration is from homogeneous freezing (test 1). Indirect modifications of the anvil glaciation are caused by processes associated with the nucleation of new ice particles in the mixed-phase region, such as collisional and heterogeneous raindrop-freezing (test 8) and primary nucleation of crystals (test 7). When such non-homogeneous nucleation processes are excluded, there is usually an increase in the concentration of droplets reaching the anvil base. This is because frozen precipitation particles are much more effective at accreting cloud water than are liquid particles of the same mass (see Johnson 1987). However, by far the greatest indirect impact on the anvil glaciation is from the warm-rain process (test 3). The warm-rain process exerts a massive impact on the anvil ice concentration, because it accounts for most of the mass of both liquid and frozen precipitation generated in the control simulation. Hence, the warm-rain process causes the depletion of most of the cloud

water in the mixed-phase region. For this reason, turbulent enhancement of coalescence produces a modification of the anvil glaciation that is comparable to, or exceeds, the indirect impacts from (non-homogeneous) ice nucleation processes in the mixed-phase region.

In-cloud droplet nucleation (test 2) produces a major impact on the anvil ice concentration. It is the source of about 99% of the number of supercooled droplets reaching the anvil base in the control simulation. Since homogeneous freezing of such droplets accounts for about 99.9% of the anvil crystals (see test 1), most of the anvil ice crystals in the control simulation must be caused by secondary droplet nucleation (see subsection 4(b)). When environmental aerosols above 5 km AMSL are neglected in a further sensitivity test with the EMM, the average concentration of supercooled droplets just below the anvil base in the updraught is reduced by about two-thirds, relative to the control.

Processes making minor contributions to the anvil ice concentration include aggregation, the H-M process, raindrop break-up and homogeneous aerosol freezing. Aggregation appears to require much longer time-scales for the production of precipitation in a deep convective cumulus cloud compared to coalescence. Homogeneous freezing of aerosols is not very significant when compared with that of cloud water, because secondary droplet nucleation usually maintains a sufficiently high concentration of droplets and anvil ice particles for the saturation ratio almost never to reach the threshold for homogeneous aerosol freezing. Some of these four nucleation processes, of limited significance for the anvil, cause appreciable modifications of the cloud-water field in the interior of the mixed-phase region. Finally, no appreciable sensitivity was found when the temperature cut-off for heterogeneous droplet freezing was changed from -30 to -60 °C.

Three extra sensitivity tests revealed that the anvil ice concentration was reduced by about 5–10% by the following exclusions: the explicit prediction of the graupel density (replaced by a constant value of 400 kg m^{-3}); the surface temperature of ice (fixed to the ambient air temperature); and the graupel drag coefficient (replaced by a formula from Beard (1980)). Significant perturbations of the total ice mixing ratio $> 10\%$ and of the droplet concentration were found in these extra runs. Clearly, explicit prediction of crystal properties with a particle-growth scheme is important for accuracy.

(g) *Intercomparison of turbulence effects*

Two simulations were performed with turbulent enhancement of raindrop-freezing and riming, respectively, prohibited. The anvil ice crystal concentration was quite similar to the control value, being altered by $< 10\%$. This alteration is a reduction because, although the supercooled-droplet concentration is increased by the order of 1–10% in the 1 km layer just below the anvil base, homogeneous aerosol freezing appears to be less prolific in these perturbation simulations than in the control. For prohibition of turbulent enhancement of the warm-rain process, corresponding alterations of the concentration of such supercooled droplets and anvil ice particles are $+30\%$ and $+20\%$ respectively. Clearly, the turbulent enhancement of the warm-rain process produces the dominant impact on the anvil glaciation out of all the various coagulation mechanisms.

Curiously, the mixed-phase region is very sensitive to the turbulent enhancement of riming. The H-M splinter concentration is reduced by an order of magnitude when the turbulent enhancement of riming is excluded. This coincides with a similar sensitivity of the mixing ratio of large graupel particles formed by raindrop freezing in the H-M region. It appears that turbulent enhancement of riming promotes the generation of the largest, millimetre-sized graupel particles that are able to fall against the updraught's

ascent into the H-M region. However, the anvil glaciation is not very sensitive to the activity of the H-M process, because most of the anvil ice particles originate from homogeneous freezing.

5. DISCUSSION AND CONCLUSIONS

We find that the vast majority of ice particles in the simulated Cb anvil originate as homogeneously frozen cloud droplets. The hypothesis proposed by Rosenfeld and Woodley (2000) of massive homogeneous droplet freezing at the anvil base is confirmed by this result. In very broad terms, it is also consistent with the parcel model calculations by Spice *et al.* (1999). This result is not globally applicable for absolutely all Cb, since IN concentrations can sometimes be so numerous in particular dusty episodes that most of the cloud-water freezes heterogeneously, or evaporates before it can freeze homogeneously. For instance, in CRYSTAL-FACE the concentration of IN was measured to be $O(1) \text{ cm}^{-3}$ during occasional Saharan dust events (DeMott *et al.* 2003), which is an increase by a factor of at least 100 beyond the control values.

Nearly all freezing droplets were created by secondary, rather than primary droplet nucleation in the model. This occurred because: (i) primary droplets from the cloud base tend to be depleted by accretion onto precipitation before reaching the anvil base; and (ii) droplet depletion aloft, in conjunction with the rapid increase with height of the vertical velocity in the updraught, combine to boost substantially the supersaturation above the freezing level. Pinsky and Khain (2002) found that the consequent nucleation of secondary droplets accelerated raindrop formation by broadening the droplet size distribution, a result duplicated here. When secondary droplet nucleation is excluded from the EMM, the amount of rain in the mixed-phase region is suppressed.

About two-thirds of the secondary droplets reaching the anvil base are formed by the activation of aerosols that have been entrained into the updraught from the lateral environment above about 5 km AMSL in the model (see also Fridlind *et al.* 2004). Consequently, very remote surface sources of atmospheric aerosol would be expected to produce an appreciable impact on anvil and cirrus glaciation. Naturally, this result depends critically on the specification of the rate of entrainment derived from the 3-D cloud model utilized by Fridlind *et al.*

Among the remaining nucleation processes, the warm-rain process produces the greatest indirect impact on the anvil ice concentration. The warm-rain process is central to the regulation of the concentration of supercooled droplets in the mixed-phase region, which determines the anvil ice concentration. This is because coalescence is the source of almost all of the mass of precipitation, whether frozen or liquid. Precipitation acts to deplete a large fraction of the cloud droplets by accretion before they can freeze homogeneously. In the mixed-phase region, the total ice mixing ratio is dominated by raindrop freezing. Without the warm-rain process, there is no H-M process in this model cloud. The explicitly predicted ice particle properties, such as axial ratio and bulk density, are also highly sensitive to the coalescence process in the mixed-phase region. The activity of the H-M process in the control, despite the peak updraught speed being $>20 \text{ m s}^{-1}$ aloft, is consistent with 3-D numerical simulations of deep convection with bulk microphysics by Aleksic *et al.* (1989; see also Ovtchinnikov *et al.* 2000).

A striking result here is that turbulent enhancement of the collision efficiency for coalescence must be accounted for if the anvil ice concentration is to be accurately predicted. Physically, this mechanism represents the modification of the relative velocities of drops of different sizes due to their inertia (see Khain and Pinsky 1995). The velocity

difference, due to turbulence, of a pair of small adjacent droplets may be comparable with their difference in terminal fall velocities. In EMM simulations presented here, it is shown that turbulent enhancement of coalescence has a greater indirect impact on the anvil glaciation than most of the (non-homogeneous) ice nucleation processes that are active in the mixed-phase region for this particular model cloud. Our simulations corroborate the result of Pinsky and Khain (2002), that the rain production rate is quite sensitive to turbulent effects. Their result is extended in this paper to cover the sensitivity of the anvil glaciation to turbulent effects. (Although giant and ultra-giant aerosol particles are not represented in the EMM here, Feingold *et al.* (1999) found that in stratocumulus clouds such giant aerosol particles tend to modify rain production appreciably only in clouds near their threshold of rain production—Cb are very far from such a threshold.)

Furthermore, it is shown that warm-rain production decreases in altitude and intensifies steadily with an increasing degree of turbulent enhancement of the warm-rain process. This steadily reduces the supercooled droplet concentration, reducing the anvil ice concentration. It can also radically alter the H-M process. It is the turbulent enhancement of the warm-rain process, rather than that of riming or raindrop freezing, that affects the anvil the most.

The present paper shows that aggregation and homogeneous aerosol freezing are not particularly important for glaciation in the updraught region of the Cb anvil in this particular model cloud, when compared with coalescence and homogeneous freezing of cloud water. Reisin *et al.* (1996) also found that aggregation is not important in deep convective clouds, partly because of low values of the sticking efficiency. The lack of homogeneous aerosol freezing in the EMM control is consistent with estimates by Knollenberg *et al.* (1993); our hydrometeor concentrations were above the low values of a few per cubic centimetre, or less than they found necessary near the anvil base for homogeneous aerosol freezing to occur in the updraught. This estimate may also be reached by scaling the analytical formula for the equilibrium supersaturation of a monodisperse population of spherical ice particles growing only by vapour deposition. That such low values are only very rarely reached in the EMM control simulation is partly because of the activity of secondary-droplet nucleation below the anvil base, and partly due to the continental nature of the environmental CN spectrum applied here.

Generally, homogeneous aerosol freezing is obviously shut down by updraught speeds being too weak (e.g. in cirrus; see Heymsfield and Sabin (1989)) because ascent is needed to force a positive supersaturation with respect to ice. But the EMM simulations here show that homogeneous aerosol freezing can also be shut down if the updraught speed is too high, due to droplet concentrations being too high below the anvil base. Another reason why homogeneous aerosol freezing is rare in this particular model Cb updraught, is that whenever the saturation ratio exceeds the critical threshold for homogeneous aerosol freezing, the largest few aerosols freeze first to form crystals. These crystals then deplete the vapour before more aerosols can freeze, reducing the saturation ratio (see Jensen *et al.* 1998). However, in the wider context it seems plausible that once the cirrus has become detached from the convective core, the slow decline in crystal concentration could conceivably allow episodes of homogeneous aerosol freezing to occur over much longer time-scales than those simulated here.

Secondary droplet nucleation in the Cb updraught would be expected to quench some of the sensitivity of the anvil glaciation, which may explain why several processes of nucleation are found to display only a weak sensitivity here. This is because any reduction in the supercooled droplet concentration will also tend to augment the equilibrium supersaturation in updraught parcels, causing extra nucleation of secondary droplets.

Of course, the present results apply only to the particular cloud simulated in this paper, which corresponds to the moderately continental CCN concentration observed in the environment on 18 July 2002 of CRYSTAL-FACE. Updraughts with a weaker rate of increase with height of the vertical air velocity than that prescribed for this case, would force a lower supersaturation below the anvil. This would probably reduce the extent of secondary droplet nucleation. Moreover, the present analysis assumes processes of ice nucleation are known and properly quantified. In fact, there is still controversy about what the full set of mechanisms are for secondary ice formation, especially with ice break-up.

In summary: this paper demonstrates a significant sensitivity of the ice microphysics with respect to the inclusion of turbulence enhancement factors in coalescence. There is clearly a need for continued laboratory studies and theoretical research to quantify such factors. Furthermore, certain nucleation processes, such as raindrop freezing and the warm-rain process, need to be accurately represented if the anvil ice properties of deep convection are to be correctly predicted in cloud models.

ACKNOWLEDGEMENTS

This project has been supported by the National Aeronautics and Space Administration (NASA; NAG5-12056) as part of the CRYSTAL-FACE campaign. The first author was supported by Princeton University's AOS Program. The authors gratefully acknowledge Ann Fridlind and colleagues at NASA (Ames) who provided the tracer profiles used in setting up the EMM. The first author is grateful to Ruei-Fong Lin, Sonia Lasher-Trapp, Bjorn Stevens and Graham Feingold for illuminating discussions, and to Professor Alexander Khain for allowing some HUCM data to be used in the EMM.

REFERENCES

- | | | |
|---|------|--|
| Aleksic, N. M., Farley, R. D. and Orville, H. D. | 1989 | A numerical cloud model study of the Hallett–Mossop ice multiplication process in strong convection. <i>Atmos. Res.</i> , 23 , 1–30 |
| Beard, K. V. | 1980 | The effects of altitude and electrical force on the terminal velocity of hydrometeors. <i>J. Atmos. Sci.</i> , 37 , 1363–1374 |
| Bleck, R. | 1970 | A fast, approximate method for integrating the stochastic coalescence equation. <i>J. Geophys. Res.</i> , 75 , 5165 |
| Blyth, A. M. and Latham, J. | 1997 | A multi-thermal model of cumulus glaciation via the Hallett–Mossop process. <i>Q. J. R. Meteorol. Soc.</i> , 123 , 1185–1198 |
| Bott, A. | 1998 | A numerical method for the numerical solution of the stochastic collection equation. <i>J. Atmos. Sci.</i> , 55 , 2284–2293 |
| Brown, P. R. A. and Heymsfield, A. J. | 2001 | The microphysical properties of tropical convective anvil cirrus: A comparison of models and observation. <i>Q. J. R. Meteorol. Soc.</i> , 127 , 1535–1550 |
| DeMott, P. J., Rogers, D. C. and Kreidenweiss, S. M. | 1997 | The susceptibility of ice formation in upper tropospheric clouds to insoluble aerosol components. <i>J. Geophys. Res.</i> , 102 , 19575–19584 |
| DeMott, P. J., Sassen, K., Poellot, M. R., Baumgardner, D., Rogers, D. C., Brooks, S. D., Prenni, A. J. and Kreidenweiss, S. M. | 2003 | African dust aerosols as atmospheric ice nuclei. <i>Geophys. Res. Lett.</i> , 30 , 14, 1732, doi: 10.1029/2003GL017410 |
| Feingold, G., Cotton, W. R., Kreidenweiss, S. M. and Davis, J. T. | 1999 | The impact of giant cloud condensation nuclei on drizzle formation in stratocumulus: Implications for cloud radiative properties. <i>J. Atmos. Sci.</i> , 56 , 4100–4117 |

- Fridlind, A. M., Ackerman, A. S., Jensen, E. J., Heymsfield, A. J., Poellot, M. R., Stevens, D. E., Wang, D., Miloshevich, L. M., Baumgardner, D., Lawson, R. P., Wilson, J. C., Flagan, R. C., Seinfeld, J. H., Jonsson, H. H., Vanreken, T. M., Varutbangkul, V. and Rissman, T. A. 2004 Evidence for the predominance of mid-tropospheric aerosols as subtropical anvil cloud nuclei. *Science*, **304**, 718–722
- Hall, W. D. 1980 A detailed microphysical model within a two-dimensional dynamical framework: Model description and preliminary results. *J. Atmos. Sci.*, **37**, 2486–2507
- Hallett, J. and Mossop, S. C. 1974 Production of secondary ice particles during the riming process. *Nature*, **249**, 26–28
- Heymsfield, A. J. and Miloshevich, L. M. 1993 Homogeneous ice nucleation and supercooled liquid water in orographic wave clouds. *J. Atmos. Sci.*, **50**, 2335–2353
- 1995 Relative humidity and temperature influences on cirrus formation and evolution: Observations from wave clouds and FIRE II. *J. Atmos. Sci.*, **52**, 4302–4326
- Heymsfield, A. J. and Sabin, R. M. 1989 Cirrus crystal nucleation by homogeneous freezing of solution droplets. *J. Atmos. Sci.*, **46**, 2252–2264
- Heymsfield, A. J., Johnson, P. N. and Dye, J. E. 1978 Observations of moist adiabatic ascent in northeast Colorado cumulus congestus clouds. *J. Atmos. Sci.*, **35**, 1689–1703
- Jensen, E. J., Anderson, D. E., Selkirk, H. B., Starr, D. O. and Toon, O. B. 2004 Overview of the Cirrus Regional Study of Tropical Anvils and Cirrus Layers—Florida Area Cirrus Experiment (CRYSTAL-FACE). *Bull. Am. Meteorol. Soc.*, in press
- Jensen E. C., Toon, O. B., Sachse, G. W., Anderson, B. E., Chan, K. R., Twohy, C. W., Gandrud, B., Aulenbach, S. M., Heymsfield, A., Hallett, J. and Gary, B. 1998 Ice nucleation processes in upper tropospheric wave-clouds observed during SUCCESS. *Geophys. Res. Lett.*, **25**, 1363–1366
- Johnson, D. B. 1987 On the relative efficiency of coalescence and riming. *J. Atmos. Sci.*, **44**, 1671–1680
- Jonas, P. R. 1996 Turbulence and cloud microphysics. *Atmos. Res.*, **40**, 283–306
- Khain, A. P. and Pinsky, M. B. 1995 Drops' inertia and its contribution to turbulent coalescence in convective clouds. Part I: Drops' fall in the flow with random horizontal velocity. *J. Atmos. Sci.*, **52**, 196–206
- Khain, A. P. and Sednev, I. 1996 Simulation of precipitation formation in the Eastern Mediterranean coastal zone using a spectral microphysics cloud ensemble model. *Atmos. Res.*, **43**, 77–110
- Khain, A. P., Ovtchinnikov, M., Pinsky, M., Pokrovsky, A. and Krugliak, H. 2000 Notes on the state-of-the-art numerical modeling of cloud microphysics. *Atmos. Res.*, **55**, 159–224
- Khain, A., Pokrovsky, A., Pinsky, M., Seifert, A. and Phillips, V. T. J. 2004 Simulation of effects of atmospheric aerosols on deep turbulent convective clouds by using a spectral microphysics mixed-phase cumulus cloud model. Part I: Model description and possible applications. *J. Atmos. Sci.*, **61**, 2963–2982
- Knollenberg, R. G., Kelly, K. and Wilson, J. C. 1993 Measurements of high number densities of ice crystals in the tops of tropical cumulonimbus. *J. Geophys. Res.*, **98**, 8639
- Koop, T., Luo, B. P., Tsias, A. and Peter, Th. 2000 Water activity as the determinant for homogeneous ice nucleation in aqueous solutions. *Nature*, **406**, 611–614
- Levine, J. 1959 Spherical vortex theory of bubble-like motion in cumulus clouds. *J. Meteorol.*, **14**, 653–662
- Lew, J. K. and Pruppacher, H. R. 1983 A theoretical determination of the capture efficiency of small columnar ice crystals by large cloud drops. *J. Atmos. Sci.*, **40**, 139–145
- Lew, J. K., Kingsmill, D. E. and Montague, D. C. 1985 A theoretical study of the collision efficiency of small planar ice crystals colliding with large supercooled water drops. *J. Atmos. Sci.*, **42**, 857–862
- Meyers, M. P., DeMott, P. J. and Cotton, W. R. 1992 New primary ice-nucleation parametrizations in an explicit cloud model. *J. Appl. Meteorol.*, **31**, 708–720

2046

V. T. J. PHILLIPS *et al.*

- Mitchell, D. 1988 Evolution of snow-size spectra in cyclonic storms. Part I: Snow growth by vapour deposition and aggregation. *J. Atmos. Sci.*, **45**, 3431–3451
- Ovtchinnikov, M., Kogan, Y. L. and Blyth, A. M. 2000 An investigation of ice production in small cumuliform clouds using a 3D model with explicit microphysics. Part II: Case study of New Mexico cumulus clouds. *J. Atmos. Sci.*, **57**, 3004–3020
- Phillips, V. T. J. 2001 ‘Simulations of the glaciation of a New Mexican storm cloud with an explicit microphysics model (EMM)’. PhD Thesis, UMIST
- Phillips, V. T. J., Blyth, A. M., Brown, P. R. A., Choullarton, T. W. and Latham, J. 2001 The glaciation of a cumulus cloud over New Mexico. *Q. J. R. Meteorol. Soc.*, **127**, 1513–1534
- Phillips, V. T. J., Choullarton, T. W., Blyth, A. M. and Latham, J. 2002 The influence of aerosol concentrations on the glaciation and precipitation of a cumulus cloud. *Q. J. R. Meteorol. Soc.*, **128**, 951–971
- Phillips, V. T. J., Choullarton, T. W., Illingworth, A. J., Hogan, R. J. and Field, P. R. 2003 Simulations of the glaciation of a frontal mixed-phase cloud with the Explicit Microphysics Model. *Q. J. R. Meteorol. Soc.*, **129**, 1351–1371
- Pinsky, M. B. and Khain, A. 1998 Some effects of cloud turbulence on water–ice and ice–ice collisions. *Atmos. Res.*, **47–48**, 69–86
- 2002 Effects of in-cloud nucleation and turbulence on droplet spectrum formation in cumulus clouds. *Q. J. R. Meteorol. Soc.*, **128**, 501–533
- Pinsky, M. B., Khain, A. P. and Shapiro, M. 2000 Stochastic effects of cloud droplet hydrodynamic interaction in a turbulent flow. *Atmos. Res.*, **53**, 131–169
- Pruppacher, H. R. and Klett, J. D. 1997 *Microphysics of clouds and precipitation*. Kluwer Academic Publishers, Dordrecht, the Netherlands
- Ramanathan, V., Pitcher, E. J., Malone, R. C. and Blackmon, M. L. 1983 The response of a spectral general circulation model to refinements in radiative processes. *J. Atmos. Sci.*, **40**, 605–630
- Rasmussen, R. M. and Heymsfield, A. J. 1987 Melting and shedding of graupel and hail. I: Model physics. *J. Atmos. Sci.*, **44**, 2754–2763
- Reisin, T., Levin, Z. and Tzivion, S. 1996 Rain production in convective clouds as simulated in an axisymmetric model with detailed microphysics. Part II: Effects of varying drops and ice initiation. *J. Atmos. Sci.*, **53**, 1815–1837
- Rogers, R. R. and Yau, M. K. 1991 *A short course in cloud physics*. Pergamon Press, New York, USA
- Rosenfeld, D. and Woodley, W. L. 2000 Deep convective clouds with sustained supercooled liquid water down to -37.5°C . *Nature*, **405**, 440–442
- Saunders, C. P. R. and Hosseini, A. S. 2000 ‘A laboratory study of the effect of velocity on Hallett–Mossop ice crystal multiplication’. Pp. 617–620 in Proceedings of the thirteenth international conference on clouds and precipitation, Reno, Nevada. American Meteorological Society, Boston, USA
- Sherwood, S. C., Minnis, P. and McGill, M. 2004 Deep convective cloud-top heights and their thermodynamic control during CRYSTAL-FACE. *J. Geophys. Res.*, **109**, D20119, doi: 10.1029/2004JD004811
- Smith, S. A. and Jonas, P. R. 1996 Observations of turbulence in cirrus clouds. *Atmos. Res.*, **43**, 1–29
- Spice, A., Johnson, D. W., Brown, P. R. A., Darlinton, A. G. and Saunders, C. P. R. 1999 Heterogeneous droplet freezing in orographic cirrus clouds: A numerical simulation of the microphysics. *Q. J. R. Meteorol. Soc.*, **125**, 1637–1667
- Stevens, B., Cotton, W. R. and Feingold, G. 1998 A critique of one- and two-dimensional models of boundary layer clouds with a binned representation of drop microphysics. *Atmos. Res.*, **47–48**, 529–553
- VanReken, T. M., Rissman, T. A., Roberts, G. C., Varutbangkul, V., Jonsson, H. H., Flagan, R. C. and Seinfeld, J. H. 2003 Toward aerosol/cloud condensation nuclei (CCN) closure during CRYSTAL-FACE. *J. Geophys. Res.*, **108**(D20), 4633

Appendix I

EVIDENCE FOR THE PREDOMINANCE OF MID-TROPOSPHERIC AEROSOLS
AS SUBTROPICAL ANVIL CLOUD NUCLEI*

*Full Citation: Fridlind, A. M., A. S. Ackerman, E. J. Jensen, A. J. Heymsfield, M. R. Poellot, D. E. Stevens, D. Wang, L. M. Miloshevich, D. Baumgardner, R. P. Lawson, J. C. Wilson, R. C. Flagan, J. H. Seinfeld, H. H. Jonsson, T. M. VanReken, V. Varutbangkul, T. A. Rissman (2004), *Science*, 304(5671), 718 – 722.

© 2004 American Association for the Advancement of Science. This appendix is reprinted with permission from the American Association for the Advancement of Science.

REPORTS

27. R. Bessinger, P. Akwara, "Trends in Sexual and Fertility-Related Behavior: Cameroon, Kenya, Uganda, Zambia, and Thailand" (The Measure Evaluation Project, United States Agency for International Development, Washington, DC, 2003) (www.cpc.unc.edu/measure/publications/pdf/sr-03-21b.pdf).
28. "South African national HIV prevalence, behavioral risk, and mass media household survey," (Nelson Mandela Children's Fund and the Human Sciences Research Council, Capetown, South Africa, 2002).
29. L. McKusick, W. Horstman, T. Coates, *Am. J. Public Health* **75**, 493 (1985).
30. K. Witte, M. Allen, *Health Educ. Behav.* **27**, 608 (2000).
31. UNAIDS, "A measure of success in Uganda" (UNAIDS, Geneva, Switzerland, 1998).
32. UNAIDS, "Trends in HIV incidence and prevalence: natural course of the epidemic or results of behavior change?" (UNAIDS, Geneva, Switzerland, 1999).
33. E. Korenromp *et al.*, *AIDS* **16**, 2209 (2002).
34. R. Stoneburner, L. Lessner, J. Fordyce, P. Bevier, M. Chiasson, *Am. J. Epidemiol.* **138**, 1093 (1993).
35. A. J. Nunn *et al.*, *Br. Med. J.* **315**, 767 (1997).
36. Peter Mugenyi, personal communication.
37. Kamali *et al.*, *Lancet* **361**, 645 (2003).
38. R. Moodie *et al.*, "An evaluation study of Uganda's AIDS control programmes' information, education, and communication activities" (WHO/Uganda Ministry of Health, 1991).
39. G. Kwasigabo *et al.*, *J. Acquir. Immune Defic. Syndr.* **23**, 410 (2000).
40. R. L. Stoneburner, D. Low-Beer, *Int. J. Epidemiol.*, in press.
41. D. Tarantola, B. Schwartzlander, *AIDS* **11**, S5 (1997).
42. M. J. Wawer *et al.*, *AIDS* **11**, 1023 (1997).
43. R. Stoneburner, M. Carballo, R. Bernstein, T. Saidel, *AIDS* **12**, 226 (1998).
44. C. Rose, *The Strategy of Preventive Medicine* (Oxford Medical Publications, Oxford, 1992).
45. "ANC sentinel surveillance of HIV/Syphilis Trends in Zambia, 1994–2002" (Central Board of Health, Lusaka, Zambia, 2004).
46. The authors thank E. C. Green for insight, advice, and support and I. Katz for support in analysis. This

work was supported in part by funding from Family Health International contract no. HRN-5972-Q-00-4002-00 (1996–1997) and USAID grant no. Afr.-G-009770008-00 (1998–2000). The opinions expressed in this article are those of the authors and in no way reflect policy of the United States government, the United States Agency for International Development, or the University of Cambridge.

Supporting Online Material

www.sciencemag.org/cgi/content/full/304/5671/714

DC1

Materials and Methods

SOM Text

Figs. S1 and S2

Tables S1 to S4

References

31 October 2003; accepted 30 March 2004

Evidence for the Predominance of Mid-Tropospheric Aerosols as Subtropical Anvil Cloud Nuclei

Ann M. Fridlind,^{1*} Andrew S. Ackerman,¹ Eric J. Jensen,¹ Andrew J. Heymsfield,² Michael R. Poellot,³ David E. Stevens,⁴ Donghai Wang,⁵ Larry M. Miloshevich,² Darrel Baumgardner,⁶ R. Paul Lawson,⁷ James C. Wilson,⁸ Richard C. Flagan,⁹ John H. Seinfeld,⁹ Hafliði H. Jonsson,¹⁰ Timothy M. VanReken,⁹ Varuntida Varutbangkul,⁹ Tracey A. Rissman⁹

NASA's recent Cirrus Regional Study of Tropical Anvils and Cirrus Layers–Florida Area Cirrus Experiment focused on anvil cirrus clouds, an important but poorly understood element of our climate system. The data obtained included the first comprehensive measurements of aerosols and cloud particles throughout the atmospheric column during the evolution of multiple deep convective storm systems. Coupling these new measurements with detailed cloud simulations that resolve the size distributions of aerosols and cloud particles, we found several lines of evidence indicating that most anvil crystals form on mid-tropospheric rather than boundary-layer aerosols. This result defies conventional wisdom and suggests that distant pollution sources may have a greater effect on anvil clouds than do local sources.

It is well understood that cloud drops form on existing atmospheric aerosols, such as sulfuric acid particles and dust. Thus, changes in aerosol number can lead to changes in drop number during cloud formation. Complex subsequent effects on cloud microphysical development vary depending on cloud type and environmental conditions (1). The overall impact of increasing anthropogenic aerosols on low clouds such as stratocumulus may be great, generally resulting in smaller, more numerous drops and leading to brighter, longer-lived clouds that reflect more sunlight (2, 3). Because stratocumulus clouds persistently cover large global areas, it has been recognized that this aerosol-induced cooling effect partially offsets the warming effect of accumulating greenhouse gas concentrations (4).

Whereas low clouds such as stratocumulus alter the global solar radiative budget with little influence on the infrared budget, high clouds such as cirrus reduce both solar incoming and infrared outgoing radiative fluxes by comparable amounts. Whether the overall impact is warming or cooling depends in a sensitive manner on cloud optical depth and ice crystal effective radius (5), among other factors. Although cirrus clouds have a much lesser influence on the net radiative budget per unit area than stratocumulus, the area covered by tropical anvil clouds may respond strongly to increasing sea surface temperatures, thereby playing a major role in global climate sensitivity (6–8). However, the properties and evolution of anvil cirrus clouds remain poorly understood and weakly constrained in models (9). Recent observations also suggest that tropical cloud cov-

erage may be rapidly changing in a manner not captured by current general circulation model simulations (10), which serves as further motivation to seek a better understanding of anvil-forming cumulonimbus clouds.

The Cirrus Regional Study of Tropical Anvils and Cirrus Layers–Florida Area Cirrus Experiment (CRYSTAL-FACE) was coordinated by NASA with the primary goal of fully characterizing subtropical cumulonimbus anvil formation and evolution. The experiment took place throughout July 2002 over southern Florida, where simultaneous measurements were made from six aircraft and three ground stations, as well as satellite platforms, over the lifetimes of many storm systems. The data gathered included simultaneous measurements of the number and size distribution of aerosols and cloud particles throughout the full depth of developing cumulonimbus columns. Whereas a handful of previous modeling studies and data analyses have addressed the potential impact of boundary-layer aerosol loading on the microphysical properties of clouds associated with deep convection (11–14), here we incorporate these extensive new measurements into a detailed three-dimensional (3D) modeling analysis with appropriate vertical variation of the aerosol field.

¹National Aeronautics and Space Administration (NASA) Ames Research Center, Moffett Field, CA 94035, USA. ²National Center for Atmospheric Research, Boulder, CO 80307, USA. ³Department of Atmospheric Sciences, University of North Dakota, Grand Forks, ND 58202, USA. ⁴Lawrence Livermore National Laboratory, Livermore, CA 94552, USA. ⁵Center for Atmospheric Sciences, Hampton University and NASA Langley Research Center, Hampton, VA 23681, USA. ⁶Centro de Ciencias de la Atmosfera, Universidad Nacional Autónoma de México, México City, DF 04510, México. ⁷Stratton Park Engineering Company, Inc., Boulder, CO 80301, USA. ⁸Department of Engineering, University of Denver, Denver, CO 80208, USA. ⁹Division of Chemistry and Chemical Engineering, California Institute of Technology, Pasadena, CA 91125, USA. ¹⁰Center for Interdisciplinary Remotely-Piloted Aircraft Studies, Marina, CA 93933, USA.

*To whom correspondence should be addressed. E-mail: ann.fridlind@nasa.gov

REPORTS

An unexpected result of this study is our finding that the fundamental source of the nuclei on which most anvil crystals initially form is the mid-troposphere at 6 to 10 km rather than the planetary boundary layer near the Earth's surface (13). Several lines of evidence for this conclusion emanate from a case study of the highest strength updraft ($>20 \text{ m s}^{-1}$) that was penetrated directly by aircraft during the CRYSTAL-FACE campaign on 18 July. Because most cloud particles are formed in high-strength updraft cores, where supersaturations reach peak values (15), these measurements provide a unique window into the microphysical environment governing the injection of cloud particles into anvil cirrus clouds. Although CRYSTAL-FACE conditions did not include deep convection in the presence of heavy smoke or active fires (14), they were representative of subtropical continental deep convection.

On 18 July, the University of North Dakota Citation aircraft measured aerosols and cloud particles at 7 to 12 km along the developing sea breeze fronts and penetrated the high-strength updraft east of Lake Okeechobee at an altitude of about 10 km (Fig. 1). Meanwhile, the Center for Interdisciplinary Remotely-Piloted Aircraft Studies (CIRPAS) Twin Otter aircraft measured aerosols and cloud particles between the surface and 4 km over the southwest Florida peninsula. NASA's WB-57 aircraft, which generally measured aerosols and cloud particles at 12 to 16 km, did not operate on 18 July, but we were able to use WB-57 aerosol and cloud observations collected under similar conditions on other days to complement this case study. We thus incorporated observations from all three aircraft making in situ measurements during CRYSTAL-FACE (16).

To simulate the development of high-strength updrafts similar to the one observed, we used 3D large-eddy simulations with size-resolved microphysics (16–19). We initialized the model domain with a meteorological profile derived from local rawinsonde measurements (16) and an aerosol profile (Table 1) derived from aircraft measurements (16). Surface heat and moisture fluxes were assimilated from mesoscale weather model predictions for 18 July (16, 20) at the location of observed convection. The model transports aerosols, liquid drops, and ice particles, accounting for activation, condensational growth, evaporation, sedimentation, and melting (21); gravitational collection (21–23); spontaneous and collision-induced drop breakup (22, 24); homogeneous and heterogeneous freezing of aerosols and drops (21, 25); and Hallett-Mossop rime splintering (21). Simulations exhibited chaotic generation of mature high-strength updrafts throughout the last 2 hours of each 3-hour simulation. We then compared simulated cloud particle properties in updrafts of similar strength with measurements made in the updraft on 18 July and in typical thick anvil clouds on 21 July.

First comparing simulations with measurements made in the updraft core on 18 July, we found that it was necessary to include tropospheric aerosols above 6 km in order to accurately simulate the large number of cloud particles observed (Fig. 2). Aerosols below 2 km, which well exceeds the typical 1-km boundary-layer height, were insufficient to account for the

observed numbers of cloud particles. Aerosols below 6 km were also insufficient, but when all aerosols up to the updraft-penetration altitude of 10 km were included in the simulation, the number of cloud particles as a function of vertical wind speed closely matched the observations. Furthermore, in both simulations and measurements, peak particle numbers were not

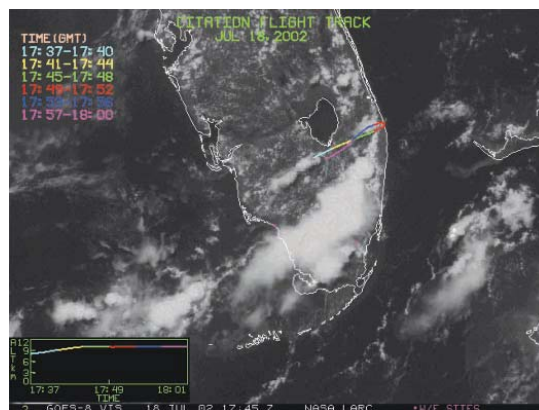


Fig. 1. Flight track of the Citation aircraft through the developing updraft core on 18 July, directly east of Lake Okeechobee. The experiment-wide peak updraft speed of about 23 m s^{-1} was measured at 17:49:10 UTC, 4 min after the underlying satellite image was taken. [Figure courtesy of Patrick Minnis and Louis Nguyen, NASA Langley Research Center]

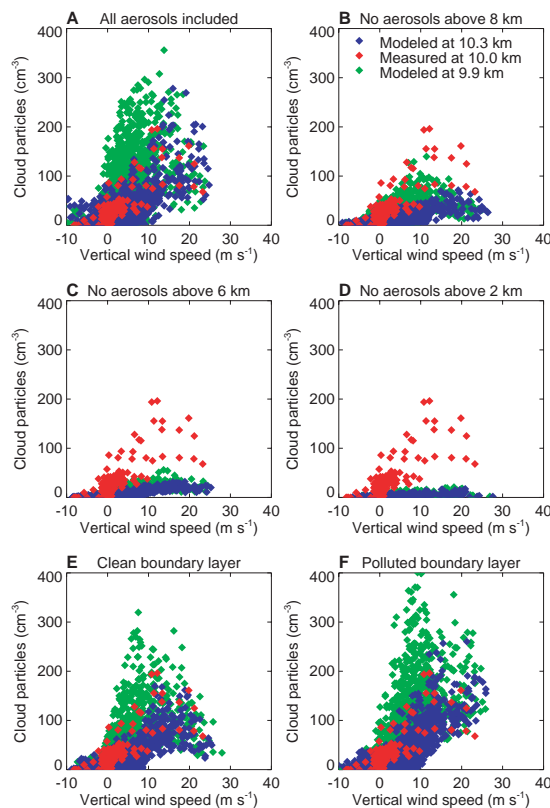


Fig. 2. Cloud particle number versus vertical wind speed measured near 10-km altitude in the updraft core (red) and simulated in the nearest layers above and below 10 km (blue and green, respectively) when simulated peak vertical wind speeds are similar to those observed. Model results show closest agreement with observations when all aerosols are included in the simulation (A). Agreement degrades when free tropospheric aerosols are excluded above 8 km (B), 6 km (C), and 2 km (D) and is less sensitive to replacing moderate aerosol concentrations of 1800 per cm^3 in the boundary layer with clean marine aerosols of 400 per cm^3 (E) or polluted aerosols of 6500 per cm^3 (F). See Table 1 for aerosol number size distribution parameters.

REPORTS

found at peak updraft speeds, where peak supersaturations are located, but instead were found at intermediate updraft speeds (Fig. 2A). This pattern, coupled with the importance of entrained mid-tropospheric aerosols to reproducing the observed cloud particle number concentrations, suggests that the highest particle numbers are found in an entraining region of the updraft core. In the entrainment region, turbulent mixing laterally brings in mid-tropospheric aerosols, which are exposed to higher supersaturations, activated, and then carried aloft.

A second line of evidence derives from a closer examination of the measured variation of cloud particle size distribution during the updraft traversal, which was flown horizontally from downwind to upwind. When we chose a similar path through a simulated updraft core and compared it with these measurements, both measurements and simulation results showed

Table 1. Aerosol profile number and log-normal size distribution parameters.

Elevation (km)	Number (cm ⁻³)	Mode diameter (μm)	Standard deviation
<i>Baseline</i>			
15*	100	0.025	1.6
10†	3000	0.025	1.6
5‡	1200	0.025	1.6
2§	1200	0.05	2.5
<1	1800	0.11	1.9
<i>Clean</i>			
<1¶	400		
	275	0.035	1.5
	125	0.11	1.4
<i>Polluted</i>			
<1#	6500		
	3000	0.03	1.5
	3500	0.12	1.8

*Because no WB-57 aircraft measurements are available for 18 July, typical number and size distribution parameters for the uppermost troposphere are derived from measurements made on 19 July. †The number concentration of aerosols at 10 km is set to the number measured by the Citation aircraft upon entering the updraft-containing cloud. Because no size distribution measurements are available for the Citation, typical size distribution parameters measured by the WB-57 on 19 July are assumed. ‡The number concentration of aerosols at 5 km is set to the typical number measured by the Citation on 18 July at that elevation. §The number concentration of aerosols at 2 km is set to the typical number measured by both Citation and Twin Otter aircraft on 18 July at that elevation. Size distribution parameters are derived from Twin Otter measurements made in the vicinity of that number concentration and elevation on 18 July. ||All 18 July Twin Otter measurements were made over the southwest peninsula, downwind of continental and pollution sources, whereas the high-strength updraft formed at the east coast in onshore winds. Baseline number concentration and size distribution are therefore derived from the cleanest boundary-layer aerosols sampled by the Twin Otter on 18 July. ¶Clean sensitivity test parameters were derived from Twin Otter measurements of marine boundary-layer aerosols sampled on 25 July, which were markedly bimodal and are therefore represented as the sum of the two modes listed. No such clean conditions were encountered on 18 July. #Polluted sensitivity test parameters were derived from measurements of boundary-layer aerosols sampled on 18 July, which were also strongly bimodal.

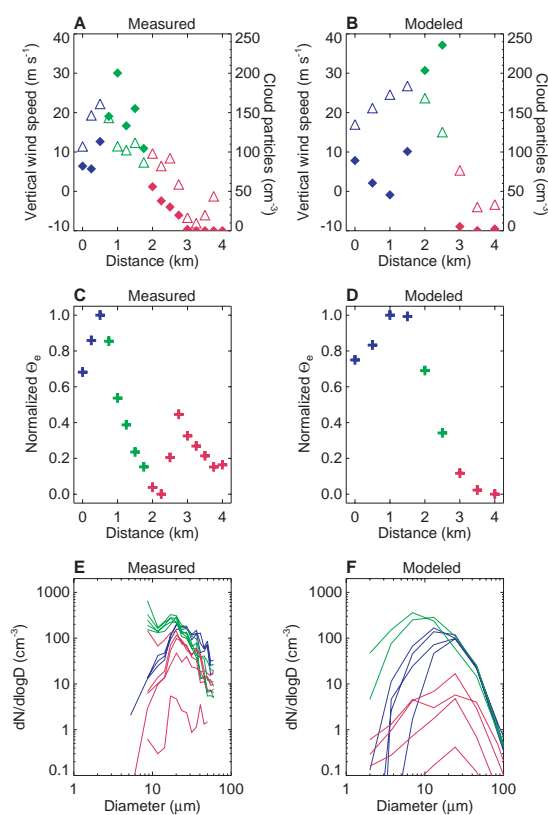
that the peak number was reached upwind of the peak vertical wind speed as the core was traversed (Fig. 3, A and B). This region in which particle numbers reached their peak values was also characterized by a mixture of source air (Fig. 3, C and D), indicative of substantial entrainment. In both simulations and observations, we also found that the additional cloud particles in this upwind entraining region were much smaller than those in the heart of the core (Fig. 3, E and F), which is the pattern that would be expected in the case of activation on recently entrained free tropospheric aerosols.

Finally, we considered whether simulated cloud particle number and size matched observations in the upper anvil cloud, where high-strength updraft cores detrain. Although the upper-level anvil cloud was not sampled on 18 July, anvil clouds from similar small cumulonimbus systems were sampled on 11, 16, 19, 21, and 28 July. Using observations in a typical thick anvil cloud between 12 and 14 km on 21 July as an example (other days appeared similar), we found that the measurements consistently indicated peak crystal number concentrations in the diameter range of 20 to 30 μm. Model simulations on 18 July

reproduced this peak accurately and consistently when aerosols were included throughout the atmospheric column, but the peak shifted to 50 to 60 μm when aerosols above 6 km were excluded, and it shifted to even larger sizes when aerosols above 2 km were excluded (Fig. 4). These comparisons in the upper-level anvil clouds support our analysis of the updraft measurements, providing a third line of evidence for the importance of mid-tropospheric aerosols. Because peak size was negligibly affected when aerosols above 10 km were excluded, those did not appear to be an important source of anvil nuclei. We estimate that the aerosols entrained between 6 and 10 km account for about two-thirds of the anvil nuclei (Fig. 4, compare B to D). We obtained similar results in simulations of convective events on other days during CRYSTAL-FACE, despite varying updraft strength and thermodynamic conditions.

It is initially surprising to find that mid-tropospheric aerosols determine fundamental anvil properties, because deep convection updraft cores are generally assumed to be relatively undiluted parcels that travel from cloud base to cloud anvil with little entrainment

Fig. 3. Comparison of 2-s average measurements across the updraft (A) with results along a 4-km path through an updraft of similar strength in the baseline simulation (B). Updraft strength (triangles) and cloud particle number concentration (diamonds) are denoted by color in three regions: downwind in the core (blue), within the entrainment region (green), and upwind of the core (red). Equivalent potential temperatures, θ_e , normalized by their respective measured and simulated ranges, demonstrate that the green points occupy an entrainment region of both the measured updraft (C) and the simulated updraft (D). Cloud particle size distributions, $dN/d\log D$, show that the entrainment region is characterized by increased numbers of the smallest particles in both measurements (E) and simulation results (F). The simulated core is generally wider and more uniform than the observed core at least in part because of limitations on model resolution (16).



REPORTS

(13). However, this assumption has recently been challenged by Zipser (26), who makes a distinction between relatively undiluted, high velocity, mid-latitude supercell updrafts and highly diluted, lower velocity, tropical marine updrafts. The updrafts observed during CRYSTAL-FACE appear to lie along this continuum, with intermediate vertical wind speed and dilution. Analysis of laboratory thermals indicates that entrainment scales inversely with updraft diameter (15), and when the toroidal rotation of rising updrafts is considered, also provides the rule of thumb that an updraft is turned "inside out" once over a vertical distance of about 1.5 diameters (27). Whereas the updraft cores of mid-latitude supercells may be 18 km in diameter (28), corresponding to less than a full toroidal rotation during ascent to the tropopause, the Florida updraft observed on 18 July exhibited an updraft diameter of less than 5 km, corresponding to about two such rotations. These order-of-magnitude estimates support the role of mid-tropospheric entrainment.

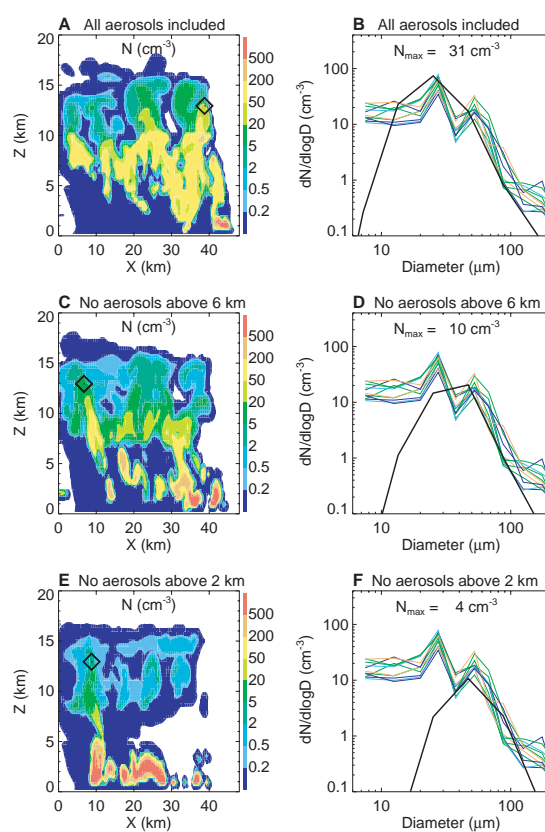
There are important implications of our finding that anvil crystal number and size are determined by the entrainment of mid-

tropospheric aerosols. Crystal size itself is a leading factor controlling cirrus radiative properties, with smaller crystals corresponding to higher cloud albedo (5). Owing to the apparently widespread presence of small anvil crystals in recent measurements, Garrett *et al.* (29) argue that there may be a need for substantial corrections to parameterizations of cirrus clouds in global climate models. It has also been suggested that the size of anvil ice crystals may control relative humidity near the tropopause and, by extension, moisture transport into the lower stratosphere (30, 31). By attributing anvil crystal formation to entrained mid-tropospheric aerosols (Fig. 4), we also provide a new explanation for the generation of copious small crystals that have been reported at anvil tops (32). The source of such crystals has been a puzzle, and they have been previously attributed to aerosol activation either at the cloud top (32) or at the cloud base (11).

Further implications hinge on our corollary finding that extreme variations in boundary-layer aerosol concentrations, from polluted to clean conditions, influence anvil properties less than do mid-tropospheric

aerosol concentrations (Fig. 2, E and F). Thus, the documented long-range transport of pollution in the middle and upper troposphere (33) may notably affect cirrus radiative properties, evolution, and lifetime. However, the details of such effects are not obvious. Recent surveys of aerosol number and size derived from multiple field experiments over tropical and subtropical regions demonstrate that there are often more than twice as many aerosols present in clean mid-tropospheric air at 6 to 10 km than in polluted air (34) and that the aerosol number at 8 to 12 km is highest when the atmosphere is devoid of nonvolatile pollution aerosols (35). Thus, pollution and aerosol number, which are closely correlated in the boundary layer, are frequently anticorrelated in the upper troposphere, perhaps owing to the scavenging of aerosol nucleation precursor gases by existing pollution aerosol surface area (35). It is thus possible that more polluted environments would yield fewer, larger anvil crystals than cleaner environments, in direct contrast to the aforementioned case of marine stratocumulus, wherein polluted environments yield more, smaller cloud particles. Because supersaturations may reach high values in cumulonimbus updrafts (22) and aerosol activation is therefore sensitive to cloud dynamics, a detailed analysis of aerosol size distributions and geographic variations in cloud dynamics is required to establish the overall effect of pollution on anvil cirrus clouds. Our analysis nonetheless indicates that long-range transport of pollution can dominate the effect of local sources on subtropical anvil clouds.

Fig. 4. A cross section (horizontal distance, X , versus elevation, Z) of simulated cloud particle number concentration, N , with a black diamond at the 13-km location of highest predicted number (A) and the ice crystal size distributions, $dN/d\log D$ (B), simulated at that location (black line) and measured at 12 to 14 km on 21 July (colored lines). Simulated peak diameters closely match measured peak diameters at 20 to 30 μm when all aerosols are included [(A) and (B)] but shift to larger sizes, exhibiting successively poorer agreement with the measurements, when aerosols are excluded above 6 km (C and D) and above 2 km (E and F).



References and Notes

- H. Graf, *Science* **303**, 1309 (2004).
- S. Twomey, *Atmos. Environ.* **8**, 1251 (1974).
- B. A. Albrecht, *Science* **245**, 1227 (1989).
- Intergovernmental Panel on Climate Change, *Climate Change 2001: The Scientific Basis*, J. T. Houghton *et al.*, Eds. (Cambridge Univ. Press, Cambridge, 2001).
- G. L. Stephens, S.-C. Tsay, P. W. Stackhouse Jr., P. J. Flatau, *J. Atmos. Sci.* **47**, 1742 (1990).
- V. Ramanathan, W. Collins, *Nature* **351**, 27 (1991).
- U. Lohmann, E. Roeckner, *J. Geophys. Res.* **100**, 16305 (1995).
- R. S. Lindzen, M.-D. Chou, A. Y. Hou, *Bull. Am. Meteorol. Soc.* **82**, 417 (2001).
- A. D. Del Genio, W. Kovari, *J. Clim.* **15**, 2597 (2002).
- B. A. Wielicki *et al.*, *Science* **295**, 841 (2002).
- A. P. Khain, D. Rosenfeld, A. Pokrovsky, *Geophys. Res. Lett.* **28**, 3887 (2001).
- V. T. J. Phillips, T. W. Choullarton, A. M. Blyth, J. Latham, *Q. J. R. Meteorol. Soc.* **128**, 951 (2002).
- S. C. Sherwood, *J. Clim.* **15**, 1051 (2002).
- M. O. Andreae *et al.*, *Science* **303**, 1337 (2004).
- R. A. Houze Jr., *Cloud Dynamics* (Academic Press, San Diego, CA, 1977).
- Materials and methods are available as supporting material on Science Online.
- D. E. Stevens, A. S. Ackerman, C. S. Bretherton, *J. Atmos. Sci.* **59**, 3285 (2002).
- E. J. Jensen, L. Pfister, A. S. Ackerman, O. B. Toon, A. Tabazadeh, *J. Geophys. Res.* **106**, 17237 (2001).
- A. S. Ackerman, O. B. Toon, D. E. Stevens, J. A. Coakley Jr., *Geophys. Res. Lett.* **30**, 10.1029/2002GL016634 (2003).

REPORTS

20. M. Xue, D.-H. Wang, J.-D. Gao, K. Brewster, K. K. Droegemeier, *Meteorol. Atmos. Phys.* **82**, 139 (2003).
21. H. R. Pruppacher, J. D. Klett, *Microphysics of Clouds and Precipitation* (Kluwer Academic Publishers, Dordrecht, Netherlands, 1997).
22. W. D. Hall, *J. Atmos. Sci.* **37**, 2486 (1980).
23. M. Z. Jacobson, R. P. Turco, E. J. Jensen, O. B. Toon, *Atmos. Environ.* **28A**, 1327 (1994).
24. R. List, N. R. Donaldson, R. E. Stewart, *J. Atmos. Sci.* **44**, 362 (1987).
25. H. P. Meyers, P. J. DeMott, W. R. Cotton, *J. Appl. Meteorol.* **31**, 708 (1992).
26. E. J. Zipser, in *Cloud Systems, Hurricanes, and the Tropical Rainfall Measuring Mission (TRMM)*, W.-K. Tao, R. Adler, Eds., vol. 29 of *Meteorological Monographs* (American Meteorological Society, Boston, MA, 2003), chap. 5.
27. R. S. Scorer, *Environmental Aerodynamics* (Wiley, New York, 1977).
28. D. J. Musil, A. J. Heymsfield, P. L. Smith, *J. Climate Appl. Meteorol.* **25**, 1037 (1986).
29. T. J. Garrett, H. Gerber, D. G. Baumgardner, C. H. Twohy, E. M. Weinstock, *Geophys. Res. Lett.* **30**, 10.1029/2003GL018153 (2003).
30. S. C. Sherwood, *Science* **295**, 1272 (2002).
31. P. K. Wang, *J. Geophys. Res.* **108**, 10.1029/2002JD002581 (2003).
32. R. G. Knollenberg, K. Kelly, J. C. Wilson, *J. Geophys. Res.* **98**, 8639 (1993).
33. J. Lelieveld *et al.*, *Science* **298**, 794 (2002).
34. A. D. Clarke, V. N. Kapustin, *J. Atmos. Sci.* **59**, 363 (2002).
35. H. B. Singh *et al.*, *J. Geophys. Res.* **107**, 10.1029/2001JD000486 (2002).
36. We thank J. Smith and B. Toon for raising questions about the relative importance of boundary-layer and free tropospheric aerosols, E. Zipser for sharing his experience with tropical convection, W. McKie for

keeping our more than 70 computer processors running in concert from Key West to Mountain View, and D. Anderson for leading CRYSTAL-FACE with long-term vision. All of the data collection and modeling associated with this work was coordinated by NASA's Earth Science Enterprise through NRA-01-OES-02, with funding and support provided by NASA, NOAA, NSF, the U.S. Department of Energy (DOE), the Office of Naval Research, and the United States Weather Research Program. We gratefully acknowledge additional computing support provided by DOE's High Performance Computing Facility.

Supporting Online Material

www.sciencemag.org/cgi/content/full/304/5671/718/DC1

Materials and Methods
References

19 December 2003; accepted 24 March 2004

Missing OH Reactivity in a Forest: Evidence for Unknown Reactive Biogenic VOCs

Piero Di Carlo,^{1,2*} William H. Brune,¹ Monica Martinez,^{1†}
Hartwig Harder,^{1‡} Robert Leshner,¹ Xinrong Ren,¹
Troy Thornberry,^{3,4‡} Mary Anne Carroll,^{3,4} Valerie Young,⁵
Paul B. Shepson,⁶ Daniel Riemer,⁷ Eric Apel,⁸ Colleen Campbell⁴

Forest emissions of biogenic volatile organic compounds (BVOCs), such as isoprene and other terpenes, play a role in the production of tropospheric ozone and aerosols. In a northern Michigan forest, the direct measurement of total OH reactivity, which is the inverse of the OH lifetime, was significantly greater than expected. The difference between measured and expected OH reactivity, called the missing OH reactivity, increased with temperature, as did emission rates for terpenes and other BVOCs. These measurements are consistent with the hypothesis that unknown reactive BVOCs, perhaps terpenes, provide the missing OH reactivity.

Emissions of natural or biogenic volatile organic compounds (BVOCs) from vegetation are estimated to exceed all emissions of anthropogenic volatile organic compounds on the global scale and are roughly equal to global emissions of methane (1, 2). They can have a dominant influence on the atmospheric chemistry of forests, rural areas, and some

cities (3). The type of vegetation, solar radiation, and temperature determine the emission rates and species of BVOCs (4).

BVOCs react with hydroxyl radicals (OH) and nitrate radicals (NO₃), and olefinic BVOCs also react with ozone (O₃). A chemical's reaction frequency with OH is the product of its rate-coefficient for reaction with OH times its concentration. The sum of the reaction frequencies with OH for all chemicals is called the OH reactivity, which is the inverse of the OH lifetime. The calculated OH reactivity for the BVOCs that are emitted annually in North America has contributions from isoprene (51%), terpenes (31%), oxygenated BVOCs such as alcohols (16%), and all other known BVOCs (2%) (4). Oxidation of BVOCs by OH in the presence of nitric oxide (NO) is the principal source of tropospheric O₃ (5, 6). At the same time, O₃ reacts with olefinic BVOCs, such as isoprene and terpenes, to produce OH (7–9). Oxidation of some BVOCs by OH, O₃, and NO₃ produces organic acids that have low

vapor pressures and thus condense to form secondary organic aerosols (10–14). Understanding the OH reactivity is key to assessing the importance of these biogenic emissions to O₃ and aerosol formation.

Recent indirect evidence indicates that forests emit unknown, reactive BVOCs, perhaps terpenes (12, 15, 16). In a Michigan forest in 1998, Faloon *et al.* observed unexpected nocturnal OH, late-evening new particle formation, and a dependence of nocturnal OH and hydroperoxyl radicals (HO₂) on O₃ (15). In a Sierra Nevada forest in 2000 and 2001, significant chemical loss of O₃ was observed (16). Finally, in the boreal Hyytiälä forest (in Finland) in 2000, new particle formation of biogenic origin was observed; ancillary measurements suggest that the particles were produced from oxidation of terpenes (12). We show that forests emit reactive, unmeasured BVOCs with properties similar to those of terpenes.

This evidence comes from the direct measurement of OH reactivity. Measurements were made from 5 July to 3 August 2000, during the Program for Research on Oxidants: Photochemistry, Emissions and Transport (PROPHET 2000) intensive campaign. The site was at the University of Michigan Biological Station (45°30'N, 84°42'W) in the Great Lakes Region in northern Michigan (17). Measurements were made 2 m below the top of a 31-m tall tower, ~10 m above the canopy height. The site is in a mixed, transition forest that consists of northern hardwood, aspen, and white pine. During this period, the site experienced both clean Canadian air from the north and polluted air from cities to the south, such as Chicago and Detroit.

Direct atmospheric measurements of total OH reactivity were made with an instrument called the Total OH Loss-rate Measurement (TOHLM) (18, 19). The TOHLM method is analogous to the discharge-flow technique used in laboratory kinetics studies (20, 21). OH is generated at mixing ratios of a few parts per trillion by volume

¹Department of Meteorology, Pennsylvania State University, University Park, PA 16802, USA. ²CETEMPS–Dipartimento di Fisica, Università di L'Aquila, 67010 Coppito, L'Aquila, Italy. ³Department of Atmospheric, Oceanic, and Space Sciences, ⁴Department of Chemistry, University of Michigan, Ann Arbor, MI 48109, USA. ⁵Department of Chemical Engineering, Ohio University, Athens, OH 45701, USA. ⁶Department of Chemistry, Purdue University, West Lafayette, IN 47301, USA. ⁷Rosenstiel School of Marine and Atmospheric Science, University of Miami, Miami, FL 33124, USA. ⁸National Center for Atmospheric Research, Boulder, CO 80305, USA.

*To whom correspondence should be addressed. E-mail: piero.dicarlo@aquila.infn.it

†Present address: Max-Planck-Institut für Chemie, D-55128 Mainz, Germany.

‡Present address: National Oceanic and Atmospheric Administration, Aeronomy Lab, Boulder, CO, USA